JOURNAL OF BIOLOGICAL REGULATORS & HOMEOSTATIC AGENTS

Volume 33, No. 5, September - October, 2019

CONTENTS

JOURNAL OF BIOLOGICAL REGULATORS & HOMEOSTATIC AGENTS Vol. 33, no. 5, 1315-1320 (2019)

EDITORIAL

USE OF CLODRONATE IN THE MANAGEMENT OF OSTEOARTHRITIS: AN UPDATE

G. SAVIOLA[1], L. ABDI-ALI[1], L. COMINI[2] and L.G. DALLE-CARBONARE[3]

[1]Rehabilitative Rheumatology Unit of the Institute of Castel Goffredo, Maugeri Clinical Scientific Institutes IRCCS, Mantova, Italy; [2]Health Directorate of the Institute of Lumezzane, Maugeri Clinical Scientific Institutes IRCCS, Brescia, Italy; [3]Department of Medicine, university of Verona, Verona, Italy

Received February 8, 2019 – Accepted June 3, 2019-06-03

Osteoarthritis (OA) is a chronic rheumatic disease characterized by joint cartilage wear and loss of normal function. Clodronate (CLO) is a first-generation non-nitrogen-containing bisphosphonate that exerts anti-inflammatory and analgesic and modulatory effects on bone and cartilage metabolism. To date, few clinical studies have evaluated the effect of CLO in OA. Current evidence suggests that CLO may represent a new type of analgesic drug as it reduces pain in bone diseases characterized by edema such as Complex Regional Pain Syndrone type-1 and vertebral fractures. Thanks to its anti-inflammatory and analgesic effects, CLO has been shown to afford benefit in knee OA, erosive OA of the hand, painful knee hip prosthesis and veterinary practice. Transforming growth factor β1 has also been found to play an important role in the pathogenesis of OA. The present review article examines recent evidence on the potential use of CLO in the treatment of OA.

Osteoarthritis (OA) is a slow progressive disabling and painful disease affecting whole joints, with inflammation involving the synovia, tendons and soft tissues. However, the pathogenesis of OA is still not completely understood, but in the past twenty years the role of subchondral bone has been shown to be crucial. Indeed, there is a functional link between articular cartilage and subchondral bone, which provides mechanical support during joint movements and is able to adapt itself to different load changes. Moreover, cartilage, subchondral bone and the nearest soft tissues form a functional and biochemical unit where cartilage and bone can communicate over the calcified tissue barrier.

Magnetic resonance imaging has demonstrated that early changes in subchondral bone (increased bone turnover, subarticular osteoporosis, microfractures and microcracks) can precede OA lesions and that subchondral bone loss is correlated with pain and subsequent cartilage loss (1, 2).

Few treatment options are currently available that can alter the course of OA. Current treatment guidelines include pain control with oral or topical analgesic drugs (e.g. NSAIDs, opioids, capsaicin) accompanied by physical therapies to maintain function. Bisphosphonates (BPs) are anti-resorptive agents (currently used in the treatment of osteoporosis). BPs have emerged as a potentially attractive therapeutic option to modulate bone remodeling in OA and could become a disease-modifying therapy (3). Meta-analyses studies and clinical trials examining the role of BPs in OA have shown mixed results, possibly due to the heterogeneous patient populations and different

Key words: clodronate; osteoarthritis; bisphosphonates; cartilage oligomeric matrix protein; COMP; TGF-β1; nanoparticle-embedded clodronate; SOX9

Corresponding Author:
Gianantonio Saviola, MD
Rheumatology and Rehabilitation Unit,
Maugeri Clinical Scientific Institutes, IRCCS of Castel Goffredo,
Via Ospedale 36, 46042, Castel Goffredo,
Mantua, ItalyTel.: +39 037677471
e-mail: gianantonio.saviola@icsmaugeri.it

0393-974X (2019)

treatment regimens of BPs used (3). The present review examines the evidence supporting the potential use of the bisphosphonate clodronate in the treatment of osteoarthritis.

Rationale for the use of bisphosphonates in osteoarthritis

The role of the subchondral bone in the pathogenesis of OA was the basis for the rationale for the use of BPs in the treatment of OA (2). BPs are the most important class of antiresorptive drugs commonly used to treat osteoporosis, complex regional pain syndrome (CRPS), bone metastasis, osteogenesis imperfecta and bone Paget's disease. BPs are chemically stable derivates of inorganic pyrophosphate with a very high affinity for bone mineral because they bind to hydroxyapatite crystals. BPs are incorporated into sites of bone remodelling where skeletal turnover is accelerated. Compounds not bound to the skeleton are rapidly cleared from the circulation via renal elimination. The most important characteristics of BPs are the ability to: i) inhibit calcifications, ii) inhibit osteoclasts and macrophages, iii) suppress bone resorption (4).

The most recognized side effects of BPs are i) osteonecrosis of the jaw, which is common during treatment with high intravenous doses of zoledronate or pamidronate for bone metastasis, in patients with poor oral hygiene or in patients with osteomalacia; and ii) atypical femural fracture, a rare side effect, described over the course of prolonged treatment (over 5 years) with oral BPs, due to severe suppression of bone turnover.

BPs can be divided into two groups with different mechanisms of action. Nitrogen containing BPs (alendronate, risedronate, zoledronate, pamidronate, neridronate) are the second generation of BPs. They reduce bone resorption and cause apoptosis of osteoclasts by the blockade of the mevalonate pathway, which induces the accumulation of intermediates able to activate circulating cytokines with consequent inflammatory effects. Non-nitrogen containing BPs (etidronate, clodronate) belong to the first generation of BPs. They are intracellularly metabolized into an analog of ATP (appCCl(2)p), which inhibits mithocondrial oxygen consumption and-differently from amino-BPs- they are recognised to exert anti-inflammatory effects (5).

Anti-inflammatory effects of clodronate

CLO has been shown to be effective in macrophage activation and the reduction of the inflammatory cytokines (IL-1β, IL-6, TNF-α), nitric oxide, cyclooxygenase 2 and prostaglandin E. CLO is also capable of inhibiting matrix metalloproteinases, a class of protease enzymes that are calcium-dependent zinc containing endopeptidases,through its ability to chelate zinc. In a rat model of adjuvant arthritis, CLO was able to reduce the number of swollen joints to the same extent as indomethacin (5). Intra-articular CLO containing liposomes was used in 10 patients affected by rheumatoid arthritis about to undergo knee replacement. CLO was administered 7 days before surgery. After surgery, macrophage depletion and decreased expression of adhesion molecules in the synovia were observed (6).

Analgesic effects of clodronate

CLO can also exert analgesic effects in bone diseases charecterized by edema as CRPS-1 syndrome, avascular osteonecrosis and vertebral fractures.

There are also pre-clinical data showing that intravenous CLO has a peripheral prolonged (up to 14 days) anti-nociceptive activity greater than that observed for acetylsalicilic acid (1). The analgesic effect of CLO in mice was also studied by Shima and colleagues (7). They demonstrated that CLO may enter neurons inhibiting SLC17-mediated transport of glutamate and/or ATP, thereby producing analgesic effects. The Authors concluded that CLO and etidronate may be candidates for a new type of analgesic drug (7). Moreover, CLO is a potent and selective inhibitor of vesicular ATP release, due to its inhibition of purinergic chemical transmission. In vivo, CLO is more effective than other therapeutic agents in attenuating neuropathic and inflammatory pain in mice, without affecting basal nociception (8).

Effect of clodronate in osteoarthritis

CLO is effective in reducing pain with a consequent improvement in functional measures in

erosive osteoarthritis of the hand (EOA) a subset of hand osteoarthritis. EOA may be the sequela of the severe development of non-erosive OA (9). In 2000, twenty-nine patients affected by EOA were successfully treated with intravenous CLO at the daily dose of 300 mg over a course of 7 days every 3 months resulting in a highly significant reduction in pain ($p=0.0001$) and number of tender joints ($p=0.00011$) (9). The dosing schedule was based on our previous experience showing that the efficacy of CLO persists for approximately 3 months. In 2012, twenty-four patients affected by EOA were treated with CLO over a period of 24-months. An initial high dose of intravenous CLO (300 mg/day for 7 days) followed by a maintenance intramuscular dose of 100 mg/day for 14 days every 3 months was administered. The following measures were significantly reduced: pain ($p<0.001$), Dreiser's score ($p=0.012$), number of tender joint ($p=0.011$) with concomitant improvement in strength of right hand ($p=0.04$), strength of left hand ($p=0.016$), physician's global assessment ($p<0.001$), and patient's global assessment ($p=0.021$). We further evaluated the effect of intramuscular CLO in EOA (5). Forty outpatients were divided into two groups: the control group consisted of 16 patients that continued standard treatment with anti-inflammatory or analgesic drugs; the second group consisted of 24 patients, who continued the previous treatment with the addition of intramuscular CLO, administered as follows: 200 mg for ten days (as initial high dose) dose followed after 3 and 6 months by 200 mg for 6 days as mainteinance dose. Our study revealed no significant changes in all parameters in the control group, while in the group treated with CLO consumption of anti-inflammatory or analgesic drugs ($p<0.0001$), pain ($p<0.0001$), number of tender joints ($p=0.0097$), number of swollen joints ($p=0.0251$), Dreiser score ($p=0.019$), and patient's and physician's global assessment of disease activity (both $p<0.001$) were significantly decreased.The functional improvement was also observed by an increase in the strength of the right ($p=0.047$) and left hand (+38%, p=ns). At 6 months, serum COMP (Cartilage Oligomeric Matrix Protein) also significantly decreased ($p<0.0029$) (5). In an earlier study, low-dose intra-articular CLO was shown to be as effective as hyaluronic acid in knee OA (10). CLO is able to induce an anabolic effect on articular chondrocytes, which results in 90% increase in extracellular matrix accumulation (11).

Recently, 23 females, affected by spondyloarthritis were treated with intramuscular CLO 200 mg weekly. CLO was able to upregulate SOX-9 gene, which encodes for the transcription factor responsible for mesenchymal chondrogenic commitment. This result supports the hypothesis of a role of CLO in preventing the degenerative process. CLO also reduced osteoarticular pain and improved mental and physical performance in these patients. In addition, nanoparticle-embedded CLO in an in vitro model of chondrogenic differentiation was also evaluated. This new formulation stimulated SOX-9 expression more efficaciously than CLO alone, suggesting the possibility to use nanoparticle-technology to optimize the efficacy of CLO to counteract the degenerative process (11).

Use of clodronate in painful knee and hip prosthesis

Evidence suggests that the risk of failure of the prosthesis is linked to the patient's pre-existing osteoporosis or osteopenia. In an observational retrospective controlled study with a follow-up period of 8 years it was shown that patients with lower bone mass have a significantly higher risk of failure. The study involved 85 female patients who underwent primary knee replacement, divided into two groups. The first group included 42 patients who had undergone a revision of knee prosthesis for aseptic loosening and the second group included 43 age-matched patients who, in the same year, underwent primary knee replacement without aseptic loosening ensuing. The evaluation of stiffness index with Achilles-QUS system showed that in the first group 20/42 patients (47.6%) had a stiffness index T-score below -2.5, while in the second group osteoporosis was present in 14/43 (32.5%) ($p=0.015$) (12). In addition, an association between BP use and implant survival after total primary arthroplasty of the knee or hip has been documented in two retrospective cohort studies.

The first study included 18,726 cases of total arthroplasty of the knee and 23,269 of the hip.

After five years, the rate of arthroplasty revision was significantly lower (0.93% vs. 1.96%) and the implant survival was significantly longer in 1,912 patients, who were identified as BPs users (13). The second paper included 95,392 patients from the Danish Nationwide Registries with a primary total joint replacement. The risk of revision surgery was lower (-59%) in bisphosphonate users (14). Given that periprosthetic bone loss is the most common complication of arthroplasty, another paper compared oral CLO, administered from 3 weeks pre-surgery until 6 months post-surgery, with placebo, showing significantly less prosthetic migration in the CLO group vs. placebo after 12 months ($p=0.01$). After 5 years, the prosthetic migration was still reduced in the CLO group (-25%). Moreover, intramuscular CLO, administered after surgery, for 12 months at a weekly dose of 100 mg, was able to reduce bone periprosthetic loss ($p<0.05$) in patients treated with total uncemented hip arthroplasty (15).

Clodronate in veterinary practice

There is a growing interest among veterinary practictioners on the use of clodronate, following the publication of a recent randomized double blind placebo controlled study by Frevel et al. in which a single intramuscular CLO dose of 1.4 mg/kg in horses was shown to be effective in reducing clinical signs of navicular disease (16). The latter is a palmar foot degenerative syndrome involving the distal sesamoid bone, with consequent lameless. Due to different clinical conditions leading to lesions of the navicular bone somewhat similar to human OA. 146 horses were divided into two groups. The first group consisted of 111 horses treated with CLO, while the second group consisted of 35 horses treated with placebo. At day 56, using the lameless scale, 75% of the horses in treatment with CLO had an improvement, with only 3% of those in the placebo group. At day 180, a positive trend was still detectable in 65% of the horses in CLO group. Most of them had an improvement by 2 lameless grade (16). Recently Michell et al. studied twelve equestrian team competition horses affected by forelimb lameless (17). In a blind manner six out of them were treated with a single dose of CLO (1.4 mg/kg), while the other six horses were treated with placebo. To detect CTX-I and osteocalcin, blood samples were weekly examinated for 8 weeks before and after CLO administration. As expected, horses treated with CLO had a significant reduction in forelimb lameless ($p=0.01$) but there was no difference in bone turnover markers between placebo or CLO treated horses (17). These findings complement and reinforce those observed in OA patients and provide further insight into other potential mechanisms by which CLO may elicit ots effects.

Potential mechanisms of action of CLO

The peculiar mechanism of action is probably the most important characteristic of CLO, which is the BP with the lowest affinity for bone crystals. Consequently, osteonecrosis of the jaw and atypical femoral fracture are- as expected- very rare during the course of treatment with CLO, even if in Italy (until 2006) intramuscular CLO was the most used drug for osteoporosis, being the pain in the injection site the most common side effect. Consequently, CLO can be used in the treatment of osteoradionecrosis of the jaw caused by radiotherapy for neck cancer to avoid orthodontic tooth movement and may prevent the side effects related to nitrogen containing BPs (7).

OA was for a long time considered as a primary disease of the hyaline cartilage, but in the past two decades the role of subchondral bone has been shown to be crucial. This is the rationale for the choice of BPs in the treatment of OA. CLO has emerged as a promising candidate because of its potent anti-inflammatory and analgesic activity. In humans, CLO has been shown to be effective on pain in knee osteoarthritis (10) and in EOA where it was demonstrated that CLO can reduce serum COMP (5).

COMP is considered to be a reliable biomarker of activity and severity in OA. In particular, in the Johnston County Osteoarthritis Project, 663 patients with hand OA were recruited. Hand symptoms were assessed by Australian-Canadian Hand Osteoarthritis Index (AUS.CAN). Higher AUS. CAN scores were independently associated with higher levels of serum COMP ($p<0.003$).

Moreover, COMP is correlated with the age and severity of synovitis in knee OA, with pre-

radigraphic knee and hip OA and with radiographic progression of knee OA (18).

The role of Transforming Growth Factor β1 (TGF–β1) in the pathogenesis of osteoarthritis has gained attention in recent years. TGF-β 1 is essential for maintenance of articular cartilage metabolic homeostasis and structural integrity has also been found to play an important role in the pathogenesis of OA (19). The association between TGF-β1 and OA severity has also been reported for human hip OA and increased levels of TGF-β1 mRNA and TGF-β3 subtypes have been detected in osteoblasts in subchondral bone from knee OA (20). TGF-β1 has been found to be increased in human OA subchondral bone. The role of TGF-β1 in subchondral bone has also been studied in mice: after anterior cruciate ligament transection TGF-β1 was activated in subchondral bone with evidence of marked changes within 7 days. On the contrary, the inhibition of TGF-β1 has been shown to reduce cartilage degeneration and systemic neutralisation of TGF-β1 relieved the disease in a rodent model of OA.

Finally, CLO in spondyloarthritis patients has been shown to upregulate the SOX-9 gene, encoding for the transcription factor responsible for mesenchymal chondrogenic commitment (11). Nanoparticle-embedded CLO was observed to stimulate SOX-9 expression more effectively than CLO alone, suggesting the possibility to use nanoparticle-technology to optimize the efficacy of CLO to counteract degenerative process.

CONCLUSION

Compared to other rheumatic diseases, there are few treatment options available that can alter the course of OA. BPs have emerged as a potentially attractive therapeutic option to modulate bone remodeling in OA. Findings from recent studies suggest that CLO is not only a symptomatic drug but could also play a role as a disease-modifying drug. Moreover CLO can be useful in the rehabilitation of painful knee or hip prosthesis and generally in painful OA joints without the common side effects normally associated with non-steroideal anti inflammatory drugs.

REFERENCES

1. Bonabello A, Galmozzi MR, Canaparo R, Serpe L, Zara GP. Long-term analgesic effect of clodronate in rodents. Bone 2003; 33:567-74.
2. Funck-Brentano T, Cohen-Solal M. Subchondral bone and osteoarthritis. Curr Opin Rheumatol 2015; 27:420-26.
3. Davis AJ, Smith TO, Hing CB, Sofat N. Are bisphosphonates effective in the treatment of osteoarthritis pain? A meta-analysis and systematic review. PLoS ONE 2013; 8:e72714.
4. Xing RL, Zhao LR, Wang PM. Bisphosphonates therapy for osteoarthritis: a meta-analysis of randomized controlled trials. Springerplus 2016; 5:1704.
5. Saviola G, Abdi-Ali L, Povino MR, Campostrini L, Sacco S, Carbonare LD. Intramuscular clodronate in erosive osteoarthritis of the hand is effective on pain and reduces serum COMP: a randomized pilot trial-The ER.O.D.E. study (ERosive Osteoarthritis and Disodium-clodronate Evaluation). Clin Rheumatol 2017; 36:2343-50.
6. Barrera P, Blom A, van Lent PL, et al. Synovial macrophage depletion with clodronate-containing liposomes in rheumatoid arthritis. Arthritis Rheum 2000; 43:1951-59.
7. Shima K, Nemoto W, Tsuchiya M, et al. The bisphosphonates clodronate and etidronate exert analgesic effects by acting on glutamate- and/or ATP-related pain transmission pathways. Biol Pharm Bull 2016; 39:770-7.
8. Kato Y, Hiasa M, Ichikawa R, et al. Identification of a vesicular ATP release inhibitor for the treatment of neuropathic and inflammatory pain. Proc Natl Acad Sci USA 2017; 114:E6297-E305.
9. Saviola G, Abdi-Ali L, Campostrini L, et al. Clodronate and hydroxychloroquine in erosive osteoarthritis: a 24-month open randomized pilot study. Mod Rheumatol 2012; 22:256-63.
10. Rossini M, Viapiana O, Ramonda R, et al. Intra-articular clodronate for the treatment of knee osteoarthritis: dose ranging study vs hyaluronic acid. Rheumatology (Oxford) 2009; 48:773-78.
11. Valenti MT, Mottes M, Biotti A, et al. Clodronate as a therapeutic strategy against osteoarthritis. Int J Mol

Sci 2017; 18:2696.
12. Saviola G, Zaghini I, Abdi-Ali L, Ferlini G, Sacco S, Rossini M. Densitometric evaluation might prevent failure of knee arthroplasty for aseptic loosening. Saudi Med j 2016;37(2):212-14.
13. Prieto-Alhambra D, Javaid MK, Judge A, et al. Association between bisphosphonate use and implant survival after primary total arthroplasty of the knee or hip: population based retrospective cohort study. BMJ 2011; 343:d7222.
14. Prieto-Alhambra D, Lalmohamed A, Abrahamsen B, et al. Oral bisphosphonate use and total knee/hip implant survival: validation of results in an external population-based cohort. Arthritis & Rheumatology (Hoboken, NJ) 2014; 66:3233-40.
15. Trevisan C, Ortolani S, Romano P, et al. Decreased periprosthetic bone loss in patients treated with clodronate: a 1-year randomized controlled study. Calcif Tissue Int 2010; 86:436-46.
16. Frevel M, King B, Kolb D. Clodronate disodium for treatment of clinical signs of navicular disease – a double-blinded placebo-controlled clinical trial. Pferdeheilkunde 2017; 33:271-9.
17. Mitchell A, Wright S, Sampson S. Clodronate improves lameness in horses without changing bone turnover markers. Equine Vet J 2018; 3:356-63.
18. Aslam I, Perjar I, Shi XA, et al. Associations between biomarkers of joint metabolism, hand osteoarthritis, and hand pain and function: the Johnston County Osteoarthritis Project. J Rheumatol 2014; 41:938-44.
19. Blaney Davidson EN, van der Kraan PM, van den Berg WB. TGF-beta and osteoarthritis. Osteoarthr Cartil 2007; 15:597-604.
20. Shen J, Li S, Chen D. TGF-β signaling and the development of osteoarthritis. Bone Res 2014; 2:14002.

JOURNAL OF BIOLOGICAL REGULATORS & HOMEOSTATIC AGENTS Vol. 33, no. 5, 1321-1326 (2019)

EDITORIAL

INTERRELATIONSHIP BETWEEN INFLAMMATORY CYTOKINES (IL-1, IL-6, IL-33, IL-37) AND ACQUIRED IMMUNITY

L. FRANZA[1,2], V. CARUSI[1,2], S. ALTAMURA[1,2], Al. CARAFFA[3], C.E. GALLENGA[4], S.K. KRITAS[5], G. RONCONI[6], P. CONTI[7] and F. PANDOLFI[1,2]

[1]Department of Internal Medicine, Fondazione Policlinico Universitario A. Gemelli IRCCS -Università Cattolica del Sacro Cuore, Roma, Italy; [2]Immunology and Allergology Department, Fondazione Policlinico Universitario A. Gemelli IRCCS -Università Cattolica del Sacro Cuore, Roma, Italy; [3]School of Pharmacy, University of Camerino, Camerino, Italy; [4]Department of Biomedical Sciences and Specialist Surgery, Section of Ophthalmology, University of Ferrara, Ferrara, Italy; [5]Department of Microbiology and Infectious Diseases, School of Veterinary Medicine, Aristotle University of Thessaloniki, Macedonia, Greece; [6]Clinica dei Pazienti del Territorio, Fondazione Policlinico Gemelli, Rome, Italy; [7]Postgraduate Medical School, University of Chieti, Chieti, Italy

Received June 30, 2019 – Accepted September 9, 2019

It is now well-known that interleukins (ILs) play a pivotal role in shaping innate immunity: inflammatory ILs are responsible for all innate aspects of immune response, from the very first vascular reactions to the chronic non-specific response to inflammation; while anti-inflammatory ILs are responsible for keeping adaptive immunity at bay. The interactions between ILs and adaptive immunity have been long considered secondary to the effects on the innate immune system, but in recent years it has appeared more clearly that IL direct interactions with adaptive immunity are extremely important both in physiologic and pathologic immune response. In the present review we analyze the role of inflammatory ILs (IL-1, IL-6, IL-33 and IL-37) on adaptive immunity and briefly discuss the possible therapeutic perspectives of IL-blockade in adaptive immunity disorders.

Inflammatory cytokines are a heterogeneous group which comprises the interleukin (IL)-1 family. The IL-1 family is made up of 11 different cytokines: IL-1α, IL-1β, IL-1Rantagonist (IL-1Ra), IL-18, IL-36Ra, IL-36α, IL-37, IL-36β, IL-36γ, IL-38 and IL-33 (1). Cytokines belonging to the IL-1 family present the same structure at the C-terminus, a β-trefoil fold made up of 12-β-strands connected by 11 loops. The pathways through which they are produced and activated are quite different from one another, ranging from nuclear expression and activation, to caspase-depending activation (2). Their functions also differ considerably, as some of these cytokines are involved in inflammatory pathways (IL-1α, IL-1β,IL-18, IL-36α,IL-36β, IL-36γ and IL-33), others have anti-inflammatory properties (IL-37) and others work as antagonists of other IL belonging to the IL-1 family (IL-1Ra and IL-36Ra). Yet, the differences in their function appear to be primarily associated to the different IL-receptors (IL-R) (3). The IL-R family is made up of 10 different receptors of which IL-1R8, IL-1R9 and IL-1R10 are anti-inflammatory pathway

Key words: inflammatory cytokines; innate immunity; IL-6; Il-37

Corresponding Author:
Prof. Franco Pandolfi,
Department of Internal Medicine,
Fondazione Policlinico Universitario A. Gemelli IRCCS
Università Cattolica del Sacro Cuore,
Roma, Italy
e-mail: franco.pandolfi@unicatt.it

0393-974X (2019)

activators, while the others work as inflammatory receptors (1).

The role of the IL-1 family has been explored particularly in the pathogenesis of auto-inflammatory diseases, as it seems that alterations of the balance between the different members of the family and the expression of IL-R are key factors in the pathogenesis of these diseases. However, the role of the IL-1 family has been studied also in other immunological diseases and disorders; for example, psoriasis, rheumatoid arthritis, gout, systemic lupus erythematosus and Crohn's disease have been specifically linked to IL-36, IL-37 and IL-38 (4), while autoimmune hepatitis has been linked to IL-1 (5). IL-36 also activates mast cells (6). Targeting members of the IL-1 family is now a common therapeutic strategy in hematologic malignancies and disorders (7) and it is being examined also in septic patients (8).

The role of the IL-1 family in human pathology has prevalently been linked to its effects on the innate immune system, promoting the activity of neutrophils, eosinophils, basophils, mast cells and natural killer cells. Yet, it appears that the IL-1 family also acts on the adaptive immune system, not only through its effects on the innate components of the system, but also directly (9).

IL-6 is another important inflammatory cytokine that is often linked to various different diseases and that may be synergic with the IL-1 family in the development of different diseases, such as macrophage activation syndrome (10) and different forms of cancer (11). It also appears to interact with the IL-1 family in the direct regulation of the adaptive immune system (12).

In this review, our main focus is to discuss the role of the IL-1 family, IL-1 and IL-33 particularly, and of IL-6 in the shaping of adaptive immunity and the possible practical consequences there could be in terms of therapies (13).

The IL-1 family in adaptive immunity: IL-1, IL-33 and IL-37

The IL-1 family plays a key role in innate immune response, sharing a similar function with Toll-like receptors (TLRs). They both stimulate the same aspecific inflammatory pathways, through cycloxigenase-2, production of cytokines and chemokines, expression of adhesion molecules and synthesis of nitric oxide. Many of these ILs present a so-called dual function, as in the case of IL-1α. The term dual-function indicates a situation in which a cytokine is expressed both as a membrane protein and as a nuclear protein, through which it promotes different pathways. The nuclear form of IL-1α is responsible for the regulation of the inflammatory response in the cell, while the membrane form promotes inflammation and interacts with interferon (IFN)-γ, allowing and promoting many of its functions. One of the key regulators of the expression of IL-1α is IL-1β, which also plays a role in determining inflammation, particularly in response to lipopolysaccharide (LPS) and IL-1α.

IL-1 is a well recognized innate immunity driver: its activity is driven by damage or pathogen-associated molecular patterns (DAMPs and PAMPs), both natural and artificial. Indeed, it has been demonstrated that the aspecific beneficial effects of vaccines are IL-1 mediated. The role of IL-1 on adaptive immunity is more complex, as it partly depends on the enhancement of innate immunity (6), but there are also other mechanisms through which it activates the adaptive system. One of the suggested mechanisms is the so called "metabolic pathway": IL-1 appears to stimulate hypoxia inducible factor 1 (HIF1), which promotes the shift from oxidative phosphorylation to aerobic glycolysis, a key factor in adaptive immunity. IL-1 can also directly stimulate the enhancement of glycolysis *vs* oxidative phosphorylation (14).

The role of IL-1 in human pathology is of great interest, particularly in the case of cancer. It has been demonstrated that IL-1 is present in tumor microenviroment, where it promotes growth and development of different tumor forms. IL-1 is fundamental in angiogenesis and it appears to act as a promoter of both colorectal and ovarian cancer. On the other hand, higher levels of IL-1 at the tumor site increase immune response to the tumor itself, with a higher number of $CD8^+$ T cells, NK cells and M1-differentiated macrophages. Nonetheless, most studies point towards the hypothesis that

IL-1 has mostly a pro-tumor activity, but local and concentrated stimulation with IL-1 at the site of tumor may have some beneficial effect (2).

IL-33 is another dual-function IL, presenting both a nuclear and a membrane form. In its nuclear form, IL-33 has been linked to an anti-inflammatory role, but as it appears to favor inflammation in rheumatoid arthritis, it is argued that its membrane form has instead inflammatory activity (15). Also in hypersensitivity diseases, such as allergies, IL-33 has an ambiguous role: indeed, it appears that its blockage, in association with the blockage of IL-17, can induce an improvement in this group of diseases (16). The different roles which IL-33 appears to play are probably secondary to the different receptors it interacts with. The bond between IL-33 and the IL-1 family orphan receptor, suppression of tumorigenicity 2 (ST2), is one of the most studied and activates a complex cascade of different events. Myeloid differentiation response protein (MyD88), IL-1R-associated kinase, TNF receptor-associated factor 6, mitogen-activated protein kinases (including JNK, p38, and ERK), and nuclear factor-kappa B (NF-κB) are only some of the different proteins and kinases which are activated and which are pivotal to different cell processes, such as the secretion of other cytokines, cell replication and survival. IL-33 can also directly interact with NF-κB, promoting among others wound healing (17).

IL-33 is capable of stimulating a Th2 type of response, especially in the gut, which is particularly rich in ST2 receptors. When it binds to ST2 on antigen presenting cells (APCs), there is an important increase in the production of type 2 immune response cytokines (IL-4, IL-5, and IL-13), which, in turn, enhance IL-33-induced type 2 innate lymphoid cell (ILC2) activation (17-18).

On the other hand, IL-33 is capable of inducing CD4+Foxp3+ regulatory T lymphocytes (TREGs), which is one of the ways through which it determines its anti-inflammatory effects. This activity is particularly evident in the gut, where IL-33 appears to be extremely active. While the activation of the Th2 pathway via IL-33 is quite straightforward, the regulatory activity of IL-33 in the gut is also influenced by the resident microbiota, which, on the other hand, is influenced by IL-33 signaling: Malik et al. have demonstrated, for instance, that IL-33-deficient mice have a different microbiota compared to wild type mice (19).

Given its intense activity in the gut, IL-33 has been studied in relation to inflammatory bowel disease (IBD) and it seems that IL-33 is linked specifically to ulcerative colitis (UC): patients with active disease have a higher level of IL-33 w compared to patients in remission, but a clear causative relationship between UC and IL-33 has not yet been established (17).

IL-37 is another member of the IL-1 family and is responsible for the modulation of IL-18 (also known as the IFN-γ inducing factor). Even though it is an inflammatory interleukin, IL-37 is responsible for an anti-inflammatory effect when it acts on the IL-18 pathway: when it binds to the IL-18R, STAT3 is activated and an inhibitory signal is started (20). Another pathway through which IL-37 exerts its immune-modulating capacity is through binding with small mother against decapentaplegic (SMAD)3, forming a complex with important nuclear regulatory capacity. Proof of the importance of this interaction has been demonstrated through inhibition of SMAD3, which resulted in IL-37's loss of immune-modulating function (21).

The modulating effects of IL-37 are particularly interesting in the context of joint and skin inflammatory conditions: in skin lesion biopsies of patients suffering from psoriasis, IL-37 levels were lower than expected. Low levels of this interleukin have been linked to an incorrect modulation of key mediators involved in murine psoriasis (e.g. IL-8, IL-6 and S100 calcium-binding protein A7-S100A7) (22).

While low levels of IL-37 have clearly been linked to an incomplete immune-modulation capacity, it seems that also very high levels of IL-37 can lead to an increase of overall inflammation. In patients suffering from rheumathoid arthritis (RA), for example, levels of IL-37 are normal in the synovium and over the normal range in peripheral blood. Such mechanism could be explained by the negative feedback mechanisms through which IL-37 appears to be regulated: when present in high concentrations IL-37 forms homodimers, which are

less effective in the blockade of the IL-18 signaling pathway. Also, it is noteworthy that IL-37 can inhibit osteoclastogenesis, resulting even more interesting in the field of future RA therapies (23).

Interestingly, both IL-33 and IL-37 have anti-inflammatory and pro-angiogenic functions, suggesting that there might be similar underlying pathways. IL-37 angiogenic efficacy has been reported to be as strong as that of VEGF (24-25).

IL-6 AND ADAPTIVE IMMUNITY

IL-6 is prevalently involved in immune reactions to infections. Its activity is deeply tied to the IL-1 family, as similar stimuli can induce their synthesis and IL-1β can also induce IL-6 production. There are different signaling pathways activated by IL-6: in the "classic" pathway IL-6 bonds with its receptor, IL-6R, which activates glycoprotein 130 (gp130) in its membrane form. This kind of signaling is typical of hepatocytes, neutrophils, monocytes, activated B cells and CD4 T cells. IL-6 can also activate gp130 through trans-signaling, activated by the bond between IL-6 and the soluble form of IL-6R (sIL-6R). This form of signaling is extremely interesting, as it allows IL-6 signaling in all those cells which do not present a membrane IL-6R.

gp130 is involved in many different signaling pathways and is activated by different factors, such as leukemia inhibitory factor (LIF), oncostatin M (OSM), ciliary neurotrophic factor (CNTF), cardiotrophin 1 (CT-1), IL-11, cardiotrophin-like cytokine factor 1 (CLCF1), IL-27 and IL-35, partly accounting for the redundancy in the functions of IL-6.

IL-6 plays a complex role in modulating immunityas it stimulates the first innate responses to a stressor, such as leukocytosis, increased blood vessel permeability and liver synthesis of acute phase proteins. As a matter of fact, the liver is extremely sensitive to the action of IL-6, as hepatocytes are among the cellular types that actually respond to classic IL-6 and they mediate the response of other organs to IL-6 signaling pathway. For example, anemia following chronic inflammation is caused by hepdicin, which is produced by the liver after IL-6 stimulation, allowing IL-6 to control indirectly erythropoiesis.

Besides its role in innate immune response, IL-6 also shapes adaptive immunity, stimulating B-lymphocytes to differentiate in plasma-cells. Also T-lymphocytes are influenced by IL-6 signaling, as they are induced to shift towards a Th17 phenotype, while TREG production is inhibited. Il-6 interferes with TGF-β, which promotes TREG differentiation, increasing the activity of its SMAD protein pathway. SMAD-I in particular can silence TGF-β. It is worth noting that IL-6, like IL-33, is extremely important in regulating immunity of the gut, but it seems to be a protective factor against IBDs. On the other hand, IL-6 may promote the development of colorectal cancer in a similar fashion to IL-1. The roles of IL-1 and IL-6 are similar also in the context of autoinflammatory diseases, but IL-6 is associated to a much vaster array of diseases, ranging from adult onset Still's disease, to depression, to myocardial infarction; different studies and case reports have reported encouraging results after blockade of IL-6 (26).

TARGETING INTERLEUKINS IN ADAPTIVE IMMUNITY DISORDERS

Blockade of ILs has worked as a therapy in different diseases. IL-6 blockade, for instance, has given positive results in different conditions, but the underlying immunologic mechanisms are not completely clear. Depression is one of the diseases in which IL-6 blockade has given encouraging results that are not yet fully understood: even though many authors report an altered inflammatory status in patients experiencing depression, the actual role of immunity is still under scrutiny. Also in heart failure and cardiovascular disease, in general, IL-6 is an interesting and apparently effective target.

Targeting ILs belonging to the IL-1 family and IL-6 began in the context of autoinflammatory diseases, but is particularly interesting and promising in the context of cancer therapy. As previously stated, IL-1 is extremely important in promoting tumor progression and growth. The use of drugs such as Anakinra, which inhibit IL-1 signaling pathway, reduce the inflammatory status induced by the tumor and correct the metabolic

alterations, possibly reducing associated symptoms such as neoplastic cachexia. Such effects are due not only to the inhibition of IL-1 expressed by the tumor, but also through the inhibition of CD14+ and CD16+ monocytes present at the tumor site. The effects on angiogenesis are also important and are enhanced by the effects of platelet blockade of IL-1 signaling. The sensitivity of platelets towards IL-1 signaling accounts for the importance of anti-IL-1 therapy, specifically IL-1β through Canakinumab, in atherosclerosis: studies conducted on patients who were at high risk of developing such condition showed that not only treated patients had a better cardiovascular health profile, but also lung cancer incidence and mortality dropped.

In the rheumatologic field, inhibition of ILs has been tested also on diseases that are not autoinflammatory, but also autoimmune, such as rheumatoid arthritis. In particular, juvenile forms benefit from blockade both of IL-1 family and IL-6. Overall, many diseases with an important inflammatory component, e.g. heart failure, diabetes, have been treated in experimental settings through IL-1 family or IL-6 blockade with interesting results. The positive effects of similar therapies obtained in such a broad spectrum of diseases is a sign of how ILs act on different aspects and components of the immune system.

CONCLUSIONS

ILs are key components of the innate immune system and determine the first stages of all immune and inflammatory reactions. However, ILs have a much broader spectrum of action, as they can interact directly and indirectly with the adaptive immune system and even with tissues and cells not belonging to the immune system. These results do not only improve our understanding of the importance of ILs specifically and the immune system in general, but also offer interesting therapeutic perspectives for a vast array of diseases.

REFERENCES

1. Dinarello CA. Interleukin-1 in the pathogenesis and treatment of inflammatory diseases. Blood 2011; 117(14):3720-32.
2. Malik A, Kanneganti T-D. Function and regulation of IL-1α in inflammatory diseases and cancer. Immunol Rev 2018; 281(1):124-37.
3. Boraschi D, Italiani P, Weil S, Martin MU. The family of the interleukin-1 receptors. Immunol Rev 2018; 281(1):197-232.
4. Hahn M, Frey S, Hueber AJ. The novel interleukin-1 cytokine family members in inflammatory diseases. Curr Opin Rheumatol 2017; 29(2):208-13.
5. Yousefi A, Najafi M, Motamed F, et al. Association of Interleukin-6 and Interleukin-1 family gene polymorphisms in autoimmune hepatitis. Ann Hepatol 2018; 17(6):1021-25.
6. Gallenga CE, Pandolfi F, Caraffa Al, et al. Interleukin-1 family cytokines and mast cells: activation and inhibition. J Biol Regul Homeost Agents 2019; 33(1):1-6.
7. de Mooij CEM, Netea MG, van der Velden WJFM, Blijlevens NMA. Targeting the interleukin-1 pathway in patients with hematological disorders. Blood 2017; 129(24):3155-64.
8. Ge Y, Huang M, Yao YM. Recent advances in the biology of IL-1 family cytokines and their potential roles in development of sepsis. Cytokine Growth Factor Rev 2019; 45:24-34.
9. Sims JE, Smith DE. The IL-1 family: regulators of immunity. Nature Rev Immunol 2010; 10:89.
10. Crayne CB, Albeituni S, Nichols KE, Cron RQ. The immunology of macrophage activation syndrome. Front Immunol 2019; 10:119.
11. Mauer J, Denson JL, Bruning JC. Versatile functions for IL-6 in metabolism and cancer. Trends Immunol 2015; 36(2):92-101.
12. Deng J, Yu XQ, Wang PH. Inflammasome activation and Th17 responses. Mol Immunol 2019; 107:142-64.
13. Iwasaki A, Medzhitov R. Control of adaptive immunity by the innate immune system. Nature Immunol 2015; 16(4):343-53.
14. Moorlag SJCFM, Röring RJ, Joosten LAB, Netea MG. The role of the interleukin-1 family in trained immunity. Immunol Rev 2018; 281(1):28-39.
15. Dinarello CA. Overview of the IL-1 family in innate inflammation and acquired immunity. Immunol Rev 2018; 281(1):8-27.

16. Gupta RK, Gupta K, Dwivedi PD. Pathophysiology of IL-33 and IL-17 in allergic disorders. Cytokine Growth Factor Rev 2017; 38:22-36.
17. Hodzic Z, Schill EM, Bolock AM, Good M. IL-33 and the intestine: The good, the bad, and the inflammatory. Cytokine 2017; 100:1-10.
18. Tettamanti, Kritas SK, Gallenga CE, et al. IL-33 mediates allergy through mast cell activation: Potential inhibitory effect of certain cytokines. J Biol Regul Homeost Agents 2018; 32(5):1061-65.
19. Malik A, Sharma D, Zhu Q, Karki R, Guy CS, Vogel P, Kanneganti TD. IL-33 regulates the IgA-microbiota axis to restrain IL-1alpha-dependent colitis and tumorigenesis. J Clin Invest 2016; 126(12):4469-81.
20. Yasuda K, Nakanishi K, Tsutsui H. Interleukin-18 in health and disease. Int J Mol Sci 2019; 20(3).
21. Boutet MA, Nerviani A, Pitzalis C. IL-36, IL-37, and IL-38 cytokines in skin and joint inflammation: a comprehensive review of their therapeutic potential. Int J Mol Sci 2019; 20(6).
22. Keermann M, Kõks S, Reimann E, Abram K, Erm T, Silm H, Kingo K. Expression of IL-36 family cytokines and IL-37 but not IL-38 is altered in psoriatic skin. J Dermatol Sci 2015; 80(2):150-52.
23. Tang R, Yi J, Yang J, Chen Y, Luo W, Dong S, Fei J. Interleukin-37 inhibits osteoclastogenesis and alleviates inflammatory bone destruction. J Cell Physiol 2019; 234(5):7645-58.
24. Yang T, Lin Q, Zhao M. IL-37 Is a novel proangiogenic factor of developmental and pathological angiogenesis. Arterioscler Thromb Vasc Biol 2015; 35(12):2638-46.
25. Castellani M. L. et al :, VEGF substance P and stress, new aspects a revisited study. J Biol Regul Homeost Agents 2010; 24(3)229-37.
26. Narazaki M, Kishimoto T. The two-faced cytokine IL-6 in host defense and diseases. Int J Mol Sci. 2018; 19(11):3528.

COOPERATION BETWEEN GALANIN AND INSULIN IN FACILITATING GLUCOSE TRANSPORTER 4 TRANSLOCATION IN ADIPOSE CELLS OF DIABETIC RATS

L.L. GUO[1], X.L. SHUN[2], B. HE[3], P.H. FANG[3], P. BO[3], Y. ZHU[3] and Z.W. ZHANG[3]

[1]Department of Physical Education, Chuzhou College, Chuzhou, Anhui, China; [2]Department of Cardiovascular and Intensive Care Unit, First People's Hospital, Yangzhou University, Yangzhou, China; [3]Department of Endocrinology, Clinical Medical College, Yangzhou University, Yangzhou, Jiangsu, China

Received February 5, 2019 – Accepted May 28, 2019

The glucose transporter 4 (GLUT4) translocation is a vital link of insulin-induced glucose uptake in adipose tissue and skeletal muscle. It is an important topic in anti-diabetic research to explore novel agents to facilitate the role of insulin. The aim of this study was to verify the hypothesis that neuropeptide galanin may enhance insulin-induced GLUT4 translocation to increase glucose uptake in adipose tissue of type 2 diabetic models. Insulin and/or galanin were injected respectively or cooperatively into type 2 diabetic rats once a day for fifteen days. The results showed that administration of galanin significantly enhanced insulin-induced GLUT4 and vesicle-associated membrane protein 2 (VAMP2) translocation, Akt phosphorylation and glucose uptake, but not GLUT4 mRNA and protein expression levels in adipose cells. The beneficial roles of galanin on insulin-induced events may be blocked by MK-2206, an Akt inhibitor, indicating that the Akt phosphorylation is essential for promoting impact of galanin on the insulin-induced events. These results suggest that galanin may benefit insulin-induced GLUT4 and VAMP2 translocation, and subsequent glucose uptake via the activated Akt-VAMP2-GLUT4 pathway in adipose cells. These findings deepen our understanding of the anti-diabetic effect of galanin and its mechanism.

It is well known that insulin is an important hormone to increase translocation of glucose transporter 4 (GLUT4) onto the plasma membrane of cells of skeletal muscle, adipose and cardiac tissues (1, 2). GLUT4 is an insulin-regulated isoform of transporters that catalyzes glucose uptake through a facilitative diffusion mechanism (3). In the basal state a majority of GLUT4 is retained in microsomes. After insulin stimulation, exocytosis of GLUT4 vesicle is markedly increased and endocytosis of the vesicle is reduced, resulting in more GLUT4 protein onto the cell surface membrane to regulate glucose uptake (4). The GLUT4 translocation is a rate-limiting step of glucose uptake (5, 6). Increased GLUT4 translocation to plasma membranes is closely associated with expedited sugar influx into adipocytes and myocytes, which directly accounts for the insulin-stimulated glucose uptake (7). After removal of insulin stimuli, the rates of exocytosis and endocytosis return to the basal states, then endocytosis of GLUT4 exceeds exocytosis, resulting in the internalization and repopulation of the GLUT4 to intracellular storage compartments, waiting for next round of insulin stimulation (8). Only at the cell surface can GLUT4 transport glucose into cells. The glucose clearance

Key words: insulin; galanin; Akt; GLUT4; VAMP2

Corresponding Author:
Dr Zhenwen Zhang,
Department of Endocrinology, Clinical Medical College,
Yangzhou University, Nantong street #98,
Yangzhou, Jiangsu, China, 225001
Tel.: +86 514 87825993 - Fax: +86 0514 87341733
e-mail: shimyyz@126.com

0393-974X (2019)

activity is directly proportional to the GLUT4 protein concentration at plasma membranes (9). An impairment of the insulin action results in hyperglycemia, which is a main hallmark of type 2 diabetes mellitus (T2DM). Recent research demonstrated that besides insulin, other hormones may regulate GLUT4 translocation too.

Neuropeptide galanin, a 29/30 amino-acid peptide, distributes widely throughout nervous and digestive system as well as other tissues. An injection of galanin into the paraventricular nucleus significantly increases food intake and body weight of subjects, which may be blocked by galanin antagonists (10). The galanin knockout mice showed impaired glucose disposal due to reduced insulin response and insulin-independent glucose elimination (11). Our and other studies indicated that central and peripheral administration of galanin increased GLUT4 translocation from intracellular membrane compartments to cell surfaces of myocytes and adipocytes, resulting in decrease in blood glucose levels in T2DM rats (2, 9, 12).

Aforementioned, administration of either insulin or galanin can benefit glucose uptake through increase in GLUT4 translocation in subjects. However, it is unknown whether galanin may promote the effect of insulin on glucose uptake in adipose cells. The purpose of current study was to investigate if galanin may benefit insulin-induced GLUT4 and vesicle-associated membrane protein 2 (VAMP2) translocation to promote glucose uptake in adipose cells of T2DM rats.

MATERIALS AND METHODS

Animal models and grouping

Eighty-two male Wistar rats (150±10 g) were obtained from the Animal Center of Yangzhou University. The rats were housed in a climate-controlled environment (22±2°C at 50% relative humidity) with 12 h light/dark cycles, fed with a high-fat diet (59% fat, 21% protein and 20% carbohydrate) and water ad libitum. Eight weeks later, the rats were intraperitoneally treated with 30 mg/kg streptozocin (2). After another four weeks the animals with fasting blood glucose levels over 11.1 mmol/L (64 rats) were used as T2DM models.

The 64 model rats were randomly divided into eight groups of 8 each: diabetic control group, MK-2206 (Santa Cruz Biotechnology Inc, USA) group, insulin (Ganli Pharmaceutical Co, Beijin, China) group, galanin (Sigma-Aldrich Inc, USA) group, insulin + galanin group, insulin + MK-2206 group, galanin + MK-2206 group and insulin + galanin + MK-2206 group. In addition, a healthy control group was included (n = 8). The insulin group, galanin group and MK-2206 group were administrated insulin glargine (2 U/kg, s.c.) , galanin (1 nmol/kg, i.v.) and MK-2206 (300 μg/kg, i.v.), respectively. The insulin + galanin group, insulin + MK-2206 group, galanin + MK-2206 group and insulin + galanin + MK-2206 group were injected the corresponding agents in combination. Both control groups were injected with the vehicle. The injection was conducted between 9:00-10:00 once a day successively for fifteen days. After the last injection all animals were intraperitoneally treated with 250 mg/kg ^{3}H-2DG (Perkin Elmer, Boston, MA, USA). At 30 min after the injection, the animals were sacrificed by an overdose of nembutal (200 mg/kg). Therewith, the epididymal fat pads were rapidly collected and stored at –80°C until further analysis. Animals were treated in accordance with the Guide for the Care and Use of Laboratory Animals and this experiment was performed with the specific acceptance of the Animal Studies Committee of Yangzhou University.

Fractionation of plasma membrane and ^{3}H-2DG uptake measurement

A differential centrifugation procedure was used to isolate plasma membrane proteins from adipose tissues, as described previously (13). Briefly, fat pads were washed, minced and homogenized in ice-cold homogenization buffer (2.5 mmol/l Tris–HCl, 2 mmol/l EDTA, 10 μg/ml leupeptin, 10 μg/ml aprotinin, 100 μmol/l phenylmethylsulfonyl fluoride and 250 mmol/l sucrose, pH 7.4). The homogenate was centrifuged at 13,000 g for 20 min at 4°C. Part of the supernatant was used for measurement of ^{3}H-2DG uptake with a liquid scintillation counting (Tri-Carb 2000, Packard Instrument Co.). The remains were centrifuged for 60 min at 31,000g to yield intracellular membranes. The pellet from the first spin was layered over a sucrose cushion and centrifuged for 60 min at 75,000 g. The pellet was removed and spun for 20 min at 39,000 g to yield the plasma membranes.

Total RNA extraction and real-time PCR

The total RNA was isolated from 100 mg of the adipose

tissue using Trizol Reagent according to the manufacturer's protocol. cDNA was obtained by M-MLV reverse transcriptase (Invitrogen, Grand Island, NY, USA). Real-time PCR was performed on a Exicycler™ 96 PCR machine (LG company, Korea) using the primer for gene amplification were: GLUT4 forward 5′-ACAGGGCAAGGATGGTAGA-3′, reverse5′-TGGAGGGGAACAAGAAAGT-3′, β-actin forward 5′-GGCTGTGTTGTCCCTGTATG-3′, reverse 5′-AATGTCACGCACGATTTCC-3′. All reactions were performed under the same conditions: 95°C for 30 min, one cycle; 95°C for 30 s, 60°C for 30 s and 72°C for 1 minute, 40 cycles. β-actin was used as the control gene and all data are represented as relative mRNA expression on gene expression (13).

Western blotting

Twenty micrograms of samples were separated on 12% sodium dodecyl sulfate-polyacrylamide gel, and then transferred to a polyvinylidene difluoride membranes. Membranes were incubated with specific primary antibody against GLUT4 (Santa Cruz Biotechnology Inc, USA), VAMP2 (Santa Cruz Biotechnology Inc, USA), Akt (Santa Cruz Biotechnology Inc, USA) and pAkt (Santa Cruz Biotechnology Inc, USA) overnight at 4°C, respectively. Then membranes were washed and incubated with HRP-conjugated secondary antibody. Protein bands were visualized by an enhanced HPIAS-2000 Image Analysis System (Championimages, China). The sum of the GLUT4 concentration in intracellular membranes and in plasma membranes was taken as the GLUT4 concentration of total cell membranes.

Statistical analysis

All data are expressed as mean ± SEM. The results

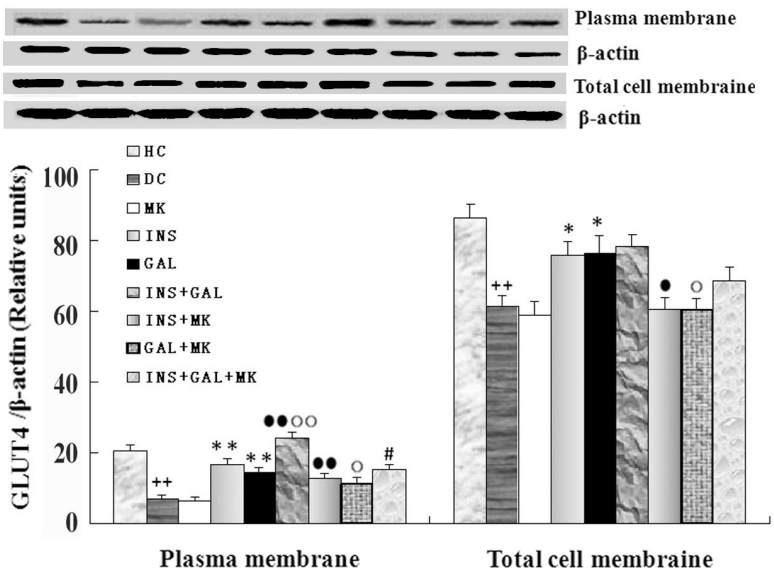

Fig. 1. *Injection with galanin increased insulin-stimulated GLUT4 trafficking to the plasma membranes of adipose cells (n = 8). The GLUT4 levels in the insulin- (INS) and galanin-treated (GAL) groups were higher in plasma membranes and total cell membranes than each diabetic control group (DC), and in INS + GAL group than either INS or GAL group in the plasma membranes, but not in total cell membranes of adipose cells. The GLUT4 levels were lower in INS + GAL + MK-2206 (MK) group than INS + GAL group in the plasma membranes. In addition, the contents in plasma membranes and total cell membranes were lower in INS + MK group than INS group, in GAL + MK group than GAL group, in DC group than each health control group (HC), respectively. While GLUT4 levels in the total cell membranes were insignificantly different between INS + GAL group and either INS or GAL group, and between INS + GAL + MK group and INS + GAL group. The sum of the GLUT4 concentration in plasma membranes and in intracellular membranes was used as the GLUT4 concentration of total cell membranes. The band sequence of representative Western blot in each panel is HC, DC, MK, INS, GAL, INS+GAL, INS + MK, GAL + MK and INS+GAL + MK group. The data shown are the means ± SEM. ++ P < 0.01 vs HC; * P < 0.05, ** P < 0.01 vs DC; ● P< 0.05, ●● P < 0.01 vs INS; # P < 0.05 vs INS+GAL".*

of experiments were analyzed by two-way ANOVA followed by Tukey's test. A p value<0.05 was considered significant.

RESULTS

GLUT4 contents in membranes of adipose cells

We first evaluated the effects of co-administrating insulin and galanin on the GLUT4 expression in adipose cells via the Western blot assay. Compared with the diabetic control group, the GLUT4 immunoreactivities in insulin- or galanin-treated group elevated by 144.2% (P<0.01) and 109.1% (P<0.01) in the plasma membranes, and 23.6% (P<0.05) and 24.3% (P<0.05) in the total cell membranes (Fig. 1). The GLUT4 levels in the plasma membranes were significantly elevated by 43.2% (P<0.01) and 66.9% (P<0.01) in the insulin + galanin group compared with either insulin or galanin group, but decreased by 37.7% (P<0.05) in the insulin + galanin + MK-2206 group compared with the insulin + galanin group. In addition, the GLUT4 levels in plasma membranes and total cell membranes were lower in the insulin + MK-2206 group than the insulin group (P<0.01, P<0.05), and in the galanin + MK-2206 group than the galanin group (P<0.05) and in the diabetic control group than each health control group (P<0.01). While the GLUT4 levels in the total cell membranes were insignificant differences between the insulin + galanin group and either insulin or galanin group (P>0.05), and between the insulin + galanin + MK-2206 group and the insulin + galanin group (P>0.05). The ratios of the GLUT4 densities in plasma membranes to total cell membranes were 23.9%, 11.2%, 10.8%, 16.9%, 18.8%, 30.7%, 20.8%, 18.8% and 21.9% in the healthy control group, the diabetic control group, the diabetic MK-2206 group, the insulin group, the galanin group, the insulin + galanin group, the insulin + MK-2206 group, the galanin + MK-2206 group and the insulin + galanin + MK-2206 group, respectively.

^{3}H-2DG uptake

We examined glucose uptake using ^{3}H-2DG assay in the adipose cells. Treatment of insulin or galanin alone significantly increased ^{3}H-2DG uptake by 53.6% (P<0.01) and 44.6% (P<0.01) compared with the diabetic control group, respectively (Fig. 2). The ^{3}H-2DG contents enhanced by 26.2% (P<0.05) and 33.9% (P<0.01) in the insulin + galanin group compared with insulin- or galanin-treated group, respectively. While the ^{3}H-2DG uptake reduced by 34.9% (P<0.01) in the insulin + galanin + MK-2206 group compared with the insulin + galanin group. The ^{3}H-2DG content was significantly lower (P<0.01) in the diabetic control group than the health controls, and in the insulin + MK-2206 group than the insulin group (P<0.05) and in the galanin + MK-2206 group than the galanin group (P<0.05), respectively.

GLUT4 mRNA expression levels

Compared with the diabetic control group, the GLUT4 mRNA levels increased by 36.8% (P<0.01) and 31.2% (P<0.05) in the insulin- and galanin-treated group (Fig. 3). While the GLUT4 mRNA expression were significantly lower in the insulin + MK-2206 group than the insulin group (P<0.05), in the galanin + MK-2206 group than the galanin group (P<0.01) and in the diabetic control group than the health control group (P<0.01), respectively. The expression levels were insignificantly different between insulin + galanin + MK-2206 group and insulin + galanin group, and between insulin + galanin and either insulin or galanin group (P>0.05).

VAMP2 levels in adipose cells

We measured the VAMP2 levels in the plasma membranes of adipose cells using subcellular fractionation and Western-blotting assay. Treatment with insulin or galanin alone significantly increased the VAMP2 levels by 58.4% (P<0.01) and 47.8% (P<0.01) compared with the diabetic control group (Fig. 4). The VAMP2 contents increased by 27.7% (P<0.05) and 36.8% (P<0.01) in the insulin + galanin group compared with insulin and galanin group, respectively. The levels reduced by 35.5% (P<0.01) in the insulin + galanin + MK-2206 group compared with the insulin + galanin group. Again, the levels in the plasma membranes were significantly lower in the diabetic control group than the health controls (P<0.01), and in the insulin + MK-2206 group than the insulin group (P<0.05) and in the galanin +

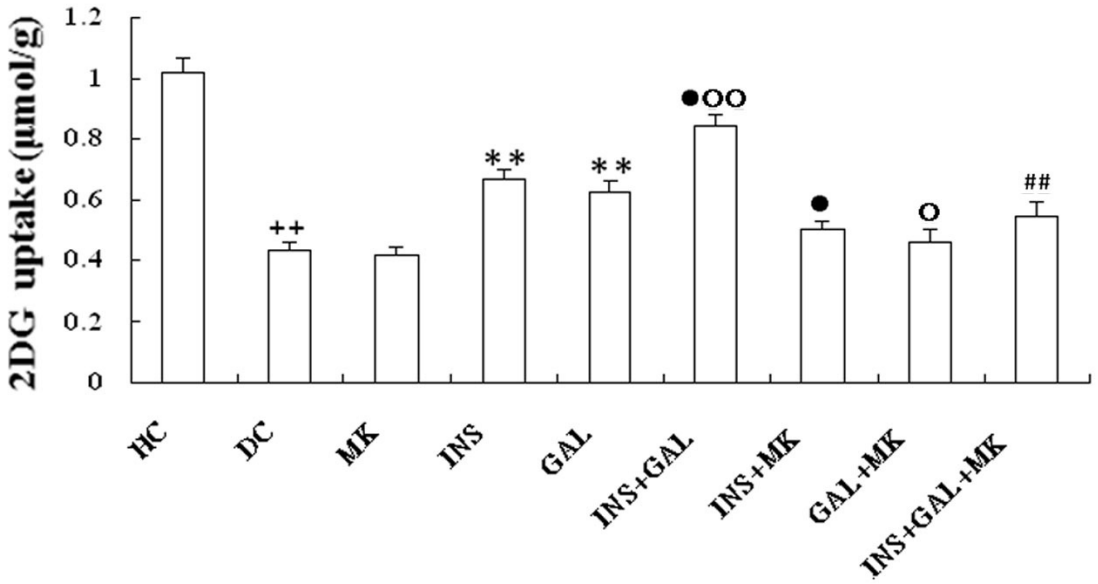

Fig. 2. *Treatment with galanin increased insulin-stimulated ^{3}H-2DG uptake in adipose cells (n = 8). The ^{3}H-2DG levels were higher in either insulin (INS) or galanin (GAL) group than the diabetic control group (DC), and in INS+GAL group than INS or GAL group. While the ^{3}H-2DG uptake were lower in INS + MK, GAL + MK, INS+GAL + MK and DC group than INS, GAL, INS+GAL and the healthy control (HC) group, respectively. The data shown are the means ± SEM. ++ P < 0.01 vs HC; ** P < 0.01 vs DC; ● P < 0.05 vs INS; ○ P < 0.05; ○○ P < 0.01 vs GAL; ## P < 0.01 vs INS+GAL.*

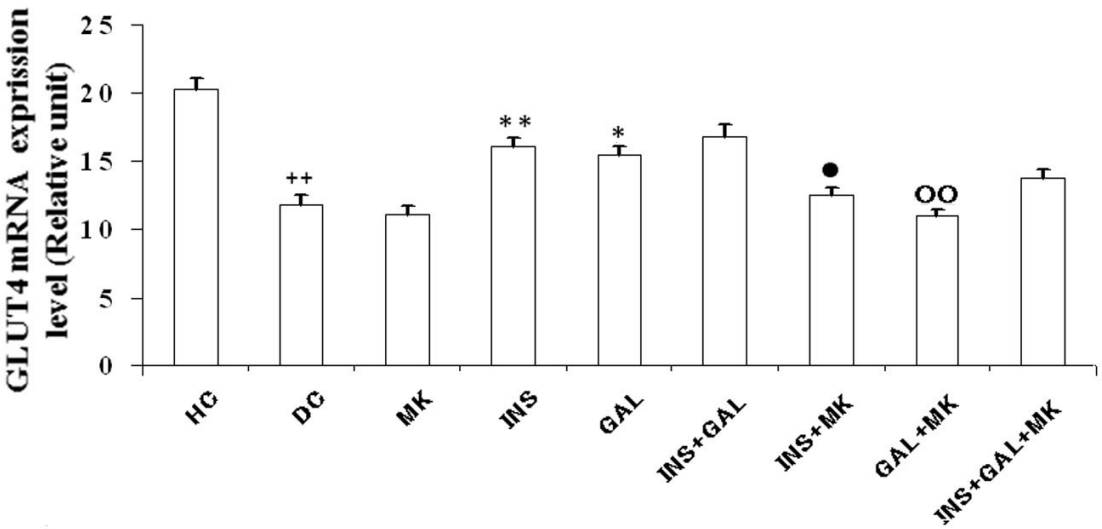

Fig. 3. *After the administration of galanin the insulin-stimulated GLUT4 mRNA expression was almost changeless in adipose cells (n = 8). The GLUT4 mRNA expression levels in the insulin (INS) and galanin group (GAL) were higher than the diabetic controls (DC). While the GLUT4 mRNA expression was lower in INS + MK-2206 (MK), GAL + MK and DC group than INS, GAL and the healthy control (HC) group, respectively. But the expression levels were insignificantly different between INS + GAL + MK and INS + GAL group, and between INS + GAL and either INS or GAL group. The data shown are the means ± SEM. ++ P < 0.01 vs HC; * P < 0.05, ** P < 0.01 vs DC; ● P < 0.05 vs INS; ○○ P < 0.01 vs GAL.*

MK-2206 group than the galanin group (P<0.05), respectively.

Galanin enhanced insulin-induced Akt phosphorylation

To determine whether injection with galanin affects insulin signaling, we measured pAkt and Akt levels in adipose cells. As shown in Fig 5A, compared with the diabetic control group, pAkt and Akt levels enhanced by 89.7% (P<0.01) and 36.9% (P<0.01) in the insulin group, and by 59.1% (P<0.01) and 27.9% (P<0.05) in the galanin group, respectively. The pAkt levels elevated by 33.2% (P<0.05) and 42.5% (P<0.01), but the Akt levels increased by only 6.3% (P>0.05) and 13.6% (P>0.05) in the insulin + galanin group compared with insulin- and galanin-treated group, respectively. While the pAkt and Akt levels attenuated by 29.8% (P<0.01) and 18.7% (P<0.05) in the insulin + galanin + MK-2206 group compared with the insulin + galanin group. Also, both parameters were lower in the diabetic control group than the healthy controls (P<0.01), and in the insulin + MK-2206 group than the insulin group (P<0.05) and in the galanin + MK-2206 group than the galanin group (P<0.05), respectively.

The ratios of pAkt/Akt increased by 38.7% (P<0.01) and 24.2% (P<0.05) in the insulin group and the galanin group compared with the diabetic control group, and by 25.3% (P<0.05) and 39.9% (P<0.01) in the insulin + galanin group compared with insulin- or galanin-treated group, respectivel. While the ratios reduced by 15.8% (P<0.01) in the insulin + galanin + MK-2206 group compared with the insulin + galanin group. The ratios were significantly lower in the diabetic control group than the health controls (P<0.01), and in the insulin + MK-2206 group than the insulin group (P<0.05) and in the galanin + MK-2206 group than the galanin group (P<0.05), respectively.

DISCUSSION

T2DM is a highly prevalent disease canonically treated with insulin, but the efficacy often is

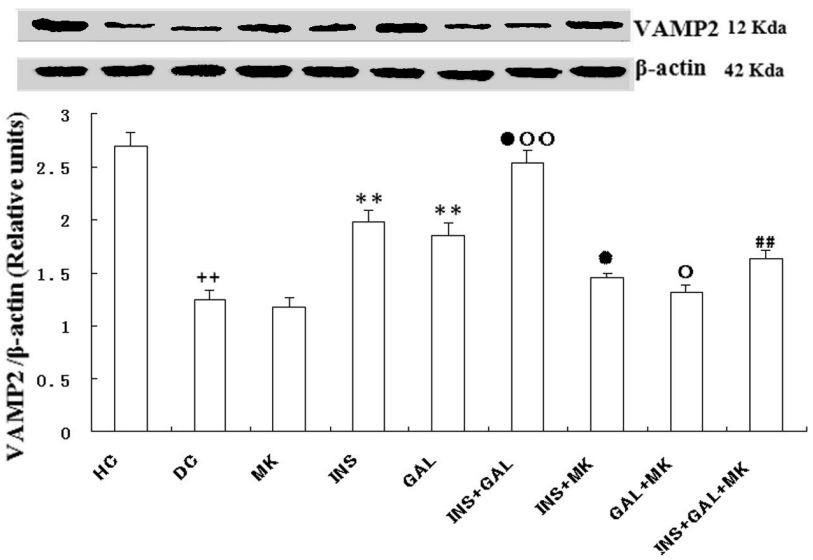

Fig. 4. *Treatment with galanin increased insulin-stimulated VAMP2 translocation in adipose cells (n = 8). The VAMP2 levels were higher in either insulin (INS) or galanin (GAL) group than the diabetic controls (DC), and in INS+GAL group than INS or GAL group. While the levels were lower in INS + MK, GAL + MK INS+GAL + MK and DC group than INS, GAL, INS+GAL and the healthy control (HC) group, respectively. The band sequence of representative Western blot is HC, DC, MK, INS, GAL, INS+GAL, INS + MK, GAL + MK and INS+GAL + MK group. The data shown are the means ± SEM. ++ P < 0.01 vs HC; ** P < 0.01 vs DC; ● P < 0.05 vs INS, ○ P < 0.05, ○○ P < 0.01 vs GAL, ## P < 0.01 vs INS+GAL.*

unsatisfying to control plasma glucose levels. Exploration of novel regulators to facilitate insulin-induced glucose clearance becomes a hot topic in the anti-diabetic research. In the current study we verified if galanin can facilitate insulin-stimulating GLUT4 translocation in adipose cells of diabetic rats from various aspects.

Firstly, it was found that co-treatment with galanin and insulin can enhance the insulin-regulated GLUT4 translocation in adipose cells. The results showed that the ratios of GLUT4 contents in plasma membranes to total cell membranes in the insulin + galanin group were higher than that in the insulin-treated group (30.7% vs 22.7%), suggesting that galanin increased insulin-stimulated GLUT4 trafficking from cytoplasm vesicles to cellular surface of adipose cells. In addition, there were not significantly differences of GLUT4 levels in the total cell membranes between insulin + galanin group and insulin- or galanin-treated group, implicating that treatment with galanin was unable further to increase the GLUT4 contents of total cell membranes in the both hormone group compared with insulin group in adipose tissues.

Secondly, co-treatment with both hormones further increased 2-DG influx into adipose cells as compared with treatment with insulin only in diabetic rats. This is consistent with our previous observation that treatment with a galanin antagonist, M35 increased plasma glucose levels and reduced insulin sensitivity in diabetic rats (9, 12, 13), i.e. endogenous galanin may decrease hyperglycemia and insulin resistance in T2DM rats. Other studies also indicated that during a glucose tolerance test insulin-independent glucose elimination was significantly blunted in galanin-knockout mice (11), while the homozygous galanin

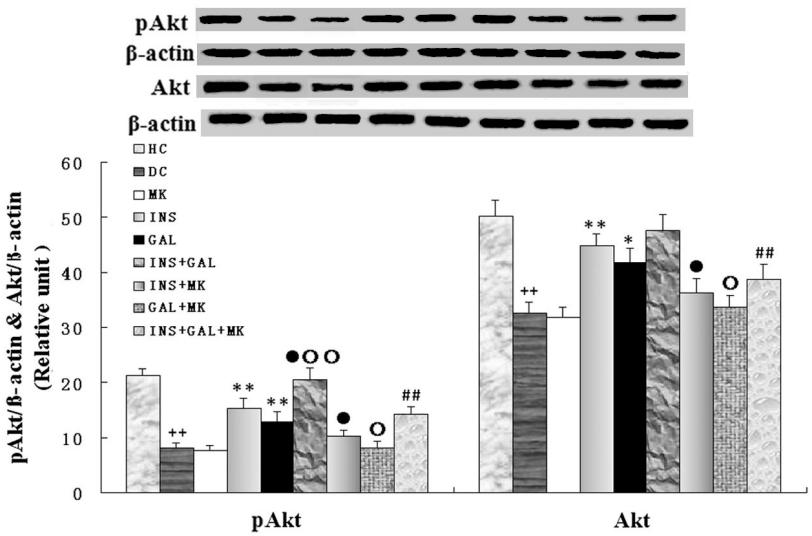

Fig. 5. *The associative effect of insulin and galanin on pAkt and Akt expression in adipose cells (n = 8). The pAkt and Akt expression was higher in either insulin (INS) or galanin (GAL) group than the diabetic controls (DC). The pAkt expression was higher also in INS+GAL group than INS or GAL group, respectively. While the levels were lower in INS + MK, GAL + MK INS+GAL + MK and DC group than INS, GAL, INS+GAL and the healthy control (HC) group, respectively. But Akt expression were insignificantly different between INS + GAL group and either INS or GAL group. The ratios of pAkt/ Akt were higher in either insulin (INS) or galanin (GAL) group than the diabetic control group (DC), and in INS+GAL group than INS or GAL group. While the ratios were lower in INS + MK, GAL + MK, INS+GAL + MK and DC group than INS, GAL, INS+GAL and the healthy control (HC) group, respectively. The band sequence of representative Western blot in each panel is HC, DC, MK, INS, GAL, INS+GAL, INS + MK, GAL + MK and INS+GAL + MK group. The data shown are the means ± SEM. ++ $P < 0.01$ vs HC; * $P < 0.05$, ** $P < 0.01$ vs DC; ● $P < 0.05$ vs INS; ○ $P < 0.05$, ○○ $P < 0.01$ vs GAL; # $P < 0.05$, ## $P < 0.01$ vs INS+GAL.*

transgenic C57BL/6J mice with the obese phenotype reduced their energy expenditure and impaired their glucose tolerance (14). The animals with galanin metabolic disorder easily suffer from T2DM (15). Regarding above results, we postulate that T2DM may result from a dysfunction of both galanin and insulin systems. Herewith, co-administration of galanin and insulin may achieve better curative efficacy to ameliorate hyperglycemia than treatment with insulin alone in T2DM rats.

Thirdly, in order to assess the effect of galanin on insulin-induced the gene change of GLUT4 protein, the GLUT4 mRNA levels of adipose cells was surveyed after the administration of galanin. Previous studies revealed that the GLUT4 mRNA level likely reflected the change in GLUT4 synthesis rate rather than its half-life (15). The elevation of GLUT4 mRNA level is associated with an increase in GLUT4 synthesis and release. The nuclear run-on assays showed that the GLUT4 transcription was decreased in adipose tissue and skeletal muscle of streptozotocin-induced diabetic animals (8). In this study we found that co-administration of galanin and insulin compared with injection of insulin alone did not further upregulate GLUT4 mRNA levels, indicating that galanin may increase insulin-induced GLUT4 translocation, not GLUT4 protein expression and synthesis in adipose tissue.

Fourthly, vesicular exocytosis involves the physical fusion of trafficking vesicles with the target membrane compartment. This fusion step involves the interactions of the vesicle-associated soluble N-ethylmaleimide-sensitive factor attachment protein receptors (SNARE) and target SNARES (16). VAMP2 regulates GLUT4 vesicle docking and fusion via forming the SNARE complex in response to insulin signaling (1, 17). An injection of VAMP2 neurotoxins or overexpression of dominant-interfering VAMP2 peptides inhibited GLUT4 translocation. The present findings revealed that administration of galanin further enhanced insulin-induced VAMP2 translocation, resulting in facilitation of GLUT4 trafficking and glucose uptake in adipose cells.

Last, we assessed Akt phosphorylation and pAkt/Akt ratios in adipose cells of T2DM rats to undestand the mechanism of the cooperative effect between galanin and insulin on GLUT4 trafficking. Akt is a key signaling molecule in the cascade of insulin-stimulating GLUT4 translocation (18, 19). Galanin may activate the PI3K/Akt signaling pathway via activated galanin receptor 2 too (20). Thus, Akt becomes a meeting-point of both signaling pathways to trigger GLUT4 exocytosis. In the current study we found that Akt phosphorylation and pAkt/Akt ratios in both hormone group were higher than that in the solitary insulin-treated group, suggesting that the interaction between both signaling cascades may enhance their intensity and transmitting efficacy, resulting in augmenting their gains in GLUT4 trafficking in adipose cells of T2DM rats.

Interestingly, the role of galanin to increase insulin-induced GLUT4 and VAMP2 translocation was blocked by Akt inhibitor, MK-2206. After administration of MK-2206, galanin was unable to potentiate insulin-induced GLUT4 and VAMP2 translocation, suggesting that Akt is essential for galanin to subserve insulin-stimulated events, and the Akt-VAMP2-GLUT4 pathway mediates the promoting effects of galanin on insulin-stimulated GLUT4 and VAMP2 translocation in adipose cells. As MK-2206, an allosteric inhibitor of Akt1, Akt2 and Akt3, may block more than one isoform of Akt (19), an additional experiment is required to further assess which specific isoform(s) of Akt mediates the promoting effect of galanin on insulin-induced GLUT4 trafficking in adipose cells.

In conclusion, the results in the present study indicated that administration of galanin enhanced insulin-induced VAMP2 and GLUT4 translocations, Akt phosphorylation and glucose uptake, not GLUT4 mRNA expression and total GLUT4 levels. The promoting effects of galanin on insulin-induced events may be antagonized by Akt inhibitor. These results suggest that Akt phosphorylation and Akt-VAMP2-GLUT4 pathway are necessary to the beneficial effect of galanin on the insulin-stimulated events. These findings provide an experimental clue for further testing whether co-administration of galanin and insulin may get better anti-diabetic efficacy than the canonical treatment with insulin alone for T2DM patients.

ACKNOWLEDGEMENTS

This work was supported by National Health, Family Planning Commission of China (W201309), Open Projects of Zoonosis Key Laboratory of Jiangsu Province (R1504), Natural Scientific Fund of Jiangsu Traditional Chinese Medicine Office (YB2015138), Natural Scientific Fund of the Anhui Higher Education Institutions of China (KJ2017A427), Six top talent project of Jiangsu Province (WSN -113) with Science and Technique Program of Chuzhou College (2014SK09) and 2018 visiting research project of key teachers of the Anhui Higher Education Institutions of China (gxgnfx2018048).

REFERENCES

1. Hiroyasu H, Makoto K. Heterotypic endosomal fusion as an initial trigger for insulin–induced glucose transporter 4 (GLUT4) translocation in skeletal muscle. J Physiol 2017; 595:5603-21.
2. Zhang Z. Sheng S. Guo L. et al. Intracerebroventricular administration of galanin antagonist sustains insulin resistance in adipocytes of type 2 diabetic trained rats. Mol Cell Endocrinol 2012; 361:213-18.
3. Hruz PW, Mueckler MM. Structural analysis of the GLUT1 facilitative glucose transporter. Mol Membr Biol 2001; 18:183-93.
4. Martin OJ, Lee A, McGraw TE. GLUT4 distribution between the plasma membrane and the intracellular compartments is maintained by an insulin-modulated bipartite dynamic mechanism. J Biol Chem 2006; 281:484-90.
5. Guo LL, Shi MY, Zhang L, et al. Galanin antagonist increases insulin resistance by reducing glucose transporter 4 effect in adipocytes of rats. Gen Comp Endocrinol 2011; 173:159-63.
6. Vijayakumar MV, Ajay AK, Bhat MK. Demonstration of a visual cell-based assay for screening glucose transporter 4 translocation modulators in real time. J Biosci 2010; 35:525-31.
7. Holman GD, Sandoval IV. Moving the insulin-regulated glucose transporter GLUT4 into and out of storage. Trends Cell Biol 2011; 11:173-79.
8. Geiger PC, Han DH, Wright DC, Holloszy JO. How muscle insulin sensitivity is regulated: testing of a hypothesis. Am J Physiol Endocrinol Metab 2006; 291:E1258-E1263.
9. He B, Shi M, Zhang L, et al. Beneficial effect of galanin on insulin sensitivity in muscle of type 2 diabetic rats. Physiol Behav 2011; 103:284-89.
10. Yun R, Dourmashkin JT, Hill J, Gayles EC, Fried SK, Leibowitz SF. PVN galaninincreases fat storage and promotes obesity by causing muscle to utilize carbohydrate more than fat. Peptides 2005; 26:2265-73.
11. Ahren B, Pacini G, Wynick D, Wierup N, Sundler F. Loss-of-function mutation of the galanin gene is associated with perturbed islet function in mice. Endocrinology 2004; 145:3190-96.
12. Bu L, Liu Z, Zou J, Gao X, Bao Y, Qu S. Blocking central galanin receptors attenuates insulin sensitivity in myocytes of diabetic trained rats. J Neurosci Res 2013; 91:971-77.
13. Liang Y, Sheng SD, Fang PH, et al. Exercise-induced galanin release facilitated GLUT4 translocation in adipocytes of type 2 diabetic rats. Pharmacol Biochem Behav 2012; 100:554-59.
14. Poritsanos NJ, Mizuno TM, Lautatzis ME, Vrontakis M. Chronic increase of circulating galanin levels induces obesity and marked alterations in lipid metabolism similar to metabolic syndrome. Int J Obes (Lond) 2009; 33:1381-89.
15. Legakis IN. The role of galanin in metabolic disorders leading to type 2 diabetes mellitus. Drug News Perspect 2005; 18:173-77.
16. Chen,YA, Scheller RH. SNARE-mediated membrane fusion. Nat Rev Mol Cell Biol 2001; 2:98-106.
17. Williams D, Pessin JE. Mapping of R-SNARE function at distinct intracellular GLUT4 trafficking steps in adipocytes. J Cell Biol 2008; 180:375-87.
18. Stretton C, Evans A, Hundal HS. Cellular depletion of atypical PKC{lambda} is associated with enhanced insulin sensitivity and glucose uptake in L6 rat skeletal muscle cells. Am J Physiol Endocrinol Metab 2010; 299:402-12.
19. Song G, Ouyang G, Bao S. The activation of Akt/PKB signaling pathway and cell survival. J Cell Mol Med 2005; 9:59-71.
20. Thimmaiah KN, Easton JB, Germain GS, Morton CL, Kamath S, Buolamwini JK, Houghton PJ. Identification of N^{10}-substituted phenoxazines as potent and specific inhibitors of Akt signaling. J Biol Chem 2005; 280:31924-35.

THE ROLE OF miR-145 IN PROMOTING THE FIBROSIS OF PULMONARY FIBROBLASTS

T. XU[1], YX. WU[1], JX. SUN[1], FC. WANG[1], ZQ. CUI[1] and XH. XU[2]

[1]Department of Critical Care Medicine (First ward), Linzi District People's Hospital, Zibo City, Shandong Province, China; [2]Department of Rheumatology and Immunology, Qilu Hospital of Shandong University (Qing Dao), Qingdao, Shandong Province, China

Received January 16, 2019 – Accepted May 22, 2019

The effects of miR-145 (microRNA 145) on *M. pneumoniae* (MP)-infected MRC-5 (Medical Research Council cell strain 5) cell TGF-β/Smad (transforming growth factor beta/Smad) fibrosis pathway were explored through constructing MP-infected MRC-5 cell models. In addition, the qPCR (quantitative real-time polymerase chain reaction) and Western blot were applied to detect the mRNA and protein expressions of miR-145, TGF-β1 (transforming growth factor beta 1), Smad3, Smad4, MMP2 (matrix metalloproteinase 2), FN1 (fibronectin 1), ELN (elastin) and COLI α1 (collagen type I alpha 1) signaling molecules in TGF-β/Smad fibrosis pathway. The results showed that the expression of miR-145 in MRC-5 cells was significantly increased after MP infection. In addition, miR-145 inhibited the fibrosis-promoting TGF-β/Smad pathway by targeting Smad3, a key factor in the TGF-β/Smad pathway. It can be concluded that, in the process of MP infection, the expression of miR-145 is stimulated to negatively regulate the fibrosis-promoting pathway of TGF-β/Smad.

As a highly pathogenic micro-organism, *M. Pneumoniae* (MP) attaches to ciliated cells through capsular mucosa, thus causing damage to its host cells and leading to infectious pleuropneumonia in humans. MP infection is widespread and its main symptoms include cough, asthma, progressive emaciation, and interstitial pneumonia, which is a chronic respiratory disease. Even if the patients have completely recovered after treatment, they would be a long-term carriers of MP. Therefore, it is difficult to control the disease or completely eliminate the bacteria, which leads to serious health risks for human beings (1).

One of the pathological features of interstitial pneumonia is pulmonary interstitial fibrosis (2), a chronic and progressive pulmonary interstitial disease, the main pathological characteristics of which are diffuse alveolitis in the early stage, diffuse pulmonary interstitial fibrosis in the middle stage, and alveolar wall fibrosis in the late stage (3). Fibrosis is indeed a type of tissue repair reaction carried out to protect the relative integrity of tissues. However, in this process, the normal structure of tissue trachea is often destroyed due to the progressive and abnormal accumulation of extracellular matrix (ECM). As a key player in pulmonary fibrosis and tissue remodeling, fibroblasts are the precursors of myofibroblasts and the major secretory cells of ECM. The long-term activation of fibroblasts, i.e. fibroblast proliferation and their phenotypic transformation

Key words: miR-145; TGF-β/Smad pathway; MRC-5 cells

Corresponding Author:
Dr Xiaohong Xu,
Department of Rheumatology and Immunology,
Qilu Hospital of Shandong University (Qing Dao),
NO.758 Hefei Road, Shibei District, Qingdao, 266000,
Shandong Province, China
e-mail: xuxiaohong08114@163.com

0393-974X (2019)

to myofibroblasts, can cause excessive secretion of extracellular matrix and subsequent pulmonary fibrosis (4). Past studies have shown that TGF-β/Smad, Fas/ERK and other signaling pathways play an important role in the development of pulmonary fibrosis (5, 6). In particular, transforming growth factor beta (TGF-β) plays an important regulatory role in the formation of fibrosis (7, 8) by interacting with other fibrogenic factors, such as platelet-derived growth factor (PDGF), and participating in the complex process of fibrosis. At present, many studies have investigated the diagnosis and etiology of MP. However, due to the difficulty of MP cultivation, the molecular mechanism of MP remains unclear.

MiR-145 (microRNA 145) is a highly conserved miRNA implicated in cancers, such as prostate cancer, colon cancer, and bladder cancer, by inhibiting the growth of cancer cells (9-12). At present, little research has been carried out to study the role of miR-145 in the regulation of pulmonary interstitial fibrosis, especially the role of miR-145 in the regulation of the TGF-β/Smad signaling pathway. Therefore, in this study, the role of miR-145 in MP infection and the activation of the TGF-β/Smad pathway was explored by constructing a MRC-5 cell model of MP infection.

MATERIALS AND METHODS

MP cultivation, passage and counting

MP standard strains (M129 strains) were preserved in the Linzi District People's Hospital laboratory at -80°C. 27.52g of mycoplasma culture medium powder (Haibo Biology Co., Ltd., China) were heated and dissolved in 800 mL of distilled water, sterilized at 121°C for 15 min, cooled to room temperature, mixed with 200 mL of inactivated complement horse serum (Hyclone Co., USA) and 800,000 units of penicillin (Shanghai Hengfei Biotechnology Co., Ltd., China), aliquoted to sterile tubes and then stored at 20°C. On a super-clean workbench (Suzhou Antai Air Technology Co., Ltd., China), 1 mL of standard strain M129 of MP was mixed with 5 mL of MP liquid culture medium and then cultured in a 37°C CO_2 incubator (Thermo Company, USA). When the medium color changed from red to orange, i.e., when the pH value was about 6.8, MP was sub-cultured. MP counting was carried out by measuring the unit of color change. The specific procedures were as follows: the MP normal culture medium was added into 12 Ep tubes, with 900 uL in each tube, and the tubes were numbered 1-12; tube 1 was added with 100 uL of MP culture medium to be tested and mixed well; then, 100 uL of the solution in tube 1 was added into tube 2 and mixed well; successively, the 1-11 tubes were diluted in gradient for 11 times; tube 12 was the negative control without MP culture medium. Afterwards, the tubes were incubated in a 37°C incubator for 1 week; then, the tubes were equilibrated under natural states; after the color was stabilized, the last tube in which the color change occurred was regarded as the CCU result.

Culture and passage of MRC-5 cells

MRC-5 cell strain (human embryonic lung fibroblasts) was from Shanghai Airui Biotechnology Co., Ltd., China. Frozen MRC-5 cells were removed from a liquid nitrogen tank (Beijing Aishan Sunshine Technology Co., Ltd., China) and immediately resuscitated in a 37°C water bath under continuous stirring. Then, a serum-free MEM (Minimum Essential Medium) and NEAA (non-essential amino acid) (Hyclone Company, USA) were added to thawed cells and centrifuged for 4 min at 800rpm. Subsequently, the cell pellet was gently suspended in 1 mL of MEM NEAA containing 10% FBS (Fetal Bovine Serum), and the cell suspension was transferred to a 10-cm cell culture dish containing 9 mL of MEM NEAA medium supplemented with 10% FBS (BI, Israel). During the cell culture in a 5% CO_2 and 37°C incubator, when the density of MRC-5 cells reached about 90% confluency, the cells were trypsinized using 1 mL of trypsin (Invitrogen Company, USA) and the number of cells in the suspension was counted under a microscope and a cytometer.

Transfection of miR-145 into MRC-5 cells using ribo FECT™ CP (A transfection agent)

MRC-5 cells were inoculated into six-well plates at a concentration of $1x10^6$ cells per well and cultured under 5% CO_2 and 37°C until the cell confluence reached about 60%. Subsequently, a ribo FECT™ CP Buffer (10x) (Guangzhou Reeber Biology Company, China) was diluted to 1x with PBS (Guangzhou Reeber Biology Company, China) and mixed with 6.25 μl of 20 μM mimics, 12.5 μl 20 μM inhibitors (Guangzhou Reeber Biology Company, China), 6.25 μl of 20 μM NC

storage solution (Guangzhou Reeber Biology Company, China) and 6.25μl of 20 μM storage solution of labeled NA oligos, respectively. After being incubated at room temperature for 5 min, 15 μl of CP Reagent (Guangzhou Reeber Biology Company, China) were gently added into the mixtures and incubated at room temperature for another 15 min. Then, the transfection reagent was added to the cells, followed by the addition of 2 mL of fresh cell culture medium in each well. Finally, the six-well plate was placed in the cell culture incubator at 37°C and 5% CO_2.

MP-infected MRC-5 cells

The cells were divided into eight groups: groups of blank, miR-145 NC, miR-145 mimics, miR-145 inhibitors, blank + MP, miR-145 NC + MP, miR-145 mimics + MP, and miR-145 inhibitors + MP. Subsequently, MRC-5 cells were cultured to a density of 10^6 for transfection. After 24 h of transfection, MRC-5 cells were infected by MP using a virus/cell ratio of 10:1, and then cultured for a further 24 h in the 37°C/CO_2 incubator, with three replicates prepared for each group.

Detection of differential expression of miR-145 and genes of the TGF-β/Smad signaling pathway

Total RNA extraction: After MRC-5 cells were infected with MP for 24 h, the total RNA in each sample was extracted by an AxyPrep kit (Full-style Gold Company, China) according to the instructions of the kit. The quality and purity of isolated RNA were detected by a nucleic acid analyzer (NANODROP, USA) and 1% agarose gel electrophoresis.

The synthesis of miR-145 cDNA and qPCR detection: A stem-ring method was used to amplify the cDNA of target genes. The qPCR detection was performed using a SYBR Premix Ex Taq TM II reagent (TaKaRa Biology Co., Ltd., Japan) in a reaction system of 25 μl. U6 was used as the internal reference gene for qPCR. The primer sequences of the target gene and internal reference gene are shown in Table I. A Bio-RadiQ5 detection system and the $2^{-\Delta\Delta t}$ method were used for gene expression quantitation. The procedure of PCR reaction was as follows: pre-denaturation at 95°C for 30 s and 40 cycles of 5 s of denaturation at 95°C and 30 s of annealing at 53°C. The fluorescence intensity signals were collected during the 55~90°C heating stage to plot the melting curve. The primer information is shown in Table I.

cDNA synthesis and qPCR detection: A TransScript One-Step gDNA Removal and cDNA Synthesis Super Mix kit (All-King Corporation, China) was used to synthesize cDNA from isolated RNA, and a SYBR Premix Ex Taq TM II (Perfect Real Time) reagent (TaKaRa Biology Co., Ltd., Japan) was used to detect the expression of target mRNAs. β-actin was used as the internal reference gene

Table I. *Primer sequences of miR-145 and related genes of the TGF-β/Smad signaling pathway.*

Gene	Forward (5'— 3')	Reverse (5'— 3')
miR-145	CGAGTCCAGTTTTCCCAGGA	GTGCAGGGTCCGAGGT
TGF-β	CCTCCTTGGCGTAGTAGTCG	CCTCCTTGGCGTAGTAGTCG
Smad3	GTTTAGCCCTGGACCCTGTT	GCTTCGCTGTGTTGAGGTTT
Smad4	CTGCCAACTTTCCCAACATT	ATCCATTCTGCTGCTGTCCT
MMP2	TATGGCTTCTGCCCTGAGAC	CACACCACATCTTTCCGTCA
FN1	ATCACCCTCACCAACCTCAC	TCCCTCGGAACATCAGAAAC
ELN	ATCACCCTCACCAACCTCAC	TCCCTCGGAACATCAGAAAC
COL1A1	CAGACAAGCAACCCAAACTGAA	TGAGAGATGAATGCAAAGGAAAAA
U6	CTCGCTTCGGCAGCACA	AACGCTTCACGAATTTGCGT
β-actin	TGAGAGGGAAATCGTGCGTGACAT	ACCGCTCGTTGCCAATAGTGATGA

for qPCR. The primer sequences of target genes and internal reference gene are listed in Table I. The relative expression of target genes was calculated using the Bio-Radi Q5 Real-time PCR detection system and $2^{-\Delta\Delta t}$ method, in conjunction with suitable negative and blank controls. The procedure of PCR was as follows: pre-denaturation at 95°C for 30 s, and 40 cycles of 5 s of denaturation at 95°C and 30 s of annealing at 55°C. The detection of fluorescence signals was carried out for every 0.5°C in the 55~90°C range of the extension stage to draw the melting curve.

Detection of differentially expressed miR-145 and proteins along the TGF-β/Smad signaling pathway

Extraction of whole cell protein: The adherent cells were washed twice with pre-cooled PBS and gently scraped off using a cell scraper before the cells and culture medium were transferred to a centrifugal tube and centrifuged at 1000rpm for 10 min. The cells were then washed twice with pre-cooled PBS via at 5 min of centrifugation at 1000rpm. The washed cells were then transferred to a pre-cooled centrifugation tube containing 1mL of a cold Lysis Buffer supplemented with 10μl of phosphatase inhibitors (Shanghai Beino Biotechnology Co., Ltd., China), 1μl of protease inhibitors (Shanghai Beino Biotechnology Co., Ltd., China), and 5 μl of 100 mM PMSF (Shanghai Hengfei Biotechnology Co., Ltd., China). The cell lysate was then gently shaken for 15 min and centrifuged at 14000rpm and 4°C for 15 min to collect whole protein extract. A BCA (Bicinchoninic acid) method was used to determine the protein concentration according to kit instructions.

Western blot detection: According to the size of the target protein, a separation gel at the corresponding concentration was prepared and 40 μl of each protein sample, which had been denatured in a boiling water bath for 5 min, were loaded onto the gel using 10 μl of 5×SDS (Shanghai Beino Biotechnology Co., Ltd., China) sample buffer. After the gel was concentrated using 25 min of 80V electrophoresis and the proteins were separated on a separate gel via 40 min of 120V electrophoresis, a PVDF membrane was treated with methanol for 15-20 s and immediately washed with distilled water. Subsequently, the membrane was immersed in a transmembrane solution for 15 min and then subjected to 1mA/cm^2 of transfer current for 1 h. In the next step, the PVDF membrane was blocked for 1 h in PBS containing 5% skimmed milk powder, washed once with the elution buffer, and then incubated overnight at 4°C with primary antibodies (1:1000 dilution, anti Smad3, Smad4, TGF-β1, FN1, ELN, MMP2, COL1A1 or anti beta-actin antibodies) (Proteintech Biology Company, USA). On the next day, the membrane was washed three times with an elution buffer and then incubated at room temperature for 1.5 h with the solution of secondary antibodies (1:10000 dilution, Zhongshan Jinqiao Company, China). Finally, the PVDF membrane was washed three times with the elution buffer (Shanghai Beino Biotechnology Co., Ltd., China), developed using a 1:1 mixture of color A and B liquids (Shanghai Beino Biotechnology Co., Ltd., China) in a dark room, scanned and visualized.

RESULTS

MP count and growth of MRC-5 Cells

The size of solid MP colonies ranged from 50 to 150 μm in diameter, with the colony morphology observed under a low power microscope. The concentration of MP was 1×10^8 CCU/mL. MRC-5 cells were adherent cells with shapes as spindles or irregular triangles and nearly parallel arrangement. The cells showed good growth with a homogeneous and transparent cytoplasm, and no signs of contamination from other organisms.

Transfection efficiency of MRC-5 cells

Fig. 1 shows the transfection efficiency result observed by fluorescent labeling of MRC-5 cells with Cy3-labeled miRNA. The fluorescence was mainly concentrated in the cytoplasm, and the transfection efficiency of miR-145 mimics, inhibitors and NC could all reach above 80%.

Expression of genes of the TGF-β/Smad signaling pathway in MP-infected MRC-5 cells

As shown in Fig. 2 and compared with that of the NC group, the expression of miR-145 was significantly increased 800-fold in the group of miR-145 mimics, while the expression of miR-145 was significantly inhibited by 80% in the group of miR-145 inhibitors. It can be seen that the transfection of miR-145 mimics successfully increased the expression of miR-145,

while the transfection of miR-145 inhibitor significantly inhibited the expression of miR-145. Compared with that in the control group, the expression level of intracellular miR-145 was increased after MP infection. Compared with that in different transfection groups, the expression level of intracellular miR-145 was about 1.53 times in the group of MP infection. It can be seen that MP infection increased the endogenous expression of intracellular miR-145. These data suggested that the differentially expressed miR-145 may play an important role in regulating the fibrosis pathway in MP -infected MRC-5 cells.

Expression of genes of the TGF-β/Smad signaling pathway in MP-infected MRC-5 cells

The mRNA and protein expression of genes of the TGF-β/Smad signaling pathway increased by different degrees in MP-infected MRC-5 cells (Fig. 3).

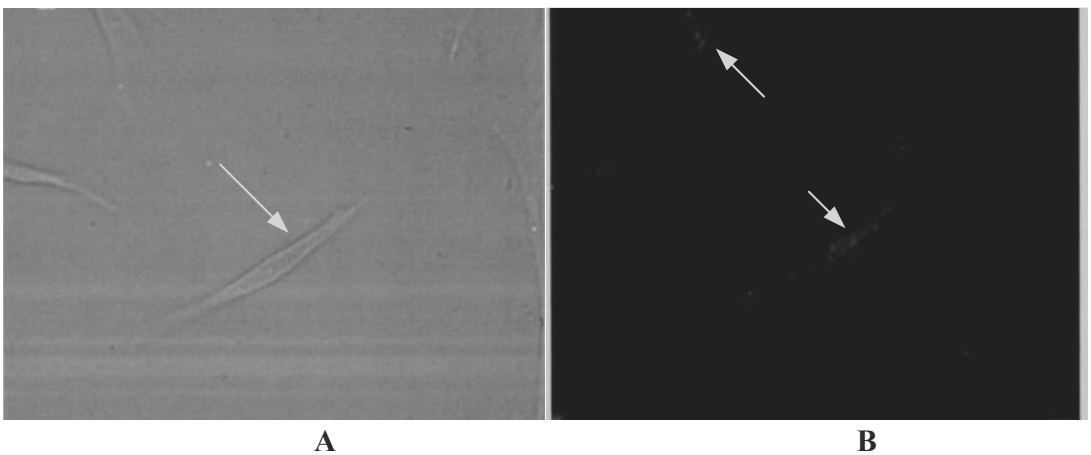

Fig. 1. *The transfection efficiency of MP-infected MRC-5 cells was observed under a fluorescence microscope (40×). **A)** infected cells under light vision; **B)** infected cells under fluorescence vision.*

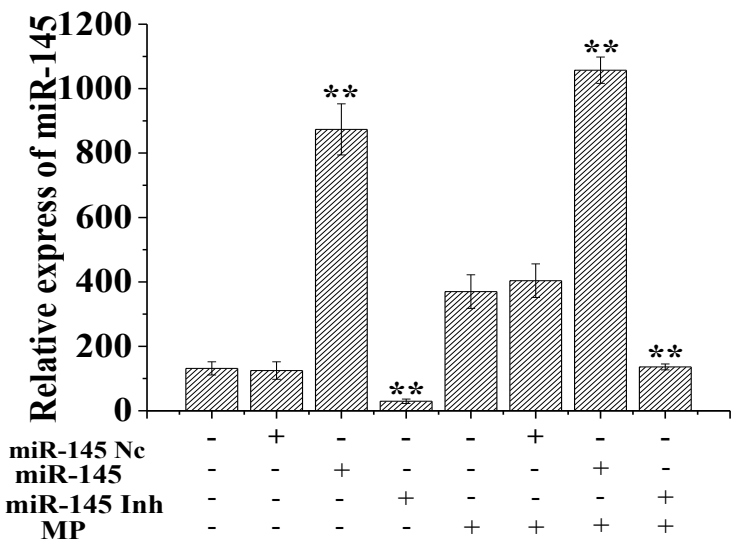

Fig.2. *Effect of MP on the expression of miR-145 in MRC-5 cells (** P < 0.01, compared with the control group)*

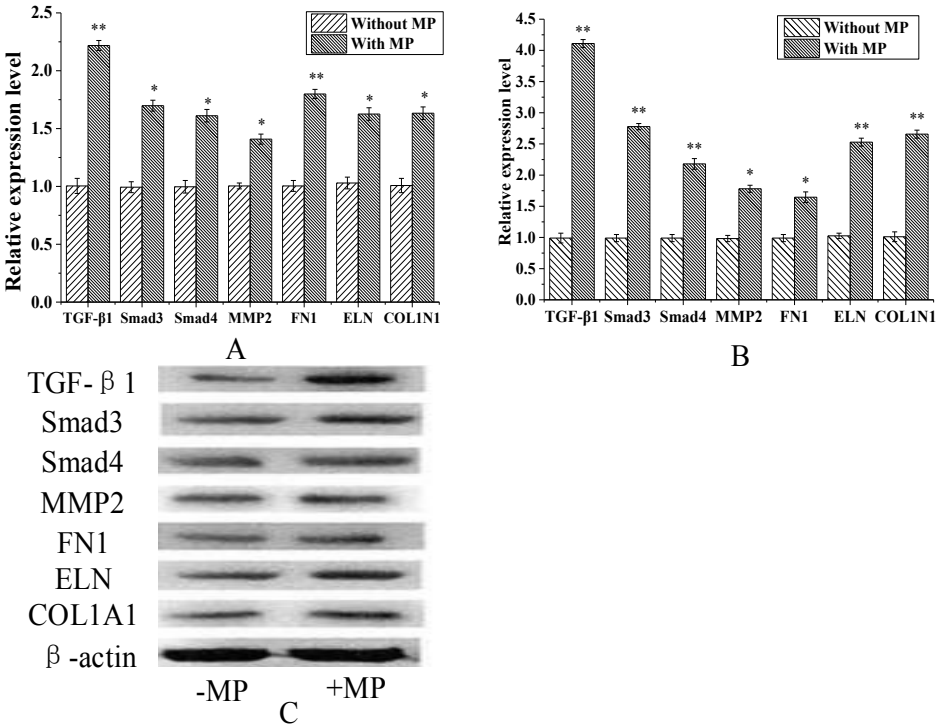

Fig. 3. *Differential expression of genes of the TGF-β/Smad pathway in MP-infected MRC-5 cells.* ***A)*** *mRNA level;* ***B)*** *protein level;* ***C)*** *Western blotting map, (* P < 0.05, ** P < 0.01, compared with the control group).*

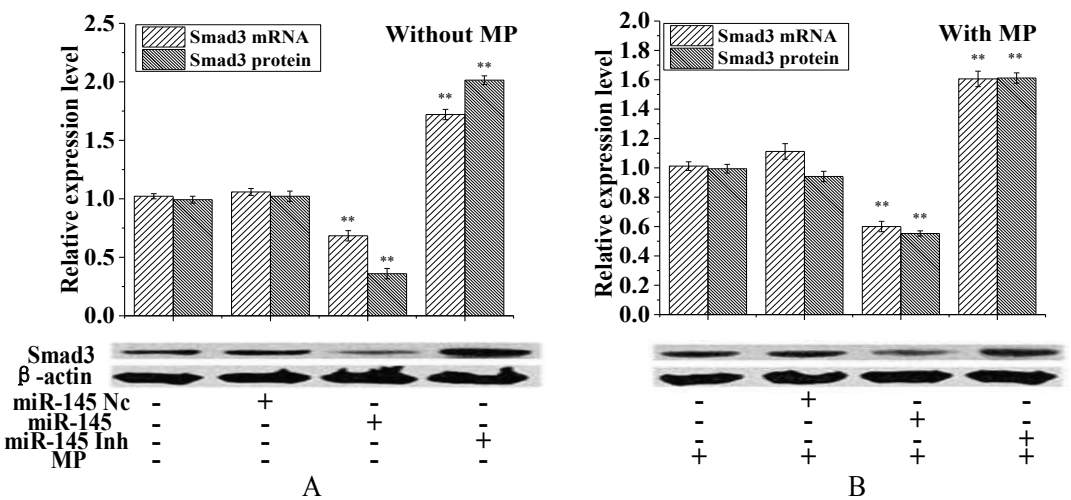

Fig. 4. *The effect of miR-145 on the mRNA and protein expression of Smad3 (** P < 0.01, compared with the transfection NC group).* ***A)*** *not infected with MP;* ***B)*** *infected with MP.*

MiR-145 inhibited Smad3 expression in MRC-5 cells

As shown in Fig. 4 and compared with that in the group transfected with NC, the expression of Smad3, a target gene of miR-145, was affected by miR-145 mimics and inhibitors. The regulatory effect of miR-145 on Smad3 expression was further confirmed by Western blotting and qPCR assays, which showed that, as compared with the control group, the MP-infected MRC-5 cells showed significantly different expression of Smad3. In particular, the expression of Smad3 in the miR-145 mimics group was significantly decreased ($P < 0.01$), while the expression of Smad3 in the miR-145 inhibitors group was significantly increased ($P < 0.01$).

Role of miR-145 in the fibrosis-promoting TGF-β/Smad pathway in MP-infected MRC-5 cells

As shown in Fig. 5 and compared with that in the NC group, the expression of genes in the TGF-β/Smad signaling pathway was inhibited by miR-145 mimics and enhanced by miR-145 inhibitors. Combining with Fig. 5, it can be seen that MP-infected MRC-5 cells showed increased expression of related factors along the TGF-β/Smad signaling pathway, whereas miR-145 inhibited the expression of related factors along the Smad3 signaling pathway, thus inhibited the activation of the fibrosis-promoting TGF-β/Smad pathway.

DISCUSSION

MiRNAs are highly conserved non-coding small RNAs with the ability to inhibit the translation of their target genes by binding to the 3'-UTR of their target mRNAs, thus affecting numerous physiological and pathological processes such as cell development, differentiation, immunity, and inflammation (13). In particular, miR-145 plays an important regulatory role in natural immune responses. When its host cells are invaded by pathogenic microorganisms, miR-145 expression is increased to fight against pathogenic microorganisms while participating in immune regulation (14). In this experiment, the expression of miR-145 in MP-infected MRC-5 cells was detected by real-time fluorescence quantitative PCR, and the results showed that the expression of miR-145 in these cells increased over time.

Excessive deposition of extracellular matrix is the most obvious feature of fibrosis, while the imbalance in extracellular matrix metabolism is usually the main cause for the excessive deposition of extracellular matrix (15). In addition, abnormal activation of signal pathways involved in tissue repair and inflammation may also cause fibrosis (16). For example, as a powerful fibroblast chemoattractant with the ability to promote the synthesis of extracellular matrix, such as type I collagen and type III collagen, to promote the synthesis of fibronectin by fibroblasts, to regulate the production of collagenogen and other proteins, and to regulate the expression of cell matrix adhesion protein receptor, TGF-β plays an important role in progressive fibrosis (17). In fact, fibroblasts can synthesize TGF-β to stimulate themselves, thus forming a positive feedback. The continuous increase in TGF-β synthesis can promote the activation of the fibrosis signaling pathway via TGF-β/Smad, resulting in the accumulation of extracellular matrix and the onset of fibrosis (18). In this experiment, the expression of fibrosis-related genes was detected after MRC-5 cells were infected with MP. The results showed that the expression of TGF-β was significantly increased by MP infection and may play an essential role in the onset of fibrosis.

The TGF-β/Smad signaling pathway plays an important role in promoting fibrosis. When the TGF-β ligand binds to its type I receptor, Smad2 and Smad3 are phosphorylated by TGF-β type I receptor kinase. As a result, phosphorylated Smad2 and Smad3 bind to Smad4 to form a complex, which then translocates into the nucleus to regulate gene expression. Interestingly, Smad2 and Smad3 belong to a receptor-binding activation type, while Smad4 belongs to a universal type. The maximum affinity of recombinant Smad3 and Smad4 to DNA is derived from their base sequence CAGAC. In addition, TGF-β-mediated phosphorylation of Smad3 increases the association between Smad3 and transcription cofactor p30, while the induction of gene expression by TGF-β requires the presence of p300. Furthermore, Smad2 does not directly bind to DNA during the above process. Instead, Smad2 binds to Fast 1 of the Fast family to activate DNA

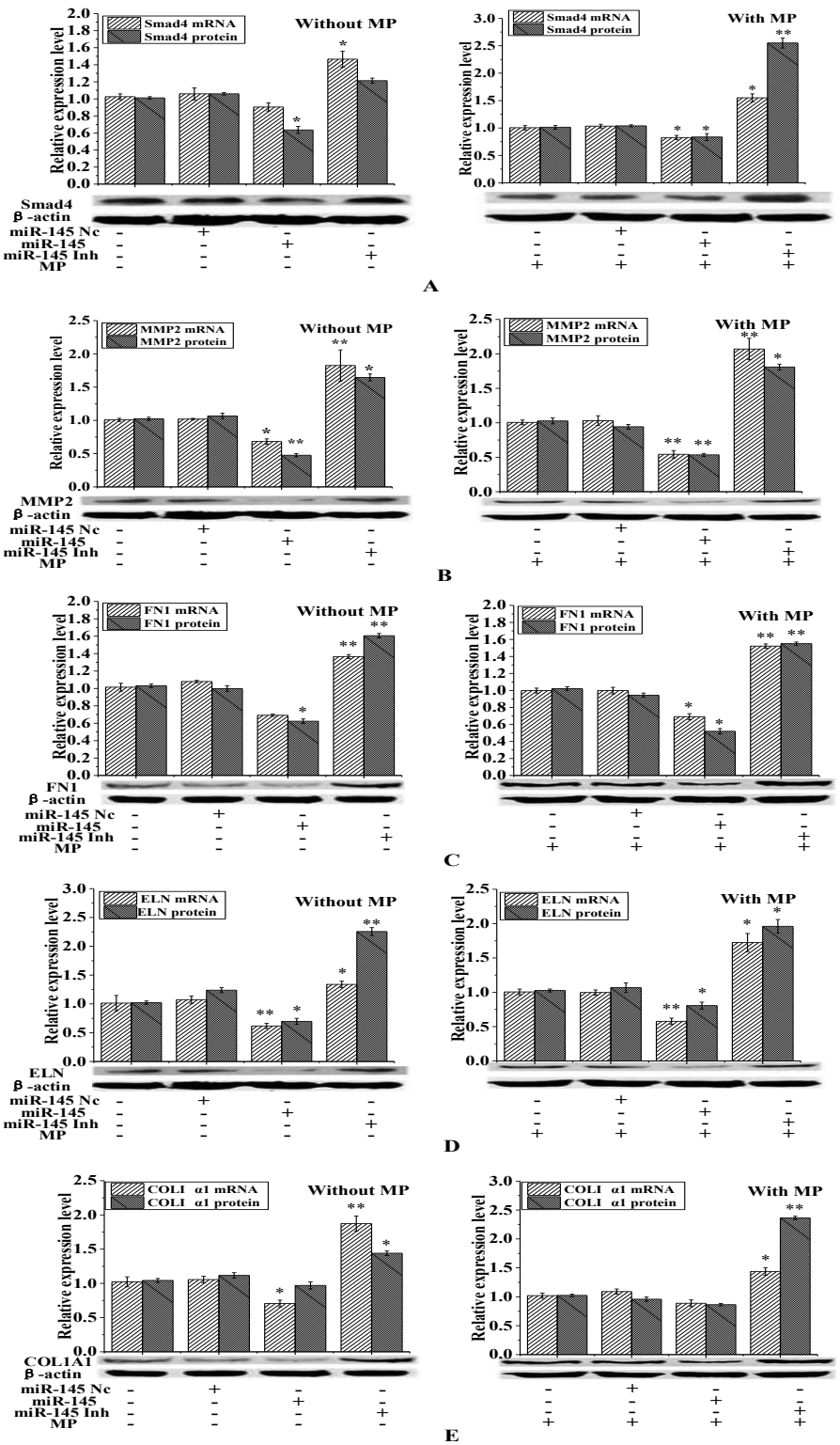

Fig. 5. *The effects of miR-145 on the mRNA and protein expressions of Smad4, MMP2, FN1, ELN and COLI α1.* ***A****) The effects of miR-145 on the mRNA and protein expression of Smad4;* ***B****) the effects of miR-145 on the mRNA and protein expression of MMP2;* ***C****) the effects of miR-145 on the mRNA and protein expression of FN1;* ***D****) the effects of miR-145 on the mRNA and protein expression of ELN;* ***E****) the effects of miR-145 on the mRNA and protein expression of COLI α1; * P < 0.05, ** P < 0.01, compared with the transfection NC group.*

transcription (19). This study confirmed that, as a target gene of miR-145, Smad3 expression is negatively regulated by miR-145. In addition, the inhibitory effect of miR-145 on Smad3 expression was confirmed at both the mRNA and protein levels in this study. The expression of factors along the TGF-β/Smad signaling pathway indicated that miR-145 exerted a certain inhibitory effect on the TGF-β/Smad signaling by targeting Smad3.

In conclusion, the infection of MRC-5 cells by MP increases the expression of miR-145, which in turn negatively regulates the expression of Smad3 and inhibits the activation of the TGF-β/Smad signaling pathway. The results of this study may provide helpful information for using miR-145 in the target gene therapy of pulmonary fibrosis.

REFERENCES

1. Xue D, Ma Y, Li M, Li Y, Luo H, Liu X, Wang Y. Mycoplasma ovipneumoniae induces inflammatory response in sheep airway epithelial cells via a MyD88-dependent TLR signaling pathway. Vet Immunol Immunopathol 2015; 163(1-2):57-66.
2. Flaherty KR, Colby TV, Travis WD, et al. Fibroblastic foci in usual interstitial pneumonia: idiopathic versus collagen vascular disease. Am J Respir Crit Care Med 2003; 167(10):1410-15.
3. Meyer KC. Pulmonary fibrosis, part I: epidemiology, pathogenesis, and diagnosis. Expert Rev Respir Med 2017; 11(5):343-59.
4. Xu X, Dai H, Wang C. Epithelium-dependent profibrotic milieu in the pathogenesis of idiopathic pulmonary fibrosis: current status and future directions. Clin Respir J 2016; 10(2):133-41.
5. Xu F, Liu C, Zhou D, Zhang L. tgf-β/smad pathway and its regulation in hepatic fibrosis. J Histochem Cytochem 2016; 64(3):157-67.
6. Sun W, Tang H, Gao L, et al. Mechanisms of pulmonary fibrosis induced by core fucosylation in pericytes. Int J Biochem Cell Biol 2017; 88:44-54.
7. Lee CM, Park JW, Cho WK, et al. Modifiers of TGF-β1 effector function as novel therapeutic targets of pulmonary fibrosis. Korean J Intern Med 2014; 29(3):281-90.
8. Park SA, Kim MJ, Park SY, et al. EW-7197 inhibits hepatic, renal, and pulmonary fibrosis by blocking TGF-β/Smad and ROS signaling. Cell Mol Life Sci 2015; 72(10):2023-39.
9. Xu Y, Qin S, An T, Tang Y, Huang Y, Zheng L. MiR-145 detection in urinary extracellular vesicles increase diagnostic efficiency of prostate cancer based on hydrostatic filtration dialysis method. Prostate 2017; 77(10):1167-75.
10. Wang W, Ji G, Xiao X, et al. Epigenetically regulated miR-145 suppresses colon cancer invasion and metastasis by targeting LASP1. Oncotarget 2016; 7(42):68674-87.
11. Minami K, Taniguchi K, Sugito N, et al. MiR-145 negatively regulates Warburg effect by silencing KLF4 and PTBP1 in bladder cancer cells. Oncotarget 2017; 8(20):33064-77.
12. Wang L, Wu X, Wang B, Wang Q, Han L. Mechanisms of miR-145 regulating invasion and metastasis of ovarian carcinoma. Am J Transl Res 2017; 9(7):3443-51.
13. Haneklaus M. Analysis of post-transcriptional gene regulation of nod-like receptors via the 3'UTR. Methods Mol Biol 2016; 1390:197-211.
14. Sasaki T, Brakebusch C, Engel J, Timpl R. Mac-2 binding protein is a cell-adhesive protein of the extracellular matrix which self-assembles into ring-like structures and binds beta1 integrins, collagens and fibronectin. EMBO J 1998; 17(6):1606-13.
15. Aschner Y, Khalifah AP, Briones N, et al. Protein tyrosine phosphatase α mediates profibrotic signaling in lung fibroblasts through TGF-β responsiveness. Am J Pathol 2014; 184(5):1489-502.
16. Kang J H, Jung M Y, Yin X, Andrianifahanana M, Hernandez DM, Leof EB. Cell-penetrating peptides selectively targeting SMAD3 inhibit profibrotic TGF-β signaling. J Clin Invest 2017; 127(7):2541-54.
17. Zheng X, Qi C, Zhang S, Fang Y, Ning W. TGF-β1 induces Fstl1 via the Smad3-c-Jun pathway in lung fibroblasts. Am J Physiol Lung Cell Mol Physiol. 2017; 313(2):L240-51.
18. Ma F, Li Z, Cao J, Kong X, Gong G. A TGFBR2/SMAD2/DNMT1/miR-145 negative regulatory loop is responsible for LPS-induced sepsis. Biomed Pharmacother 2019; 112:108626.
19. Paloschi MV, Pontes AS, Soares AM, Zuliani JP. An update on potential molecular mechanisms underlying the actions of snake venom L-amino acid oxidases (LAAOs). Curr Med Chem 2018; 25(21):2520-30.

STAT3 SIGNALING PATHWAY IN DRUG-RESISTANT BLADDER CANCER CELL LINE

T. LEI[1,2*], S. ZHOU[1*], Q. MENG[1,2] and M. ZHANG[1,2,3]

[1]Department of Clinical Laboratory Medicine, Beijing Shijitan Hospital, Capital Medical University, Beijing, China; [2]Beijing Key Laboratory of Urinary Cellular Molecular Diagnostics, Beijing, China; [3]Department of Clinical Laboratory Medicine, Peking University Ninth School of Clinical Medicine, Beijing, China

Received February 18, 2019 – Accepted June 10, 2019

[*]These authors contributed equally to this work

STAT3 signaling pathway is related to the proliferation, apoptosis and metastasis of tumor cells. The relationship between STAT3 and drug resistance is still unknown. We studied the inhibitors in STAT3 pathway and its downstream molecules to analyze the unique effects in drug-resistant bladder cancer cells. qRT-PCR and Western blot were implemented to study the expression level of JAK2, STAT3, p-STAT3, MMP2 and Cyclin D1 in Pumc-91 and Pumc-91/ADM cell lines, respectively. The effects of AG490 on the expression of STAT3, p-STAT3, MMP2 and Cyclin D1 in Pumc-91 were evaluated using qRT-PCR and Western blot. Pumc-91/ADM cells were treated with AG490. CCK-8 and wound healing assay were used to detect the cell proliferation and metastasis. Compared to Pumc-91, an obvious decrease of JAK2, p-STAT3 and increase of MMP2 were shown in Pumc-91/ADM cell line. After inhibition of STAT3 signaling pathway, the mRNA and protein levels of STAT3, p-STAT3, MMP2 and Cyclin D1 obviously decreased in the test group. The proliferation and migration of Pumc-91/ADM were suppressed by inhibiting of STAT3. STAT3 pathway regulated the proliferation and migration of bladder cancer drug-resistant cells by modulating the expression of Cyclin D1 and MMP2.

Bladder cancer is one of the most common tumors in the genitourinary system (1), and its biological characteristics make it susceptible to drug resistance, migration and recurrence (2). Approximately 30% of bladder tumors are muscle invasive and have a high risk of death from metastases; 70% of bladder cancer is non-muscle invasive tumors with a high rate of recurrence, despite several post-operative chemotherapeutic agents or immune-therapy for its prevention (3). Drug resistance is also a nearly intractable issue widespread in many kinds of tumor, including bladder cancer. Numerous studies have revealed several mechanisms that contribute to drug resistance including drug inactivation and alterations in the drug target, modification of cell cycle checkpoints and increased DNA damage repair, drug efflux and decreasing drug influx (4). The development of drug resistance greatly hinders effective cancer therapy. Several lines of evidence indicated that acquisition of multidrug resistance by cancer cells is usually accompanied by enhanced cell proliferation and metastasis (5). Recent advances

Key words: bladder cancer; signal transducer and activator of transcription 3(STAT3) AG490; signaling pathway; drug resistance bladder cancer

Corresponding Author:
Man Zhang, M.D., Ph.D,
No.10 Tieyi Road,
Haidian District, Beijing Shijitan Hospital,
Capital Medical University, Beijing, 100038, China
Tel.: +86 010 63926389 - Fax: +86 010 63926283
e-mail: zhangman@bjsjth.cn

0393-974X (2019)

in cancer research have demonstrated that cross activation of other signaling pathways during development of drug resistance may increase the potential of drug-resistant cancer cells (6). Recently, many studies focused on increasing chemotherapy drug sensitivity and reducing tumor metastasis. However, the signaling pathway of metastasis and recurrence is not very clear in bladder cancer drug resistance.

Signal transducers and activators of transcription 3 (STAT3) are transcription factors which can be activated by growth factor receptors and non-receptor tyrosine kinases in cytoplasm (7). When cytokine or growth factor (e.g. EGF, TGF-α, IL-6, HGF and oncogenic kinases) induced its upstream Janus-associated kinase (JAK), STAT3 was activated. The activated STAT3 translocated into nucleus and bound with DNA to regulate the expression of the target genes including Cyclin D1, Bcl-2, Bcl-xL, matrix metalloproteinases (MMPs) and vascular endothelial growth factor (VEGF) (8). These proteins encoded by the target genes are related to the proliferation, apoptosis and metastasis of tumor cells, which could cause tumor initiation, progression and metastasis. Consequently, constitutive activation of STAT3 is responsible for a variety of human cancers, including head and neck, breast, gastric, ovarian, prostate and pancreatic cancers, as well as leukemia (9-12). STAT3 expresses in a variety of cells and tissues *in vivo*. In normal cells, the activation of STAT3 is fast and short and the normal physiological process is essential (13-15). Blocking JAK/STAT3 signal might inhibit the growth of human cancers.

AG490, a STAT3 inhibitor, has been shown to effectively inhibit STAT3 activation, block JAK2/STAT3 signaling pathway, inhibit tumor cell proliferation, induce apoptosis and increase the sensitivity of chemotherapy drugs (16). In recent years, AG490 was reported to inhibit the growth of head and neck squamous cell, lung, colorectal, breast, prostate and bladder cancers as well as leukemia, lymphoma and other tumor cells, while the toxicity of normal cells was very small (17-20).

In this study, the expression levels of JAK2, STAT3, p-STAT3, MMP2 and Cyclin D1 were detected in human bladder cancer adriamycin-resistant cell line (Pumc-91/ADM) and its parental cell line (Pumc-91). When AG490 inhibited the activity of STAT3 signaling pathway, we studied the expression of STAT3 and the downstream molecules, and then verified with functional experiments.

MATERIALS AND METHODS

Cell culture and treatments

The human bladder cancer cell (Pumc-91) was kindly provided by the Cell Laboratory of Peking Union Medical College Hospital. Pumc-91/ADM was a drug-resistant cell line established by adding the dosage of adriamycin (aladdin, China) gradually. The final concentration of adriamycin was 1.0 ug/ml. Pumc-91 cells were cultured in RPMI 1640 medium (Gibco, USA) supplemented with 10% fetal bovine serum (Dingguo Biotechnology, China), and Pumc-91/ADM cells with 18% fetal bovine serum. Cell cultures were maintained at 37°C in a humidified incubator with 5% CO_2.

qRT-PCR

Total RNA was extracted with TRIzol reagent (Ambition, Life Technologies, USA) from Pumc-91 and Pumc-91/ADM cells according to the manufacturer's instructions. cDNA was generated by 2 μg of total RNA from each sample, Oligo d (T) (Dingguo Biotech), dNTP (Genview) under the action of M-MLV reverse transcriptase (Promega). qRT-PCR was performed using Roche LightCycler 480 Real Time PCR System with TransStart Top Green qPCR SuperMix (TransGen Biotech, China). The PCR primer sequences used were as followed: JAK2 forward: 5'-TACCAACCTCACCAACATTA-3' and reverse: 5'-TAGTCTCCTACTTCTCTTCGT-3'; GAPDH forward: 5'-TTTGGTATCGTGGAAGGACT-3' and reverse: 5'-AGTAGAGGCAGGGATGATGT-3'; STAT3 forward: 5'-AGAAAACTCTCACGGACGA-3' and reverse: 5'- TTGTTGACGGGTCTGAAGT-3'; MMP2 forward: 5′-TTGATGGCATCGCTCAGATC-3′ and reverse: 5′-CTGCGAAGAACACAGCCTTC-3′; Cyclin D1 forward: 5′-TGACTGCCGAGATGTTGTGC-3′ and reverse: 5′-GAGGGTGGGTTGGAAATGAA-3′; ANXA1 forward: 5' -TGTGAATGAAGACTTGGCTG-3' and reverse: 5'-ACTCTGCGAAGTTGTGGATA-3'; GAPDH forward: 5'-TTTGGTATCGTGGAAGGACT-3' and

reverse: 5'-AGTAGAGGCAGGGATGATGT-3'. Relative mRNA expression normalized to GAPDH expression was calculated. $2^{-\Delta\Delta Ct}$ method was used to evaluate the relative gene mRNA expression. All of the tests were repeated at least three times.

Western blot

Pumc-91/ADM and Pumc-91 cell lines were collected and washed three times with PBS. Protein extracts were prepared using a total protein extraction kit (KeyGen, Nanjing, China) according to the manufacturer's instructions. RIPA buffer (1%Triton X-100, 1% SDS, 20 mM Na_2HPO_4 and 0.2 mM PMSF) was used to lyse cells. Protein (100 μg) per sample was separated in 8% sodium dodecyl sulfate polyacrylamide gel electrophoresis (SDS-PAGE) and electrotransferred to a polyvinylidene difluoride (PVDF) membrane (Bio-Rad, USA) for 1 h at 12V. The membranes were blocked in solution with 5% nonfat dry milk in phosphate buffered saline with Tween-20 (PBST) for 2 h at room temperature. The membranes were incubated overnight at 4°C with mouse or rabbit primary antibodies (Abcam, USA) against JAK2, STAT3, p-STAT3, MMP2 and Cyclin D1 dilutions of 1:1000, 1:1000, 1:1000, 1:500, 1:500, respectively and β-actin (ZhongShan Co., China) at a dilution of 1:300. Subsequently, the membranes were incubated peroxidase-conjugated goat anti-mouse IgG antibody or anti-rabbit IgG antibody at a dilution of 1:1000 in horseradish for 1.5 h at room temperature. Immunobands were detected by enhanced HRP-DAB chromomeric kit. The Image-Pro Plus v 6.0 software (MEDIA CYBERNETICS, USA) was adopted to analyze the integrated optical density (IOD) value of every band. All of the tests were repeated at least three times.

Cell viability assay

The Cell Counting Kit-8 (CCK-8) (Dojindo) cell proliferation assay system was used to analyze the effects of AG490 on Pumc-91/ADM cell proliferation. Pumc-91/ADM cells were seeded to a final density of 8×10^3 cells per well in 96-well culture plates and incubated at 37°C in 5% CO2 for 12 h. The cells were incubated with 0, 50, 100, 200 μM of AG490, respectively. RPMI-1640 cultured medium without cells served as a vehicle control and 0 μM group served as a negative control. After cells were treated with AG490 for 24 h, 48 h and 72 h, 10 μl of CCK-8 was added to each well and incubated for 2 h at 37°C. The microplate reader (Model 680, BioRad Laboratories, Hercules, CA, USA) was used to measure the absorbance at a wavelength of 450 nm and 655 nm. All of the tests were repeated at least three times.

Scratch wound assay

Scratch wound assay was used to analyze the effects of AG490 on Pumc-91/ADM cell migration. Pumc-91/ADM cells were seeded to a final density of 10^4 cells per well in 24-well culture plates and incubated at 37°C in 5% CO2 for 12 h to create confluent mono-layers. The mono-layers were scratched using a pipette tip and washed with PBS. The cells

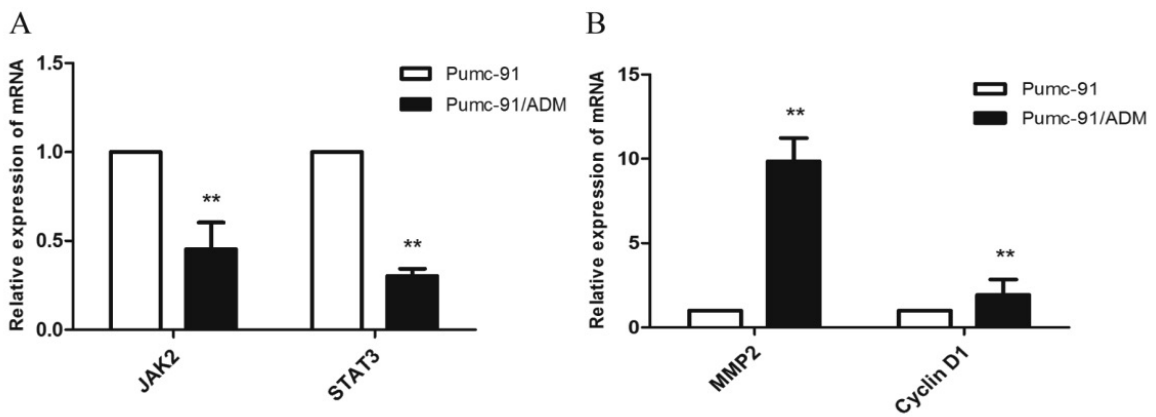

Fig. 1. *The relative expression of mRNA levels in Pumc-91 and Pumc-91/ADM cells. Results were expressed as a ratio of target gene to housekeeping gene (GAPDH). **P<0.01. **A**)The mRNA levels of JAK2 and STAT3 in Pumc-91 and Pumc-91/ADM cells. **B**) The mRNA levels of MMP2 and Cyclin D1 in Pumc-91 and Pumc-91/ADM cells.*

were treated with 0, 100, 200 μM of AG490, respectively. 0 μM acted as the control group. To measure cell migration, the images of wound were captured at 3 random fields 0, 24, 48 and 72 h after scratching. The cure rate was calculated using the following equation: cure rate (%) = (mono-layers distance before healing − mono-layers distance after healing)/mono-layers distance before healing.

Statistical analysis

All results were expressed as mean ± SEM. Statistical analysis was performed by Student's *t*-test for comparisons between two groups and ANOVA-test for multiple comparison test using SPSS 17.0 software (SPSS lnc., Chicago, USA). $P<0.05$ was considered statistically significant.

RESULTS

The mRNA levels of STAT3 signaling pathway molecules in multidrug-resistant bladder cancer cells

qRT-PCR was implemented to research the mRNA levels of JAK2, STAT3, MMP2 and Cyclin D1 in Pumc-91 and Pumc-91/ADM cell lines (Fig. 1). The levels of mRNA in Punc-91/ADM cells were 0.45±0.15-fold lower than in Pumc-91 cells for STAT3, 0.30±0.04-fold lower than in Pumc-91 cells for JAK2. The levels of mRNA in Punc-91/ADM cells were 9.86±1.37-fold higher than in Pumc-91 cells for MMP2, 1.93±0.92-fold higher than in Pumc-91 cells for Cyclin D1. Compared to Pumc-91, an obvious decrease of JAK2, STAT3 and increase of MMP2 were shown in Pumc-91/ADM. The difference was statistically significant ($P<0.05$). However, there was no difference in Cyclin D1 expression between two cell lines ($P>0.05$).

The expression of STAT3 signaling pathway molecules in multidrug resistance bladder cancer cells

Western blot analysis was performed to determine the protein expression level of JAK2, STAT3, p-STAT3, MMP2 and Cyclin D1 in Pumc-91/ADM and Pumc-91 cell lines (Fig. 2). The expression

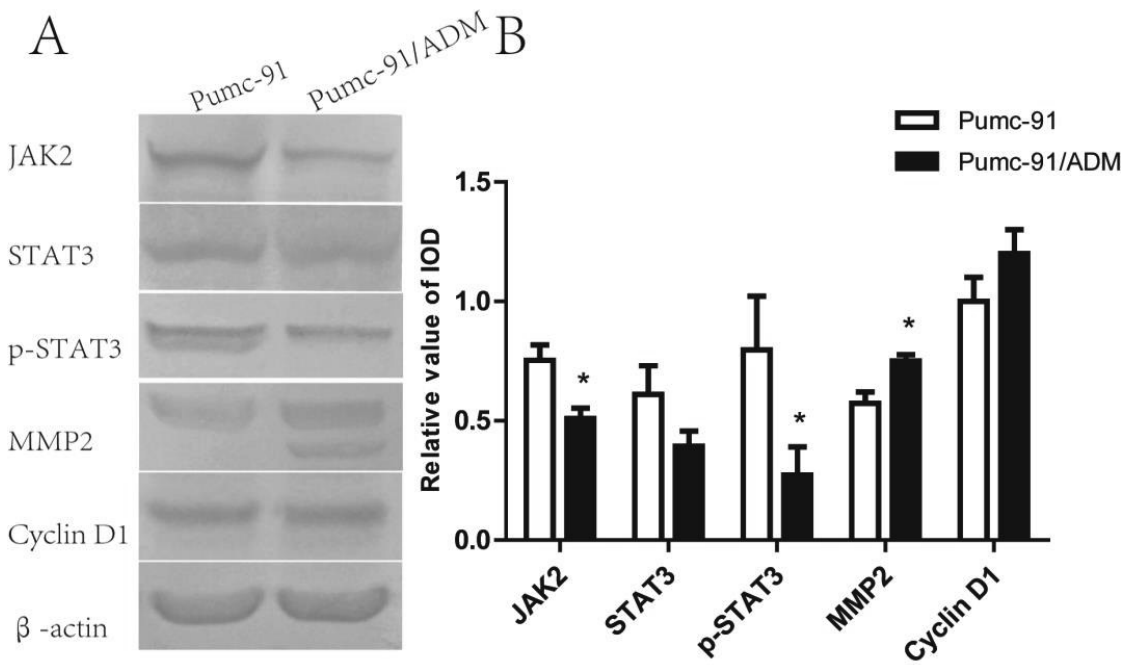

Fig. 2. *The expression of JAK2, STAT3, p-STAT3, MMP2 and Cyclin D1 at the protein levels examined by Western blot in Pumc-91 and Pumc-91/ADM cells. **A**) Electrophoregram. **B**) bar graph. *p<0.05.*

level of JAK2 was 0.75±0.06 in Pumc-91 cells, 0.51±0.04 in Pumc-91/ADM cells. The expression level of STAT3 was 0.61±0.12 in Pumc-91 cells, 0.39±0.06 in Pumc-91/ADM cells. The expression level of p-STAT3 was 0.79±0.22 in Pumc-91 cells, 0.27±0.11 in Pumc-91/ADM cells. The expression level of MMP2 was 0.57±0.04 in Pumc-91 cells, 0.75±0.02 in Pumc-91/ADM cells. The expression level of Cyclin D1 was 1.03±0.07 in Pumc-91 cells, 1.20±0.08 in Pumc-91/ADM cells. The expression levels of JAK2, p-STAT3 were up-regulated in the Pumc-91/ADM compared to Pumc-91 cell line, while MMP2 expression increased. The difference was statistically significant (P<0.05). However, there was no difference in STAT3 and Cyclin D1 expression between two cell lines (P>0.05).

After inhibition of STAT3 signaling pathway, the mRNA levels of STAT3 signaling pathway molecules in multidrug-resistant bladder cancer cells

After Pumc-91/ADM cells were treated with 200 μM of AG490 for 48 h, qRT-PCR was implemented to research the mRNA levels of STAT3, MMP2 and Cyclin D1 in control group and test group (Fig. 3). The levels of mRNA in AG490 group were 0.34±0.07-fold lower than in control group for STAT3, 0.32±0.06-fold lower than in control group for JAK2. The levels of mRNA in AG490 group were 2.50±0.50-fold higher than in control group for MMP2, respectively. Compared to the control group, an obvious decrease of STAT3, MMP2 and Cyclin D1 in test group was found. The difference was statistically significant (P<0.05).

After inhibition of STAT3 signaling pathway, the expression of STAT3 signaling pathway molecules in multidrug resistance bladder cancer cells

After Pumc-91/ADM cells were treated with 200 μM of AG490 for 48 h, Western blot analysis evaluated the effects of AG490 on the expression of STAT3, p-STAT3, MMP2 and Cyclin D1 in the control group and test group (Fig. 4). The expression

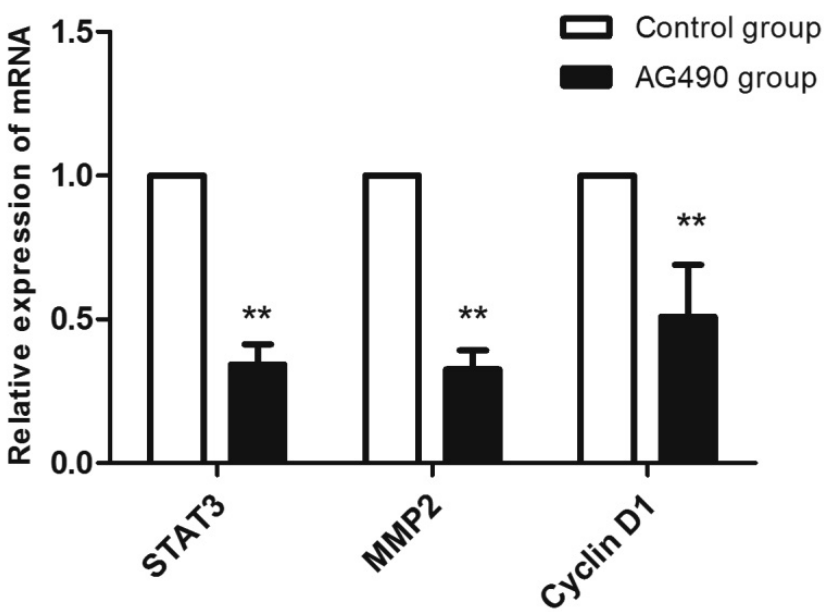

Fig. 3. *The expression of STAT3, MMP2 and Cyclin D1 at the mRNA level examined by q-PCR in Pumc-91/ADM cells. Cells were treated with 200 mM of AG490 for 48 h. Results were expressed as a ratio of target gene to housekeeping gene (GAPDH). **P<0.01 compared with the control group.*

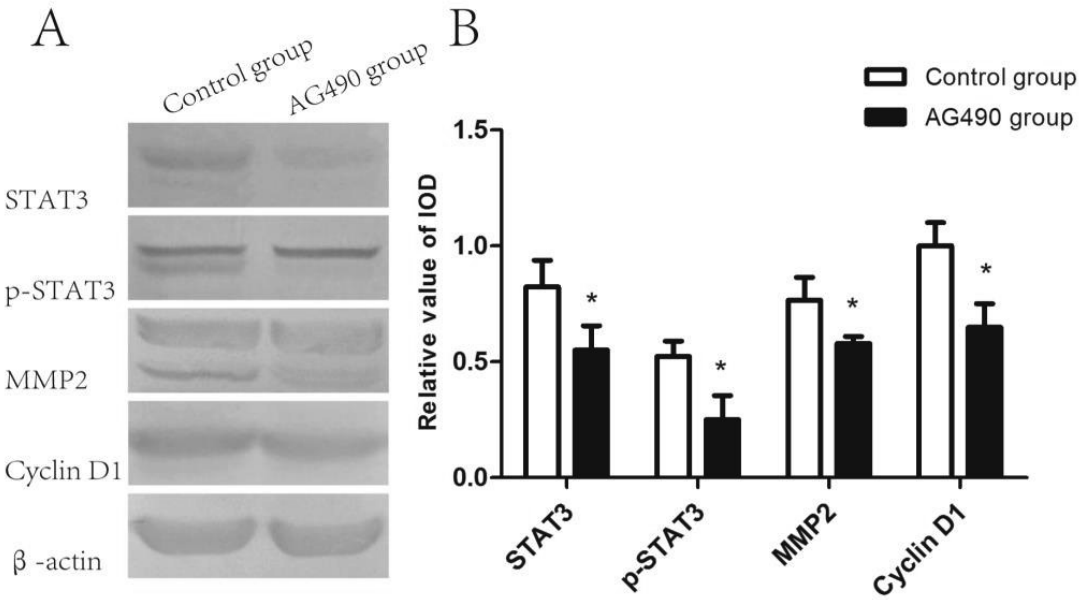

Fig. 4. *The expression of STAT3, p-STAT3, MMP2 and Cyclin D1 at the protein level examined by Western blot in Pumc-91/ADM cells. Cells were treated with 200 μM of AG490.* ***A****) Electrophoregram.* ***B****) bar graph. *P<0.05.*

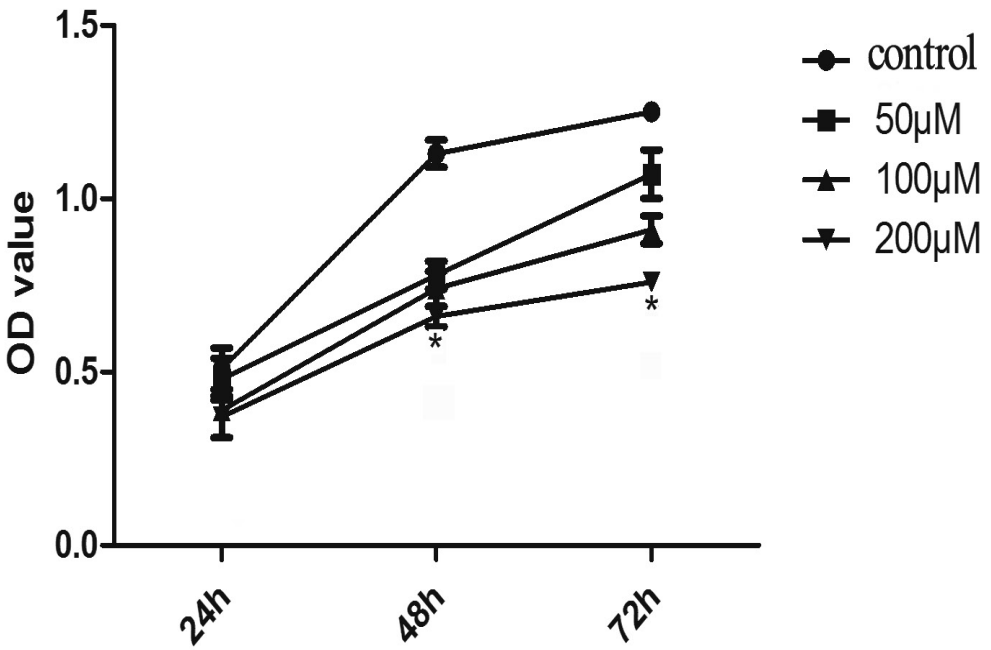

Fig. 5. *Proliferation inhibitory effect of AG490 in Pumc-91/ADM cells. Pumc-91/ADM cells were treated with 0, 50, 100, 200 μM of AG490. The cells were cultured for 24, 48 and 72 h respectively.*

level of STAT3 was 0.82±0.11 in the control group, 0.55±0.10 in AG490 group. The expression level of p-STAT3 was 0.52±0.06 in the control group, 0.25±0.10 in AG490 group. The expression level of MMP2 was 0.76±0.09 in the control group, 0.58±0.03 in AG490 group. The expression level of Cyclin D1 was 1.00±0.11 in control group, 0.65±0.09 in AG490 group. The expression levels of STAT3, p-STAT3, MMP2 and Cyclin D1 were down-regulated in the test group compared to the control group. The difference was statistically significant (P<0.05).

Proliferation inhibitory effect of AG490 in Pumc-91/ ADM cells

Cell Counting Kit-8 (CCK-8) was used to detect the impact of AG490 on cell proliferation (Fig .5). At the action time of 24 h, the OD value of control, 50 μM, 100 μM and 200 μM groups were 0.50±0.06, 0.48±0.04, 0.39±0.02, 0.37±0.06, respectively. Compared to the control group, 50 μM group was not statistically significant (p>0.05), 100 μM and 200 μM groups were significantly different (p<0.05). In the 50 μM group compared with the 100 μM and 200 μM groups, respectively, the difference was statistically significant (p<0.05). There was no significant difference between the 100μM and 200 μM groups (p>0.05). At the action time of 48 h, the OD value of control, 50 μM, 100 μM and 200 μM groups were 1.13±0.04, 0.78±0.04, 0.74±0.05, 0.66±0.03, respectively. Compared to the control group, there was significant difference in the 50 μM, 100 μM and 200 μM groups (p<0.05). In the 50 μM group compared with 100 μM group, the difference was not statistically significant (p>0.05), but compared with 200 μM group, the difference was statistically significant (p<0.05). There was significant difference between the 100 μM and 200 μM groups (p<0.05). At the action time of 72 h, the OD value of control, 50 μM, 100 μM and 200 μM groups were 1.25±0.01, 1.07±0.07, 0.91±0.04, 0.76±0.02, respectively. There were significant differences among the groups (p<0.05). AG490 inhibited the proliferation of Pumc-91/ ADM cells, and the inhibition depended on the dose of AG490.

Migration inhibitory effect of AG490 in Pumc-91/ ADM cells

Wound closure assay was adopted to analyze the effects of AG490 on cell migration (Fig. 6). After Pumc-91/ADM cells were treated with100 μM, 200 μM of AG490, the cells were cultured for 0, 24, 48 and 72 h, respectively. We used wound healing assay to analyze the effects of AG490 on cell migration and drew the cure rate curves of cells treated with different times. In control group, the healing rates of 24, 48, 72 h were 10.67±0.57%, 49.00±1.00% and 98.00±2.00%, respectively. In the 100 μM group, the cure rates of 24, 48, 72h were 10.33±0.57%, 23.67±3.05% and 48.00±3.00%, respectively. The difference was statistically significant (p<0.05). In the 200 μM group, the cure rates of 24, 48, 72 h were 9.67±1.15%, 15.67±2.51% and 24.66±2.52%, respectively. The difference was statistically significant (p<0.05). Compared to the control group, the cure rates of the 100 μM, 200 groups were reduced gradually along with the increasing concentration of AG490. AG490 inhibited the migration of Pumc-91/ADM cells, and the inhibition depended on the dose of AG490.

DISCUSSION

STAT3 is a member of the transcription factors that plays major roles in cytokine signaling (21). This transcription factor has been shown to regulate the expression of genes involved in cell proliferation, anti-apoptosis angiogenesis and metastasis, such as cyclin D1, VEGF, Bcl-2, Bcl-xL, survivin and MMPs (22). In our present study, we used AG490, a well-known inhibitor of Jak2/ STAT3 signal transduction pathway, to block this signaling pathway (23). AG490 is one of the natural organic sulfur-containing compounds with no known side-effects. Therefore, AG490 has been widely used in the treatment of many kinds of tumors, such as leukemia, lymphoma, liver and bladder cancers (24). It was reported that AG490 could inhibit the proliferation of bladder cancer cells by inhibiting STAT3 phosphorylation and blocking the STAT3 signal transduction pathway (25). Eriksen et al. (26) reported that AG490 inhibited cytokine-induced tumor cell mitosis

by blocking STAT3 signal pathway and reducing Mcl-1 expression in T-cell lymphoma cells. Recently, many groups have reported synergistic anti-cancer effect in combination treatment with chemotherapeutic agents and AG490 in *in vitro* and *in vivo* cancer models. Joung et al. (27) showed that oral administration of AG490 and MSM (a natural sulfur compound) combination significantly inhibited the growth of tumor xenografts *in vitro*. In our study, AG490 could successfully block STAT3 signaling pathway by inhibiting the expression of p-STAT3 in Pumc-91 cell line. The results clearly demonstrated that the predominant effect of AG490 was the reduction of signaling molecules including STAT3, p-STAT3, Cyclin D1 and MMP2, which were involved in the growth, progression and migration.

In the process of tumor invasion, MMP2

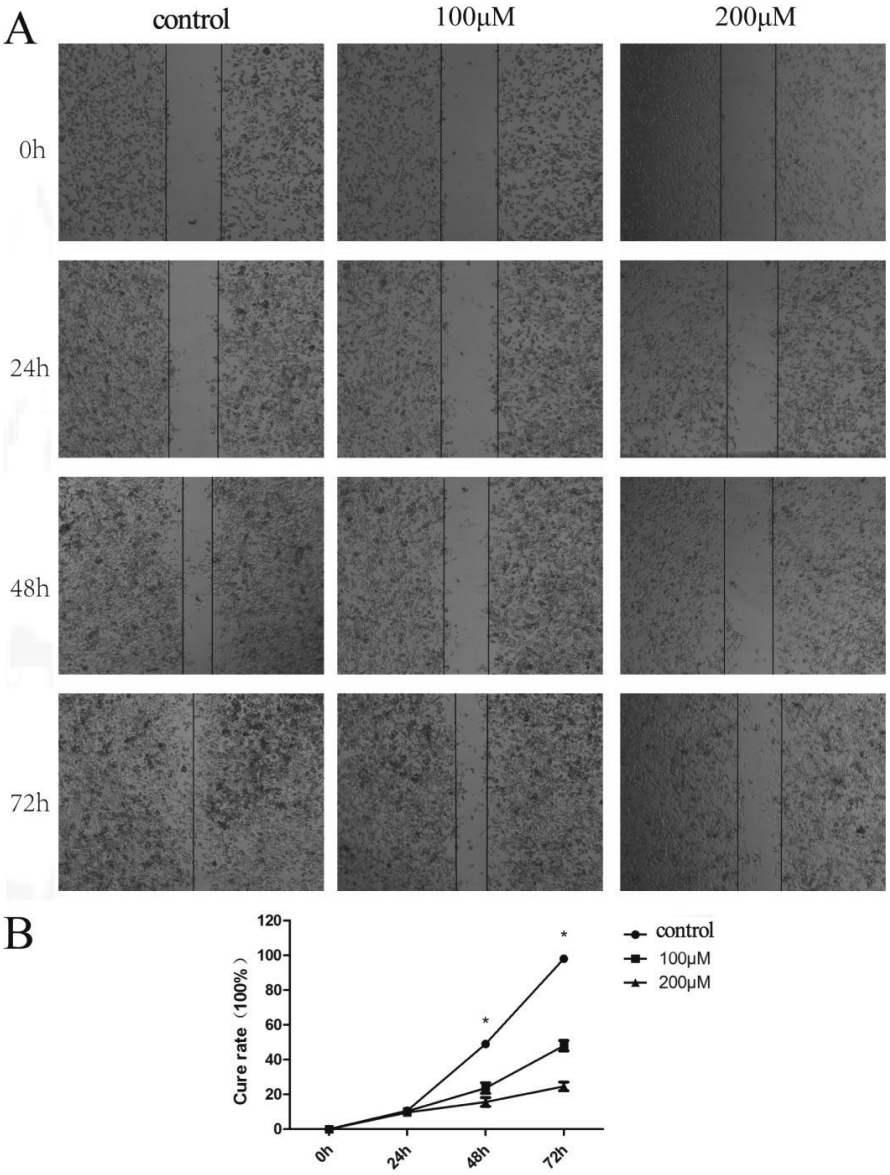

Fig. 6. *The metastasis inhibitory effect of AG490 in Pumc-91/ADM cells. Pumc-91/ADM cells were treated with 0, 200 μM of AG490. The cells were cultured for 0, 24, 48 and 72h respectively.* ***A****) Images showing the wound area before and after incubation.* ***B****) The cure rate curves of cells treated with 0, 24, 48 and 72 h.*

plays an important role in the degradation of extracellular matrix and neovascularization induced by angiogenesis factor. Huang W et al. (28) found that AG490 significantly inhibited activity of angiotensin II-induced STAT3 and reduced expression of MMP2 and VEGF in gastric cancer cells. Wang et al. (29) considered that MMP2 was the STAT3 signaling pathway downstream target gene. The dimeric STAT3 translocates to the nucleus, where it binded to consensus STAT3 binding sequences within the promoter region of MMP2 gene and thereby activated its transcription (30). MMP2 expression was tightly and positively regulated by JAK/STAT3 pathways. Our research demonstrated that after inhibition of STAT3 signaling pathway, the mRNA and protein levels of MMP2 obviously decreased in the test group. In the scratch healing experiment, compared to the control group, the cure rates of test groups were reduced gradually along with the increasing concentration of AG490. The result illustrated that AG490 inhibited the migration of Pumc-91/ADM cells, and the inhibition depended on the dose of AG490. AG490 successfully suppressed STAT3 signaling pathway and down-regulated the expression of MMP2 protein, which affected the migration ability of tumor cells. STAT3 signaling pathway mediated the migration of tumor cells through regulating the expression of MMP2 molecules in bladder cancer drug-resistant cells.

It was reported that Cyclin D1 was a proto-oncogene critical regulator of cell proliferation and anti-apoptosis, acting as a major mitogen sensor that links cellular signaling networks to the cell cycle machinery (31). This protein promoted cell proliferation through interaction with transcription factors such as the estrogen receptor and tumor suppressor protein (32). Cyclin D1 was one of the downstream target genes of STAT3 signaling pathway which promoted cell proliferation by regulating G1 phase to S phase. Abnormally high levels of Cyclin D1 might accelerate the cell cycle and keep it in a split state, leading to the continued cell proliferation (33). Cyclin D1 overexpression was found in a variety of tumor cells. Liang et al. (34) studied that the si-STAT3 inhibited prostate tumor growth by blocking STAT3 signal pathway. In our study, there was no significant difference in Cyclin D1 expression between Pumc-91/ADM cells and Pumc-91 cells. The results of qRT-PCR and Western blot showed that compared with the control group, the expression of Cyclin D1 was significantly decreased at the gene level and protein level after being treated with AG490. After Pumc-91/ADM cells were treated with AG490, the cell OD value of the test group was gradually reduced along with the increasing concentration of AG490. The CCK-8 test result certified that AG490 inhibited the migration of Pumc-91/ADM cells, and the inhibition depended on the dose of AG490.

In conclusion, compared to Pumc-91, an obvious decrease of JAK2, p-STAT3 and increase of MMP2 were shown in Pumc-91/ADM cell line. After inhibition of STAT3 signaling pathway, the mRNA and protein levels of STAT3, p-STAT3, MMP2 and Cyclin D1 obviously decreased in the test group. The proliferation and migration of Pumc-91/ADM were suppressed by inhibiting of STAT3. STAT3 signal pathway is closely related to the occurrence, development and drug resistance of bladder cancer cells. Inhibition or complete silencing of STAT3 expression is an effective anticancer therapy strategy and may be a new approach for treatment of bladder cancer.

ACKNOWLEDGEMENTS

This research was supported by Beijing Natural Science Foundation (No.7172106), Beijing Municipal Administration of Hospitals' Ascent Plan (DFL20150701) and Beijing Shijitan Hospital Youth Fund (2015-QB07, 2012-c15), and Enhancement Funding of Beijing Key Laboratory of Urinary Cellular Molecular Diagnostics (2019-JS02).

REFERENCES

1. Siegel RL, Miller KD, Jemal A. Cancer statistics, 2015. CA Cancer J Clin 2015; 65:5-29.
2. Yu S, Meng Q, Hu H, Zhang M, Correlation of ANXAl expression with drug resistance and relapse in bladder cancer. Int J Clin Exp Pathol 2014; 7:5538-48.

3. Arantes-Rodrigues R, Pinto-Leite R, Fidalgo-Goncalves L, Palmeira C, Santos L, Colaco A, Oliveira P. Synergistic effect between cisplatin and sunitinib malate on human urinary bladder-cancer cell lines. Biomed Res Int 2013; 2013:791406.
4. Longley DB, Johnston PG. Molecular mechanisms of drug resistance. J Pathol 2005; 205:275-92.
5. Housman G, Byler S, Heerboth S, Lapinska K, Longacre M, Snyder N, Sarkar S. Drug resistance in cancer: An overview. Cancers 2014; 6:1769-92.
6. Zhang F, Wang Z, Fan Y, Xu Q, Ji W, Tian R, Niu R. Elevated STAT3 Signaling-Mediated Upregulation of MMP-2/9 Confers Enhanced Invasion Ability in Multidrug-Resistant Breast Cancer Cells. Int J Mol Sci 2015; 16:24772-90.
7. Turkson J, Jove R. STAT proteins: novel molecular targets for cancer drug discovery. Oncogene 2000; 19:6613-26.
8. Wegrzyn J, Potla R, Chwae YJ, Sepuri NB, Zhang Q, Koeck T. Function of mitochondrial Stat3 in cellular respiration. Science 2009; 323:793-7.
9. Blaskovich MA, Sun J, Cantor A, Turkson J, Jove R, Sebti SM. Discovery of JSI-124 (cucurbitacin I), a selective Janus kinase/signal transducer and activator of transcription 3 signaling pathway inhibitor with potent antitumor activity against human and murine cancer cells in mice. Cancer Research 2003; 63:1270-9.
10. Huang WW, Yang JS, Lin MW. Cucurbitacine induces G2/M phase arrest through STAT3/p53/p21 signaling and provokes apoptosis via Fas/CD95 and mitochondria-dependent pathways in human bladder cancer T24 cells. Evid Based Complement Alternat Med 2012; 11:9527-62.
11. Poli V, Camporeale A. STAT3 mediated metabolic reprograming in cellular transformation and implications for drug resistance. Front Oncol 2015; 5:121.
12. Han Z, Feng J, Hong Z, Chen L, Li W. Silencing of the STAT3 signaling pathway reverses the inherent and induced chemoresistance of human ovarian cancer cells. Biochem Biophys Res Commun 2013; 435: 188-94.
13. Luo X, Tarbell KV, Yang H, et al. Dendritic cells with TGF-beta differentiate naive CD4+ CD25+/-T cell into islet-protective Foxp3 +regulatory T cells. Pro Natl Acad Sci USA 2007; 104:2821-16.
14. Kortylewski M, Kujawski T, Wang S, et al. Inhibiting Stat3 signaling in the hematopoietic system elicits multicomponent antitumor immunity. Nat Med 2005; 11:1314-21.
15. Fuke H, Shiraki K, Sugimoto K, et al. Jak inhibitor induces S phase cell-cycle arrest and augments TRAIL-induced apoptosis in human hepatocellular carcinoma cells. Biochen Biophys Res Commun 2007; 363:738-44.
16. Miyamoto N, Sugita K, Goi K, et al. The JAK2 inhibitor AG490 predominantly abrogates the growth of human B-precursor leukemic cells with 11q23 translocation or Philadelphia chromosome. Leukemia 2001; 15:1758-68.
17. Gritsko T, Williams A, TurkSon J. Persistent activation of Stat3 Signaling induces survivin gene exp ression and confers resistance to apoptosis in human breast cancer cells. Clin Cancer Res 2006; 12:11-19.
18. Aziz MH, Hafeez BB, Sand JM, Pierce DB, Aziz SW, Dreckschmidt NE, Verma AK. Protein kinase C mediates Stat3 Ser727 phosphorylation, Stat3-regulated gene expression and cell invasion invarious human cancer cell lines via integration with MAPK. Oncogene 2010; 29: 3100-9.
19. Sun Y, Cheng MK, Griffiths TR, Mellon JK, Ksi B, Kriajevska M, Manson MM. Inhibition of STAT signaling in bladder cancer by diindolylmethane-relevance to cell adhesion, migration and proliferation. Curr Cancer Drug Targets 2013; 13:57-68.
20. Chen RJ, Ho YS, Guo HR. Long-term nicotine exposure induced chemoresistance is mediated by activation of Stat3 and down regulation of ERK1/2 via nAChR and Beta adrenoceptors in human bladder cancer cells. Toxicoi Sci 2010; 115:118-30.
21. Yokogami K, Wakisaka S, Avruch J, Reeves SA. Serine phosphorylation and maximal activation of STAT3 during CNTF signaling is mediated by the rapamycin target mTOR. Current Biology 2000; 10:47-50.
22. Hazan-Halevy I, Harris D, Liu Z, et al. STAT3 is constitutively phosphorylated on serine 727 residues, binds DNA, and activates transcription in CLL cells. Blood 2010; 115:2852-63.
23. Tsui KH, Cheng AJ, Chang Pe, Pan TL, Yung BY. Association of nucleophosmin/B23 mRNA expression within clinical outcome in patients with

bladder carcinoma. Urology 2004; 64:839-44.
24. Meydan N, Grunberger T, Dadi H, et al. Inhibition of acute lymphoblastic leukaemia by a Jak-2 inhibitor. Nature 1996; 379:645-48.
25. Mo-Li Wu, Hong Li, Li-Jun Yu, et al. Short-Term resveratrol exposure Causes in vitro and in vivo growth inhibition and apoptosis of bladder cancer cells. Plos One 2014; 9:e89806.
26. Eriksen KW, Kaltoft K, Mikkelsen G, et al. Constitutive STAT3-activation in Sezary syndrome: tyrphostin AG490 inhibits STAT3-activation, interleukin-2receptor expression and growth of leukemic Sezary cells. Leukemia 2001, 15:787-93.
27. Joung YH, Yoon MN, Young BY, Sp N. Combination of AG490, a Jak2 inhibitor, and methylsulfonylmethane synergistically suppresses bladder tumor growth via the Jak2/STAT3 pathway. Int J Oncol 2014; 44:883-95.
28. Huang W, Yu LF, Zhong J, Wu W, Zhu JY, Jiang FX, Wu YL. Stat3 is involved in angiotensin II-induced expression of MMP2 in gastric cancer cells. Dig Dis Sci 2009; 54:2056-62.
29. Wang L, Ling Y, Chen Y, Li CL, Feng F, You QD, Lu N, Guo QL. Flavonoid baicalein suppresses adhesion, migration and invasion of MDA-MB-231 human breast cancer cells. Cancer Lett 2010; 297:42-48.
30. Xie TX, Wei D, Liu M, Gao AC, Ali-Osman F, Sawaya R, Huang S.Stat3 activation regulates the expression of matrix metalloproteinase-2 and tumor invasion and metastasis. Oncogene 2004; 23:3550-60.
31. Fu M, Wang C, Li Z, Sakamaki T, Pestell RG. Minireview: cyclin D1: normal and abnormal functions. Endocrinology 2004; 145:5439-47.
32. Kim JK, Diehl JA. Nuclear cyclin D1: an oncogenic driver in human cancer. Cell Physiol 2009; 220:292-96.
33. Pysz MA, Hao F, Hizli AA, Lum MA, Swetzig WM, Black AR, Black JD. Differential regulation of Cyclin D1 expression by protein kinase Cα and ϵ signaling in intestinal epithelial cells. J Biol Chem 2014; 289: 22268-83.
34. Liang ZW, Guo BF, Li Y, Li XJ. Plasmid-based Stat3 siRNA delivered by hydroxyapatite nanoparticles suppresses mouse prostate tumour growth in vivo. Asian J Androl 2011; 13:481-86.

EXPRESSION CHANGES OF INFLAMMATORY CYTOKINES TNF-α, IL-1β AND HO-1 IN HEMATOMA SURROUNDING BRAIN AREAS AFTER INTRACEREBRAL HEMORRHAGE

XW. ZHANG, Y. WU, DK. WANG, X. JIN and CH. LI

Department of Neurosurgery, Tongde Hospital of Zhejiang Province, Hangzhou, China

Received April 15, 2019 – Accepted June 25, 2019

To study the expression changes of inflammatory factors heme oxygenase-1 (HO-1), tumor necrosis factor-α (TNF-α), and interleukin-1β (IL-1β) in intracerebral hemorrhage (ICH), brain tissues surrounding hematoma were collected from ICH patients. The expressions of HO-1, TNF-α, IL-1β, and other genes were examined at different time points of ICH. Changes in HO-1, TNF-α, and IL-1β positive cell numbers after ICH were detected by immunohistochemical staining. The results showed that the expressions of HO-1, TNF-α, and IL-1β had no significant changes in brain tissues surrounding hematoma within 6 hours after ICH (P > 0.05). Their expressions during 6-24 hours and 24-72 hours after ICH increased constantly. After reaching the peak, they remained steady or slightly decreased after 72 hours. The dynamic expression changes of HO-1, TNF-α, and IL-1β were observed and their development trends were interfered timely to alleviate the secondary neurological impairment after ICH, which was significant to prevent ICH.

Intracerebral hemorrhage (ICH), which has high morbidity and mortality, refers to non-traumatic cerebral parenchymal hemorrhage (1). Among the many factors that lead to ICH, high-risk diseases, such as hypertension and cerebrovascular disease, are the main causes. ICH also takes place during intracranial surgery (2, 3). An increasing number of studies are focusing on certified and functional damage after ICH.

The mechanism of secondary injury caused by ICH is not fully known. Inflammation, oxidative stress and apoptosis are considered as the main factors of secondary injury (4-6). Previous studies have confirmed that ICH induced inflammatory reactions, such as leukocyte infiltration, microglia activation, significant expressions of cytokines and activation of complement system (7, 8), in the hemorrhagic sites and surrounding brain tissues. Inflammation plays two roles in the pathophysiological process after ICH. On one hand, it absorbs hematoma and removes necrotic tissues; on the other hand, it causes nerve injury though immune response (9-11). In ICH-related research, many inflammatory molecules and inflammation-related reaction mechanisms have been discovered. The role of HO-1 (heme oxygenase-1) in ICH has been studied in recent years, and researchers found the abnormal expression level of HO-1 after ICH shows neuroprotective effects (12). In this study, we detected the expression changes of HO-1, TNF-α and IL-1β in the brain tissues surrounding hematoma at different time points after ICH. Our research will provide a new therapeutic idea for the prevention and treatment of secondary brain injury after ICH.

Key words: intracerebral hemorrhage; secondary brain injury; human brain tissues; inflammatory factors

Corresponding Author:
Dr Chenhao Li,
Department of Neurosurgery,
Tongde Hospital of Zhejiang Province,
No.234 Gucui Road,
Hangzhou 310012, China
e-mail: li_chenhao186@126.com

0393-974X (2019)

MATERIALS AND METHODS

Study subjects

This study enrolled 28 patients with hypertensive ICH admitted to Tongde Hospital of Zhejiang Province between October 2013 and October 2018. The selected patients, included 18 males and 10 females, aged 35-65 years, (average 55.6±15.32 years). The bleeding volume of these patients was 30-60 ml, while the bleeding areas in the brain varied: 20 cases of basal ganglia hemorrhage, 8 lobar hemorrhage, and 14 lesions in both left and right brain. Among these patients, 9 had stroke history, and 23 had alcoholism history. Their mean systolic blood pressure was 201±20.3 mm Hg, and diastolic blood pressure was 130±11.2 mmHg. Two patients had Glasgow scores of 3-6, 24 had 7-10, and 2 had 11-15. All the selected cases met the criteria for ICH diagnosis and treatment in China. All patients involved in this study signed the informed consent, and the study was approved by the Ethics Committee of Tongde Hospital of Zhejiang Province. Patient inclusion criteria were: diagnosed as ICH by pathological diagnosis; no history of taking any medication affecting blood pressure while receiving surgical treatment in the previous six months; and willing to sign the informed consent. Exclusion criteria were: patients with motor system trauma in the previous months; patients with diseases affecting blood pressure; patients twho had taken medication affecting blood pressure in the previous six months.

Sample preparation

The 28 hypertensive ICH patients in this study were treated with craniotomy surgery to remove hematoma. During the surgical procedure, brain tissues less than or equal to 1 cm diameter were collected. Tissues taken from the hematoma surrounding areas were used for the experimental groups, while normal brain tissues from the same ICH patient in areas far away from the hematoma were used as the control group. Four experimental groups (≤6 h, 6-24 h, 24-72 h and 72 h) were set based on the onset-to-surgery time frame of patients. In each group, brain tissues were collected from 7 patients (n=7). Tissues used for Western blotting and RT-PCR were stored at -80°C until use. Tissues used for immunohistochemistry were fixed in 10% formaldehyde fixative solution, and cut into 5-μm thick slices.

Determination of bicinchoninic acid protein concentrations

Brain samples at -80°C were taken and put on ice for Western blotting. For 0.1 g of tissues, 0.9 ml Radio Immunoprecipitation Assay (RIPA) lysate buffer with protease inhibitors (Biyuntian Biotechnology Co., Ltd, China) (ratio 1:9) was added, and homogenized with an electric homogenizer (GILSON, Finland) on ice. Constant rotation was maintained for 45 min at 4°C to make sure samples were fully dissociated. Protein lysates were transferred to 2-ml Eppendorf (Ep) tubes with a transporter (GILSON, Finland). Ep tubes containing protein lysates were kept on ice for another 30 min, followed by centrifugation for 20 min at 12,000 rpm at 4°C. The tubes were gently removed from the centrifuge, and the supernatant was aspirated, which was placed in a fresh Ep tube. Bicinchoninic acid (BCA) assay was used to measure protein concentrations in the supernatant samples. Afterwards, 25 mg/ml bovine serum albumin (BSA) stock solution was prepared by adding 0.8 ml protein standard formulation solution to 20 mg BSA, which was diluted to 0.5 mg/ml standard solution with phosphate buffered saline (PBS) (Boshide Engineering Co., Ltd., China), and stored at -20°C in the dark. An appropriate amount of 25mg/mL protein standard mother concentrate was diluted with PBS (BOSTER Biological Technology, China) to formulate the 0.5mg/mL standard solution, which was stored at -20°C in the dark . Preparation of BCA working fluid: Reagent A (1% BCA disodium salt, 2% anhydrous sodium carbonate, 0.16% sodium tartrate, 0.4% sodium hydroxide, and 0.95% sodium bicarbonate were mixed and the pH value was adjusted to 11.25) (BOSTER Biological Technology, China) and Reagent B (4% copper sulphate) (BOSTER Biological Technology, China) were thoroughly mixed at a ratio of 50:1 to formulate the BCA working fluid. A total of 8 gradients were set, and the absorbance value of A562 was measured by using an enzyme mark instrument. The standard curve was plotted, and the protein concentrations of the samples were calculated in accordance with the absorbance values of samples.

Detection of target protein expressions by Western blotting

The volume of the supernatant sample per pore was calculated from the protein concentration measured by the BCA protein concentration test, and the total protein amount of each supernatant sample was equal. The loading buffer

was added to the supernatant sample protein in each pore, and the samples were boiled. Then they were placed in the SDS (sodium dodecylsulfate)-polyacrylamide gel for electrophoresis for 1 h. Then, the membrane was transferred by wet method. The protein on the polyacrylamide gel was transferred to a nitrocellulose membrane at a constant voltage of 100V; after 1.5 h, the membrane was rinsed with TBST (Tris Buffered Saline Tween) buffer and soaked in a container for subsequent experiments. Then, the membrane was blocked by using the blocking solution (20 mL of TBST, 0.75g of BSA, and 3 scoops of skimmed milk powder) at room temperature for 60 min. The membrane was incubated overnight at 4°C by using the corresponding primary antibody (Shanghai Beyotime Biotechnology, China). On the next day, the membrane was washed 3 times with TBST for 5 min each time. The polyvinylidene fluoride (PVDF) membrane was then incubated with the corresponding secondary antibody for 1 h at room temperature on a horizontal shaker; the secondary antibody was diluted at a ratio of 1:5000 as indicated. After incubation, the membrane was washed with PBS for 4 times, 15 min each time. After the above operations were successfully completed, the image analysis software processing system (Image pro plus) (BIO-RAD, USA) was used to analyze the protein band of the nitrocellulose (NC) membrane specimen. The gray value of the target protein band on the NC membrane (BIO-RAD, USA) was compared with the gray value of the β-actin protein band to obtain the ratio, and the ratio of the bands was compared. After 3 times of repetition, the mean number and standard deviation of the ratios were calculated.

Detection of HO-1, TNF-α and IL-1β mRNA expressions by real-time quantitative PCR (RT-PCR)

The primers used to detect the expression level of HO-1, TNF-α and IL-1β by RT-PCR were synthesized and provided. The list of primers are as follows:

The target gene length of HO-1 is 525, with the following primers:

F: CAGCCGTACAAGCCTAAGGGC;

R: GATGTTGAGCACCGGATCGCT;

The target gene length of TNF-α is 397, with the following primers:

F: TGAGGCTGAGATCCATATGAGC;

R: TCCGGTCCCATCGTACGACCTA

The target gene length of IL-1β is 207, with the following primers:

F: GTCCACCAAATTCAATACCG;

R: TCAGAATGGCCTCCTGAGGA

The target gene length of GAPDH is 146, with the following primers:

F: ATCATGTTTGAGACCTTCAACA;

R: CATCTCTTGCTCGAAGTCCAAG

RNA extraction

Tissues used for RNA preparation were either freshly collected from ICH patients or from samples stored at -80°C. 1 mg of each sample was put in a glass grinding container containing 0.5 ml Trizol RNA extracting reagent (Abbkine, USA). After grinding, the homogenate was transferred to a 2-ml Ep tube, and the grinder was washed with 0.5 ml Trizol RNA extracting reagent, which was mixed with the homogenate. The samples were shaken and mixed evenly, and incubated at room temperature for 15 min. Then, the RNA solution was obtained in accordance with the instructions of the RNA extraction kit. First, the spectrophotometer was zeroed. A small amount of RNA solution was diluted with TE at a ratio of 1:100, and the absorption values at 260 nm and 280 nm of the spectrophotometer (BIO-RAD, USA) were read. The ratio at 260mm/280nm of the RNA solution was the purity of the RNA, which ranged from 1.8 to 2.0. The obtained RNA solution was stored at -80°C until use.

RNA reverse transcription

The RNA Ep tube stored in the -80°C cryocontainer was taken out, and 20 μL of the reverse transcription reaction system were prepared as shown in Table I. The reverse transcription reaction conditions: at 42°C on PCR instrument (BIO-RAD, USA) for 30 min; at 4°C for 10 min; and cooled on ice. The obtained cDNA could be used directly for subsequent PCR or cryopreservation at -80°C.

The mRNA was detected by using an ABI fluorescence quantitative PCR instrument (ABI, USA), and each sample was set with 3 repeated pores. During the PCR process, the sample was first denatured at 95°C for 10 s, then refracted at 60°C for 31 s, and finally extended at 68°C for 50 s. The cycle was repeated for 40 times. Then, the PCR products obtained from amplification were subjected to electrophoresis to harvest the target band. The gray value of the target protein band on the PCR products was compared with the gray value of the β-actin protein band to obtain the ratio, and the ratios of the bands were

Table I. *Reaction system.*

	Components	Volume
A	Total RNA	2 μL
	5×first-strand Buffer	4 μL
	M-Mu LV Reverse Transcriptase (200U/μl)	0.8 μL
	Oligo dT Primer (50 μM)	2 μL
	dNTP Mixture (10 mM each)	2 μL
	RNase Inhibitor (40U/μL)	0.5 μL
	RNase Free dH_2O	up to 50 μL
B	2×Super SYBR premixture	9 μl
	PCR Forward Primer (10 μM)	0.5 μl
	PCR Reverse Primer(10 μM)	0.5μl
	cDNA	4μl
	RNase Free dH_2O	up to 20 μl

A) *reverse transcription;* ***B)*** *real-time PCR*

compared. After repeating 3 times, the mean number and standard deviation of the ratio were calculated.

Detection of the expression of HO-1, TNF-α and IL-1β at ICH patient samples by immunohistochemical staining

The frozen tissue slices were recovered at room temperature for 70 min, and immersed in 75% alcohol for 5 min. 75% alcohol was changed for 3 times, and then washed with PBS for 4 times, 5 min each washing. Sodium citrate buffer solution (BOSTER Biological Technology, China) (0.01M, pH6.0) was made using 100°C boiling water. The slices were slowly pressurized on a staining rack, and immersed in sodium citrate buffer solution for 15 min. Then the slices were cooled down in cold water. Tissue slices were washed with PBS for 4 times, 5 min each time. Then, slices were blocked with sheep serum at room temperature for 30 min, The slices were incubated overnight with the primary antibody (BOSTER Biological Technology, China), rabbit anti-human HO-1 polyclonal antibody (1:200), TNF-α polyclonal antibody (Shanghai Beyotime Biotechnology, China) (1:1000), or IL-1β polyclonal antibody (1:1000) on a shaker at 4°C. On the second day, the tissue slices were prewarmed for 60 min at room temperature (approximately 37°C), and washed with PBS for 4 times, 5 min each time. The slices were incubated with anti-rabbit monoclonal antibody (1:2000) at room temperature for 90 min, and rinsed in PBS for 4 times, 5 min each time. The processes were repeated by using the secondary antibody. The slices were stained with 3,3-N-Diaminobenzidine Tetrahydrochloride (DAB) (Boster Biological Technology, China) for 15 min, followed by PBS washing for 5 min. They were then re-stained with hematoxylin for 3 min, and washed with saline for 15-20 min. The brain tissue sections were dehydrated, dried, mounted and observed under a microscope (BIO-RAD, USA) using 100x objective. A digital camera was used to capture images under optical microscope. Six field images were randomly taken from each brain slice. The number of positive cells and total cells was counted using Image Pro plus, and the immunohistochemical staining image analysis system.

Statistical analysis

All data were shown as mean±standard deviation. SPSS13.0 for Windows statistical software was used for statistical analysis. Rank sum test was used for comparison within two groups. The *t*-test was used for comparison between two groups. P values < 0.05 were considered statistically different, and $P < 0.01$ were considered significantly statistically different.

RESULTS

Detection of HO-1, TNF-α and IL-1β protein expressions in ICH patients by Western blot

Using Western blotting, we examined the expression changes of HO-1, TNF-α and IL-1β protein levels in the brain samples from ICH patients. Fig. 1B shows the linear regression for the entire set of the standard points. The standard curve R^2 was 0.99989 in our BCA protein concentration assay. Western blotting results showed the change of protein expressions of HO-1, TNF-α, IL-1β and β-actin in brain areas surrounding hematoma in ICH patients (Fig. 1A). We found the protein levels of all the target proteins were increased significantly in hematoma-surrounding brain areas compared to control brain areas from ICH patients (Fig. 1A, 1C, 1D and 1E). The increase was seen 6 h after bleeding, kept going up over time, and lasted for at least 72 h. Fig. 1C shows the expression level of HO-1 protein was low in normal tissues and not increased significantly in hematoma-surrounding when onset time was ≤6 h ($P > 0.05$); the HO-1 protein level started to markedly increase at 6-24 h ($P < 0.05$), reached the peak at 24-72 h, and still remained high after 72 h. The basal protein level of

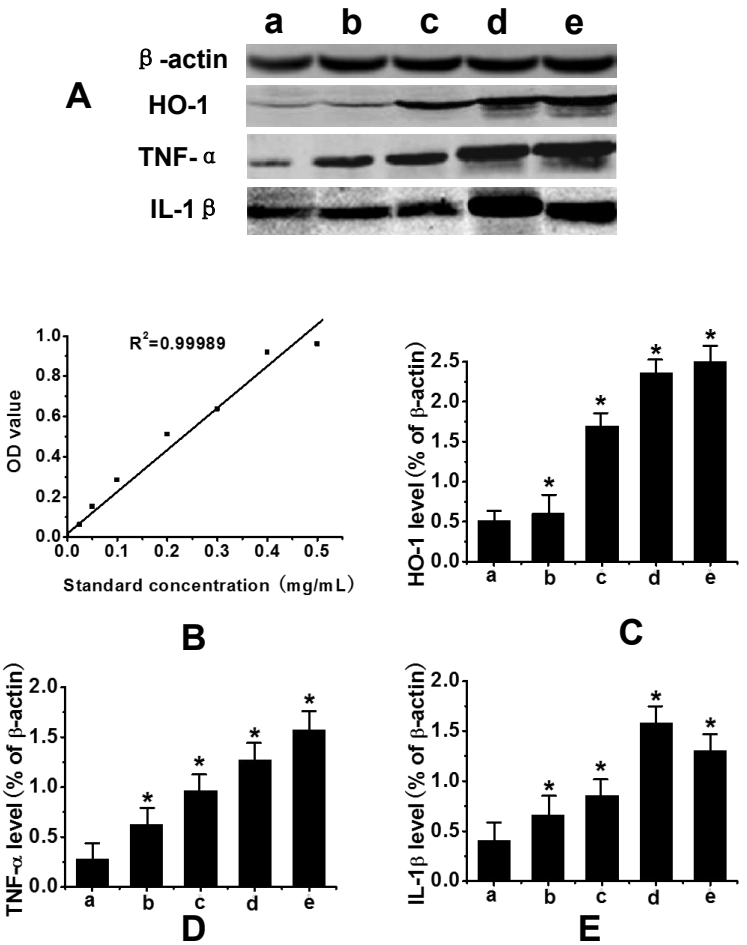

Fig. 1. *The protein expression changes of HO-1, TNF-α and IL-1β in human brain tissues after ICH and the standard curve (a: control group; b: ≤6 h group; c: 6-24 h group; d: 24-72 h group; e: > 72 h group;* ***A****) Western blotting detection of HO-1, TNF-α, IL-1β and β-actin;* ***B****) BCA protein concentration determination standard curve;* ***C****) HO-1 protein expression levels;* ***D****) TNF-α protein expression levels;* ***E****) IL-1β protein expression levels; (* represents the significance of the experimental groups compared to the control group, $P < 0.05$, $n = 7$).*

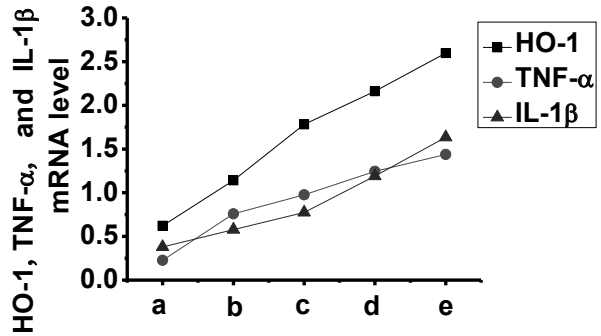

Fig. 2. *The mRNA expression changes of HO-1, TNF-α and IL-1β in human brain tissues after ICH (a: control group; b: ≤6 h group; c: 6-24 h group; d: 24-72 h group; e: >72 h group).*

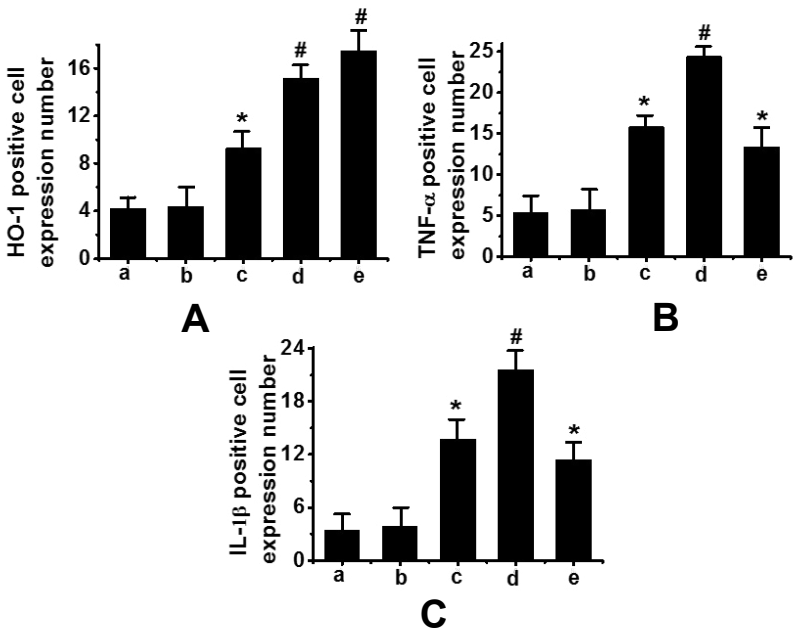

Fig. 3. *The positive cells that expressed HO-1, TNF-α and IL-1β in human brain tissues after ICH (a: control group; b: ≤6 h group; c: 6-24 h group; d: 24-72 h group; e: >72 h group; **A**) HO-1 positive cells expression; **B**) TNF-α positive cells expression; **C**) IL-1β positive cells expression; * represents statistical significance when compared to control group, P < 0.05; # represents statistical significance when compared to control group, P < 0.01, n=7).*

TNF-α in the control group was relatively low, and the expression of TNF-α in the brain tissues around hematoma after ICH was slightly increased in ≤6 h and 6-24 h groups, but not significantly (Fig. 1D). The expression of TNF-α was increased significantly in the 24-72 h group, and kept rising after 72 h ($P < 0.05$). There was no significant difference in the expression of IL-1β protein in the experimental groups of ≤ 6h and 6-24 h after ICH compared to the control, while the expression level of IL-1β increased significantly and reached the peak at 24-72 h (Fig. 1E). After 72 h, IL-1β protein levels decreased slightly. After ICH, IL-1β protein expression levels were significantly higher ($P < 0.05$) in the experimental groups of 24-72 h and >72 h.

Table II. *HO-1, TNF-α and IL-1β positive cells after ICH.*

Group	Control group	≤6 h group	6-24 h group	24-72 h group	>72 h group
A	4.2±1.4	4.4±1.6	9.3±2.1*	15.2±2.2#	17.5±1.5#
B	5.4±2 .2	5.7±2.3	15.8±3.9*	24.4±4.5#	13.4±3.7*
C	3.4±0.7	3.9±1.6	13.7±3.5*	21.6±4.9#	11.4±3.1*

***A)** HO-1; **B)** TNF-α; **C)** IL-1β. * Statistical significance when compared to control group, P < 0.05; # Statistical significance when compared to control group, P < 0.01.*

Detection of HO-1, TNF-α and IL-1β mRNA levels by RT-PCR

Using RT-PCR, we detected HO-1, TNF-α and IL-1β mRNA expression levels in human brain tissues from ICH patients. RT-PCR results showed that the expression level of HO-1, TNF-α and IL-1β in normal brain tissues are relatively low, while the expression of HO-1 mRNA in normal brain tissues was the highest among the three (Fig. 2). The mRNA level of HO-1, TNF-α and IL-1β in brain areas surrounding hematoma were increased in ICH patients, compared to the expression level of normal brain tissues (Fig. 2). After ICH, the mRNA level of all three genes started to rise in the experimental group ≤6 h, increased significantly at 6-24 h, and reached the peak at 72 h. After 72 h, the expression of HO-1 and TNF-α mRNA kept increasing, while the expression of IL-1β mRNA level decreased slightly. The expression of HO-1, TNF-α and IL-1β mRNA in human brain tissues after ICH was significantly higher than that in control group, and there was obvious statistical significance ($P < 0.05$).

Immunohistochemical staining was used to detect the expression changes of HO-1, TNF-α and IL-1β after ICH

Using immunohistochemical staining, the changes were examined of positive cell numbers that expressed HO-1, TNF-α and IL-1β after ICH. As can be seen in Fig. 3A and Table I, only a small number of cells (4.2±1.4) were HO-1 positive in the control group. The HO-1 positive cell number in ≤6 h group was 4.4±1.6, not different from control. The HO-1 expression cell number was two-fold at 6-24 h compared to that in control group, and increased significantly at 24-72 h and >72 h ($P < 0.01$). Only a few TNF-α positive cells were found in normal brain tissues (Fig. 3B and Table I). Within 6 h after ICH, the number of TNF-α positive cells in the experimental group was not significantly different compared to that in the control group ($P > 0.05$). TNF-α positive cells began to increase significantly at 6-24 h after ICH ($P < 0.05$), and reached the peak at 24-72 h ($P < 0.01$), while decreasing gradually at > 72 h after ICH ($P < 0.05$). The number of IL-1β positive cells in experimental group was similar to that in the control group within 6 h after ICH ($P > 0.05$) (Fig. 3C and Table I). IL-1β positive cell number began to increase dramatically at 6-24 h after ICH, with significant difference ($P < 0.05$). The number of cells that expressed IL-1β was significantly increased at 24-72 h ($P < 0.01$), and reached the peak at 72 h after ICH. While IL-1β positive sell number decreased gradually > 72 h after ICH.

DISCUSSION

The hemoglobin released by secondary injury after ICH activates the inflammatory pathway around the hematoma and leads to the blood-brain barrier destruction and brain cell apoptosis (13, 14). Studies have shown that the main function of HO-1 is to promote heme degradation (15-17). The severity of brain edema in ICH patients is related to the expression of TNF-α in brain tissues (18). In this study, Western blot and RT-PCR were used to detect the expression of HO-1, TNF-α, and IL-1β in brain tissues at different time points after ICH. The results showed that the expressions of HO-1, TNF-α, and IL-1β within 6 hours after ICH were less than those

in the control group with no significant differences ($P > 0.05$). In addition, their expressions began to increase at 6-24 h and reached the peak at 24-72 h. Afterwards, their expressions remained steady or slightly declined.

Previous studies have found that the upregulated expressions of HO-1, TNF-α, and IL-1β are important markers for secondary brain injury (19-21). It was found that the expressions of HO-1, TNF-α and IL-1β were lower within 6 h after ICH compared to the control group ($P > 0.05$). Afterwards, their expressions tended to keep stable or gradually decreased. Therefore, there were statistically significant differences ($P<0.01$) between the 24-72 h and the control group.

In summary, it was supposed that the expression levels of HO-1, TNF-α, and IL-1β were timely intervened at certain time points, which may alleviate the secondary neurological impairment after ICH. Our study provides new ideas for clinical treatment of ICH.

REFERENCES

1. Sansing LH. Intracerebral hemorrhage. Semin Neurol 2016; 36(3):223-24.
2. Lattanzi S, Cagnetti C, Provinciali L, Silvestrini M. Neutrophil-to-lymphocyte ratio and neurological deterioration following acute cerebral hemorrhage. Oncotarget. 2017; 8(34):57489-94.
3. Keep RF, Andjelkovic AV, Xiang J, Stamatovic SM, Antonetti DA, Hua Y, Xi G. Brain endothelial cell junctions after cerebral hemorrhage: changes, mechanisms and therapeutic targets. J Cereb Blood Flow Metab 2018; 38(8):1255-75.
4. Li Z, He Q, Zhai X, et al. Foxo1-mediated inflammatory response after cerebral hemorrhage in rats. Neurosci Lett 2016; 629:131-36.
5. Ye L, Gao L, Cheng H. Inflammatory profiles of the interleukin family and network in cerebral hemorrhage. Cell Mol Neurobiol 2018; 38(7):1321-33.
6. Zhang Z, Zhang Z, Lu H, Yang Q, Wu H, Wang J. Microglial polarization and inflammatory mediators after intracerebral hemorrhage. Mol Neurobiol 2017; 54(3):1874-86.
7. Zhou HX, Gao LH, Meng LL, Zhang YX, Wei ZF, Si DW. Preventive and therapeutic effect of simvastatin on secondary inflammatory damage of rats with cerebral hemorrhage. Asian Pac J Trop Med 2017; 10(2):152-56.
8. Chen C, Li T, Zhao Y, et al. Platelet glycoprotein receptor Ib blockade ameliorates experimental cerebral ischemia–reperfusion injury by strengthening the blood–brain barrier function and anti-thombo-inflammatory property. Brain Behav Immun 2018; 69:255-63.
9. Doerfler S, Faerber J, McKhann GM, et al. The Incidence and Impact of Secondary Cerebral Insults on Outcome After Aneurysmal Subarachnoid Hemorrhage. World Neurosurg 2018; 114:e483-e494.
10. Zhou K, Zhong Q, Wang YC, et al. Regulatory T cells ameliorate intracerebral hemorrhage-induced inflammatory injury by modulating microglia/macrophage polarization though the IL-10/GSK3β/PTEN axis. J Cereb Blood Flow Metab 2017; 37(3):967-79.
11. Yang Y, Dong B, Lu J, Wang G, Yu Y. Hemopexin reduces blood–brain barrier injury and protects synaptic plasticity in cerebral ischemic rats by promoting EPCs though the HO-1 pathway. Brain Res 2018; 1699:177-85.
12. Ren H, Kong Y, Liu Z, et al. Selective NLRP3 (pyrin domain–containing protein 3) inflammasome inhibitor reduces brain injury after intracerebral hemorrhage. Stroke 2018; 49(1):184-92.
13. Wang J, Doré S. Inflammation after intracerebral hemorrhage. J Cereb Blood Flow Metab 2007; 27(5):894-908.
14. Lattanzi S, Cagnetti C, Provinciali L, Silvestrini M. Neutrophil-to-lymphocyte ratio and neurological deterioration following acute cerebral hemorrhage. Oncotarget 2017; 8(34):57489-94.
15. Keep RF, Andjelkovic AV, Xiang J, Stamatovic SM, Antonetti DA, Hua Y, Xi G. Brain endothelial cell junctions after cerebral hemorrhage: changes, mechanisms and therapeutic targets. J Cereb Blood Flow Metab 2018; 38(8):1255-75.
16. Ruan S, Xiao Y, Ma T. Correlation of IL-6 and TNF-α levels in cerebrospinal fluid and serum in patients with subarachnoid hemorrhage: a meta-analysis. Int J Clin Exp Med 2017; 10(8):11549-62.

17. Takeda TA, Sasai M, Adachi Y, Ohnishi K, Fujisawa JI, Izawa S, Taketani S. Potential role of heme metabolism in the inducible expression of heme oxygenase-1. Biochim Biophys Acta Gen Subj 2017; 1861(7):1813-24.
18. Rendevski V, Aleksovski B, Stojanov D, Aleksovski V, Rendevska AM, Kolevska M, Stojanoski K, Gjorgoski I. Peripheral glutamate and TNF-α levels in patients with intracerebral hemorrhage: Their prognostic values and interactions toward the formation of the edemal volume. Neurol Neurochir Pol 2018; 52(2):207-14.
19. Aronowski J, Roy-O'Reilly MA. Neutrophils, the felons of the brain. Stroke 2019; 50(3):e42-e43.
20. Fan X, Mu L. The role of heme oxygenase-1 (HO-1) in the regulation of inflammatory reaction, neuronal cell proliferation and apoptosis in rats after intracerebral hemorrhage (ICH). Neuropsychiatr Dis Treat 2016; 13:77-85.
21. Zhang Z, Wu Y, Yuan S, et al. Glutathione peroxidase 4 participates in secondary brain injury though mediating ferroptosis in a rat model of intracerebral hemorrhage. Brain Res 2018; 1701:112-25.

EFFECTS OF APELIN-13 ON THE EXPRESSION OF IL-6, TNF-α, AND IFN-γ IN RATS WITH EXPERIMENTAL AUTOIMMUNE NEURITIS

YF. WEI[1*], P. YIN[1*], L. LIU[1], SS. WU[1], L. JIA[2] and S. SUN[3]

[1]Department of Neurology, Heilongjiang Provincial Hospital, Harbin, Heilongjiang, China;
[2]Department of Nursing, Heilongjiang Provincial Hospital, Harbin, Heilongjiang, China;
[3]Department of Geriatric Neurology, Heilongjiang Provincial Hospital, Harbin, Heilongjiang, China

Received April 24, 2019 – Accepted June 20, 2019

[*]These authors contributed equally to this work

The objective of this paper was to study the effects of PYR-ARG-PRO-ARG-LEU-SER-HIS-LYS-GLY-PRO-MET-PRO-PHE-OH (APELIN-13) on the expression of inflammatory factors interleukin-6 (IL-6), tumor necrosis factor-α (TNF-α), and interferon-γ (IFN-γ) in rats with experimental autoimmune neuritis (EAN). A total of 30 rats were divided into a control group, an EAN group, and an APELIN-13 group. Enzyme-linked immunosorbent assay (ELISA) was used to detect the levels of IL-6, TNF-α, and IFN-γ in rat plasma. Real-time quantitative Polymerase Chain Reaction (PCR) and Western blot were used to detect the protein and mRNA expression of IL-6, TNF-α, and IFN-γ in rat lymph nodes. In the EAN group, the infiltration of various types of inflammatory cells and focal demyelination were observed near the nerve fascicles of sciatic nerves. Compared with the EAN group, the infiltration of inflammatory cells and demyelination in the APELIN-13 group decreased significantly. The levels of plasma IL-6, TNF-α, and IFN-γ in the EAN group were significantly higher than those in the control group (P<0.05) but significantly lower than those in the APELIN-13 group (P<0.05). Compared with the control group, the mRNA and protein expression of IL-6, TNF-α, and IFN-γ increased significantly (P<0.05) in the EAN group but decreased significantly in the APELIN-13 group (P<0.05). In conclusion, APELIN-13 exerted a protective effect against EAN in rats.

Guillain-Barre syndrome (GBS) is a common peripheral nerve disease caused by nerve demyelination (1). The pathological features of GBS mainly include infiltration of inflammatory cells into peripheral nerve tissues and changes in the structure of nerve fiber myelins (2). As an autoimmune disease mediated by $CD4^+$T cells, experimental autoimmune neuritis (EAN) is also featured by inflammatory cell infiltration into peripheral nerve tissues and demyelination of nerve fibers (3, 4). EAN and GBS are very similar in terms of their clinical manifestations, neuro-electrophysiological changes, and immunological pathology (5). EAN is currently recognized as an ideal animal model for GBS research (6). APELIN is a natural ligand of the putative receptor protein related to the angiotensin receptor (AT1/APJ), which was first isolated from the secretion of the bovine stomach by Tatemoto

Key words: APELIN-13, experimental autoimmune neuritis; inflammatory factor; lymphocyte; nerve myelin antigen

Corresponding Author:
Dr Shuang Sun,
Department of Geriatric Neurology,
Heilongjiang Provincial Hospital,
No. 82 Zhongshan Road, Xiangfang District,
Harbin150036, Heilongjiang, China
e-mail: sunshuang6637@163.com

0393-974X (2019)

et al. in 1998 (7). The APELIN/APJ system is widely distributed in the nervous system and has a protective effect on the nervous system, which is a novel neuroprotective factor (8). Under the influence of proteolytic enzymes, APELIN propeptide is decomposed into polypeptide fragments of different lengths, mainly including APELIN-36, APELIN-17, APELIN-13, and APELIN-12 fragments (9). Different APELIN polypeptide fragments exert different physiological and pharmacological effects both *in vivo* and *in vitro*. Of all APELIN polypeptide fragments, APELIN-13 is highly expressed in the nervous system (10). The main pathological changes of GBS and EAN are observed in inflammatory cell infiltration and inflammatory responses (11). Studies have shown that APELIN exerts a regulatory effect on inflammatory responses in many diseases (12, 13). Therefore, the correlation between the anti-inflammatory effect of APELIN-13 and its role in relieving the clinical symptoms of EAN were explored in this study by measuring the effect of APELIN-13 on the expression of IL-6, TNF-α, IFN-γ in EAN rats.

MATERIALS AND METHODS

Animal model establishment

A total of 30 female Lewis SPF rats (Beijing Vital River Laboratory Animal Technology Co., Ltd., China), which weighed 150~170g, were selected for this research. All rats were housed under a relative humidity of 50-70% and a room temperature of 18-22°C, with a 12h:12h light-dark cycle and were allowed free access to food and water. The experiments were carried out after the rats were allowed to acclimate for 1 week. Then, the rats were randomly divided into 3 groups: a control group, EAN group, and APELIN-13 group, with 10 rats in each group. Rats in the EAN group and the APELIN-13 group were sensitized as explained below.

Each rat was injected with 10% chloral hydrate for anaesthetization. Then, 0.9% saline was added with bovine peripheral myelin (BPM) and H37Ra trunk thermal inactivation mycobacterium tuberculosis (5:1) to formulate the suspension; next, the suspension was completely emulsified with equivalent Freund's adjuvant (Sigma, USA), and a total of 200 μL of antigen emulsion (containing 5 mg of BMP and 1 mg of mycobacterium tuberculosis) were injected through a 1 mL syringe to the footpad of both hindlimbs of each rat to establish the antigen immune Lewis rats. The day of sensitization was recorded as day 0; on the day after sensitizer injection, the rats in the APELIN-13 group were given APELIN-13 (0.1mg/kg) through caudal intravenous injection once a day for 15 consecutive days. At the same time, the rats in the control and EAN groups were given the same amount of saline through caudal intravenous injection. The day of injection was recorded as day 0, and other operations were the same as those of the EAN and APELIN-13 groups. The criteria for EAN establishment included the clinical assessment of signs of the nervous system being 2-9, and presence of obvious inflammatory cell infiltration and demyelination (14).

Assessment of signs of the nervous system in rats

The signs of the nervous system in the rats were assessed on a daily basis after sensitization. The criteria for EAN assessment: 0 indicated no obvious abnormality; 1 indicated reduced tail and muscle tone; 2 indicated tail paralysis and partial disappearance of the righting reflex; 3 indicated more significant disappearance of the righting reflex; 4 indicated the occurrence of ataxia and abnormal postures; 5 indicated incomplete paralysis of hind limbs; 6 indicated moderate paralysis; 7 indicated severe paralysis of hind limbs; 8 indicated paralysis of all limbs; 9 indicated a near death situation; and 10 indicated death. Rats with a score of 2-9 were included in the study.

Pathological observation of sciatic nerves

On the 15th day after sensitization, rats were anesthetized by intraperitoneal injection of 10% chloral hydrate (Xi'an Kanghua Pharmaceutical Corporation, China). After being successfully anesthetized, the rats were fixed on the operating table in prone position. Their fur in the surgical areas was shaved and the exposed skin was disinfected and covered. According to the bone landmarks, the skin of rats was cut to the shallow layer of femurs. The projection position of the femur on the body surface was incised. Then, the myofascial fascia was cut to expose the sciatic nerve trunks, which were fully dissociated. Both ends of the sciatic nerve trunks were cut and trimmed into sciatic nerve segments of about 15 mm in length. The sciatic nerves on both sides were obtained.

One nerve sample from each rat was quickly fixed with 4% paraformaldehyde (PFA) (Qingdao JISSKANG Biological Technology, China) and stained with Hematoxylin-Eosin (HE) to observe the infiltration of inflammatory cells. An imaging system for pathological analysis (Chongqing Tianhong Corporation, China) was used to measure the cross-sectional area of sciatic nerve trunks and to record the number of inflammatory cells on each mm^2 of this cross-sectional area. Another nerve sample from each rat was fixed with 2.5% glutaraldehyde (Shanghai Muyuan Biotech, China) and examined by electron microscopy to observe the loss of myelin and the damages to neurites.

Detection of inflammatory factors in rat plasma using the enzyme-linked immunosorbent assay

On the 15th day after sensitization, rat blood samples were collected from the caudal veins using test tubes containing an anticoagulant. Then, the test tubes were centrifuged at 1500 rpm for 5 min to collect the plasma fraction, whose levels of serum TNF-α, IFN-γ, and IL-6 were detected by enzyme-linked immunosorbent assay (ELISA). Next, the micro-plate was coated with the single antibody for preparation of the solid phase antibody. Then, the samples to be tested and the monoclonal antibody marked by horseradish peroxidase (HRP) were added to formulate the compound of the marked antibody of "coating antibody-TNF-α, IFN-γ, and IL-6-enzyme". Afterward, the optical density (OD) values were measured after color development, and the contents of TNF-α, IFN-γ, and IL-6 in the samples were calculated from the standard curve.

Real-time PCR

On the 15th day after sensitization, rats were given 10% chloral hydrate through intraperitoneal injection and decapitated quickly to harvest their inguinal lymph nodes, which were homogenized to extract total RNA using a Trizol kit (Thermo Fisher Scientific, USA). A reverse transcription kit (Thermo Fisher Scientific, USA) was used to convert extracted total RNA into the first strand of cDNA, which was then subjected to real-time PCR to determine the mRNA expression of target genes using the 2^{-CT} method. The primer sequences: TNF-α: upstream: 5'-TGATCGGTCCCAACAACGA-3', downstream: 5'-TGCTTGGTGGTTTGCTACGA-3'; IFN-γ: upstream: 5'-AAAGACAACAGGCCTAGA-3', downstream: 5'-CTAATCCGCTTCGTTAGGCT-3'; IL-6: upstream: 5'-TGGACTCTGAGCCGCATTGA-3', downstream: 5'-GACGCATGGCGGACAATAGA-3'.

Western blot analysis

On the 15th day after sensitization, rats were given 10% chloral hydrate through intraperitoneal injection and decapitated quickly to harvest their inguinal lymph nodes. The collected lymph nodes were homogenized and the total RNA in the homogenate was resolved by 12% sodium dodecyl sulfate-polyacrylamide gel electrophoresis (SDS-PAGE) at 60V for 1 h followed by 120V for 2 h using 50μg/well of samples. Once the bromophenol blue colorant (Beijing Solarbio Science & Technology, China) reached the juncture of separation gel (15 mL, 12%) and stacking gel (5 mL, 4%), the voltage was shifted to 120V and the electrophoresis was continued for another 2 h. In the next step, the resolved proteins were transferred to a polyvinylidene fluoride (PVDF) membrane at 200mA for 60-80 min. Subsequently, the PVDF membrane was blocked by a blocking solution for 1-2 h and then incubated with diluted primary antibodies (1:200 dilution, rabbit anti-mouse IL-6 monoclonal antibody, rabbit anti-mouse TNF-α monoclonal antibody, rabbit anti-mouse IFN-γ monoclonal antibody, rabbit anti-mouse β-actin monoclonal antibody) at 4°C in a sealed hybridization bag overnight. Afterward, the PVDF membrane was washed three times with TBST, 3 min each time, and incubated at room temperature with a HRP-tagged secondary antibody working solution (1:2000) for 2 h on a shaker. Then, the PVDF membrane was rinsed three times with TBST, 3 min each time. The results were shown on X-ray films by using a Western blot fluoroscopic examination kit (Shanghai Westang Biological Technology, China), and the images were scanned and saved by a gel electrophoretogram scanner. The protein bands were scanned using a gel image scanner to analyze their grey values using a Quantity One Western Blot image system (BIO-RAD Corporation, USA). The expression of each target protein was calculated using the OD ratio of the target protein to the internal reference β-actin.

Statistical analysis

Experimental data were analyzed by SPSS 22.0 statistics software and expressed in the form of $\overline{x} \pm s$. The comparisons between two groups were tested by

LSD *t*-tests while the comparisons among multiple groups were analyzed by one-way ANOVA. P<0.05 indicated the difference was significant.

RESULTS

Assessment of animals

As indicated in Table I, the time of initial onset of EAN in the APELIN-13 group was significantly delayed compared with the EAN group (P<0.05). On the 15th day after sensitization, the rats in the APELIN-13 group showed significantly decreased assessment scores compared with the EAN group (P<0.05). However, the rats in the control group showed no symptoms of neurological deficiency.

Pathological changes of sciatic nerves

The results of HE (Fig. 1, A1, B1, and C1) staining showed the infiltration of various types of inflammatory cells in and around the nerve fascicles of rat sciatic nerves, along with significant focal demyelination. However, no obvious infiltration of inflammatory cells and demyelination were found in the sciatic nerves of the control group. Compared with the EAN group, the infiltration of inflammatory cells and demyelination in the APELIN-13 group decreased significantly.

The results of electron microscopy (Fig. 1, A2, B2, and C2) showed that certain sciatic nerve myelins of rats in the EAN group were injured and demyelinated, while injuries to neurites and stromata were found in serious cases of EAN. For rats in the control group, no demyelination and injuries to neurites and stromata were found. Compared with the EAN group, myelin damage and neurite injuries in the APELIN-13 group were alleviated significantly.

Table I. *Assessment of animals*

Group	The time of initial onset of EAN (d)	The assessment of peak-hours
The EAN group	8.6±0.6	7.9±0.6
The APELIN-13 group	12.2±1.1	3.6±0.4

** Comparison with the EAN group, P<0.05.*

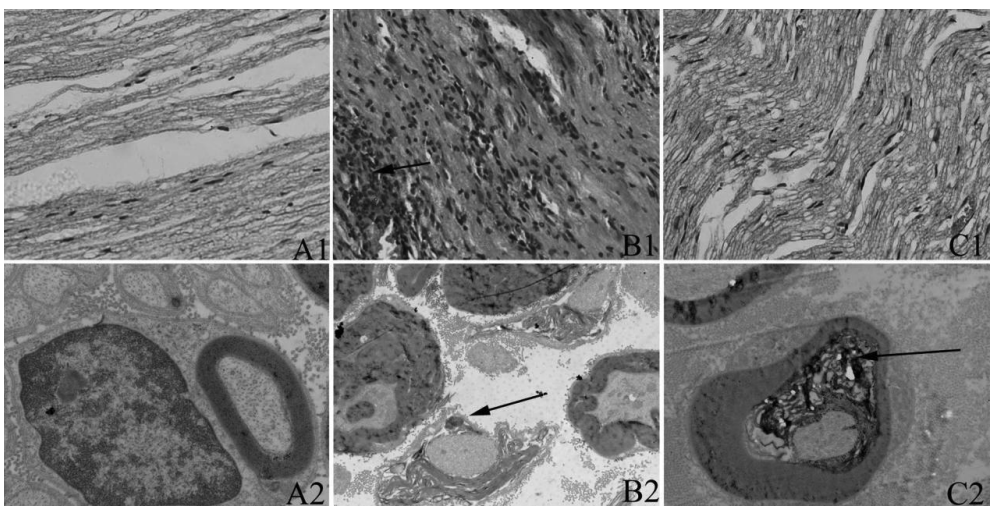

Fig. 1. *Pathological sections of sciatic nerves of rats in each group and electron microscopic results of rat sciatic nerves in each group. **A**) Control group; **B**) EAN group; **C**) APELIN-13 group. (1: Pathological sections, the arrow indicates inflammatory cell infiltration, HE×400; 2: Electron microscopic results, the arrows indicate the injured positions of myelin sheath and neurites, 1 μm)*

Table II. *Infiltration of inflammatory cells into sciatic nerves of rats in each group*

Group	The control group	The EAN group	The APELIN-13 group
Count of inflammatory cells (unit/mm^2)	37.2±6.4	476.8±51.2*	167.4±20.2#

** Comparison with the control group, P<0.05; # comparison with the EAN group, P<0.05.*

Table III. *Impacts of APELIN-13 on plasma levels of TNF-α, IFN-γ, and IL-6 in EAN rats*

Group	The control group	The EAN group	The APELIN-13 group
TNF-α (pg/mL)	11.23±2.14	51.57±6.25*	15.65±4.36*#
IFN-γ (pg/mL)	8.42±1.25	28.67±3.64*	14.71±2.68#
IL-6 (pg/mL)	13.09±0.97	25.36±3.83*	19.27±3.11*#

** comparison with the control group, P<0.05; # comparison with the EAN group, P<0.05.*

Table IV. *Relevant mRNA and protein expressions of TNF-α, IFN-γ, and IL-6 in lymph nodes*

Group		The control group	The EAN group	The APELIN-13 group
The relevant mRNA expressions of each factor	TNF-α (%)	100.00±0.00	381.31±22.43*	116.37±12.25#
	IFN-γ (%)	100.00±0.00	393.27±26.74*	125.51±8.96#
	IL-6 (%)	100.00±0.00	418.35±31.66*	151.34±9.06#
The relevant protein expressions of each factor	TNF-α	0.29±0.05	0.77±0.12*	0.42±0.09#
	IFN-γ	0.39±0.08	0.91±0.11*	0.48±0.08#
	IL-6	0.22±0.04	0.66±0.09*	0.39±0.08#

** comparison with the control group, P<0.05; # comparison with the EAN group, P<0.05.*

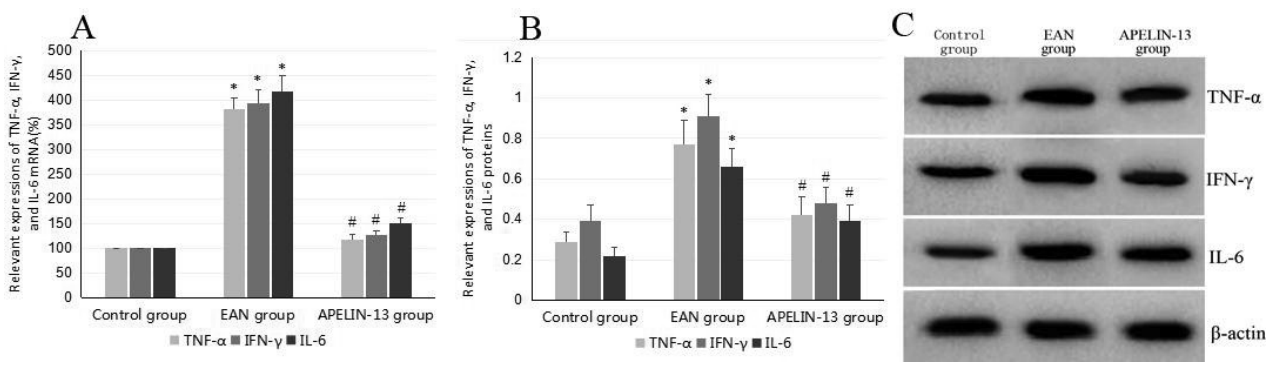

Fig. 2. *The mRNA and protein expressions of inflammatory factors TNF-α, IFN-γ, and IL-6 in lymph nodes. **A)** Relevant mRNA expressions of TNF-α, IFN-γ, and IL-6; **B)** Relevant protein expressions of TNF-α, IFN-γ, and IL-6; **C)** Immunity proteins of the 3 groups) (*P<0.05, compared with the control group; # P<0.05, compared with the EAN group).*

Infiltration of inflammatory cells into the sciatic nerves of rats in each group

As indicated in Table II and compared with the control group, the infiltration of inflammatory cells into the sciatic nerves of rats increased significantly in the EAN group on the 15th day after sensitization ($P<0.05$). Compared with the EAN group, the infiltration of inflammatory cells into the sciatic nerves of rats decreased significantly in the APELIN-13 group ($P<0.05$).

The plasma levels of TNF-α, IFN-γ, and IL-6 in each group

As shown in Table III, compared with the control group, the plasma levels of TNF-α, IFN-γ, and IL-6 of rats in the EAN group increased significantly on the 15th day after sensitization ($P<0.05$). Compared with the EAN group, the plasma levels of TNF-α, IFN-γ, and IL-6 in the APELIN-13 group decreased significantly ($P<0.05$).

Lymph node expressions of TNF-α, IFN-γ, and IL-6 in each group

As shown in Table IV and Fig. 2, the mRNA and protein expressions of TNF-α, IFN-γ, and IL-6 in lymph node tissues of rats in the EAN group increased significantly compared with the control group ($P<0.05$). Compared with the EAN model group, the APELIN-13 group showed significantly decreased mRNA and protein expressions of TNF-α, IFN-γ, and IL-6 in lymph node tissues ($P<0.05$).

DISCUSSION

Most of the previous studies have focused on the correlation between APELIN and diseases in the central nervous system (15, 16). Since GBS is a peripheral neurological disease while nerve fibers are a part of nerve cells (neurites or long dendrites) (17, 18), this study has speculated that APELIN exerts neuroprotective effects on peripheral nerve lesions. In this study, APELIN-13 was identified as an APELIN polypeptide most closely related to the nervous system and hence was used for the prevention and treatment of EAN. The results of the study showed that APELIN-13 delayed the incidence of EAN, shortened the course of disease, and significantly reduced the degree of inflammatory cell infiltration and demyelination of sciatic nerves.

TNF-α is a pleiotropic pro-inflammatory cytokine (19, 20). It has been shown that the serum level of TNF-α in GBS patients is significantly higher than that in normal people (21). Moreover, TNF-α is positively correlated with the severity of EAN, while the reduction in the TNF-α expression is conducive to the recovery of EAN. IL-6 is an inflammatory cytokine directly or indirectly participating in the pathogenesis of immune diseases of the central and peripheral nervous systems (22). IL-6 and the colony stimulating factor (CSF) can synergistically promote the growth and differentiation of primary bone marrow-derived cells (23, 24). IFN-γ is also involved in the development of various autoimmune diseases (25) by activating macrophages to release oxygen free radicals, so as to promote the migration of macrophages and T lymphocytes to the nervous system while promoting the expression of MHC II molecules on macrophages, thereby aggravating the inflammatory responses of EAN (26, 27). The results of this study have shown that APELIN-13 significantly reduced the plasma levels of TNF-α, IL-6, and IFN-γ in EAN rats. Also, APELIN-13 significantly down-regulated the mRNA and protein expression of TNF-α, IL-6, and IFN-γ in the lymph nodes of EAN rats.

In summary, the results of this study indicated that APELIN-13 can be used as an effective preventive treatment of EAN. Furthermore, the results also suggested that APELIN-13 could be used as a new prevention and treatment method for GBS.

ACKNOWLEDGEMENT

This work was supported by Youth Science Fund of Heilongjiang Provincial Science and Technology Department.

REFERENCES

1. Shen D, Chu F, Lang Y, Geng Y, Zheng X, Zhu J, Liu K. Beneficial or harmful role of macrophages in Guillain-Barré syndrome and experimental

autoimmune neuritis. Mediators Inflamm 2018; 2018:4286364.
2. Zhang HL, Wu J, Zhu J. The role of apolipoprotein E in Guillain-Barré syndrome and experimental autoimmune neuritis. J Biomed Biotechnol 2010; 2010:357412.
3. Zhang HL, Zheng XY, Zhu J. Th1/Th2/Th17/Treg cytokines in Guillain–Barré syndrome and experimental autoimmune neuritis. Cytokine Growth Factor Rev 2013; 24(5):443-53.
4. Yuan F, Yosef N, Lakshmana Reddy C, Huang A, Chiang SC, Tithi HR, Ubogu EE. ccr2 gene deletion and pharmacologic blockade ameliorate a severe murine experimental autoimmune neuritis model of Guillain-Barré syndrome. PLoS One 2014; 9(3):e90463.
5. Wang X, Zheng XY, Ma C, et al. Mitigated Tregs and augmented Th17 cells and cytokines are associated with severity of experimental autoimmune neuritis. Scand J Immunol 2014; 80(3):180-90.
6. Han R, Xiao J, Zhai H, Hao J. Dimethyl fumarate attenuates experimental autoimmune neuritis through the nuclear factor erythroid-derived 2-related factor 2/hemoxygenase-1 pathway by altering the balance of M1/M2 macrophages. J Neuroinflammation 2016; 13(1):97.
7. Chantal B, Angelica P, Estelle W, et al. Effects of dietary eicosapentaenoic acid (EPA) supplementation in high-fat fed mice on lipid metabolism and Apelin/APJ system in skeletal muscle. PLoS One 2013; 8(11):e78874.
8. Pope GR, Roberts EM, Lolait SJ, O'Carroll AM. Central and peripheral apelin receptor distribution in the mouse: Species differences with rat. Peptides 2012; 33(1):139-48.
9. Kidoya H, Kunii N, Naito H, Muramatsu F, Okamoto Y, Nakayama T, Takakura N. The apelin/APJ system induces maturation of the tumor vasculature and improves the efficiency of immune therapy. Oncogene 2012; 31(27):3254-64.
10. Bao HJ, Zhang L, Han WC, Dai DK. Apelin-13 attenuates traumatic brain injury-induced damage by suppressing autophagy. Neurochem Res 2015; 40(1):89-97.
11. Yu S, Zhang Y, Li MZ, et al. Chemerin and apelin are positively correlated with inflammation in obese type 2 diabetic patients. Chin Med J (Engl) 2012; 125(19):3440-44.
12. Yu S, Zhang Y, Li MZ, et al. Chemerin and apelin are positively correlated with inflammation in obese type 2 diabetic patients. Chin Med J (Engl) 2012; 125(19):3440-4.
13. Leeper NJ, Tedesco MM, Kojima Y, et al. Apelin prevents aortic aneurysm formation by inhibiting macrophage inflammation. Am J Physiol Heart Circ Physiol 2009; 296(5):H1329-35.
14. Xiao J, Zhai H, Yao Y, et al. Chrysin attenuates experimental autoimmune neuritis by suppressing immuno-inflammatory responses. Neuroscience 2014; 262:156-64.
15. Acar N, Parlak H, Ozkan A, Soylu H, Avcı S, Ustunel I, Izgut-Uysal VN, Agar A. The effect of docosahexaenoic acid on apelin distribution of nervous system in the experimental mouse model of Parkinson's disease. Tissue Cell 2019; 56:41-51.
16. Wu D, He L, Chen L. Apelin/APJ system: a promising therapy target for hypertension. Mol Biol Rep 2014; 41(10):6691-703.
17. Previtali SC, Archelos JJ, Hartung HP. Expression of integrins in experimental autoimmune neuritis and Guillain-Barre syndrome. Ann Neurol 1998; 44(4):611-21.
18. Willison HJ, Jacobs BC, van Doorn PA. Guillain-Barré syndrome. Lancet 2016; 388(10045):717-27.
19. Shen D, Lang Y, Chu F, et al. Roles of macrophage migration inhibitory factor in Guillain-Barré syndrome and experimental autoimmune neuritis: beneficial or harmful?. Expert Opin Ther Targets 2018; 22(7):567-77.
20. Lu MO, Duan RS, Quezada HC, et al. Aggravation of experimental autoimmune neuritis in TNF-α receptor 1 deficient mice. J Neuroimmunol 2007; 186(1-2):19-26.
21. Han F, Luo B, Shi R, Han C, Zhang Z, Xiong J, Jiang M, Zhang Z. Curcumin ameliorates rat experimental autoimmune neuritis. J Neurosci Res 2014; 92(6):743-50.
22. Gijbels K, Van Damme J, Proost P, Put W, Carton H, Billiau A. Interleukin 6 production in the central nervous system during experimental autoimmune encephalomyelitis. Eur J Immunol 1990; 20(1):233-35.
23. Rallidis LS, Zolindaki MG, Manioudaki HS, Laoutaris NP, Velissaridou AH, Papasteriadis EG.

Prognostic value of C-reactive protein, fibrinogen, Interleukin-6, and macrophage colony stimulating factor in severe unstable angina. Clin Cardiol 2002; 25(11):505-10.

24. Kim K, Duramad O, Qin XF, Su B. MEKK3 is essential for lipopolysaccharide-induced interleukin-6 and granulocyte-macrophage colony-stimulating factor production in macrophages. Immunology 2007; 120(2):242-50.
25. Zhang HL, Azimullah S, Zheng XY, et al. IFN-γ deficiency exacerbates experimental autoimmune neuritis in mice despite a mitigated systemic Th1 immune response. J Neuroimmunol 2012; 246(1-2):18-26.
26. Zou LP, Ma DH, Wei L, van der Meide PH, Mix E, Zhu J. IFN-beta suppresses experimental autoimmune neuritis in Lewis rats by inhibiting the migration of inflammatory cells into peripheral nervous tissue. J Neurosci Res 1999; 56(2):123-30.
27. Pineda AA, Minohara M, Kawamura N, et al. Preventive and therapeutic effects of the selective Rho-kinase inhibitor fasudil on experimental autoimmune neuritis. J Neurol Sci 2011; 306(1-2):115-20.

DYSREGULATION OF miR-195-5p/-218-5p/BIRC5 AXIS PREDICTS A POOR PROGNOSIS IN PATIENTS WITH GASTRIC CANCER

J. ZOU[1*], X. LIAO[2*], J. ZHANG[1] and L. WANG[1]

[1]Department of Gastroenterology, Shanghai Jiao Tong University Affiliated Sixth People's Hospital, Shanghai, China; [2]Department of Gastroenterology, Baoan Central Hospital of Shenzhen, the Fifth Affiliated Hospital of Shenzhen University, Shenzhen, Guangdong, China

Received April 11, 2019 – Accepted July 12, 2019

[*]These Authors contributed equally to this article

MicroRNAs (miRNAs) function by negatively regulating their target genes. Aberrant expression of baculoviral IAP repeat containing 5 (BIRC5) is associated with the tumor growth and metastasis, however, the clinical significance of miRNAs/BIRC5 axis in gastric cancer (GC) remains unknown. The association of BIRC5 or miR-195-5p/-218-5p expression levels with the clinicopathological characteristics and prognosis in patients with GC was analysed by using a tissue microarray and TCGA dataset. Pearson correlation analysis was used for analysing the correlation of BIRC5 with miR-195-5p/-218-5p expression in GC tissues. Cox proportional hazard regression model was conducted to assess whether BIRC5 or miR-195-5p/-218-5p was an independent prognostic factor in patients with GC. We found that BIRC5 expression levels were increased in GC tissues as compared with the adjacent normal tissues, and acted as an independent prognostic factor of tumor recurrence in patients with GC. Increased expression of BIRC5 was traceable to the dysregulation of miR-195-5p/-218-5p rather than its genetic and epigenetic alterations in GC tissues. MiR-195-5p/-218-5p displayed a negative correlation with BIRC5 expression, and acted as independent prognostic factors of poor prognosis in patients with GC. In conclusion, dysregulation of miR-195-5p/-218-5p/BIRC5 axis predicts a poor prognosis in patients with gastric cancer

Gastric cancer (GC) ranks the third place in malignancies and exhibits the third leading cause of cancer-related death in China (1). The outcomes of patients with advanced GC are undesirable due to their invasive and metastatic potential. Accumulating data indicate that the pathogenesis and progression of GC are ascribed to the genetic and epigenetic alterations in oncogenes or tumor suppressors (2). Thus, screening the promising biomarkers related to the carcinogenesis of GC is urgently needed.

Baculoviral inhibitor of apoptosis repeat-containing 5 (BIRC5) has been proved to be associated with the progression of GC. The expression levels of BIRC5, increased in GC tissues and associated with TNM stage and lymph node metastasis (3), act as an independent prognostic factor of poor survival (4, 5), as well as a predictor of response to chemotherapy in patients with GC (6). Moreover, BIRC5 promotes metastases by augmenting VEGF-C expression (7), and inhibition of BIRC5 represses the tumor growth

Key words: BIRC5; miR-195-5p; miR-218-5p; survival; recurrence; gastric cancer

Corresponding Author:
Dr Jing Zhang,
Department of Gastroenterology,
Shanghai Jiao Tong University
Affiliated Sixth People's Hospital,
Yishan Road 600, Shanghai 200233, China
Tel.: +86 021-24058969
e-mail: jing5522724@163.com

0393-974X (2019)

(8), indicating BIRC5 as a prognostic factor in patients with GC.

It is known that microRNAs (miRNAs) function by negatively modulating their targets. Increasing evidence showed that miR-138-5p/-203/-542-3p/-195 contribute to the repression of cell proliferation and invasion by targeting BIRC5 in multiple malignancies (9-13). In addition, miR-218 enhances the cisplatin sensitivity by targeting BIRC5 in GC cells (14, 15). These studies reveal the interaction between BIRC5 and miRNAs in cancer. In the present study, we found that BICR5 expression levels were increased in GC tissues, and acted as an independent prognostic factor of tumor recurrence in patients with GC. Upregulation of BICR5 was attributable to the dysregulation of miR-195-5p/-218-5p, and they were regarded as independent prognostic factors of poor prognosis in patients with GC.

MATERIALS AND METHODS

Clinical samples

A tissue microarray (TMA) including 30 pair-matched GC tissue samples was purchased from Xi'an Alena Biotech Co. Ltd (ST8018, Xi'an, China). The clinicopathological data in another cohort for 383 cases of GC samples and 30 adjacent normal tissues as well as the relative expression levels of BIRC5 and 11 miRNAs (has-miR-135a-5p, has-miR-144-3p, has-miR-184, has-miR-195-5p, has-miR-204-5p, has-miR-218-5p, has-miR-335-5p, has-miR-485-5p, has-miR-497-5p, has-miR-499a-5p and has-miR-501-5p) were downloaded from The Cancer Genome Atlas (TCGA) RNA-seq database (https://genome-cancer.ucsc.edu). The protocols used in our study were approved by the Ethics Committee of Shanghai Sixth People's Hospital.

Immunohistochemical analysis

The protein expression of BIRC5 was examined by using immunohistochemical (IHC) analysis in 30 pair-matched GC tissues from the TMA. These tissues were stained by using anti-BIRC5 (ab469, Abcam, Cambridge, MA, USA). The detailed description of the IHC method as well as the quantification of BIRC5 protein expression was performed as previously described (16).

Identification of BIRC5-specific binding with miRNAs

Eleven miRNAs (has-miR-135a-5p, has-miR-144-3p, has-miR-184, has-miR-195-5p, has-miR-204-5p, has-miR-218-5p, has-miR-335-5p, has-miR-485-5p, has-miR-497-5p, has-miR-499a-5p and has-miR-501-5p) that target BIRC5 3'UTR were identified by using the StarBase v2.0 (http://starbase.sysu.edu.cn/starbase2/ index.php) according to the number of supporting experiments (n >5) and number of cancer types (n = 3).

Statistical analysis

Statistical analysis was performed by SPSS 20.0 (IBM, SPSS, Chicago, IL, USA) and GraphPad Prism. Student's *t*-test or *Chi*-squared test were used to evaluate the statistical significance for the comparisons of two groups. Pearson's correlation coefficient analysis was used to analyze the correlations of BIRC5 with miRNAs. Overall survival was recurrence curves analyzed with the Kaplan-Meier plotter and log-rank test. Univariate analysis and multivariate models were performed by using a Cox proportional hazards regression model. $P < 0.05$ was considered statistically significant.

RESULTS

Increased expression of BIRC5 was associated with tumor recurrence in patients with GC

BIRC5 protein expression levels were detected in 30 paired GC tissue samples by using IHC analysis, indicating that the positive expression of BIRC5 was elevated in GC tissues as compared with the adjacent normal tissues ($P = 0.030$; Fig. 1A). TCGA dataset further demonstrated that the expression levels of BIRC5 were dramatically increased in unpaired (n = 383, $P < 0.0001$) and paired GC tissues (n = 30, $P < 0.0001$; Fig. 1B). These studies indicated that increased expression of BIRC5 was frequent even in GC.

In addition, according to the survival time, survival status and BIRC5 expression levels, a cutoff value of BIRC5 was achieved by using a Cutoff Finder tool (http://molpath.charite.de/cutoff/load.jsp) in GC tissue samples (Fig. 1C), and divided the patients into high BIRC5 expression (n = 53) and low BIRC5 expression groups (n = 237; Fig. 1D). We then analysed the association of BIRC5

expression with the clinicopathological parameters and prognosis in patients with GC, and found that high expression of BIRC5 was associated with age ($P = 0.027$) and distant metastasis ($P < 0.0001$), but had no association with other factors (each $P > 0.05$) in patients with GC (Table I).

Kaplan-Meier analysis further indicated that the patients with high BIRC5 expression had a higher tumor recurrence (Fig. 1E), but showed no difference in overall survival (Fig. 1F), as compared with those with low BIRC5 expression. Univariate and multivariate analysis demonstrated that high BIRC5 expression, as well as age and pathological stage, was an independent prognostic factor of tumor recurrence in patients with GC (Table II).

BIRC5 showed a negative correlation with miR-195-5p/-218-5p expression in GC tissue samples

To elucidate the reason why BIRC5 expression was increased in GC samples, we investigated the genetic and epigenetic alterations of BIRC5 in GC (n = 372), indicating that BIRC5 had no obvious alterations in genetic mutation (Fig. 2A), copy number (Fig. 2B) or methylation levels (Fig. 2C).

It was therefore hypothesized that BIRC5 expression might be regulated by miRNAs at post-transcriptional levels. To verify this hypothesis, we identified 11 miRNAs that may bind to BIRC5

Table I. *The association of BIRC5 expression with clinicopathological characteristics in patients with gastric cancer.*

Variables	Cases (n)	BIRC5		*P* value
		High	Low	
Total	290	53	237	
Age (years)				
≥60	201	30	171	
<60	89	23	66	0.027
Gender				
Male	184	29	155	
Female	106	24	82	0.145
Pathological stage				
I/II	133	24	109	
III/IV	157	29	128	0.926
T stage				
T1/T2	72	16	56	
T3/T4	218	37	181	0.318
N stage				
Negative	104	19	85	
Positive	186	34	152	0.998
M stage				
Negative	263	41	222	
Positive	27	12	15	< 0.0001

3'UTR by using StarBase v2.0, and examined their expression levels in GC tissue samples, of which miR-195-5p, miR-204-5p and miR-218-5p displayed a significantly decreased expression in unpaired (Fig. 3A) and paired GC tissue samples (Fig. 3B) as compared with the adjacent normal tissues. Pearson correlation analysis indicated that BIRC5 displayed a negative correlation with miR-195-5p and miR-218-5p rather than miR-204-5p in GC tissues (Fig. 3C).

Table II. *Cox regression analysis of BIRC5 expression as a predictor of tumor recurrence in patients with gastric cancer.*

Variables	Univariate Cox regression analysis		Multivariate Cox regression analysis	
	RR (95% CI)	*P* value	RR (95% CI)	*P* value
Age (years)				
<60 *vs* ≥60	1.561 (1.008 to 2.415)	0.046	1.892 (1.210 to 2.959)	0.005
Gender				
Male *vs* Female	1.088 (0.726 to 1.633)	0.682	NA	NA
Pathological stage				
III/IV *vs* I/II	1.802 (1.198 to 2.711)	0.005	1.968 (1.303 to 2.975)	0.001
T stage				
T3+T4 *vs* T1+T2	1.486 (0.910 to 2.428)	0.114	NA	NA
N staging				
Positive *vs* Negative	1.539 (0.997 to 2.377)	0.052	NA	NA
M stage				
Positive *vs* Negative	1.789 (1.017 to 3.147)	0.043	1.755 (0.996 to 3.093)	0.052
BIRC5 expression				
High *vs* Low	0.449 (0.277 to 0.727)	0.001	0.386 (0.238 to 0.627)	<0.0001

NA: not analyzed

Table III. *Cox regression analysis of miR-195-5p expression as a survival predictor in gastric cancer patients.*

Variables	Univariate Cox regression analysis		Multivariate Cox regression analysis	
	RR (95% CI)	*P* value	RR (95% CI)	*P* value
Age (years)				
<60 *vs* ≥60	1.575 (1.018 to 2.438)	0.041	1.845 (1.184 to 2.876)	0.007
Gender				
Male *vs* Female	1.072 (0.715 to 1.608)	0.736	NA	NA
Pathological stage				
III/IV *vs* I/II	1.781 (1.184 to 2.680)	0.006	1.823 (1.207 to 2.755)	0.004
T stage				
T3+T4 *vs* T1+T2	1.497 (0.916 to 2.445)	0.107	NA	NA
N staging				
Positive *vs* Negative	1.516 (0.981 to 2.341)	0.061	NA	NA
M stage				
Positive *vs* Negative	1.779 (1.012 to 3.128)	0.046	1.584 (0.895 to 2.803)	0.114
miR-195-5p expression				
High *vs* Low	1.966 (1.076 to 3.595)	0.028	2.027 (1.103 to 3.723)	0.023

NA: not analyzed

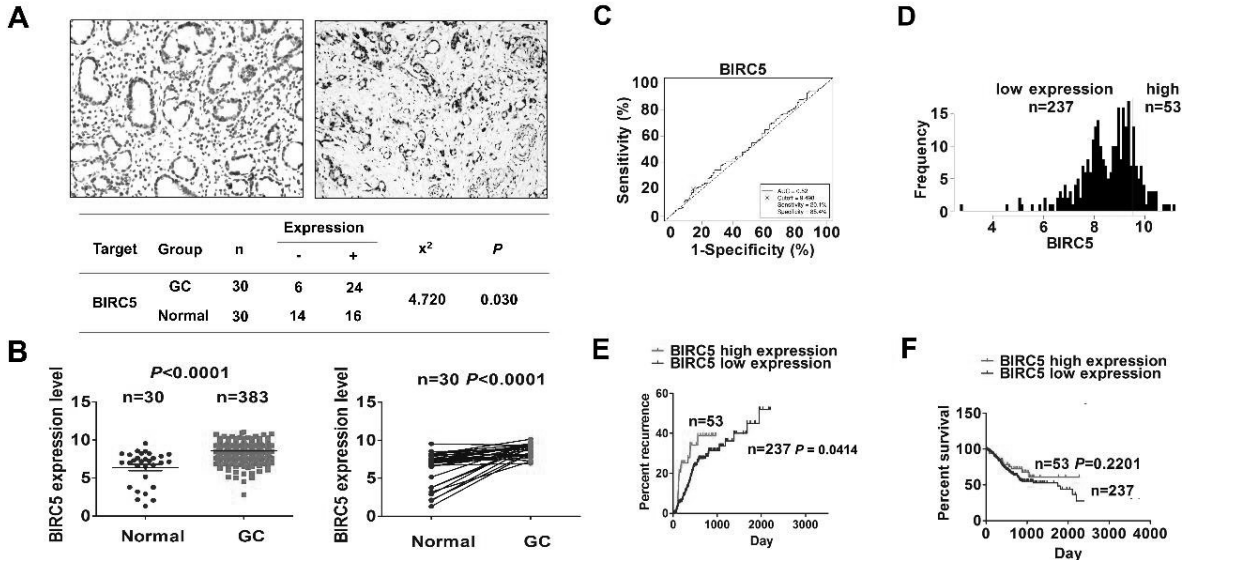

Fig. 1. *The association of BIRC5 expression with the prognosis in patients with GC. A) IHC analysis of the protein expression levels of BIRC5 in GC tissue samples. B) TCGA validation of the expression levels of BIRC5 in unpaired and paired GC tissue samples. C) ROC curve analysis of the cutoff value of BIRC5 in GC samples (n=290). D) The cutoff value of BIRC5 divided the GC patients into high BIRC5 expression and low BIRC5 expression groups. E, F) Kaplan Meier analysis of the association of high or low BIRC5 expression with the tumor recurrence and poor survival in patients with GC.*

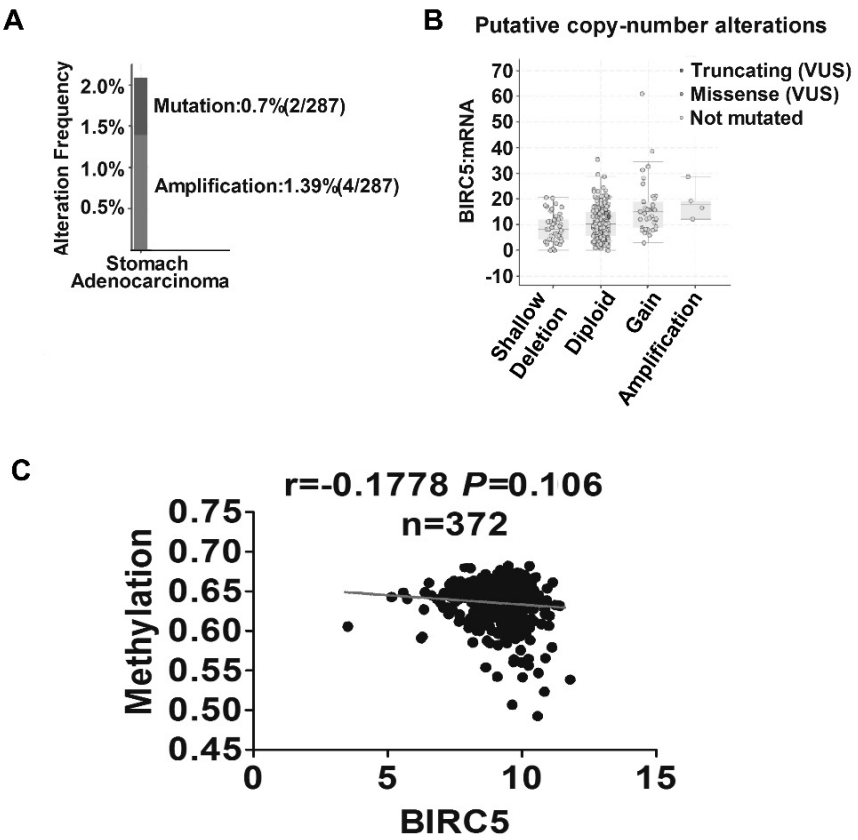

Fig. 2. *TCGA analysis of the association of BIRC5 expression with its (**A**) genetic mutation, (**B**) copy number and (**C**) methylation levels in GC tissue samples.*

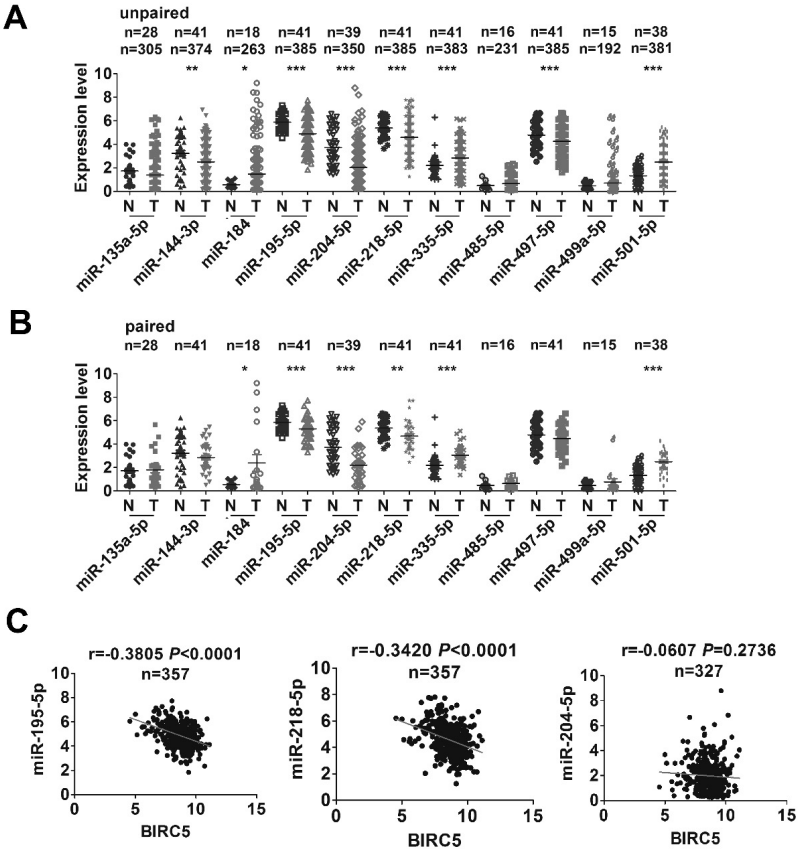

Fig. 3. *The correlation of BIRC5 with miR-195-5p/-218-5p expression in GC tissues.* ***A, B****) TCGA analysis of the expression levels of 11 miRNAs in unpaired and paired GC tissues.* ***C****) Pearson correlation analysis of the correlation of BIRC5 with miR-195-5p/-218-5p/-204-5p expression in GC tissues.*

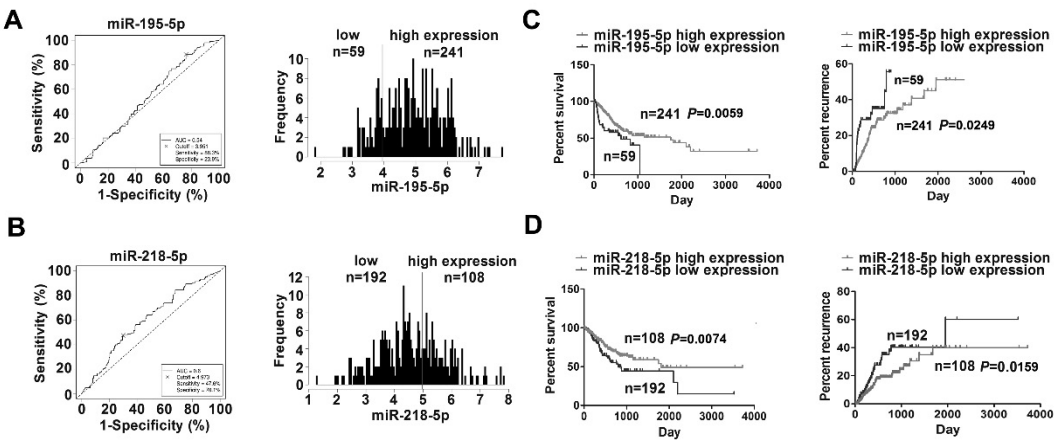

Fig. 4. *Low expression of miR-195-5p/-218-5p was associated with poor prognosis in GC patients.* ***A, B****) ROC curve analysis of the cutoff value of miR-195-5p/-218-5p in GC samples (n=300), and their cutoff values divided the patients into high miR-195-5p/-218-5p and low miR-195-5p/-218-5p expression groups.* ***C, D****) Kaplan Meier analysis of the association of high or low miR-195-5p/-218-5p expression with the poor survival and tumor recurrence in GC patients.*

Table IV. *Cox regression analysis of miR-218-5p expression as a survival predictor in gastric cancer patients.*

Variables	Univariate Cox regression analysis		Multivariate Cox regression analysis	
	RR (95% CI)	*P* value	RR (95% CI)	*P* value
Age (years)				
<60 *vs* ≥60	1.575 (1.018 to 2.438)	0.041	1.765 (1.136 to 2.742)	0.012
Gender				
Male *vs* Female	1.072 (0.715 to 1.608)	0.736	NA	NA
Pathological stage				
III/IV *vs* I/II	1.781 (1.184 to 2.680)	0.006	1.856 (1.229 to 2.802)	0.003
T stage				
T3+T4 *vs* T1+T2	1.497 (0.916 to 2.445)	0.107	NA	NA
N staging				
Positive *vs* Negative	1.516 (0.981 to 2.341)	0.061	NA	NA
M stage				
Positive *vs* Negative	1.779 (1.012 to 3.128)	0.046	1.755 (0.995 to 3.096)	0.052
miR-218-5p expression				
High *vs* Low	1.779 (1.207 to 2.622)	0.004	1.830 (1.241 to 2.699)	0.002

NA: not analyzed

Low expression of miR-195-5p/-218-5p was associated with a poor prognosis in patients with GC

Having confirmed the decreased expression levels of miR-195-5p/-218-5p in GC tissues (Fig. 4 A, B), we further analysed the association between miR-195-5p/-218 -5p expression and clinicopathological features and prognosis in patients with GC. The cutoff values of miR-195-5p/-218-5p were acqured in GC tissues (Fig. 4A, B) and divided the patients into high miR-195-5p/-218-5p expression and low miR-195-5p/-218-5p expression groups (Fig. 4A, B).

Furthermore, we found that miR-195-5p/-218-5p expression showed no association with the clinicopathological factors in patients with GC (each $P > 0.05$). Kaplan-Meier analysis indicated that the patients with low miR-195-5p/-218-5p expression possessed a shorter survival time and a higher tumor recurrence as compared with those with high miR-195-5p/-218-5p expression (Fig. 4C, D). Univariate and multivariate analyses revealed that low miR-195-5p/-218-5p expression was an independent prognostic factor of poor survival and tumor recurrence in patients with GC (Tables III, IV).

DISCUSSION

BIRC5 expression has been reported to be increased and to act as an oncogenic factor in GC (3-7). However, the association of BIRC5 expression with the prognosis of GC is still undocumented. In the present study, BIRC5 expression levels were verified to be increased in GC tissues in TMA and TCGA cohorts, which indicated that high expression of BIRC5 was associated with age and distant metastasis in GC patients. BIRC5 expression has been regarded as a poor prognostic biomarker in pancreatic ductal adenocarcinoma (17). We also found that high expression of BIRC5 was associated with tumor recurrence, acting as an independent prognostic factor of tumor recurrence in GC patients.

Furthermore, we found that the increased expression of BIRC5 in GC tissues might be attributable to the post-transcriptional regulation of miRNAs instead of its genetic and epigenetic alterations. Previous studies indicated that miR-203/-542-3p/-485-5p represses the tumor growth and metastasis and favors the chemosensitivity by

targeting BIRC5 in ovarian cancer (12), hepatocellular carcinoma (18) and breast cancer (19). MiR-195-5p and miR-218-5p, which were screened to bind with BIRC5 3'UTR, were identified to be downregulated, and exhibited a negative correlation with BIRC5 expression in GC tissues. Some studies showed that miR-195-5p acts as a tumor suppressor and a predictive factor of poor prognosis in melanoma by targeting hTERT (20), in lung cancer by targeting CIAPIN1 (21) and NOTCH2 in colorectal cancer (22). We also found that low expression of miR-195-5p was an independent prognostic factor of poor survival and tumor recurrence in patients with GC.

In addition, miR-218-5p represses growth and invasion via LYN/NF-κB signaling in cervical cancer (23), and via CDK6/CyclinD1/E2F1 axis in GC (24), and inhibition of miR-218-5p facilitates the invasion of oral carcinoma via activation of CD44-ROCK signaling (25). Low expression of miR-218-5p is associated with distant metastasis and poor prognosis in patients with GC (24). In accordance with these studies, we also found that low expression of miR-218-5p acted as an independent prognostic factor of poor survival and tumor recurrence in patients with GC. Our findings indicate that increased expression of BIRC5 might be directly regulated by miR-195-5p/-218-5p in GC.

The present study demonstrated that increased expression of BIRC5 or decreased expression of miR-195-5p/-218-5p were associated with poor survival and tumor recurrence, and acted as independent prognostic factors of poor prognosis in GC patients. miR-195-5p/-218-5p/BIRC5 axis might represent promising biomarkers for predicting poor prognosis in GC patients.

REFERENCES

1. Chen W, Zheng R, Zhang S, et al. Cancer incidence and mortality in China, 2013. Cancer Lett 2017; 401:63-71.
2. Yamashita S, Kishino T, Takahashi T, et al. Genetic and epigenetic alterations in normal tissues have differential impacts on cancer risk among tissues. Proc Natl Acad Sci U S A 2018; 115:1328-33.
3. Gu Y, Jin S, Wang F, et al. Clinicopathological significance of PI3K, Akt and survivin expression in gastric cancer. Biomed Pharmacother 2014; 68:471-75.
4. Chen J, Li T, Liu Q, Jiao H, Yang W, Liu X, Huo Z. Clinical and prognostic significance of HIF-1α, PTEN, CD44v6, and survivin for gastric cancer: a meta-analysis. PLoS One 2014; 9:e91842.
5. Cerda-Opazo P, Valenzuela-Valderrama M, Wichmann I, et al. Inverse expression of survivin and reprimo correlates with poor patient prognosis in gastric cancer. Oncotarget 2018;9:12853-67.
6. Bozkaya Y, Özdemir NY, Sezer S, et al. Is serum survivin expression a predictive biomarker in locally advanced gastric cancer patients treated with neoadjuvant chemotherapy? Cancer Biomark 2018; 22:143-49.
7. Zhang J, Zhu Z, Sun Z, Sun X, Wang Z, Xu H. Survivin gene expression increases gastric cancer cell lymphatic metastasis by upregulating vascular endothelial growth factor-C expression levels. Mol Med Rep 2014; 9:600-606.
8. Habib R, Akhtar J, Taqi M, Yu C, Zhang C. Lentiviral vector-mediated survivin shRNA delivery in gastric cancer cell lines significantly inhibits cell proliferation and tumor growth. Oncol Rep 2015; 34:859-67.
9. Yang R, Liu M, Liang H, et al. miR-138-5p contributes to cell proliferation and invasion by targeting Survivin in bladder cancer cells. Mol Cancer 2016; 15:82.
10. Chen X, Chen XG, Hu X, et al. MiR-34a and miR-203 inhibit survivin expression to control cell proliferation and survival in human osteosarcoma Cells. J Cancer 2016; 7:1057-65.
11. Althoff K, Lindner S, Odersky A, et al. miR-542-3p exerts tumor suppressive functions in neuroblastoma by downregulating Survivin. Int J Cancer 2015; 136:1308-20.
12. Wang B, Li X, Zhao G, et al. miR-203 inhibits ovarian tumor metastasis by targeting BIRC5 and attenuating the TGFβ pathway. J Exp Clin Cancer Res 2018; 37:235.
13. Yu X, Zhang Y, Cavazos D, Ma X, Zhao Z, Du L, Pertsemlidis A. miR-195 targets cyclin D3 and survivin to modulate the tumorigenesis of non-small cell lung cancer. Cell Death Dis 2018; 9:193.
14. Jingjing L, Wangyue W, Qiaoqiao X, Jietong Y. MiR-218 increases sensitivity to cisplatin in esophageal

cancer cells via targeting survivin expression. Open Med (Wars) 2016; 11:31-35.

15. Zhang Z, Kong Y, Yang W, Zhang B, Ma F, Liu H, Hua Y. MicroRNA-218 enhances gastric cancer cell cisplatin sensitivity by targeting survivin. Exp Ther Med 2018; 16:4796-802.
16. Zhang J, Jin M, Chen X, Zhang R, Huang Y, Liu H1, Zhu J. Loss of PPM1F expression predicts tumour recurrence and is negatively regulated by miR-590-3p in gastric cancer. Cell Prolif 2018; 51:e12444.
17. Zhou L, Lu J, Liang ZY, et al. High nuclear Survivin expression as a poor prognostic marker in pancreatic ductal adenocarcinoma. J Surg Oncol 2018; 118:1115-1121.
18. Wang XP, Yao J, Guan J, Zhou ZQ, Zhang ZY, Yang J. MicroRNA-542-3p functions as a tumor suppressor via directly targeting survivin in hepatocellular carcinoma. Biomed Pharmacother 2018; 99:817-24.
19. Wang M, Cai WR, Meng R, et al. miR-485-5p suppresses breast cancer progression and chemosensitivity by targeting survivin. Biochem Biophys Res Commun 2018; 501:48-54.
20. Chai L, Kang XJ, Sun ZZ, et al. MiR-497-5p, miR-195-5p and miR-455-3p function as tumor suppressors by targeting hTERT in melanoma A375 cells. Cancer Manag Res 2018; 10:989-1003.
21. Zheng J, Xu T, Chen F, Zhang Y. MiRNA-195-5p Functions as a tumor suppressor and a predictive of poor prognosis in non-small cell lung cancer by directly targeting CIAPIN1. Pathol Oncol Res 2019; doi: 10.1007/s12253-018-0552-z. [Epub ahead of print]
22. Lin X, Wang S, Sun M, et al. miR-195-5p/NOTCH2-mediated EMT modulates IL-4 secretion in colorectal cancer to affect M2-like TAM polarization. J Hematol Oncol 2019; 12:20.
23. Xu Y, He Q, Lu Y, Tao F, Zhao L, Ou R. MicroRNA-218-5p inhibits cell growth and metastasis in cervical cancer via LYN/NF-κB signaling pathway. Cancer Cell Int 2018; 18:198.
24. Deng M, Zeng C, Lu X, et al. miR-218 suppresses gastric cancer cell cycle progression through the CDK6/Cyclin D1/E2F1 axis in a feedback loop. Cancer Lett 2017; 403:175-85.
25. Li X, He J, Shao M, et al. Downregulation of miR-218-5p promotes invasion of oral squamous cell carcinoma cells via activation of CD44-ROCK signaling. Biomed Pharmacother 2018; 106:646-54.

EFFECT OF RhoC SILENCING ON MULTIPLE MYELOMA XENOGRAFTS AND ANGIOGENESIS IN NUDE MICE

K. LIU[1*], MM. SUN[1*], ZH. ZHAO[1], N. WEI[1], GZ. JIANG[1], ZY. WANG[1], L. ZHANG[1], XY. ZHU[2], LP. DAI[3], HM. YANG[4], T. WANG[1] and KS. CHEN[1]

[1]Department of Pathology, The First Affiliated Hospital of Zhengzhou University, Henan Key Laboratory of Tumor Pathology, Zhengzhou, China; [2]Histology and Embryology Teaching and Research Center, School of Basic Medical Sciences, Zhengzhou University, Zhengzhou, China; [3]Henan Academy of Medical and Pharmaceutical Sciences Department of Epidemmiology, Zhengzhou, China; [4]Henan Medical College Basic Medical Department, Zhengzhou, China

Received January 11, 2019 – Accepted July 12, 2019

[*] These authors equally contributed to this work

In this study, we investigated the expression of RhoC in the multiple myeloma (MM) cell line RPMI-8226, as well as the effects of silencing RhoC on the growth of tumor xenografts and tumor-induced angiogenesis in nude mice with MM. For this purpose, we transduced RPMI-8226 cells with lentiviral particles overexpressing short hairpin RNAs (shRNA) targeting RhoC. Tumor xenografts were generated by subcutaneously injecting nude mice with RPMI-8226 cells overexpressing control shRNA [negative control (NC) group] or the RhoC shRNA [the experimental (S) group], respectively. RhoC protein and mRNA levels in the tumor xenografts were measured. Nude mice were also subcutaneously inoculated with Matrigel mixed with vascular endothelial growth factor, and CD31 and KI67 levels in the tumor xenografts were measured by immunohistochemistry. Similarly, we assessed tumor xenograft growth and angiogenesis in Matrigel implants in the mice of both groups. We found that RhoC levels, microvessel density, and CD31 labeling index were more reduced in the S group than in the NC group. However, there was no significant difference in the size of tumor xenografts between the 2 groups. The number of new vessels and the neovascular length in the Matrigel implants were significantly lower in the S group than in the NC group. Therefore, we concluded that RhoC expression in myeloma xenografts has important effects on the induction of angiogenesis.

Multiple myeloma (MM) is the second most common hematologic malignancy and is mainly characterized by the abnormal proliferation of B cells (1). Studies on tumor angiogenesis have found that MM is similar to tumors in other sites in that tumor growth and development requires angiogenesis (2). The process of tumor angiogenesis is highly complex and involves the participation of many factors, which primarily include the tumor microenvironment, tumor cells and associated interstitial cells, as well as various cytokines (3, 4). As such, the sole use of myeloma cells as a target in the suppression of tumor angiogenesis for the treatment of MM has not achieved satisfactory results (5). The angiogenic

Key words: blood vessels; matrigel implants; multiple myeloma; RhoC; xenografts

Corresponding Author:
Dr Kuisheng Chen,
Department of Pathology,
The First Affiliated Hospital, Zhengzhou University,
Henan Key Laboratory of Tumor Pathology,
Zhengzhou, 450052, China
Tel.: 037167966358 - Fax: +86037166658175
e-mail: kuishengc@126.com

0393-974X (2019)

process involves endothelial cell proliferation and migration, lumen formation, and vascularization (6, 7). RhoC, a member of the Rho (Ras homologous) family, mainly functions as a regulator of the actin cytoskeleton, and plays a key role in cell proliferation and migration, and lumen formation (8-10).

Related study has found that RhoC expression is associated with cellular escape in MM cells (11), and RhoC expression in the tumor tissue is closely associated with angiogenesis (12). Therefore, we hypothesized that RhoC expression in MM cells is not only associated with angiogenesis, but also pivotal in tumor growth and development.

In this study, we silenced the expression of RhoC in RPMI-8226 cells by using a lentiviral vector overexpressing short hairpin RNA (shRNA) targeting RhoC, and used the RhoC-silenced cells to generate tumor xenografts in nude mice. The construction of myeloma animal models is complex and difficult to replicate in the clinical myeloma, and researchers can construct different animal models for the purposes of the research (13). This allowed us to investigate the *in vivo* effects of RhoC silencing on tumor growth and angiogenesis. By investigating the relationship between RhoC and RPMI-8226 xenografts, through this study we aim to provide new approaches for the clinical suppression of myeloma tissue growth and angiogenesis.

MATERIALS AND METHODS

Cell culture and animals

RPMI-8226 MM cells were grown in RPMI 1640 (Invitrogen /Gibco, California, USA) culture medium containing 10% fetal bovine serum (Invitrogen /Gibco, California, USA), and cultured in an incubator at 37°C and 5% CO_2. Cells were subcultured when they reached 80% confluency. For each experimental group, 5 BALB/c nude mice (aged 4 weeks, male) were used. Stably transduced RPMI-8226 myeloma cell lines (1×10^6) were injected into the left anterior axilla of the mice, and regular measurements of tumor volumes were made (14). When tumor size reached approximately 1 cm^3, Matrigel (BD Biosciences, New Jersey, USA) implants (of approximately 0.5 mL) containing VEGF165 (100 ng/mL) (PeproTech, New Jersey, USA) were injected into the right anterior axilla. The mice were sacrificed after 1 month of tumor formation. Tumors and Matrigel implants were then removed from the mice, and angiogenesis was quantified by performing vessel count under a microscope (Nikon, ECLIPSE Ti, Japan) (15).

All experiments were approved by the Animal Care and Ethics Committee of the University of Zhengzhou (China) and were conducted in accordance with the guidelines issued by the International Association for the Study of Pain.

RhoC shRNA lentiviral particles and transduction of cells

The packaging of the RhoC shRNA lentiviral particles was performed by Suzhou Gene Pharma. The recombinant lentivirus contains the (green fluorescent protein) *GFP* marker gene to enable the expression of green fluorescence in the transduced cells. The *RhoC* targeting sequence of the experimental group (S Group) was GGACACTGATGTCATCCTCAT; the non-targeting sequence of the negative control (NC) group was GTTCTCCGAACGTGTCACGT. RPMI-8226 cells (5×10^4 cells/well) were added to a 24-well plate and cultured. The following day, the cells were infected with viral particles overexpressing RhoC shRNA or NC shRNA diluted 1:10 with culture medium: 500 μL of the diluted lentivirus suspension were added to each well, and the medium was replaced after 12 h. The efficiency of lentiviral transduction was calculated by the percentage of cells that, upon observation under a fluorescence microscope, exhibited green fluorescence in 5 random fields at 200 × magnification (16). Stably transduced cells were selected by the addition of 1μg/mL puromycin (Merck, Darmstadt, Germany) to the culture medium.

Measurement of RhoC mRNA expression in RPMI-8226 myeloma cells by quantitative PCR (qPCR)

Total RNA was extracted using 300 μL of Ezol, and reverse transcribed using the SYBR PCR Master Mix (GenePharma, Shanghai, China). The PCR conditions were set as follows: initial denaturation at 95°C for 3 min, denaturation at 95°C for 3 s, annealing at 62°C for 40 s, elongation at 72°C for 5 min. Forty cycles were performed, with the amplified fragment having a length of approximately 113 bp. The following primer sequences were used: *RhoC*, forward CAGTGCCTTTGGCTACCTTG and reverse CCCTCCGACGCTTGTTCTT; glyceraldehyde

3-phosphate dehydrogenase (*GAPDH*), forward CATGAGAAGTATGACAACAGCCT and reverse AGTCCTTCCACGATACCAAAGT. The $2^{-\Delta\Delta CT}$ method was used to compare the relative *RhoC* mRNA expression levels between groups. *GAPDH* was used as internal standard. Three replicate wells were used for each group.

Measurement of RhoC protein expression in RPMI-8226 myeloma cells by Western blot analysis

Cells of the NC and S groups were lysed on ice for protein extraction using M-PER. Proteins were quantified, and, after heat denaturation, 10 µL of sample were loaded to each well of a sodium dodecyl sulfate-polyacrylamide gel, and electrophoresis was performed at 80 V for 30 min and 120 V for 60 min. After electrophoresis, protein transfer onto a PVDF membrane was performed at 80 V for 90 min. The membrane was incubated with anti-RhoC antibody (Abcam,1:500 Cambridge, UK), anti-actin antibody (Abcam,1:10000) overnight at 4°C, and with anti-mouse and anti-rabbit antibodies (Proteintech, 1:5,000) the following day at 25°C for 2 h. An ECL reagent (Thermo Fisher, Massachusetts, USA) was used for chemiluminescence detection. The images were obtained using a Tanon 4200 automatic chemiluminescence image analysis system (Tanon 4200, Beijing Yuanping Hao Biological Technology Co. Ltd). The experiment was repeated thrice for each group, and grayscale analysis of the images and quantification was performed using the Image J software (National Institute of Health, Bethesda, MD, USA).

Immunohistochemical detection of CD31 and KI67 expression

Tumor tissues were formalin-fixed and paraffin-embedded. Three slides were immunostained from each tissue samples. The slides were oven-dried for 30 min, sequentially passed through xylene for dewaxing and a series of decreasing concentrations of alcohols for hydration. After washing with tap water, antigen retrieval was carried out by boiling. The slides were then soaked in 3% H_2O_2 for 15 min. KI67 and CD31 antibodies (Proteintech, Chicago, USA) were diluted in PBS (1:500). The slides were incubated with the diluted antibodies overnight at 4°C, and then with the secondary antibody (Jackson ImmunoResearch, USA, 1:10,000) for 2 h at 25°C. Slides were stained with a DAB staining solution for 3 min, then photographed and observed under a microscope at 400× magnification.

KI67 was immunohistochemically localized in the cell nucleus, and positive labeling was indicated by a yellow or brownish-yellow staining. The KI67 labeling index (LI) was calculated as the mean percentage of positively labeled cells out of the total number of cells in 10 randomly selected fields at 400× magnification.

CD31 was used to label vascular endothelial cells, and microvessel densities (MVD) of the various groups were calculated by counting the number of microvessels at 400× magnification: a clear separation between brownish yellow-stained vascular endothelial cells and other cells, such as surrounding tumor cells, was regarded as one microvessel (17). For each group, counting was performed thrice, and the mean value was used for MVD calculation.

Statistical analysis

The SPSS 17.0 software (SPSS Inc., Chicago, IL, USA) was used to test the normality of data, and quantitative data that fulfilled the normality criterion were expressed as $\bar{x}\pm S$. The *t*-test was used to compare differences between 2 samples, and differences were considered statistically significant when $p < 0.05$.

RESULTS

Assessment of lentiviral transduction efficiency in RPMI-8226 myeloma cells

Forty-eight hours after lentiviral transduction, the expression of GFP was observed using a fluorescence microscope (Fig. 1). The transduction efficiency in RPMI-8226 cells was (48.85±2.10)%.

RhoC expression levels in tumor xenografts

Western blot and qPCR were used to measure RhoC protein and mRNA expression, respectively, in the tumor xenografts generated upon injection of control (NC) or RhoC-silenced (S) RPMI-8226 cells. Our results indicated that the relative RhoC protein levels in the S group were significantly lower than in the NC group ($p < 0.05$; Fig. 2, A and B). Similarly, the relative *RhoC* mRNA levels in the S group were significantly lower than in the NC group ($p < 0.05$; Fig. 2C). Therefore, the infection of RPMI-8226 cells with the RhoC shRNA lentiviral particles effectively

reduced RhoC expression levels in the cells of the tumor xenografts.

Effects of downregulated RhoC expression in RPMI-8226 cells on tumor xenografts and angiogenesis in nude mice

Two months after injection of the RPMI-8226 cells in the nude mice, no significant difference in the xenograft size was observed in the S group compared with the NC group ($p > 0.05$, Fig. 2D). Next, the effects were observed of RhoC silencing on angiogenesis in the Matrigel implants isolated from both groups.

The Matrigel implants were removed from the

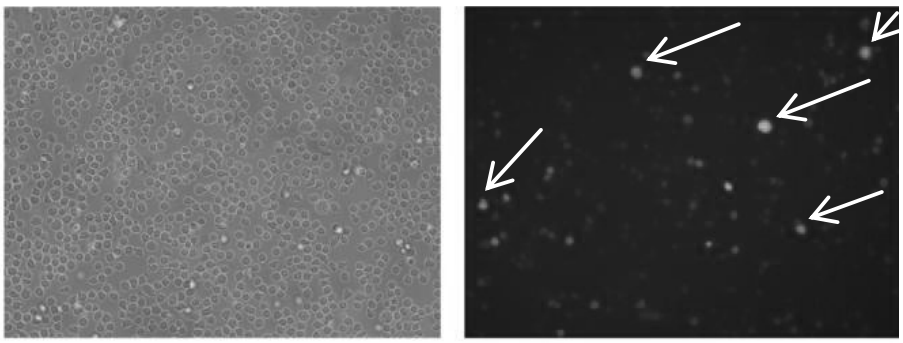

Fig. 1. *Evaluation of the efficacy of lentiviral transduction. The fluorescence was evaluated in RPMI-8226 cells after transduction. Arrows indicate cells transfected successfully on the right. Left, phase contrast image; right, fluorescence image. Magnification 200×.*

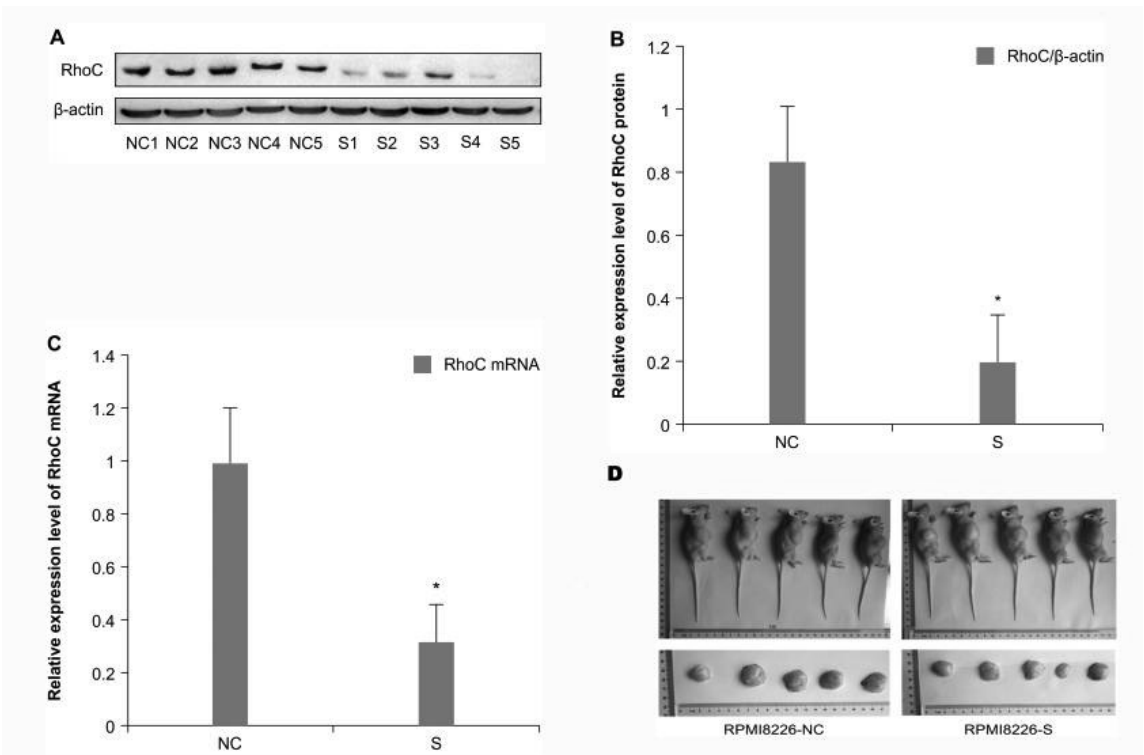

Fig. 2. *Expression of RhoC in tumor xenografts. Relative RhoC expression levels in RPMI-8226 cells of tumor xenografts in the control (NC) and RhoC-silenced (S) groups (n = 5 for both).* ***A****) Western blot.* ***B****) Quantification of the Western blot in A.* ***C****) Quantification of the quantitative PCR data.* ***D****) Size of RPMI-8226 xenografts in the control (NC) and RhoC-silenced (S) groups (n = 5), 2 months after injection.*

mice after 2 months. The Matrigel implants from the NC group exhibited a reddish color, and significant angiogenesis, while the implants from the S group were transparent with extremely low levels of angiogenesis (Fig. 3A, a and b). The Matrigel implants of the NC group were also larger in size than the ones from the S group. Observation under a microscope (Fig. 3A, c and d) found that the number of new vessels was significantly lower in the S group compared with the NC group (Fig. 3B; $p < 0.05$), and the neovascular length in the S group was significantly shorter than that of the NC group (Fig. 3C $p < 0.05$). Therefore, we concluded that the angiogenesis-inducing capability of the S group was significantly lower than that of the NC group.

Immunohistochemical detection of CD31 and KI67 in tumor tissues

We then analyzed the expression of CD31 and KI67 in the tumor xenografts generated upon injection of RPMI-8226 cells in the mice (Fig. 4). The KI67 LI of the NC and S groups were (78.49±3.03)% and (49.14±3.64)%, respectively, with the LI of the S group being significantly lower than that of the NC group ($p < 0.05$). The MVD of the NC and S groups were 19.00±2.65 and 6.67±1.53, respectively, with

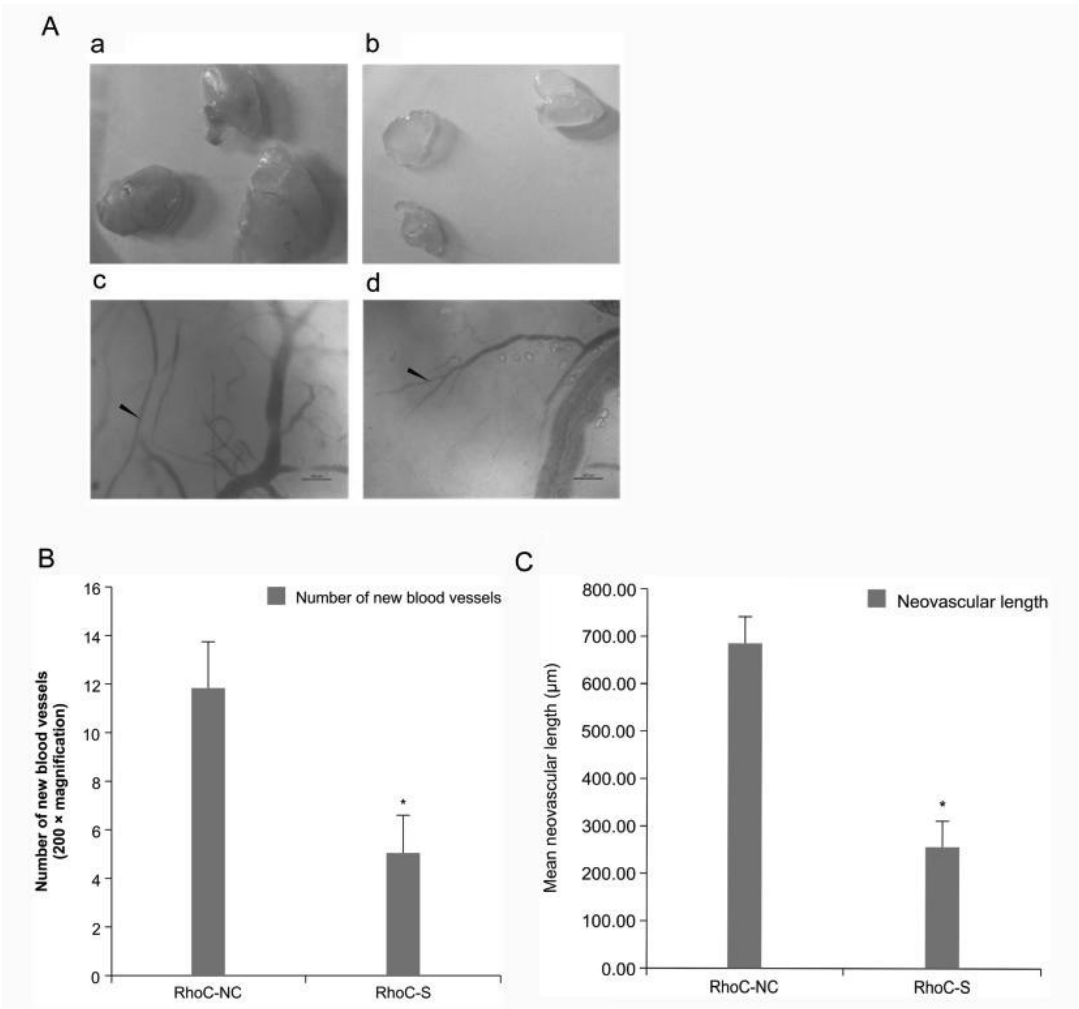

Fig. 3. *Angiogenesis in subcutaneous Matrigel implants in nude mice.* ***A****) Matrigel implants isolated from the control (NC) group (a) or the RhoC-silenced (S) group (b). c-d) Blood vessels in the Matrigel implants isolated from the NC (c) or S (d) group. Magnification, 100×; Scale bar = 100 μm.* ***B****) The number of new blood vessels in the Matrigels implants in the control (NC) group or the RhoC-silenced (S) group (n = 5).* ***C****) Neovascular length in the Matrigels implants in the control (NC) group or the RhoC-silenced (S) group (n=5). Arrow indicates blood vessel position. *: $p < 0.05$ compared with the NC group.*

the MVD of the S group being significantly lower than that of the NC group ($p < 0.05$), confirming impaired angiogenesis upon RhoC silencing.

DISCUSSION

RhoC is a member of the Rho (Ras homologous) family that functions as a regulator of the actin cytoskeleton and also plays key roles in cell migration and proliferation (10, 18). Studies have found that RhoC is expressed in various types of tumors, such as breast cancer (19), head and neck squamous cell carcinoma (20, 21), epithelial ovarian cancer (22), and cervical cancer (23). RhoC expression is closely and positively correlated with tumor cell infiltration and metastasis (11, 24). Studies on MM have indicated that RhoC plays an important role in MM cell migration and metastasis (11). Specifically, researchers have found that RhoC is critically involved in the interaction between cancer cells and vascular endothelial cells, and participates in tumor metastasis and development through the promotion of angiogenesis (25, 26).

In the present study, we used a shRNA lentiviral vector that enables the long-term and stable expression of shRNA in host cells, to interfere with RhoC expression in cells (27) and investigate RhoC-related functions in RPMI-8226 cells. Western blot and qPCR analyses indicated that the lentiviral particles we used could effectively downregulate RhoC expression in RPMI-8226 cells.

The RhoC-silenced cells were subsequently inoculated in nude mice. After 2 months, the size of tumor xenografts generated in the Rho-silenced (S) and control (NC) group was similar. It is possible that we did not find any effect of RhoC on tumor size because we measured the tumors 2 months after injection, and this could be an interval too long to notice any difference. On the contrary, relevant factors

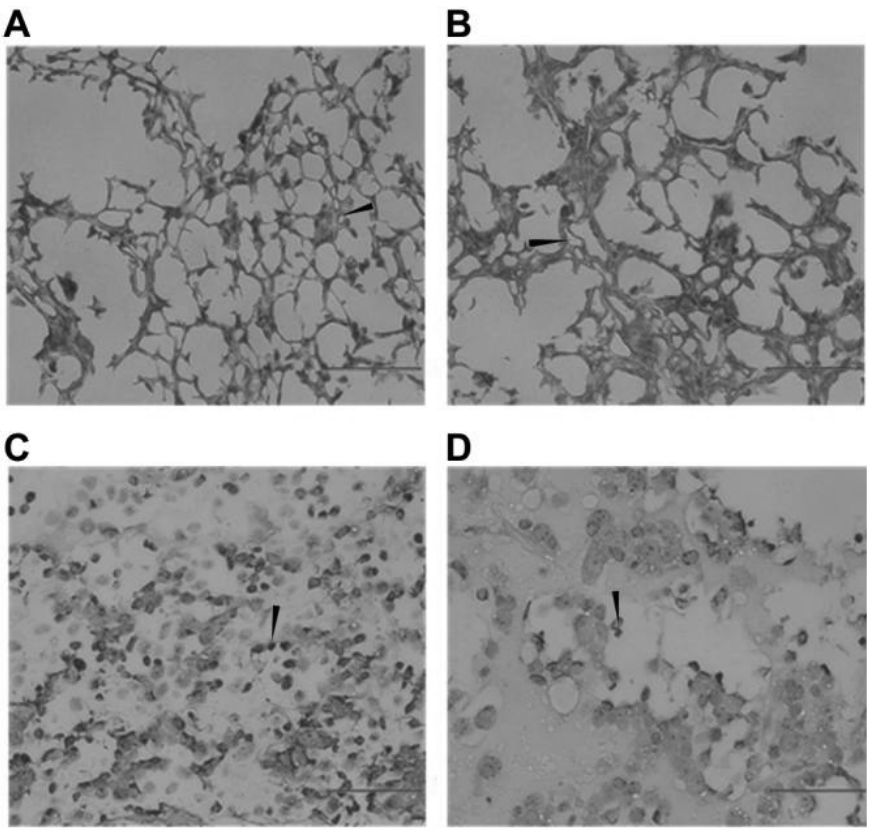

Fig. 4. *Immunohistochemical detection of CD31 and KI67 expression in the tumor xenografts.* ***A****) CD31 expression in the control (NC) group.* ***B****) CD31 expression in S group. Arrow indicates blood vessel position.* ***C****) KI67 expression in the NC group.* ***D****) KI67 expression in the S group. Magnification, 400×; scale bar = 50 μm. Arrow indicates positive cells*

that stimulate the growth of RPMI-8226 cells in nude mice might exist, and these might mask any RhoC-related effect. One study (28) revealed that the tumor microenvironment, tumor-associated macrophages and various cytokines play important roles in xenograft growth in nude mice. Some researchers believe that tumor growth and angiogenesis are associated with the Rho-associated protein kinase (ROCK) signaling pathway (29), with ROCK being a downstream effector of RhoC. A previous study on the association between RhoC and microvessel density in esophageal cancer found that RhoC can promote angiogenesis in esophageal cancer tissues through the upregulation of VEGF expression (30). In this study, immunohistochemical techniques were used to measure KI67 and CD31 expression in tumor xenografts from the 2 groups of mice, and the results indicated that the KI67 LI and the MVD of the S group were both significantly reduced compared with that of the NC group.

The angiogenic process is highly complex and involves multiple steps, including the proliferation and migration of vascular endothelial cells, and lumen formation. Several studies have highlighted that RhoC is expressed in vascular endothelial cells, and RhoC expression promotes cell proliferation and migration, and lumen formation and blood vessel sprouting (25, 31). In the present study, we found that the length and number of new blood vessels were both reduced in the S group compared with the NC group. The mechanism through which RhoC promotes angiogenesis may be related to its role in the regulation of VEGF, and/or to the suppression of endothelial cell network formation and blood vessel sprouting through the suppression of F-actin reorganization (12, 32, 33).

In conclusion, this study shows that RhoC expression in RPMI-8226 myeloma cells plays a key role in the induction of microvessel formation around tumor tissues.

ACKNOWLEDGEMENTS

The authors would like to express gratitude to Professor Kuisheng Chen for his supervision and guidance.

This study (Project 81570199) was supported by the National Natural Science Foundation of China.

REFERENCES

1. Willenbacher W, Seeber A, Steiner N, et al. Towards molecular profiling in multiple myeloma a literature review and early indications of its efficacy for informing treatment strategies.Int J Mol Sci 2018; 19:2344.
2. Du W, Hattori Y, Hashiguchi A, et al. Tumor angiogenesis in the bone marrow of multiple myeloma patients and its alteration by thalidomide treatment. Pathol Int 2004; 54:285-94.
3. Ribatti D. Mast cells and macrophages exert beneficial and detrimental effects on tumor progression and angiogenesis. Immunol Lett 2013; 152:83-88.
4. Ricciuti B, Foglietta J, Bianconi V, Sahebkar A, Pirro M. Enzymes involved in tumor-driven angiogenesis: A valuable target for anticancer therapy. Semin Cancer Biol 2019; 56:87-99.
5. Richardson PG, Barlogie B, Berenson J, et al. Extended follow-up of a phase II trial in relapsed, refractory multiple myeloma: Final time-to-event results from the SUMMIT trial. Cancer 2006; 106:1316-19.
6. Mombeinipour M, Zare MA, Mansuri K, Lotfi M. In vivo and in vitro anti-angiogenesis effect of venom-derived peptides (ICD-85). Arch Iran Med 2013; 16:109-13.
7. Wijk X, Kuppevelt T. Heparan sulfate in angiogenesis: a target for therapy. Angiogenesis 2014; 17:1-20.
8. Lang S, Busch H, Boerries M, et al. Specific role of RhoC in tumor invasion and metastasis. Oncotarget 2017; 8:87364-78.
9. Srivastava S, Ramdass B, Nagarajan S, Rehman M, Mukherjee G, Krishna S. Notch1 regulates the functional contribution of RhoC to cervical carcinoma progression. Br J Cancer 2010; 102:196-05.
10. Xu XD, Shen HB, Zhu L, Lu JQ, Zhang L, Luo ZY, Wu YQ. Anti-RhoC siRNAs inhibit the proliferation and invasiveness of breast cancer cells via modulating the KAI1, MMP9, and CXCR4 expression. Onco Targets Ther 2017; 10:1827-34.
11. Lv J, Xiao Q, Wang L, et al. Fucoidan prevents multiple myeloma cell escape from chemotherapy-induced drug cytotoxicity. Fitoterapia 2013; 84:257-63.
12. Wang W, Wu F, Fang F, Tao YM, Yang LY. RhoC is essential for angiogenesis induced by hepatocellular

carcinoma cells via regulation of endothelial cell organization. Cancer sci 2008; 99:2012-18.
13. Libouban H. The use of animal models in multiple myeloma. Morphologie 2015; 99:63-72.
14. Schmidt M, Kim Y, Gast SM, Endo T, Lu D, Carson D, Schmidt-Wolf IG. Increased in vivo efficacy of lenalidomide and thalidomide by addition of ethacrynic acid. In Vivo 2011; 25:325-33.
15. Chigurupati S, Kulkarni T, Thomas S, Shah G. Calcitonin stimulates multiple stages of angiogenesis by directly acting on endothelial cells. Cancer Res 2005; 65:8519-29.
16. Durán MC, Willenbrock S, Barchanski A, et al. Comparison of nanoparticle-mediated transfection methods for DNA expression plasmids: efficiency and cytotoxicity. J Nanobiotechnology 2011; 9:47.
17. Al-Ghorbani M, Vigneshwaran V, Ranganatha VL, Prabhakar BT, Khanum SA. Synthesis of oxadiazole–morpholine derivatives and manifestation of the repressed CD31 Microvessel Density (MVD) as tumoral angiogenic parameters in Dalton's Lymphoma. Bioorg Chem 2015; 60:136-46.
18. Chen R, Cheng Y, Zhang Y, Li Z, Geng L. RhoC mediates invasion and migration of caski cells through the Rho-associated serine-threonine protein kinase 1 signaling pathway. Int J Gynecol Cancer 2014; 24:184-91.
19. .Kaushal N, Durmaz YY, Bao LW, Merajver SD, ElSayed ME. "Smart" nanoparticles enhance the cytoplasmic delivery of anti-RhoC Silencing RNA and inhibit the migration and invasion of aggressive breast cancer cells. Mol Pharm 2015; 12:2406-17.
20. Islam M, Sharma S, Teknos TN. rhoc regulates cancer stem cells in head and neck squamous cell carcinoma by overexpressing IL-6 and phosphorylation of STAT3. PLoS ONE 2014; 9:e88527.
21. Tumur Z, Katebzadeh S, Guerra C, Bhushan L, Alkam T, Henson BS. RhoC mediates epidermal growth factor-stimulated migration and invasion in head and neck squamous cell carcinoma. Neoplasia 2015; 17:141-51.
22. Chen X, Chen S, Xiu YL, Sun KX, Zong ZH, Zhao Y. RhoC is a major target of microRNA-93-5P in epithelial ovarian carcinoma tumorigenesis and progression. Mol Cancer 2015; 14:31.
23. He XQ, Qian Y, Cai HL, Yang SH, Cai J, Wang ZH. RhoC is essential in TGF-β1 induced epithelial-mesenchymal transition in cervical cancer cells. Oncol Lett 2015; 10:985-89.
24. Sang XB, Sun KX, Wang LL, Chen S, Wu DD, Zong ZH, Zhao Y. Effects and mechanism of RhoC downregulation in suppressing ovarian cancer stem cell proliferation, drug resistance, invasion and metastasis. Oncol Rep 2016; 36:267-74.
25. Chang GH, Lay AJ, Ting KK, et al. ARHGAP18: an endogenous inhibitor of angiogenesis, limiting tip formation and stabilizing junctions. Small GTPases 2014; 5:1-15.
26. Reymond N, Im JH, Garg R, et al. RhoC and ROCKs regulate cancer cell interactions with endothelial cells. Mol Oncol 2015; 9:1043-55.
27. Hutson TH, Foster E, Moon LD, Yáñez-Muñoz RJ. Lentiviral vector-mediated RNA silencing in the central nervous system. Hum Gene Ther Methods 2014; 25:14-32.
28. Cho HJ, Jung JI, Lim DY, Kwon GT, Her S, Park JH, Park JH. Bone marrow-derived, alternatively activated macrophages enhance solid tumor growth and lung metastasis of mammary carcinoma cells in a Balb/C mouse orthotopic model. Breast Cancer Res 2012; 14:R81.
29. Croft DR, Sahai E, Mavria G, et al. Conditional ROCK activation in vivo induces tumor cell dissemination and angiogenesis. Cancer Res 2004; 64:8994-9001.
30. Zhao ZH, Tian Y, Yang JP, Zhou J, Chen KS. RhoC, vascular endothelial growth factor and microvascular density in esophageal squamous cell carcinoma. World J Gastroenterol 2015; 21:905-12.
31. Hoeppner LH, Sinha S, Wang Y, et al. RhoC maintains vascular homeostasis by regulating VEGF-induced signaling in endothelial cells. J Cell Sci 2015; 128:3556-68.
32. Ming J, Liu N, Gu Y, Qiu X, Wang EH. PRL-3 facilitates angiogenesis and metastasis by increasing ERK phosphorylation and up-regulating the levels and activities of Rho-A/C in lung cancer. Pathology 2009; 41:118-26.
33. van Golen KL, Wu ZF, Qiao XT, Bao L, Merajver SD. RhoC GTPase overexpression modulates induction of angiogenic factors in breast cells. Neoplasia 2000; 2:418-25.

17β-ESTRADIOL REPLACEMENT THERAPY INDUCES eNOS, nNOS AND ESTROGEN RECEPTOR β IN HYPOPHYSECTOMIZED RATS WITH INFLAMED FOOTPADS

C. VERA-ARZAVE[1], J. PACHECO-YEPEZ[1], C.M. MEJÍA-BARRADAS[1], L.M. CÁRDENAS-JARAMILLO[2], R. CAMPOS-RODRÍGUEZ[1] and E. ABARCA-ROJANO[1]

[1]National Polytechnic Institute, Graduate Studies and Research Section, Superior School of Medicine, Mexico City, Mexico; [2]National Polytechnic Institute, Superior School of Medicine, Mexico City, Mexico

Received February 14, 2019 – Accepted July 22, 2019

Nitric oxide (NO) plays a key role in inflammation. It is partly produced by three forms of NOS: eNOS of inflammatory cells, nNOS of neural cells and iNOS (inducible isoform). Estrogens can cause an anti-inflammatory effect, although it is not yet clear through which NOS isoforms. The aim of this study was to evaluate the role of the different NOS isoforms, as well as estrogen receptors (ERs) α and β, on the anti-inflammatory effects of estrogens. To avoid the influence of endogenous glucocorticoids or sexual hormones, male rats were hypophysectomized. Animals were segregated into two control groups (no-treatment control group and SHAM-operated animals) and three hypophysectomized groups (no-hormonal treatment, with estradiol-17β, or with testosterone replacement treatment). Freund's complete adjuvant (1 mg) was administered to the footpad of all animals. Measurements were made based on footpad inflammation (with a plethysmometer) such as eNOS, nNOS, iNOS and ER α and β protein expression (by immunohistochemistry principle/method) on days 1, 7 and 14. Only estradiol decreased inflammation, accompanied by increased levels of eNOS and nNOS and differential expression of ERs α and β in the inflammatory infiltrate. The higher levels of estradiol-induced eNOS and nNOS ocurred perhaps through the activation of ER β.

Inflammation, which is an essential component of the immune system, is regulated by hormones and other factors. During the tissue repair process after damage or trauma, it is well established that neurotransmitters, hormones and cytokines (1, 2) have effects on the central nervous system (CNS), which in turn up-regulates the immune system through the pituitary hormones, growth hormone (GH) and prolactin (PRL) (3), or down-regulates the same through the hypothalamus-pituitary-adrenocortical axis (the latter is activated by diverse stress factors, including infections and toxemias) (4-6). Nitric oxide (NO) promotes local inflammation (7) and sexual hormones regulate NO production (8).

In addition, estradiol is a hormone that activates eNOS, and therefore, the NO production. NO is produced during the conversion of L-Arginine to citruline by the nitric oxide synthase (NOS) (9). There are three isoform of NOS: neuronal (nNOS, NOS 1), inducible (iNOS, NOS 2), and endothelial (eNOS, NOS 3) (10). Estrogen can induce the eNOS expression in endothelium (11) and nNOS in neutrophilis (12). The inducible form is commonly controlled by inflammatory cytokines (7).

Key words: hypothalamic-pituitary-adrenal axis, inflammation, estradiol, eNOS, iNOS, nNOS, as estrogen receptors α and β

Corresponding Author:
Dr E. Abarca-Rojano,
Escuela Superior de Medicina,
Plan de San Luís y Díaz Mirón Col.
Casco de Santo Tomás, Alcaldía Miguel Hidalgo,
Ciudad de México, México, CP 11340
Tel.: +52 55 57296300, ext. 62743
e-mail: rojanoe@yahoo.com

0393-974X (2019)

For over 20 years, it has been recognized that cytokine synthesis is modulated in inflammatory cells by estrogens. More recently, Kovats demonstrated that estrogen receptors (ER) regulate immune functions and the signaling mechanisms in macrophages and dendritic cells (13). Estrogen and testosterone are known to affect the immune system function, but the relative contribution of NOS isoforms and of the ERs α and β is unclear.

The *in vivo* effects of testosterone and estrogens on NOS isoforms in inflamed tissue have been reported (14), however, to our knowledge, no studies have evaluated these effects in a model of hypophysectomized animals. Such model assures the absence of influence by endogenous glucocorticoids or sexual hormones (4).

The aim of this paper was to analyze the effect of estrogen and testosterone replacement therapy on the labeling of eNOS, iNOS and nNOS as well as the ERs α and β during inflammation (provoked in the footpad by Freund's complete adjuvant) on hypophysectomized male rats. It was found that 17β-estradiol, but not testosterone, caused a decrease in inflammation (estimated by a plethysmometer). Likewise, inflammation was accompanied by higher levels of eNOS in the mononuclear cells of hypophysectomized rats with estrogen treatment on days 1 and 7, and greater expression of nNOS in lymphocytes of hypophysectomized and testosterone-treated rats on days 7 and 14. The iNOS stainning was significant. Regarding ERs in hypophysectomized rats, the β receptor was found to be marked principally on lymphocytes on days 1, 7 and 14, and receptor α on neutrophils on days 1 and 14.

MATERIALS AND METHODS

Animals and groups

Male Wistar rats weighing 250 to 300 g were obtained from the animal facility of the Escuela Superior de Medicina, Instituto Politécnico Nacional, Mexico City. They were housed in transparent plastic cages in groups of three, under 12/12 h light/dark cycle in a room with little noise, and were provided with food and water *ad libitum*. The protocol of this study was developed based on the ARRIVE guidelines for reporting animal research, and was approved by the Ethics in Research Committee of the Escuela Superior de Medicina. Animals were randomly divided into five groups: passive control (n = 3) without any surgical treatment, active control (n =9) with a SHAM procedure, and three experimental groups (n = 9) which were all hypophysectomized. One experimental group was given no hormonal treatment, while the other two were administered either 17β-estradiol or testosterone replacement therapy. These five groups were labeled in control, SHAM, HYPOX, HYPOX-E_2 and HYPOX-T procedures, respectively.

Hypophysectomy

A parapharyngeal hypophysectomy was carried out according to a previously described method. Briefly, the animals were anaesthetized with ether, and the application of atropine (40 μg/100g body weight) to reduce rhinotracheal secretions. A rat was placed in a dorsal position at an angle of approximately 70°, so that the endotracheal probe could be introduced. On SHAM-operated animals, the surgical procedure was simulated, opening and closing the animals without removing the pituitary gland. After the procedure, the animals had a duration of 7-day recovery.

Treatments

After the recovery period, hormonal implants were subcutaneously administered in a SILASTIC tube (Dow Corning, Midland, MI, USA) placed in the cervical region. The tubes used for 17β-estradiol (Sigma) were 1.5 cm long, and those for testosterone (Sigma) 2.5 cm long. These tubes have the advantage of administering a precise and constant dosage of each hormone in rats rats during the 14-day period of this study. The success of this technique lies in the fact that the rate of dosing is not related to the quantity of hormone in the tube, but instead is proportional to the surface area of the implant (14).

At the end of the 7-day recovery period, an inflammatory stimulus (1 mg Freund's complete

adjuvant) was administered to the footpad of all animals (day 1). Inflmmation measurements were made by plethysmometer based on water displacement volume, and three NOS isoforms (by immunohistochemistry) on days 1, 7 and 14 (post-administration of Freund's complete adjuvant).

Immunohistochemistry

Footpad tissue samples were fixed with embedded paraformaldehyde, and paraffin histological cuts of 7 μm were made, then mounted on slides previously coated with poly-L-lysine (Sigma, St. Louis, MO, USA) and rehydrated with descendent alcohol concentrations and PBS. These immunohistochemistry samples were placed in 10 mM Sodium Citrate Buffer (pH = 6.0) with 0.05% Tween at 20-90°C for 10 min for antigen recovery. The samples were washed with cold citrate buffer for 20 min, then PBS for 5 min. Endogen peroxidase was blocked with 3% H_2O_2 in PBS for 30 min. Non-specific binding was blocked with 3% fetal bovine serum for 30 min.

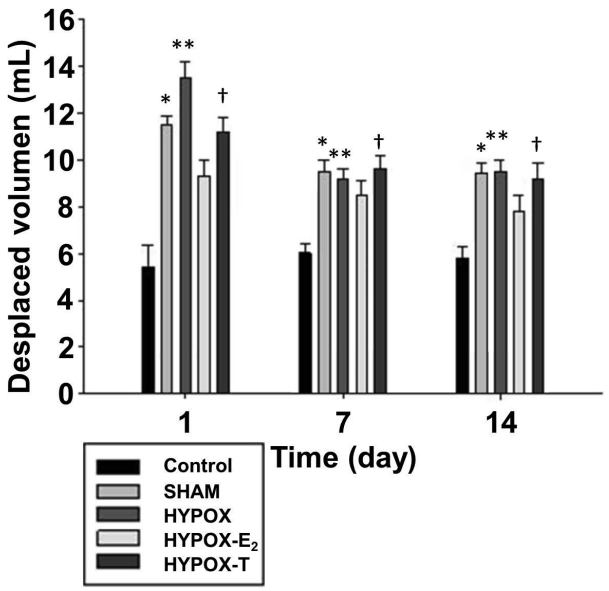

Fig. 1. *Degree of inflammation. Edema measured by plethysmometer on days 1, 7 and 14 post-administration of Freund's complete adjuvant. Data are expressed in ml to displace water volume taken from the footpad in rats. Rats with E_2 replacement therapy had the lowest edema of all groups. Values were analyzed by one-way analysis of variance. Bars correspond to the mean ± standard error. * P = 0.002; ** P ≤ 0.001; † P = 0.019.*

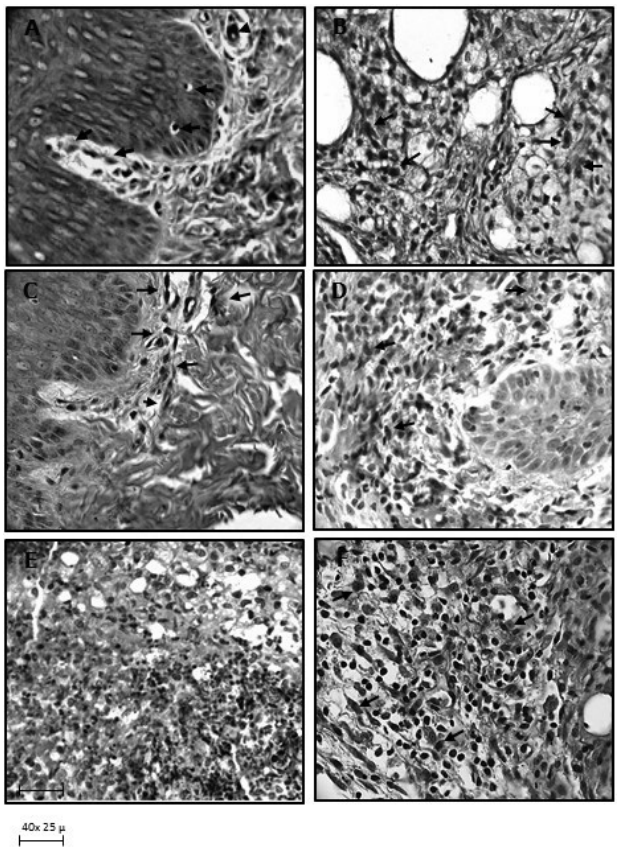

Fig. 2. *Immunohistochemical staining of NOS isoforms of footpads in rats. Tissues were treated with anti-nNOS, eNOS and iNOS antibodies as described in Materials and Methods section.* ***A****) Rats treated with HYPOX on footpads (7 days) labeled for nNOS in mononuclear cells (arrowheads) of connective tissue and intraepithelial lymphocytes (arrows).* ***B****) Rats treated with HYPOX on footpads (day 1) with eNOS staining in mononuclear cells (arrows).* ***C****) Rats treated with HYPOX E_2 on footpads labeled for nNOS in mononuclear cells of dermal connective tissue (arrows) at day 1.* ***D****) Rats treated with HYPOX E_2 on footpads labeled for eNOS for chronic leukocytes (arrows) in interstitial connective tissue on day 1.* ***E****) Rates treated with HYPOX E_2 labeled for iNOS in subepidermal and dermal tissue on day 1.* ***F****) Rats treated with HYPOX T with nNOS staining in dermal lymphocytes (arrows) on day 7. Magnifications of A, B, C, D and F 40x. Magnification of E 20 ×.*

The expression of the NOS isoforms were evaluated by directed mouse polyclonal IgG: C-20 for eNOS (sc-654), A-11 for nNOS (sc-5302) and C-11 for iNOS (sc-7271). All antibodies were acquired from Santa Cruz Biotechnology Inc., and the avidin-biotin system was used for film

development. The dilution of eNOS and nNOS was 1:500, and iNOS was 1:250. Cells were observed under an Axiovert 200M microscope (Carl Zeiss Co., Germany). The images, both of the epidermis and dermis samples, were sent to a KS 300 image analyzer, which evaluates the tissue area with immunofluorescence derived by the presence of immunolabelled NOS isoforms (expression area). Three independent readings were made of each slide, and data is expressed as the average μm^2 value.

For ER, samples were incubated overnight at 4°C with primary anti-ERα (Santa Cruz, CA, USA) or anti-ERβ (Santa Cruz, CA, USA), in both cases with 0.4 µg/100 µl. Then, samples were incubated with a secondary antibody 1:200: peroxidase-goat anti-mouse IgG (Invitrogen, Camarillo, CA, USA) for ERα and peroxidase-goat anti-rabbit IgG 1 mg/1 ml (Millipore, Temecula, CA, USA) for ERβ, in both cases for 1 h at room temperature. The

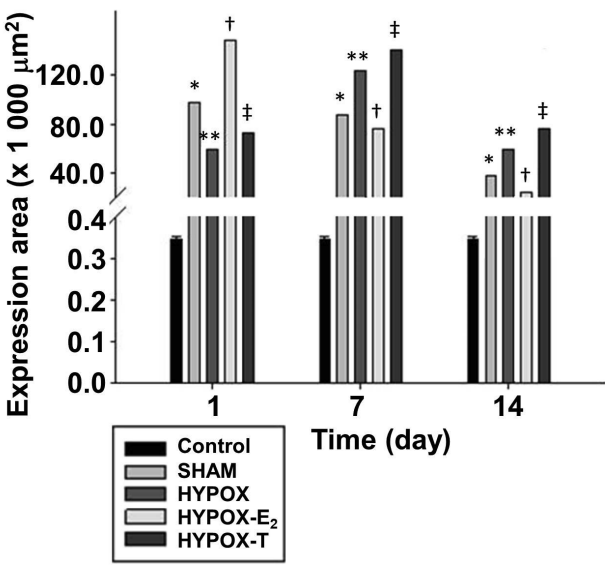

Fig. 3. *nNOS in inflammatory tissue. Rats with E_2 replacement therapy showed a notable increase in nNOS on day 1 post-administration of Freund's complete adjuvant, which was not the case for animals with testosterone therapy. In the latter group, the value of this parameter increased abruptly sharply by day 7. *, **, † and ‡ $P \leq 0.001$. Bars represent the mean of isoform expression area ± standard error measured in μm^2 by microscopy and immunohistochemistry, as an indicator of the nNOS expression in inflammatory tissue of rat footpads.*

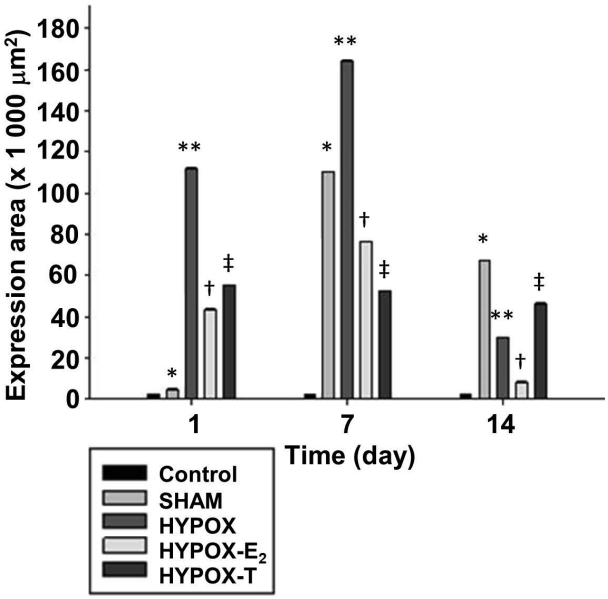

Fig. 4. *iNOS in inflammatory tissue. Rats with E_2 replacement therapy showed a lesser increase in cells labeled for iNOS than those labeled for the other two NOS isoforms evaluated. *, **, † and ‡ $P \leq 0.001$. Bars represent the mean isoform expression area ± standard error measured in μm^2 by microscopy and immunohistochemistry, as an indicator of the iNOS in inflammatory tissue of rat footpads.*

substrate of the DAB enzyme was added (Thermo Fisher Scientific, Rockford, Illinois, USA) for 5 min. The samples were washed and counterstained with hematoxylin (1:9) for 1-2 min. The slides were dehydrated in ascendant alcohol concentration (96-100%) and Xylene. After adding a drop of resin, the slide was observed under a Nikon ECLIPSE E600 microscope. Using the Image-Pro Plus 5.1 software with 40 × magnification a count was made of positive cells to ERβ in three fields of the samples. Then, the positive cells were calculated.

Statistical analysis

Statistical analysis of data was carried out with SigmaPlot ver. 11.0. One-way ANOVA and paired multiple comparison procedures (Holm-Sidak method) to examine statistical significance between days. The Kruskal-Wallis one-way analysis of variance on ranks was used to examine statistical significance between groups on each measurement day. Comparisons between groups were made

with Tukey Test. Data are presented as the mean ± standard error, and significance was considered with $P \geq 0.05$. Inflammation was correlated with NOS expression by using the Pearson product-moment correlation, where the pairs of variables with a positive correlation coefficient tend to increase together, while those with a negative one change in an opposite sense (one decreases and the other increases).

RESULTS

Edema of footpads

On day 1 postadministration, using the Freund's complete adjuvant, the HYPOX rats (without hormone treatment) showed significantly more edema than all other groups (Fig. 1). On days 1, 7 and 14, the HYPOX-E2 group had significantly less edema than the other two hypophysectomized groups (HYPOX and HYPOX-T) and the SHAM group.

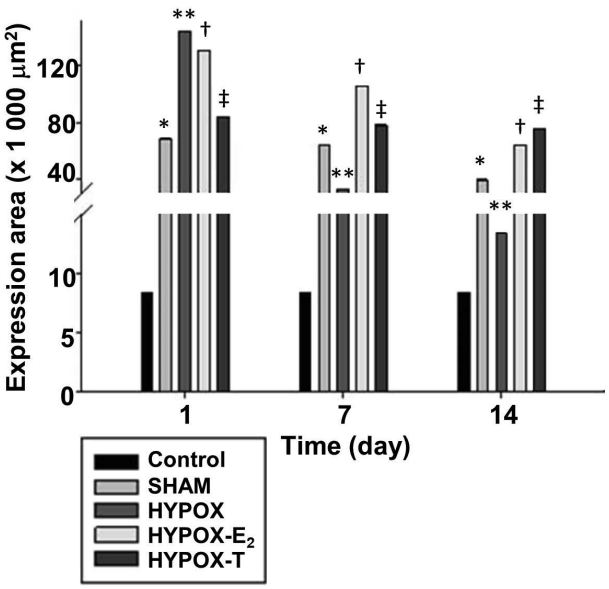

Fig. 5. *eNOS in inflammatory tissue. Rats with E_2 replacement therapy showed much higher levels for eNOS on day 1 post-administration of Freund's complete adjuvant compared to the control group. Although these levels gradually decrease in the E_2 group on days 7 and 14, they remained higher compared to the control group. *, **, † and ‡ $P \leq 0.001$. Bars represent the mean isoform expression area ± standard error measured in μm^2 by microscopy and immunohistochemistry, as an indicator of the eNOS in inflammatory tissue of rat footpads.*

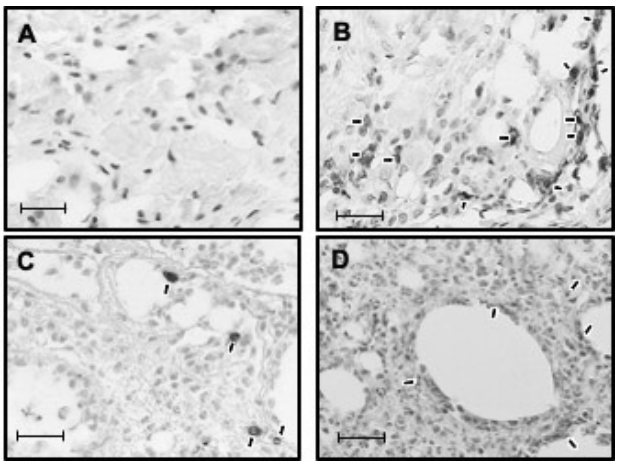

Fig. 6. *Immunohistochemical analysis of ERβ. From hypophysectomized rats with estradiol or testosterone replacement therapy, tissue samples from inflamed footpads were obtained on days 1, 7 and 14 post-administration of Freund's complete adjuvant. Sections of these samples were stained with anti-ERβ. **A**) No label for ERβ was observed in the cells of connective tissue of control rats. **B**) In animals treated with HYPOX on Day 7, ERβ was labeled for lymphocytes (arrows). **C**) ERβ was present in lymphocytes of connective tissue (arrows) in the HYPOX-E_2 group on Day 14. **D**) the HYPOX-T group label was present in lymphocytes on Day 7. At Magnifications 40 ×.*

Between day 1 and days 7 and 14 there were significative changes. At this stage, the edema decreased in all groups, but was still above the basal level. Nevertheless, there was no significant change between days 7 and 14. The only significant differences in this parameter between groups were found on day 1. These results show a strong association between the surgical elimination of the pituitary gland and greater inflammation of the rat footpad, as well as between 17β-estradiol replacement therapy and an attenuation of inflammation.

NOS detection in rats with inflamed footpads

The inflamed footpad tissue was subjected to immunohistochemical NOS staining for all groups (HYPOX, HYPOX-E_2, HYPOX-T, SHAM procedures and control) on days 1, 7 and 14. The control group produced a mixed inflammatory

infiltrate in tissue and some leukocytes labeled for NOS enzymes throughout the tissue (Fig. 2).

nNOS protein detection

Statistical analysis of immunohistochemical samples showed an increase in the nNOS protein on day 1 for all groups with hypophysectomy. On day 1, the HYPOX-E2 group had the highest number of cells labeled for nNOS (Fig. 3), and underwent a gradual reduction until day 14. This isoform was labeled in cells of chronic inflammatory infiltrate in dermal connective tissue. Diversely, the HYPOX and HYPOX-T groups had their maximum number of cells labeled for nNOS on day 7. For the HYPOX group, nNOS was positive in the lymphocytes of connective tissue (Fig. 2A) and some intraepithelial lymphocytes in the stratified epithelium. The only positive correlation between edema and nNOS expression was om the HYPOX-E2 group ($r = 0.999$, $p = 0.034$).

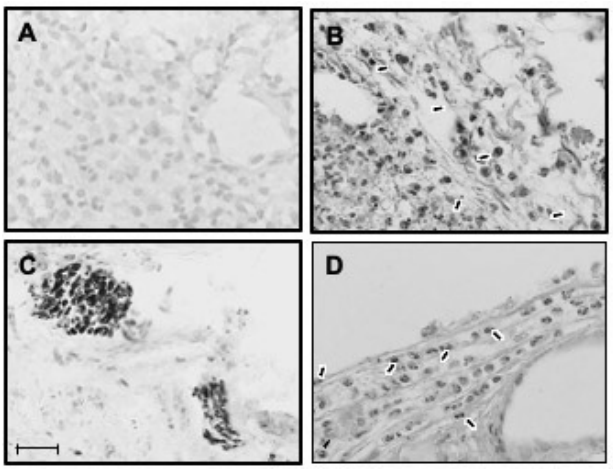

Fig. 7. *Immunohistochemical analysis of ERα. The inflamed footpad tissue samples of hypophysectomized rats treated with estradiol or testosterone replacement therapy were obtained on days 1, 7 and 14 post-administration of Freund's complete adjuvant and sections were stained with anti-ERα.* ***A****) No label for ERα was observed in the control rats.* ***B****) Animals belonging to the HYPOX group showed immunostaining for ERα in neutrophils observed in connective tissue of the reticulated dermis on day 14.* ***C****) HYPOX-E_2 group present axons of the nerve in the connective tissue stained for receptor alpha on day 14.* ***D****) Neutrophils stained for ERα were observed in the inflammatory infiltrate in HYPOX-T rats on day 1 (arrows). Magnifications 40 ×.*

iNOS detection

In all hypophysectomized and SHAM-operated animals, the number of cells labelled for iNOS increased after surgery (Fig. 4). In HIPOX and HYPOX-E_2 animals, the number of iNOS-labeled cells increased from day 1 to day 7 and decreased from day 7 to day 14. Contrary to the HYPOX-T group, there was a constant number of cells labeled for iNOS on days 1, 7 and 14. On day 14, among the operated groups (SHAM and hypophysectomized), the HYPOX-E2 group showed the greatest reduction in cells labeled for iNOS, suggesting that the 17β-Estradiol down-regulates this NOS isoform in the latter stages of the inflammatory procedure. This pattern of iNOS has been reported in the literature of inflammatory process. In the HYPOX group of this study, the iNOS label was mainly located in connective tissue and some leukocytes of the papillary dermis (Fig. 2C). It was not possible to find a correlation between the expression of this immunolabeled isoform and the edema that would be able to show the relation of its expression with a degree of inflammation in each experimental group.

eNOS protein detection

Statistical analysis of immunohistochemical samples showed higher levels of the eNOS protein, compared to the control, for all groups with hypophysectomy on day 1. For the group treated with 17β-Estradiol, the same pattern was found for eNOS and nNOS, with a gradual decrease in levels of the former protein from day 1 to day 14 (Fig. 5). Whereas on day 1, the largest number of cells labeled for eNOS was found in the HYPOX group, this value dramaticaly or severely decreased by day 7, which was lower than that of the HYPOX-E_2 group.

In the reticular dermis of HYPOX rats, the inflammatory infiltrate was composed by lymphocytes, mononuclear cells and macrophages labeled for eNOS (Fig. 2B). The inflammatory process included polymorphonuclear and mononuclear cells in the interstitial conjunctive tissue of the reticular dermis, and these were stained for eNOS in HYPOX-E_2 animals (Fig. 2D). This confirms the well-established fact that estrogens increase NO production through higher eNOS expression, and

suggests that 17β-Estradiol down-regulates eNOS in the latter stages of the inflammatory process. It was not possible to find a correlation between the expression of this immunolabeled isoform and the edema that would be able to show the relation of its expression with a degree of inflammation in each experimental group.

Estrogen receptors alpha and beta in rats with inflamed footpads

We analyzed footpad inflammation using HYPOX, HYPOX-E_2 and HYPOX-T groups on days 1, 7 and 14. Regarding the HYPOX group, the inflammatory infiltrate was constituted mainly by lymphocytes strongly labeled for ERβ on days 7 and 14 (Fig. 6B). In HYPOX-E_2 rats on day 14, the label was mainly observed in lymphocytes present in connective tissue of the reticulated dermis (Fig. 6C). In the HYPOX-T group, there were lymphocytic cells stained for ERβ on day 7 (Fig. 6D), cells were also labeled for this receptor on day 1. For this group, no label for ERβ was detected on day 14. The control did not show label (Fig. 6A). The count of positive cells to ERβ showed a significant increase on day 14 *vs* days 1 and 7 in the HYPOX-E_2 group (Table I). In the HYPOX-T group, a decrease in the number of labeled cells to ERβ was observed at day 7. No positive cells were observed at day 14 (Table I).

In HYPOX rats, the inflammatory infiltrate was mainly composed by polymorphonuclear cells and lymphocytes in dense connective tissue of reticulated dermis. Label for ERα was detected on day 7 (data not shown). In the HYPOX-E_2 group, neutrophils had infiltrated into the inflammatory tissue. Neutrophils in the connective tissue of the reticular dermis were stained for ERα on day 14 (Fig. 7B). A high label was observed in axons of the nerve present in the connective tissue (Fig. 7C), while no label for α receptor was found at any other time points. Neutrophils present in the inflammatory infiltrate were labeled for ERα in HYPOX-T rats on day 1 (Fig. 7D). Furthermore, high label was observed in axons of the nerve present in the connective tissue (data not shown). The control samples did not show label (Fig. 7A).

Table I. *Count of positive cells to estrogen receptor β.*

Days of hormone replacement	HYPOX-E_2[a] (mean±SD)	HYPOX-T[b] (mean±SD)
1	6.78±1.40	11.16±0.95
7	9.17±0.41	1.33±0.47
14	12.11±2.78	0±0.00

[a] *Positive cells to ERβ in HYPO-E_2 group.*
[b] *Positive cells to ERβ in HYPOX-T group.*
The number of positive cells was compared at each time point.

DISCUSSION

The use of hypophysectomized rats guaranteed that the inflammatory process was not influenced by the action of endogenous glucocorticoids or sexual hormones. It is well-established that with an interruption of the HPA axis, whether surgically (by adrenalectomy or hypophysectomy) or pharmacologically (by antagonists of glucocorticoids), there is an increased susceptibility to infection and mortality in animals (5). Accordingly, in this study, the hypophysectomized group treated without hormonal treatment (HYPOX) was the most vulnerable group to inflammation (2). It has been shown that an intense inflammatory reaction and the presence of a large number of inflammatory cells increases susceptibility to damage (15). This is the first study, to our knowledge, that serves to analyze the effect of estrogens and testosterone on the expression of the three NOS isoforms in hypophysectomized animals subjected to an inflammatory process.

Studies on pregnant rats and other animal models, for example ovariectomized animals, have documented the contribution of pituitary hormones; especially estradiol, in nNOS and eNOS expressions, even though these are considered as the two calcium-dependent NOS isoforms (16). However, it has been well-documented that eNOS expression can also be activated by adenosine and salbutamol through a calcium independent pathway (17, 18). Despite the fact that these two isoforms are constitutive, it has been demonstrated that their activity and expression are induced by E2, but not through testosterone in diverse tissues (19). A recent study reported that nNOS contributed to E_2-induced vascular relaxation

in mesenteric arteries in female rats. However, the same authors demonstrated a drastic change towards the superoxide production in relation to nNOS enzymatic function during aging or after an ovariectomy. Evidence has consistently led to the availability or deficiency of the tetrahydrobiopterin (BH4) co-factor and L-Arginine substrate in the control of coupling or uncoupling during NOS catalysis. Contrary to the absence of BH4 and/or L-Arginine, NOS is uncoupled and generates ROS/RNS, which is detrimental to vascular function (20).

To evaluate the NOS expression, in this study, the immunohistochemical staining technique. The images were analyzed computationally in a quantitative way. This technique measures the amount of label per area indicating the presence of protein. Higher levels of eNOS and nNOS found in this study with 17β-estradiol replacement therapy could rely upon the lesser extent of edema in the HYPOX-E_2 group compared to all other groups. In this sense, the significant increase in nNOS on day 1 for rats treated with HYPOX-E_2 probably contributed to the reduction of inflammation. Indeed, the only positive correlation between edema and NOS expression occured with nNOS in the HYPOX-E_2 group ($r = 0.999$, $p = 0.034$).

The iNOS expression was high in rats treated with HYPOX and HYPOX-E_2 on day 1 and even greater by day 7. Contrarily, the inflammation was more pronounced in HYPOX and HYPOX-E_2 groups on day 1 and decreased by day 7. The highest value of iNOS on days 1 and 7 was found in the HYPOX group. Among the three hypophysectomized groups on day 1, the protein leve lof iNOS was the lowest in animals treated with HYPOX-E_2.

The influence of estrogens on immune responses is well-documented. It seems that the key role played by estrogens in controlling inflammation is partly carried out by inducing high levels of eNOS and nNOS, which is an effect apparently not induced by testosterone (21). The phenomenon of the conversion of testosterone to estradiol through the aromatase enzyme, found in another study, does not seem to have taken place here. The current results show that in the HYPOX-E_2 group, the stain for ERβ was predominantly found in intraepithelial lymphocytes on day 1 while lymphocytes and connective tissue were found on day 14. There were a scarce number of cells labeled for ERβ on day 7 vs day 14.

Interestingly, ERα were labeled on neutrophils and lymphocytes in connective tissue of the reticulated dermis on day 7 in the HYPOX group, but only on polymorphonuclear cells on day 1 in the HYPOX-T group. Evidence in humans and mice indicates a differential expression of ER on lymphocytes, with ERα being predominantly expressed on CD4+ T cells and ERβ on B cells. This difference may be involved in the maturation and differentiation of T cells in the thymus as well as the alteration of B lymphopoiesis in bone marrow (22).

It has been demonstrated that 17β-estradiol inhibits NF-kB binding to the IL-6 promoter, suggesting that ERs work by blocking NF-kB-mediated activtion of inflammatory genes (23). On the other hand, evidence shows that ERβ is the predominant receptor in secondary lymphoid organs, while expression of ERα is restricted to the active germinal center during systemic inflammation. However, the responsiveness of the immune cells to estrogens and testosterone could be determined by the receptor subtypes, as well as the activation/differentiation status of cells. Since the aim of this study was the labeling of enzymes NOS and ERs in hypophysectomized rats, the scope of this paper is not focused on the role of receptors, but the confirmation of a possible role of the ERs in a subsequent study with the administration of ER antagonists. In this study, the HPA axis was interrupted by hypophysectomy, followed by hormone replacement therapy with 17β-estradiol or testosterone. The results suggest that, unlike testosterone, estradiol could have had an anti-inflammatory effect on the footpad of rats by the administration of Freund's complete adjuvant This protective effect was apparently related to the high estradiol-induced levels of eNOS and nNOS as well as the protein expression of β estrogens.

ACKNOWLEDGEMENTS

This work was supported in part by grants from SEPI-Instituto Politécnico Nacional. R. Campos-Rodríguez, J. Pacheco-Yepez. and E. Abarca-Rojano

are fellows of COFAA and SEPI-Instituto Politécnico Nacional. CM Mejía-Barradas, R. Campos-Rodríguez, J. Pacheco-Yepez and E. Abarca-Rojano are fellows of CONACYT.

REFERENCES

1. Madden KS, Felten DL. Experimental basis for neural-immune interactions. Physiol Rev 1995; 75:77-106.
2. Scarborough DE. Cytokine modulation of pituitary hormone secretion. Ann N Y Acad Sci 1990; 594:169-87.
3. Nagy E, Berczi I. Prolactin and contact sensitivity. Allergy 1981; 36:429-31.
4. Edwards CK 3rd., Lorence RM, Dunham DM, et al. Hypophysectomy inhibits the synthesis of tumor necrosis factor alpha by rat macrophages: partial restoration by exogenous growth hormone or interferon gamma. Endocrinology 1991; 128:989-86.
5. Sternberg EM, Hill JM, Chrousos GP, et al. Inflammatory mediator-induced hypothalamic-pituitary-adrenal axis activation is defective in streptococcal cell wall arthritis-susceptible Lewis rats. Proc Natl Acad Sci U S A 1989; 86:2374-78.
6. Ruzek MC, Pearce BD, Miller AH, et al. Endogenous glucocorticoids protect against cytokine-mediated lethality during viral infection. J Immunol 1999; 162:3527-33.
7. Bogdan C. Nitric oxide and the immune response. Nat Immunol 2001; 2(10):907-16.
8. Chambliss KL, Shaul PW. Estrogen modulation of endothelial nitric oxide synthase. Endocr Rev 2002; 23:665-686.
9. Moncada S, Higgs A. The L-arginine-nitric oxide pathway. N Engl J Med 1993; 329:2002-12.
10. Sessa WC. The nitric oxide synthase family of proteins. J Vasc Res 1994; 31:131-143.
11. Moncada S, Higgs EA. Nitric oxide and the vascular endothelium. Handb Exp Pharmacol 2006; 213-54.
12. Garcia-Duran M, de Frutos T, Diaz-Recasens J, et al. Estrogen stimulates neuronal nitric oxide synthase protein expression in human neutrophils. Circ Res 1999; 85:1020-26.
13. Kovats S. Estrogen receptors regulate innate immune cells and signaling pathways. Cell Immunol 2015; 294:63-69.
14. Sommerville EM, Tarttelin MF. Plasma testosterone levels in adult and neonatal female rats bearing testosterone propionate-filled silicone elastomer capsules for varying periods of time. J Endocrinol 1983; 98:365-71.
15. Webster JI, Sternberg EM. Role of the hypothalamic-pituitary-adrenal axis, glucocorticoids and glucocorticoid receptors in toxic sequelae of exposure to bacterial and viral products. J Endocrinol 2004; 181:207-21.
16. Weiner CP, Lizasoain I, Baylis SA, et al. Induction of calcium-dependent nitric oxide synthases by sex hormones. Proc Natl Acad Sci U S A 1994; 91:5212-16.
17. Edwards CK 3rd, Yunger LM, Lorence RM, et al. The pituitary gland is required for protection against lethal effects of Salmonella typhimurium. Proc Natl Acad Sci U S A 1991; 88:2274-77.
18. Figueroa XF, Poblete I, Fernandez R, et al. NO production and eNOS phosphorylation induced by epinephrine through the activation of beta-adrenoceptors. Am J Physiol Heart Circ Physiol 2009; 297:134-43.
19. Gingerich S, Krukoff TL. Estrogen modulates endothelial and neuronal nitric oxide synthase expression via an estrogen receptor beta-dependent mechanism in hypothalamic slice cultures. Endocrinology 2005; 146:2933-41.
20. Lekontseva O, Chakrabarti S, Jiang Y, et al. Role of neuronal nitric-oxide synthase in estrogen-induced relaxation in rat resistance arteries. J Pharmacol Exp Ther 2011; 339:367-75.
21. Nathan L, Shi W, Dinh H, et al. Testosterone inhibits early atherogenesis by conversion to estradiol: critical role of aromatase. Proc Natl Acad Sci U S A 2001; 98(6):3589-93.
22. Shim GJ, Gherman D, Kim HJ, et al. Differential expression of oestrogen receptors in human secondary lymphoid tissues. J Pathol 2006; 208:408-14.
23. Yang L, Hu Y, Hou Y. Effects of 17beta-estradiol on the maturation, nuclear factor kappa B p65 and functions of murine spleen CD11c-positive dendritic cells. Mol Immunol 2006; 43:357-66.

EXPRESSION OF PROTEINASE-ACTIVATED RECEPTOR-2 AND TRANSIENT RECEPTOR POTENTIAL A1 IN VAGAL AFFERENT NERVE OF RAT AFTER LUNG ISCHEMIA-REPERFUSION INJURY

XH. ZHANG[1], HX. QI[2], DS. XU[3], XC. PANG[4], CY. WANG[5] and WJ. YU[6]

[1]Department of Pulmonary Medicine, The First Hospital, Jilin University, Changchun, China; [2]Department of Nephrology, The First Hospital (Eastern Division), Jilin University, Changchun, China; [3]Tumor Center; The First Hospital, Jilin University, Changchun, China; [4]Clinical Laboratory; The First Hospital, Jilin University, Changchun, China, [5]Department of Neurosurgery; The First Hospital (Eastern Division), Jilin University, Changchun, China; [6]Department of Hand Surgery; The First Hospital (Eastern Division), Jilin University, Changchun, China

Received July 17, 2018 – Accepted October 4, 2018

The first two Authors contributed equally to this work

Lung ischemia-reperfusion injury (LIRI) is a common and severe clinical complication. As the injury occurs, the pulmonary afferent nerves play an important role in regulating respiratory functions under pathophysiological conditions. The purpose of this study was to examine expression of proteinase-activated receptor-2 (PAR2) and transient receptor potential A1 (TRPA1) in pulmonary vagal afferent nerves of LIRI and further to determine molecular mediators linking activation of PAR2 and TRPA1. A rat model of LIRI was used. Enzyme-linked immunosorbent assay (ELISA) and Western blot analysis were employed to examine pro-inflammatory cytokines (PICs, i.e., IL-1β, IL-6 and TNF-α), and the protein levels of PIC receptors, PAR2, TRPA1, and intracellular signals. In the results, IL-1β, IL-6 and TNF-α along with their receptors were amplified in afferent nerves of LIRI rats as compared with control rats. Sensory PAR2 and TRPA1 were also upregulated by LIRI. Blocking PAR2 by infusion of FSLLRY-NH2 attenuated upregulation of TRPA1 via intracellular signals, namely p38-MAPK and JNK. Moreover, blocking individual PIC receptor attenuated PAR2 and TRPA1 in pulmonary vagal afferent nerves. Our data showed specific signaling pathways leading LIRI to activation of PIC signal and activation of PAR2 and TRPA1 in pulmonary vagal afferent nerves via intracellular mediators. Targeting one or more of these signaling molecules may present opportunities to improve the abnormalities in vagal afferent nerve-mediated respiratory functions observed as LIRI occurs.

Lung ischemia-reperfusion injury (LIRI) is a common and severe postoperative complication that often occurs after lung transplantation, cardiopulmonary bypass, cardiopulmonary resuscitation, pulmonary embolism, and sepsis (1, 2). Although surgical technology is developed, an inevitable surge in LIRI has been seen in clinics due to its wide application. The underlying mechanisms leading to LIRI are primarily due to oxidative stress, inflammation, cellular apoptosis, intracellular calcium overload, etc. (3). Nonetheless, it is noteworthy to study molecular mediator involved in

Key words: PAR2, TRPA1, lung ischemia, cytokines, vagal afferent nerve

Mailing address:
Dr Wenjun Yu,
Department of Neurosurgery, Department of Hand Surgery,
The First Hospital (Eastern Division) of Jilin University,
3302 Jilin Avenue, Changchun, Jilin 130031, China
Tel.: +86 15804300636
e-mail: wenjuny@aol.com

0393-974X (2019)

pathophysiological process of LIRI.

Mast cells are present around blood capillaries and lymph vessels in connective tissue of the respiratory system in involvement of respiratory function (4). Activation of mast cells in the lungs further contributes to allergic and inflammatory diseases of the respiratory system (5). Evidence has demonstrated that mast cell migration and activation play a regulatory role in LIRI in animal model (6, 7). It has been found that pretreatment with mast cell stabilizer (i.e., cromolyn sodium) attenuated the inflammatory response and thereby alleviated LIRI (6, 7).

Tryptase, one of the characteristic and unique mediators released from mast cell activation, has been revealed to facilitate and exacerbate inflammation (6). Prior studies have shown that tryptase stimulates eosinophils, neutrophils, endothelial cells, and epithelial cells in lung to release pro-inflammatory cytokines (PICs) (8, 9).

Proteinase-activated receptors (PARs) are a family member of G-protein-coupled receptors and are activated by a proteolytic mechanism (10). Among the four members of PARs, subtype PAR2 is largely distributed in various tissues including neural, gastrointestinal, cardiovascular, and respiratory systems, and is activated by mast cell product tryptase (11). Prior studies have also shown that PAR2 activation is implicated in lung inflammatory responses and contributes to the enhancement of inflammatory signaling by increasing PICs (12, 13).

Pulmonary sensory nerves play an important role in regulating respiratory functions to maintain homeostasis (14). A large subset of sensory nerves in the vagal nerves can also respond to inflammatory mediators and noxious stimuli (14). Under pathophysiological conditions, stimulation of PAR2 in sensory nerves has been reported to mediate neurogenic inflammatory responses (15). Thus, we hypothized that as LIRI occurs, the levels of PICs are increased and PAR2 protein expression is upregulated in nodose ganglions (NG) mainly supplying sensory pulmonary vagal nerves in rats.

Transient receptor potential ankyrin 1 (TRPA1) plays a functional role in regulating neurogenic inflammation resulting from channel activation to a variety of compounds including pungent agents, irritant chemicals, reactive oxygen, and products of oxidative stress-induced lipid peroxidation (16). TRPA1 has been shown to appear in pulmonary sensory nerves and is engaged in development of inflammation-mediated responses and ischemic injury (16). A recent study also suggests a role of PAR2 in regulating TRPA1 functions in sensory nerves, and blocking PAR2 decreases TRPA1expression in engagement of neurogenic response (17).

Thus, we hypothesized that LIRI amplifies the levels of PICs (such as IL-1β, IL-6 and TNF-α) and upregulates expression of their receptors (IL-1R, IL-6R and TNFR1) in the NG of rats, which increases in expression of PAR2 and TRPA1. Blocking PAR2 by systemic injection of FSLLRY-NH2 (FSLL), an antagonist to PAR2, decreases the expression levels of TRPA1 in LIRI rats via intracellular signal pathways p38-MAPK and JNK. We further hypothesized that inhibition of each PIC receptor decreases PAR2 and TRPA1 in the NG of LIRI rats.

MATERIALS AND METHODS

Animals

A total of male Wistar rats (200-250 g) were housed in individual cages with free access to food and water and were kept in a temperature-controlled room (25°C) on a 12/12 h light/dark cycle. All animal protocols were in accordance with the guidelines of the International Association for the Study of Pain and approved by the Animal Care and Use Committee of Jilin University.

Model of lung ischemia-reperfusion injury and administration of drugs

The rats were initially anesthetized using pentobarbital sodium (60 mg/kg, i.p.) and then anesthesia was maintained by continuous infusion of pentobarbital (0.05 mg/kg/min). An endotracheal tube was inserted and the rats were ventilated using a rat ventilator (Harvard Apparatus, Boston, MA, USA). The ventilating parameters were set with an inspiratory oxygen fraction (FiO2) of 40% at a rate of 50-60 breaths/min and a tidal volume of 6-8 mL/kg.

Catheters were inserted into the femoral artery and vein for monitoring arterial blood pressure and administration of fluids (saline, 1 mL/h) and drugs (vecuronium bromide,

0.1 mg/kg/h; heparin, 250 U/kg), respectively. A left anterolateral thoracotomy was performed in the fifth intercostal space, and the pleura were exposed to allow the left hilum of the lung to be isolated. After stabilizing for 15 min, the tidal volume was decreased to 5-7 mL/kg, and the rate was increased to 70-75 breaths/min. Lung ischemia was induced by clamping the left pulmonary hilum, including the left main bronchus, artery and vein, for 1 hour, followed by reperfusion induced by removing the clamp and ventilating the left lung for 4 h. The sham control group underwent the left thoracotomy without clamping hilus and were ventilated for 5 h.

The thoracic incision was protected from evaporative losses using a covering of wet absorbent gauze. The body heat of the rats was maintained using a heating lamp at a rectal temperature within the normal range (36-37°C). Arterial blood (0.3 mL) was collected from each rat before induction of ischemia and 30 min and 4 h after reperfusion, and then blood gas analyses were performed (ABL 800; Radiometer, Copenhagen, Denmark). Arterial partial pressure of oxygen (PaO2) and arterial partial pressure of carbon dioxide (PaCO2) were also recorded. The arterial

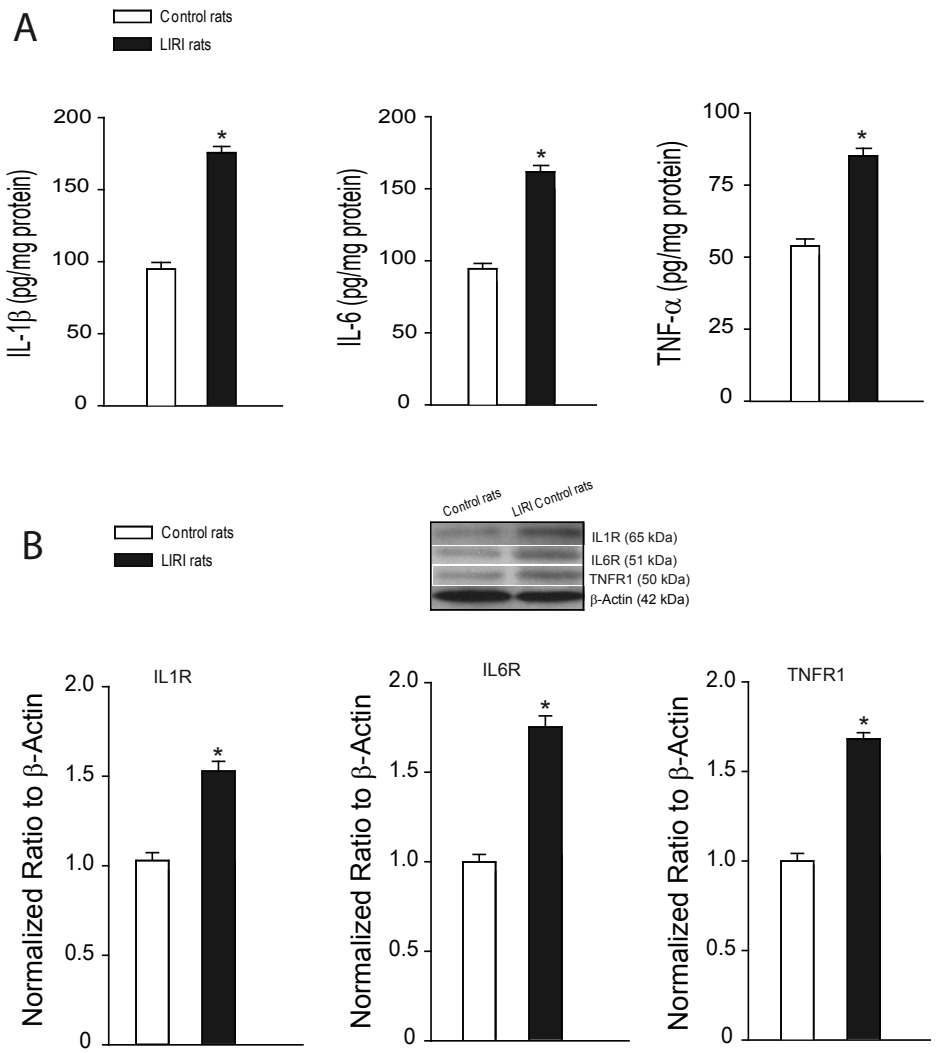

Fig. 1. *Levels of PIC and expression of PIC receptors.* ***A****) LIRI amplified the levels of PICs (IL-1β, IL-6 and TNF-α) in the NG as compared with controls. *P < 0.05, LIRI rats (n=15) vs control rats (n=15).* ***B****) Top panel and bottom panel are typical band and average data, showing that protein expression levels of PIC receptors (IL-1R, IL-6R and TNFR1) were upregulated after LIRI. *P < 0.05, LIRI rats vs control rats. The number of rats = 6-10 in each group.*

pressure, heart rate, and temperature of each rat were also monitored continuously throughout the study.

In subgroups of experiments, FSLL (1mg/kg; PAR2 inhibitor), IL1Ra (3mg/kg; IL-1β antagonist; ProSpec Inc), SC144 (1mg/kg; IL6R-gp130 inhibitor; Tocris Co) and etanercept (ETAN; 1mg/kg, TNF-α receptor antagonist, Tocris Co.) were injected (i.p.) in control rats and LIRI rats after induction of ischemia. At the end of the experiment, the rats were euthanized with pentobarbital sodium (120 mg/ kg, i.p.), and the nodose ganglions were taken out.

ELISA measurement

All the tissues from individual rats were sampled for the analysis. In brief, nodose ganglion tissues of the rats were removed. Total protein was then extracted by homogenizing the sample in ice-cold immunoprecipitation assay buffer with protease inhibitor cocktail kit. The lysates were centrifuged and the supernatants were collected for measurements of protein concentrations using a bicinchoninic acid assay reagent kit. The levels of IL-1β, IL-6 and TNF-α were obtained according to the provided description and modification (Promega Corp. Madison, WI, USA).

Polystyrene 96-well microtiter immunoplates were coated with affinity-purified polyclonal rabbit anti- IL-1β, anti- IL-6 and anti-TNF-α antibodies. Parallel wells were coated with purified rabbit IgG for evaluation of nonspecific signal. After overnight incubation at room temperature and 2 h of incubation with the coating buffer containing 50 mM carbonate buffer (pH 9.5) in 2% BSA, plates were washed with 50 mM Tris-HCl. After extensive washing, the diluted samples and the IL-1β, IL-6 and TNF-α standard solution were distributed in each plate and left at room temperature overnight. The plates were washed and incubated with anti-IL-1β, anti-

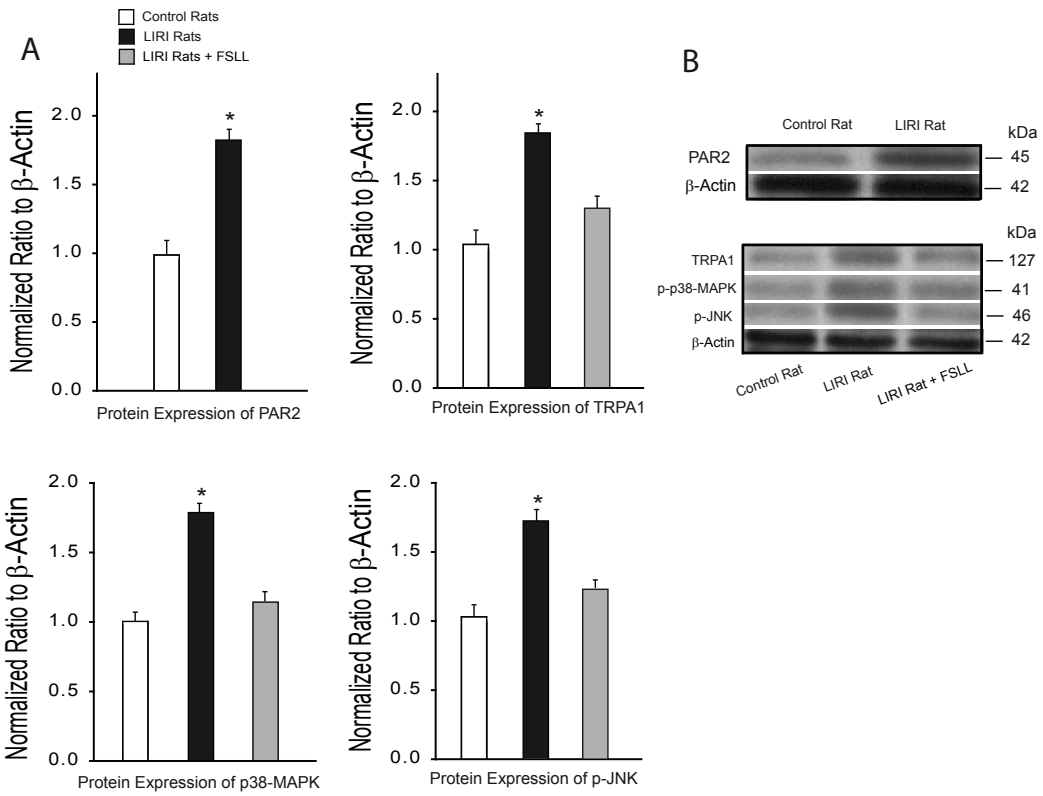

Fig. 2. *Expression of PAR2 and TRPA1.* ***A)*** *The protein levels of PAR2 were amplified in the NG tissues of LIRI rats and attenuation of PAR2 by systemic administration of FSLLRY-NH2 (FSLL) decreased expression of TRPA1, intracellular signals p38-MAPL and JNK. *P < 0.05, LIRI rats vs control rats and LIRI rats treated with FSLL. The number of rats in each group =6-8.* ***B)*** *Typical bands show that LIRI increased the protein levels of PAR2 (top panel), TRPA1 and p38-MAPK/p-JNK (bottom panel) and that FSLL inhibited amplification of TRPA1, p38-MAPK and p-JNK evoked by LIRI (bottom panel).*

IL-6 and anti-TNF-α galactosidase per well. Then, the plates were washed and incubated with substrate solution. After an incubation of 2 h at 37°C, the optical density was measured using an ELISA reader.

Western blot analysis

Briefly, nodose ganglion tissues were removed and total protein was extracted. The lysates were centrifuged and the supernatants were collected. After being denatured, the supernatant samples containing 20 μg of protein were loaded onto gels and electrically transferred to a polyvinylidene fluoride membrane. The membrane was incubated with respective primary antibodies (at 1:500, Abcam): rabbit anti-IL-1R, anti-IL-6R, anti-TNFR1, anti-PAR2, anti-TRPA1, anti-p-p38-MAPK and anti-p-JNK. The membranes were washed and incubated with an alkaline phosphatase conjugated anti-rabbit secondary antibody (1:1000). The immunoreactive proteins were detected by enhanced chemiluminescence. The bands recognized by the primary antibody were visualized by exposure of the membrane onto an X-ray film. The membrane was stripped and incubated with anti-β-actin to show equal loading of the protein. The film was then scanned and the optical density of IL-1R/IL-6R/ TNFR1/ PAR2/TRPA1/p-p38-MAPK/ p-JNK/β-actin bands was analyzed using Scion Image software.

Statistical analysis

All data were analyzed using a two-way repeated-measures analysis of variance. Values were presented as means ± standard error of mean. For all analyses, differences were considered significant at $P < 0.05$. All statistical analyses were performed by using SPSS for Windows version 13.0 (SPSS Inc.).

RESULTS

Blood gas and arterial blood pressure

The arterial-alveolar oxygen pressure gradient ($A\text{-}aDO_2$) was calculated using the following formula: $A\text{-}aDO_2$ = fraction inspired O_2 x (Patm-PH_2O) - ($PaCO_2$/RQ) - PaO_2, where Patm = 760 mmHg, PH_2O = 47mm Hg, and RQ = 0.8. In controls (n=31), no significant differences in PaO2 and A-aDO2 were observed over baseline at any time point. In the LIRI group (n=48), PaO2 decreased by 25% (30 min post-reperfusion) and by 17% (4 h post-reperfusion) as compared with baseline ($P < 0.05$ *vs* baseline), whereas the A-aDO2 increased by 21% (30 min post-reperfusion) and by 16% (4 h post-reperfusion) ($P < 0.05$ *vs* baseline).

Arterial blood pressure and heart rate were stable throughout the whole study in control rats. Although the mean arterial pressure (MAP) appeared to slightly decrease in LIRI rats, no significance difference was seen between the control group and the LIRI group 4 h after reperfusion (i.e., MAP: 105±9 mmHg in control and 99±7 mmHg in LIRI; $P > 0.05$ between two groups). There was no significant difference in heart rate between the two groups at any time point (i.e., 376±12 beats/min in control group and 382±15 beats/min in LIRI group 4 h after reperfusion; $P > 0.05$ between two groups).

Levels of PICs and their receptors expression

Fig. 1A demonstrates that IL-1β, IL-6 and TNF-α were increased in the NG of LIRI rats (n=16) as compared with sham control rats (n=15; $P < 0.05$, LIRI *vs* controls). Likewise, Fig. 1B illustrates that LIRI increased the protein expression of IL1R, IL6R and TNFR1 in the NG of rats ($P < 0.05$, LIRI rats *vs* control rats; n=6-10 in each group).

Expression of PAR2 and TRPA1

We further examined the regulatory effects of PAR2 on TRPA1 and intracellular signal pathways. Fig. 2A&B demonstrates that LIRI amplified the levels of PAR2 and TRPA1 in the NG as compared with control rats ($P < 0.05$, LIRI rats vs control rats, n=6 in control; and n=8 in LIRI group). LIRI also upregulated protein expression of intracellular signal p38-MAPK and JNK as compared with control rats ($P < 0.05$, LIRI rats vs control rats, n=6-8 in each group). This Fig. further shows that PAR2 inhibition using FSLL decreased upregulation of p-p38-MAPK, p-JNK and TRPA1 induced by LIRI ($P<0.05$ vs LIRI rats without FSLL).

Effects of blocking PIC receptors on PAR2 and TRPA1

The effects of PIC receptor inhibition on PAR2 and TRPA1 expression were examined in additional

groups. In this experiment, IL-1Ra, SC144 and ETAN were administered to attenuate PIC receptors, IL-1R, IL-6R and TNFR1, respectively. Fig. 3 (A, B, C) demonstrates that LIRI amplified the levels of PAR2 and TRPA1 in the NG as compared with control rats ($P < 0.05$, LIRI rats vs control rats; n=6-10). As individual PIC receptor was given, upregulation of PAR2 and TRPA1 expression in the NG of LIRI rats was attenuated ($P < 0.05$, LIRI rats vs LIRI rats with inhibitors; n=6-10).

DISCUSSION

Our results showed that LIRI amplifies the levels of IL-1β, IL-6 and TNF-α and upregulates eIL-1R, IL-6R and TNFR1 in the NG of rats. This process is likely to increase in expression of PAR2 and TRPA1. Blocking PAR2 decreases TRPA1 in LIRI rats via intracellular signal pathways: p38-MAPK and JNK. In addition, inhibition of each PIC receptor decreases PAR2 and TRPA1 in the NG of LIRI rats.

Sensory input from nerve endings in the lungs is mediated to vagal afferent neurons in the lower nodose and superior jugular ganglions. The nodose ganglion is derived from epibranchial placodes and the jugular ganglions originates from the neural crest cells, which defines the phenotypes of the vagal fibers (18) . The central endings of vagal afferent neurons innervating the airways terminate in the medulla oblongata and release a variety of neurotransmitters and neuromodulators (14). This thereby affects vagal motor neurons in the brainstem. Primary respiratory vagal reflexes modifying the pattern of breathing are evoked via lung inflation and activation of chemoreceptors by chemical substances affecting vagal afferents (14).

In the present study, we first examined the levels of PICs in the NG innervating the vagal afferent nerves and found that LIRI amplified IL-1β, IL-6 and TNF-α in the NG of rats. Since prior studies have observed mast cell migration and activation with LIRI and tryptase released from mast cell activation facilitates and exacerbates inflammation (6, 7), it is well reasoned that upregulation of IL-1β, IL-6 and TNF-α seen in the present study was linked to tryptase as LIRI was induced. In addition to PICs, we found that the protein levels of PAR2 were increased in the NG after LIRI. Under pathophysiological

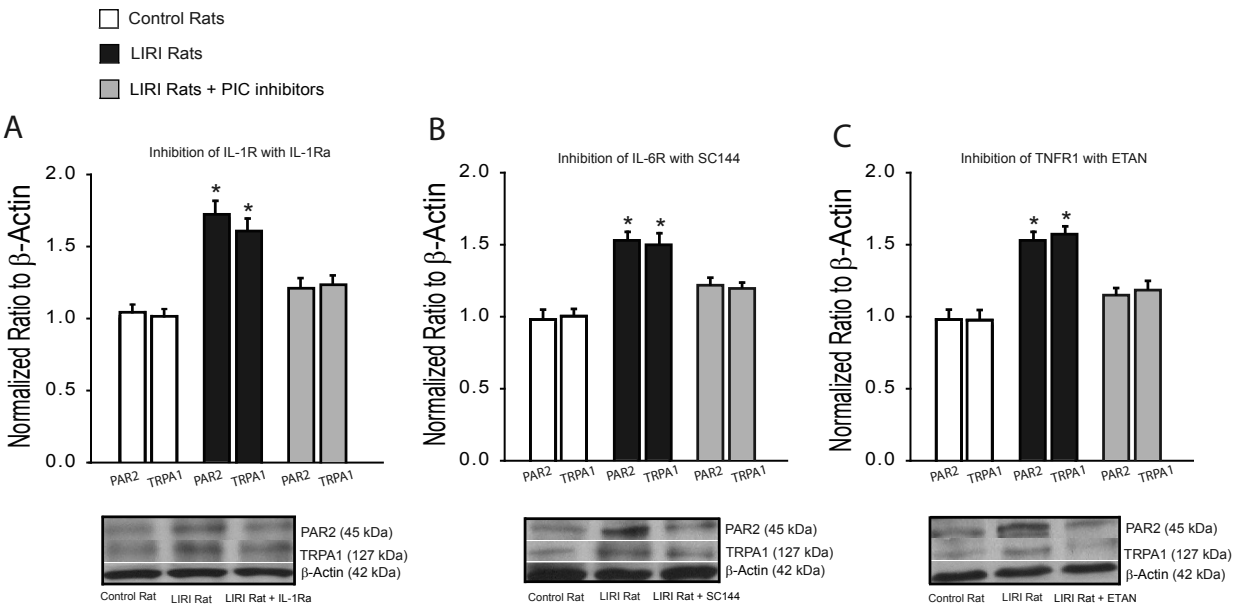

Fig. 3. *Effects of PIC receptor inhibition on PAR2 and TRPA1. Averaged data and typical bands showing the protein levels of PAR2 and TRPA1 expression were decreased in the NG of LIRI rats after blocking IL-1R with IL-1Ra (A), IL-6R with SC144 (B), and TNFR1 with ETAN (C). *P < 0.05 vs control rats and LIRI rats with respective inhibitor. n=6-10 in each group.*

conditions, activation of PAR2 in sensory nerves has been reported to mediate neurogenic inflammatory responses (15). Accordingly, it is likely that as LIRI occurs, PIC-PAR2 signal pathways are stimulated in engagement of neurogenic inflammation in pulmonary vagal afferent nerves.

TRPA1 activation may explain a wide variety of symptoms in patients suffering from asthma or COPD and might also play a crucial role in infection-induced exacerbations. TRPA1 expression has been identified in bronchopulmonary vagal C-fiber afferents (19) and evidence for a role in asthma was provided (20). In this prior study, it was demonstrated that airway hyper-reactivity as well as respiratory system inflammation were markedly reduced after genetic ablation of TRPA1 or after treatment with a TRPA1 antagonist. TRPA1 may represent one of the most promising targets for pharmaceutical interventions in inflammatory respiratory diseases. To the best of our knowledge, there has not been any proof for a dysregulation of TRPA1 in pulmonary vagal nerves following LIRI.

PICs including IL-1β, IL-6 and TNF-α have been reported to be involved in sensory vagal nerve-mediated reflex response. Among those PICs, TNF-α activates multiple signaling pathways, including the p38-MAPK and JNK pathways (21), which are recognized as important regulators of inflammatory noxious response. In the current study, we have also demonstrated upregulation of TNF-α subtype TNFR1 in the NG of LIRI rats and that blocking TNFR1 using ETAN attenuated increases of PAR2 and TRPA1. Also, inhibition of PAR2 decreased expression of TRPA1 as well as p38-MAPK and JNK. Taken together, our data suggest that p38-MAPK and JNK signal pathways are activated in the vagal afferent nerves by LIRI and likely mediate upregulation of TRPA1 via PIC-PAR2 pathways. We demonstrated, for the first time, a novel mechanism by which TNF-α contributes to enhanced TRPA1 expression likely via p38-MAPK and JNK signal in the NG of LIRI animals, which are likely involved in regulating respiratory functions to maintain homeostasis.

TNF-α produces its effects via activation of two TNF-α receptor subtypes: TNFR1 and TNFR2 (22). TNFR1 is expressed exclusively on neuronal cells and plays a functional role, whereas TNFR2 is located predominantly on macrophages and/or monocytes in response to inflammation. TNF-α activation appears most relevant to the development of afferent nerve-mediated behavior via the TNFR1. Mechanical noxious response induced by exogenous TNF-α and/or by inflammation is reduced in TNFR1 but not TNFR2 knockout mice and TNFR1 but not TNFR2 neutralizing antibodies reduce experimental hyperalgesia (23, 24). Thus, in our current study ETAN attenuated expression of PAR2 and TRPA1 in the NG of LIRI rats likely via TNFR1.

Likewise, LIRI upregulated IL-1R and IL-6R in the NG and blocking of these receptors using IL-1Ra and SC144 attenuated PAR2 and TRPA1 expression. p38-MAPK and JNK are thought to mediate physiological functions by IL-1β and IL-6. i.e., JNK is activated by IL-1β in cultured sensory cells (25, 26). p38-MAPK is also downstream molecules of IL-1β-mediated signaling since intrathecal injection of IL-1β increased p38-MAPK in the sensory nerve system in mice (27). Another study suggests that inhibition of IL-1β significantly suppressed JNK activation induced by chemotherapeutic agents (28).

IL-6 complexes with membrane-bound or soluble IL6R to activate cells expressing the signal transducer glycoprotein (gp130) (29). Most cells are devoid of membrane-bound IL-6R and are thus unresponsive to IL-6; however, they can still react to IL-6 complexed with a soluble form of the IL6R (sIL-6R) to activate gp130, a pathway called "trans-signaling" (30). Thus, in the current study we used SC144, a gp130 inhibitor, to block IL-6-mediated signal transduction to examine engagement of IL-6R in activation of PAR2 and TRPA1 induced by LIRI. Our data showed that SC144 attenuated increases of PAR2 and TRPA1 in the NG of LIRI animals.

In conclusion, LIRI increased IL-1β, IL-6 and TNF-α and expression of their receptors such as IL-1R, IL-6R and TNFR1 in the NG. This leads to upregulation of PAR2 and TRPA1 receptors via intracellular p38-MAPK and JNK signals. We revealed specific signaling pathways by which LIRI leads to activation of PIC signal and PAR2-TRPA1 via intracellular mediators.

REFERENCES

1. Ailawadi G, Lau CL, Smith PW, et al. Does reperfusion injury still cause significant mortality after lung transplantation? J Thorac Cardiovasc Surg 2009; 137:688-94.
2. Rubenfeld GD, Caldwell E, Peabody E, et al. Incidence and outcomes of acute lung injury. N Engl J Med 2005; 353:1685-93.
3. Laubach VE, Sharma AK. Mechanisms of lung ischemia-reperfusion injury. Curr Opin Organ Transplant 2016; 21:246-52.
4. Kay LJ, Yeo WW, Peachell PT. Prostaglandin E2 activates EP2 receptors to inhibit human lung mast cell degranulation. Br J Pharmacol 2006; 147:707-13.
5. Kaur D, Hollins F, Woodman L, et al. Mast cells express IL-13R alpha 1: IL-13 promotes human lung mast cell proliferation and Fc epsilon RI expression. Allergy 2006; 61:1047-53.
6. Caughey GH. Mast cell tryptases and chymases in inflammation and host defense. Immunol Rev 2007; 217:141-54.
7. Su M, Chi EY, Bishop MJ, Henderson WR, Jr. Lung mast cells increase in number and degranulate during pulmonary artery occlusion/reperfusion injury in dogs. Am Rev Respir Dis 1993; 147:448-56.
8. Wang H, He S. Induction of lactoferrin and IL-8 release from human neutrophils by tryptic enzymes via proteinase activated receptor-2. Cell Biol Int 2006; 30: 688-97.
9. Wang H, Zheng Y, He S. Induction of release and up-regulated gene expression of interleukin (IL)-8 in A549 cells by serine proteinases. BMC Cell Biol 2006; 7:22.
10. Cottrell GS, Amadesi S, Schmidlin F, Bunnett N. Protease-activated receptor 2: activation, signalling and function. Biochem Soc Trans 2003; 31:1191-97.
11. D'Andrea MR, Derian CK, Leturcq D, et al. Characterization of protease-activated receptor-2 immunoreactivity in normal human tissues. J Histochem Cytochem 1998; 46:157-64.
12. Ramachandran R, Sadofsky LR, Xiao Y, Botham A, Cowen M, Morice AH, Compton SJ. Inflammatory mediators modulate thrombin and cathepsin-G signaling in human bronchial fibroblasts by inducing expression of proteinase-activated receptor-4. Am J Physiol Lung Cell Mol Physiol 2007; 292:L788-98.
13. Zang N, Zhuang J, Deng Y, et al. Pulmonary C Fibers Modulate MMP-12 Production via PAR2 and Are Involved in the Long-Term Airway Inflammation and Airway Hyperresponsiveness Induced by Respiratory Syncytial Virus Infection. J Virol 2015; 90:2536-43.
14. Lee LY, Yu J. Sensory nerves in lung and airways. Compr Physiol 2014; 4:287-324.
15. Poole DP, Amadesi S, Veldhuis NA, et al. Protease-activated receptor 2 (PAR2) protein and transient receptor potential vanilloid 4 (TRPV4) protein coupling is required for sustained inflammatory signaling. J Biol Chem 2013; 288:5790-5802.
16. Zygmunt PM, Hogestatt ED. TRPA1. Handb Exp Pharmacol 2014; 222:583-630.
17. Wei H, Wei Y, Tian F, Niu T, Yi G. Blocking proteinase-activated receptor 2 alleviated neuropathic pain evoked by spinal cord injury. Physiol Res 2016; 65:145-53.
18. Undem BJ, Carr MJ. Pharmacology of airway afferent nerve activity. Respir Res 2001; 2:234-44.
19. Nassenstein C, Kwong K, Taylor-Clark T, Kollarik M, Macglashan DM, Braun A, Undem BJ. Expression and function of the ion channel TRPA1 in vagal afferent nerves innervating mouse lungs. J Physiol 2008; 586:1595-604.
20. Caceres AI, Brackmann M, Elia MD, et al. A sensory neuronal ion channel essential for airway inflammation and hyperreactivity in asthma. Proc Natl Acad Sci U S A 2009; 106:9099-104.
21. Miller RJ, Jung H, Bhangoo S, White FA. Cytokine and chemokine regulation of sensory neuron function; in (Canning BJ, and Spina DV, eds) Handbook of Experimental Pharmacology. Berlin Heidelberg, Springer, 2009, vol. p.^pp. 417-49.
22. MacEwan DJ. TNF receptor subtype signalling: differences and cellular consequences. Cell Signal 2002; 14:477-92.
23. Sommer C, Schmidt C, George A. Hyperalgesia in experimental neuropathy is dependent on the TNF receptor 1. Exp. Neurol. 1998; 151:138-42.
24. Parada CA, Yeh JJ, Joseph EK, Levine JD. Tumor necrosis factor receptor type-1 in sensory neurons contributes to induction of chronic enhancement of inflammatory hyperalgesia in rat. Eur J Neurosci. 2003; 17:1847-52.

25. Hou L, Li W, Wang X. Mechanism of interleukin-1 beta-induced calcitonin gene-related peptide production from dorsal root ganglion neurons of neonatal rats. J Neurosci Res 2003; 73:188-97.
26. Pollock J, McFarlane SM, Connell MC, Zehavi U, Vandenabeele P, MacEwan DJ, Scott RH. TNF-alpha receptors simultaneously activate Ca2+ mobilisation and stress kinases in cultured sensory neurones. Neuropharmacology 2002; 42:93-106.
27. Meotti FC, Posser T, Missau FC, Pizzolatti MG, Leal RB, Santos AR. Involvement of p38MAPK on the antinociceptive action of myricitrin in mice. Biochem Pharmacol 2007; 74:924-31.
28. Li ZY, Zhang YP, Zhang J, Zhang SB, Li D, Huang ZZ, Xin WJ. The possible involvement of JNK activation in the spinal dorsal horn in bortezomib-induced allodynia: the role of TNF-alpha and IL-1beta. J Anesth 2016; 30:55-63.
29. Wolf J, Rose-John S, Garbers C. Interleukin-6 and its receptors: a highly regulated and dynamic system. Cytokine 2014; 70:11-20.
30. Rose-John S, Heinrich PC. Soluble receptors for cytokines and growth factors: generation and biological function. Biochem J 1994; 300(Pt 2):281-90.

microRNA-155 ATTENUATES PROFIBROTIC EFFECTS OF TRANSFORMING GROWTH FACTOR-BETA ON HUMAN LUNG FIBROBLASTS

L. CHI[1*], Y. XIAO[2*], L. ZHU[2], M. ZHANG[2], B. XU[3], H. XIA[2], Z. JIANG[2] and W. WU[1]

[1]School of Basic Medical Sciences, Zhejiang Chinese Medical University, Hangzhou, Zhejiang, China; [2]Institute of Occupational Medicine, Zhejiang Academy of Medical Sciences, Hangzhou, Zhejiang, China; [3]Department of General Surgery, Zhejiang Rehabilitation Medical Center, Hangzhou, Zhejiang, China

Received March 13, 2019 – Accepted August 6, 2019

*These two authors contribute equally to this work

Transforming growth factor-beta (TGF-β) functions in fibrogenesis as a profibrotic mediator, regulating cell proliferation, migration, apoptosis and collagen production of fibroblasts. microRNA-155 (miR-155), the expression of which has been related to bleomycin-induced idiopathic pulmonary fibrosis, has been involved in TGF-β induced epithelial-mesenchymal transition. Here, we found that miR-155 expression was decreased in human pulmonary fibroblasts by TGF-β treatment. We overexpressed miR-155 in fibroblasts to investigate the functional impact of miR-155 on TGF-β-induced fibrotic phenotype of fibroblasts. It is suggested that miR-155 overexpression attenuated the stimulatory effect of TGF-β on fibroblast proliferation, migration and collagen synthesis, by evidence from assessment of cell cycle, viability, apoptosis, migration and collagen content. Furthermore, quantitative measurement showed that SMAD1 gene expression was decreased following miR-155 inhibition, thereby demonstrating an indirect miRNA-SMAD interaction that links miR-155 to TGF-β signaling. Our work helped uncover an miRNA-mediated mechanism of fibroblast response to TGF-β. Moreover, it will help to achieve a better understanding of the regulatory roles of miR-155 in fibrogenesis.

Idiopathic pulmonary fibrosis is a progressive, devastating lung disease with no effective therapy or cure. It is characterized by the proliferation of fibroblasts, resulting in excessive production, deposition and contraction of extracellular matrix (ECM), and leads to clinical outcomes including lung dysfunction or death. Idiopathic pulmonary fibrosis is generally considered a consequence of dysregulated wound healing in response to epithelial injuries. During early phase of wound healing or injury repair, macrophages release cytokines that are important for cell proliferation and migration in this process. Mesenchymal fibroblasts proliferate and migrate into the wound region, and extracellular matrix proteins (e.g. collagen and fibronectin) are deposited there, due to the stimulation of growth factors such as transforming growth factor-beta (TGF-β) (1). Fibroplasia is then initiated to help with wound contraction. Fibroblasts start to differentiate into myofibroblasts, which essentially

Key words: pulmonary fibrosis; fibroblasts; miRNA; transforming growth factor beta; SMAD proteins

Corresponding Author:
Dr Wei Wu,
548# Binwen Road,
Zhejiang Chinese Medical University,
Hangzhou, Zhejiang 310053, China
Tel.: +86 571 86613694
e-mail: wuwei5759@163.com

0393-974X (2019)

contribute to tissue remodeling through the massive production of ECM and fibrogenic factors. While successful healing involves gradual disappearance of myofibroblasts, the persistence of these cells leads to the deposition of excessive ECM, resulting in overgrowth, hardening or scarring at the site of the injured tissue, termed fibrogenesis.

TGF-β is a pleiotropic cytokine that has been closely related to development of fibrotic disease in various organs. TGF-β induces growth arrest and apoptosis in most epithelial cells, including cancer cells, endothelial cells, and lymphocytes. In contrast, TGF-β promotes proliferation and ECM production in mesenchymal cells, such as fibroblasts, to induce a fibrotic response in various tissues (2). Adenovector-mediated transfer of active TGF-β1 to lungs of adult rats resulted in prolonged and severe interstitial fibrosis, while inhibiting TGF-β by a peptide inhibitor in mice with already established fibrosis significantly attenuated the progression of lung fibrosis (3, 4). TGF-β signals through a serine/threonine kinase pathway to induce multiple pro-fibrotic behaviors of fibroblasts. Active TGF-β initially binds to its type II receptor that recruits type I receptor to form an active ligand–receptor complex. In the canonical TGF-β signaling pathway, the TGF-β receptor I/activin-like kinase receptor 5 (ALK5) was recruited to activate the R-SMADs (receptor-regulated SMAD proteins), SMAD2 and SMAD3. The R-SMADs then form complexes with the common partner SMAD4 and transduce the TGF-β signal from cell membrane to nucleus, where they bind the TPA-responsive (TRE) elements in the promoter region of various profibrotic genes to activate transcription. ALK1 (activin A receptor like type 1) is an alternative TGF-β type I receptor that activates SMAD1, SMAD5 and SMAD8. Nonetheless, it is suggested by several studies that ALK1/Smad1/5 pathway acts as an antagonistic mediator of ALK5/Smad2/3 signaling in ECM synthesis (5). Moreover, the balance between ALK1 and ALK5 may regulate the effect of TGF-β on cartilage homeostasis (5, 6).

As key mediators in a wide range of biological process, microRNAs (miRNAs) are involved in pathogenesis of various diseases. Our knowledge of fibrosis-related miRNAs is continually growing. The presumable mechanism by which miRNAs regulate fibrogenesis is the interaction between these non-coding RNAs and their mRNA targets. Recent studies have demonstrated that miR-155 is a multifunctional miRNA that can be associated to immunity, malignancy and viral infection (7-9). In a mouse model of lung fibrosis, the expression level of miR-155 increased in response to bleomycin treatment, and was correlated with the degree of fibrosis (10). Apoptosis and cell motility were both promoted in miR-155-overexpressing fibroblasts. In recent years, many studies have found important roles of miRNAs in mediating TGF-β function, and miR-155 has been related to TGF-β in diverse cellular contexts. Some studies linked miR-155 to TGF-β function in cancer cells and macrophages via SMAD signaling (11-13). Elevated level of miR-155 was detected in the *in vitro* models of TGF-β-induced epithelial-mesenchymal transition (EMT), and it is suggested that miR-155 mediates TGF-β-induced EMT by targeting RhoA signaling or by mediating loss of CCAAT-enhancer binding protein beta (C/EBPβ) (14, 15). To date, there is still a lack of experimental evidence of the functional impact of miR-155 on TGF-β responsiveness in fibroblasts.

The present study aimed to investigate the miR-155 function in TGF-β-induced fibrotic response of lung fibroblasts. We found that TGF-β promoted cell viability, cell motility and collagen synthesis. miR-155 negatively mediated the profibrotic effect of TGF-β, suggesting a potential antifibrotic role of miR-155 in pulmonary fibrosis. Finally, the regulatory relationship between miR-155 and TGF-β signaling was established by the evidence that miR-155 influenced SMAD1 expression in lung fibroblasts.

MATERIALS AND METHODS

Cell culture and treatment

The human lung fibroblast cells HFL1 were kindly provided by Stem Cell Bank, Chinese Academy of Sciences. HFL1 cells were cultured in Ham's F-12K medium (Corning cellgro, Manassas, VA, USA) supplemented with 10% fetal bovine serum (Life Technologies, Grand Island, NY, USA) at 37°C in a

humidified atmosphere containing 5% CO_2. Recombinant human TGF-β1 (PeproTech, Rocky Hill, NJ, USA) were used at a final concentration of 10 ng/ml for phenotype analysis.

Overexpression and Inhibition of miR-155 in HFL1

miR-155 mimics, miR-155 inhibitor and the respective negative control were purchased from Genepharma (Shanghai, China). HFL1 cells were grown in 6-well plates and transfected at 60% confluency using Lipofectamine™ 2000 (Invitrogen, Carlsbad, CA, USA) with mimics/inhibitor and control at a final concentration of 100 nM for 48 h.

Quantitative real-time PCR

HFL1 cells were exposed to different treatment for 48 h. For collagen gene COL1A1, total RNA was isolated and reverse transcribed using the First-Strand cDNA Synthesis kit (Thermo Scientific Fermentas, Waltham, MA, USA). Quantitative real-time PCR was performed using the SYBR® Premix Ex Taq™ (TaKaRa, Otsu, Shiga, Japan) on LightCycler 2.0 Real-time Detection System (Roche Diagnostics, Rotkreuz, Switzerland). Concentrations of PCR components and cycling conditions were set strictly following the manufacturer's instructions. Quantification of miR-155 was performed using stem-loop primers for reverse transcription followed by real-time PCR (16). Quantitative PCR Primers used for miR-155 detection are: RT primer 5'-GTCGTATCCAGTGCAGGGTCCGAGGTATT-CGCACTGGATACGACACCCC-3', forward 5'-TGCGCTTAATGCTAATCGTGATA-3', reverse 5'-CCAGTGCAGGGTCCGAGGTATT-3'. Small RNA U6 is used as an internal control. Quantitative PCR Primers used for mRNA detection are: COL1A1: forward 5'- AGCCAGCAGATCGAGAACA -3', reverse 5'-TCCTTGGGGTTCTTGCTGAT -3'; SMAD1: forward 5'-CTCCCAATAGCAGTTACCCA -3', reverse 5'-ATAAGCAACCGCCTGAACAT -3'; SMAD2: forward 5'- TCCATCTTGCCATTCACGCC -3', reverse 5'-CTTCCTGCCCATTCTGCTCT -3'; SMAD3: forward 5'- TGACTGTGGATGGCTTCACC -3', reverse 5'-CCTCTTCCGATGTGTCTCCG -3'; SMAD5: forward 5'- ACAGCCCTTATCCCCCTTCT -3', reverse 5'-ATATAGGCAGGAGGAGGCGT -3'. Here β-actin was used as internal control. Relative quantification was calculated using the comparative cycle threshold method ($2^{-\Delta\Delta Ct}$).

Cell viability assay

We added 100 µl of cell suspension into each well of the 96-well plate at $2x10^4$ cells/ml and allowed the cells to adhere for 24 h. After 48 h treatment, cells were subjected to viability assay by using the Cell Counting Kit-8 (CCK-8; Beyotime, Haimen, Jiangsu, China) according to the manufacturer's instructions.

Apoptosis assay

Cell apoptosis was evaluated by using an annexin V-FITC kit (KeyGen Biotech, Nanjing, Jiangsu, China) according to the manufacturer's protocol. After treatment, cells were harvested and double stained with annexin V and PI in the dark at room temperature for 15 min. Samples were then analyzed with the FACSCalibur (BD Bioscience, San Jose, CA, USA). Data were collected, and cells at early stage and late stage of apoptosis were both included.

Cell cycle analysis

Cellular DNA content was detected by flow cytometry. After treatment, cells were harvested, washed and fixed with 70% ice-cold ethanol at 4°C for at least 4 h. The cells were then washed twice with ice-cold PBS and treated with 50 µg/ml RNase A at 37°C for 30 min. For DNA labeling, the cells were stained in the dark in 50 µg/ml propidium iodide (PI) solution at 4°C for 30 min. Finally, the stained cells were transferred to the flow cytometer (BD Bioscience, San Jose, CA, USA) for cell cycle analysis.

In vitro migration assay

Cell migration was evaluated by using 24-well transwell with 8-µm polyethylene terephthalate inserts (BD Biosciences, Bedford, MA, USA). The lower Transwell chamber was filled first with 800 µl F-12K medium containing 10% FBS. HFL1 cells were adjusted to a density of 2×10^5/ml using serum-free F-12K medium, and 200 µl of cell suspension was added into the upper chambers. After 24 h, unmigrated cells from the upper surface of the inserts were removed with a cotton swab, and migrated cells on the lower surface were fixed with methanol for 30 s, stained with crystal violet for 30

min, rinsed with PBS, and observed under high-power magnification. A total of five random fields were counted, and the average was calculated.

Hydroxyproline assay

Cell culture supernatant was collected after treatment. Hydroxyproline content was determined by using a hydroxyproline assay kit purchased from Nanjing Jiancheng Bioengineering Institute (Nanjing, Jiangsu, China) following the manufacturer's instructions. Briefly, samples added with hydrolysate solution were hydrolyzed in boiling water for 20 min, and then the pH adjusted to 6.8 after cooling down. Then 1 ml colorless supernatant was prepared by adding active carbon and centrifuged at 3500 rpm for 10 min, after which 0.5 ml solution I was added, mixed and incubated for 10 min; 0.5ml solution II was added, mixed and incubated for 5 min; 0.5 ml solution III was added, mixed and incubated for 15 min at 60°C. Samples were centrifuged at 3500 rpm for 10 min for subsequent measurement of absorbance (OD550 nm).

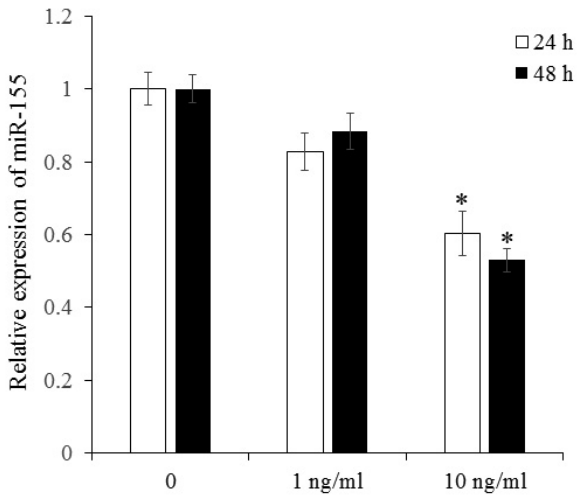

Fig. 1. *TGF-β suppressed miR-155 expression in HFL1 cells. HFL1 cells were exposed to 1 ng/ml and 10 ng/ml of TGF-β for 24 h and 48 h, respectively, followed by quantitative real-time PCR analysis of miR-155. The quantification was repeated three times. * p<0.05 was considered statistically significant, compared with untreated cells.*

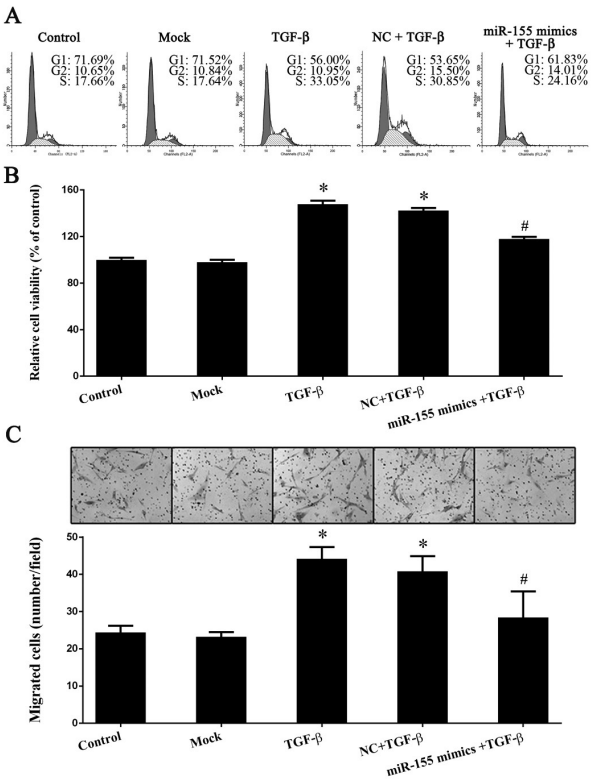

Fig. 2. *miR-155 reduced the stimulatory effects of TGF-β on cell proliferation and migration. HFL1 cells exposed to each treatment for 48 h were subjected to (**A**) flow cytometry analysis of cell cycle, (**B**) CCK-8 analysis of proliferation and (**C**) Transwell assay analysis of cell migration. Migrated cells were stained with crystal violet for observation, and cell number was calculated from five random images of each group. Each experiment was repeated three times. p<0.05 was considered statistically significant, * compared with control, # compared with TGF-β treatment.*

Masson trichrome staining

HFL1 cells were seeded into a 6-well microplate with coverslips placed in each well and allowed to adhere for 24 h. After treatment, the coverslips with plated cells were washed three times with PBS and fixed with 4% paraformaldehyde. Cells were stained with Weigert Iron Hematoxylin, Ponceau-acid fuchsin, Aniline blue and dehydrated in ethanol. The coverslips were finally mounted onto slides to be viewed under a bright-field microscope. The collagen proteins were stained in blue against a red background.

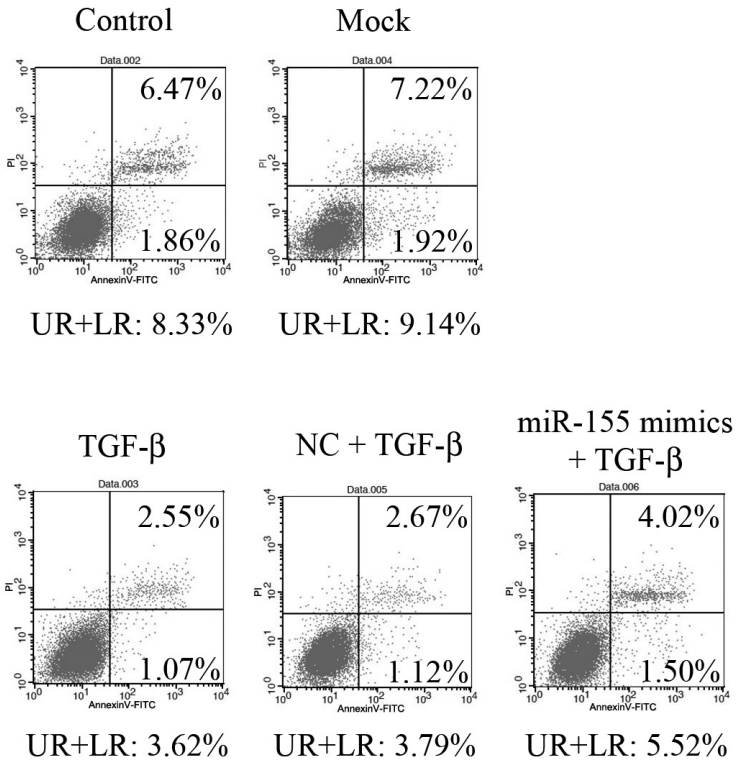

Fig. 3. *miR-155 hardly reduced the inhibitory effects of TGF-β on apoptosis. HFL1 cells exposed to each treatment for 48 h were stained with Annexin V/PI and analyzed by flow cytometry. The early apoptotic rate (lower right) and late apoptotic rate (upper right) are shown, and the total apoptotic rate (sum of the early and late apoptotic rate) was calculated. The experiment was repeated three times. UR, upper right; LR, lower right.*

Statistical analysis

All data were analyzed with SPSS 17.0 (IBM Corp., Amonk, NY, USA). Comparisons between treatment group and control group or those between miR-155 mimics-transfected group and TGF-β-treated group were determined by the Student's *t*-test, and a p value of <0.05 was considered significant. Data acquired from triplicate experiments were presented as mean ± standard deviation.

RESULTS

miR-155 level was decreased in response to TGF-β treatment

HFL1 cells were exposed to TGF-β1 (1 ng/ml and 10 ng/ml) for 24 h and 48 h, respectively. Quantitative analysis showed that miR-155 level was decreased by TGF-β1 treatment, and 48-h treatment induced significant downregulation of miR-155 compared with that of control group (Fig. 1).

miR-155 attenuated the stimulatory effects of TGF-β on fibroblast proliferation and migration

TGF-β induces proliferative response of fibroblasts, therefore, we investigated the potential function of miR-155 in the alteration of HFL1 proliferation caused by TGF-β1 treatment. HFL1 cells were subjected to mock treatment (Lipofectamine only), TGF-β1 treatment (10 ng/ml), TGF-β1 treatment (10 ng/ml) with transfection of miR-155 mimics, and TGF-β1 (10 ng/ml) treatment with transfection of negative control of miR-155 mimics, respectively. Phenotypic alteration was

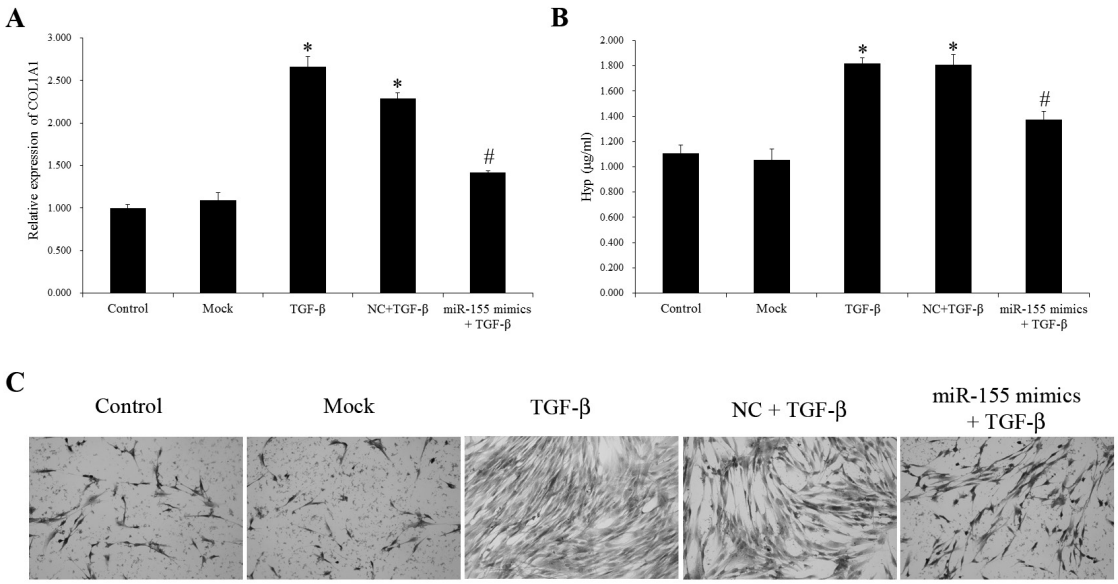

Fig. 4. *miR-155 reduced the stimulatory effects of TGF-β on collagen synthesis. HFL1 cells were exposed to each treatment for 48 h, and collagen synthesis was examined by (**A**) quantitative analysis of COL1A1 expression, (**B**) hydroxyproline assay and (**C**) Masson trichrome staining. Each experiment was repeated three times. p<0.05 was considered statistically significant, * compared with control, # compared with TGF-β treatment.*

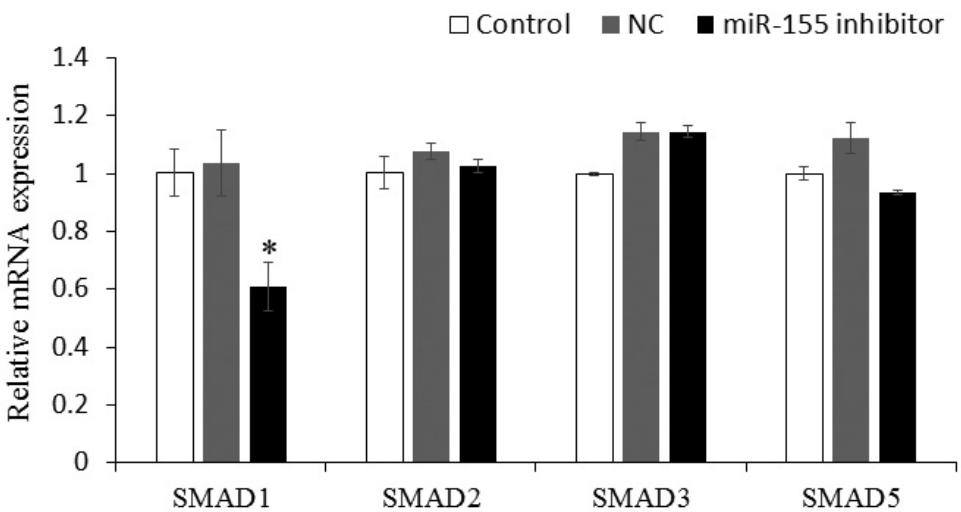

Fig. 5. *miR-155 modulated mRNA expression of SMAD1 in lung fibroblasts. miR-155 expression was suppressed in HFL1 cells by transfection with miRNA inhibitor, and the mRNA levels of SMAD1, SMAD2, SMAD3 and SMAD5 was measured by quantitative real-time PCR. The mRNA quantification was repeated three times. * p<0.05 was considered statistically significant, compared with control.*

determined 48 h after each treatment.

We then investigated the alteration of cell cycle due to each treatment using flow cytometry. Percentage of S-phase cells increased from 17.66% to 33.05% after 48-h treatment of TGF-β1, while the overexpression of miR-155 led to a decline of S-phase proportion to 24.16% (Fig. 2A). miR-155 exerted moderately negative effect on the TGF-β1-mediated cell cycle progression.

We examined the viability of HFL1 cells 48 h after treatment, and found 2.5-fold increase in TGF-β1-treated cells. The overexpression of miR-155 reduced cell proliferation significantly to less than 1.5-fold change, which demonstrated an inhibition of the proliferative effect of TGF-β1 (Fig. 2B).

Fibroblast migration function in repair of injuries, and its dysregulation is regarded as a critical feature of idiopathic pulmonary fibrosis (17). Thus, we examined cell migration using Transwell assay to find out whether miR-155 affects TGF-β1-mediated fibroblast motility. By visualizing and quantifying the migrated cells, we found elevated migration of HFL1 cells resulting from TGF-β1 treatment (Fig. 2C). However, the increased number of migrated cells declined from 40.8±4.1 to 28.4±7.0 when TGF-β1 worked together with an overexpression of miR-155 (Fig. 2C). miR-155 weakened the enhancement of cell motility induced by TGF-β1.

miR-155 did not affect cell apoptosis that was inhibited by TGF-β

We investigated the alteration of cell apoptosis due to each treatment by flow cytometry using Annexin-V/PI double staining, and found that TGF-β1 inhibited HFL1 apoptosis, as compared to control levels (Fig. 3). The total apoptotic rate hardly changed when miR-155 was overexpressed in TGF-β1-treated cells. miR-155 hardly restored the inhibited cell apoptosis by TGF-β1.

miR-155 Attenuated the stimulatory effects of TGF-β on collagen synthesis

As a pivotal mediator of fibrosis in multiple organs, TGF-β causes matrix deposition in fibroblasts by promoting expression of extracellular matrix genes including collagen genes, and suppressing genes that degrade ECM (2). To find out whether miR-155 regulates the collagen deposition resulting from TGF-β treatment, we investigated the expression of type I collagen gene (COL1A1), collagen contents, and fibrotic area staining in HFL1 cells exposed to each treatment.

Quantitative analysis showed that COL1A1 expression in HFL1 was significantly induced by TGF-β1 treatment, and decreased from 2.5-fold to 1.5-fold when miR-155 was overexpressed (Fig. 4A). We then evaluated the collagen content using hydroxyproline assay and found, as expected, a significant increase of hydroxyproline content following TGF-β1 treatment. Meanwhile, the hydroxyproline content decreased in HFL1 cells overexpressing miR-155, compared with that in TGF-β1-treated cells (Fig. 4B). We also examined the appearance of the fibrotic area using Masson trichrome staining, and found a prominent increase of both cell proliferation and the blue-stained collagen protein after TGF-β1 treatment. Cells transfected with miR-155 mimics showed regression of fibrotic response to TGF-β1 treatment (Fig. 4C). Thus, our results indicated that miR-155 negatively mediated TGF-β1-stimulated collagen synthesis in fibroblasts.

miR-155 regulated SMAD1 expression in HFL1 cells

SMAD proteins act as transcription factors that are essential for the transduction of TGF-β signaling. To find out which SMAD protein(s) might be responsible for the crosstalk between TGF-β signaling and miR-155, we detected the mRNA expression of the receptor-regulated SMADs including SMAD1, SMAD2, SMAD3 and SMAD5. According to the quantitative real-time PCR analysis, the expression of SMAD1 was found decreased, while the expression levels of SMAD2, SMAD3 and SMAD5 were not modified by miR-155 inhibitor (Fig. 5). Our finding that SMAD1 expression varied with miR-155 in the same direction suggested that SMAD1 is not a direct target of miR-155 in HFL1 cells.

DISCUSSION

miR-155, a multifunctional regulator, has been previously associated to TGF-β function in

endothelial mesenchymal transition or immunity (12, 15, 18). In the present study, we found that miR-155 was downregulated by TGF-β1 in human lung fibroblasts. Therefore, we overexpressed miR-155 by transfecting miR-155 mimics into the fibroblasts. Phenotypic examination demonstrated a negative effect of miR-155 on TGF-β1 function. Based on our results, TGF-β1 promoted proliferation, migration of lung fibroblasts as well as collagen synthesis. Fibroblasts overexpressing miR-155 exhibited weakened phenotypic response to TGF-β1.

TGF-β is a pleiotropic molecule that controls tissue homeostasis by regulating a variety of biological processes. Diseases including fibrosis, cardiovascular diseases and cancer have been reported in which dysregulation of TGF-β leads to excessive deposition of extracellular matrix, aberrant tissue repair, induction of angiogenesis, and promotion of the EMT (2, 19, 20). Phenotypic observation in the current study confirmed the profibrotic effect of TGF-β, consistent with previous studies (2, 21). Recent studies have focused on the crosstalk between TGF-β signaling and miRNA machinery, and a series of miRNAs have been related to the regulation of TGF-β signaling pathway, mostly in the fibrogenesis of various organs. According to the involvement of miR-155 in TGF-β-induced EMT (15), we intended to establish a relationship between miR-155 and TGF-β function in lung fibroblasts. By *in vitro* evaluation of cellular phenotype, we found that TGF-β-induced fibrotic response was attenuated in fibroblasts overexpressing miR-155.

miRNAs are a class of non-coding RNAs that regulate protein-coding genes by destabilizing target mRNAs or repressing their translation. Each miRNA may have several targets and vice versa one target may be regulated by several miRNAs. The complex miRNA-mRNA interactions allow a variety of physiological and pathological effects in different cellular and tissue contexts, including development, differentiation, tumorigenesis and fibrogenesis. miR-155 is one of the most extensively studied miRNAs, and has been detected in macrophages, dendritic cells as well as fibroblasts. miR-155 expression is modulated in multiple physiological and pathological processes such as hematopoiesis, immunity, tumorigenesis and inflammation. Recent studies demonstrated additional functions of miR-155 in fibroblasts, related to the fibrosis of lung, liver and skin (22-24). In the mouse model of alcohol liver disease, profibrotic genes were found downregulated in miR-155 knockout mice after alcohol diet (22). Treatment of miR-155 antagomir reduced skin fibrosis at wound sites, and inhibited collagen synthesis as well as profibrotic pathways *in vitro* (23, 24). Serum miR-155 was found elevated in lung fibrosis clinically, and furthermore, a correlation between miR-155 expression and the degree of fibrosis was demonstrated *in vivo* (10, 25). Here, the reduced profibrotic phenotype of lung fibroblasts attributed to overexpression of miR-155 also related this small RNA molecule to the TGF-β-induced fibrogenesis, suggesting a potential antifibrotic role of miR-155 in pulmonary fibrosis.

SMAD proteins are intracellular molecules that transduce extracellular signals from TGF-β to the nucleus and then regulate transcription of downstream target genes. The SMAD–miRNA interaction and following consequences have been extensively investigated in recent years, and there has been evidence determining SMADs as miR-155 targets in different cell lines. Louafi *et al.* suggested that miR-155 regulates the cellular response of monocytes to TGF-β by directly targeting SMAD2, with potential implications in fibrosis, angiogenesis, and immunity (12). A study using primary B cell lymphoma cell lines showed that miR-155 influenced SMAD5 expression and activity by directly binding to the 3' UTR, affecting a non-canonical TGF-β pathway and lymphomagenesis (13). Similar results were obtained from studies of miR-155 function in lymphoma both *in vivo* and *in vitro* (11). miR-155 is also able to inhibit BMP signaling and BMP-induced Epstein-Barr virus reactivation by directly targeting SMAD1 and SMAD5, as demonstrated by Qin *et al.* (26). To date, the impact of miR-155 on TGF-β or BMP-mediated SMAD signaling has been well investigated in immune cells or cancer cells. However, the relationship between miR-155 and SMAD signaling has not been established in fibrogenesis or fibrotic changes involving phenotypic alteration of fibroblasts. Therefore, we examined the receptor-regulated SMADs, SMAD2/3 and SMAD1/5, which are responsible for the canonical and non-canonical

TGF-β signaling, respectively. Despite the evidence that miR-155 directly targets SMAD2 and SMAD5 (12, 13), the mRNA expression levels of SMAD2 and SMAD5 were not found altered, nor did the level of SMAD3 change in response to miR-155 inhibitor. Although previous study described a direct targeting of SMAD1 by miR-155 in the lung epithelial cell line A549 (26), our results herein showed that the mRNA level of SMAD1 was decreased following miR-155 inhibition, suggesting an indirect miRNA-mRNA interaction. miR-155 may bind to one or more of its targets which can mediate SMAD1 expression at the transcriptional level. We used PROMO (http://alggen.lsi.upc.es/cgi-bin/promo_v3/promo/promoinit.cgi?dirDB=TF_8.3/) to identify the putative transcription factor binding site of SMAD1, and found multiple candidates as potential regulators of SMAD1 mRNA expression. Among these candidates, there are several (e.g. STAT4, c-Myc and c-Jun) that have been proved direct targets of miR-155 (27-29). These transcription factors likely mediated SMAD1 expression in response to miR-155 overexpression in HFL cells. Despite the evidence that miR-155 reduces the profibrotic effect of TGF-β by the potentially indirect interaction with SMAD1, the mechanism underlying the negative regulation of TGF-β signaling by miR-155 remains unclear. A possible explanation is that miR-155 may enhance ALK1 pathway by regulating SMAD1 expression. ALK1/SMAD1 pathway antagonizes the canonical TGF-β/ALK5/SMAD2/3 pathway (5), thus inhibiting the profibrotic effect of TGF-β.

In summary, miR-155 overexpression attenuated the profibrogenic effect of TGF-β on lung fibroblasts, suggesting a potential antifibrogenic role of miR-155. The downregulation of SMAD1 expression by miR-155 inhibition might relate miR-155 to TGF-β signaling via a non-canonical SMAD signaling. Our work thus helped uncover an miRNA-mediated mechanism of fibroblast activation by TGF-β and prompted us to evaluate the potential therapeutic role of miR-155 in pulmonary fibrosis.

ACKNOWLEDGEMENTS

This work was supported by National Natural Science Foundation of China (No. 81202244, 81300298, 81302464, 81502752), Natural Science Foundation of Zhejiang Province (No. LQ12H26001, LQ16H220001), Project of Zhejiang Province Science and Technology Plan (2013F20004), and the Health and Family Planning Commission of Zhejiang Province (No. 2013KYB071, 2014RCA003, 2015RCA007, 2016KYB068).

REFERENCES

1. Eickelberg O, Kohler E, Reichenberger F, et al. Extracellular matrix deposition by primary human lung fibroblasts in response to TGF-beta1 and TGF-beta3. Am J Physiol 1999; 276:L814-24.
2. Leask A, Abraham DJ. TGF-beta signaling and the fibrotic response. FASEB J 2004; 18:816-27.
3. Sime PJ, Xing Z, Graham FL, Csaky KG, Gauldie J. Adenovector-mediated gene transfer of active transforming growth factor-beta1 induces prolonged severe fibrosis in rat lung. J Clin Invest 1997; 100:768-76.
4. Arribillaga L, Dotor J, Basagoiti M, et al. Therapeutic effect of a peptide inhibitor of TGF-beta on pulmonary fibrosis. Cytokine 2011; 53:327-33.
5. Finnson KW, Parker WL, Chi Y, Hoemann CD, Goldring MB, Antoniou J, Philip A. Endoglin differentially regulates TGF-beta-induced Smad2/3 and Smad1/5 signalling and its expression correlates with extracellular matrix production and cellular differentiation state in human chondrocytes. Osteoarthritis Cartilage 2010; 18:1518-27.
6. Blaney Davidson EN, Remst DF, Vitters EL, et al. Increase in ALK1/ALK5 ratio as a cause for elevated MMP-13 expression in osteoarthritis in humans and mice. J Immunol 2009; 182:7937-45.
7. Wu XY, Fan WD, Fang R, Wu GF. Regulation of microRNA-155 in endothelial inflammation by targeting nuclear factor (NF)-kappaB P65. J Cell Biochem 2014; 115:1928-36.
8. Ranganath P. MicroRNA-155 and its role in malignant hematopoiesis. Biomark Insights 2015; 10:95-102.
9. Dudda JC, Salaun B, Ji Y, et al. MicroRNA-155 is required for effector CD8+ T cell responses to virus

infection and cancer. Immunity 2013; 38:742-53.
10. Pottier N, Maurin T, Chevalier B, et al. Identification of keratinocyte growth factor as a target of microRNA-155 in lung fibroblasts: implication in epithelial-mesenchymal interactions. PLoS One 2009; 4:e6718.
11. Jiang D, Aguiar RC. MicroRNA-155 controls RB phosphorylation in normal and malignant B lymphocytes via the noncanonical TGF-beta1/SMAD5 signaling module. Blood 2014; 123:86-93.
12. Louafi F, Martinez-Nunez RT, Sanchez-Elsner T. MicroRNA-155 targets SMAD2 and modulates the response of macrophages to transforming growth factor-{beta}. J Biol Chem 2010; 285:41328-36.
13. Rai D, Kim SW, McKeller MR, Dahia PL, Aguiar RC. Targeting of SMAD5 links microRNA-155 to the TGF-beta pathway and lymphomagenesis. Proc Natl Acad Sci U S A 2010; 107:3111-16.
14. Bijkerk R, de Bruin RG, van Solingen C, et al. MicroRNA-155 functions as a negative regulator of RhoA signaling in TGF-beta-induced endothelial to mesenchymal transition. Microrna 2012; 1:2-10.
15. Johansson J, Berg T, Kurzejamska E, et al. MiR-155-mediated loss of C/EBPbeta shifts the TGF-beta response from growth inhibition to epithelial-mesenchymal transition, invasion and metastasis in breast cancer. Oncogene 2013; 32:5614-24.
16. Chen C, Ridzon DA, Broomer AJ, et al. Real-time quantification of microRNAs by stem-loop RT-PCR. Nucleic Acids Res 2005; 33:e179.
17. Lam AP, Flozak AS, Russell S, et al. Nuclear beta-catenin is increased in systemic sclerosis pulmonary fibrosis and promotes lung fibroblast migration and proliferation. Am J Respir Cell Mol Biol 2011; 45:915-22.
18. Das LM, Torres-Castillo MD, Gill T, Levine AD. TGF-beta conditions intestinal T cells to express increased levels of miR-155, associated with down-regulation of IL-2 and itk mRNA. Mucosal Immunol 2013; 6:167-76.
19. Munjal C, Opoka AM, Osinska H, James JF, Bressan GM, Hinton RB. TGF-beta mediates early angiogenesis and latent fibrosis in an Emilin1-deficient mouse model of aortic valve disease. Dis Model Mech 2014;7:987-96.
20. Chiechi A, Waning DL, Stayrook KR, Buijs JT, Guise TA, Mohammad KS. Role of TGF- in breast cancer bone metastases. Adv Biosci Biotechnol 2013; 4:15-30.
21. Conte E, Gili E, Fagone E, Fruciano M, Iemmolo M, Vancheri C. Effect of pirfenidone on proliferation, TGF-beta-induced myofibroblast differentiation and fibrogenic activity of primary human lung fibroblasts. Eur J Pharm Sci 2014; 58:13-9.
22. Bala S, Csak T, Saha B, et al. The pro-inflammatory effects of miR-155 promote liver fibrosis and alcohol-induced steatohepatitis. J Hepatol 2016; 64(6):1378-87.
23. Yan Q, Chen J, Li W, Bao C, Fu Q. Targeting miR-155 to treat experimental scleroderma. Sci Rep 2016; 6:20314.
24. Yang LL, Liu JQ, Bai XZ, et al. Acute downregulation of miR-155 at wound sites leads to a reduced fibrosis through attenuating inflammatory response. Biochem Biophys Res Commun 2014; 453:153-59.
25. Kurowska-Stolarska M, Hasoo MK, Welsh DJ, et al. The role of microRNA-155/liver X receptor pathway in experimental and idiopathic pulmonary fibrosis. J Allergy Clin Immunol 2017; 139:1946-56.
26. Yin Q, Wang X, Fewell C, et al. MicroRNA miR-155 inhibits bone morphogenetic protein (BMP) signaling and BMP-mediated Epstein-Barr virus reactivation. J Virol 2010; 84:6318-27.
27. Song J, Liu P, Yang Z, Li L, Su H, Lu N, Peng Z. MiR-155 negatively regulates c-Jun expression at the post-transcriptional level in human dermal fibroblasts in vitro: implications in UVA irradiation-induced photoaging. Cell Physiol Biochem 2012; 29:331-40.
28. Litvinov IV, Cordeiro B, Fredholm S, et al. Analysis of STAT4 expression in cutaneous T-cell lymphoma (CTCL) patients and patient-derived cell lines. Cell Cycle 2014; 13:2975-82.
29. Sun S, Sun P, Wang C, Sun T. Downregulation of microRNA-155 accelerates cell growth and invasion by targeting c-myc in human gastric carcinoma cells. Oncol Rep 2014; 32:951-6.

PAEONIFLORIN REDUCED THE CARDIOTOXICITY OF ACONITINE IN H9c2 CELLS

J. LI[1], SH. ZHANG[1], D. HE[1], JF. WANG[1] and JQ. LI[1,2]

[1]School of Medicine, University of Electronic Science and Technology of China & Department of Pharmacy, Sichuan Provincial People's Hospital, Chengdu, China; [2]Personalized Drug Therapy Key Laboratory of Sichuan Province & Sichuan Academy of Medical Sciences, Chengdu, China

Received June 20, 2019 - Accepted August 5, 2019

Aconitine (ACO), the main active component in *Aconitum carmichaelii* Debeaux (family: Ranunculaceae), has high cardiotoxicity, however the mechanisms of this effect remain unclear. Paeoniflorin (PF), the main chemical ingredient in herbaceous peony, can protect the heart from damage through antioxidant, vasodilatory and other effects. In this study, we focused on the mechanism by which PF reduces ACO cardiotoxicity. We selected H9c2 cells as the experimental model. MTT assay, Western blot analysis and real-time PCR were used to measure cell proliferation, apoptosis, ion channels and oxidative stress. Cell proliferation was significantly increased, the Bcl-2/Bax ratio and p53 level were upregulated, and Caspase-3 was slightly reduced in the ACO+PF group compared with the ACO group. SCN5A mRNA expression was significantly increased in the ACO+PF group compared with the ACO group, while RyR2 and Cx43 mRNA expression was decreased. Compared with the ACO group, the ACO+PF group showed marked decreases in extracellular lactate dehydrogenase (LDH) and intracellular malondialdehyde (MDA), while there was no difference in intracellular superoxide dismutase (SOD). The above data demonstrate that the cardiotoxicity of ACO in H9c2 cells was significantly decreased by PF.

Traditional Chinese medicines (TCMs) are popular and self-prescribed treatments for many diseases in China and other Asian countries. A U.S. survey suggested that approximately 90% of patients with arthritis use herbal medicines as alternative therapies (1).

Aconitum plants (Ranunculaceae family) (2), one of the most famous herbal medicines in China and other Asian countries, are well known for their medicinal value in clinical practice, including rheumatism, knee pain, chronic diarrhea and so on. Aconitine (ACO, $C_{34}H_{47}NO_{11}$, Fig. 1) is the main bioactive component in Aconitum plants (3, 4). Shi et al. (5) revealed that ACO is effective against adjuvant arthritis by inhibiting the production of PGE and restoring the function of T cells. Recently, Li et al. (6) found that ACO is a potential novel treatment for systemic lupus erythematosus. However, ACO has high cardiotoxicity, and because of this, the use of Aconitum plants is limited in clinical care. A high content of Paeoniflorin (PF, $C_{23}H_{28}O_{11,}$ Fig. 1) is present in the total glucosides from *Paeonia suffruticosa* Andrews and PF has been used clinically for its antiarrhythmic, analgesic, immune-regulatory and other effects. A study published in 2011 (7) showed that PF has anti-inflammatory and

Key words: aconitine; paeoniflorin; cardiotoxicity, H9c2 cells

Corresponding Author:
Prof. Jin-qi Li,
Department of Pharmacy,
Sichuan Provincial People's Hospital,
No.32 West Second Section First Ring Road,
Chengdu 610072, China
Tel.: +86 17708130627
e-mail: lijinqi2002@126.com

0393-974X (2019)

immunoregulatory effects and that it can not only decrease the release of IL-1, TNF-α and PGE_2 but also upregulate the expression of cAMP and EP_4 in CIA rats. In addition, PF could inhibit platelet aggregation, dilate arteries, increase coronary flow and protect against acute myocardial ischemia. Zhang et al. (8) found that PF inhibited L-type Ca^{2+} current (*Ica,L*) by 51% and markedly shifted the steady-state inactivation curve of *Ica,L* towards a more negative potential, indicating that PF obviously inhibited the Ca^{2+} channels in rat ventricular myocytes.

A previous pharmacological study supported that the acute toxicity of ACO was markedly relived by treatment with *P. suffruticosa* Andrews (9), and coadministration of ACO and PF in rats was shown to reduce the acute toxicity of ACO, which might relate to the pharmacokinetic alteration of ACO in rats (10). However, the mechanism by which the combined use of these two herbs reduces toxicity remains unclear.

In the present study, we focused on investigating the effect and mechanism of ACO combined with PF on reducing ACO cardiotoxicity in H9c2 cells. The H9c2 cell line is a subclone of the original clonal cell line derived from embryonic BD1X rat heart tissue by B. Kimes and B. Brandt and exhibits many of the properties of skeletal muscle (ATCC® CRL-1446™).

Table I. *H9c2 cell processing conditions*

Time (h)	ACO μg/mL	ACO:PF
0.5	3200	1:4
1	1600	1:4

Cell culture

H9c2 was purchased from Procell Life Science & Technology Co., Ltd. (Wuhan, China, Cat No. CL-0089). Cells were incubated in complete growth medium which consisted of 89% DMEM (HyClone, Cat NO. SH30022.01B, USA), 10% FBS (Clark Bioscience, Richmond, USA, Cat NO. FB25015) and 1% P/S (HyClone, Cat NO. C40505, USA) and maintained in a Thermo BB15 CO_2 incubator (Thermo Scientific, USA). The medium was replaced every 48-72 h.

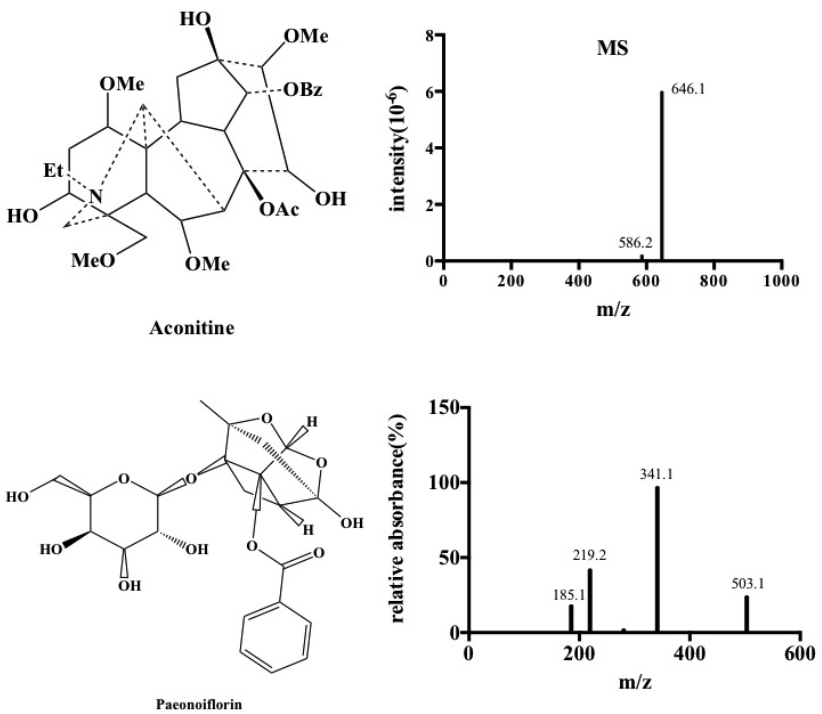

Fig. 1. *Chemical structure of ACO and PF.*

Preparations of the drugs

A stock solution of ACO (Chengdu Mansite Biotechnology Co., Ltd., China, Cat No. A0196, purity>98%) was prepared with dimethyl sulfoxide (DMSO, BioFroxx, Germany, Cat NO. 1084ML500) (50 mg ACO was dissolved in 800 μL DMSO), and PF (Chengdu Push Biotechnology Co., Ltd., China, Cat No. PS0220-0025, purity>98.5%) was dissolved in complete growth medium at a concentration of 80 mg/mL to prepare a stock solution. Before use in this research, all of the stock solutions were diluted in complete growth medium to the desired concentrations.

The toxicity concentration and effective duration as measured by MTT

The cells were incubated in 96-well plates for 24 h, and every well had a density of 8000 cells/well. Then, the cells were treated with several concentrations of ACO (3200, 1600, 800, 400, or 200 μg/mL, per well), except the normal group (with complete growth medium) and control group (with DMSO) for 0.5 h, 1 h, 2 h and 4 h. The concentration of DMSO in the control group at every time point was equal to the concentration of DMSO in the ACO group. The medium was then removed, and the cells were incubated with 10 μL of MTT and 190 μL of complete growth medium for an additional 4 h at 37°C in a CO_2 incubator. The viable cells change the color of MTT to blue-purple after the addition of 150 μL of DMSO. The absorbance at 490 nm was measured using a Thermo Multiskan FC microplate reader (Thermo Scientific, USA), and the absorbance (optical density, OD) represented the cell viability. All experiments were carried out with six replicates.

Protective effect of PF on H9c2 cells as detected by MTT

According to the Chinese Pharmacopeia (2005 Edition), the recommended clinical dosages of ACO and PF are 3–15 g/day/person and 6–15 g/day/person, respectively. Therefore, the ratio of ACO to PF used in this research was less than 5:1.

H9c2 cells were prepared in the same way as in the measurement of toxicity. The cells were divided into a control group, ACO groups, ACO+PF groups (the concentration of ACO was the same, the ratio of

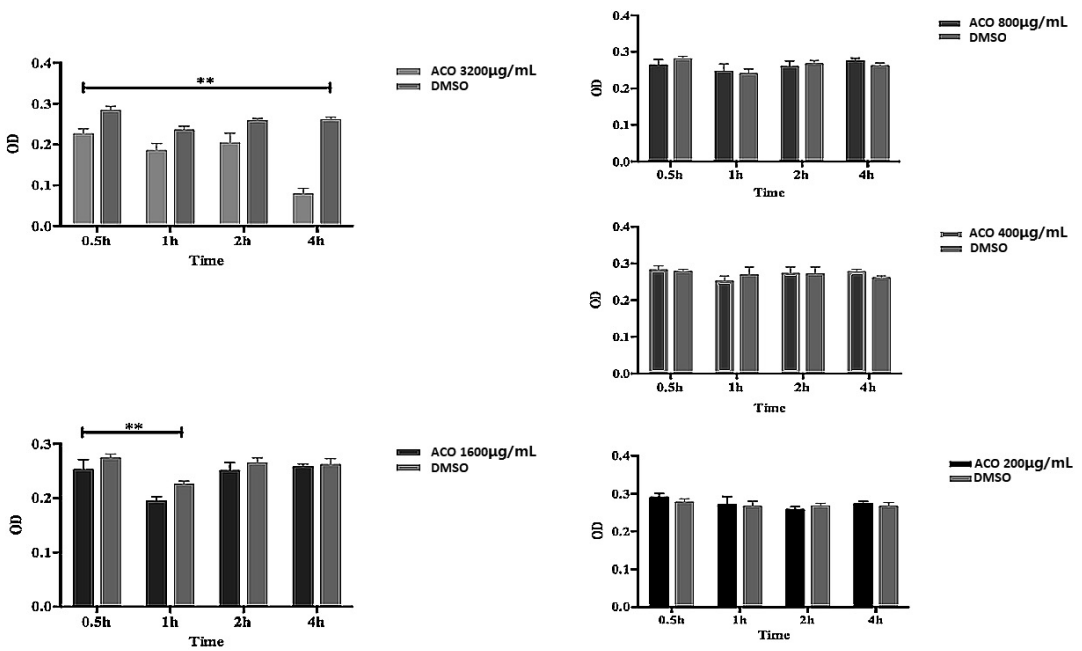

Fig. 2. *Toxicity concentration and effective duration of aconitine by culturing with different concentrate of aconitine alone to H9c2 cells for 0.5 h to 4 h. Each point represents mean±S.D. (n = 6). Compared with DMSO, *P<0.05, **P<0.01.*

the drugs was 4:1, 2:1, 1:1, 1:2, 1:4), and PF groups. The volume of drugs used was 100 µl per well. After processing as described, all of the cells were cultured for 0.5 h or 1 h before the MTT assay was performed. The inhibition rate was calculated (Formula 1), and the effect was confirmed with the Q value method (11).

Inhibition rate=the OD of experimental wells/the OD of DMSO ⋯ Formula 1

The Q value method uses the following equation:

$$Q=E_{A+B}/(E_A+E_B-E_A*E_B)$$

where E_{A+B} is the inhibition rate of A combined with B, and E_A and E_B are the inhibition rates of A and B, respectively. Q=0.85-1.15 indicates that the effects of the two drugs were additive. Q>1.15 represents a synergetic effect, and Q<0.85 represents an antagonistic effect.

Intracellular superoxide dismutase and malondialdehyde measurements

H9c2 cells were incubated in 6-well plates at a density of 80000 cells/well for 24 h, and then the cells were divided into the following five groups: a control group (treated with DMSO, the same

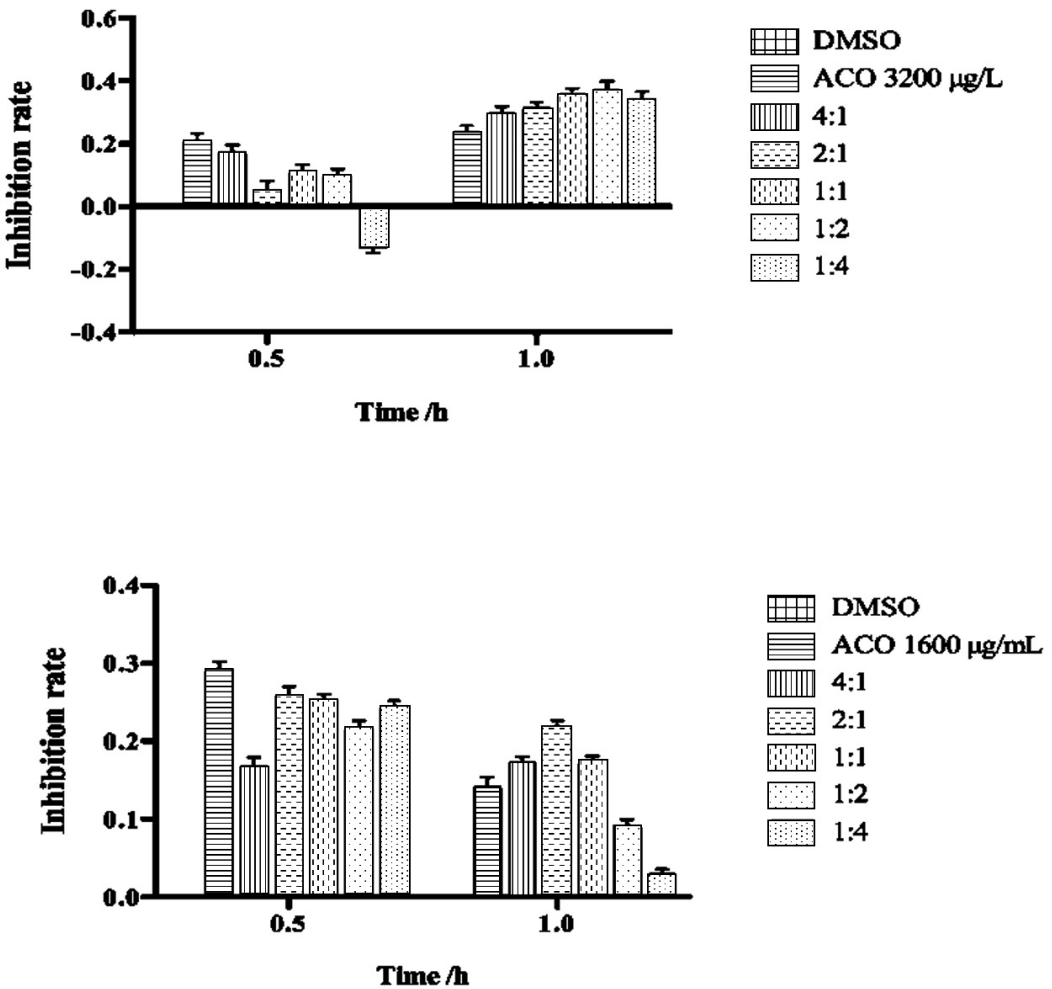

Fig. 3. *The inhibition rate of ACO combined with PF (n=3).*

volume and concentration as the ACO group), a normal group (treatment with complete growth medium, the same volume), an ACO group, an ACO+PF group, and a PF group. The volume of drugs was 1 mL per well. All of the cells were incubated for 0.5 h or 1 h. The media were removed and stored in a centrifuge tube until use, and the cells were collected. Intracellular superoxide dismutase (SOD) and malondialdehyde (MDA) contents were measured according to the SOD and MDA kit instructions (Nanjing Jincheng Bioengineering Institute, China).

Intracellular SOD generation was measured by xanthine oxidase, and the absorbance was detected

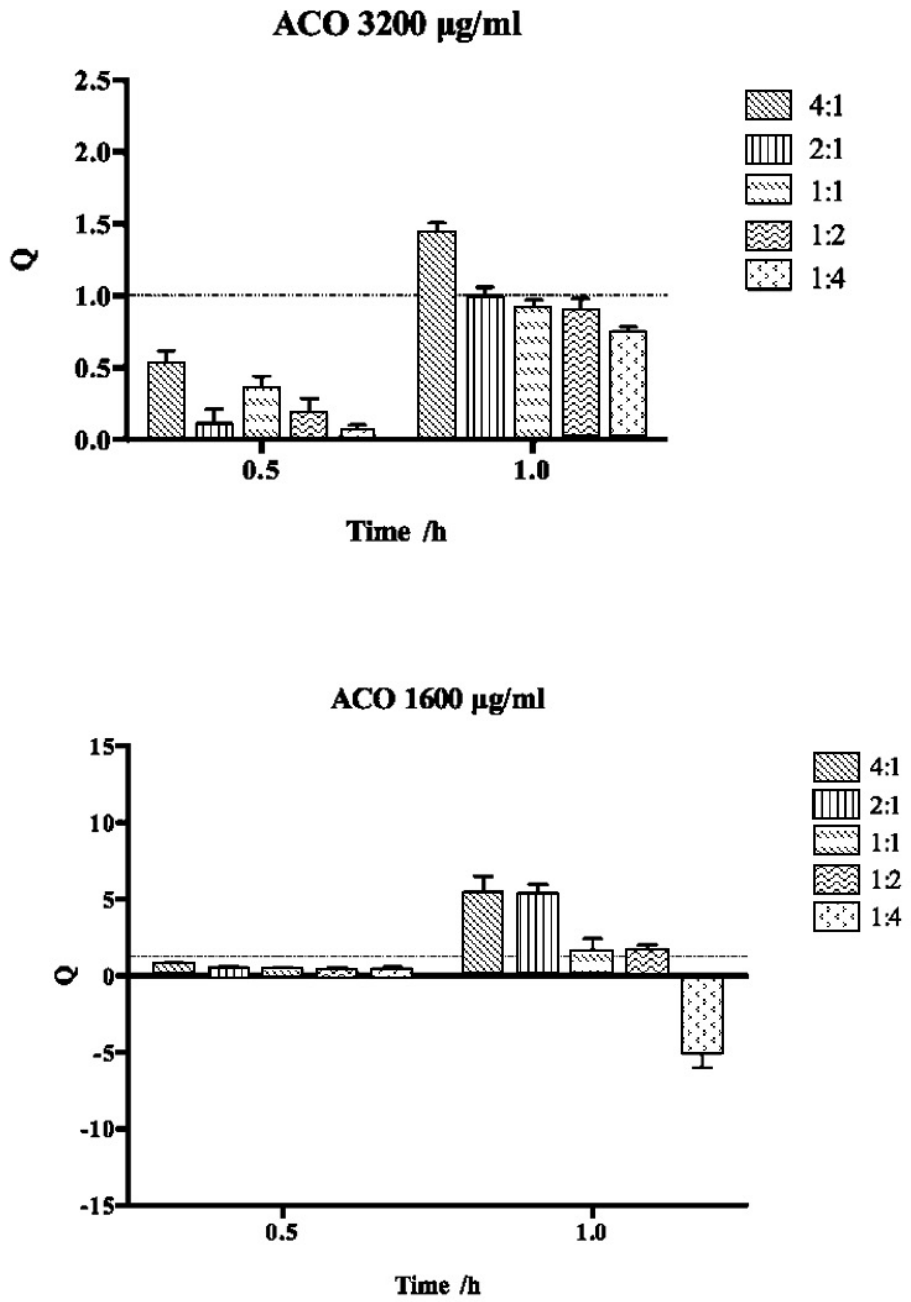

Fig. 4. *The Q value of ACO combined with PF (n-3).*

by a spectrophotometer at a wavelength of 550 nm. Intracellular MDA generation was measured by thiobarbituric acid, and the peak OD was detected by a spectrophotometer at a wavelength of 532 nm.

Extracellular lactate dehydrogenase measurement

The media collected in the same way as for the measurement of SOD and MDA were used to measure extracellular lactate dehydrogenase (LDH) release, and the methods were performed according to the LDH assay kit instructions (Changchun Huili Biotech Co., Ltd., China).

Extracellular LDH release was measured by a lactate dehydrogenase release assay, and the absorbance was detected by an automated chemistry analyzer (Rayto Life and Analytical Sciences Co., Ltd., China) at a wavelength of 320 nm.

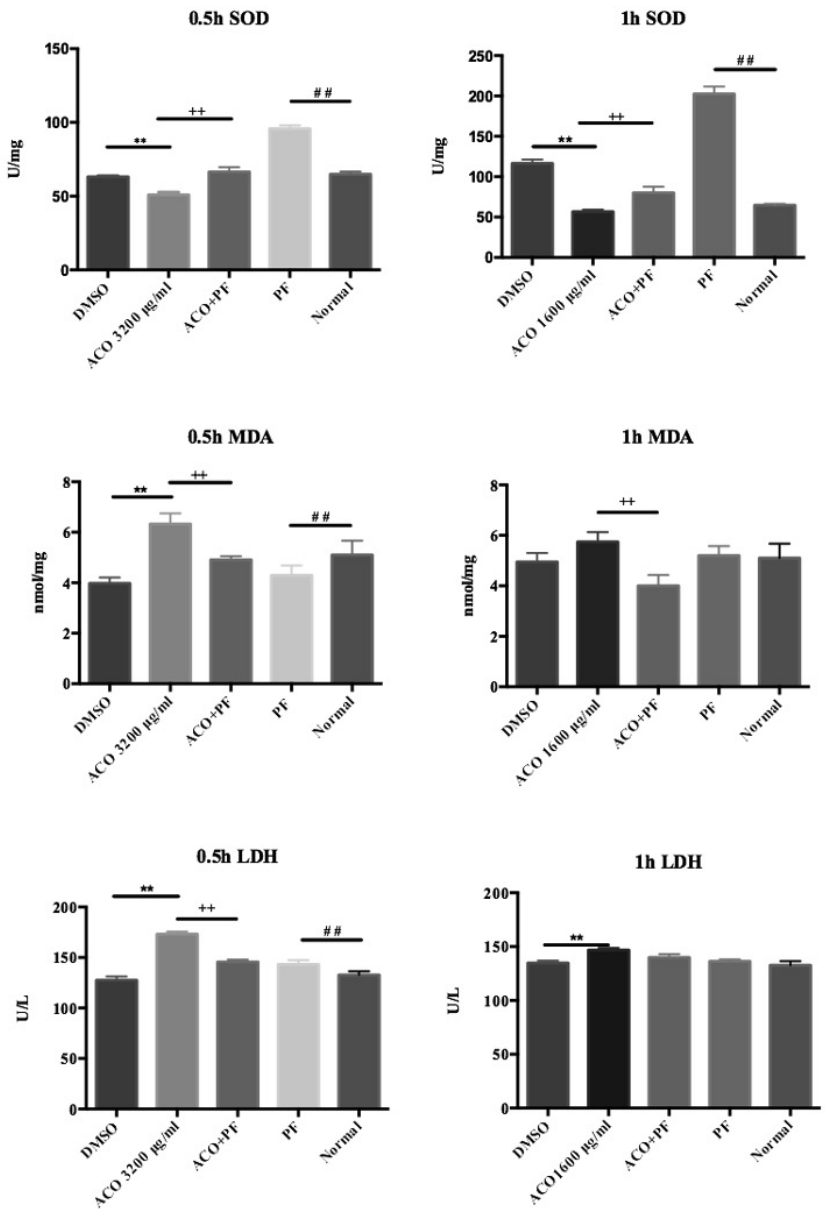

Fig. 5. *Intracellular SOD, MDA and extracellular LDH. Each point represents mean±S.D. (n = 3). Compared with DMSO, *P<0.05, **P<0.01, compared with ACO, $^{+}$P<0.05, $^{++}$P<0.01, compared with normal, $^{\#}$P<0.05, $^{\#\#}$P<0.01.*

Analysis of mRNAs by real-time PCR

The division was the same as for the measurement of SOD and MDA, and H9c2 cells were collected at 0.5 h or 1 h after treatment with drugs. Total RNA was extracted, and the final concentration was 200 ng/μL. Then, 2 μg of RNA was used for first strand cDNA synthesis by using 1 μL of oligo (dT)18 as the first strand primer. After cDNA synthesis, the expression levels of SCN5A, RyR_2 and Cx43 were detected by real-time PCR (ABI, USA) using FastStart Universal SYBR Green Master (Roche, USA). Actin was used as an internal reference to quantify mRNA content. Finally, relative quantities were calculated by the $^{\Delta\Delta}$CT method as follows:

$^{\Delta\Delta}$CT method: target gene expression=2^{-K}

where A=CT (genes, drug)- CT (Actin, drug); B=CT (genes, DMSO)- CT (Actin, DMSO); and K=A-B.

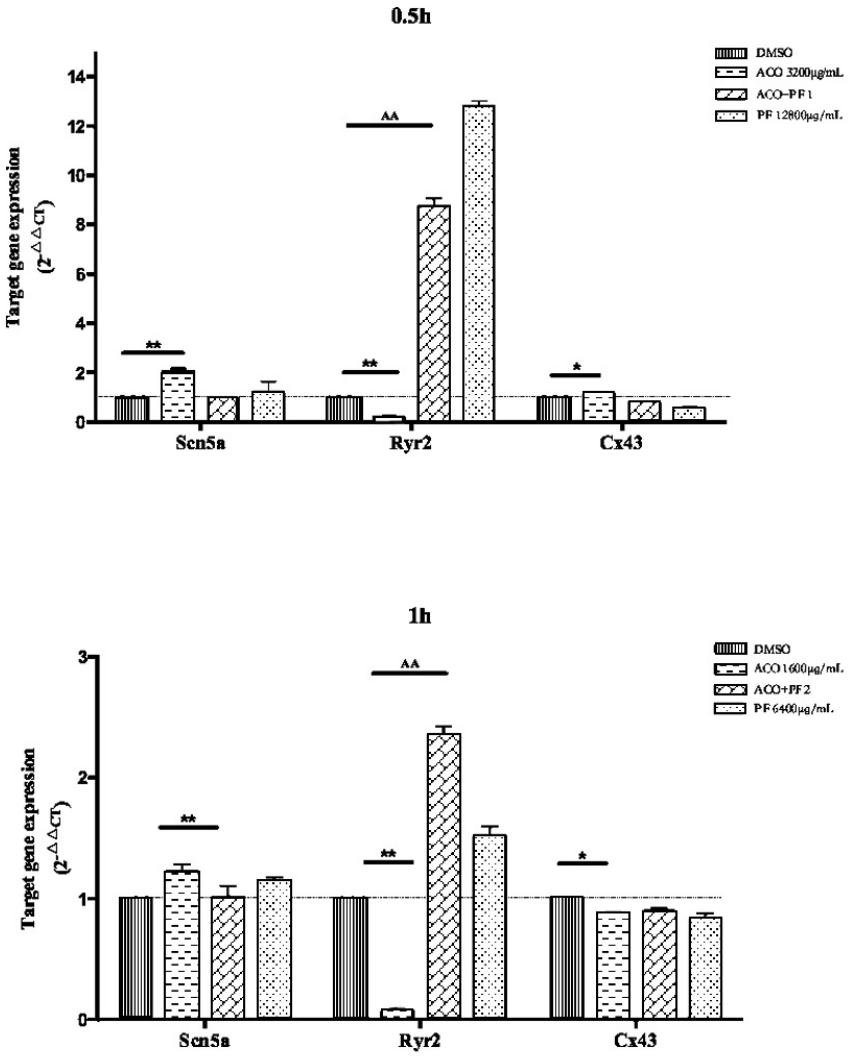

Fig. 6. *Effect of ACO combined with PF on the ion channel protein. Each point represents mean±S.D. (n = 3). Compared with DMSO, *P<0.05, **P<0.01, compared with ACO+PF, ^{A}P<0.05, ^{AA}P<0.01.*

Western blot analysis

The groups were the same as for the measurement of SOD and MDA, and H9c2 cells were collected for immunoblotting analysis at 0.5 h or 1 h after treatment with drugs. Briefly, total cellular proteins were extracted and estimated by a BCA test, separated by SDS-PAGE, and transferred onto Immobilon-P transfer membranes (PVDF) (Millipore, USA). The membranes were incubated with primary antibodies at 4°C overnight, followed by high-temperature incubation with secondary antibodies for 45 min. The signals were detected by electrochemiluminescence (ECL). The intensities of Bcl, Bax, p53 and Caspase-3 on the PVDF membraned were quantified by densitometry and then analyzed with AlphaEase FC software (Alpha Innotech, USA). GAPDH bands served as loading controls.

Statistical analysis

Data are expressed as the means ± standard deviations. Groups were statistically compared using two-way analysis of variance (ANOVA) with GraphPad Prism 6 (GraphPad Software, USA). A value of $P < 0.05$ was considered statistically significant.

RESULTS

The toxic concentration and effective treatment duration of ACO

Based on the OD value of H9c2 cells, which was measured by a microplate reader (Fig. 2), ACO had an inhibitory effect on the proliferation of H9c2 cells in a concentration-dependent manner. At an ACO concentration of 1600 μg/mL or above, obvious cytotoxicity was observed (compared with DMSO, $P<0.05$), while the concentration of 800 μg/mL or below had little effect ($P>0.05$).

Regarding the four time points (0.5 h, 1 h, 2 h, 4 h), the results indicated that ACO had obvious cardiotoxicity after culturing for 0.5 h or 1 h (compared with DMSO, $P<0.05$). However, in the 1600 μg/mL group, the inhibitory effect of ACO after culturing for 2 h or 4 h was weakened (compared with that of DMSO,

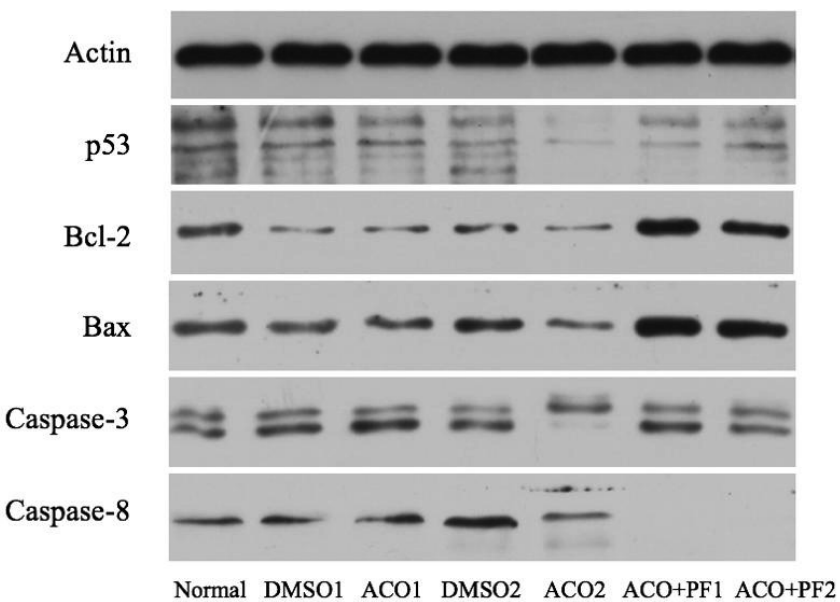

Fig. 7. *Representative Western blot of various apoptosis factors protein isoforms in cultures. (Group1: 0.5h, 3200 μg/mL; Group2: 1h, 1600 μg/mL, n=3).*

P>0.05). Thus, the toxic concentrations of ACO used in the subsequent test were 1600 μg/mL and 3200 μg/mL, and the culture time was 0.5 h and 1 h.

Protective effect of PF on H9c2 cell proliferation

The inhibition rate was calculated based on the OD data (Fig. 3). The following conclusions can be drawn from the above data: i) in the groups treated with 1600 μg/mL for 0.5 h, all of the PF proportions had similar antagonistic effects; ii) among the groups treated with 3200 μg/mL for 0.5 h, the 1:4 proportion had strong antagonistic effects; iii) among the groups treated with 1600 μg/mL for 1 h, only the 1:2 and 1:4 proportions had antagonistic effects, and the 1:4 proportion was the best; and iv) among the groups treated with 3200 μg/mL for 1 h, only the 1:4 proportion had antagonistic effects, and the inhibition rate at the 1:4 proportion was higher than that of ACO alone, indicating that the cardiotoxicity of the 1:4 proportion was higher than that of ACO.

In addition, according to the lowest Q value (Fig. 4), the H9c2 cell processing conditions for the follow-up study are shown in Table I.

Effect on LDH and oxidative stress

The intracellular SOD and MDA and extracellular LDH were measured according to kit instructions, and the results are shown in Fig. 5. LDH release was significantly increased in the ACO group (compared with the DMSO group, P<0.01), which showed that ACO strongly damaged H9c2 cells. In the ACO+PF group, LDH release was decreased (compared with the ACO group, P<0.01), which indicated that PF relieved LDH release in H9c2 cells. SOD activity was decreased in the ACO group (compared with the DMSO group, P<0.01), showing that the H9c2 cell damage caused by ACO may be related to oxidative stress. Compared with the DMSO group, both the ACO+PF group and the PF group had significantly increased SOD activity (P<0.01), indicating that PF can alleviate the oxidative damage induced by ACO. The MDA content of the ACO group was increased, especially at 0.5 h (compared with that of the DMSO group, P<0.01), while in the PF group and ACO+PF group, the content of MDA was decreased (P<0.05), indicating that PF inhibited intracellular MDA.

Therefore, this study proved that PF improved

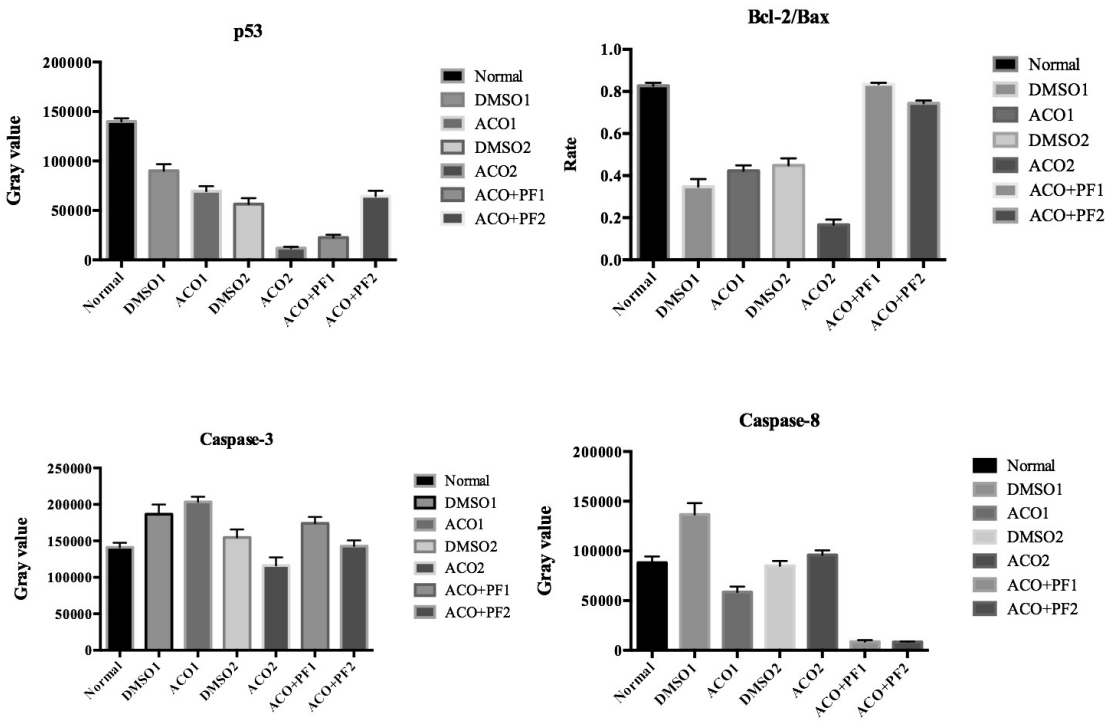

Fig. 8. *Representative Western blot of p53, caspase-3, -8 and Bcl-2, Bax protein isoforms in cultures. (Group1:0.5h, 3200 μg/mL; Group2: 1h, 1600 μg/mL, n=3).*

the cell condition by changing the levels of LDH, SOD and MDA.

Effect on ion channels

The mRNA expression levels of Scn5a, Ryr2 and Cx43 are shown in Fig. 6. Compared with the DMSO group, the ACO group had decreased Scn5a mRNA expression ($P<0.01$), showing that the cardiotoxicity caused by ACO may be associated with Na^+ channels. Moreover, the Scn5a mRNA expression in the ACO+PF group was not obviously different from that in the DMSO group ($P>0.05$), demonstrating that PF-mediated cardioprotection may be related to the Scn5a protein. The expression of Ryr2 mRNA was elevated in the ACO group compared with the DMSO group ($P<0.01$), showing that the toxicity caused by ACO may be related to Ca^{2+} channels. Additionally, Ryr2 mRNA expression was significant inhibited in the ACO+PF group compared with the ACO group ($P<0.05$), suggesting that the PF-mediated alleviation of myocardial damage was associated with the Ryr2 protein. The expression of Cx43 mRNA was increased by high ACO and decreased by low ACO compared with DMSO ($P<0.05$), indicating that the ACO-induced myocardial injury may be related to cardiac gap-junctional channels, and Cx43 mRNA expression was not different between the in ACO+PF group and the DMSO group ($P>0.05$), which meant that PF relieved myocardial damage through a process involving the Cx43 protein. These findings suggested that the protective effect of PF was closely related to various channels in the heart.

Effect on cell apoptosis

ACO had an inhibitory effect on the level of p53, and compared with the ACO group, ACO+PF group 2 had an increased level of p53, showing that PF had a certain inhibitory activity against p53. After 0.5 h of incubation, ACO increased Caspase-3 expression in cells, but the expression of Caspase-3 was suppressed after 1 h of culture. The results also suggested that compared with DMSO, ACO+PF can inhibit the expression of Caspase-3. From the Caspase-8 expression pattern, it can be seen that a high concentration of DMSO obviously activated the expression of Caspase-8, but ACO had little effect on Caspase-8 expression. In addition, PF combined with ACO strongly decreased Caspase-8 expression. As shown in Fig. 8, the ratio between Bcl-2 and Bax was calculated, and the results clearly showed that the Bcl-2/Bax ratio was inhibited more by DMSO than by ACO alone, but the combination of ACO and PF significantly improved the ratio, indicating that this treatment had a better effect on cell apoptosis.

The results of the Western blot analysis of various apoptosis-related proteins are listed in Fig. 7-8. In conclusion, although ACO had different effects on the expression of p53, Caspase-3, Caspase-8 and Bcl-2/Bax, the results proved that the combined use of ACO and PF improved these factors, indicating that PF can effectively decrease the apoptosis caused by ACO.

DISCUSSION

In the present work, we proved the protective effects of PF on ACO cardiotoxicity and showed that many mechanisms are involved.

Cell proliferation plays an important role in life, including biological cell development and cell division (reproduction). Apoptosis is an active process of programmed cell death that occurs in multicellular organisms; aging and diseased cells are eliminated by apoptosis to protect the body from injury. Cell proliferation and apoptosis are the basic characteristics of life and are also the basic measures that maintain the dynamic balance of cell number in various organs. The main responsibility of these processes is to ensure the health of the body.

In the present study, it was found that cell proliferation was promoted more when ACO was combined with PF than when only ACO was administered. In addition, the expression of Capase-3 and Caspase-8 was decreased, and p53 and the ratio of Bcl-2 to Bax were increased, indicating that apoptosis was relieved by PF.

Ion channels are large structural pores in the cell membrane and interact with various ionophoric proteins to allow ions to freely pass through the pore. Ion channels are crucial components in a wide variety of biological processes, such as cardiac and nerve processes.

The condition of the heart depends on various ion channels (12), such as potassium channels, sodium channels, and calcium channels. Ion channels maintain the normal function of the heart.

In the current study, the expression of SCN5A mRNA was decreased, and RyR_2 mRNA was increased by ACO. Moreover, it was discovered that PF played a protective role in ion channels because the expression of SCN5A mRNA was increased and RyR_2 mRNA was decreased with ACO+PF treatment compared with ACO treatment alone.

Gap junctions are also protein pores; they are specialized intercellular junctions that connect the cytoplasm of two cells, allowing various molecules, ions and electrical impulses to directly pass through a regulated gate between the cells. One gap junction channel is made up of two connexons (13). In cardiovascular disease, changes in the expression of connexin 43 (Cx43) (14), a subunit of a connexon, may cause abnormalities in the heart and lead to arrhythmia.

We investigated the expression of Cx43 mRNA and found that ACO treatment led to the abnormal expression of Cx43 mRNA, while PF changed this unusual condition. The results indicated that PF reduced the cardiotoxicity of ACO and may be associated with changes in Cx43 expression.

Energy metabolism in the body is composed of several complex chemical processes. These processes generally involve various metabolic pathways within the cell, including catabolic or anabolic pathways. In humans, research that investigates how energy is processed in the body is termed bioenergetics, and this field is mainly focused on how the three main nutrients (carbohydrates, proteins and fats) break down to release energy for cell growth, cell repair, physical activity and energy storage.

LDH, SOD and MDA (15, 16) are all important substances for energy metabolism, LDH is widely expressed in some tissues, and the expression of LDH will increase when tissues are damaged; LDH is a marker of injuries and diseases such as heart failure. SOD is an antioxidant enzyme within cells and can convert the superoxide radical into other nonreactive chemicals, such as molecular oxygen. Superoxide is a byproduct of oxygen metabolism, and a high level of superoxide will cause unpredicted cell damage. MDA is a product of lipid peroxidation and is one of the best markers of oxidative damage. The high expression of MDA reflects serious damage to the cell membrane.

The present results showed that the expression of LDH and MDA were suppressed and that the expression of SOD was increased with ACO+PF treatment compared with ACO treatment alone. Therefore, PF can improve cell status by modifying some components of energy metabolism. Although we have shown that PF can protect the heart from ACO-induced cardiotoxicity, how strong is the curative effect of PF when it is combined with ACO? In ancient times, ACO was used to treat rheumatoid arthritis (RA). According to many reports, ACO has anti-inflammatory effects (5, 6), and PF is widely used in the treatment of adjuvant arthritis (AA) or RA (17, 18). Therefore, we hypothesize that the combination of PF with ACO may enhance the effect on RA. This hypothesis needs to be confirmed through animals, cells and other models. In-depth exploration of the mechanism of the improvement may have extraordinary significance for treating RA.

In conclusion, we found that PF reduced the cardiotoxicity of ACO in H9c2 cells and that this effect was closely related to cell proliferation, apoptosis, ion channels and energy metabolism. The proliferation of cells was suppressed, and the expression of apoptosis-related factors such as Bcl, Bax, p53, and Caspase-3 in cells was changed in different ways. The level of ion channel-related proteins, such as SCN5A, RyR2 and Cx43, was disordered. Additionally, the amount of extracellular LDH and intracellular MDA was increased, while intracellular SOD was decreased, which indicated that the *in vivo* environment of cells was damaged by ACO and further disrupted energy metabolism. When ACO and PF were combined, the condition of H9c2 cells was significantly improved, possibly resulting from PF-mediated inhibition of the deterioration of cell proliferation, apoptosis, ion channels and energy metabolism.

REFERENCES

1. Herman CJ, Allen P, Hunt WC, et al. Use of complementary therapies among primary care clinic

patients with arthritis. Prev Chronic Dis 2004; 1(4):A12.
2. Wang Z, He S, Xu S. Determination of aconitine alkaloids in aconitum plants and related proprietary medicines by liquid chromatography/mass spectrometry/mass spectrometry. Chinese J Anal Che 2001; 29(4):394-95.
3. Shu Y, Jin ZH, Yang XD, et al. Progress in studies on chemical constituents and pharmacological functions of Aconitum L. plants. J Yunnan Agri Univ 2007; 22(2):229-233.
4. Liu W, Pi Z, Wang X, et al. HPLC/ESI-MSn and ESI-MS studies on the Aconitum alkaloids in three Chinese medicinal herbs. J Sep Sci 2015; 33(17-18):2898-906.
5. Shi HB, Zhou CC, Li YZ, et al. The anti-inflammatory effect of total alkaloids of Radix Aconiti. China J Chin Mater Med 1990; 15(3):46-49.
6. Li X, Gu L, Yang L, et al. Aconitine: A potential novel treatment for systemic lupus erythematosus. J Pharmacol Sci 2017; 133(3):115-21.
7. Chang Y, Zhang L, Wang C, et al. Paeoniflorin inhibits function of synoviocytes pretreated by rIL-1α and regulates EP4 receptor expression. J Ethnopharmacol 2011; 137(3):1275-82.
8. Zhang G-Q, Hao X-M, Chen S-Z, Zhou P-A, Cheng H-P, Wu C-H**.** Blockade of paeoniflorin on L-type calcium channel in isolated rat ventricular myocytes. Chin Pharmacol Bull 2003; 19(8):863-66.
9. Qin L, Peng X, Li XL, Zhang SH, Sun R. Acute toxicity experiment of white peony root and Radix Aconiti using together or separately. J Shangdong Univ Tradit Chin Med 2000; 24:453-55.
10. Fan YF, Xie Y, Liu L, et al. Paeoniflorin reduced acute toxicity of aconitine in rats is associated with the pharmacokinetic alteration of aconitine. J Ethnopharmacol 2012; 141(2):701-8.
11. Jin ZJ. The addition effect of concomitant drugs. Acta Pharmacol Sin 1980; 1(2):70-76.
12. Roden DM, George AL, Jr. The cardiac ion channels: relevance to management of arrhythmias. Anu Rev Med 1996; 47(1):135-48.
13. Lampe PD, Lau AF. The effects of connexin phosphorylation on gap junctional communication. Int J Biochem Cell B 2004; 36(7):1171-86.
14. Kostin S, Rieger M, Dammer S, et al. Gap junction remodeling and altered connexin43 expression in the failing human heart. Mol Cell Biochem 2003; 242(1-2):135-44.
15. Brooks GA, Dubouchaud H, Brown M, et al. Role of mitochondrial lactate dehydrogenase and lactate oxidation in the intracellular lactate shuttle. P Natl Acad Sci USA 1999; 96(3):1129-34.
16. Qi Z, Da Fang Z. Effects of Aconitum alkaloids on myocardial SOD activity and MDA content in chronic heart failure rats. Lishizhen Med Mater Med Res 2010; 21(11):2812-13.
17. Jia Z, He J. Paeoniflorin ameliorates rheumatoid arthritis in rat models through oxidative stress, inflammation and cyclooxygenase 2. Exp Ther Med 2015; 11(2):655-59.
18. Wu HX, Chen JY, Wang QT, et al. Expression and function of β-arrestin 2 stimulated by IL-1β in human fibroblast-like synoviocytes and the effect of paeoniflorin. Int Immunopharmac 2012; 12(4):701-6.

INFLUENZA A VIRUS AND *STREPTOCOCCUS PNEUMONIA* COINFECTION POTENTIALLY PROMOTES BACTERIAL COLONIZATION AND ENHANCES B LYMPHOCYTE DEPRESSION AND REDUCTION

L. XIANG[1], T.J. ZHOU[2], L.L. ZHOU[1], J. LUO[3], Z. QIN[1], J.Z. YOU[1], J. JIAN[1], Z.Y. ZHAO[1], Y.S. ZHOU[4], Y.C. YE[5], H.R. WANG[1], B.N. WANG[1] and M.Y. LI[1]

[1]Department of Microbiology, West China School of Basic Medical Sciences and Forensic Medicine, Sichuan University, Chengdu City, Sichuan P.R. China; [2]Department of Pathology, the Affiliated Hospital of Southwest Medical University, Luzhou City, Sichuan Province, China; [3]Department of Clinical Laboratory, the First Affiliated Hospital of Chengdu Medical College, Chengdu City, Sichuan Province, China; [4]Department of Pathogen Biology, Preclinical Medicine College, Southwest Medical University, Luzhou City, Sichuan Province, China; [5]Experiment Center of Pathogen Biology and Immunology, Preclinical Medicine College, Southwest Medical University, Luzhou City, Sichuan Province, China

Received June 9, 2019 – Accepted August 8, 2019

Influenza has frequently been epidemic in recent years. However, the mechanisms of severe pneumonia with postinfluenza *Streptococcus pneumoniae* (SP) secondary infection have not been fully understood. In this study, we explored the mechanisms of pneumonia in postinfluenza A virus (IAV) infection via a mouse model. Mice were intranasally inoculated with SP three days after IAV inoculation. We then collected samples at three time points to dynamically observe the pathological progression. In IAV infection alone, lymphocyte infiltration and widened alveolar intervals were observed. In the blood, levels of the $CD19^+$, $CD19^+CD21^+$ and $CD19^+CD79\beta^+$B lymphocyte subpopulations were reduced, and IFN-γ and IL-10 were elevated. Slight atrophy was seen in the spleen, which was due to splenic B lymphocyte-initiated apoptosis through the mitochondrial pathway. When SP infection occurred after IAV infection, the pulmonary inflammation was significantly aggravated; a fair number of lymphocytes and neutrophils infiltrated simultaneously with exfoliated bronchial epithelial cells, vascular endothelial cells, widened alveolar septum and hemorrhaging. Increasing edema fluid and bacteria accumulated in the alveolar cavity. Decreased $CD19^+$, $CD19^+CD21^+$ and $CD19^+CD79\beta^+$B lymphocyte subpopulations and increased interferon gamma (IFN-γ) or interleukin 10 (IL-10) were more prominent compared to those with viral infection alone. Spleen atrophy resulting from coinfection was more obvious because of massive splenic B lymphocyte apoptosis through the mitochondrial pathway compared to viral infection alone. This study shows that although inflammation caused by SP infection alone was temporary, preceding IAV infection provided favorable conditions for SP colonization and multiplication by destroying lung structure and suppressing humoral immunity. Synergistic IAV-SP coinfection is likely to facilitate more SP colonization and promote B lymphocyte-suppression and reduction. Eventually, the pneumonia worsened.

Key words: influenza A virus; Streptococcus pneumoniae; B lymphocyte; pneumonia

Corresponding Author:
Prof. Mingyuan Li,
Department of Microbiology, West China School of Basic Medical Sciences & Forensic Medicine, Sichuan University,
Chengdu City, 610041, Sichuan, P.R. China
e-mail: mingyuan0707@163.com

0393-974X (2019)

DISCLOSURE: ALL AUTHORS REPORT NO CONFLICTS OF INTEREST RELEVANT TO THIS ARTICLE.

Postinfluenza A viruses (IAV) are important respiratory pathogens, as they are highly contagious, infect many kinds of birds and mammals and are prone to widespread epidemic. Since the 1800s, there have been several large epidemics of influenza that spread across the globe, and the subtypes involved were H1N1, H2N2, and H3N2. The H1N1 subtypes appeared most frequently, such as the 1918 "Spanish flu," 1889 and 1977 "Russian flu" and 2009 "swine flu" (1). It has been reported that worldwide annual flu epidemics cause up to five million cases of severe illness, which result in 250,000-500,000 deaths per year (2).

IAV infection damages bronchociliary columnar epithelial cells, inhibits cilia movement, and prevents timely excretion of mucus and bacteria (3). IAV infection might upregulate bacterial adhesion receptors in the respiratory tract and increase the chance of bacterial infection (4). During the 2009 H1N1 pandemic, a study in 35 pediatric intensive care units (PICUs) in the United States found that, of 838 children with pH1N1 infection, 33% were diagnosed with bacterial pneumonia (5). In China, a multicenter study of 810 children with influenza showed that 72.3% had pneumonia, and 100 of them were positive for fungal or bacterial culture, accounting for 88% of the bacteria (6). Maclntyre et al. analyzed 75 studies published (between 01/01/2009 and 05/07/2012) that described cases of fatal or hospitalized A (H1N1) pdm09 and included data on bacterial testing or coinfection. The results showed that SP was the most common bacteria found in secondary bacterial infections. SP was particularly associated with causing high mortality and morbidity during influenza epidemics and pandemics (7).

Some studies have demonstrated that IAV can downregulate immunity. H3N2 causes the apoptosis of fresh human PBMCs (peripheral blood mononuclear cells) (2). When mice are infected with H3N2, their bone marrow (BM) B cells, particularly $CD43^{low/-}B220^{+}$ pre-B and immature B cells, decrease substantially. Depletion of BM B lineage cells results primarily from cell cycle arrest and most likely apoptosis within the BM environment (8). Highly pathogenic H9N2 virus infection in mice leads to depletion of spleen B cells and bone marrow (BM) early B cells (9). The 2009 H1N1 pandemic virus might lead to an impaired T cell response in mice models (10).

Destruction of the respiratory tract structure by IAV infection provides suitable conditions for colonization by SP, while an immune system impaired by IAV promotes the progression of pneumonia. Some studies have suggested that coinfection of IAV-SP can further enhance IAV replication in the lung and significantly reduce both the number and percentage of $CD19^{+}$B lymphocytes and $CD3^{+}CD4^{+}$T lymphocytes in the lungs and spleen. Coinfection also significantly reduces the percentage of $CD3^{+}CD4^{+}$T lymphocytes in peripheral blood (11). T lymphocytes and B lymphocytes play important roles in antimicrobial immunity. Their reduction inevitably affects the development of pneumonia. However, it is unclear what the mechanism of IAV-SP coinfection is with regard to the suppression of specific immune cells, such as B lymphocytes. Our study aimed to demonstrate that IAV-SP coinfection promotes SP colonization and accelerates the decline in B lymphocyte activity, thus ascertaining the mechanisms of post-flu pneumococcus pneumonia aggravation, which could provide new insights for the prevention and treatment of severe pneumonia.

MATERIALS AND METHODS

Viruses and bacteria

Mouse-adapted influenza A H1N1 (A/Puerto Rico/8/1934) viruses were grown in MDCK cells and then collected from supernatant and quantified by plaque formation assays (in plaque-forming units; PFUs), as previously described (12). The infection titer of viruses was set at 4×10^{2} PFU/ml in 60 µl PBS (pH 7.2~7.4). SP (ATCC6303) was cultured on blood agar. The infection dose of SP was set at 2×10^{7} CFU/ml in 60 µl PBS (pH 7.2~7.4) (13).

Construction of the mouse model

All experimental animals, 8- to 10-week-old female BALB/c mice, were provided by Beijing Bioscience Co. LTD. Specific-pathogen free (SPF) mice were maintained separately in a room at the Sichuan University animal care facilities and had unlimited access to food and water. The mice were randomly divided into 5 groups:

Blank control group, PBS control group, SP infection group, H1N1 infection group and H1N1-SP coinfection group. Independent experiments consisting of 20 mice per experimental group were performed. The mice were anesthetized by inhalation of isoflurane and intranasally administered H1N1, SP and/or PBS (pH 7.2~7.4) (14). All interventions were performed under light anesthesia with inhalation of isoflurane. At least five animals per group were sacrificed by cervical dislocation at each time point. Best efforts were made to minimize suffering and to reduce the number of animals used. The animal experiment schedule is shown in Table I.

All institutional and national guidelines for the care and use of laboratory animals were followed. The protocol was approved by the Animal Ethical and Welfare Committee of the West China School of Basic Medical Sciences and Forensic Medicine, Sichuan University (Animal Welfare Assurance Number SCXK2013-24, protocol number 20160026).

Hematoxylin and eosin staining

The lungs and spleens were fixed in 4% buffered formalin, embedded, and divided into tissue sections (3-μm thick) with H&E staining (15). Routine histopathological examinations were performed by pathologists. For each section, randomly selected microscopic fields were scanned at a magnification of ×400.

RNA isolation and qRT-PCR

Total RNA was extracted from lungs using TRIzol reagent (TIANGEN, China) according to the manufacturer's instructions. PrimeScript™ RT-PCR Kit (TAKARA, Japan) was used to detect the influenza virus M1 gene using real-time fluorescent quantitative PCR (Roche, Switzerland) (16, 17). A TIANamp FFPE DNA Kit (TIANGEN, China) was used to extract DNA from blocks of embedded lungs, and the SP Nucleic Acid Detection Kit (PCR-fluorescent probe, DAAN GENE, China) was used to detect the lytA gene (18). The relative expression values of the M1 and lytA genes were normalized to the expression of the GAPDH gene. The primer sequences are displayed in Table II.

Flow cytometry

For every 100 μl of EDTA anticoagulant, 2 μl of fluorescent antibody was added. The antibodies were CD19-APC-H7, CD21-PerCP-Cy5.5 and CD79β-FITC (BD, USA), and the samples were incubated with the antibodies in the dark for 15 to 30 min, combined with 2 ml erythrocyte lysate, placed at room temperature for 15 min, washed with PBS, and centrifuged for 5 min at 2000 rpm. The supernatant was then discarded, 200 μl of PBS was added per tube, and the samples were analyzed by flow cytometry (BD, USA). BD FACSuite software was used to analyze the results.

ELISA

Because it was difficult to collect bronchoalveolar

Table I. *Animal experiment schedule.*

Time (hours)	Groups				
	Blank control group	PBS control group	SP infection group	H1N1 infection group	H1N1-SP coinfection group
0		PBS	PBS	H1N1	H1N1
24					
48					
72 (+SP 0 h)		PBS	SP	PBS	SP
76 (+SP 4 h)			sampling		
96 (+SP 24 h)			sampling		
108 (+SP 36 h)			sampling		

lavage fluid from weak mice and to observe the endocrine action of IFN-γ and IL-10 on extrapulmonary organs, the measurement of cytokines in the blood was performed instead of measuring local lung cytokines. The cytokine concentrations were determined using mouse ELISA kits (Neobioscience, China). Each sample was tested in duplicate according to the manufacturer's protocol.

TUNEL

The spleens were fixed in 4% buffered formalin, embedded, and divided into tissue sections (3 μm thick). An *In Situ* Cell Death Detection Kit POD (Roche, Switzerland) was used to measure cell apoptosis in sections, and experiments were performed strictly according to the instruction manual. Positive cells were photographed and counted by light microscope; apoptosis index (AI) = positive cells number/ total cell number × 100%.

Immunohistochemistry

Spleen immunohistochemical studies were performed using standard protocols (19). Antibodies were purchased from Bioworld (USA). Primary antibodies included anti-caspase-3, anti-caspase-8, anti-caspase-9, anti-caspase-12 (rabbit anti-mouse, 1:100 dilution), and the secondary antibody was goat anti-rabbit IgG (1:100 dilution). Staining of caspase proteins was documented using a digital camera (Olympus, Japan) on a microscope (Olympus, Japan) at 400-fold magnification. Staining in the cytoplasm and membrane were considered positive. For each section, six randomly selected microscopic fields were scanned at a magnification of ×400. IHC results were analyzed by Image-Pro Plus 6.0 Software.

Statistics

All data were analyzed using SPSS 19.0 software (Version 17.0, Chicago, IL, USA). Sample results were described using means and standard deviations. Multiple samples were compared using one-way ANOVA. Two samples were compared using the independent-samples *t* test or Mann-Whitney *U* test, as appropriate. *P* values less than 0.05 were considered statistically significant.

RESULTS

H1N1-SP coinfection aggravated lung inflammation

In the blank control group, PBS control group and SP infection group, the lungs appeared to be pink, with no hyperemia or edema. In the viral infection group, hyperemia and edema were obvious. In the coinfection group, more prominent hyperemia, edema and hemorrhage were observed, and the degree and area of the lesions increased with time.

Using H&E staining, we observed the microstructure of the lung. In the blank control group, the lung showed no visible pathological changes (Fig. 1a). In the PBS control group (Fig. 1b), the lung showed slight dilatation and congestion because of the inoculated PBS. In the SP infection group (Fig. 1, c-e), only slight vasodilatation, hyperemia, and scattered neutrophils were observed, and the neutrophils decreased with time. In the viral infection group (Fig. 1, f-h), massive lymphocyte and macrophage infiltration were apparent, the alveolar septum had widened, and pulmonary

Table II. *Primers and probes.*

Template	Forward primer 5'-3'	Reverse primer 5'-3'	Probe
M1	5'-cctggtatgtgcaacctg tg-3'	5'-agcctgactagcaacct aa-3'	6FAM-cagctaaggctatggagc aaatggctg-TAMRA
lytA	5'-attcgtactataactcttg ccgaa-3'	5'-gttctatacctattcccag ttgcac-3'	6FAM-tttaccccgtaatcggcac tcgtca-TAMRA
GAPDH	5'-aactttggcattgtggaa gg-3'	5'-ggatgcagggatgatgt tct-3'	6FAM-atcactgccacccagaag actgtggat-TAMRA

bronchial epithelial cells fell off. In the coinfection group (Fig. 1, i-k), more lymphocytes, neutrophils and SP accumulated in the lung; lesions were evident in the bronchi, capillaries, alveoli and interstitium. At the later stages, parts of the bronchial lumen were closed; the area of pathological regions was enlarged.

SP increased with time in the lungs of the coinfection group

To verify the success of the animal models, we performed qualitative and semiquantitative detection of H1N1 and SP in the lungs. The amplification curve of the influenza virus M1 gene rose in both the viral infection group and the coinfection group, but the $2^{-\Delta\Delta Ct}$ value differences were not statistically significant between the two groups nor were they between different time points in the same group (P>0.05) (Fig. 2a), which meant that H1N1 did not multiply quickly in the two groups over time. The amplification curve of the SP lytA gene only emerged in the coinfection group, which showed that SP was only present in the coinfection group rather than in the SP infection group. The $2^{-\Delta\Delta Ct}$ value of the lytA gene increased over time (P<0.05) (Fig. 2b).

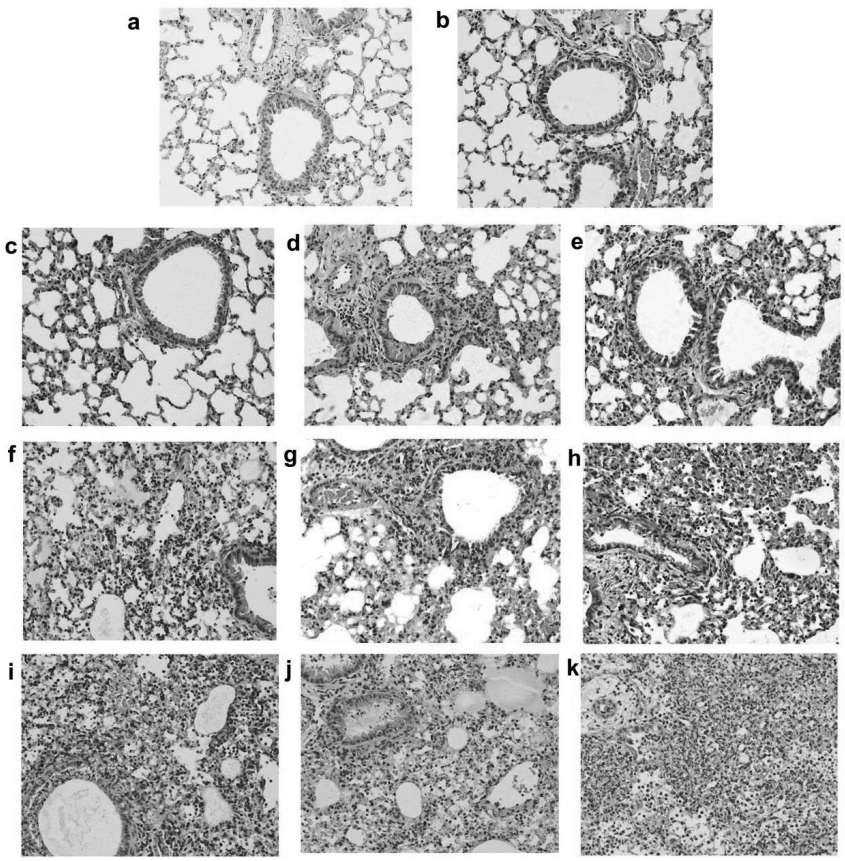

Fig. 1. *The changes in morphology in mice lungs by H&E staining (×400). In the blank control group, the alveolar, bronchial and vascular structures were intact (**a**). In the PBS control group, light pulmonary vascular dilation and congestion were evident (**b**). In the SP infection group at 76 h (**c**), 96 h (**d**) and 108 h (**e**), pulmonary vascular dilatation, infiltration by scattered neutrophils and inflammation weakened with time. In the viral infection group at 76 h (**f**), 96 h (**g**) and 108 h (**h**), lymphocyte infiltration was apparent, the alveolar cavity had effusion, the alveolar interval widened, bronchial epithelial cells fell off, the number of macrophages increased, and hyperemia, edema and bleeding were obvious. In the coinfection group at 76 h (**i**), 96 h (**j**) and 108 h (**k**), serious pathological changes appeared in both the interstitium and parenchyma of the lung. The lung had both lymphocyte and neutrophil infiltration in the alveolar cavity, which contained a large amount of edema fluid and SP, alveolar septum widening, bronchial epithelial shedding, bronchial epithelia degeneration, partial bronchi exudation and occlusion, and endovasculitis.*

$CD19^+$, $CD19^+CD21^+$ and $CD19^+CD79\beta^+$ B lymphocyte subpopulations in blood obviously decreased in the coinfection group

To clarify the functional status of B lymphocytes in blood, we measured the level of signal molecules closely related to B lymphocyte activation. The data showed that the percentages of $CD19^+$ (Fig. 3a), $CD19^+CD21^+$ (Fig. 3b) and $CD19^+CD79\beta^+$ (Fig. 3c) B lymphocyte subpopulations in the SP infection group were not significantly different from those in the two control groups ($P>0.05$) but were significantly higher than those in the coinfection group ($P<0.05$). In the viral infection group, the B lymphocyte subpopulations decreased compared to levels in the control groups. In the coinfection group, especially at 108 h, the cell numbers were significantly lower than those in the viral infection group ($P<0.05$).

Concentration of IFN-γ and IL-10 increased in the coinfection group

IFN-γ and IL-10 are two important anti-inflammatory cytokines. To understand their role in disease development, we examined them in the blood. IFN-γ concentration in blood was not significantly different among the control groups and SP infection group ($P>0.05$). After viral infection, IFN-γ was elevated compared with the control groups ($P<0.05$). When coinfection occurred, IFN-γ was higher than it was in any other group ($P<0.05$) (Fig. 4a). The concentration of IL-10 was tested only at 108 h in the viral infection and coinfection groups because, at other time points in the other groups, the IL-10 concentration was too low to be detected. IL-10 in the coinfection group was higher than it was in the viral infection group ($P<0.05$) (Fig. 4b).

B lymphocytes in the atrophied spleen obviously decreased in the coinfection group

When collecting tissue specimens, we found that the spleens from the viral infection and coinfection groups were smaller than those of the control groups, so we observed the pathological characteristics of the spleens using H&E staining. In the blank control group (Fig. 5a), PBS control group (Fig. 5b) and SP infection group (Fig. 5c), there were small amounts of pyknosis dispersed throughout the entire spleens. In the viral infection group (Fig. 5, d-f), especially in the coinfection group (Fig. 5, g-i), there was more pyknosis appearing in the lymph nodules of the white pulp — the main area containing B lymphocytes — and pyknosis in the region of the splenic cells was significantly reduced.

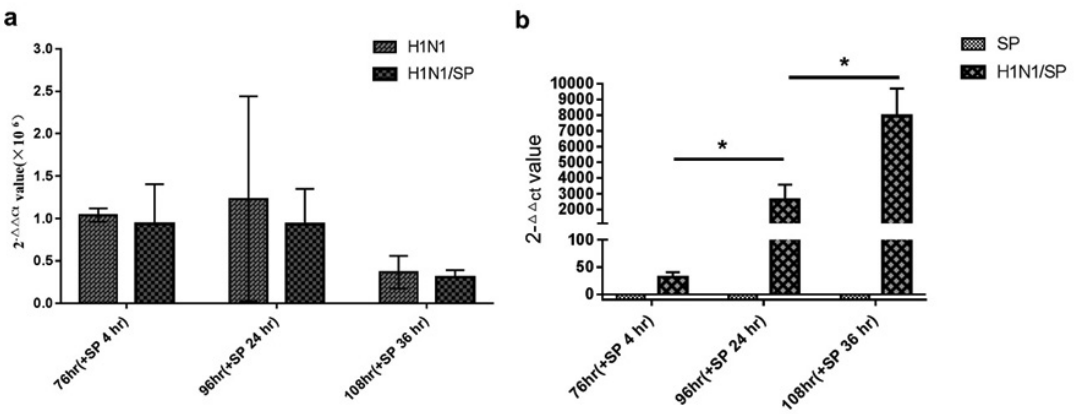

Fig. 2. *Change in $2^{-\Delta\Delta Ct}$ values for the M1 and lytA genes. **a)** The $2^{-\Delta\Delta Ct}$ value for the M1 gene first increased and then decreased in the viral infection group. It decreased with time in the coinfection group, but the differences were not all statistically significant ($P>0.05$). In a word, the viral quantities in the two groups did not prominently change with time. **b)** The $2^{-\Delta\Delta Ct}$ value for the lytA gene in the coinfection group increased with time ($P<0.01$), which indicated that the quantity of SP increased with time. *, $P<0.05$, by one-way ANOVA.*

Massive splenic B lymphocyte apoptosis in the coinfection group

Considering that only small amounts of pyknosis and cell debris appeared in the SP infection group, and abundant pyknosis and cells debris appeared in the viral infection and coinfection groups, the TUNEL-POD method was used to detect apoptotic spleen cells. The results showed that only a few apoptotic cells appeared in the blank control group (Fig. 6a), PBS control group (Fig. 6b) and SP infection group (Fig. 6c). However, apoptotic cells in the viral infection group (Fig. 6, d-f) were obvious and distributed mainly in the lymphoid nodule of the white pulp. In the coinfection group (Fig. 6, g-i), apoptotic cells also mainly appeared in the lymphoid nodule of the white pulp. The quantity of apoptotic cells was much higher in the coinfection group in comparison to the other groups, and it increased with time.

Splenic caspase-3 and caspase-9 proteins showed high expression in the coinfection group

To clarify the molecular pathways of B lymphocyte apoptosis in the spleen, the caspase proteins were assayed by immunohistochemistry (IHC) staining. Cells positive for caspase-3 (Fig. 7a) and caspase-9 (Fig. 7b) were found mainly in the lymphoid nodule of the splenic white pulp in the viral infection and coinfection groups. In the coinfection group, there were more positive cells than there were in the viral infection group. The integrated optical density (IOD) in the viral infection group was higher than that in the control groups ($P<0.05$). In the coinfection group, the IOD was the highest among the five groups, and it increased over time ($P<0.05$). Expression of caspase-8 and caspase-12 did not significantly differ among the five groups across the different time points ($P>0.05$, data not shown).

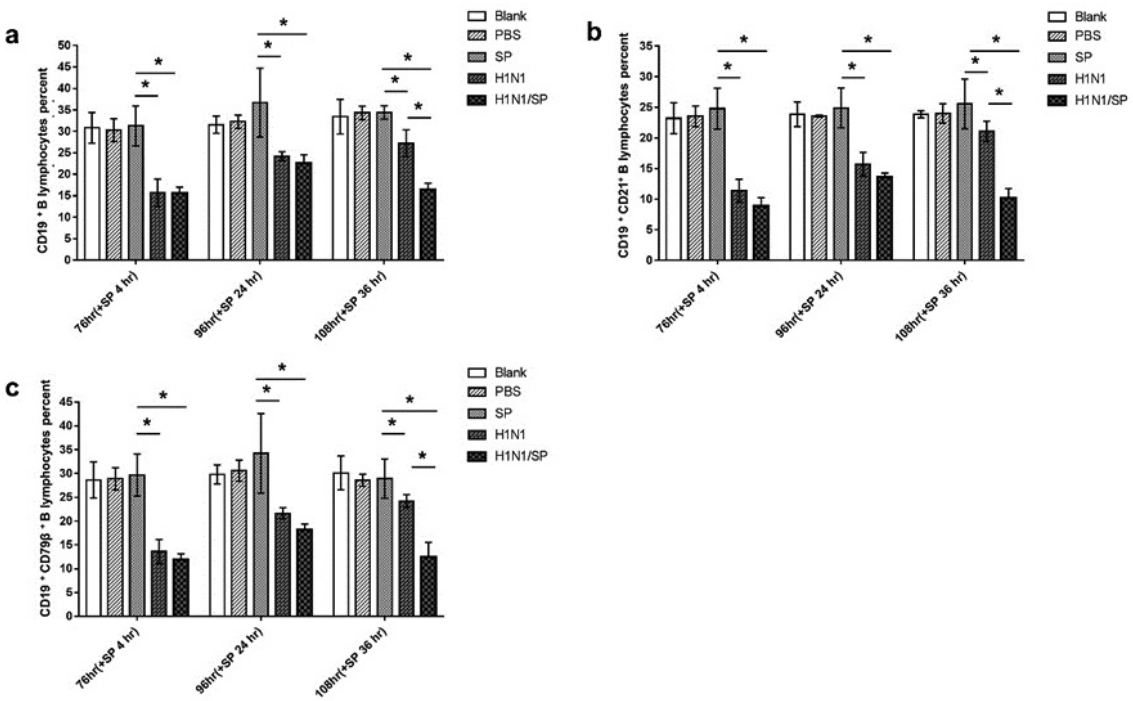

Fig. 3. *Percentage of $CD19^+$, $CD19^+CD21^+$ and $CD19^+CD79\beta^+$ B lymphocyte subpopulations at three time points in blood.* ***a)*** *The percentage of $CD19^+$ B lymphocytes in the SP infection group was higher than those of the other groups. This difference was significant for the coinfection group ($P<0.01$) but not for the control groups ($P>0.05$). In the viral infection group, the percentage was lower than those in the control groups. The percentage for the coinfection group was the lowest ($P<0.01$). The results for $CD19^+CD21^+$ (**b**) and $CD19^+CD79\beta^+$ (**c**) agreed with $CD19^+$ ($P<0.01$). *, $P<0.05$, by one-way ANOVA.*

DISCUSSION

Cytokines and chemokines have long been considered to play an important role in severe pathological lesions caused by IAV infection. IFN-γ can induce apoptosis in many types of cells through various pathways, such as by activating caspase-9 and caspase-3 and significantly enhancing STAT-1 phosphorylation. It also promotes cell apoptosis by increasing the production of reactive oxygen species or endoplasmic reticulum stress (20, 21). IL-10 is an effective anti-inflammatory cytokine for inhibiting excessive immune response (22). In our experiment, inflammation caused by viral infection was strong and recruited a large number of lymphocytes and other immune cells to the lung, thus inducing massive IFN-γ and IL-10 production. CD19, CD21 and CD79 are important signaling molecules related to B lymphocyte activity (23). Viral infection resulted in a decrease in all of the $CD19^+$, $CD19^+CD21^+$ and $CD19^+CD79\beta^+$B lymphocyte subsets in the blood. (Because the percentage of $CD19^+CD79\alpha^+$ B lymphocytes was too low for detection, was greatly affected by operational factors and had a similar function to CD79β, it was not suitable for result analysis.) Accordingly, we inferred that IFN-γ possibly induced apoptosis of the B lymphocytes, and IL-10 inhibited their activity. (Because of the limited number of specimens, the apoptosis of B lymphocytes in blood was not analyzed.)

SP infection alone did not successfully colonize the lung, only led to slight and temporary inflammation and low IFN-γ and IL-10 production. Thus, $CD19^+$, $CD19^+CD21^+$ and $CD19^+CD79\beta^+$B lymphocyte subsets did not decrease but rather increased, producing less obvious inflammation. In SP infection post-IAV, the early viral infection caused structural destruction of the respiratory tract, providing a location for SP invasion. The synergistic effect of IAV-SP coinfection impaired more

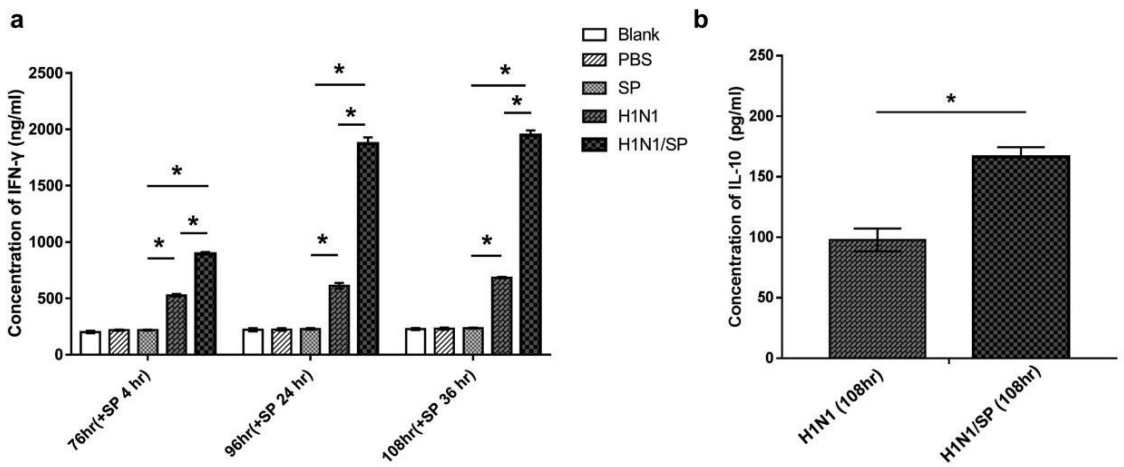

Fig. 4. *Coinfection induced robust IFN-γ and IL-10 production in the peripheral blood. At three time points, these levels were significantly higher in the viral infection group and coinfection group than in the other three groups (P<0.05), and the increases were time-dependent (P<0.05). At each time point, the IFN-γ concentration in the coinfection group was higher than it was in the viral infection group (P<0.05) (**a**). At 108 h, the IL-10 concentration in the coinfection group was higher than it was in the viral infection group (P<0.05) (**b**). *, P<0.05, by one-way ANOVA (a) and independent samples t test (b).*

respiratory tract structures, including pulmonary bronchi, blood vessels and alveoli. Increasing amounts of SP colonized the lung, increasing the number of lymphocytes and neutrophils in the lung and resulting in an increased release of IFN-γ and IL-10. Therefore, the $CD19^+$, $CD19^+CD21^+$ and $CD19^+CD79\beta^+$ B lymphocytes clearly decreased, and their activity was intensely suppressed. As a result, this process also accelerated the growth of SP.

Apoptosis is the death of a single cell in a normal cell population. Because the dead cell nucleus loses water and the chromatin condenses, the nucleus becomes small and the basophilia strengthens, and this phenomenon is called pyknosis (24). Apoptosis pathways include the following: (i) the exogenous pathway; (ii) the endogenous pathway (mitochondrial pathway); (iii) endoplasmic reticulum stress-induced caspase-12 activation and cell apoptosis. Caspase-3 is the most important terminal shear enzyme in apoptosis and the convergence point of much apoptosis stimuli signaling (25). Caspase-8 is the key starting caspase in the exogenous pathway (26). Caspase-9 is an important pro-apoptotic factor in the endogenous pathway (27). RNA polymerase (PB1, PB2 and PA), the nonstructural protein (NS) and the nucleocapsid protein (NP) of IAV can induce cell apoptosis. IAV can also lead to cell apoptosis by causing mitochondrial dysfunction

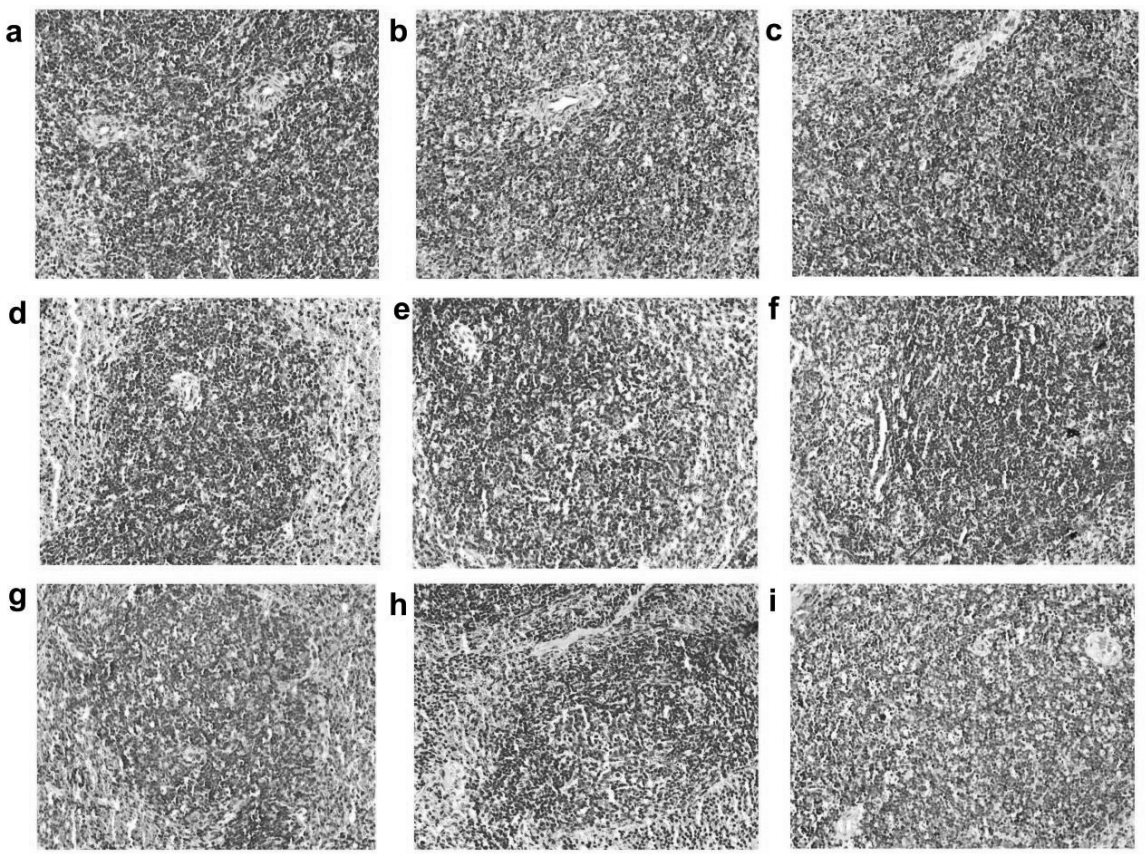

Fig. 5. *Morphological changes in mice spleens by H&E staining (×400). In the blank control group (**a**), PBS control group (**b**) and SP infection group (**c**), the white pulp, splenic sinus and splenic cord structures were normal, and there was no obvious pyknosis or cell debris. At 76 h (**d**), 96 h (**e**) and 108 h (**f**) in the viral infection group, the spleen white pulp progressively atrophied, and pyknosis and cell debris increased with time. At 76 h (**g**), 96 h (**h**) and 108 h (**i**) in the coinfection group, spleen white pulp atrophy was obvious, and pyknosis and cell debris were greater than those in the viral infection group, and they constantly increased with time.*

through P53 aggregation. In IAV-infected mice, the spleen presents obvious atrophy, and the number of B lymphocytes in the spleen, peripheral blood and mediastinal lymph nodes decreases gradually. Some virulence factors of SP (e.g., pneumolysin) can also induce cell apoptosis by various mechanisms (28).

The spleen is the primary location for B lymphocytes and the place where B lymphocytes receive blood antigen stimulation, thus producing immune responses. In our study, the spleen atrophy in IAV-SP coinfection mice was more obvious than it was in IAV-alone infection mice. TUNEL staining showed numerous apoptotic B lymphocytes appearing in the atrophic spleen lymphoid nodule in coinfection mice. Across each group and at each time point, the expressions of caspase-8 and caspase-12 did not significantly differ. Caspase-3 and caspase-9 expression was high in the spleens of viral infection and coinfection mice. Splenic B lymphocyte apoptosis induced by IAV and IAV-SP occurred through the mitochondrial pathway rather than the nonmitochondrial pathway. IFN-γ possibly induced apoptosis by increasing caspase-9 and caspase-3 activity. Accordingly, we deduced that IAV possibly reached the spleen through the bloodstream and directly induced B lymphocyte apoptosis by

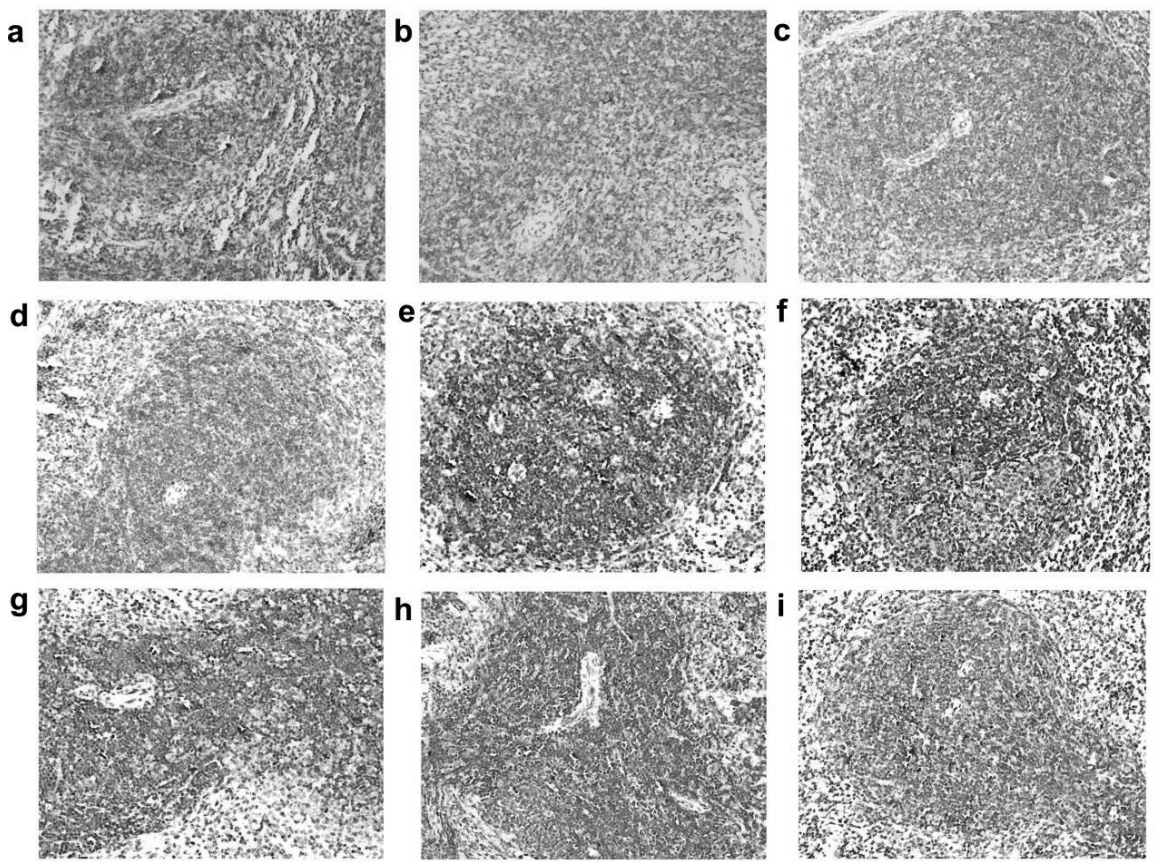

Fig. 6. *Pathological changes in the spleen evident by TUNEL staining (×400). Granules with positive staining are apoptotic cells. In the bank control group (**a**), PBS control group (**b**) and SP infection group (c), only a few apoptotic B lymphocytes occurred from 76 h to 108 h in the entire spleen. At 76 h (**d**), 96 h (**e**) and 108 h (**f**) in the viral infection group, the number of apoptotic B lymphocytes increased with time (P<0.05). At 76 h (**g**), 96 h (**h**) and 108 h (**i**) in the coinfection group, the apoptotic B lymphocytes were significantly increased compared with the other groups, and they increased with time (P<0.05). By one-way ANOVA.*

the mitochondrial pathway or that IFN-γ reached the spleen through the bloodstream and induced B lymphocyte apoptosis by a similar pathway. In the mitochondrial pathway, the pro-apoptotic protein Bax and anti-apoptotic proteins Bcl-2 and Bcl-xl also play vital roles. Whether non-mitochondrial apoptosis-induced signaling participates in IAV/SP mediated pneumonia is of great interests to be validated. Therefore, in the future, we plan to conduct researches examining Bax, Bcl-2 and Bcl-xl, in order to reveal more key signal transduction pathways involving in IAV/SP mediated pneumonia.

Taken together, either SP or IAV infection alone can cause mild to moderate pneumonia. When SP infection occurs post-IAV infection, the IAV infection damages the pulmonary structure and suppresses B lymphocyte function, which is advantageous for SP invasion and growth. IAV-SP coinfection further destroy the respiratory tract structure while suppressing B lymphocyte function. Thus, more SP colonize the lung, resulting in aggravated pneumonia. In this study, B lymphocytes under given conditions were analyzed from different perspectives at different time points in different tissues, comprehensively and dynamically showing the occurrence and development of pneumonia, thus helping us better understand the mechanism by which post-flu pneumococcus pneumonia is exacerbated.

ACKNOWLEDGEMENTS

The authors are very grateful to Dr. Xianglin Hu of Zhongshan Hospital of Fudan University for his instruction regarding the arrangement of the figures

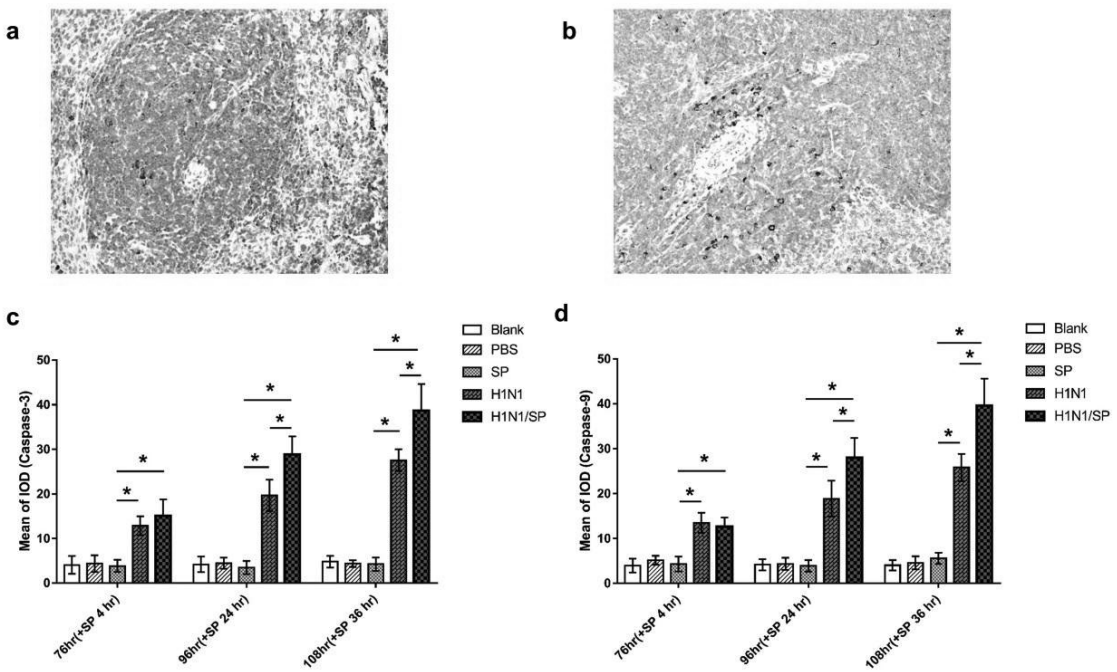

Fig. 7. *The expressions of caspase-3 and caspase-9 in spleen by IHC staining (×400). Granules with positive staining represents the protein expression. Caspase-3 (**a**) and caspase-9 (**b**) were expressed in the cell membrane and cytoplasm. Most cells positive for caspase-3 and caspase-9 appeared in the lymphoid nodule of the splenic white pulp in the viral infection and coinfection groups. Caspase-3 (**c**) and caspase-9 (**d**) expression in the SP infection group did not differ from those in the control groups but was different from that in the coinfection group. In the viral infection group, caspase-3 and caspase-9 expression was higher than it was in the control groups at each time point, and it was time-dependent (P<0.01). Caspase-3 and caspase-9 expression in the coinfection group was higher than that in the viral infection group (P<0.01). *, P<0.05, by one-way ANOVA. IOD, integrated optical density.*

and English writing. This study was supported by the National Natural Science Foundation of China (no. 81071362, 31500114), State Key Laboratory of Oral Diseases (no. SKLOD2015OF08), Science & Technology Department of Sichuan Province (no. 2016JY0223), and Office of Science & Technology and Intellectual Property of Luzhou (no. 2017LZXNYD-J25)

REFERENCES

1. Morris DE, Cleary DW, Clarke SC. Secondary bacterial infections associated with influenza pandemics. Front Microbiol 2017; 8:1041.
2. Xie D, Bai H, Liu L, Xie X, Ayello J, Ma X, Zhang J. Apoptosis of lymphocytes and monocytes infected with influenza virus might be the mechanism of combating virus and causing secondary infection by influenza. Int Immunol 2009; 21(11):1251-62.
3. Bakaletz LO. Viral-bacterial co-infections in the respiratory tract. Curr Opin Microbiol 2017; 35:30-35.
4. Vimalanathan S, Schoop R, Suter A, Hudson J. Prevention of influenza virus induced bacterial superinfection by standardized Echinacea purpurea, via regulation of surface receptor expression in human bronchial epithelial cells. Virus Res 2017; 233:51-59.
5. Randolph AG, Vaughn F, Sullivan R, et al. Critically ill children during the 2009-2010 influenza pandemic in the United States. Pediatrics 2011; 128(6):e1450-8.
6. 2009 Influenza A (H1N1) Clinical Case Investigation Group. Multi-center investigation of the hospitalized children with 2009 influenza A (H1N1) infection. Zhonghua Er Ke Za Zhi 2010; 48(10):733-8.
7. MacIntyre CR, Chughtai AA, Barnes M, Ridda I, Seale H, Toms R, Heywood A. The role of pneumonia and secondary bacterial infection in fatal and serious outcomes of pandemic influenza a (H1N1) pdm09. BMC Infect Dis 2018; 18(1):637.
8. Sedger LM, Hou S, Osvath SR, Glaccum MB, Peschon JJ, van Rooijen N, Hyland L. Bone marrow B cell apoptosis during in vivo influenza virus infection requires TNF-alpha and lymphotoxin-alpha. J Immunol 2002; 169(11):6193-201.
9. Qi W, Tian J, Zhang C, He J, Ning Z, Jiao P, Liao M. Potential role of HPA axis and sympathetic nervous responses in depletion of B cells induced by H9N2 avian influenza virus infection. PLoS One 2012; 7(12):e51029.
10. Meunier I, Morisseau O, Garneau É, Marois I, Cloutier A, Richter MV. Infection with a mouse-adapted strain of the 2009 pandemic virus causes a highly severe disease associated with an impaired T cell response. PLoS One 2015; 10(9):e0138055.
11. Wu Y, Tu W, Lam KT, et al. Lethal coinfection of influenza virus and Streptococcus pneumoniae lowers antibody response to influenza virus in lung and reduces numbers of germinal center B cells, T follicular helper cells, and plasma cells in mediastinal lymph Node. J Virol 2015; 89(4):2013-23.
12. Tanaka A, Nakamura S, Seki M, et al. Toll-like receptor 4 agonistic antibody promotes innate immunity against severe pneumonia induced by coinfection with influenza virus and Streptococcus pneumoniae. Clin Vaccine Immunol 2013; 20(7):977-85.
13. Blevins LK, Wren JT, Holbrook BC, Hayward SL, Swords WE, Parks GD, Alexander-Miller MA. Coinfection with Streptococcus pneumoniae negatively modulates the size and composition of the ongoing influenza-specific CD8□ T cell response. J Immunol 2014; 193(10):5076-87.
14. Walters KA, D'Agnillo F, Sheng ZM, et al. 1918 pandemic influenza virus and Streptococcus pneumoniae co-infection results in activation of coagulation and widespread pulmonary thrombosis in mice and humans. J Pathol 2016; 238(1):85-9.
15. Kalhoro DH, Gao S, Xie X, Liang S, Luo S, Zhao Y, Liu Y. Canine influenza virus coinfection with Staphylococcus pseudintermedius enhances bacterial colonization, virus load and clinical presentation in mice. BMC Vet Res 2016; 12:87.
16. Hardison SE, Herrera G, Young ML, Hole CR, Wozniak KL, Wormley FL Jr. Protective immunity against pulmonary cryptococcosis is associated with STAT1-mediated classical macrophage activation. J Immunol 2012; 189(8):4060-8.
17. Nakamura S, Davis KM, Weiser JN. Synergistic stimulation of type I interferons during influenza virus coinfection promotes Streptococcus pneumoniae colonization in mice. J Clin Invest 2011; 121(9):3657-65.
18. Dhoubhadel BG, Yasunami M, Yoshida LM, et al. A novel high-throughput method for molecular serotyping and serotype-specific quantification of Streptococcus

pneumoniae using a nanofluidic real-time PCR system. J Med Microbiol 2014; 63(Pt 4):528-39.
19. Ogiwara H, Yasui F, Munekata K, et al. Histopathological evaluation of the diversity of cells susceptible to H5N1 virulent avian influenza virus. Am J Pathol 2014; 184(1):171-83.
20. Cho SJ, Pyo S. Interferon-gamma enhances the apoptosis of macrophages under trophic stress through activation of p53 and the JAK1 pathway. Arch Pharm Res 2010; 33(2):285-91.
21. Cao ZH, Zheng QY, Li GQ, Hu XB, Feng SL, Xu GL, Zhang KQ. STAT1-mediated down-regulation of Bcl-2 expression is involved in IFN-γ/TNF-α-induced apoptosis in NIT-1 cells. PLoS One 2015; 10(3):e0120921.
22. Madan R, Demircik F, Surianarayanan S, et al. Nonredundant roles for B cell-derived IL-10 in immune counter-regulation. J Immunol 2009; 183(4):2312-20.
23. Huang YC, Yan XY, Cai SH, et al. Characterization and expression analysis of B cell receptor accessory molecule CD79 gene in Humphead Snapper (Lutijanus sanguineus). Ocean Univ China 2016; 15: 318.
24. Nainu F, Shiratsuchi A, Nakanishi Y. Induction of apoptosis and subsequent phagocytosis of virus-infected cells as an antiviral mechanism. Front Immunol 2017; 8:1220.
25. Wall DM, McCormick BA. Bacterial secreted effectors and caspase-3 interactions. Cell Microbiol 2014; 16(12):1746-56.
26. Tummers B, Green DR. Caspase-8: regulating life and death. Immunol Rev 2017; 277(1):76-89.
27. Eeva J, Nuutinen U, Ropponen A, et al. Feedback regulation of mitochondria by caspase-9 in the B cell receptor-mediated apoptosis. Scand J Immunol 2009; 70(6):574-83.
28. Zhou A, Wang H, Lan K, et al. Apoptosis induced by pneumolysin in human endothelial cells involves mitogen-activated protein kinase phosphorylation. Int J Mol Med 2012; 29(6):1025-30.

BRAIN GLIOMAS AND GROWTH FACTORS: IMMUNOHISTOCHEMICAL, IMMUNOFLUORESCENCE, FLOW CYTOMETRY AND RT-PCR PROFILE IN PEDIATRIC AGE

S. TAURONE[1*], M. SPOLETINI[2*], C. CHIAPPETTA[3], C. DI GIOIA[4], R. CARLETTI[4], A. GRECO[1], E. AGOSTINELLI[5], M. RALLI[1], F. GIANGASPERO[4,6], M. ARTICO[1], F.S. PASTORE[7], S. SCARPA[8], P. GOBBI[9*] and R. DI LIDDO[10*]

[1]Department of Sensory Organs, "Sapienza" University of Rome, Rome, Italy; [2]Department of Anatomy, Histology, Forensic Medicine and Orthopedics, "Sapienza" University of Rome, Rome, Italy; [3]Department of Medical-Surgical Sciences and Biotechnologies,"Sapienza" University of Rome, Rome, Italy; [4]Department of Radiology, Oncology and Pathology, "Sapienza" University of Rome, Rome, Italy; [5]Department of Biochemical Sciences "A. Rossi Fanelli", "Sapienza" University of Rome, Rome, Italy; [6]IRCCS Neuromed, Pozzilli (Is), Italy; [7]Department of Systems Medicine, "Tor Vergata" University of Rome, Rome, Italy; [8]Department of Experimental Medicine, "Sapienza" University of Rome, Rome, Italy; [9]Department of Biomolecular Sciences, University of Urbino "Carlo Bo", Urbino, Italy; [10]Department of Pharmaceutical and Pharmacological Sciences, University of Padua, Padua, Italy

Received February 21, 2109 – Accepted June 7, 2019

[*]These Authors contributed equally to this work

Gliomas represent over 50% of tumors occurring in children. Evidence suggests that glioma stem cells (GSCs), maintained by the transforming growth factor-beta (TGF-β_1) pathway, and vascularization substantially contribute to tumor aggressiveness. The identification of important angiogenic factors such as vascular endothelial growth factor (VEGF) may represent a crucial step in the therapeutic approach against tumor growth and metastatic diffusion. The aim of this study was to identify the expression of TGF-β_1, VEGF and VEGF-receptors in brain gliomas. Specimens of 16 gliomas and 4 controls from children aged 0.2-14 years were used in the study. Immunohistochemical analysis and gene expression study from specimens was performed. Flow cytometry analysis on GSCs was performed to ascertain the expression of VEGF and VEGF-R2 in the tumor stem cell compartment. Newly diagnosed gliomas mainly showed moderate to strong VEGF immunostaining and increased expression of pro-inflammatory molecules in glioma cells. The proportion of TGF-β_1 positive endothelial cells was markedly lower in normal brain vessels compared to tumor vessels. These findings demonstrate that the glioma mass is constituted by a phenotypically immature anoxic central area with a proliferating hypoxic layer; the peripheral area is characterized by cell types with a higher degree of differentiation expressing pro-angiogenic factors. Our data have proven that GSCs play a central role in promoting glioma neovascularization. These findings are useful to understand glioma vascularization, have relevant implications in the therapeutic options and may favor new insights into stem cells biology and suggest therapeutic opportunities for the anti-vascular treatment strategy.

Key words: childhood cancers; brain gliomas; angiogenesis; growth factors; IHC; RT-PCR

Corresponding Author:
Dr Massimo Ralli,
Department of Sensory Organs,
"Sapienza" University of Rome.
V.le del Policlinico 155, 00161 Rome, Italy
Tel./fax: +39 0649976808
e-mail: massimo.ralli@uniroma1.it

0393-974X (2019)

DISCLOSURE: ALL AUTHORS REPORT NO CONFLICTS OF INTEREST RELEVANT TO THIS ARTICLE.

Gliomas represent one of the most common primary brain neoplasms in children (1-3). The therapeutic strategies against glioma in the pediatric population have led to an increase of positive prognosis. Although the results are encouraging, the treatment of these tumors, in particular glioblastomas (GBMs), remains a clinical challenge. Nearly 20% of childhood tumors are brain tumors, which are characterized by a significant variety of entities (1). In the United States, the most common cerebral cancer in children and young adults is represented by gliomas, which represent over 50% of brain tumors (2). In particular, gliomas represent 52.9% of all primary brain neoplasms in children between 0 and 14 years old (3).

Gliomas are classified according to the World Health Organization (WHO) Classification of Central Nervous System Tumors, most recently revised in 2016 (4); gliomas are classified based not only on histopathologic appearance, but also on well-established molecular parameters (4).

Tumor vascularity of glioma is accompanied by a higher WHO grade, and neovascularization influences the glioma progression. A distinctive histopathologic hallmark of GBMs is a relevant vascular endothelial proliferation, making GBMs highly vascularized solid malignancies. The development of specific intratumoral vascularization and GBM stem-like cells (GSCs) are considered the most important components of the pitfall to a successful treatment of these tumors. Accumulating evidence suggests that glioma stem cells (GSCs) are a population of markedly tumorigenic cells whose properties may perform critical roles in tumor invasiveness and therapeutic resistance (5). An intensive search has therefore been stimulated for pro- and anti-angiogenic molecules, with the purpose of identifying some significant factors including epidermal growth factor receptor (EGFR), vascular endothelial growth factor (VEGF) and platelet derived growth factor (PDGF). The development of angiogenesis is essential for tumor growth and metastatization. Intratumoral vascularization has been usually considered to be developed from existing blood vessels through angiogenesis (6). New evidence supports the theory that the complex system of tumoral vascularization may originate from cancer stem cellS due to a phenomenon of vasculogenesis. It has been demonstrated that hypoglycemia, hypoxia, growth factors, and deregulation of different genes play a significant role in the up-regulation of VEGF expression (7). VEGF increases neoangiogenesis and induces the fast proliferation of tumor cells. Transforming growth factor-beta (TGF-β_1) is a factor secreted by different tissues and contributes to the maintenance of pluripotent and cancer stem cells (8). TGF-β_1 signaling is modified in neoplastic patients, and the uncorrected signaling could influence the beginning and progression of many tumors including glioma. In fact, the TGF-β_1 pathway is involved in the preservation of stemness of GSCs (9).

Expansion of a tumor mass depends on the engagement of its own vascular supply. When the tumor is newly formed, previously developed blood vessels may feed the nutrition necessary to tumoral stem cells. When the infinite multiplication of the tumor cells has been established, the microenvironment in which the cells are growing demonstrates a relevant anoxic condition (10). Diabira and Morandi (10) postulated the hypothesis of a neo-niche, which remarks the role of hypoxia in facilitating tumor growth. In fact, hypoxia is considered a stimulator of angiogenesis in GBMs (11). The presence of hypoxia in neoplastic tissues causes the recruitment of residential or mobile myeloid cells in the cancer stroma (12).

Moreover, these pleiotropic agents and cytokines may play a role in the regulation of both tumor vasculogenesis and GSC self-renewal, likely implying a close link between these two processes. Cancer is comparable to a neo-organ, formed by cancer cells at different stages of development; they include cancer stem-like cells (CSCs), precancerous stem-like cells (PCSCs) and cancer cells (13). CSCs have been recognized to facilitate neoplastic angiogenesis by the secretion of VEGF and through their potential for trans-differentiation into endothelial cells. However, extracellular matrix remodeling, macrophage and fibroblast recruitment following oxidative stress are necessary to tumor development. Increasing evidence indicates that cytokines and chemokines modify numerous profiles of brain pathology and

physiology. A modified cytokine expression pattern is described during various conditions, comprising head and neck tumors. Current studies demonstrated that growth factors and inflammatory cytokines play a significant role in tumor growth and progression (14, 15). Neovascularization is represented by the development of new blood vessels from a preexisting network and plays a crucial role in the growth of the tumor, as it supplies it with oxygen and nutrients. Angiogenesis and inflammation play relevant roles in neoplasm development. These processes are administered by the balance of a few factors, acting as pro- or anti-angiogenic and pro- or anti-inflammatory molecules.

The aim of this experimental study was to determine the expression of TGF-β_1 in relation to VEGF and VEGF-receptor involved in inflammatory and angiogenetic pathways in children with head and neck tumors.

MATERIALS AND METHODS

Clinical evaluation

Written informed consent concerning the donation of pediatric tumor brain tissues was provided by parents of the patients prior to tissue acquisition, following the protocol for the acquisition of human brain tissues of the Ethics Committee of the University Hospital Policlinico Umberto I, Rome Italy, which specifically approved the study protocol. All specimens were acquired according to the principles of the Helsinki Declaration. Samples harvested for this study were obtained from pediatric patients admitted to the Department of Radiology, Oncology and Pathology, "Sapienza" University of Rome. No patient had received chemotherapy or radiation therapy before surgery. Specimens consisted of 16 gliomas (9 males and 7 females, mean age 8.4, range 0.2–14 years) and 4 control samples (normal brain samples contained no visible tumor cells; three males and one female) from archival paraffin embedded blocks with a sufficient sample size. The histopathological diagnosis of the 16 observed gliomas was confirmed by university pathologists based on the 2016 WHO guidelines grading system (malignancy scale) for tumors of the central nervous system. No patient had received anti-VEGF therapy. Samples were coded anonymously. However, patient sex, age, histopathological grade, therapy and outcome data (time to recurrence and overall survival) were available.

Immunohistochemistry

The immunohistochemical analysis was conducted using the ABC/HRP technique (avidin complexed with biotinylated peroxidase) on 4-µm thick paraffin sections that were cut using a rotative microtome. These sections were deparaffinized and hydrated through decreasing ethanol series to distilled water, then subjected to microwave irradiation and immersed in citrate buffer (pH= 6) twice for 5 min each time. Subsequently, endogenous peroxidase activity was quenched using 0.3% hydrogenous peroxide in methanol for 30 min. To evaluate the immunolocalization of TGF-β_1, VEGF-A, VEGF-RI and VEGF-RII the following antibodies were employed: i) rabbit anti-TGF-β_1 polyclonal antibody (Santa Cruz, CA, USA); ii) mouse anti-VEGF monoclonal antibody (Santa Cruz, CA, USA); iii) mouse anti-VEGF Receptor 1 (Flt-1/EWC) monoclonal antibody (Abcam, ab9540); iiii) mouse anti-VEGF Receptor 2 (KDR/ EIC) monoclonal antibody (Abcam, ab9530). Overnight incubation with the primary antibodies was carried out at 4°C. Optimal antibody dilution and incubation times were assessed from data of preliminary experiments. As negative control, the primary antibodies were omitted. After having exposed all slides to the primary antibodies, they were rinsed twice using a phosphate buffer (pH=7.4) and incubated for 1 h with the appropriate secondary biotinylated antibody at the final dilution of 1:200. The secondary biotinylated antibodies against rabbit and mouse immunoglobulins were provided by Abcam (biotinylated goat anti-rabbit antibody and biotinylated goat anti-mouse antibody). The slides were then incubated with peroxidase-conjugated avidin (Vector laboratories, Burlingame, CA, USA, Vectastain Elite ABC kit Standard*PK 6-100) for 30 min. Slides were washed in phosphate buffer (pH=7.4) and treated with 0.05% 3,3-diaminobenzidine (DAB) and 0.1% H_2O_2. Sections were then

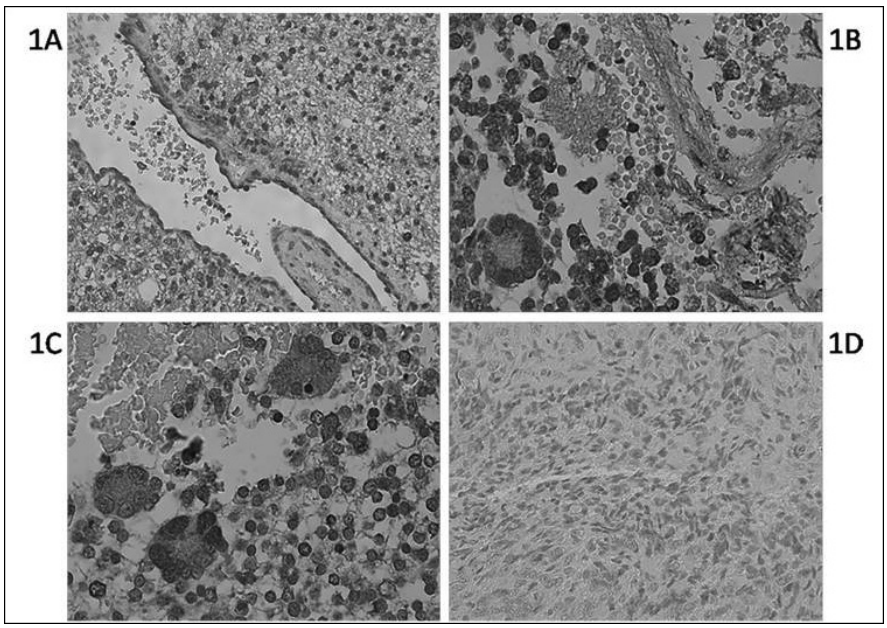

Fig. 1. *Immunohistochemical analysis of VEGF-A in glioma tissues (A, B, C) and control tissues (1D). VEGF-A positive tumor cells were found in the peripheral and more vascularized area of the tumor mass (**A-C**). The most intense immunostaining of VEGF-A is seen in the cytoplasm, but nuclear and perinuclear immunoreactivity is also observed in some tumor cells at higher magnification (**B-C**). VEGF-A-positive cells are accumulated around the blood vessels (**A**). Glioma tissues show a relatively strong expression of vascular endothelial growth factor-A (VEGF-A), when compared with the control tissue (**D**). Magnification (A-D) x20; (B-C) x40.*

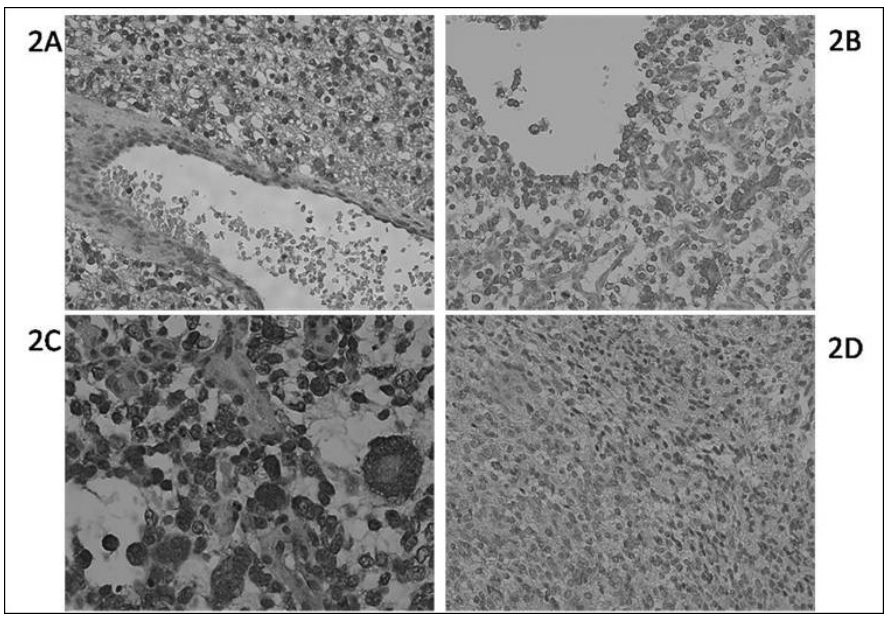

Fig. 2. *Immunohistochemical analysis of TGF-β in glioma tissues (A, B, C) and control tissues (2D). TGF-β positive immunostaining signal was localized on the membrane and in the cytoplasm of tumor cells (**A-C**). TGF-β immunoreactivity is particularly strong in areas surrounding necrosis (**B**), the most intense immunostaining of TGF-β is seen in the cytoplasm, but nuclear immunoreactivity is also observed in a few tumor cells (**C**). Positive staining of TGF-β was shown focally and weakly in control tissues. Magnification (A, B, D) x20; (C) x40.*

counterstained using Mayer's hematoxylin and dehydrated rapidly. Staining was performed by three experts. Microdensitometry was used to assess the intensity of the immune reaction (IAS 2000 image analyzer, Delta Sistemi, Rome, Italy) connected to the microscope using a TV camera. Twelve 100 μm^2 areas were identified in each section by diaphragm measurements; the system was calibrated setting the background obtained in non-immune serum-exposed sections as zero. Analysis of variance (ANOVA) followed by Duncan's multiple range test as a post hoc test were used for quantitative data analysis of the intensity of immune staining. The expression levels of each antigen between pathologic tissue and control tissue was compared using Student's *t*-test.

RT-PCR

RNA extraction from formalin-fixed and paraffin-embedded specimens was performed with the Recover All Total Nucleic Acid Isolation Kit (Thermofisher, Foster City, CA, USA) following the supplier's instructions, with a final elution volume of 50 µL. The extracted RNA was quantitated by OD260/280 measurement; High Capacity cDNA Reverse Transcription Kit (Life Technologies, Foster City, CA, USA) was used to reverse-transcribe in a final volume of 20 uL next total RNA. Then, 30 ng cDNA was added to TaqMan Fast Master Mix (Life Technologies, Foster City, CA, USA) in a final volume of 10µl. ABI PRISM 7500 Fast Real Time PCR System (Life Technologies, Foster City, CA, USA) equipped with ABI PRISM 7500 software was used to analyze the mRNA expression level of Transforming Growth Factor beta (TGFB1), Vascular Endothelial Growth Factor A (VEGFA), Vascular Endothelial Growth Factor Receptor 1 (VEGFR1) and Receptor 2 (VEGFR2) by Real-Time PCR. In parallel, the expression of Actin beta (ACTB) was considered as housekeeping gene. The amplification of cDNA was performed at defined conditions (20 s at 95°C, 3 s at 95°C and 30s at 60°C for 40 cycles) using oligo primers and probes labeled with reporter dye FAM (Life Technologies, Foster City, CA, USA) (Table I). The expression level of target genes from

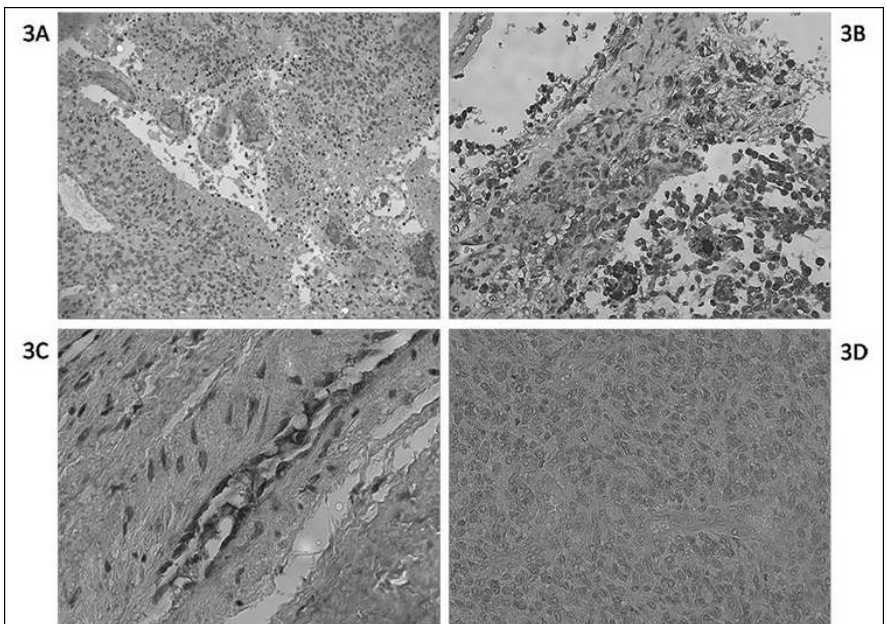

Fig. 3. *Immunohistochemical analysis of VEGF-RII in glioma tissues (A, B, C) and control tissues (D). VEGF-RII was not only expressed in the brain capillaries and on the endothelial cells (**C**) but also on GSCs (**B**). VEGF-RII positive immunostaining signal was localized on the membrane and in the cytoplasm of tumor cells. Most high-grade gliomas showed high expression of VEGF-RII. The immunopositivity for VEGF-RII was significantly lower in the control tissues. Magnification (A, B, D) x20; (C) x40.*

healthy patients (n=2, Control) was considered as reference for the analysis of pathological samples (n=5, Glioma). Data from three replicas of each sample were analyzed using the comparative CT method ($2^{-\Delta\Delta Ct}$).

Flow cytometry analysis

In order to ascertain the expression of VEGF and VEGF-R2 in tumor stem cell compartment, we performed a flow cytometry analysis on GBM cells (GCs) isolated from surgical specimens. The samples were collected under written informed consent of donors as approved by local ethics committee. GBM cells were isolated and functionally validated; flow cytometry (FCM) analysis was performed on cells in exponential growth phase, using three replicas of three independent populations. After treatment with 0.5 mM EDTA-trypsin (Sigma-Aldrich,S.r.l., Milan, Italy) and trypsin-neutralization in 0.2% BSA/PBS, the cells were centrifuged at 1200 rpm, for 5 min and then were reconstituted to a final concentration of 0.5-1.0 x 10^6 cells/mL in 0.2% BSA/PBS for labeling. To detect intracellular VEGF, the cells were fixed with BD Cytofix/Cytoperm™ (BD Biosciences, San Jose, CA) for 20 min at 4°C. Following two washings in BD Perm/Wash™ (BD Biosciences), the samples were resuspended in 50 µL of a saponin-containing buffer and then were incubated for 30 min at 4°C, in the dark with 5 µL of rabbit polyclonal anti-human VEGF (Abcam, Cambridge, UK). After rinsing with a buffer solution, the indirect staining was carried out with goat anti-rabbit phycoerythrin/PE-conjugated secondary antibody (Santa Cruz Biotechnology, Dallas, Texas, USA) for 15 min at room temperature (RT) in the dark. In parallel, the samples treated with only PE-conjugated secondary antibody were prepared as controls. Moreover, the expression of VEGFR2 was investigated on unfixed GBM cells incubating for 15 min at RT in the dark, with mouse anti-human VEGFR2 Fluorescein-conjugated monoclonal antibody (R&D Systems, Minneapolis, MN, USA). The corresponding level of nonspecific binding was defined in samples treated with mouse isotype control (R&D Systems). Cells were then washed twice using PBS and resuspended in 0.3 mL of 0.2% BSA/PBS and analyzed by FACSCanto™ II (BD Bioscience) equipped with BD FACSDiva™ software v6.1.3. Data were graphically processed with FlowJo™ software (Tree Star Inc., Ashland, OR). The percentage of cells positives for VEGF or VEGFR2 was defined against the corresponding control, using the Substraction tool of Summit software v4.3 (Beckman Coulter, Inc., Brea, CA, USA). Per each target protein, the mean percentage value of three independent measurements was reported with Standard Deviation (SD) in the overlay histograms.

Statistical analysis

Statistical analysis was performed with the Student's *t*-test, using the GraphPad Prism (La Jolla, CA). A p-value <0.05 was considered for statistical significance.

RESULTS

Immunohistochemistry

Cancer tissues macroscopically appeared as yellowish-gray masses with multiple areas of hemorrhage and necrosis. Histological evaluation revealed a poorly demarcated, non-encapsulated infiltrating tumor with marked cell atypia, elevated mitotic index, and areas of hemorrhage and necrosis. VEGF immunoreactivity was observed as brown staining located in the cytoplasm. Newly diagnosed gliomas mainly showed moderate-to-strong VEGF immunostaining associated with increased expression of pro-inflammatory molecules in glioma cells, including TGF-β_1. Furthermore, the proportion of TGF-β_1- positive endothelial cells was markedly lower in normal brain vessels compared to tumor vessels. Nevertheless, VEGF highly expressing cells were found in the peripheral and highly vascularized areas of the neoplastic tissue, as we found elevated expression of VEGF along the peripheral layer. These findings demonstrate that the glioma mass is constituted by a phenotypically immature anoxic central area with a proliferating hypoxic layer; the more oxygenated peripheral area is characterized by cell types with a higher degree of differentiation and with an astroglial population expressing pro-angiogenic factors. For TGF-β_1, we observed a high

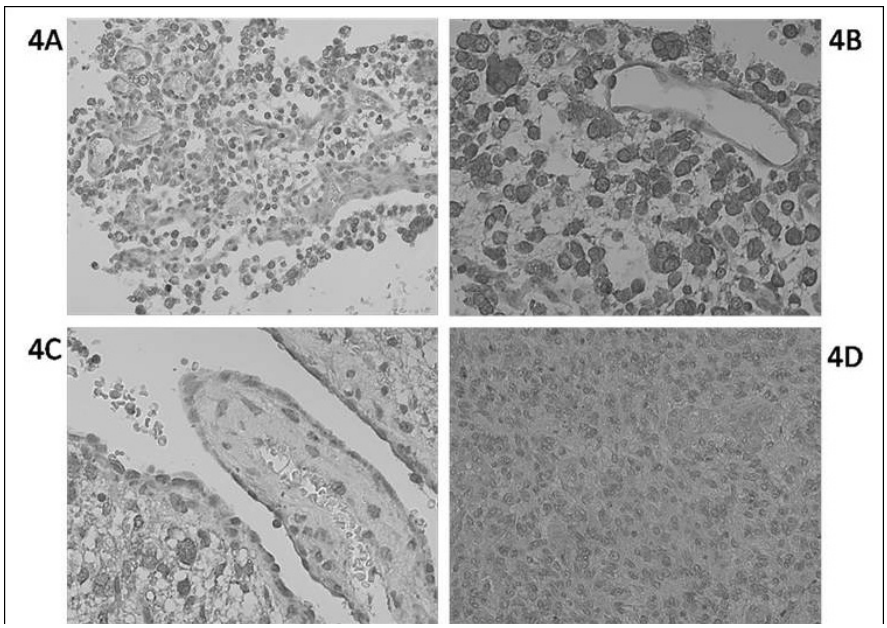

Fig. 4. *Immunohistochemical analysis of VEGF-RI in glioma tissues (A, B, C) and control tissues (D). VEGF-RI expression was confined to the cytoplasm of tumor cells (**A-C**). It is expressed weakly in nerve cell bodies and in reactive astroglial cells and is consistently negative in glial cells in normal brain tissue (**D**). Magnification (A, D) x20; (B, C) x40.*

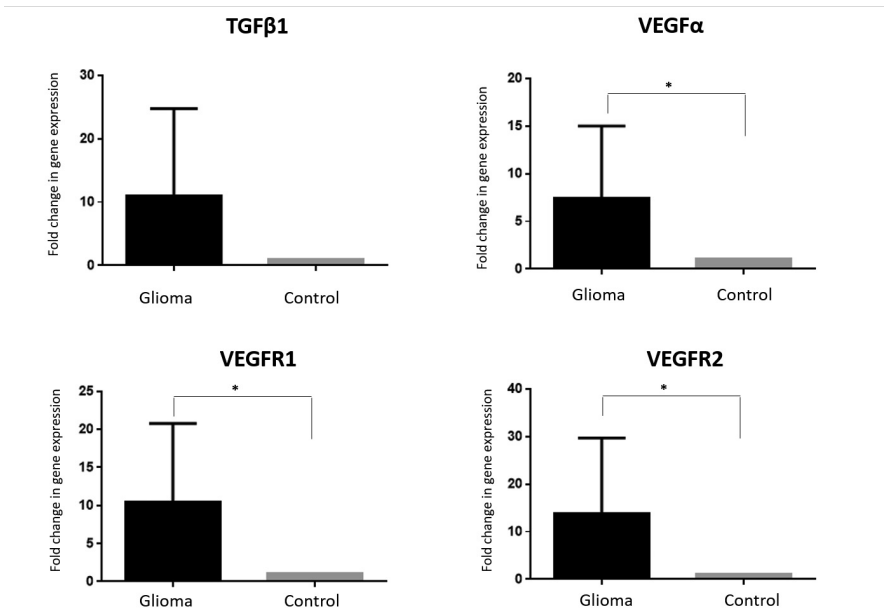

Fig. 5. *RT-PCR analysis of TGFB1, VEGFA, VEGFR1 and VEGFR2 in gliomas of pediatric patients compared to healthy donors. The quantification of gene expression level was performed using the comparative Ct method ($2^{-\Delta\Delta Ct}$). *p value ≤ 0.05 vs control.*

cancer-specific immunoreactivity in most GBM samples with a pattern characterized by extra-cellular staining mainly in neoplastic cells and in malignant vasculature endothelial cells, while staining was negative in normal brain tissues. Furthermore, TGF-β1, a negative prognostic factor for gliomas, has a role in angiogenesis and in VEGF-RII regulation. Our target was to associate expression of VEGF-RII and TGF-β1 activity with clinico-pathological features of GBM. The evaluation of immunoreactive specimens shows that the largest part of normal brain vessels is nearly completely unprovided for detectable VEGF-RII, and the opposite is true for tumor vasculature. The VEGF-A, whose production is induced by hypoxia, enhances microvascular permeability, goads endothelial division and migration and promotes angiogenesis. VEGF-A shows the most intense immunostaining in the cytoplasm. Perinuclear and nuclear immunoreactivity is also found in different tumor cells when using higher magnification (Fig. 1).

TGF-β1 immunostaining was localized in the cytoplasm and surface of cells (Fig. 2). On serial sections, VEGF-RII and TGF-β1 were observed in a portion of tumor cells (Figs. 2 and 3). High expression of TGF-β1 showed a strict correlation with marked expression of VEGF-RII in tumor cells (Figs. 2 and 3). The VEGF-A was significantly increased in GBMs with high expression of VEGF-RII and TGF-β1. The microvessels stained by VEGF-RII appeared to be more evident in high- compared to low-grade gliomas. VEGF-RI immunostaining was limited to the cytoplasm of glial cells (Fig. 4) and appeared weakly expressed in neuronal bodies and in reactive astroglial cells and was clearly negative in glial cells of normal brain. VEGF-RII signaling, but not VEGF-RI signaling, has a role in GBSCs proliferation. The data concerning percentage of positive cells in the pathological tissues in comparison to the control tissues are provided in detail in Table II.

RT-PCR

As shown in Fig. 5, a significant ($p<0.05$) up-regulated gene expression of *VEGFA*, *VEGFR1* and *VEGFR2* was detected in pediatric brain gliomas compared to control samples. In particular, approximately six-(*VEGFA*), nine- (*VEGFR1)*

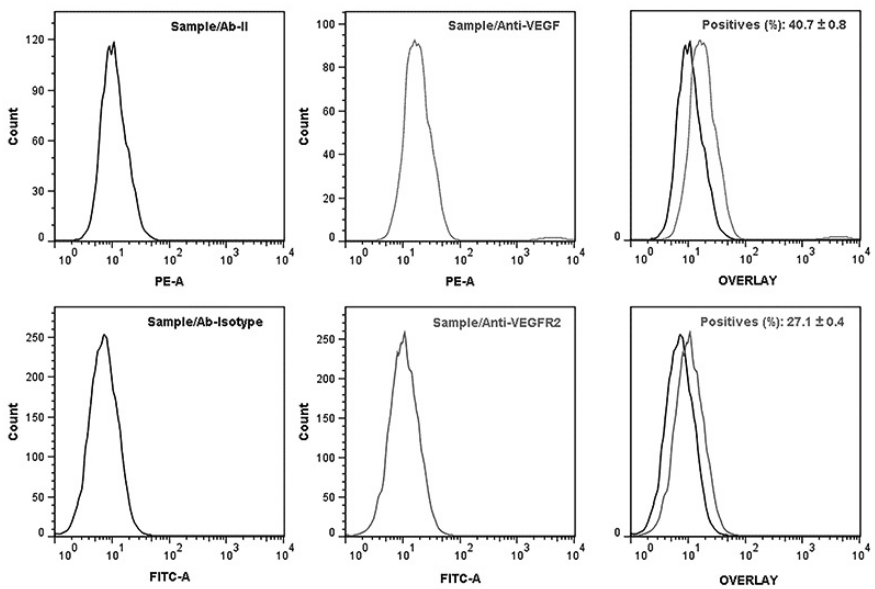

Fig. 6. *Flow cytometry analysis on glioblastoma cells in logarithmic phase of growth. Histograms and overlay were prepared using FlowJo™ software. The percentage of positive cells (grey line) compared with control (black line) was defined using the substraction tool of Summit software v4.3. Data were reported in overlay histograms as the mean percentage value of three independent measurements ± SD.*

and eleven- (*VEGFR2*) fold increases of gene expression were observed in pathological specimens, suggesting an active stimulation of glioma growth and angiogenesis.

Flow cytometry analysis

Glioma stem-like cells (GSLCs) are reported to interact with tumor vascular niche and stimulate angiogenesis by releasing VEGF to stimulate the proliferation of host endothelial cells (ECs) (16). Recently, GSLCs have been suggested to participate in the tumor angiogenic response by transdifferentiating into vascular EC-like cells (17). As the frequency of GLSC-EC conversion has not been defined, and no alterations in the endothelial compartment of human GBMs have been detected, another hypothesis would be a lineage commitment of GLSCs to endothelial precursor cells. The potentiality of GSLCs to acquire an endothelial like-phenotype could explain several aspects of the complex mechanism of tumor vascularization. VEGF and VEGFR-2 play a pivotal role in the control of the self-renewal, the tumorigenicity and the neoangiogenesis in tumors by GSLCs. In our study, FCM analysis evidenced that GBM-derived cells include immature subsets due to: i) responsiveness to angiogenic stimuli by VEGFR-2; and ii) potential to trigger angiogenic response through the production of VEGF. In particular, as shown in Fig. 6, GCs showed 40.7±0.8% and 27.1±0.4% positive cells for VEGF and VEGFR2, respectively.

DISCUSSION

The complex microenvironment of GBM is composed of several cell types, signaling molecules, soluble factors and extracellular matrix components, which control the development of neoplasm progression. Tumor stem cells (CSCs) are postulated to sustain the growth of neoplasm mass and to survive at metastatic sites. Moreover, CSCs respond to environmental stressors, such as reactive oxygen species (ROS), upregulating glutathione-dependent metabolism and acquiring malignant phenotype.

Table I. *Oligonucleotides used for RT-PCR analysis.*

Genes	Gene ID	Assay ID	Amplicon length
TGFβ1	7040	Hs00998133_m1	57 bp
VEGFA	7422	Hs00900055_m1	59 bp
VEGFR1	2321	Hs01052961_m1	72 bp
VEGFR2	3791	Hs00911700_m1	83 bp
ACTB	60	Hs99999903_m1	171 bp

F: forward; R: reverse

Table II. *Percentage of positive cells in the pathological tissue in comparison to the control tissue.*

	PATHOLOGICAL TISSUE	CONTROL TISSUE	p-value
VEGF-A	70.36±8.10	25.75±3.53	< 0.00001
TGF-β1	57.77±5.78	18.40±4.35	< 0.00001
VEGF-RI	38.76±3.83	9.93±3.03	< 0.00001
VEGF-RII	47.01±5.14	19.314.40	< 0.00001

The result is significant at $p < 0.05$.

Cancer progression depends on remodeling of the extracellular matrix, proliferation of fibroblasts and activation of macrophages in response to oxidative stress, epithelial mesenchymal transition (EMT)-related signals and chemotactic stimuli for the recruitment of perivascular and endothelial cells. Furthermore, neoplasm-associated pathologic vessels facilitate dissemination through GBM cell migration into the circulatory system to permit the formation of pre-metastatic niche. The induction of angiogenesis is a fundamental prerequisite for the growth and spread of tumor mass as well as the malignant neoplasm formation (18-20). VEGF is a main mediator of angiogenesis and promotes the proliferation of vascular endothelial cells. Neoangiogenesis is directly correlated with tumor aggressiveness, degree of malignancy and recurrence rate, while it is inversely correlated with postoperative survival in patients affected by GBM (19, 20). In accordance with these accumulated data, our findings demonstrated an overexpression of VEGF in many glioma patients with a relevant tumor grade-dependent increase, as observed by immunohistochemistry and gene expression. These findings confirm that VEGF plays a significant role in sustaining tumor growth in pediatric age by promoting neo-vascularization.

Angiogenesis has been largely studied in GBM, one of the most frequent brain tumors in the adult population. Better knowledge of the angiogenesis processes and mediators in gliomas has been derived from the adult GBM model and adapted to pediatric brain tumors. A limited number of studies on angiogenesis in pediatric brain tumors is available in the literature (21, 22). Current evidence supports the finding that during tumorigenesis, tumor cells co-opt adjacent blood vessels to reach the diffusion distance between vessels and induce hypoxia. Structural changes of the endothelial lining are at the base of a modified microvascular permeability and blood–brain barrier function loss (20). All these modifications in tumor vasculature could depress the effectiveness of codified therapeutic approaches. Moreover, VEGF-A can be released from different cells, and interacts with two high-affinity tyrosine kinase receptors (VEGFR-1 or Flt-1 and VEGFR-2 or KDR); VEGFR-2 mediates endothelial cell migration/proliferation, microvascular permeability, and anti-apoptotic effects, while VEGFR-1 stimulates cell migration and mitigates the signaling pathways mediated by VEGFR-2 (23). Therefore, further studies of the molecular mechanisms implicated in the regulation of biological behavior of GBSCs could represent significant therapeutic approaches in the treatment of glioma tumors.

Published data reported that endothelial-derived factors promote the initiation and growth of brain neoplasms, further confirming the close relationship between endothelial and brain tumor stem cells. Nevertheless, the mechanisms underlining the cross-interaction of these growth factors remain unclear. To propose an answer to this question it is mandatory to understand the effects of VEGF, which might be the most important endothelial-derived factor in the regulation of GBSC proliferation. VEGF stimulates GBSC proliferation through VEGFR2. Ki8751, a specific inhibitor of VEGFR2, which has the ability to suppress VEGF-induced GBSC proliferation (24). VEGFR1 down-regulates the promoting effect of VEGF on the development of GBSCs. This “crosstalk” with VEGFR2 may influence the biological outcome of inhibiting or stimulating the activity of VEGFR1. Many researchers have reported that VEGFR1 can negatively regulate VEGFR2 signals. In this study, we found that TGF high immunoreactivity and PCR expression in GBMs were significantly correlated with a marked expression of VEGF and with a higher histological grade and an increased neo-angiogenesis in GBM. To date, the complete mechanisms through which TGF can promote GBM-associated angiogenesis are not clear, but it could be hypothesized that TGF-β1 is an initial regulator of factors inducing angiogenesis, such as IL-8 and VEGF. The elevated expression of TGF-β1 in GBM cells stimulates neoplasm neo-vascularization by mediating the secretion of main angiogenic factors through an autocrine mechanism. In accordance with other authors, the expression of VEGF and VEGFR-2 by GBM-derived cells suggest the contribution of GLSCs to the rearrangement of endothelial niche and their capability to control the self-renewal of the GBM stem cell compartment.

Exponential development of new blood vessels is between the main histological parameters to determine the grade of neoplasms and the outcome of tumors. Taking this evidence together with the results obtained in our study, in which the expression of VEGF-A, VEGF-RII and TGF-β1 in GBMs were ascertained to be positively correlated with each other, we could hypothesize that VEGF and TGF-β1 may be significantly involved in the malignant evolution of GBM. The overexpression of TGF-β1 up-regulates the expression of VEGF-A and VEGF-RII by activating the PI3K/AKT pathway under hypoxic conditions. As reported by Cheng et al. (25), GBM stem cell compartment is sensitive to TGF-β1 stimulation, promoting the proliferation of vascular pericytes to support vessel function and tumor growth. All these conditions increase tumorigenesis and progression of GBM, promoting anti-apoptosis, angiogenesis, invasiveness, and abnormal propagation. Our research enrolled a small number of tumor samples, therefore further studies on a larger number of specimens could improve the efficacy of such comparisons. Based on our present data, we propose that VEGF might influence not only the tumor vessels, but also the functionality of GBM stem cells.

Several therapeutic approaches have targeted VEGF and VEGFRs for their central roles in promoting angiogenesis and GBSCs proliferation. Anti-VEGF and VEGFR2 inhibitors are commonly used in patients with GBM to target the VEGF-VEGFR2 cascade. Nevertheless, the utility of these two combined approaches has often been disappointing (25, 26). Antiangiogenic therapy induces devascularization, which contrasts tumor growth; however, the benefits of angiogenesis inhibitors are mainly transient, and tumor cells often develop resistance (25). In addition, some antiangiogenic therapies have been found to reduce blood supply and increase invasiveness of GBM cells. Several mechanisms may be involved, and the induction of hypoxia, which has been shown to promote GBSC proliferation, could represent one of the possible mechanisms (26, 27). In GBM, anti-VEGF treatments have proven scarce effectiveness due to evasive mechanisms put into effect by the neoplasm. A previous study determined that GBM resistance was positively correlated with the up-regulation of some genes related to pro-inflammatory response and mesenchymal origin (28). Prolonged anti-VEGF therapy can also favor the differentiation of GBM into stem cell and mesenchymal phenotypes. The latter inhibit the effectiveness of the anti-VEGF therapy (28). It is not surprising that hypoxia induces stem cell and mesenchymal phenotypes as both cell populations are preferentially located in environments characterized by low oxygen concentration. Therefore, research has turned its attention on the role of hypoxia in maintaining GBM CSCs and GBM resistance against anti-angiogenic treatments.

There is increasing attention on the possible molecules that participate in the interaction between endothelial cell types involved in tumor vasculogenesis. Ricci-Vitiani et al. (29) have demonstrated that GSC-derived angiogenesis is fundamental for GBM survival. The newly-formed microvascular system can supply the nutrition required for GSC growth and ameliorate its capability of self-renewal and proliferation. Therefore, the neo-microvascular system may preserve GSCs from chemo- and radiotherapy, enabling these cells to reconstitute a GBM mass following an initial clinical response. Endothelial cells were also found to facilitate the recrudescence and metastatization of the GBM. Hypoxia stimulates CSCs to develop metastatic transformation with increased survival. Continuous progress has to be made to elucidate the mechanisms driving causative roles of CSCs under hypoxia in tumor recurrence and therapeutic failure. It is also difficult to investigate the role of different microenvironmental factors associated with hypoxic stress on CSC behavior using *in vivo* models due to difficulties associated with multiple specific microenvironmental interactions.

Our data have proven that GSCs, associated with high expression of VEGF-A and TGF-β, play a central role in promoting GBM neovascularization. This finding is useful to understand GBM vascularization and it has relevant implications in the therapeutic options. Lineage relationships between GBM stem-like cells and endothelial progeny may

favor new insights into stem cell biology and suggest new therapeutic opportunities for the anti-vascular treatment strategy.

ACKNOWLEDGEMENTS

The authors thank Sapienza University of Rome and Italian MIUR (Ministero dell'Istruzione, dell'Università e della Ricerca) for financial support. E.A. also thanks the Fondazione 'Enrico ed Enrica Sovena'. The research for this paper was financially supported by Fondazione NOBILE S.p.A.

REFERENCES

1. Braunstein S, Raleigh D, Bindra R, Mueller S, Haas-Kogan D. Pediatric high-grade glioma: current molecular landscape and therapeutic approaches. J Neurooncol 2017; 134(3):541-59.
2. Ostrom QT, Gittleman H, Truitt G, Boscia A, Kruchko C, Barnholtz-Sloan JS. CBTRUS Statistical Report: Primary Brain and Other Central Nervous System Tumors Diagnosed in the United States in 2011-2015. Neuro Oncol 2018; 20(suppl 4):iv1-iv86.
3. Ostrom QT, de Blank PM, Kruchko C, et al. Alex's Lemonade Stand Foundation Infant and Childhood Primary Brain and Central Nervous System Tumors Diagnosed in the United States in 2007-2011. Neuro Oncol 2015; 16(S10):1-36.
4. Villa C, Miquel C, Mosses D, Bernier M, Di Stefano AL. The 2016 World Health Organization classification of tumours of the central nervous system. Presse Med 2018; 47(11-12 Pt 2):e187-e200.
5. Ghosh D, Nandi S, Bhattacharjee S. Combination therapy to checkmate Glioblastoma: clinical challenges and advances. Clin Transl Med 2018; 7(1):33.
6. Guo S, Deng CX. Effect of stromal cells in tumor microenvironment on metastasis initiation. Int J Biol Sci 2018; 14(14):2083-93.
7. Ameratunga M, Pavlakis N, Wheeler H, Grant R, Simes J, Khasraw M. Anti-angiogenic therapy for high-grade glioma. Cochrane Database Syst Rev 2018; 11:CD008218.
8. Han J, Alvarez-Breckenridge CA, Wang QE, Yu J. TGF-beta signaling and its targeting for glioma treatment. Am J Cancer Res 2015; 5(3):945-55.
9. Salmaggi A, Boiardi A, Gelati M, et al. Glioblastoma-derived tumorospheres identify a population of tumor stem-like cells with angiogenic potential and enhanced multidrug resistance phenotype. Glia 2006; 54(8):850-60.
10. Diabira S, Morandi X. Gliomagenesis and neural stem cells: Key role of hypoxia and concept of tumor "neo-niche". Med Hypotheses 2008; 70(1):96-104.
11. Semenza GL. Defining the role of hypoxia-inducible factor 1 in cancer biology and therapeutics. Oncogene 2010; 29(5):625-34.
12. Piao Y, Liang J, Holmes L, Zurita AJ, Henry V, Heymach JV, de Groot JF. Glioblastoma resistance to anti-VEGF therapy is associated with myeloid cell infiltration, stem cell accumulation, and a mesenchymal phenotype. Neuro Oncol 2012; 14(11):1379-92.
13. Hong D, Gupta R, Ancliff P, et al. Initiating and cancer-propagating cells in TEL-AML1-associated childhood leukemia. Science 2008; 319(5861):336-39.
14. Presti M, Mazzon E, Basile MS, et al. Overexpression of macrophage migration inhibitory factor and functionally-related genes, D-DT, CD74, CD44, CXCR2 and CXCR4, in glioblastoma. Oncol Lett 2018; 16(3):2881-86.
15. Xu X, Wang B, Ye C, et al. Overexpression of macrophage migration inhibitory factor induces angiogenesis in human breast cancer. Cancer Lett 2008; 261(2):147-57.
16. Yao XH, Ping YF, Chen JH, et al. Glioblastoma stem cells produce vascular endothelial growth factor by activation of a G-protein coupled formylpeptide receptor FPR. J Pathol 2008; 215(4):369-76.
17. Shao R, Taylor SL, Oh DS, Schwartz LM. Vascular heterogeneity and targeting: the role of YKL-40 in glioblastoma vascularization. Oncotarget 2015; 6(38):40507-18.
18. Artico M, Bardella L, Ciappetta P, Raco A. Surgical treatment of subependymomas of the central nervous system. Report of 8 cases and review of the literature. Acta Neurochir (Wien) 1989; 98(1-2):25-31.
19. Jensen RL. Brain tumor hypoxia: tumorigenesis, angiogenesis, imaging, pseudoprogression, and as a

therapeutic target. J Neurooncol 2009; 92(3):317-35.
20. Argyriou AA, Giannopoulou E, Kalofonos HP. Angiogenesis and anti-angiogenic molecularly targeted therapies in malignant gliomas. Oncology 2009; 77(1):1-11.
21. Cao WD, Kawai N, Miyake K, Zhang X, Fei Z, Tamiya T. Relationship of 14-3-3zeta (zeta), HIF-1alpha, and VEGF expression in human brain gliomas. Brain Tumor Pathol 2014; 31(1):1-10.
22. Sie M, den Dunnen WF, Hoving EW, de Bont ES. Anti-angiogenic therapy in pediatric brain tumors: an effective strategy? Crit Rev Oncol Hematol 2014; 89(3):418-32.
23. Melincovici CS, Bosca AB, Susman S, et al. Vascular endothelial growth factor (VEGF) - key factor in normal and pathological angiogenesis. Rom J Morphol Embryol 2018; 59(2):455-67.
24. Rosenstein JM, Krum JM. New roles for VEGF in nervous tissue--beyond blood vessels. Exp Neurol 2004; 187(2):246-53.
25. Cheng L, Huang Z, Zhou W, et al. Glioblastoma stem cells generate vascular pericytes to support vessel function and tumor growth. Cell 2013; 153(1):139-52.
26. Bikfalvi A, Moenner M, Javerzat S, North S, Hagedorn M. Inhibition of angiogenesis and the angiogenesis/invasion shift. Biochem Soc Trans 2011; 39(6):1560-64.
27. Heddleston JM, Wu Q, Rivera M, et al. Hypoxia-induced mixed-lineage leukemia 1 regulates glioma stem cell tumorigenic potential. Cell Death Differ 2012; 19(3):428-39.
28. Piao Y, Liang J, Holmes L, Henry V, Sulman E, de Groot JF. Acquired resistance to anti-VEGF therapy in glioblastoma is associated with a mesenchymal transition. Clin Cancer Res 2013; 19(16):4392-403.
29. Ricci-Vitiani L, Pallini R, Biffoni M, et al. Tumour vascularization via endothelial differentiation of glioblastoma stem-like cells. Nature 2010; 468(7325):824-28.

MOLECULAR EVALUATION OF TISSUE PROTEINS *IN VIVO* DURING CONTROLLED ORTHODONTIC MOVEMENT

M. MATARESE[1], M. MANUELLI[2,3,4], L. GRASSI[1], G. CALDARA[2,3], A. LIGUORI[2,3], G. MATARESE[1] and A. LUCCHESE[2,3]

[1]Department of Biomedical, Odontostomatological Sciences and of Morphological and Functional Images, School of Dentistry, University of Messina, Italy; [2]School of Dentistry, Department of Orthodontics, Vita-Salute San Raffaele University, Milan, Italy; [3]Unit of Dentistry, Division of Orthodontics, Research area in Dentofacial Orthopedics and Orthodontics, IRCCS San Raffaele Scientific Institute, Milan, Italy; [4]Private practice Milano and Bologna Italy

Received April 5, 2019 – Accepted July 12, 2019

Orthodontic tooth movement determines a biological response of all the tissues surrounding the teeth to which force is applied. The aim of this study is to evaluate which ideal orthodontic force, at the biological level, arouses an acute inflammatory response on periodontal tissues, and the duration of the force in order to establish an ideal experimental model of dental movement. The periodontal ligament and the alveolar bone change abruptly due to the biochemical adaptive response, resulting in a re-organization of the intracellular and the extracellular matrix. There is a modification of the local vascularization which stimulates a cascade production, synthesis and the release of arachidonic acid, metabolites, proteins, such as cytokines, and growth factors. Every dentist can control and should know the above-mentioned mechanism. Moreover, the production of proteins by modulating the direction and the intensity of the force can be changed but, above all, the duration.

Orthodontic movement is a very complex problem from a periodontal point of view and from the alveolar bone that depends on the characteristics of the strength and the response of tissues. In 1932, Schwarz argued that continuous force optimally leads to compressing the capillaries so that occlusion is prevented during applied force to the periodontal ligament (1). Subsequently, this conception was slightly modified by Oppenheim, who supported the use of the lightest possible force capable of initiating tooth movement (2), and in 1967 by Reitan who, demonstrating the absence of cells in some areas compressed by light force, proposed the use of even lighter force (3). According to current thinking, optimal force should be low and can be different for each tooth and for each patient. From a cellular point of view, stress distribution (force/unit of surface), deformation of the periodontal ligament (shear stress, tension) and bone (tension) are the critical factors of the remodelling response (4). The aim of this study is to evaluate which ideal orthodontic force, at the biological level, arouses an acute inflammatory response on periodontal tissues, and the duration of the force in order to establish an ideal experimental model of dental movement.

Key words: molecular evaluation, orthodontic, tooth movements

Corresponding Author:
Prof. Alessandra Lucchese,
School of Dentistry,
Dept. of Orthodontics,
Vita-Salute San Raffaele University,
Milan, Italy
e-mail: lcclsn@unife.it

0393-974X (2019)

DISCLOSURE: ALL AUTHORS REPORT NO CONFLICTS OF INTEREST RELEVANT TO THIS ARTICLE.

MATERIALS AND METHODS

Patients

Twenty patients with a mean age of 13.8 years (SD=±0.7 years), of both sexes, were selected for orthodontic treatment in a private practice and in the Dental School of Vita-Salute San Raffaele University, Milan, Italy. The 20 patients needed dental extractions for a total of 40 premolars (5-7). The inclusion criteria for this study were patients with: a full natural permanent dentition (excluding third molars extracted or not erupted); a severe Class II, a light Class III or dental crowding in a Class I Angle classification; absence of previous orthodontic treatment or tooth extraction. The exclusion criteria were patients with prosthetic rehabilitation and those who needed corrective jaw surgery, and multiple and/or advanced caries. The study was approved by the Medical Ethics Committee of the University Vita-Salute San Raffaele Hospital, Milan, Italy, (106/NT/2017) and the parents or guardians of each participant signed informed consent for sampling. All methods used in the study were non-invasive.

Treatment

The patients were randomly divided into two groups; group one was treated with NiTi coilspring which expresses 50 grams; in group two a NiTi Closed Coil Spring was used, with a resultant force of 30 gr (G4™ NiTi Coil Springs produced by G&H® Orthodontics) (Fig. 1)**.** The two groups were divided into five subgroups, depending on the time used to applied force: 1, 7, 14, 21 or 28 days. Depending on the application of the spring, each patient underwent the extraction of the two premolars, the right one where the force was applied (with coilspring on the first molar to the first premolar) and the left one with no strength. After extraction, a periodontal ligament was removed by scarifying the root surface from the pressure side and from the tension side and it was placed in two different test tubes (Fig. 2). The samples were compared with the periodontal ligament samples of the homologous contralateral teeth not subjected to any force.

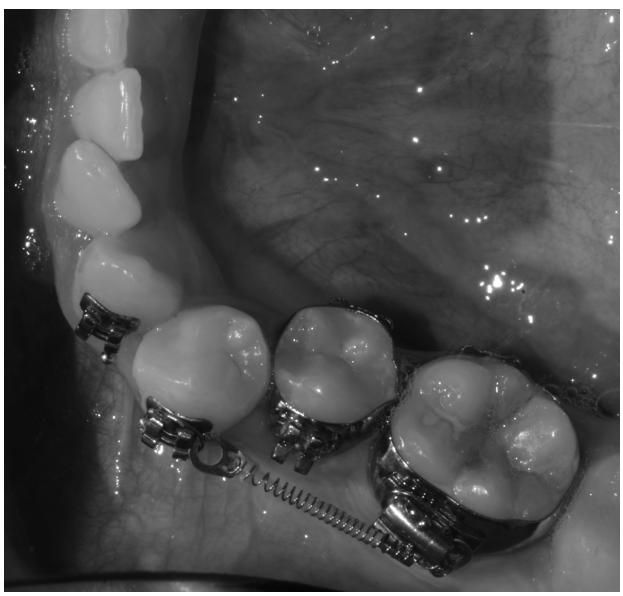

Fig. 1. *NiTi coil springs on which the premolars were forced.*

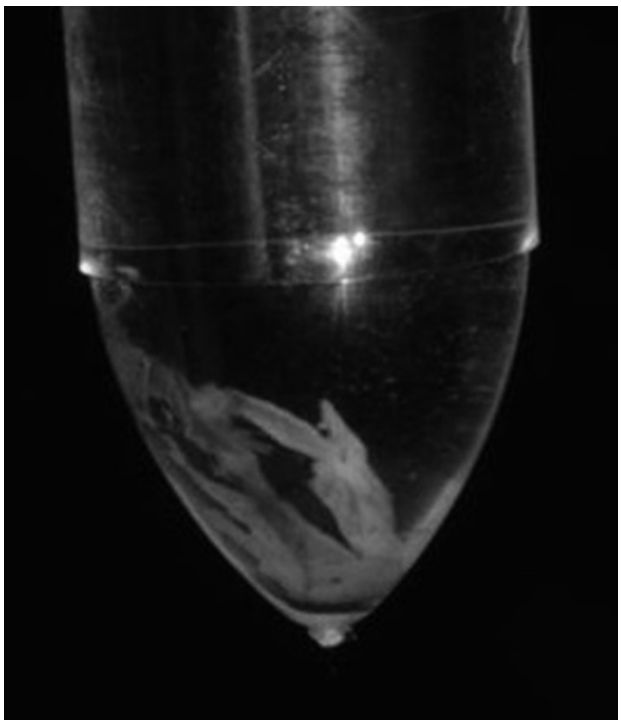

Fig. 2. *Test tube containing the periodontium tissue from the tooth surface.*

Sample analysis

The removal of the periodontal ligament was carried out to effect indirect immunofluorescence and the sections were then observed and photographed using a Zeiss LSM DUO confocal microscope, equipped with META using laser Argon (458 e 488 nm) (Fig. 3).

Immunofluorescence reactions were performed to verify the immunolocalization patterns of type I collagen, type IV collagen, fibronectin and vascular endothelial

growth factor (VEGF) in the periodontal human ligament and at 1, 7, 14, 21 and 28 days after orthodontic treatment in both groups. Furthermore, to check the presence of the tested proteins, the software display profile was applied.

RESULTS

The data confirmed that collagen I showed a 1-day reduction in protein from the site-of-tension treatment until day 14. After that, at day 28 it quickly rose to return to the same starting point as T0. The reactions of the type IV collagen confirm an intensity of the fluorescence values at 14, 21 and 28 days in the pressure and tension sites of the orthodontic treatment. Instead, these fluorescence peaks were considerably reduced at the beginning of the treatment, at days 1 and 7, both at the pressure and tension site. The results obtained from the VEGF display profile confirm that the data from the anti-VEGF immunofluorescence reaction show peaks similar to anti-collagen IV antibodies. Furthermore, the display profile related to fibronectin confirms the previous data, compared to the control group, especially at 21 and 28 days after orthodontic treatment, on the pressure side. Thus, a biologically more active force was observed in group two, where cellular but, above all, protein activity was greater (Fig. 4).

DISCUSSION

The cells of the periodontal ligament and all their secretions therefore play a fundamental role in the adaptation of mechanical forces in the repair and regeneration of the periodontium (8). This study shows that from day 1 there are variations of the molecular components. Collagen I is the major constituent of the extracellular matrix and its functional importance consists in contributing significantly as a support to masticatory forces (9-11). The mechanical stimulation of the periodontal ligament alters the production of collagen I, tropoelastine and fibronectin, through the alteration of the extracellular matrix synthesis by fibroblasts of the periodontal ligament. The data from the pressure site in which the expression of collagen I increases significantly also increased slightly (12, 13). The immunohistochemical study of VEGF lies in the importance of the activation of the vascular system, as an indispensable process for periodontal remodelling during orthodontic movement. The initial response of the mechanically compressed or expanded periodontal tissue consists in the release of vaso-active neuropeptides through the stimulation of sensitive nerve endings (14). The blood vessels respond with an increase in permeability through the formation of endothelial fenestrations which increase in number and size (15, 16), allowing the extravasation of leukocytes in the interstitial tissue (17) that release cytokines. The latter induce the activation of osteogenetic cells and, finally, the remodelling and tooth movement (18) in which VEGF plays a fundamental role. VEGF also intervenes in the

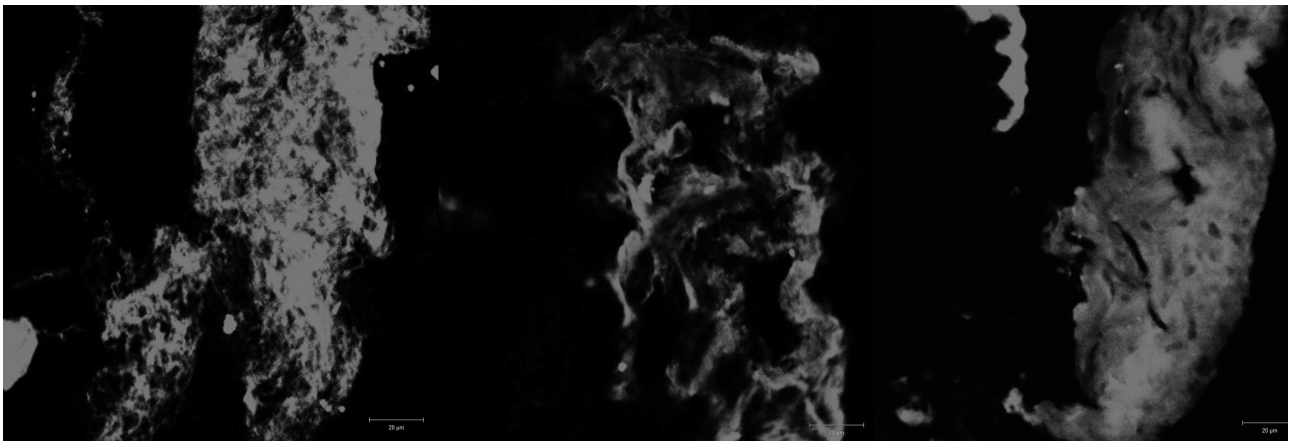

Fig. 3. *Immunofluorescence photos, Collagen I at days 1, 7 and 28.*

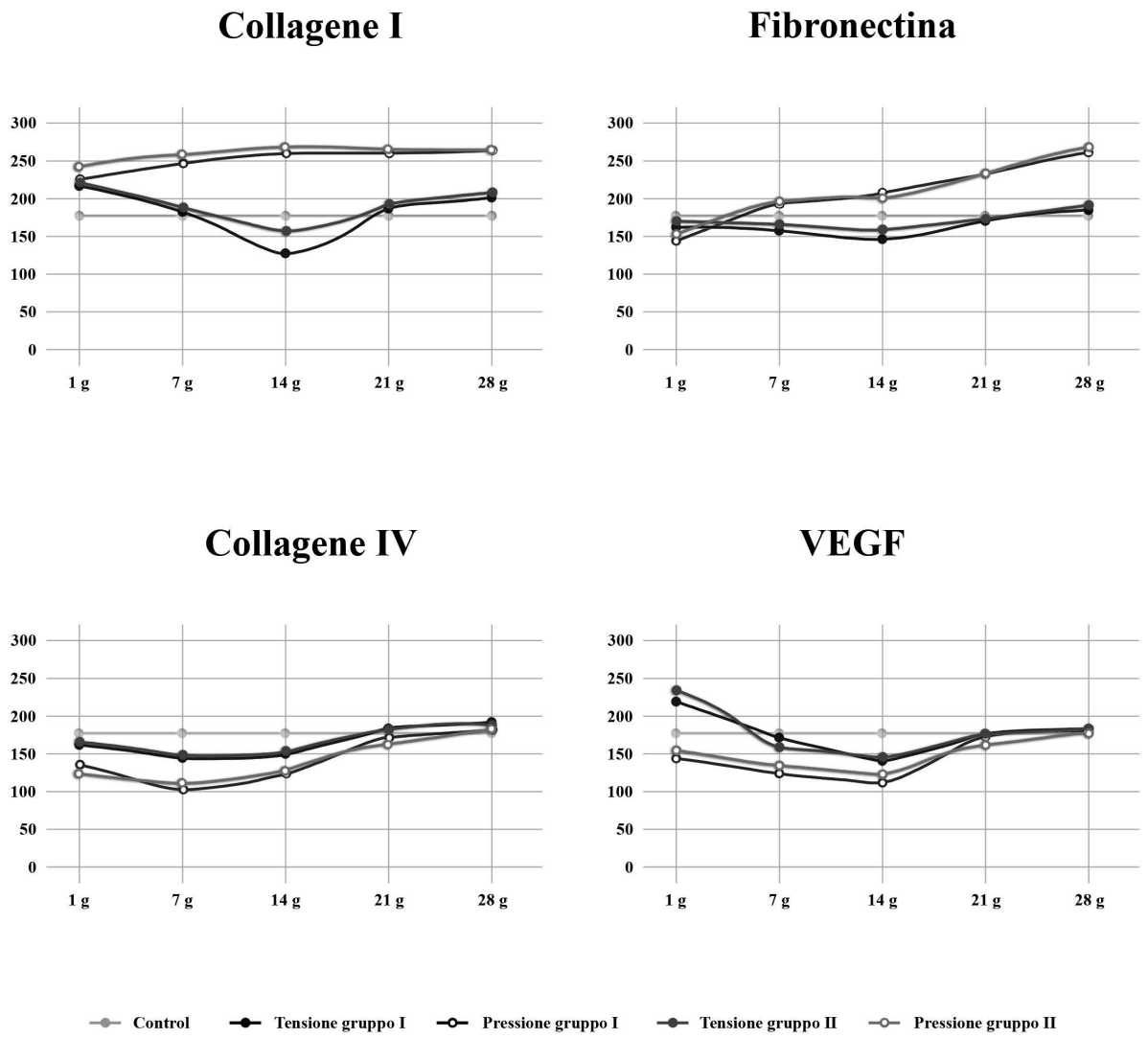

Fig. 4. *Graphics based on the results of display profile obtained with confocal laser scanning microscopy with type I collagen, type IV collagen, and fibronectin and VEGF in the two groups.*

processes of inflammation and healing (19). The change in VEGF immunostaining intensity on the first day confirms that orthodontic treatment induces a variation in the periodontal vasculature, even in the early stages of treatment (20). Twenty-four hours after the application of the orthodontic force, at the compression site, a partial (group 2) or almost complete (group 1) occlusion of the blood vessels was observed. At 7 days, a decrease in collagen IV, a reduction in collagen I at the site of tension, and an increase in the site of pressure was observed; the VEGF was strongly reduced at the pressure site, while it remained expressed at the site of tension; fibronectin presented a pattern of immunolocalization similar to that of collagen I (21). Collage IV is a protein mainly located on a perivasal level, the decrease of which indicates a reduction in the vascular component and an increase in blood vessel density. At 14 days, the lowest peak, and also VEGF, for both

sites was observed in the pattern of collagen I immunostaining; an increase in collagen IV, and, finally, fibronectin, maintained its positivity in both sampling sites. At 14 days, studies in the literature indicate that the density of blood vessels shows a tendency to normalization. At 21 days there was an increase in the immunofluorescence of collagen I at the tension site, which remained strongly expressed at the pressure site; there was an increase in the fluorescence of collagen IV, VEGF and fibronectin in both study sites and groups. On this basis, the increase in the fluorescence of type I collagen at the pressure site can be hypothesized to represent a process of thickening of the fibrillar component as a defense response to mechanical stress. Fibronectin increases and can promote the growth of periodontal ligament cells and may have different effects on the attack and proliferation of ligament cells as an increase in the metabolic activity in response to the application of an orthodontic force.

We observed that an induction force up to 21 days resulted in a reactive response of the periodontal ligament with changes in collagen and fibronectin, proteins of the matrix, which are functionally important in the response to orthodontic forces. The increase in VEGF at 21 days, induced by tissue hypoxia, would indicate the beginning of an angiogenetic process. This is a process involving the remodelling of the extracellular matrix, migration, proliferation and functional maturation of blood vessels. At 28 days, collagen I and fibronectin showed a positive tendency of immunostaining intensity, which meant that the tissue remodelling phase was still active.

At 28 days there was a restoration of the normal periodontal ligament structure which led to a re-organization of the fibers and their orientation. The vascular component of the periodontium, after an initial slight suffering, showed a tendency to normalization. In any case, a light force is preferable for a long stability (22-24) and to avoid damage to the tooth or periodontal tissues. It is therefore important that the orthodontist considers these differences in both cellular and tissue responses due to orthodontic light force, unlike those from heavy force produced by palatal expansion (25), in order to obtain a rapid tooth displacement without damage and with maximum comfort for the patient, who may suffer from some other pathology (27, 27).

REFERENCES

1. Schwarz AM. Tissue changes incident to tooth movement. Int J Orthod Oral Surg 1932; 18(4):331-52.
2. Oppenheim A. Human tissue response to orthodontic intervention of short and long duration. Am J Orthod Oral Surg 1942; 28(5):263-301.
3. Reitan K. Clinical and histological observations on tooth movement during and after orthodontic treatment. Am J Orthod 1967; 53(10):721-45.
4. Isola G. Matarese G, Cordasco G, Perillo L, Ramaglia L. Mechanobiology of the tooth movement during the orthodontic treatment: a literature review. Minerva Stomatol 2016; 65(5):299-327.
5. Matarese G, Isola G, Alibrandi A, Gullo AL, Bagnato G, Cordasco G, Perillo L. Occlusal and MRI characterizations in systemic sclerosis patients: A prospective study from Southern Italian cohort. Joint Bone Spine 2016; 83(1)57-62.
6. Jamilian A, Lucchese A, Darnahal A, Zamali Z, Perillo L. Cleft sidedness and congenitally missing teeth in patients with cleft lip and palatale patients. Progr Orthod 2016; 17:14.
7. Cavuoti S, Matarese G, Isola G, Abdolreza J, Femiano F, Perillo L. Combined orthodontic-surgical management of a transmigrated mandibular canine. Angle Orthodontist 2016; 86(4):681-91.
8. Anastasi G, Cordasco G, Matarese G, et al. An immunohistochemical, histological, and electron-microscopic study of the human periodontal ligament during orthodontic treatment. Int J Mol Med 2008; 21(5):545-54.
9. Rodriguez y Baena R, Lupi SM, Pastorino R, Maiorana C, Lucchese A, Rizzo S. Radiographic evaluation of regenerated bone following poly (Lactic-Co-Glycolic) acid/hydroxyapatite and deproteinized bovine bone graft in sinus lifting. J Craniofac Surg 2013; 24(3):845-48.
10. Nakagawa M, Kukita T, Nakasima A, Kurisu

K. Expression of the type I collagen gene in rat periodontal ligament during tooth movement as revealed by in situ hybridization. Arch Oral Biol 1994; 39(4):289-94.
11. Zhao Z, Fan Y, Bai B, Wang J, Li Y. The adaptive response of periodontal ligament to orthodontic force loading – A combined biomechanical and biological study. Clin Biomech 2007; 23(l1):S59-S66.
12. Howard PS, Kucich U, Taliwal R, Korostoff JM. Mechanical forces alter extracellular matrix synthesis by human periodontal ligament fibroblasts. J Periodontal Res 1998; 33(8):500-508.
13. Zaki AE, Vanhuysen G. Histology of the Periodontium Following Tooth Movement. J Dent Res. 1963; 42:1373-79.
14. Vandevska-Radunovic V, Kvinnsland S, Kvinnsland IH. Effect of experimental tooth movement on nerve fibres immunoreactive to calcitonin gene-related peptide, protein gene product 9.5, and blood vessel density and distribution in rats. Eur J Orthod 1997; 19(5):517-29.
15. Iida J, Inage S, Kurihara S, Miura F. Changes in the microvasculature after mechanical pressure on the hamster cheek pouch. J Dent Res 1992; 71(6):1304-9.
16. Lew KK. Orthodontically induced microvascular injuries in the tension zone of the periodontal ligament. J Nihon Univ Sch Dent 1989; 31(3):493-501.
17. Rygh P, Bowling K, Hovlandsdal L, Williams S. Activation of the vascular system: a main mediator of periodontal fiber remodeling in orthodontic tooth movement. Am J Orthod 1986; 89(6):453-68.
18. Davidovitch Z. Tooth movement. Crit Rev Oral Biol Med 199; 2(4):411-50.
19. Dvorak HF, Detmar M, Claffey KP, Kagy JA, van de Water L, Senger DR. Vascular permeability factor/vascular endothelial growth factor: an important mediator of angiogenesis in malignancy and inflammation. Int Arch Allergy Immunol 1995; 107(13):233-35.
20. Ren Y, Maltha JC, Stokroos I, Liem RSB, Kuijpers-Jagtman AM. Effect of duration of force application on blood vessels in young and adult rats. Am J Orthod Dentofacial Orthop 2008; 133(5):752-57.
21. Matarese G, Isola G, Anastasi GP, et al. Immunohistochemical analysis of TGF-β1 and VEGF in gingival and periodontal tissues: A role of these biomarkers in the pathogenesis of scleroderma and periodontal disease. Int J Mol Med 2012; 30(3):502-508.
22. Raucci G, Pachêco-Pereira C, Grassia V, d'Apuzzo F, Flores-Mir C, Perillo L. Maxillary arch changes with transpalatal arch treatment followed by full fixed appliances. Angle Orthod 2015; 85(4):683-89.
23. Raucci G, Pachêco-Pereira C, et al. Predictors of long-term stability of maxillary dental arch dimensions in patients treated with a transpalatal arch followed by fixed appliances. Prog Orthod 2015; 16-24.
24. Lucchese A, Manuelli M, Bassani L, et al. Fiber reinforced composites orthodontic retainers. Minerva Stomatol 2015; 64(6):323-33.
25. Lucchese A, Sfondrini MF, Manuelli M, Gangale S. Fixed space maintainer for use with a rapid palatal expander. J Clin Orthod 2005; 39(9):557-58.
26. Palmieri A, Zollino I, Clauser L, et al. Biological effect of resorbable plates on normal osteoblasts and osteoblasts derived from Pfeiffer syndrome. J Craniofacial Surg 2011; 22(3):860-63.
27. Lucchese A, Matarese G, Manuelli M, et al. Reliability and efficacy of palifermin in prevention and management of oral mucositis in patients with acute lymphoblastic leukemia: a randomized, double-blind controlled clinical trial. Minerva Stomatol 2016; 65(1):43-50.

LETTER TO THE EDITOR

CHANGES IN THE LEVELS OF NF-κB SIGNALING MEDIATORS AND IL-1β IN RATS WITH RADIATION-INDUCED LUNG INJURY

ZJ. SHEN and JH. QIU

Department of Anesthesiology, Ruijin Hospital North, Shanghai Jiaotong University School of Medicine, Shanghai, P.R. China

Received April 8, 2019 – Accepted June 4, 2019

To the Editor,

Radiotherapy is one of the main treatment options for thoracic malignant tumors, such as lung cancer, esophageal cancer, and breast cancer (1). Even if several other therapeutic options with less side effects, such as plant extracts or combination of chemotherapeutic drugs, have been tested and used, the results are still not comparable to radiotherapy (2, 3). Radiotherapy not only destroys cancer cells, but also creates different degrees of injury to the surrounding healthy tissues (4, 5). This not only limits the dose of radiotherapy and reduces the quality of life of patients, but also affects the local control of tumors and long-term survival of patients.

Increasing evidence has shown that the NF-κB signaling pathway participates in the inflammatory reaction of various organs and tissues, such as the lung, nerve, and pancreas (6), suggesting that the NF-κB signaling is closely related to the occurrence and development of organ injury and inflammation. Therefore, it is hypothsized that this signaling pathway and its key proteins, such as IκBα and NF-κBp65, may also participate in the development of radiation-induced lung injury (7). Currently, the dynamic changes in the protein levels of NF-κBp65 and IκBα remain unclear in the process of radiation-induced lung injury. Therefore, a rat model of radiation lung injury was established by a single high dose irradiation to the right lung of rats (8). The study aimed to investigate the dynamic changes in the serum level of IL-1β and the expression of NF-κBp65, IκBα and IL-1β in rat lung tissues in order to elucidate the molecular mechanism and possible new targets for the prevention and treatment of radiation-induced lung injury.

MATERIALS AND METHODS

Animals

Specific pathogen free (SPF) grade male Sprague-Dawley (SD) rats were purchased from Shanghai Slack Laboratory Animal Co. Ltd., China. A total of 64 rats 6-8 weeks old and with a body weight between 180 and 220 grams were selected. All rats had free access to feed and drinking water. The temperature and humidity of the animal room were controlled at 25±1°C and 55±5%, respectively. After 7 days of acclimatization, the rats were randomly divided into a blank group and an irradiation group (32 in each group). In addition, the rats in each group were further randomly divided into 4 sub-groups corresponding to the four time points of analysis: end of the 2nd week, 6th week, 12th week, and 24th week, 8 animals per subgroup. The rats in the blank group were not exposed to any treatment, while the rats in the irradiation group

Key words: radiation-induced lung injury; NF-κB p65; IκBα; IL-1β

Corresponding Author:
Dr Jianhua Qiu,
Department of Anesthesiology, Ruijin Hospital North,
Shanghai Jiaotong University, School of Medicine,
No.227 South Chongqing Road,
Shanghai 201801, P.R. China
e-mail: qiujianhua_2011@163.com

0393-974X (2019)

were treated with a single dose of ^{60}Co to the right lung to establish a model of radiation-induced lung injury. The protocol was approved by the ethics committee of Ruijin Hospital North, Shanghai Jiaotong University School of Medicine and the experiment followed the regulations of the State Science and Technology Commission on the management of laboratory animals.

Establishment of a radiation-induced lung injury model

After intraperitoneal anesthesia with 10% chloral hydrate solution (0.35mL/100g) (Kodi Biology Company, China), the rats were fixed in a supine position on a radiotherapy simulator (Siemens China Limited, China). The contour of the inspiratory phase of the rat lungs was positioned with a fuse, and the contour of the inspiratory phase was fixed and positioned on a computed tomography (CT) simulator (Siemens China Limited, China), while a red or black marker pen was used to draw the rough contour of the right lung on the chest of the rat to reposition the contour of the lung with the fixed fuse, so as to eliminate the error caused by skin movement as far as possible. After positioning, a lead block baffle was used to block the exposure of other parts except the right lung of the rat to the irradiation field (GWXJ80 ^{60}Co radiotherapy instrument, China Nuclear Power Research and Design Institute Equipment Manufacturing Plant, China). The irradiation field was aligned vertically with a total dose of 18 Gy (the size of the irradiation field was 2cm x3cm, the distance from skin was 80 cm, the treatment depth was 2 cm, and the dose absorption rate was 2.083Gy/min). After irradiation, the rats were removed from the fixator and placed in an incubator (Shanghai Yuyan Scientific Instruments Co., Ltd., China) for resuscitation. At the end of the 2nd, 6th, 12th and 24th week after irradiation, 8 rats were anesthetized and sacrificed in each group by intraperitoneal injection of 10% chloral hydrate 0.35mL/100g to collect blood and right lung tissue samples.

Sample collection and detection

Rats were anesthetized by intraperitoneal injection of 10% chloral hydrate (0.35mL/100g), and their blood samples were obtained by heart puncture. After blood collection, thoracotomy was performed immediately to take the entire right lung. The lung was rinsed in normal saline solution (Kodi Biology Company, China) before photographing. The middle lobe of the lung was placed in 4% paraformaldehyde (Kodi Biology Company, China), while the rest of the lung was deposited in a 1.5 mL EP tube (Kodi Biology Company, China) and kept at –80°C until analyis. After 48 h of fixation, the middle lobe of the right lung was embedded in paraffin (Kodi Biology Company, China), cut into - μm serial sections, stained by hematoxylin & eosin (H&E) and Masson dyes, and observed under a 200 x magnification to detect the pathological changes in lung tissues.

The collected blood samples were centrifuged for 15 min at 4°C and 1000 rpm. The serum was separated and stored at –80°C until analysis.

Hematoxylin & eosin staining

After the lung tissue was fixed and embedded, it was sliced by a tissue slicing machine (Leica Company, Germany) to a thickness of about 4 μm and stained with H&E. The slides were visualized under a microscope (Olympus, China).

The scoring criteria of pathological pneumonia included: pneumonia grade 0: no alveolar inflammation; grade I mild alveolitis: enlarged alveolar septum due to cell infiltration, with the size of lesion accounting for less than 20% of the whole lung; grade II moderate alveolitis: the size of lesion exceeded 20%-50% of the whole lung; grade III diffuse alveolitis: the size of lesion exceeded 50% of the whole lung.

Masson staining

Procedures of pulmonary tissue immobilization, embedding, slicing, dewaxing and dehydration were the standard used also for the H&E staining. After washing, tissue slices were quickly dyed in hematoxylin for 5-10 min, and then rinsed with tap water. The rinsed slices were incubated with hydrochloric alcohol (Kodi Biology Company, China) for 1 min and then fully rinsed with distilled water. The acid fuchsin of Lichunhong (Kodi Biology Company, China) was used to dye the slides for 10 min and the slices were rinsed with 2% glacial acetic acid aqueous solution (Kodi Biology Company, China). After that, the slices were differentiated with 1% phosphomolybdic acid aqueous solution (Kodi Biology Company, China) for 3-5 min, dyed with a light green liquid (Kodi Biology Company, China) for 5 min without washing, and soaked in 2% glacial acetic acid aqueous solution for a short time. They were dehydrated with

95% anhydrous alcohol (Kodi Biology Company, China), made transparent using xylene, and sealed with neutral gum (Kodi Biology Company, China). After drying they were analyzed under a microscope (Olympus, China).

Detection of hydroxyproline level

30-100 mg of right lung tissues were put into a sterile test tube labeled with a sample number. Then, 1 mL of hydrolysate was added to the test tube, fully mixed, and the sample was incubated in a 95°C water bath for 20 min. The total volume of the sample was adjusted to 10 mL using distilled water and its pH was adjusted to 6-6.8. Subsequently, 3-4 mL of diluted hydrolysate was transferred into a new sterile test tube before adding 25 mg of activated carbon. The tube was centrifuged at 3500rpm/s for 10 min and 1 mL of supernatant was taken to measure its optical density (OD) using a hydroxyproline (HYP) assay kit (Nanjing Jiancheng Institute of Bioengineering, China) according to the manufacturer's instructions. Finally, the HYP content was calculated according to the following formula: HYP content (μg/mg wet weight) = (OD of the sample tube – OD of the blank tube) x content of standard substance (5μg/mL) x total volume of hydrolyte (10mL)/(OD of the standard tube - OD of the blank tube)/tissue wet weight (mg).

Detection of serum IL-1β levels and protein expressions levels of NF-κBp65, IL-1β and IκBα in lung tissues

A rat IL-1β ELISA Kit (Wuhan Huamei Bioengineering Co., Ltd., China) was used to determine the IL-1β serum levels according to the manufacturer's instructions. The right lung tissue was dried, weighed and placed into a tissue grinder containing 2 mL of saline solution (Shanghai Shifeng Biotechnology Co., Ltd., China). The tissue homogenate was then placed in an ice bath and its supernatant was collected by centrifugation at a low temperature (Gene Company, USA) for 10 min at 1000r/min. The supernatant was then diluted 1:1 with normal saline and the protein contents of NF-κBp65, IL-1β and IκBα were detected using corresponding ELISA kits (Wuhan Huamei Bioengineering Co., Ltd, China) according to the manufacturer's instructions.

Statistical analysis

SPSS17.0 (SPSS Inc., Chicago, IL, USA) statistical software was used for data analysis. Data were expressed as mean ± standard deviation. Variance analysis was used for the comparison between different groups. Least Significant Difference (LSD) test was used for data with a homogeneous variance, while Dunnett's T3 test was used for data with an uneven variance. $P < 0.05$ indicated statistical significance.

RESULTS

Gross observation of lung tissues

The lung tissues of the blank group appeared bright pink with a smooth and soft texture. There was good elasticity and no inflammatory exudation. In the irradiation group, the lung tissues showed slight edema and a slight increase in volume at the end of the 2nd week after irradiation. At the end of the 6th week, the lung tissues became swollen and the degree of hyperemia increased. At the end of the 12th week, the lung tissues became gradually atrophic with a slightly hardened texture and poorer elasticity. In addition, there were small nodules and obvious white spots on the surface. At the end of the 24th week, the atrophy of lung tissues was more obvious, their surface became concave or convex and uneven with obvious gray-white flakes, and their texture became harder with poorer elasticity (Fig.1).

H&E staining of lung tissues

There was no congestion, edema, inflammation or fibrosis in alveolar and interstitial tissues of the right lung in the blank group, and their alveolar structure was intact. At the end of the 2nd week after irradiation, there were slight hyperemia of capillaries, partial alveolar epithelial exfoliation and slight interstitial edema in the lung tissues of the irradiation group. At the end of the 6th week after irradiation, the alveolar wall and septum were slightly thickened, the alveolar cavity was slightly reduced, and the edema became more obvious, along with inflammatory cell infiltration. At the end of the 12th week, the alveolar wall and septum became even thicker with disappeared local alveoli and the presence of fibroblasts. At the end of the 24th week, some alveolar cavities were replaced, fused and substantiated by connective tissues, while the lung structure was destroyed by connective tissues. The

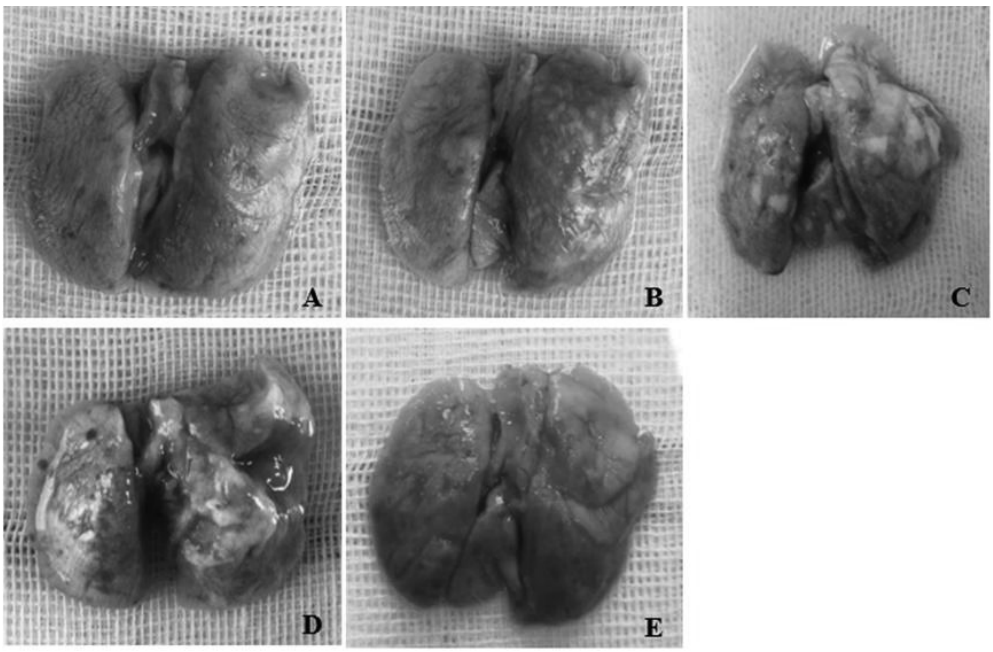

Fig. 1. *Gross changes of rat lung tissues.* ***A****) gross changes of rat lung tissues at the end of the 2nd week after irradiation;* ***B****) gross changes of rat lung tissues at the end of the 6th week after irradiation;* ***C****) gross changes of rat lung tissues at the end of the 12th week after irradiation;* ***D****) gross changes of rat lung tissues at the end of the 24th week after irradiation;* ***E****) gross changes of rat lung tissues in the blank group)*

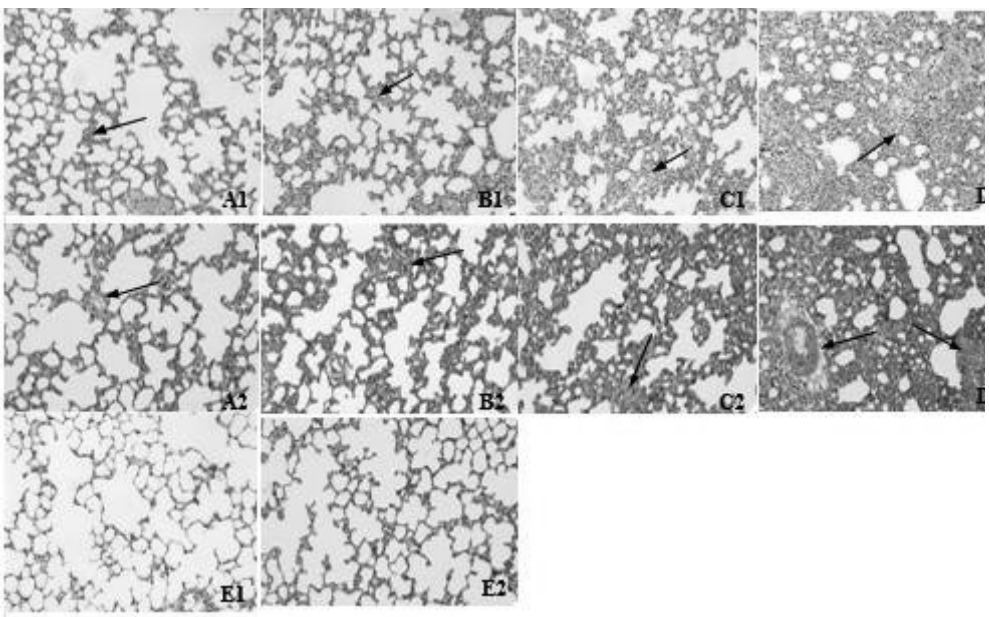

Fig. 2. *H&E staining and Masson staining of rat lung tissues after irradiation (*200) (1: H&E staining, 2: Masson staining.* ***A****) rat lung tissues at the end of the 2nd week after irradiation;* ***B****) rat lung tissues at the end of the 6th week after irradiation;* ***C****) rat lung tissues at the end of the 12th week after irradiation;* ***D****) rat lung tissues at the end of the 24th week after irradiation;* ***E****) rat lung tissues in the blank group) (Arrow in A1: capillary congestion; arrow in B1: alveolar wall and alveolar septum thickening; arrow in C1: proliferative fibroblasts; arrow in D1: proliferative fibroblasts; arrows in A2-D2: collagen deposition)*

alveolar wall became significantly thicker while a large number of fibroblasts proliferated and replaced local normal tissues (Fig.2).

Hydroxyproline levels in lung tissue

The HYP levels in the lungs of rats in the blank group showed no significant difference at the 4 time points ($P > 0.05$). The HYP levels in the irradiation group increased gradually over time until the end of the 24th week; at the end of the 2nd week after irradiation, the HYP levels increased compared to the levels in the blank group, but the difference was not statistically significant ($P > 0.05$). At the end of 6th, 12th and 24th week, the HYP levels in the irradiation group increased significantly compared to blank group ($P < 0.05$) (Fig.3A).

Cytokine IL-1β levels in serum

There was no significant difference in serum IL-1β concentration between the blank group and the control group at different time points ($P > 0.05$). In the irradiation group, the serum IL-1β levels began to increase in the 2nd week and reached its peak in the 6th week before gradually declining at the end of 12th and 24th week. The serum IL-1β levels in the irradiation group were significantly higher than those in the

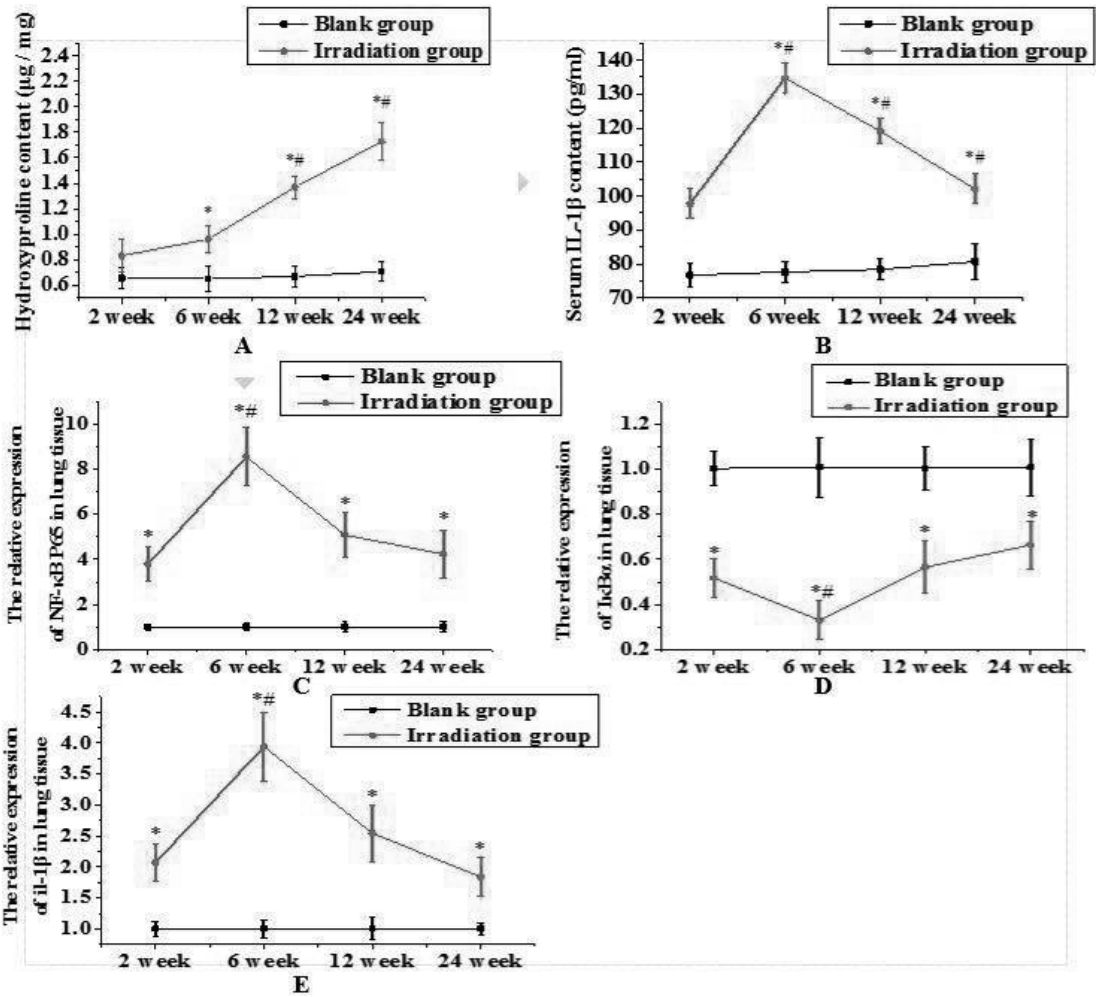

Fig. 3. *The expression levels of NF-κBp65, IκBα and IL-1β in rat lung tissues and changes of serum IL-1β.* ***A****) Changes in the expression level of hydroxyproline in rat lung tissues;* ***B****) Changes in the expression level of serum IL-1β;* ***C****) Changes in the expression level of NF-κBp65 in rat lung tissues;* ***D****) Changes in the expression level of IκBα in rat lung tissues;* ***E****) Changes in the expression level of IL-1β in rat lung tissues. Compared with the blank group, * $P < 0.05$; compared with other time points in the same group, #$P < 0.05$.*

blank group at each time point ($P < 0.05$). At the end of the 6th, 12th and 24th week, significant difference was observed in serum IL-1β levels at different time points of the same group ($P < 0.05$) (Fig.3B).

Expression of NF-κBp65, IκBα and IL-1β in rat lung tissues

The expression level of NF-κB P65 protein in the blank group was stable at different time points, and there was no significant difference ($P > 0.05$). The expression of NF-κBp65 in the irradiation group was increased compared with the blank group ($P < 0.05$), showing an increasing trend from the end of the 2nd week to the 6th week before reaching a stable level. In addition, the expression of NF-κBp65 in the irradiation group was higher than that in the blank group, but the difference was not statistically significant (Dunnett's T3 test, $P > 0.05$). Moreover, the expression of NF-κBp65 in the irradiation group at the end of the 6th week was higher than that of other time points in the irradiation group ($P < 0.05$) (Fig. 3C).

The expression of IκBα in the lung tissues in the blank group was relatively stable at each time point, and there was no obvious statistical significance ($P > 0.05$). Compared with the blank group, the expression level of IκBα in the irradiation group significantly decreased at each time point ($P < 0.05$). The level of IκBα in the irradiation group began to decrease at the end of the 2nd week before reaching its lowest point at the end of the 6th week and then increasing again at the end of the 12th week. There was significant difference in the expression of IκBα in the irradiation group between the levels from the end of the 6th week and the levels from other time points ($P < 0.05$) (Fig. 3D).

There was no significant difference in the expression of IL-1β protein between the blank group and the control group at different time points ($P > 0.05$). The expression of IL-1β protein in the lung tissues of rats in the irradiation group was increased compared with the blank group at any time points ($P < 0.05$). In the irradiation group the trend showed an increasing in IL-1β protein expression levels from the end of the 2nd week to the end of the 6th week before reaching a peak and then a decrease after the 12th and 24th week. Finally, there was no significant difference in the expression of IL-1β protein between the two groups (Dunnett's T3 test, $P > 0.05$), while the expression of IL-1β protein in the irradiation group was lower at the end of the 6th week than that of other time points ($P < 0.05$) (Fig. 3E).

DISCUSSION

In radiation-induced lung injury in rats, the expression of IL-1β increased first and then decreased. The relative expression of NF-κB was also increased first and then decreased, while the expression of NF-κBp65 was reversed. It is hypothized that inflammation may be caused by early lung tissue injury (2 and 6 weeks after irradiation) in rats caused by high dose Y-ray (9). In later stages (12 and 24 weeks after irradiation), with the absorption and gradual subsidence of inflammation, the expression of inflammation inhibitor IL-1β gradually decrease along with the expression of inflammatory factors IL-1β and NF-κBp65. In addition, the expression of inflammatory factors reached a peak at the end of 6th week after radiation-induced lung injury, which may be due to the recruitment of various inflammatory cells and the expression of inflammatory factors (IL-1β, TNF-α, etc.). The latter further activates the downstream NF-κB signaling pathway and leads to the phosphorylation of NF-κBp65 into the nucleus. After nuclear entry, NF-κBp65 can also regulate the expression of inflammatory cell factors such as IL-1, IL-6 and TNF-α, forming a positive feedback loop and causing a "Cascade Fall" (10) of inflammatory factors, which eventually leads to and aggravates radiation pneumonia. In the later stage, the expression of these inflammatory factors, especially NF-κBp65, did not completely decrease, and still remained at a certain high level. It can be concluded that the DNA binding activity of NF-κBp65 and the deletion of IκBα in the nucleus of rats increased continuously in several months after irradiation. In conclusion, abnormal NF-κBp65 expression and sustained activation of NF-κBp65 signaling pathways play an essential role in regulating radiation-induced lung injury, although further research is still needed.

REFERENCES

1. Woolf DK, Slotman BJ, Faivre-Finn C. the current role of radiotherapy in the treatment of small cell lung cancer. Clin Oncol (R Coll Radiol) 2016; 28(11):712-19.
2. Yang L, Fan JH, Liu LL, et al. Comparison of gefitinib and platinum-based chemotherapy and only platinum-based chemotherapy to treat lung adenocarcinoma. J Biol Regul Homeost Agents 2018; 32(3):613-8.
3. Sani TA, Mohammadpour E, Mohammadi A, et al. Cytotoxic and apoptogenic properties of dracocephalum kotschyi aerial part different fractions on calu-6 and mehr-80 lung cancer cell lines. Farmacia 2017; 65(2):189-99.
4. Yue Z, Xu B. The feather model for chemo- and radiation therapy-induced tissue damage. Methods Mol Biol 2017; 1650:299-307.
5. Fujio K, Komai T, Inoue M, Morita K, Okamura T, Yamamoto K. Revisiting the regulatory roles of the TGF-β family of cytokines. Autoimmun Rev 2016; 15(9):917-22.
6. Han X, Li B, Ye X, et al. Dopamine D2 receptor signaling controls inflammation in acute pancreatitis via PP2A-dependent Akt/NFκB signaling pathway. Br J Pharmacol 2017; 174(24):4751-70.
7. Michaelis KA, Agboke F, Liu T, et al. IκBβ-mediated NF-κB activation confers protection against hyperoxic lung injury. Am J Respir Cell Mol Biol 2014; 50(2):429-38.
8. Jing W, Chunhua M, Shumin W. Effects of acteoside on lipopolysaccharide-induced inflammation in acute lung injury via regulation of NF-κB pathway in vivo and in vitro. Toxicol Appl Pharmacol 2015; 285(2):128-35.
9. Low JT, Hughes P, Lin A, et al. Impact of loss of NF□κB1, NF□κB2 or c□REL on SLE□like autoimmune disease and lymphadenopathy in Faslpr/lpr mutant mice. Immunol Cell Biol 2016; 94(1):66-78.
10. Yan J, Zhang H, Xiang J, Zhao Y, Yuan X, Sun B, Lin A. The BH3-only protein BAD mediates TNFα cytotoxicity despite concurrent activation of IKK and NF-κB in septic shock. Cell Res 2018; 28(7):701-18.

JOURNAL OF BIOLOGICAL REGULATORS & HOMEOSTATIC AGENTS Vol. 33, no. 5, 1479-1483 (2019)

LETTER TO THE EDITOR

APOPTOSIS SIGNAL-REGULATING KINASE CONTROLS PORCINE OVARIAN GRANULOSA CELL FUNCTIONS AND THEIR RESPONSE TO GHRELIN

A.V. SIROTKIN[1,2], A. BENČO[1], J. KOTWICA[3], S. ALWASEL[4] and A.H. HARRATH[4]

[1]Constantine the Philosopher University, Nitra, Slovakia ; [2]Research Institute of Animal Production, National Agricultural and Food Centre, Lužianky, Slovakia; [3]Institute of Animal Reproduction and Food Research, Olsztyn-Kortowo, Poland; [4]King Saud University, Department of Zoology, College of Science, Riyadh, Saudi Arabia

Received March 11, 2019 – Accepted June 6, 2019

To the Editor,

Apoptosis signal-regulating kinase 1 (ASK1 or MAP3K5) belongs to the mitogen-activated protein kinase (MAP3K) family (1). It can mediate the stimulatory effect of stress on apoptosis and the development of several diseases (1–3). Pharmacological inhibitors of ASK-1 are considered a promising tool for increasing cell viability and treating the diseases (1-3). It has not yet been established whether ASK-1 is involved in the control of healthy cell functions, and response to the upstream physiological regulators.

Ovarian functions are under the control of hormones. One such hormonal regulator is the metabolic hormone ghrelin, which was shown to be a potent regulator of porcine ovarian cell proliferation, apoptosis, and secretory activity (4-6). Changes in the ASK-1 accumulation in ovarian cells after ghrelin (4) administration indicate that ASK-1 might mediate the action of this hormonal regulator of ovarian functions. Nevertheless, the involvement of ASK-1 in the control of ovarian cell functions and in modification and mediation of their response to the upstream hormonal regulator ghrelin has not yet been examined.

This study aimed to investigate the involvement of ASK-1 in the control of ovarian granulosa cell proliferation, hormone release, and their response to the metabolic hormone ghrelin. We examined the effect of transfection with ASK-1 cDNA on the basic functions of cultured porcine ovarian granulosa cells cultured with and without ghrelin. The accumulation of ASK-1 and PCNA (cell proliferation marker) (7), as well as the release of ovarian hormones progesterone (P4) and prostaglandin E (PGE), known markers and regulators of ovarian functions (6), was evaluated.

MATERIALS AND METHODS

Preparation, culture, and processing of ovarian cells

The ovaries of non-cycling pubertal Slovakian White gilts aged 180 days were processed after slaughter at a local abattoir; their granulosa cells were transfected and cultured as described previously (4). Briefly, follicular fluid containing granulosa cells was aspirated from 3–5 mm diameter follicles, isolated by centrifugation for 10 min at 200 × *g*, rinsed with sterile DMEM/F12 1:1 medium (BioWhittaker™, Verviers, Belgium), and resuspended in the same medium supplemented with 10% fetal calf serum (BioWhittaker™) and 1% antibiotic-antimycotic solution (Sigma, St. Louis, MO, USA). Thereafter, granulosa cells (1×10^6 cells/ml) were cultured for 2 days in the medium described above in

Key words: apoptosis signal-regulating kinase (ASK-1); ghrelin; hormones; ovarian granulosa cells; pig; proliferation; transfection

Corresponding Author:
Prof. Dr. Alexander V. Sirotkin, PhD., DrSc.,
Constantine the Philosopher University,
Tr. A Hlinku 1, 949 74 Nitra, Slovakia
Tel.: +421 903561120,
e-mail: asirotkin@ukf.sk

0393-974X (2019)

Falcon 24-well plates (Becton Dickinson, Lincoln Park, NJ, USA) and chamber slides (Nunc Inc. Naperville, TN, USA) at 38°C and 5% CO_2 in humidified air, with 2 ml and 200 µl medium per well, respectively. After 2 days of culture, the granulosa cells were transfected using Roti-Fect (Carl Roth, GmBH, Karlsruhe, Germany) transfection reagent according to the manufacturer's instructions. Cells were transfected with plasmids for HA-ASK-1 WT pcDNA3 obtained from Dr. Atsushi Matsuzawa (Tokyo Medical and Dental University, Tokyo, Japan) and a pEGFP-N1 reporter plasmid for green fluorescent protein EGFP and resistance to kanamycin (Clontech laboratories, now Takara Bio USA, Mountain View, CA, USA). Control cells were transfected with a "scramble" control plasmid vector without ASK-1 provided by Dr. Neil Perkins (University of Dundee, Dundee, UK) and pEGFP-N1. All the constructs were sub cloned as indicated previously (4). After transfection, granulosa cells were cultured as described previously with and without biological grade human recombinant ghrelin (Peptides International Int., Louisville Kentucky, USA) at 0, 1, 10, or 100 ng/ml medium. The hormone was dissolved in culture medium immediately before the experiment. After 48 h, cell numbers and viability were determined by Trypan blue staining and counting using a hemocytometer. Thereafter, cells and medium were collected and stored for analysis as described previously (4).

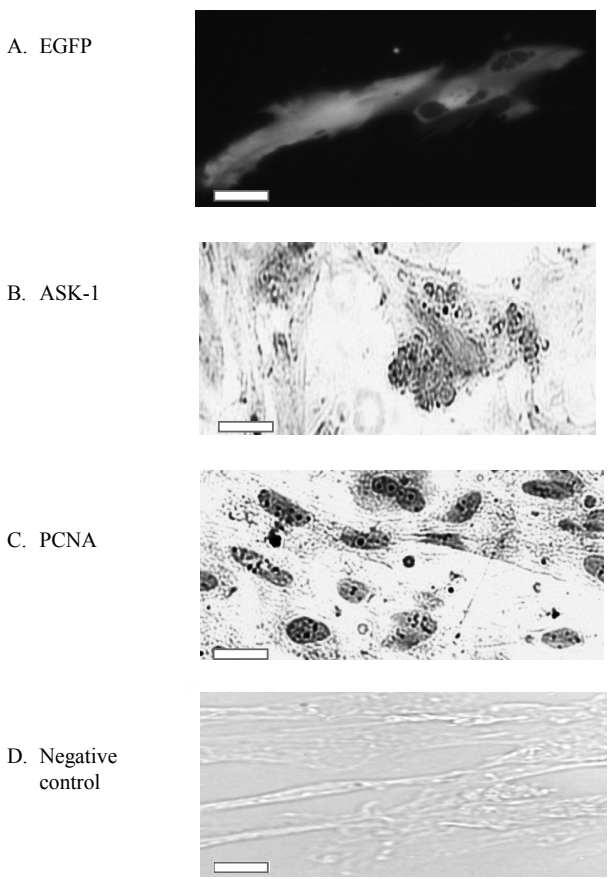

Fig. 1. *Fluorescence and light microscopy images of porcine granulosa cells containing EGFP (bright) (**A**), apoptosis signal-regulating kinase 1 (ASK1; dark) (**B**), proliferating cell nuclear antigen (PCNA; dark) (**C**), and negative control (cells processed with secondary, but not primary antibody for PCNA, no staining) (**D**). Scale bars represent 10 µm.*

Immunoassays

P_4 concentration was measured in 50 µl of incubation medium using a radioimmunoassay (RIA) kit (DSL, Webster, TX, USA) according to the manufacturer's instructions. The antiserum used had <0.01% cross-reactivity with pregnenolone, androstenediol, testosterone, estradiol, cortisol, and IGF1. The sensitivity of the assay was 0.12 ng/mL, and the intra- and inter-assay coefficients of variation were 13.1% and 8.0%, respectively.

PGE2 was assayed in 25 µl of incubation medium using our RIA system (8,9). The cross-reactivity of the antiserum against PGE was <28.0% to PGA-1, <7.0% to PGA-2, <0.6% to PGB-1, <1.4% to PGB-2, <5.0% to PGF-1, <1.5% to PGF-2, 165% to PGE-1, and 100% to PGE-2. The sensitivity of the RIA was 0.015 ng/mL, and the intra- and inter-assay coefficients of variation were 7.5% and 4.0%, respectively.

Both RIAs were validated for use in culture medium samples by serial dilution tests.

Immunocytochemical analysis

The presence of ASK-1 and PCNA was detected using immunocytochemistry as it was described previously (4) by cross-reacting primary mouse monoclonal antibodies against them (Santa Cruz Inc., Santa Cruz, CA, USA; 1:500 dilution) with corresponding human, rat, mouse, and yeast antigens. Secondary porcine polyclonal antibodies against the mouse IgGs, labelled with horseradish peroxidase (Sevac, Prague, Czech Republic; 1:1000 dilution) and 3-3' diaminobenzidine (DAB) (Boehringer Mannheim GmbH, Mannheim, Germany), were used to visualize the primary antibody. The presence of immunoreactivity in the cells was determined by one blinded observer under a light microscope (Leica Microsystems GmbH, Wetzlar,

Germany). The ratio of cells containing ASK1 or PCNA to the total cell number was calculated manually (without use of software). Cells processed without the primary antibody were used as negative controls. The presence of cells expressing EGFP (marker of construct integration and expression) was inspected using a fluorescence microscope (Leica Microsystems) equipped with specific wave-length filters for green fluorescence.

Statistical analysis

Each series of experiments was performed three times on different days with separate groups of granulosa cells obtained from 15–20 animals. Data are the means of these values.

RIA: Each experimental group was formed of four culture wells; i.e., each mean value represents 4 wells × 3 experiments = 12 replicates. Assays of hormone concentration in the incubation medium were performed in duplicate. The negative control values (serum-supplemented medium incubated without cells) were subtracted from the values determined using RIA in cell-conditioned medium to exclude non-specific background signal (<10% of all values). Secretion rates were calculated per 10^6 viable cells/day.

Immunocytochemistry: In each chamber (3 per group), 1000 cells were scored; i.e., each mean value represents 9 replicates with 9000 cells in total. The percentage of antigen-containing cells was calculated for each group.

Significant differences ($P < 0.05$) between treatments were evaluated by two-way analysis of variance (ANOVA) followed by Tukey's or *chi*-squared tests, using Sigma Plot 11.0 (Systat Software, GmbH, Erkhart, Germany) software.

RESULTS

After transfection, 18-59% of cells produced EGFP (Fig.1A), with 96–98% cell viability. After culture, ovarian cells contained ASK-1 (Fig.1B, Fig. 2A) and PCNA (Fig. 1C, Fig. 2B), and secreted substantial amounts of P4 (Fig. 2C) and PGE2 (Fig. 2D). No statistically significant difference in cell number (range 0,85 – 1,1 x 10^6 cells) or viability (range 0,92-0,96%) was observed between the control and experimental groups.

Quantitative immunocytochemistry demonstrated that transfection of the cultured granulosa cells with ASK-1 cDNA resulted in a substantial increase in the percentage of cells containing ASK-1 (Fig. 2A, see differences between transfected and non-transfected cells cultured with 0 ng/ml of ghrelin). Transfection also increased the proportion of cells containing PCNA (Fig. 2B). Furthermore, transfected cells released less P4 (Fig. 2C) but more PGE2 (Fig. 2D).

The addition of ghrelin at a dose of 100 ng/ml but not at 1 or 10 ng/ml to the untransfected granulosa cells increased the accumulation of ASK-1 (Fig. 2A). Ghrelin administration at all doses reduced PCNA accumulation in non-transfected cells (Fig. 2B). Ghrelin, when added at doses of 10 or 100 ng/ml (but not at 1 ng/ml), promoted P4 (Fig. 2C) and PGE2 (Fig. 2D) release.

Transfection of granulosa cells with ASK-1 cDNA promoted the inhibitory action of ghrelin on ASK-1 accumulation; in transfected cells, ghrelin suppressed ASK-1 accumulation at all doses (Fig. 2A). In transfected cells, ghrelin inhibited PCNA accumulation when added at doses of 1 or 10 ng/ml but stimulated it when added at a dosage of 100 ng/ml (Fig. 2C). In granulosa cells transfected with ASK-1 cDNA construct, ghrelin at doses of 1 or 10 ng/ml reduced P4 output (Fig. 2C), and at doses of 10 or 100 ng/ml, it promoted PGE release (Fig. 2D).

DISCUSSION

Immunocytochemical analysis demonstrated that the transfection of cells with ASK-1 cDNA promoted ASK-1 accumulation, and hence transfection was successful and resulted in increased ASK-1 expression. This was accompanied by an increase in the proportion of cells accumulating PCNA, a decrease in P4, and an increase in PGE output.

To our knowledge, we are the first to demonstrate that ASK-1 can promote proliferation of healthy ovarian granulosa cells without influencing their viability (see above). Furthermore, our results demonstrate the involvement of ASK-1 in controlling the release of ovarian steroid hormone (P4) and prostaglandin (PGE2), which play an important role in the control of ovarian cell proliferation, apoptosis, folliculogenesis, oogenesis, and thus fertility (6). The effects of ASK-1 on ovarian cell proliferation

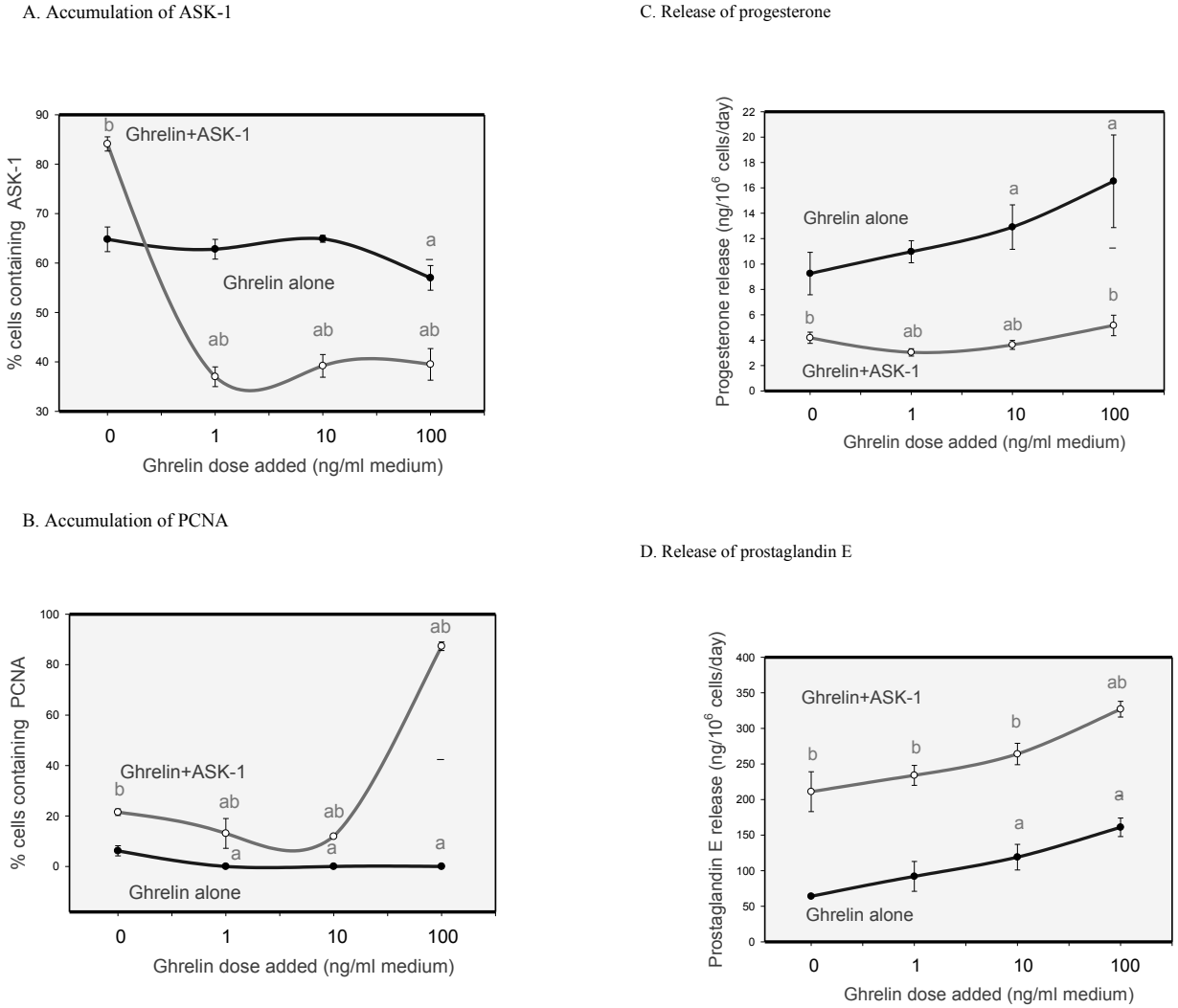

Fig. 2. *Effects of ghrelin at different concentrations on the expression of ASK-1 (**A**), PCNA (**B**), and on the release of progesterone (**C**), and prostaglandin E (**D**) by cultured porcine granulosa cells transfected and non-transfected with ASK-1 cDNA construct. Data from quantitative immunocytochemistry (A, B) and radioimmunoassay (C, D). "a" indicates a significant ($P < 0.05$) difference between the hormone-treated (1, 10, or 100 ng/ml) and control (0 ng/ml) cells; "b" indicates a significant ($P < 0.05$) difference between transfected and untransfected cells.*

could therefore be mediated by changes in ovarian hormone release.

The present experiments showed the inhibitory action of ghrelin on PCNA accumulation, as well as its inhibitory influence on P4 and stimulatory action on PGE2 output. These observations confirm the previous findings that ghrelin is a potent physiological regulator of porcine ovarian cell proliferation and secretory activity (4-6). Furthermore, the findings demonstrate the ability of ghrelin to down-regulate ASK-1 in ovarian cells. This represents the first indication of the involvement of ASK-1 in mediating ghrelin action in ovarian cells. The second indication is the ability of ASK-1 to modify the ghrelin effect; overexpression of ASK-1 promoted ghrelin action on ASK-1 and induced the stimulatory ghrelin action on PCNA and inhibitory action of ghrelin on P4. Therefore, ASK-1 overexpression was associated with promotion of ghrelin action on ASK-1 and the reversal of ghrelin effects on PCNA and P4. Only the

stimulatory action of ghrelin on PGE2 did not change after transfection with the ASK-1 gene construct.

The effect of ghrelin on ASK-1 along with the modification of ghrelin effects by ASK-1 suggest that ASK-1 is an intracellular mediator of the effects of this hormone on ovarian granulosa cells.

Taken together, our observations demonstrate that ASK-1 is a new-found regulator of basic ovarian functions and that it can mediate ghrelin action on these functions.

ACKNOWLEDGEMENTS

These studies were supported by the Slovak Research and Development Agency (APVV) under contract numbers APVV-0854-11, APVV-14-001, and APVV-15-0296, the Slovak Grant Agency of the Ministry of Education, Science, and Sport, the Slovak Academy of Science (VEGA) projects (VEGA 1/0392/17, VEGA 1/0022/15, and VEGA 1/0327/16).

This work was financed by Researchers Supporting Project number RSP-2019/17, King Saud University, Riyadh, Saudi Arabia.

The authors express their gratitude to Ing. Ž. Kuklová and Ms. K. Tóthová (Research Institute of Animal Production, Nitra, Slovakia) for their help analyzing the samples, Dr. A. Matsuzawa (Tokyo Medical and Dental University, Tokyo, Japan) and Dr. N. Perkins (University of Dundee, Dundee, UK) for kindly providing gene constructs, and Dr. W.W. Thatcher (University of Florida, Gainesville, FL) for the gift of antiserum against PGE.

REFERENCES

1. Chen Z, Seimiya H, Naito M et al. ASK1 mediates apoptotic cell death induced by genotoxic stress. Oncogene 1999; 18:173-80.
2. Hattori K, Naguro I, Runchel C, Ichijo H. The roles of ASK family proteins in stress responses and diseases. Cell Commun Signal 2009; 24:7-9. DOI: 10.1186/1478-811X-7-9.
3. Hayakawa R, Hayakawa T, Takeda K, Ichijo H. Therapeutic targets in the ASK1-dependent stress signaling pathways. Proc Jpn Acad Ser B Phys Biol Sci 2012; 88:434-53.
4. Sirotkin AV, Benco A, Tandlmajerova A, Vasícek D, Kotwica J, Darlak K, Valenzuela F. Transcription factor p53 can regulate proliferation, apoptosis and secretory activity of luteinizing porcine ovarian granulosa cell cultured with and without ghrelin and FSH. Reproduction 2008; 136:611-8. DOI:10.1530/REP-08-0229.
5. Rak-Mardyla A. Ghrelin role in hypothalamus-pituitary-ovarian axis. J Physiol Pharmacol 2013; 64:695-704.
6. Sirotkin AV. Regulators of Ovarian Functions. Nova Publishers Inc. New York, 2014; p. 194.
7. Shiomi Y, Nishitani H. Control of genome integrity by RFC complexes; conductors of PCNA loading onto and unloading from chromatin during DNA replication. Genes 2017; 8:52. DOI:10.3390/genes8020052.
8. Kotwica J, Skarzynski D. Influence of oxytocin removal from corpus luteum on secretory function and duration of estrous cycle in cattle. J Reprod Fertil 2014; 97:411-17
9. Duras M, Mlynarczuk J, Kotwica J. Non-genomic effect of steroids on oxytocin-stimulated intracellular mobilization of calcium and on prostaglandin F2α and E2 secretion from bovine endometrial cells. Prostaglandins Other Lipid Mediat 2005; 76:105-16.

LETTER TO THE EDITOR

CORRELATION BETWEEN THE EXPRESSION OF Rap1GTPase ACTIVATING PROTEIN AND THE CLINICOPATHOLOGICAL FEATURES OF INVASIVE BREAST CANCER

CM. JIN[1], FY. GONG[1], JQ. GUI[2], RH. LI[1], YY. WANG[3], CY. XU[4], Y. LIN[5] and HF. LIU[6]

[1]Clinical Lab, Affiliated Hongqi Hospital of Mudanjiang Medical University, Mudanjiang, Heilongjiang, China; [2]Department of Pathogenic Microbiology, Mudanjiang Medical University, Mudanjiang, Heilongjiang, China; [3]Basic Medical College, Harbin Medical University, Harbin, Heilongjiang, China; [4]Pathology Department, Mudanjiang Tumor Hospital, Mudanjiang, Heilongjiang, China; [5]Department of Thoracic Surgery, Affiliated Hongqi Hospital of Mudanjiang Medical University, Mudanjiang, Heilongjiang, China; [6]Department of Biochemistry and Molecular Biology, Mudanjiang Medical University, Mudanjiang City, China

Received March 7, 2019 – Accepted May 22, 2019

To the Editor,

As a common malignant tumor in women, breast cancer occurs in the ductal epithelium of the breast (1). The current research found that genetic changes related to breast cancer include GATA binding protein 3 (GATA3), MYB proto-oncogene, transcription factor (c-myb), cell cycle-related genes, and cell proliferation genes (2). As a Rap1-specific protein activated by guanosine triphosphate (GTP), Rap1 GTPase-activating protein 1 (Rap1GAP) catalyzes the conversion of Rap1 from an active GTP-binding form to an inactive Guanosine diphosphate (GDP) form, while Rap1 is a small-molecule G protein involved in a variety of cellular functions (3, 4).

As a tumor suppressor, Rap1GAP is involved in the regulation of cell proliferation, differentiation, and adhesion by regulating the activity of Rap1 (5). In addition, the inhibitory effect of Rap1GAP on some tumors has been clarified. Nevertheless, although a certain progress has been made in the study of Rap1GAP family members, past studies have focused on the mechanisms underlying the role of Rap1GAP family members in the pathogenesis of tumors. Therefore, the function and mechanism of Rap1GAP gene remain unclear (6-8).

In recent years, studies on Rap1GAP have mainly focused on the low expression of Rap1GAP in pancreatic cancer and thyroid cancer tissues, while few studies have reported the role of Rap1GAP in breast cancer (9). In this study, the expression of Rap1GAP in invasive breast cancer, benign breast diseases and normal breast tissues was detected to explore the correlation between Rap1GAP expression and the development of invasive breast cancer, to provide scientific basis for clinical treatment of invasive breast cancer.

MATERIALS AND METHODS

Patients

From June 2012 to June 2018, 96 patients with breast cancer who underwent surgical resection in the Affiliated Hongqi Hospital of Mudanjiang Medical University were selected for this study. Inclusion and exclusion criteria were developed in accordance with international multi-center clinical

Key words: Rap1; GTPase activating protein; invasive breast cancer; risk factors; SP immunohistochemistry

Corresponding Author:
Dr Hongfeng Liu,
Department of Biochemistry and Molecular Biology,
Mudanjiang Medical University,
No.3 TongXiang Road,
Mudanjiang, Heilongjiang, 157011, China
e-mail: liuhongfeng006@163.com

0393-974X (2019)

trial guidelines. The age of the patients ranged from 24 to 79 years (average 49.5 years). At the same time, 30 specimens of benign breast diseases and 30 normal breast tissue samples were randomly selected as controls. Prior to sample collection, the patients or their family members signed an informed consent which was conserved with the medical record. This study was approved by the medical ethics committee of the Affiliated Hongqi Hospital of Mudanjiang Medical University, China.

Inclusion criteria were: breast cancer patients aged 24-79 years undergoing surgical resection of breast cancer during the previous 5 years; patients not treated by chemoradiotherapy, endocrine therapy or biological target therapy; patients undergoing at least 4 cycles of first-line chemotherapy after surgery.

Exclusion criteria: patients with other physiological or pathological conditions that could affect the observation and judgment of the study indicators; patients with certain clinical characteristics whose enrollment would violate medical ethics; patients unable to follow-up with the study; patients unwilling to sign the informed consent.

Detailed steps of SP immunohistochemistry

In brief, SP immunohistochemistry sections (Thereto, America) were put into a 50-60□ oven (Changzhou Zhongwei Electronics, China) for 1 h and then dewaxed in xylene for 5 min×2, soaked in anhydrous ethanol (Beijing Zhongshan Jinqiao Biological Technology Co., Ltd, China) for 10 min x 2 to remove residual xylene, successively soaked in 100%, 95%, 80%, and 70% of gradient ethanol (5 min each), rinsed with distilled water, and then repaired in a 0.01 ml citrate buffer (Beijing Zhongshan Jinqiao Biological Technology Co., Ltd, China) (pH 6.0) at high temperature and high pressure for 3 min. After the sections were cooled to room temperature, they were washed with distilled water for 3 min×3, rinsed with phosphate buffered saline (PBS) (Beijing Zhongshan Jinqiao Biological Technology Co., Ltd, China) for 3 min x 2, and then incubated at room temperature for 10 min with a 1:50 ul endogenous peroxidase blocking solution (Beijing Zhongshan Jinqiao Biological Technology Co., Ltd, China) to eliminate the effect of endogenous peroxidase. Then, sections were thoroughly rinsed with PBS for 3min x 3 and incubated at room temperature for 10 min with a normal sheep serum working fluid. In the next step, the sections were incubated for 1 h at room temperature with 50 ul/section of primary anti-Rap1GAP (diluted to 1:100 in PBS), anti-ER anti-PR or anti-Her2 antibodies, while PBS was used as the negative control. Thereafter, the sections were fully rinsed with PBS for 5 min×3 and then incubated at room temperature for 10 min with a secondary antibody (Goat anti Mouse, Ig G) (Abcam, America) working solution. After being thoroughly rinsed with PBS for 3 min×3, the sections were incubated for 10 min at room temperature with 50 u1/section of streptomycin avidin (Beijing Zhongshan Jinqiao Biological Technology Co., Ltd, China)-labeled HRP, fully rinsed with PBS for 3 min × 3, developed using 50 u1/section of diaminobenzidine (DAB, 1:19) (Guangzhou Anbiping Co. Ltd., China) and then observed under a light microscope (OYLMPUS, Japan). When the optimal color rendering effect was observed, the reaction was terminated by tap water and the sections were counterstained with hematoxylin (Beijing Zhongshan Jinqiao Biological Technology Co., Ltd, China) for 2 min. Subsequently, the sections were rinsed with tap water and ammonia water (Beijing Zhongshan Jinqiao Biological Technology Co., Ltd, China) before being immersed in gradient alcohol, dehydrated, dried and sealed with neutral gum. Under the light microscope, the brown-yellow or yellow cytoplasm indicated positive expression. The evaluation criteria of the results are detailed in the following section. In each experiment, known positive sections were used as positive controls while PBS was used as the negative control.

Follow-up

All breast cancer patients in this group were regularly followed-up. Disease-Free Survival (DFS) and Overall Survival (OS) were used as prognostic indexes. In particular, DFS was calculated from the date of surgery to the date of tumor recurrence or metastasis, while OS was calculated from the date of surgery to the date of tumor-related death.

The follow-up was 9-84 months, with a median of 61 months. During the follow-up period, 41 cases presented local recurrence, distant metastasis or regional lymph node metastasis, along with 36 deaths, which included 2 deaths caused by other diseases and subsequently treated as deleted cases.

Statistical analysis

SPSS19.0 statistical software was used to analyze the data, while *chi*-squared test or Fisher's exact probability test was used to count the data. Univariate analysis was used to screen out the factors affected by Rap1GAP expression, while the relationship between Rap1GAP expression and the above factors was analyzed with binary multivariate Logistic analysis. The difference was statistically significant at $P<0.05$.

RESULTS

Expression of Rap1GAP in invasive breast cancer, benign breast diseases and normal breast tissues

The positive rates of Rap1GAP expression were 35.42% in invasive breast cancer tissues,

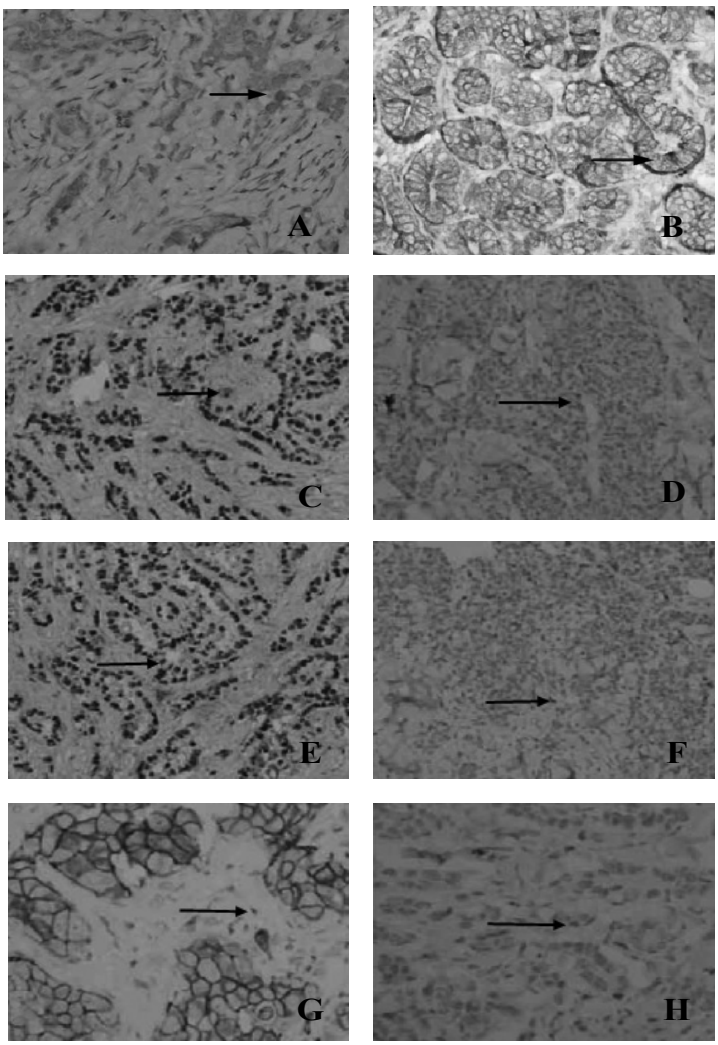

Fig. 1. *Expression of Rap1GAP, ER, PR, and Her2.* ***A****) expression of Rap1GAP in invasive breast cancer, 400×;* ***B****) expression of Rap1GAP in benign breast, 400×;* ***C****) positive expression of ER receptor, 400×;* ***D****) negative expression of ER receptor, 400×;* ***E****) positive expression of PR receptor, 400×;* ***F****) negative expression of PR receptor, 400×;* ***G****) positive expression of Her2 receptor, 100×;* ***H****) negative expression of Her2 receptor, 100×*

60% in tissues of benign breast diseases and 90% in normal breast tissues. Significant difference was found between invasive breast cancer tissues and normal breast tissues (χ^2 = 12.388 and P = 0.000), as well as between invasive breast cancer tissues and tissues of benign breast diseases (χ^2 = 4.534 and P = 0.033), while no significant difference was found between tissues of benign breast diseases and normal breast tissues (χ^2=2.678 and P=0.033). Rap1GAP expression in invasive breast cancer tissues was significantly lower than that in benign breast diseases and normal breast tissues. SP staining showed that the expression of Rap1GAP in normal breast tissues and benign breast diseases was mainly located in the cytoplasm, and the degree of staining was strongly positive or moderately positive. In contrast, invasive breast cancer tissues showed little or no Rap1GAP expression, as shown in Fig. 1, A and B.

The expression of estrogen receptor, progesterone and human epidermal growth factor receptor 2 in invasive breast cancer

In invasive breast cancer, the positive expression rates of estrogen receptor (ER), progesterone (PR), and human epidermal growth factor receptor 2 (Her2) were 70.58%, 52.95%, and 20.58%, respectively. SP staining showed that the positive expression of ER and PR receptors in invasive breast cancer was mainly located in the nucleus, while the positive expression of Her2 was located on the cell membrane, as shown in Fig. 1, C-H.

Table I. *Correlation analysis of Rap1GAP expression in invasive breast cancer.*

Relevant factors	Rap1GAP		χ^2	P value
	Positive	Negative		
Less than 50 years old	16	34	0.524	0.469
Over 50 years old	18	28		
Premenopausal	17	35	1.756	0.186
Postmenopausal	17	27		
Positive ER	22	39	0.144	0.706
Negative ER	12	23		
Positive PR	14	33	2.488	0.116
Negative PR	20	29		
Positive Her2	11	12	0.774	0.379
Negative Her2	23	50		
Tumor less than 2cm in diameter	24	34	1.268	0.261
Tumor greater than 2cm in diameter	10	28		
Stage I-II of TNM staging	29	36	4.026	0.045
Stage III of TNM staging	5	26		
I-II histological grading	28	30	9.140	0.003
III histological grading	6	32		
No axillary lymph node metastasis	26	25	7.168	0.007
Axillary lymph node metastasis	8	37		

Univariate analysis of Rap1GAP expression in invasive breast cancer

The positive expression of Rap1GAP in invasive breast cancer was not correlated with the patient's age, menstrual status, tumor diameter, or receptor expression (ER, PR, and Her2), and the difference was not statistically significant ($P > 0.05$), but it related to TNM stage, histological grade, and axillary lymph node metastasis. Among them, the positive expression rate of Rap1GAP in invasive breast cancer tissues with stage I-II in TNM stage was higher than that in stage III, the difference was statistically significant ($P<0.05$). The Rap1GAP positive expression rate in histologically graded I-II of invasive breast cancer tissues was higher than that in grade III, and the difference was statistically significant ($P < 0.05$). The Rap1GAP positive expression rate in invasive breast cancer tissues without axillary lymph node metastasis was higher than that with axillary lymph node metastasis, and the difference was statistically significant ($P < 0.05$). The results are shown in Table I.

Logistic regression analysis of Rap1GAP expression in invasive breast cancer

Taking the expression of Rap1GAP in invasive breast cancer as a dependent variable and the risk factors (including TNM stage, histological grade and axillary lymph node metastasis) as independent variables, a binary multivariate unconditional Logistic regression analysis was carried out. Through the verification of the regression coefficient of the Wald *chi*-squared value, it can be concluded that the logistic regression analysis is feasible. TNM staging, histological grading and the OR value (defined odds ratio) of axillary lymph node metastasis were all greater than 1, indicating that all three were risk factors for the downregulation of Rap1GAP expression, and the differences were statistically significant ($P < 0.05$), as shown in Table II.

Relationship between Rap1GAP expression and prognosis of invasive breast cancer

All breast cancer patients were followed up for 9-84 months, with a five-year disease-free survival

Table II. *Binary multivariate unconditioned Logistic analysis of Rap1GAP expression in breast cancer*

Factors	Regression coefficient	Standard error	Wald value	P value	OR value	95% confidence interval for OR
TNM stage	0.988	0.453	4.782	0.028	2.688	1.108 6.525
Histological grade	1.392	0.444	9.856	0.003	4.018	1.686 9.571
Axillary lymph node metastasis	0.944	0.398	5.572	0.017	2.568	1.173 5.615
Constant term	-0.538	0.345	2.425	0.118	0.584	

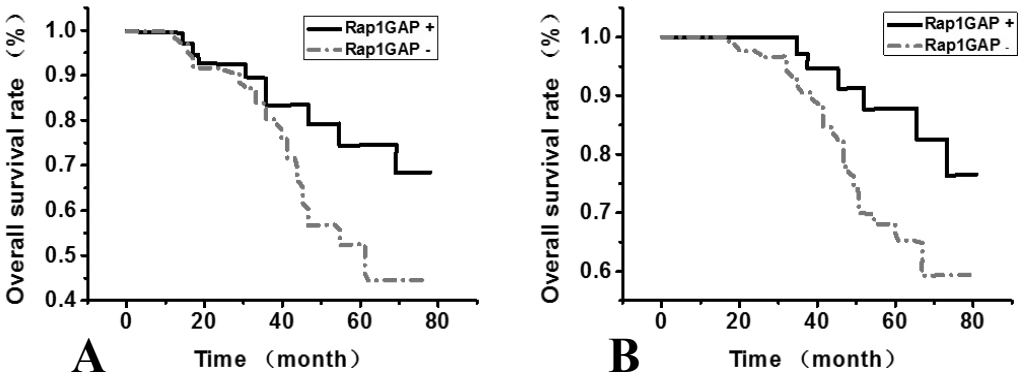

Fig. 2. *Rap1GAP expression and survival curves of DFS/OS of invasive breast cancer.* ***A)*** *survival curve of DFS;* ***B)*** *survival curve of OS.*

rate of 66.18% and a five-year overall survival rate of 75.1%, respectively. The patients were divided into two groups based on their Rap1GAP expression. Kaplan-Meier survival curves of the two groups of patients (as shown in Fig. 2, A and B) were subjected to a log-rank test, and the results showed significant difference in the survival rates between the two groups ($P < 0.05$). In addition, the DFS and OS of breast cancer patients showing positive Rap1GAP expression were significantly higher than those showing negative Rap1GAP expression.

DISCUSSION

Rap1GAP participates in the regulation of cell proliferation, differentiation, and adhesion by regulating the activity of Rap1. In addition, Rap1GAP overexpression can inhibit the proliferation, invasion and metastasis of malignant tumor cells (10). Further study found that there was no correlation between Rap1GAP positive expression in invasive breast cancer tissues and patient age, menstrual status, tumor diameter and receptor expression (ER, PR, Her2), and the differences were not statistically significant ($P>0.05$). Stage III of TNM staging, III histological grade, and axillary lymph node metastasis were risk factors for the down-regulation of Rap1GAP expression, with statistically significant differences ($P < 0.05$), suggesting that the decreased expression of Rap1GAP may be related to some malignant biological behaviors of breast cancer. Past studies have confirmed the lack of Rap1GAP heterozygosity in pancreatic cancer and oral squamous cell carcinoma, suggesting the presence of a tumor suppressor gene in this region the reduced expression of which may lead to the occurrence and development of tumors (11, 12). The results of this study showed that the DFS and OS of patients in the Rap1GAP positive expression group were significantly higher than those in the Rap1GAP negative expression group.

In summary, Rap1GAP was down-regulated in invasive breast cancer, which could be used as an indicator to judge the prognosis of breast cancer. It would provide a new direction for the diagnosis and treatment of invasive breast cancer in humans, but a comprehensive understanding of the mechanism of Rap1GAP still needs to be confirmed by other aspects. With the further understanding of Rap1GAP by researchers, Rap1GAP will have a broader clinical application prospect.

ACKNOWLEDGEMENT

This work was supported by Heilongjiang Natural Science Foundation Project (No.H201493).

REFERENCES

1. Yang D S, Roh S, Jeong S. The axon guidance function of Rap1 small GTPase is independent of PlexA RasGAP activity in Drosophila. Dev Biol 2016; 418(2):258-67.
2. Battram AM, Durrant TN, Agbani EO, et al. The Phosphatidylinositol 3,4,5-trisphosphate (PI (3,4,5) P3)-binder Rasa3 Regulates Phosphoinositide 3-kinase (PI 3-kinase)-dependent Integrin αIIbβ3 Outside-in Signaling. J Biol Chem 2017; 292(5):1691-704.
3. Wang JC, Lee JY, Christian S, Dang-Lawson M, Pritchard C, Freeman SA, Gold MR. The Rap1-cofilin pathway coordinates actin reorganization and MTOC polarization at the B-cell immune synapse. J Cell Sci 2017; 130(6):1094-109.
4. Kam CY, Dubash AD, Magistrati E, et al. Desmoplakin maintains gap junctions by inhibiting Ras/MAPK and lysosomal degradation of connexin-43. J Cell Biol 2018; 217(9):3219-35.
5. Wong SM, Freedman RA, Sagara Y, Aydogan F, Barry WT, Golshan M. Growing use of contralateral prophylactic mastectomy despite no improvement in long-term survival for invasive breast cancer. Ann Surg 2017; 265(3):581-89.
6. Kajiho H, Kajiho Y, Frittoli E, et al. RAB2A controls MT1-MMP endocytic and E-cadherin polarized Golgi trafficking to promote invasive breast cancer programs. EMBO Rep 2016; 17(7):1061-80.
7. Williams LA, Olshan AF, Tse CK, Bell ME, Troester MA. Alcohol intake and invasive breast cancer risk by molecular subtype and race in the Carolina Breast Cancer Study. Cancer Causes Control 2016; 27(2):259-69.
8. Gaudet MM, Carter BD, Brinton LA, et al. Pooled analysis of active cigarette smoking and invasive breast cancer risk in 14 cohort studies. Int J Epidemiol 2017; 46(3):881-93.
9. Chu CY, Jin YT, Zhang W, et al. CA IX is upregulated in CoCl2-induced hypoxia and associated with cell invasive potential and a poor prognosis of breast cancer. Int J Oncol 2016; 48(1):271-80.
10. Ko ES, Kim JH, Lim Y, Han BK, Cho EY, Nam SJ. Assessment of Invasive Breast Cancer Heterogeneity Using Whole-Tumor Magnetic Resonance Imaging Texture Analysis: Correlations With Detailed Pathological Findings. Medicine (Baltimore) 2016; 95(3):e2453.
11. Elshof LE, Schaapveld M, Schmidt MK, Rutgers EJ, van Leeuwen FE, Wesseling J. Erratum to: Subsequent risk of ipsilateral and contralateral invasive breast cancer after treatment for ductal carcinoma in situ: incidence and the effect of radiotherapy in a population-based cohort of 10,090 women. Breast Cancer Res Treat 2017; 161(2):389-90.
12. Kuerer HM, Vrancken Peeters MTFD, Rea DW, Basik M, De Los Santos J, Heil J. Nonoperative Management for Invasive Breast Cancer After Neoadjuvant Systemic Therapy: Conceptual Basis and Fundamental International Feasibility Clinical Trials. Ann Surg Oncol 2017; 24(10):2855-62.

JOURNAL OF BIOLOGICAL REGULATORS & HOMEOSTATIC AGENTS Vol. 33, no. 5, 1493-1496 (2019)

LETTER TO THE EDITOR

ANNUALLY OVER 9 BILLION DOLLARS LESS FOR ONE-STEP MELANOMA SURGERY: SOUNDS GOOD?

G. TCHERNEV[1,2] and I. TEMELKOVA[1,2]

[1]Department of Dermatology, Venereology and Dermatologic surgery, Medical Institute of Ministry of Interior (MVR), Sofia, Bulgaria; [2]Onkoderma, Clinic for Dermatology, Venereology and Dermatologic Surgery, Sofia, Bulgaria

Received May 22, 2019 – Accepted June 19, 2019

To the Editor,

The rules for surgical treatment of cutaneous melanomas are subject to lively discussions without finding a definitive solution to date (1). We present a short comparison between the American Joint Committee of Cancer (AJCC) and One Step Melanoma Surgery (OSMS) recommendations (Table I, Table II), proving our thesis that OSMS at present is certainly the most effective methodology (2).

In a number of our papers, we examined in detail the possibility of performing melanoma surgery within one surgical session (OSMS), (Table II) (3, 4). What is interesting is the fact that the final post-surgical result achieved by conducting OSMS therapy is completely consistent with the one achieved after following the recommendations for AJCC treatment for cutaneous melanoma (4). Thus, the result of AJCC recommendations is respected and clearly defined but within one surgical intervention (3).

We are of the opinion that the two-step model of melanoma treatment is one of the main reasons for disrupting the standards for correct or more reliable treatment, hence, in all likelihood, for the progression of cutaneous melanoma, as problems occur most often due to:

i. the impossibility of the field of surgical security to be precisely defined or outlined in the context of the second intervention, especially if it is carried out by another surgeon (2). The reasons for this can be attributed, on the one hand, to the absence of detailed data in the patient‘s epicrisis (aregarding the extent of the resection field) and to the lack of evidence-based imaging material that actually/practically illustrates with what field of surgical security the patient was initially treated (1,2);
ii. failure to comply with the time limits within which the secondary excision should be performed (2);
iii. time-consuming histopathological preparations and a desire/wish for control of tumor thickness with another pathologist, which further delays the timely performance of a secondary excision (2).

The following two additional circumstances are also important, however are completely ignored if the dermatological surgeon is guided by the AJCC recommendations:

i. the lack of adequacy of guidelines or additional recommendations for expansion of the surgical fields in case of non-compliance/disparity of the clinically marked preoperative with the histopathologically established postoperative resection margins (5)

Key words: OSMS; drug-induced melanoma; Olmesartan; surgical approach; sartans

Corresponding Author:
Prof. Georgi Tchernev,
Department of Dermatology,
Venereology and Dermatologic Surgery
Medical Institute of Ministry of Interior (MVR)
General Skobelev 79, 1606 Sofia, Bulgaria
e-mail: georgi_tchernev@yahoo.de

0393-974X (2019)

DISCLOSURE: ALL AUTHORS REPORT NO CONFLICTS OF INTEREST RELEVANT TO THIS ARTICLE.

Table I. *AJCC recommendation.*

Breslow thickness	Recommended surgical margins/AJCC
Melanoma in situ	**0.5 cm** (primary excision with 0.5 cm in all directions, followed by secondary excision)
<1mm	**0.5 cm** primary excision (followed by secondary excision with 0.5 cm in all directions)
1.01 - 2.0mm	**0.5 cm** primary excision (followed by secondary excision with 0,5 cm- 1.5 cm/ with SLND)
2mm- 4mm	**0.5 cm** primary excision (followed by secondary excision with 1.5 cm in all directions/with SLND)
> 4mm	**0.5 cm** primary excision (followed by secondary excision with 1.5 cm in all directions/without SLND if nodes not enlarged)

ii. the same recommendations for treatment/surgical security margins of nodular and superficial spreading melanomas (5).

Precisely these are probably some of the key links that could be responsible for tumor progression.

Of particular interest is the final financial result ensuing from the application/performance of the two methodologies (4). With treatment in accordance with the current AJCC guidelines [performed always in two stages- primary excision followed by re-excision (Table I)], the median calculated sum for recurrence (secondary excision with sentinel lymph node, for example) is $5,000 considering the current number of melanoma cases leads to an extra cost of $1,500,000,000 per year. OSMS reduces this cost in any phase of melanoma patients, namely from Stage 1 to Stage 4 (2, 3), making it attractive for further discussion.

According to the American Institute for Cancer Research, in 2018 the number of new melanoma cases reached nearly 300,000 worldwide (6, 7). According to the statistics, advancement and mortality were reported in 60,712 of these cases (6), i.e. advancement and mortality in 21% of the cases (6, 7). These are supposed to be patients subject to a mandatory targeted therapy, although the exact percentage of patients on a target therapy is not disclosed (6,7). The concept of "positively influenced by target therapy" is also blurred, as there are cases that have been treated for six months with pembrolizumab and, in the absence of efficacy or

Table II. *One-step melanoma surgery*

Breslow thickness	Recommended surgical margins/ Tchernev et al.
Melanoma in situ	**1.0 cm** (clinical/ dermatoscopical evaluation obligate/if possibility for echographical examination - from benefit)
<1mm	**1.0 cm** (clinical/dermatoscopical evaluation obligate/if possibility for echographical examination - from benefit)
1.01 - 2.0mm	**1.0 cm (with SLND),** (echographical tumour thickness measurement preoperatively)
2mm- 4mm	**2.0 cm (with SLND)** echographical tumour thickness measurement preoperatively
> 4mm	**2.0 cm** **a)** no enlarged lymph nodes- 2cm resection is sufficient, **b)** in the presence of enlarged lymph nodes - to be removed together with the reexcison of the primary tumorous tissue!

(OSMS) recommendations.

loss of this, ipiliulumab has been added. There is no precise literature data about applied target therapy, initially non-responsive, or primary and secondary resistance. According to US statistics, only the number of invasive melanomas was around 70,000 per year between 2007-2011 and it is expected to reach more than 116,000 per year in 2026-2031, i.e. around 70,000 people will be subject to target therapy (8). In this regard, one of the main and first introduced therapies for advanced melanoma cases is treatment with Ipilimumab (9). The currently approved dosing schedule for ipilimumab is 3 mg/kg every 3 weeks for a total of 4 doses, and according to available literature, the price is $30,000 per injection or $120,000 for the full treatment cycle (9). If those 70,000 cases are subject to the therapy in question, the incurred cost is $8,400,000,000 per year. We are talking about monotherapy in advanced melanoma.

On the other hand, according to the Food and Drug Administration for advanced or inoperable melanoma, a combination of ipilimumab and niulumab cost $256,000 a year for patients who respond to treatment. Other analyses showed that nivolumab monotherapy had the lowest total cost, followed by ipilimumab monotherapy, and the combination therapy: $169,320, $213,763 and $228,352, respectively (10).

Thus 70,000 patients for one year cost $17.5 billion to the health insurance system. If the therapy is not combined, these numbers are about 35% lower. If the inoperable or advanced melanomas are half of the amounts mentioned and calculated by us, the cost of the health system is at least $8.5 billion a year.

According to certain authors, not only are new „breakthrough“ products expensive, but existing products tend to outgrow general inflation, making the pharmaceutical industry very profitable and resulting in many patients skipping or cutting down the doses of such critical medicines (11). They share the opinion that companies spend large sums on lobbying and influencing medical leaders in order to keep their profits high (11).

We are of the opinion that one-step melanoma surgery is capable of drastically changing the number of advanced melanomas to at least 35-50% of the current numbers, which in practice signifies that, with more than 60,000 probable deaths, on a yearly basis (4), it is expected that they would have been, at least theoretically, on combined target therapy, which has been estimated at $ 256,000 per year for „respondents“, whatever that means (12). Which makes over $15 billion minimum for targeting melanoma therapy per year. Although, it is assumed that the number of melanomas which have undergone target therapy (combined or monotherapy) should be at least two-fold higher than that of the deceased - namely at least 120,000 registered patients annually out of approximately 300,000 worldwide.

We believe that the interval between the two surgical excisions is at risk for patients‘ late presentation and, in some cases, even refusal of reoperation, which is probably associated with an increased risk for metastatic melanoma occurrence (1). By optimizing the approach through one-step melanoma surgery, we eliminate precisely this key/turning point - the cost of treatment with the second surgical intervention: the direct overpayment of $1,500,000,000. We share the opinion that one-step melanoma surgery will also reduce the need for additional target therapy in advanced melanomas by at least 50%, which is practically around $7.6 billion per year. Or a general/total benefit of at least $9.1 billion.

REFERENCES

1. Tchernev G, Temelkova I. The novel surgical margin for One Step Melanoma Surgery (OSMS) (without using ultrasonography preoperatively): the end of conformity! „Vivere militare est!“ Open Access Maced J Med Sci 2018; 6(7):1263-66.
2. Tchernev G, Temelkova I. The one step melanoma surgery (OSMS): a new chance for more adequate surgical treatment of melanoma patients!? Open Access Maced J Med Sci 2019; 7(3):504-6.
3. Tchernev G, Temelkova I. Comparative analysis of the „Scholastic“ recommendations of the AJCC from 2011 for the surgical treatment of cutaneous melanoma with the newly suggested guidelines for OSMS from the Bulgarian Society For Dermatologic Surgery! Open Access Maced J Med Sci 2018; 18; 6(12):2369-72.

4. Tchernev G, Temelkova I, Stavrov K. One Step Melanoma Surgery (OSMS) without using ultrasonography for preoperative tumour thickness measurement? – "A question that sometimes drives me hazy: am I or are the others crazy!". Open Access Maced J Med Sci 2018; 6(6):1085-90.
5. Swetter S, Tsao H, Bichakjian C, et al. Guidelines of care for the management of primary cutaneous melanoma. J Am Acad Dermatol 2019; 80(1):208-50.
6. Bray F, Ferlay J, Soerjomataram I, Siegel R, Torre L, Jemal A. Global cancer statistics 2018: GLOBOCAN estimates of incidence and mortality worldwide for 36 cancers in 185 countries. CA Cancer J Clin 2018; 68(6):394-424.
7. WCRF International. Skin cancer statistics. Online available at https://www.wcrf.org/dietandcancer/cancer-trends/skin-cancer-statistics
8. Whiteman D, Green A, Olsen C. The growing burden of invasive melanoma: projections of incidence rates and numbers of new cases in six susceptible populations through 2031; J Invest Dermatol 2016; 136(6):1161-71.
9. Fellner C. Ipilimumab (yervoy) prolongs survival in advanced melanoma: serious side effects and a hefty price tag may limit its use. P T 2012; 37(9):503-30.
10. Oh A, Tran D, McDowell L, et al. Cost-effectiveness of nivolumab-ipilimumab combination therapy compared with monotherapy for first-line treatment of metastatic melanoma in the United States. J Manag Care Spec Pharm 2017; 23(6):653-64.
11. Hoffer E. America's Health Care System is Broken: What went wrong and how we can fix it. Part 4: The pharmaceutical industry. Am J Med 2019. pii: S0002-9343(19)30333-X.
12. Beasley D (Reuters). The cost of cancer: new drugs show success at a steep price. Online available at https://www.reuters.com/article/us-usa-healthcare-cancer-costs/the-cost-of-cancer-new-drugs-show-success-at-a-steep-price-idUSKBN1750FU.

LETTER TO THE EDITOR

PSEUDOVITELLIFORM MACULOPATHY SECONDARY TO BRAF AND MEK INHIBITORS IN A PATIENT WITH METASTASIC MELANOMA

C. ALBA-LINERO[1], C. ROCHA DE LOSSADA[1], AS. DELGADO-FERNÁNDEZ[1], M. JÓDAR-MÁRQUEZ[1], M. RODRÍGUEZ CALVO DE MORA[1] and MA. BERCIANO-GUERRERO[2]

[1]Ophthalmology Department, Hospital Regional Málaga, Plaza del Hospital Civil, Málaga, Spain; [2]Oncology Department. Hospital Regional Málaga, Málaga, Spain

Received March 4, 2109 – Accepted june 10, 2019

To the Editor,

Malignant melanoma is the seventh most common cancer worldwide and the main cause of skin cancer deaths. Sun exposition and type 1 phenotype are the major risk factors for this illness. Its incidence has been rising faster than other types of cancer in the last decade, but fortunately we have also seen the dawn of a new era in the treatment options available for patients with metastatic disease (1).

Combination regimens of BRAF inhibitors (BRAFi) and MEK inhibitors (MEKi) have improved clinical benefit. Combinations approved for the management of metastatic melanoma are cobimetinib plus vemurafenib (1) and dabrafenib plus trametinib (2). Treatment with BRAFi and MEKi can lead to serious iatrogenic responses such as rash, diarrhea or pyrexia (3). Ocular toxicity has been reported in clinical trials as serous retinopathy and, rarely, central vein occlusion or retinal detachment (3).

The aim of this report is to describe a case of a patient treated with the combination vemurafenib-cobimetinib who suffered ocular adverse effects and was under observation in our ophthalmology department. The patient read, understood and signed informed consent to participate in the study.

Clinical case

A 55-year-old man was diagnosed in 2013 of anteriorcervical intradermal nodular melanoma with liver metastasis. As it was positive for V600E mutation (gene BRAF), in October 2017, the patient started oral treatment with vemurafenib (960 mg oral administration) and cobimetinib (60 mg oral administration) in a continuous regimen.

The ophthalmologic examination carried out prior to the treatment did not reveal any alteration. During the first ophthalmologic examination, one month after the beginning of the treatment, the patient reported a slight decrease of his visual acuity with a feeling of blurred vision and metamorphopsia. Visual acuity was 20/25 (Snellen chart) in the right eye (OD) and 20/20 in the left eye (OS). Funduscopy exam revealed the presence of a yellowish deposit at foveolar level in both eyes that was rated as vitelliform material (Fig. 1). Optical Coherence Tomography (OCT) revealed a bilateral subfoveal neuroepithelial retinal detachment of 202 microns in OD and 167 in OS (Fig. 2). Together with the oncology department it was decided not to suspend the treatment and close observation of the patient.

During the second ophthalmologic examination,

Key words: neuroepithelial detachment; metastasic melanoma; BRAF inhibitors; MEK inhibitors; pseudovitelliform

Corresponding Author:
Carmen Alba Linero, MD, PhD
Ophthalmology Department ,
Hospital Regional Málaga,
Plaza del Hospital Civil, s/n 29009, Málaga, Spain
Tel.: +951290000
e-mail: carmen.alba.linero@gmail.com

0393-974X (2019)

3 months after the beginning of the treatment, the patient reported improvement in the symptoms. Visual acuity was 20/20 for both eyes. Slight alteration of the retinal pigment epithelium could be seen in the retinography.

The new OCT examination reported a neurosensorial detachment of 125 microns for OD and 150 microns for OS (Fig. 3).

DISCUSSION

New combination therapy of BRAFi and MEKi in metastatic melanoma has improved survival in this cohort of patients (4). One of the combinations used nowadays is cobimetinib plus vemurafenib, as in reported. Despite the benefit of this combination being well known, it is not exempted from systemic and ocular adverse events. The most described one is serous neuroepithelial detachment, and in severe cases, retinal vein occlusion (5).

Cancer, as a disease itself, can cause visual disturbances and affects up to 12% of patients (6). Retinopathy can also develop in patients with melanoma as an autoimmune complication (7). Opthalmologist advise is crucial to achieve a better management of this kind of patients and their possible complications. We report a clinical case of serous neuroepithelial detachment with pseudovitelliform macular deposit.

Optical coherence tomography is useful to detect and characterize the fluid distribution pattern and to distinguish it from corticosteroids-related subretinal fluid accumulation of central serous corioretinopathy (CSC), as glucocorticoids are often taken by oncologic patients, although sometimes it is necessary to carry out a fluoresceine angiography in case of doubt.

Serous detachment related to BRAFi and MEKi have different qualities, being multifocal, bilateral, not associated to retinal pigment epithelium (RPE) detachment and not necessarily dome-shaped, in contraposition of serous detachment in CSC (8).

Choroidal thickness was within normal range in our patients. This suggests that MEK inhibitor-induced serous detachments may not be associated with a pachychoroid phenotype, highlighting another distinction between CSC and MEKi-BRAFi serous detachment (9).

Other causes of pseudoviteliform deposition, such as choroidal folds, macular degeneration or chronic macular edema, should be ruled out as well as real vitelliform deposit secondary to retinal dystrophy.

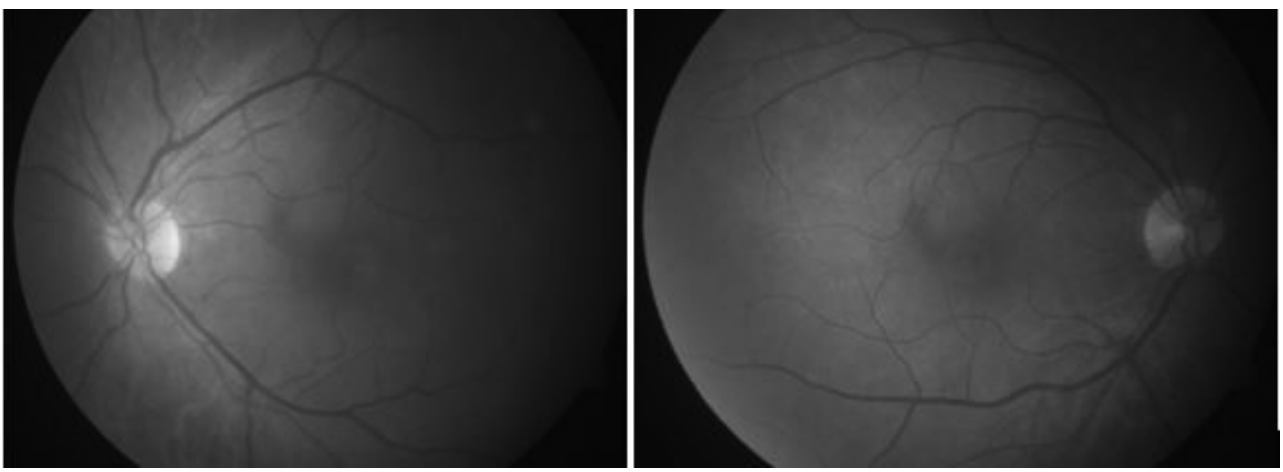

Fig. 1. *Fundus photography of OD and OS showing pseudovitelliform macular deposit.*

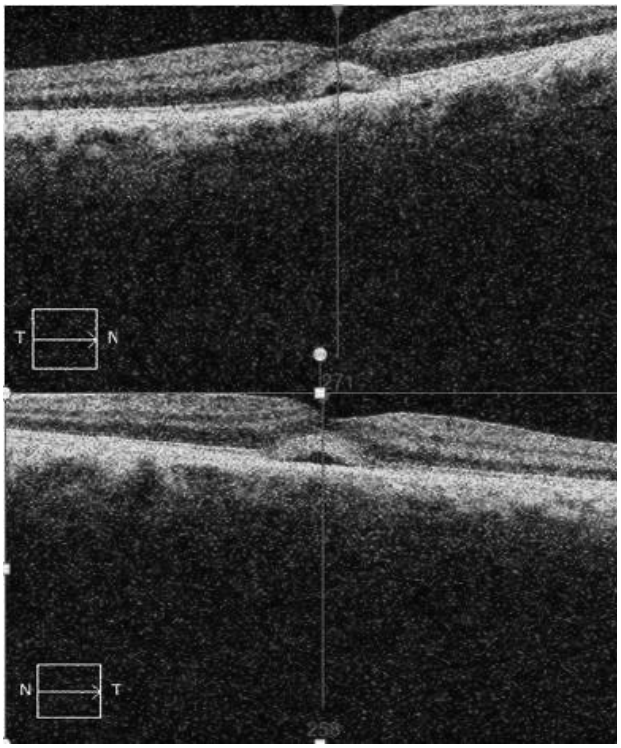

Fig. 2. *OCT of OD and OS in the first exam.*

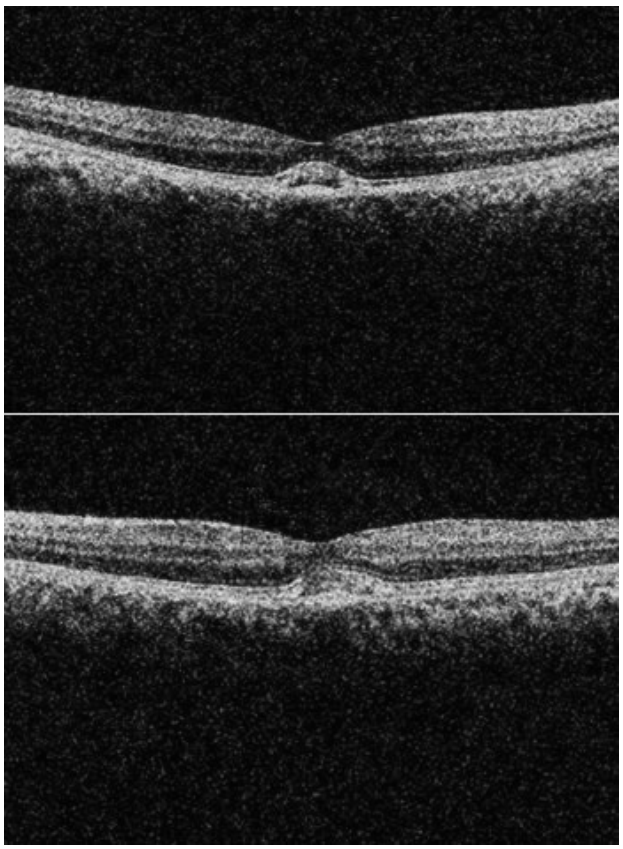

Fig. 3. *OCT of OD and OS in the second exam.*

In the trial by Stjepanovic (Phase 3, coBRIM or GO28141)**,** forty-nine percent (49%) of patients receiving the combination treatment experienced grade ≥2 CTCAE scale toxicity that occurred before study day 12 in 52% of patients and resolved after dose interruption, reduction or discontinuation of cobimetinib in 75% of the patients at the time of presentation of the results (10).

We agree with these results, as in our case, retinopathy was established 30 days after drug administration but we decided to continue with the treatment due to risk-benefit situation in our patient.

In our experience, as metastatic melanoma is a very aggressive neoplasia and new combined therapies of MEKi and BRAFi have changed survival prognosis, patients should be monitored, but it is not necessary to stop drug administration as these ocular adverse events are mild and usually reversible. A risk-benefit and an individualized decision must be taken.

Therapy expansion in oncology is just beginning. Clinicians should pay attention to detect new ocular adverse events and learn how to manage them properly.

REFERENCES

1. Ascierto PA, McArthur GA, Dreno B, et al. Overall survival with cobimetinib combined with vemurafenib in advanced BRAFV600-mutated melanoma: updated efficacy results from the phase 3, randomized coBRIM study. Lancet Oncol 2016; 17:1248-60.
2. Niro A, Strippoli S, Alessio G, Sborgia L, Recchimurzo N, Guida M. Ocular toxicity in metastatic melanoma patients treated with mitogen-activated protein kinase inhibitors: a case series. Am J Ophthalmol 2015; 6:959-67.
3. Robert C, Karaszewska B, Schachter J, et al. Improved overall survival inmelanoma with combined dabrafenib and trametinib. N Engl J Med 2015; 372(1):30-39.

4. Sullivan RJ, Weber JS, Patel SP, et al. A phase Ib/II study of BRAF inhibitor (BRAFi) encorafenib (ENCO) plus MEK inhibitor (MEKi) binimetinib (BINI) in cutaneous melanoma patients naive to BRAFi treatment. J Clin Oncol 2015; 33:90-97.
5. Singh P, Singh A. Ocular adverse effects of anti-cancer chemotherapy. J Cancer Ther Res 2012; 1:5.
6. Francis JH, Habib LA, Abramson DH, et al. Clinical and morthological characteristics of MEK inhibitore associated retinopathy differences from central serous chorioretinopathy. Ophthalmology 2017; 124(12):1788-1798.
7. Staurenghi G, Sadda S, Chakravarthy U, Spaide RF. Clinical and morphologic proposed lexicon for anatomic landmarks in normal posterior segment spectral-domain optical coherence tomography: the INSOCT consensus. Ophthalmology 2014:1572-78.
8. Jiang Q, Cao C, Lu S, et al. MEK/ERK pathway mediates UVB-induced AQP1 downregulation and water permeability impairment in human retinal pigment epithelial cells. Int J Mol Med 2009; 23:771-77.
9. Urner-Bloch U, Urner M, Stieger P, Frauchiger AL, Dummer R, Goldinger SM. Transient MEK inhibitor-associated retinopathy inmetastatic melanoma. Ann Oncol 2014; 25(7):1437-41.
10. Stjepanovic JP, Velazquez-Martin PL, Bedard. Ocular toxicities of MEK inhibitors and other targeted therapies. Ann Oncol 2016; 27:998-1005.

LETTER TO THE EDITOR

EXPRESSIONS OF CYCLOOXYGENASE 2 IN GASTROINTESTINAL STROMAL TUMORS

KH. TONG and J. QIAN

Department of Gastrointestinal Surgery, Yinzhou People's Hospital, School of Medicine, Ningbo University, Ningbo, Zhejiang, P.R. China

Received April 8, 2019 – Accepted May 22, 2019

To the Editor,

Gastrointestinal stromal tumor (GIST) is a common mesenchymal tumor of the digestive tract (1). GISTs mainly affect the stomach and small intestine, although rare cases ofhave also been observed in the esophagus and rectum (2). Cyclooxygenase (COX) is a rate-limiting enzyme involved in the synthesis of prostaglandins and can be divided into three subtypes: COX1, COX2 and COX3. COX2 is an inducible gene whose expression cannot be detected in most normal tissues under normal physiological conditions (3). COX2 participates in a variety of pathological processes and its synthesis is initiated upon stimulation. Dickens et al. found that COX2 was positively correlated with tumor malignancy and invasiveness (4). However, Herceg et al. found that the expression of COX2 in leiomyosarcoma is mainly limited to tumor cells around the necrotic tissues, and it was suggested that COX2 is not an effective target in the clinical therapy of leiomyosarcoma (5). Therefore, it remains controversial as to whether a correlation exists between the expression of COX2 and clinicopathological features of GIST. This study aimed to analyze the expression of COX2 in GIST to explore the relationship between the COX2 expression and clinicopathological features of GIST, thus providing a theoretical reference for the clinical treatment of GIST.

MATERIALS AND METHODS

Subjects

The wax blocks and clinical data of 68 GIST patients diagnosed at Yinzhou People's Hospital from June 2015 to January 2019 were studied. The gender, ages, and location and histological types of GIST were recorded. The morphology, arrangement, tumor necrosis, secondary changes, infiltration, and metastasis of GIST tumor cells were observed under an optical microscope. Informed consent was signed by all patients or their families and this study was approved by the Ethics Committee of Yinzhou People's Hospital.

Exclusion criteria: Patients with smooth muscle-derived tumor, neurogenic tumors, and gastric complications; those who were too old or too young; those with poor medical compliance.

GIST risk stratification

In accordance with the GIST risk stratification criteria recommended by the Chinese Society of Clinical Oncology (CSCO), the tumors (6) were divided into groups of extremely low risks (tumor size <2 cm, mitotic count <5/50 HPF, and any primary site of the tumor), low risks (tumor size <2.1-5 cm, mitotic count <5/50 HPF, and any primary site of the tumor), intermediate risks (tumor size ≤2.1-5 cm,

Key words: gastrointestinal stromal tumors; cyclooxygenase 2; immunohistochemistry; in situ hybridization histochemistry

Corresponding Author:
Dr Kehui Tong,
Departments of Gastrointestinal Surgery,
Yinzhou People's Hospital,
School of Medicine, Ningbo University,
Ningbo, Zhejiang, 315040, P.R. China
e-mail: kehuitong_nbyz@yeah.net

0393-974X (2019)

mitotic count ≤6-10/50 HPF, and the primary site of the tumor in the stomach; or tumor size ≤2 cm, mitotic count ≤6-10/50 HPF, and any primary site of the tumor; or tumor size ≤5.1-10 cm, mitotic count ≤5/50 HPF, and the primary site of the tumor in the stomach), and high risks (any tumor size, any mitotic count, and rupture of the tumor; or tumor size > 10 cm, any mitotic count, and any primary site of the tumor; or any tumor size, mitotic count > 10/50 HPF, and any primary site of the tumor; or tumor size > 2 cm and ≤ 5cm, any mitotic count, and non-primary gastric tumor; or tumor size > 5 cm and ≤ 10 cm, mitotic count ≤ 5/50 HPF, and non-primary gastric tumor) according to the maximum tumor diameter, mitotic count, location of primary tumor site, and presence of tumor rupture.

Immunohistochemistry staining

A 5μm-thick paraffin-embedded tissue section was cut and baked in a 65°C oven for 60 min, after which the section was dewaxed by xylene and hydrated by gradient alcohol. Then, the section was washed three times with PBS for 5 min each time. Afterwards, the section was dried and incubated with 3% H_2O_2 for 20 min at 37°C to block the activity of peroxidase. High-pressure heat repair of antigens was then performed using citric acid (PH 6.0). After the section was cooled to room temperature, it was washed three times with PBS for 5 min each time. Thereafter, the section was wiped dry, incubated again with 3% H_2O_2 for 20 min at 37°C, washed three times with PBS for 5 min each time, and blocked with goat serum at 37°C for 20 min. Subsequently, the section was wiped dry before 50 μL of primary antibody (CST Corporation, USA) was added dropwise onto the surface and incubated at 4°C overnight. The next day, the section was warmed to 37°C, washed three times with PBS for 5 min each time, dried again, and incubated at 37°C for 20 min with 50 μL (1:400) of secondary antibody added onto its surface. After three washes with PBS for 5 min each, the section was wiped dry, stained for 5 min with 50 μL of DAB working fluid, rinsed with tap water to terminate the staining reaction, counterstained with a ready-to-use hematoxylin solution for 1 min, rinsed with tap water for 3 min to terminate the reaction, differentiated by 0.1% hydrochloric acid alcohol for 1s , developed with 0.1% ammonia solution, dehydrated by gradient alcohol, cleared with xylene, sealed, and dried in the air. The staining result of the section was observed under an optical microscope using images of well-stained parts. The positive control of the two antigens was colon adenocarcinoma cells, and the positive markers were brown granular in cytoplasm and/or cell membrane. The corresponding positive control was set up in each test, and PBS was used as the blank control instead of primary antibody.

In situ *hybridization histochemistry*

The paraffin-embedded tissues were cut into 3 μm-thick sections and baked in a 65°C oven for 45 min (COX2 *in situ* hybridization kit, Tianjin Haoyang Biological Products Technology Co., China). After that, the section was dewaxed following the instructions and washed three times with PBS for 5 min each time. Next, the section was incubated at 37°C for 20 min with 50 μL of perforation solution (0.5% Tranton X-100) so that the probe (1.5'-GTC AAATCCCACACTCATACATACACCTCGG,2.5'-CAGAAGGGGATGCCAGTGATAGAGGGTGT TA) could penetrate the cell membrane. Then, the section was washed three times with PBS for 5 min each time, incubated at 37°C for 20 min with 3% H_2O_2, and then washed three times with PBS for 5min each time, and incubated at 37°C for 20 min with 50 μL of complex digestive working fluid (Protease K 100 μg, pepsin 2 mg, and EDTA Na4 10 mg were dissolved in 100 mL citric acid buffer). After washing with PBS three times for 5 min each time and rinsed with 0.2×SSC for 3 min, the section was wiped dry. Tissue slices were covered with 50 μL pre-hybridization working fluid, covered with glasses and sealed with rubber sealant (CST Company, USA) and incubated at 37°C for 2 h with 50 μL of pre-hybrid working fluid, washed three times with 0.2×SSC (saline sodium citrate) for 5 min each time at room temperature, wiped dry, and incubated at 37°C for 12 h with 50 μL of the hybrid working fluid. After incubation, the section was washed at 37°C with 2×SSC and PBS, incubated at 37°C for 45 min with 50 μL of mouse anti-digoxigenin biotinylated antibody working fluid, washed three

times with PBS (phosphate buffer saline) for 5 min each time, and incubated at 37°C for 45 min with high-sensitivity peroxidase streptavidin complex working fluid. Afterwards, the section was washed three times with PBS for 5 min each time, wiped dry, stained for 10 min with 50 μL of DAB working fluid (Dako REALTM EnVisionTM Detection System, Peroxidase/DAB+), and washed with tap water to terminate the staining reaction. Then, the section was counterstained for 1 min with the ready-to-use hematoxylin solution, rinsed with tap water for 3 min to terminate the staining reaction, differentiated by 0.1% hydrochloric acid alcohol for 1 s, rinsed with tap water, treated with 0.1% ammonia solution, dehydrated by gradient ethanol, cleared with xylene, sealed, and dried in the air. The staining result of the section was observed under an optical microscope (Suzhou Huiguang Technology Co., Ltd., China) using images of well-stained parts. The positive signal of COX2 gene expression was brown granular in the cytoplasm of the corresponding cells. In each experiment, oligonucleotide probe hybridization solution was used as the negative control.

Statistical analysis

The results were analyzed by SPSS 19.0 statistics software. Grouped data were examined by *Chi*-squared test. Ranked data were analyzed by Spearman-associated analysis. The significance of differences was checked by log-rank test. $P<0.05$ was considered statistically significant

RESULTS

Cytological classification

Microscopic results showed that GIST could be divided into three categories in accordance with the morphology of tumor cells: GIST dominated by spindle-shaped cells (Fig. 1A), GIST dominated by epithelioid cells (Fig. 1B), and GIST dominated by mixed cells (Fig. 1C).

Spindle cells were dominant. Tumor cells were short spindle or spindle, and arranged in interlaced bundles, spokes, whirlpools, herring bones, organ-like or pseudochrysanthemum-like clusters. Occasionally, palisade structures were observed, which were similar to schwannomas, and nuclear end vacuoles were often seen. In some cases, tumor cells were abundant and closely arranged. The mitotic figures were easily seen, and the changes of nuclear atypia were different. In a few cases, giant cells and multinucleated cells were found. Epithelioid cells were predominant: tumor cells were polygonal, nested, flaky or pseudoglandular, with clear, vacuolar or eosinophilic cytoplasm. Occasionally, nuclear deviation was seen, and the tumor cells resembled plasma cells. Mixed cell type: tumor cells were fusiform and epithelioid in part. Tumor cells in the very low risk group and low risk group were sparse, and their morphology and size were similar. The mitotic figures were absent or occasionally visible, and secondary changes were rare.

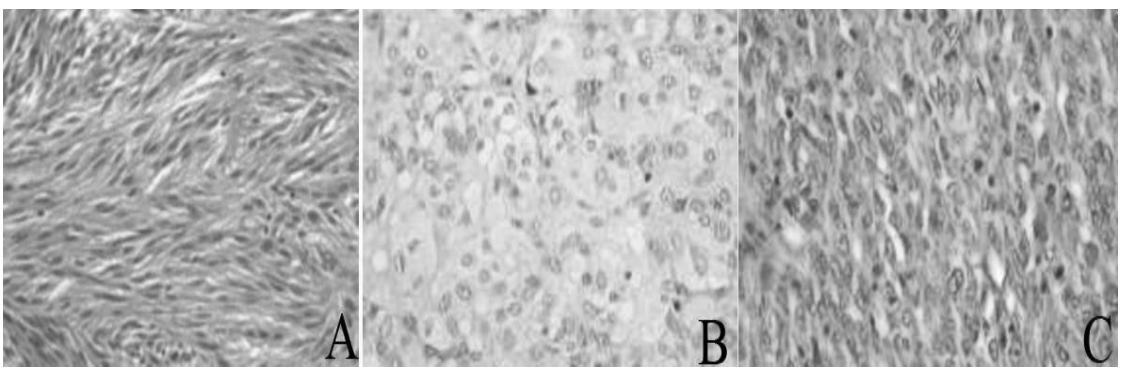

Fig. 1. *Cells of GIST.* ***A****) spindle-shaped cells;* ***B****) epithelioid cells;* ***C****) mixed cells.*

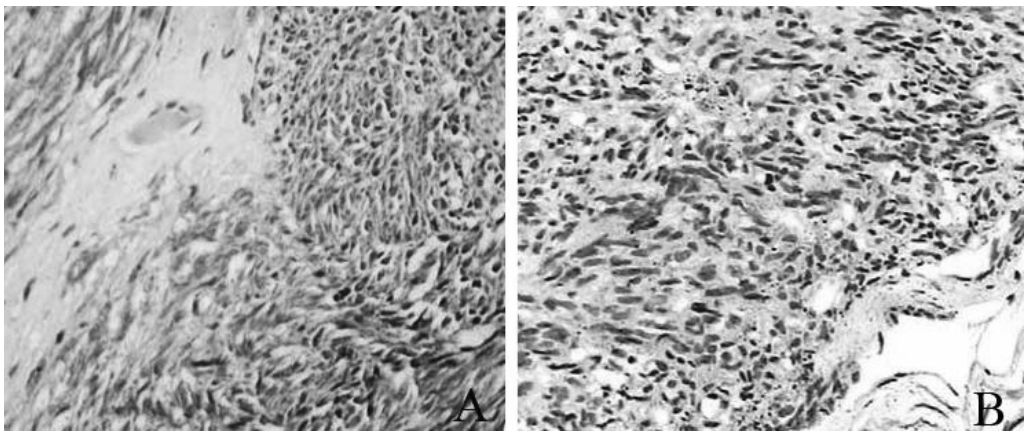

Fig. 2. *The COX2 expression in GIST.* ***A)*** *Strong positive expressions of COX2 in GIST;* ***B)*** *negative expressions of COX2 in GIST) (x200).*

Expression of COX2 and its correlation with clinicopathological features

Among the 68 tissue samples, the COX2 protein expression was positive in 56 cases (82.35%) and negative in 12 cases (17.65%) The strong positive expression of COX2 in GIST is shown in Fig. 2A, and the negative expression is shown in Fig. 2B. The expression of COX2 protein was significantly different among different risk groups of GIST ($P<0.05$). However, the expression of COX2 protein was not affected by age, gender, location or histological types of GIST ($P>0.05$) (Table I).

The rate of positive expressions of COX2 in the intermediate risk and high risk groups was higher than that in the groups of extremely low risk and low risk. Besides, the expression of COX2 was positively correlated with the risk stratification of GIST.

mRNA expression of COX2 and its correlation with clinicopathological features

Among the 68 GIST cases, COX2 mRNA was positively expressed in 52 cases and negatively expressed in 16 cases. The expression of COX2 mRNA was significantly different among different risk groups ($P<0.05$). With an increased level of risk, the positive rate of COX2 mRNA expressions also increased. In addition, the expression of COX2 mRNA was positively correlated with the risk stratification of GIST. Moreover, the expression of COX2 mRNA was not affected by age, gender, location or histological types of GIST ($P>0.05$) (Table I).

Analysis of the correlation between COX2 protein expressions and mRNA expressions

Among the 68 GIST cases, 47 cases were positive for both COX2 protein and mRNA expressions; 6 cases were positive for the COX2 mRNA expression only; 10 cases were positive for the COX2 protein expression only; and 5 cases were negative for COX2 protein and/or mRNA expressions. The correlation analysis showed that the expression of COX2 protein and mRNA in GIST was positively correlated ($P=0.015$).

DISCUSSION

Some GIST patients show symptoms of obstruction or compression, while other patients show symptoms of dysphagia if their GIST are located in the esophagus (7, 8). Studies have shown that the protein and mRNA expression of COX2 and vascular endothelial growth factor (VEGF) are increased in colorectal cancers and are of great

Table I. *The expression of COX2 in GIST and its correlation with clinicopathological features.*

Category			COX2 protein expression		P Value	COX2 mRNA expression		P Value
			-	+		+	- +	
Gender	Male		7	29	0.515	7	26	0.634
	Female		5	27		9	26	
Age	<55		5	29	0.183	6	25	0.226
	≥55		7	27		10	27	
Tumor site	Stomachs		10	34	0.102	13	30	0.158
	Intestines		2	16		2	13	
	Parenteral		0	6		1	9	
Histological type	Spindle-shaped cells		11	45	0.237	14	43	0.817
	Epithelioid cells		0	6		2	4	
	Mixed cells		1	5		0	5	
	Extreme	-	6			6		
	low risk	+	3			3		
	Low risk	++	2			1		
	Intermediate risk	+++	2			2		
	High risk							
	Extreme	-	2			6		
Risk stratification	low risk	+	6			4		
	Low risk	++	4			7		
Risk stratification	Intermediate risk	+++	7		<0.001	5		<0.001
Risk stratification	High risk							
	Extreme	-	1			2		
Risk stratification	low risk	+	1			3		
	Low risk	++	3			3		
	Intermediate risk	+++	5			2		
	High risk							
		-	3			2		
	Extreme	+	3			3		
	low risk	++	3			7		
		+++	17			12		

importance to the angiogenesis, invasion, and metastasis of colorectal cancer cells (9, 10). It is hypothesized that COX2 can affect the regeneration of tumor blood vessels through VEGF.

One study showed that COX2 is commonly expressed in GIST, especially in tissues with weak/focal positive expressions of CD117 or in tumors dominated by epithelioid cells (11). Thus, COX2 plays an important role in the differential diagnosis of GIST. This paper showed that the positive expression rates of COX2 protein and mRNA in GIST were 80.56% and 76.74%, respectively. In addition, the expression of COX2 protein and mRNA was significantly different among different risk groups of GIST, although the expression of COX2 protein and mRNA was not affected by gender, age, tumor site or histological type. This discrepancy could be caused by the small proportion of epithelioid cell-dominated GIST and mixed cell-dominated GIST in this research. Nevertheless, the positive rate of COX2 protein expression is higher than the positive rate of COX2 mRNA expressions in this study, which could be related to the type of tissue fixation, the duration of fixation, and the degradation of COX2 mRNA.

It was also found that COX2 can promote the occurrence and development of GIST. The correlation analysis showed that the expression of COX2 protein was positively correlated with the expression of COX2 gene. It was hypothesized that the expression of COX2 gene promoted the occurrence and development of GIST. Therefore, the results of this study indicated that there was a relationship between the expression of COX2 protein in GIST and the transfer of GIST.

REFERENCES

1. Kang G, Park YS, Jung ES, et al. Gastrointestinal stromal tumors in children and young adults: a clinicopathologic and molecular genetic study of 22 Korean cases. APMIS 2013; 121(10):938-44.
2. Shirahama T, Arima J, Akiba S, Sakakura C. Relation between cyclooxygenase-2 expression and tumor invasiveness and patient survival in transitional cell carcinoma of the urinary bladder. Cancer 2001; 92(1):188-93.
3. Morita Y, Hata K, Nakanishi M, Nishisho T, Yura Y, Yoneda T. Cyclooxygenase-2 promotes tumor lymphangiogenesis and lymph node metastasis in oral squamous cell carcinoma. Int J Oncol 2012; 41(3):885-92.
4. Dickens DS, Kozielski R, Khan J, Forus A, Cripe TP. Cyclooxygenase-2 Expression in Pediatric Sarcomas. Pediatr Dev Pathol 2002; 5(4):356-64.
5. Herceg ME, Tsiatis AC, Halpern JL, Holt GE, Schwartz HS, Keedy VL, Cates JM. Cyclooxygenase 2 Expression in Soft Tissue Leiomyosarcoma. Anticancer Res 2009; 29(8):2913-7.
6. He YL. [Consensus and controversy of surgical diagnosis and treatment for gastrointestinal stromal tumor]. Zhonghua Wei Chang Wai Ke Za Zhi 2013; 16(3):201-3.
7. Johnston FM, Kneuertz PJ, Cameron JL, et al. Presentation and management of gastrointestinal stromal tumors of the duodenum: a multi-institutional analysis. Ann Surg Oncol 2012; 19(11):3351-60.
8. Kitamura Y, Hirota S, Nishida T. Gastrointestinal stromal tumors (GIST): a model for molecule-based diagnosis and treatment of solid tumors. Cancer Sci 2003; 94(4):315-20.
9. Wu AW, Gu J, Li ZF, Ji JF, Xu GW. COX-2 expression and tumor angiogenesis in colorectal cancer. World J Gastroenterol 2004; 10(16):2323-6.
10. Choi J, Chang H. The expression of MAGE and SSX, and correlation of COX2, VEGF, and survivin in colorectal cancer. Anticancer Res 2012; 32(2):559-64.
11. Stewart AE, Heslin MH, Arch J, et al. Cyclooxygenase-2 Expression and Clinical Outcome in Gastrointestinal Stromal Tumors. J Gastrointest Surg 2006; 10(2):315-19.

LETTER TO THE EDITOR

PATHOLOGICAL MECHANISM OF FOCAL CEREBRAL ISCHEMIA AND REPERFUSION INJURIES IN MICE

Y. GAO, LL. WEN, X. YANG, J. WANG and J. FENG

No. 1 Department of Neurology, Shengjing Hospital Affiliated Hospital of China Medical University, Shenyang, Liaoning, China

Received April 1, 2019 – Accepted June 18, 2019

To the Editor,

Arteries are the major blood-supply of the brain and are vulnerable to cerebrovascular diseases (1). Stenosis and embolism of cerebral arteries are likely to cause cerebral ischemia. Both the incidence and mortality of patients with cerebral ischemia as well as the disability rate of those with cerebral ischemia reperfusion are high (2). Heat shock protein (HSP) is conserved in the process of biological evolution; once organs are stimulated by cerebral ischemia and hypoxia, the synthesis of HSP increases (3). It has been reported that Hsp60 is a mitochondrial matrix stress-inducing protein, which is important for the folding and functions of mitochondrial proteins (4, 5). Mitochondrial dysfunction is considered as an important factor in oxidative stress-induced cellular dysfunction. In addition, cerebral ischemia is strongly related to Hsp60 induction. Therefore, through exploring the changes of Hsp60 at different time points, the injury mechanism of cerebral ischemia could be further understood (6, 7). The thioredoxin peroxidase (Prxs) family is a newly discovered antioxidant protein family with antioxidant and ROS scavenging effects (8). In the Prxs family, Prx2 is an antioxidant enzyme found in recent years, which has anti-peroxidation and H2O2 regulation functions in cells. Over the years, studies have reported that Prx2 has protective effects on neurons induced by cerebral ischemia (9). However, the expression changes of Prx2 in the pathophysiological processes of neurological diseases and the reasons still need further clarification.

MATERIALS AND METHODS

Animals

For this study, 24 white mice (aged 8-10 weeks; weighing 240-290 g) were purchased from Shenzhen Feipeng Biological Co., Ltd., China. All the mice were maintained at a 12-h light-dark cycle at temperature of 22±2°C and humidity of 40-60%, permitted free access to food and water, and were allowed acclimatization for 1 week prior to intervention. All animal procedures were approved by the Animal Care Committee of Shengjing Hospital Affiliated Hospital of China Medical University.

Grouping

The 24 mice were randomly divided into two groups: an operated group and a sham-operated group, with 12 mice in each group. For each group, all parameters at 0, 6, 24 and 168 hours post-operation were observed and recorded. Three mice were required for each group from the biological repetition 2×4 groups, i.e., 2×4×3=24 mice. Reperfusion was given to mice 2 h after the threads were successfully inserted into the arteries.

Key words: cerebral ischemia; reperfusion injury; Hsp60 protein; Prx2 protein

Corresponding Author:
Dr Juan Feng,
NO.1 Department of Neurology,
Shengjing Hospital Affiliated Hospital of
China Medical University, No.36 Sanhao Street,
Heping District, Shenyang, 110004, Liaoning, China
e-mail: fengjuanyisheng99@163.com

0393-974X (2019)

Establishment of animal models with focal cerebral ischemia and reperfusion injuries

All mice were fasting 12 h before the operation. Isoflurane (Sigma-Aldrich, St. Louis, MO, USA) was utilized to anesthetize the mice; after the mice were successfully anesthetized, the inlet was switched to 2% v/v isoflurane and 98% v/v oxygen. The modified Longa's method was applied to establish the MCAO/R model.

After the mice were successfully anesthetized, they were placed in a supine position, in which their head and limbs were fixed to the operation table; thefur in the abdominal side of the neck was shaved, and then the skin was disinfected. For each mouse, the central part of the neck was cut vertically to observe the carotid artery. The superficial cervical fascia was separated from the intermuscular space of digastric, sternocleidomastoid, and omohyoid, and then along with the internal carotid artery to the area of the skull base, and a single branch of the carotid artery was separated from the internal carotid artery and ligated. At the carotid artery, the proximal part, the distal part, and the part between the proximal part and distal part of the right common carotid artery were reserved with 5-0 thread for pulling and ligation. A small cut was made between the proximal part and distal part of the right common carotid artery, and then asilica gel-covered nylon thread was inserted into the root of the internal carotid artery. The inserted part of the thread was 20±2 mm in length. After insertion, the wound was quickly sutured, and the tail of the thread was left outside the body. The operative time was shortened to attenuate postoperative damage to the animals.

Additionally, 2 h after operation, the mice were again anesthetized with 3% isoflurane and 97% oxygen; then, the thread was gently pulled out of the mice for blood reperfusion.

Model validation

Laser Doppler flowmeter (Perimed AB, Järfälla, Sweden) was adopted to validate the models. This instrument could measure the perfusion value with relatively open wounds (approximately 1-3 mm) of the mice. The time nodes of measurement were adopted respectively before ischemia, after ischemia, and after reperfusion.

The cerebral perfusion values of the mice were also accurately measured. If the perfusion value measured after the operation decreased within 30% compared with before the operation, the ischemia operation was successful, that was the precondition of ischemic neuronal injuries. After reperfusion, if the blood perfusion value increased to 60% of that before the operation, the perfusion experiment was successful since no proof of bleeding in skull base surgery was found. If the mice models of cerebral ischemia/reperfusion injuries made by Longa's Method failed to meet the aforementioned two criteria, they were not allowed to be used in following stages of research.

Detection of physiological parameters

A mouse was put on the blanket with constant temperature (37ºC) and its body temperature was measured continuously with a rectal thermometer. During the operation, PowerLab data acquisition system (ADInstruments, Dunedin, New Zealand) was utilized to measure the electrocardiogram and heart rate (HR) of the mice in real-time. An animal pulse oximeter was applied to measure the oxygen saturation (SpO_2) and respiratory rate of the mice. Then, neurological assessment of recovery was carried out. This assessment system had 5 levels: 0, normal and no neurological deficiency; 1, the left front claw of the mouse was unable to stretch normally; 2, the mouse turns towards its paralyzed side during walking; 3, the mouse falls towards its paralyzed side during walking, demonstrating severe neurological deficiency; 4, the mouse cannot walk spontaneously or loss of consciousness.

Protein extraction

After neurological assessment, 5% sodium pentobarbital solution (40 mg/kg) (Sigma-Aldrich, St. Louis, MO, USA) was injected into the mice intraperitoneally. When the mice were deeply anesthetized, the abdomen was immediately opened. The right auricle was cut till blood splashed out and phosphate-buffered saline (PBS; 60-90 mL 4ºC) was injected. The volume of injected PBS depended on the observation of the eyes, lungs, front claws, etc. of the mice; if the aforementioned organs of the mice became white then the PBS injection was stopped. Next, the brain tissues were obtained through craniotomy.

Western blotting

During the first experiment, the regular Western

blotting was carried out. For this purpose, experimental conditions and procedures remained unchanged.

Sodium dodecyl sulfate polyacrylamide gel electrophoresis (SDS-PAGE)

SDS-PAGE was performed to detect the cerebral proteins of mice. When the process was completed, the well-exposed films were put under the gel imaging system for taking photos and image analysis. Each set of experiments was repeated at least 3 times.

The most appropriate gel system obtained from the experiment above was applied in electrophoresis of the cerebral proteins of the mice, and the SDS-polyacrylamide gel was prepared (4.2%-17.85% linear gradient, 5% crosslinking degree, and 0.5%-1%w/v SDS).

Sample preparation: The volume of protein samples was 20μg. 12.6μg/μL of mouse cerebral tissue proteins were added into 50 mM of sample buffer, and the volume of samples was added to 20 μL with Milli-Q water; afterward, the sample was boiled for 5 min in 95°C water. Protein marker: The volume of the sample was 4 uL.

SDS-polyacrylamide gel preparation: The glass plates were washed and dried for reservation. The stacking gel was prepared. After gel production, solution was formulated, and the separation gel was prepared. 4.5 mL of the gel were poured downwards perpendicular to the glass plates, sealed with Milli-Q water, and stood for 30 min. If the gel was totally solidified, there was an obviously broken line between the water layer and the gel layer. The water was slowly poured out, and the gel was dried with a filter paper. Then, the stacking gel was added, and the 1-mm-thick comb was inserted. After the gel was solidified, the comb was taken out. The PAGE device was installed in the electrophoresis tank, and 20 μL of the above-mentioned protein samples and 4 μL of protein markers were added to the corresponding lane of PAGE gel by a 20 μL pipette. The power was established, and the stacking gel underwent electrophoresis at 60V voltage. Once the protein was stacked onto the separation gel for separation, the voltage was switched to 80V; the electrophoresis was terminated until the bromophenol blue line ran to the bottom of the gel plate. The gel plate was gently unclenched, and the stacking gel was removed. The separation gel was placed into a box with 10 mL of staining solution and stained for 15 min. Then, the staining solution was discarded, and the staining box was added with 15 mL of destaining solution and destained for 30 min. Afterward, the used destaining solution was replaced with another 15 mL of destaining solution and the gel was destained for 90 min. Finally, the destaining solution was discarded, and the gel was added with 15mL of hydrating solution and hydrated for 30min. The gel was placed into a plastic bag and sealed with an appropriate hydrating solution. Then, the gel was scanned under the resolution of 600dpi. When the electrophoresis was finished, the well-exposed films were put under the gel imager for photo-taking and image analysis. Each set of experiments was repeated at least 3 times.

Statistical analysis

SPSS 15.0 statistical software (IBM, Armonk, NY, USA) was used for data analysis. The normally distributed quantitative data were expressed as mean ± standard deviation (SD). Intra-group comparisons were made by independent-samples *t*-test or rank-sum test. Inter-group comparisons were conducted by *chi*-squared test.

RESULTS

Values of cerebral perfusion for mice

Fig. 1, A and B show the cerebral perfusion values detected before ischemia, after ischemia, and after reperfusion of the mice in the sham-operated group and operated group, respectively. As shown in Fig. 1A, the trend in the sham-operated group was stable, while fluctuation was observed in the operated group, indicating the high credibility of the results.

Fig. 1A showed the cerebral perfusion values which were respectively detected before ischemia, after ischemia, and after reperfusion of mice in the sham-operated group. Fig. 1B shows the cerebral perfusion values which were respectively detected before ischemia, after ischemia, and after reperfusion of mice in the operated group. It was inferred, as seen in Fig. 1A, that the perfusion variation of the sham-operated group was stable, and that of the MCAO/R group was extremely obvious, indicating the high credibility of the results. As seen in Fig. 1B, in the sham-operated group, there were few changes in the occupation ratio of cerebral perfusion attention amount in basic values during the three periods. However, the same ratio of the operated group fluctuated obviously after ischemia and perfusion.

Physiological parameters

The results showed that all these physiological parameters were approximately in the normal ranges as follows: HR, 350-450; oxygen saturation, 99-99.9%; respiratory rate, 60-70; and body temperature, 36.5-37.5; there was no significant difference between physiological parameters in the operated group and sham-operated group. During the operation, no significant differences in physiological parameters were found, indicating that the mice in both groups were comparable.

Neurological assessment

The assessment process was carried out with respect to the criteria 2 h after the ischemia. The assessment result after 0/6/22/168 hours revealed 0 points for the sham-operated group, while after 0/6/22/168 hours, 0 points, 3±0.4 points,

Table I. *Ethological scores of mice after reperfusion following ischemia for different periods.*

Reperfusion at 2 h after ischemia/h	0 h	6 h	22 h	168 h
Scores of the sham-operated group	0	0	0	0
Scores of the operated group	0	3±0.4	3.4±0.6	3.1±0.4

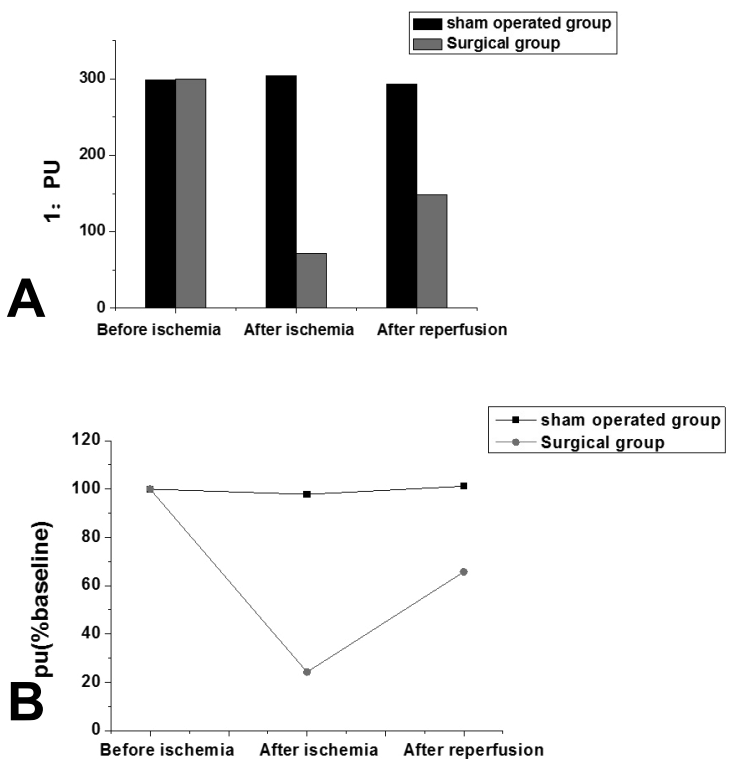

Fig. 1. *Variations of the preoperative and postoperative cerebral perfusion values. **A)** Cerebral perfusion values before ischemia, after ischemia, and after reperfusion in the sham-operated group and operated group; **B)** Variations in the values of cerebral perfusion in the operated group and sham-operated group*

3.4±0.6 points, and 3.1±0.4 points were indicated, respectively, for the operated group (Table I).

Western blotting of cerebral proteins

The experimental results of Western blotting are shown in Fig. 2. It was observed that, given the conditions of 5%T, 2.6%C stacking gel-15%T, and 2.6%C separation gel, the separation effects of markers were preferable; however, the cerebral protein samples were not well separated. In addition, the separation effects of markers were preferable but the protein samples were still not well separated (Fig. 2B)., It was observed that, given the conditions of the SDS-PAGE system of 4.2%-17.85T (linear

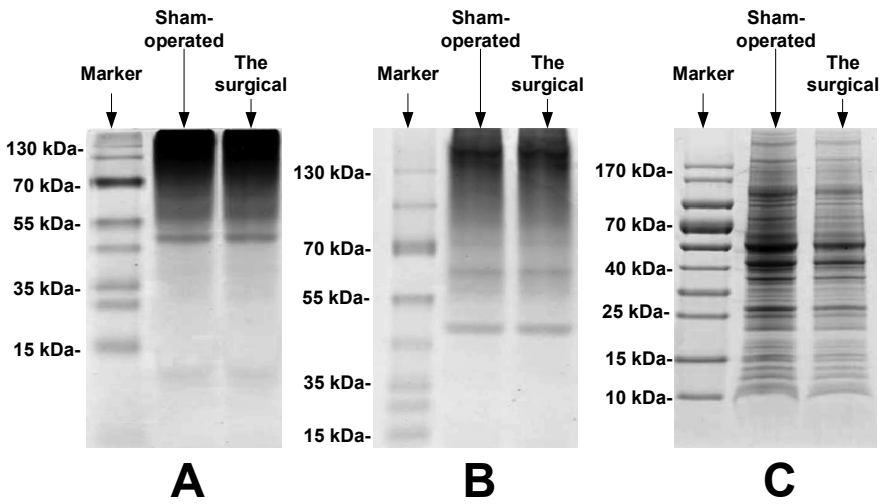

Fig. 2. *Results of electrophoresis. **A)** Image of cerebral protein CBB staining using 5%T, 2.6%C stacking gel-15%T, and 2.6%C separation gel. **B)** Cerebral protein stained using 5%T, 2.6%C stacking gel-10%T, and 2.6%C separation gel. **C)** SDS-PAGE cerebral protein CBB stained using 4.2-17.85% T (linear gradient), and 5% C (crosslinking degree)*

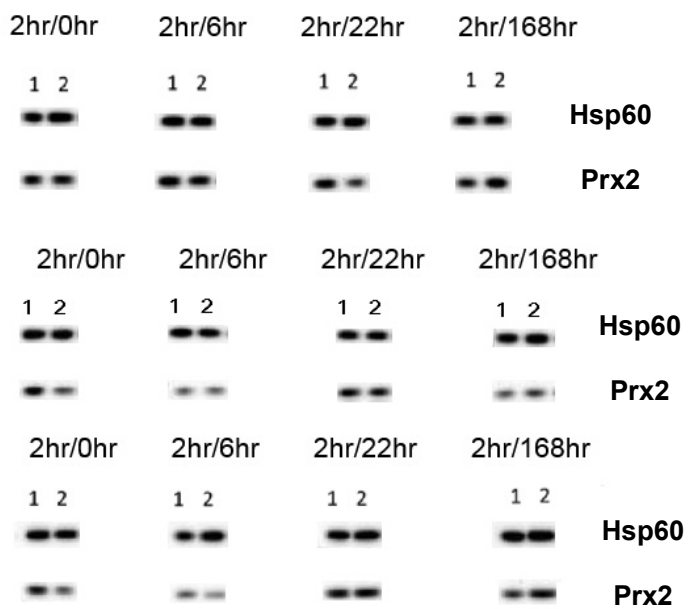

Fig. 3. *Hsp60 and Pxr2 ribbon diagrams for the sham-operated group and operated group at different time points after reperfusion (1 indicated the sham-operated group, and 2 represented the operated group).*

gradient) and 5%C (degree of crosslinking), both the marker and the cerebral protein samples were well separated (Fig. 2C).

The effects of oxidative stress on proteins in cerebral ischemia

As shown in Fig. 3, the first and the second lanes expressed the sham-operated group and the operated group, respectively. The horizontal axis represented the duration of ischemia/reperfusion. The expression levels of Hsp60 declined, which reduced the stress responses of brain tissues. However, increased expression levels of Prx2 significantly enhanced the antioxidation effect after cerebral ischemia, protecting brain tissues from massive generation of free radicals.

DISCUSSION

Prx2 is a strong antioxidant (10), protecting cells from oxidative stress responses and apoptosis. The over-expression of Prx2 effectively reduces damage to the brain caused by cerebral ischemia. The decreased Prx2 protein expression indicated damage of cerebral ischemia reperfusion injury. Therefore, Hsp60 and Prx2 are significant in oxidative stress responses and antioxidation reactions (11). In this study, the models of mice with focal cerebral ischemia and reperfusion injuries were successfully established and validated. It was revealed that the expression level of Hsp60 increased after ischemia, which is an important criterion for damage to brain tissues after cerebral ischemia.

It has been found that the fat content of brain tissues was extremely high. The cerebral proteins were surrounded by fat, contributing to higher measured volume compared to the theoretical volume (12). In this research, the Western blotting results indicated that in the mono-concentration gel, the marker could be well separated, but the separation results of cerebral protein samples were unsatisfactory. In the gradient SDS-PAGE separation system, both the marker and the cerebral protein samples were well separated. Thus, the results of this paper were basically consistent with previous studies (12).

There were several limitations in this study that can be eliminated through adding sample sizes in the future studies. The individual difference of subjects was relatively obvious; cerebral ischemia and variations after reperfusion were relatively different.

In summary, the research on focal cerebral ischemia and reperfusion injuries in mice is of great significance, providing a reference for its clinical application on humans

ACKNOWLEDGEMENT

This work was supported by The National Nature Science Foundation of China (NSFC; NO.81771271).

REFERENCES

1. Han JQ, Liu CL, Wang ZY, Liu L, Cheng L, Fan YD. Anti-inflammatory properties of lipoxin A4 protect against diabetes mellitus complicated by focal cerebral ischemia/reperfusion injury. Neural Regen Res 2016; 11(4):636-40.
2. Yamato M, Shiba T, Yamada K, Watanabe T, Utsumi H. Separable detection of lipophilic and hydrophilic phase free radicals from the ESR spectrum of nitroxyl radical in transient MCAO mice. Free Radic Res 2009; 43(9):844-51.
3. Lou J, Cao G, Li R, Liu J, Dong Z, Xu L. β-Caryophyllene attenuates focal cerebral ischemia-reperfusion injury by Nrf2/HO-1 pathway in rats. Neurochem Res 2016; 41(6):1291-304.
4. Zhang X, Xue X, Zhao J, Qian C, Guo Z, Ito Y, Sun W. Diosgenin attenuates the brain injury induced by transient focal cerebral ischemia-reperfusion in rats. Steroids 2016; 113:103-12.
5. Ikeda S, Harada K, Ohwatashi A, Kamikawa Y. Effects of Edaravone, a free radical scavenger, on photochemically induced cerebral infarction in a rat hemiplegic model. ScientificWorldJournal 2013; 2013:175280.
6. Qian GQ, Peng X, Cai C, Zhao GP. Effect on eNOS/NO Pathway in MIRI rats with reconditioning of GFPC from Dang Gui Si Ni decoction. Pharmacognosy Res 2014; 6(2):133-37.
7. Zhang Q, An R, Tian X, et al. β-Caryophyllene Pretreatment Alleviates Focal Cerebral Ischemia-Reperfusion Injury by Activating PI3K/Akt Signaling

Pathway. Neurochem Res. 2017; 42(5):1459-69.
8. Huang Q, Li C, Xia N, Zhao L, Wang D, Yang Y, Gao H. Neurochemical changes in unilateral cerebral hemisphere during the subacute stage of focal cerebral ischemia-reperfusion in rats: an ex vivo 1 H magnetic resonance spectroscopy study. Brain Res 2018; 1684:67-74.
9. Chen J, Yang C, Xu X, Yang Y, Xu B. The effect of focal cerebral ischemia-reperfusion injury on TLR4 and NF-κB signaling pathway. Exp Ther Med 2018; 15(1):897-903.
10. Stvolinsky SL, Fedorova TN, Devyatov AA, Medvedev OS, Belousova MA, Ryzhkov IN, Tutelyan VA. A neuroprotective action of carnosine in conditions of experimental focal cerebral ischemia-reperfusion. Zh Nevrol Psikhiatr Im S S Korsakova 2017; 117(12):60-64.
11. Qi W, Zhou F, Li S, et al. Remote ischemic postconditioning protects ischemic brain from injury in rats with focal cerebral ischemia/reperfusion associated with suppression of TLR4 and NF-κB expression. Neuroreport 2016; 27(7):469-75.
12. Li Z, Fang F, Wang Y, Wang L. Resveratrol protects CA1 neurons against focal cerebral ischemic reperfusion-induced damage via the ERK-CREB signaling pathway in rats. Pharmacol Biochem Behav 2016; 146-147:21-27.

LETTER TO THE EDITOR

CLINICAL ASSESSMENT OF PATIENTS WITH SEVERE CORONARY ARTERY DISEASE TREATED WITH YIQI TONGLUO

XQ. YANG[1*], CL. DU[2*], W. WANG[1], Z. LIU[1], YR. DONG[1], QM. FENG[1] and LP. YAO[3*]

[1]Shanghai municipal Hospital of Traditional Chinese Medicine, Shanghai University of Traditional Chinese Medicine, Shanghai, China; [2]Zhenxin Community Health Service Center, Jiading, Shanghai, China; [3]Department of Cardiothoracic Surgery, Xinhua hospital Affiliated to Shanghai Jiaotong University School of Medicine, Shanghai, China

Received January 9, 2019 – Accepted June 26, 2019

[*]These Authors contributed equally to this work

To the Editor,

Coronary artery disease (CAD) causes 1/4 of all deaths, and 30% of CAD patients are not suitable for coronary artery bypass grafting due to severe pathologies in their coronary arteries (1, 2). Since the aging population is growing rapidly and the number of such CAD patients is positively correlated with increasing age (3), new therapies are needed. Traditional Chinese medicine (TCM) is effective for CAD patients and has few side effects, thus improving the long-term quality of life (4).

CAD is categorised as 'chest obstruction with pain' in TCM, which involves the heart, kidney, Qi, blood, arteries, veins, phlegm and stasis. The TCM Yiqi Tongluo (YQTL) compound is for treatment of severe CAD with Qi-deficiency and blood-stasis (QDBS) syndrome, and its main therapeutic components are Isoflavones and saponins. In the compound, *Astragalus* invigorates Qi and nourishes blood. *Ligusticum chuanxiong* hort, *Prunus persica* (L.) Batsch, *Eupolyphaga sinensis* and *Scirpus fluviatilis* promote blood circulation. *Ramulus Cinnamomi* dredges the meridians (TCM states that the human body contains a network of meridians which transport Qi and blood around the body). *Rehmannia glutinosa*, and *Epimedium brevicornum* Maxim have an anti-inflammatory effect on the kidneys and replenish the Jing (Jing is loosely translated as 'Essence', a substance stored in the kidneys). *Trichosanthes kirilowii* and *Pinellia ternata* relieve chest congestion and reduce phlegm. *Aurantii Trifoliata* Fructus, *Ostrea gigas Thunberg* and *Prunella vulgaris* soften and break down lumps. We previously found that combination of YQTL and Western medicine improved ventricular remodeling and left ventricular diastolic function in patients with CAD and three-vessel disease (5), however less is known about the efficacy of YQTL for patients with severe CAD and QDBS syndrome.

We, therefore, investigated the effects of YQTL on angina pectoris, Nitroglycerin/ heart-protecting musk pill (HMP) dosage and TCM QDBS syndrome scores in patients with severe CAD and QDBS syndrome.

MATERIALS AND METHODS

The present study was approved by the Ethics

Key words: severe coronary artery disease; Yiqi Tongluo formulation; Qi-deficiency and blood-stasis syndrome

Corresponding Author:
Qi-Mao Feng, PhD,
Shanghai Municipal Hospital
of Traditional Chinese Medicine,
No. 274 Zhijiang Road,
Jing'an District, Shanghai 200071, China
e-mail: qimao_guo337@163.com

0393-974X (2019)

Committees of Shanghai Municipal Hospital of Traditional Chinese Medicine, Shanghai Changzheng Hospital, and Jingan District Hospital of Traditional Chinese Medicine. An informed consent was obtained from all patients. The present study enrolled a total of 155 patients with severe CAD and QDBS syndrome who were not suitable for coronary stent placement and/or coronary artery bypass grafting. These patients were admitted to the above-mentioned three clinical research centers or cardiology outpatient clinics. All participating patients were randomly divided into two groups: a treatment group and a control group. These two groups were comparable (Table I), and the difference in gender, age, height, weight, smoking history, course of disease, medication, and distribution of complications was not statistically significant ($P \geq 0.05$, Table I).

Inclusion criteria

According to the diagnostic criteria for severe CAD in China's Guidelines for Percutaneous Coronary Intervention (2012) (6), severe CAD is diagnosed when coronary computed tomography (CT) or angiography

Table I. *General information.*

Item	Treatment group	Control group	Statistical value	P-value
Male/Female	40 (53.3%)/35 (46.7%)	30 (40.0%)/45 (60.0%)	1.433	0.231
Age (years old)	67.23±8.58	67.94±8.43	-0.441	0.659
Height (cm)	163.74±7.63	163.29±8.00	-0.182	0.855
Body weight (kg)	68.69±7.77	70.60±8.28	-1.277	0.193
Smoking history (years)	16.86±11.83	14.00±11.68	-0.976	0.329
Course of disease (years)	5.37±1.11	5.63±0.81	-0.685	0.493
Antiplatelet drug				
Aspirin	70 (93.3%)	66 (88.0%)	-0.848	0.397
Clopidogrel	6 (8.0%)	11 (14.6%)	-0.746	0.456
Antihypertensive drugs				
β-blockers	11 (14.6%)	15 (20.0%)	-0.630	0.529
ACEI	32 (42.7%)	34 (45.3%)	-0.238	0.812
ARB	42 (56.0%)	40 (53.3%)	-0.241	0.810
CCB	40 (53.3%)	40 (53.3%)	0.000	1.000
Diuretics	12 (16.0%)	14 (18.7%)	-0.305	0.760
Statins	16 (21.3%)	20 (26.7%)	-0.543	0.587
Nitrates	28 (37.3%)	30 (40.0%)	-0.241	0.810
Complications				
Hypertension	75 (100.0%)	75 (100.0%)	0.000	1.000
Hyperlipidemia	16 (21.3%)	20 (26.7%)	-0.543	0.587
Cardiac insufficiency	30 (40.0%)	32 (42.7%)	-0.239	0.811
Diabetes	8 (10.7%)	14 (18.7%)	-0.978	0.328

Data compared using the χ^2 test and Wilcoxon Rank-Sum Test.
ACEI, angiotensin converting enzyme inhibitor; ARB, angiotensin receptor blocker; CCB, calcium channel blocker

indicates moderate stenosis in the left anterior descending (LAD) coronary artery, left circumflex coronary artery, and triple-vessel right coronary artery. In addition, there should be at least one blood vessel with stenosis of more than 75%. Patients were only included when both cardiology and cardiac surgical diagnoses demonstrated that he/she was not suitable for coronary stent placement or coronary artery bypass grafting, or both the patient and his/her family did not consent to coronary stent placement or coronary artery bypass grafting.

According to the diagnostic criteria for QDBS syndrome in The Guidelines for Clinical Research of New TCM Drugs (2002) (7), the primary symptom is chest pain, and secondary symptoms include chest tightness, palpitations, shortness of breath, lassitude, dark purple-colored tongue, and weak yet astringent pulse. A patient who has the primary symptom and at least two of the secondary symptoms listed above can be diagnosed with QDBS syndrome.

Only patients who met these criteria were recruited. Male and female patients who were 40–80 years old, diagnosed with QDBS syndrome by TCM, and were willing to receive treatment with the consent of their families for at least three months with regular follow-ups were included in the study. Furthermore, these patients were not participating in any other concurrent clinical trials for TCM or Western medicine.

Exclusion criteria

The present study employed the following exclusion criteria: patients <40 or >80 years old; patients with class IV cardiac function or pulmonary edema; patients with severe liver and/or kidney dysfunction; patients with TCM intolerance; patients with concurrent malignant diseases; patients with concurrent severe inflammatory diseases; patients with concurrent hemorrhagic disease; patients with concurrent acute coronary syndrome (ACS); patients who participated in other clinical trials within the previous month; pregnant or lactating women.

Therapeutic methods

Patients in the control group were treated using the standard treatment regimens recommended by the Guidelines for the Diagnosis and Treatment of Coronary Heart Disease (8), depending on the patient's condition. The standard treatment regimens included, but were not limited to, antiplatelet drugs, antihypertensive drugs, nitrates, statins.

Patients in the treatment group, in addition to the treatment received by subjects in the control group, were administered the granulated YQTL compound once a day. The granules were dissolved in 300 mL of boiling water, and 150 mL was given each morning and night. The compound included *Astragalus*, *Ligusticum chuanxiong* Hort, *Prunus persica* (L.) Batsch, *Eupolyphaga sinensis*, *Scirpus fluviatilis*, *Typha angustifolia* L., *Ramulus Cinnamomi*, *Aurantii Trifoliata* Fructus, *Cornu Cervi* Pantotrichum, *Rehmannia glutinosa*, *Epimedium brevicornum* Maxim., *Trichosanthes kirilowii* Maxim., *Allium macrostemon*, *Pinellia ternata*, *Ostrea gigas* Thunberg, *Prunella vulgaris*. All granules mentioned above were obtained from E-FONG Pharmaceutical Corp. (Guangzhou, China).

Observational indicators

All patients filled-in the Angina Pectoris Score Sheet (9), Nitroglycerin/HMP Dosage Sheet, and TCM QDBS Score Sheet (7) before the treatment, and at one month and three months post-treatment.

Statistical analyses

In collaboration with the Center for the Study of Clinical Drug Trials (Shanghai University of Traditional Chinese Medicine), a database was established using the electronic clinical trial management system, and statistical analyses were performed using SPSS 18.0 software. Continuous data were presented as the mean and standard deviation, and compared using Wilcoxon rank-sum test. Categorical variables were presented as number of cases (percentages), and compared using *chi*-squared test. Repeated measurement data were subjected to repeated measures analysis. All results were considered statistically significant at $P \leq 0.05$.

RESULTS

In the present study, 150 patients completed the follow-ups, while five patients were lost to follow-up. None of the patients experienced severe adverse reactions; three patients experienced stomach discomfort and nausea, and two patients had diarrhea. All symptoms were alleviated after stopping treatment upon completion of the follow-up.

Comparison of angina pectoris scores

The comparisons of angina pectoris scores before and after treatment are shown in Table II. It was found that the angina pectoris in the treatment group was alleviated in terms of the number of episodes, duration, pain level and total score, which gradually decreased over time. Furthermore, the effect of the treatment became more significant three months after treatment. The difference between the treatment and the control groups was statistically significant ($P \leq 0.05$).

Comparison of nitroglycerin/HMP dosage

The comparison of nitroglycerin/HMP dosage at pre- and post-treatment is shown in Table II. It was revealed that the nitroglycerin/HMP dosage in the treatment group gradually decreased over time. Furthermore, therapeutic efficacy became more significant at three months post-treatment. The difference between the treatment and control groups was statistically significant ($P \leq 0.05$).

Comparison of TCM syndrome scores

The comparison of TCM syndrome scores before and after the treatment is shown in Table II. It could be observed that the TCM syndrome score in the treatment group improved. Furthermore, the scores for chest pain, chest tightness, shortness of breath, palpitations and lassitude, and the total score of the treatment group gradually decreased over time. Furthermore, treatment efficacy became more significant at three months after treatment. The difference between the treatment group and the control group was statistically significant ($P \leq 0.05$).

DISCUSSION

We found that combination of YQTL with standard Western medicine therapy significantly improved TCM QDBS syndrome, angina pectoris and nitroglycerin/HMP dosage in patients with severe CAD and QDBS syndrome and was better than standard Western medicine treatment alone. Furthermore, its effect was more significant over a prolonged period of treatment.

Severe CAD is a chronic disease with specific symptoms, including the conventional 'chest pain'. Its root causes can include a Qi deficiency, blood circulation problems, and an imbalance of yin and yang and less severe symptoms can consist of Qi stagnation, a build-up of phlegm, and blood stasis. Moreover, most patients are elderly, leading to frequent complications with a deficiency of Qi and Jing in the kidney. Based on the complicated pathogenicity, we created YQTL compound. It replenishes Qi and coordinates the kidney, promotes blood circulation, invigorates Qi, relieves chest stuffiness and resolves phlegm and lumps. Modern pharmacology (10-12) demonstrated that the effectively active components of *Astragalus*, *Ligusticum chuanxiong* hort and *Rehmannia glutinosa* exhibit antithrombotic, antiplatelet aggregation, blood viscosity reducing, anti-atherosclerotic, anti-inflammatory, free-radical scavenging, blood circulation-improving and anti-myocardial ischemia effects.

Our study was constrained by time, where the patients were treated and followed-up for only three months. Prolonged treatment and follow-up time will provide more scientific and objective results. Subsequently, we will carry out a follow-up study for up to 6–12 months. Animal experimentation has confirmed that our compound may potentially exhibit a protective effect on vascular endothelial function, improve the collateral circulation, and stabilize atherosclerotic plaques. In addition, YQTL compound is currently only approved in China, so whether the drug as well as the results of our study are applicable to patients outside China remains to be observed in the future.

ACKNOWLEDGEMENTS

This study was supported by Key R&D Program Projects of the Ministry of Science and Technology (No. 2018YFC1704100); Traditional Chinese medicine Dominant Disease Cultivation Project of Shanghai municipal commission of health and family planning system (No. ZY(2018-2020)-ZYBZ-18); The program for accelerating the development of traditional Chinese medicine through a 3-year action plan on inheritance and innovation of traditional Chinese medicine development in Shanghai (No. ZY3-CCCX-3-3024).

Table II. *Comparison of angina pectoris scores, nitroglycerin/HMP dosage, and TCM syndrome scores of the two groups before and after treatment.*

Item	Time	Treatment group	Control group	Statistical value	P-value
Angina pectoris scores					
Episodes	Pre-treatment	2.74±0.98	2.51±0.89	1.046	0.310
	One month post-treatment	2.34±1.03*	2.57±0.92	0.965	0.330
	Three months post-treatment	1.26±0.98*#	2.34±0.91#	23.158	0.000
Nitroglycerin/HMP dosage					
Duration	Pre-treatment	2.91±1.48	3.09±1.48	0.234	0.630
	One month post-treatment	2.69±1.08	3.03±1.32	1.420	0.238
	Three months post-treatment	4.17±5.53*#	2.63±1.06*#	6.819	0.011
TCM syndrome scores					
Pain level	Pre-treatment	3.49±1.40	3.49±1.12	0.000	1.000
	One month post-treatment	2.86±1.12*	3.20±0.99*	1.843	0.179
	Three months post-treatment	2.06±2.14*#	2.80±1.11*#	7.024	0.010
Total score	Pre-treatment	9.14±3.15	9.09±2.54	0.007	0.934
	One month post-treatment	7.89±2.37*	8.80±2.44*	2.530	0.116
	Three months post-treatment	5.26±2.91*#	7.77±2.46*#	15.202	0.000
Dosage	Pre-treatment	10.46±7.80	9.77±5.76	0.175	0.677
	One month post-treatment	7.91±6.48*	9.17±5.34*	0.785	0.379
	Three months post-treatment	4.17±5.53*#	7.83±4.88*#	8.594	0.005
Chest pain	Pre-treatment	3.66±1.41	3.94±1.14	0.869	0.354
	One month post-treatment	3.14±1.31*	3.71±0.99*	4.250	0.043
	Three months post-treatment	2.11±1.28*#	3.09±1.12*#	11.426	0.001
Chest tightness	Pre-treatment	2.09±0.45	2.06±0.34	0.091	0.763
	One month post-treatment	1.54±0.51*	2.03±0.38	20.556	0.000
	Three months post-treatment	1.06±0.34*#	1.89±0.40*	86.648	0.000
Shortness of breath	Pre-treatment	2.26±0.61	2.51±0.56	3.359	0.071
	One month post-treatment	1.51±0.51*	1.51±0.51*	51.503	0.000
	Three months post-treatment	1.03±0.38*#	2.14±0.55*#	96.843	0.000
Palpitations	Pre-treatment	1.89±0.58	2.06±0.42	2.007	0.161
	One month post-treatment	1.63±0.55*	2.00±0.42	10.152	0.002
	Three months post-treatment	1.09±0.51*#	1.89±0.53*#	41.650	0.000
Lassitude	Pre-treatment	2.40±0.60	2.40±0.55	0.000	1.000
	One month post-treatment	1.77±0.55*	2.29±0.52	16.296	0.000
	Three months post-treatment	1.49±0.56*#	2.20±0.58	27.174	0.000
Total score	Pre-treatment	12.29±2.76	12.97±2.02	1.405	0.240
	One month post-treatment	9.60±2.57*	12.46±1.85*	28.480	0.000
	Three months post-treatment	6.77±2.31*#	11.20±2.14*#	69.096	0.000

**Compared with the same group before the treatment, P≤0.05; #Compared with the same group one month post-treatment, P≤0.05.*

REFERENCES

1. National Health and Family Planning Commission of the People's Republic of China (NHFPC). Diagram: 2015 Report on Chinese Nutrition and Chronic Disease [R/OL]. (2015/6/30) ttp://www.nhfpc.gov.cn/jkj/s5879/201506/4505528e65f3460fb88685081ff158a2.shtml. [Accessed on: 2016/3/1].
2. De Maria GL, Patel N, Banning AP. Obstructive left main stem coronary disease: is it time to recommend coronary stenting. Heart 2018; 104:614-20.
3. Chen WW, Gao RL, Liu LS, et al. The report on cardiovascular diseases in China, 2017. Chin Circ J 2018; 33:1-8.
4. Li JG, Xu H, Shi DZ. Randomized controlled clinical study of coronary heart disease with integrated traditional Chinese and western medicine: progress and prospect. Chin J Integr Tradit West Med 2017; 37:517-21.
5. Xing JD, Dong YR, Zhao Y, et al. Effect of Tongxin Decoction on Ventricular Remodeling and Cardiovascular Events in Patients with Triple-vessel Coronary Artery Disease. JETCM 2010; 19:1649-51.
6. Interventional Cardiology Group of Chinese Society of Cardiology, Chinese Medical Association, Editorial Board of the Chinese Journal of Cardiovascular Diseases. China's guidelines for percutaneous coronary artery treatment in 2012. Chin J Crit Care Med 2012; 40:271-77.
7. Zheng XY. The guidelines for clinical research of new TCM drugs. Beijing, China: Chinese medical science and technology press 2002:68-73.
8. Yan HB, Ma CS, Huo Y. Guidelines for clinical diagnosis and treatment of coronary artery disease. Beijing, China: People's Medical Publishing House 2010:46-58.
9. Integrative treatment of angina pectoris and cardiac arrhythmias forum. Coronary heart disease angina and ECG efficacy evaluation standard. Chin Pharm Aff 1987; 2:71.
10. Chen CJ, Fu Q, Li YJ, Li ZL. Effect of Astragalus mongholicus polysaccharides on gene expression profiles of dendritic cells isolated from healthy donors. J South Med Univ 2015; 35:1802-5.
11. Zhu Y, Liu WW, Gu N, Shi AW. Research progress on the active components of rhizoma chuanxiong and its protective effect on cardiovascular system. Lishizhen Med Mater Med Res 2016; 27:1701-4
12. Cui XH, Liang SM, Yao PA, Wei KZ, Gao JP. Experimental study of catalpol against myocardial hypertrophy induced by isoproterenol in mice. Shanghai J Tradit Chin Med 2017; 51:73-75.

LETTER TO THE EDITOR

LOW TRIIODOTHYRONINE SYNDROME IS ASSOCIATED WITH PROCEDURE COMPLEXITY IN EMERGENCY PERCUTANEOUS CORONARY INTERVENTION

DL. ZHOU[1,3], LF. YU[2], M. ZHANG[1], L. WEI[3] and QM. ZHAO[1]

[1]Department of Cardiology, Beijing Anzhen Hospital, Capital Medical University, Beijing, China; [2]Clinical Pharmacy, First Affiliated Hospital, Heilongjiang University of Chinese Medicine, Harbin, Heilongjiang Province, China; [3]Department of Cardiology, First Hospital of Harbin City, Harbin, Heilongjiang Province, China

Received April 26, 2019 – Accepted June 10, 2019

To the Editor,

In recent years, studies have found that low triiodothyronine syndrome (LT3S) is frequently seen in patients with acute myocardial infarction (AMI) (1). The typical characteristics of LT3S are the absence of clinical symptoms of hypothyroidism, but decreased serum levels of total triiodothyronine (TT3) or free triiodothyronine (FT3), normal-to-low free thyroxin (FT4) and total thyroxin (TT4), increased reverse triiodothyronine (rT3), and normal thyroid stimulating hormone (TSH) (2, 3).

In the past, experts believed that LT3S is a protective adaptation mechanism of the hypothalamus, thereby requiring no special attention (4). However, recent studies have shown that LT3S is associated with poor outcomes in patients with heart disease, especially in those with myocardial infarction or heart failure (5). In clinical practice, we found that patients with LT3S have complicated changes in vascular status, which is more difficult to manage during percutaneous coronary intervention (PCI); thus, we suspected that LT3S may be associated with procedure complexity in emergency PCI. This study discusses the relationship between LT3S and the complexity of emergency PCI. To the best of our knowledge, there are no reports about the relationship between LT3S and the complexity of emergency PCI.

MATERIALS AND METHODS

Patients

The study population and design are shown in Fig. 1; 532 patients over 18 years of age who were admitted to Beijing Anzhen Hospital between April 2016 and April 2017 with a confirmed AMI diagnosis were considered for enrollment into the study. AMI diagnosis was based on (a) Chest pain lasting for more than 30 min, (b) increased serial cardiac troponin, and (c) typical electrocardiographic changes (6). Two hundred and ninety-four patients were excluded because: they had known thyroid diseases, prior myocardial infarction; autoimmune disease; prior renal insufficiency; anemia; prior CABG or PCI; receiving treatment with statins, amiodarone, or corticosteroids. All subjects gave informed, signed consent to participate in the study and the study was approved by the Ethics Committee of Beijing Anzhen Hospital.

Definitions of LT3S and grouping

The reference ranges of thyroid hormone were as

Key words: *low T3 syndrome; procedure complexity; acute myocardial infarction; percutaneous coronary intervention*

Corresponding Author:
Dr Quanming Zhao,
Department of Cardiology,
Beijing Anzhen Hospital, Capital Medical University,
No.2, Anzhen Road, Chaoyang District,
Beijing, 100029, China
e-mail: zhaoquanming9421@163.com

0393-974X (2019)

follows: TSH (0.49–4.91 mIU/L), TT3 (1.01–2.48 nmol/L), FT3 (3.28–6.47 pmol/L), and FT4 (7.64–16.03 pmol/L). Patients were divided based on thyroid hormone profile. The euthyroid group had normal values of TSH, fT3, and fT4, while the LT3S group had TT3<1.01 nmol/L or FT3<3.28 pmol/L, and normal values of TSH.

Data collection

All patients had blood samples collected within 24 h of presentation and were tested for thyroid hormone, high-sensitivity C-reactive protein (hsCRP), blood routine, uric acid, lipids, and homocysteine.. The peak values of cardiac troponin I (cTnI) and N-terminal pro-brain natriuretic peptide (NTproBNP) after serial measurements were used as indicators of myocardial injury. The normal range of cTnI was 0–0.04ng/mL. Echocardiography was performed on the second day of hospitalization. The results of coronary angiography and the failure rate of PCI were recorded in each patient.

The extent and severity of coronary artery disease (CAD) was evaluated by using the Gensini score (7). In this system, a severity score is derived for each coronary stenosis on the basis of the degree of luminal narrowing and its topographic importance. Reductions in luminal diameter of 1–25%, 26–50%, 51–75%, 76–90%, 91–99%, and 100% (occlusion) are scored as 1, 2, 4, 8, 16, and 32, respectively. Each principal vascular segment is assigned a multiplier that represents its functional importance in maintaining myocardial blood supply. Multipliers are 5 for the left main (LM) coronary artery; 2.5 for the proximal segments of the left anterior descending (LAD) and left circumflex (LCX); 1.5 for the mid segment of the LAD; 1 each for the right coronary artery (RCA), distal segment of the LAD, posterolateral artery, and obtuse marginal (OM) branch; and 0.5 for other segments.

In-hospital outcomes were collected and confirmed by medical records. The primary outcome was in-hospital cardiovascular death and adverse cardiac events, which were defined as reinfarction, fatal arrhythmia, and stroke. Secondary outcomes included the severity of myocardial injury, cardiac ejection fraction, and length of hospital stay.

Statistical analysis

Continuous variables are expressed as mean±SD or median (25^{th}–75th percentile) and were compared across groups using Student's *t*-test or the Wilcoxon rank-sum test as appropriate. Categorical variables are presented as counts and percentages and were compared across groups using the χ^2 test or Fisher's exact test as appropriate. Linear correlation regression analysis was used for continuous variables, while binary logistic regression analysis was used for classification variables, after adjusting for gender, age, smoking, hypertension, diabetes, and dyslipidemia. All analyses were performed using the SPSS 24 statistical package.

RESULTS

Baseline characteristics

Two hundred and thirty-eight patients met the inclusion criteria for this study, of whom 68 (28.6%) had LT3S. Baseline characteristics recorded prior to admission in the study groups are presented in Table I. Compared with the euthyroid groups, the LT3S group had more female patients.

Laboratory parameters, coronary angiography characteristics, clinical outcomes in and LT3S cohort euthyroid

The LT3S group had lower total T3 0.89(0.76-0.98) *vs* 1.27 (1.14-1.38), FT3 4.14 (3.86-4.43) *vs*

Table I. *Baseline patient characteristics*

Clinical variables	Euthyroid (n =170)	LT3S (n = 68)	P values
Age, years	55.49±11.13	57.85±12.66	0.229
female, n(%)	21(12.4)	17(25)	0.02
Hypertension, n(%)	91(53.5)	36(52.9)	0.886
DM, n(%)	42(24.7)	20(29.4)	0.455
Dyslipidemia, n(%)	13(7.6)	2(2.9)	0.177
Smoker, n(%)	53(31.2)	20(29.4)	0.789

DM: diabetes mellitus; LT3S: low triiodothyronine syndrome

4.75 (4.42-5.19), hemoglobin level 141.5(132.2-153) *vs* 150 (141.74-160), total cholesterol 3.12 (3.68-4.96) *vs* 4.68 (3.99-5.34), low-density lipoprotein cholesterol 2.55 (2.22-3.24) *vs* 3.04 (2.45-3.66) (all P<0.001) and higher neutrophil count 6.96 (5.01-9.79) *vs* 5.59 (4.25-8.08) and hsCRP levels 9.81 (1.88-32.12) *vs* 4.56 (1.67-11.27) (both P<0.01) than the euthyroid group (Table II). Homocysteine and uric acid were not statistically significant parameters.

As shown in Table II, compared with the euthyroid group, the LT3S group had more stenosis of the three vessels (30.8 *vs* 10.6%, P<0.001); left main disease (17.6 *vs* 7%, P=0.027); severe vascular calcification (16.2 *vs* 5.8%, P=0.023); coronary bifurcation lesions (7.3 *vs* 1.2%, P=0.034); and high thrombus burden (17.6 *vs* 5.8%, P=0.01), Gensini scores, and failed PCI rates (20.6 *vs* 5.3%, P=0.001). Considering triple-vessel stenosis, left main disease, severe vascular calcification, coronary bifurcation lesions, high thrombus burden, Gensini scores, and failed PCI rates as the dependent variables, and the study groups as the independent variables, linear regression or logistic regression were performed, after adjusting for age, sex, smoking, hypertension, diabetes, and dyslipidemia. The results showed that the LT3S group was associated with triple-vessel stenosis, left main disease, severe vascular calcification, coronary bifurcation lesions, high thrombus burden, Gensini score, and failed PCI rate (Fig. 2).

Compared with the euthyroid group, The peak values of cTnI, NTproBNP were significantly higher 3.53 (0.67-11.62) *vs* 7.16 (1.94-18.36) and 1450 (906-2200) *vs* 3645 (1250-10925) p < 0.001, left ventricular ejection fraction were lower (7.6 *vs* 26.5%, p < 0.001) in LT3S, Subjects with LT3S had greater length of hospital stay than those without (P < 0.001). The inter-group differences in respect to major adverse cardiac events (MACE), defined as in-hospital cardiovascular death, and adverse cardiac events, defined as re-infarction, fatal arrhythmia, and stroke, were not statistically significant (3.5 *vs* 8.8%, P= 0.174).

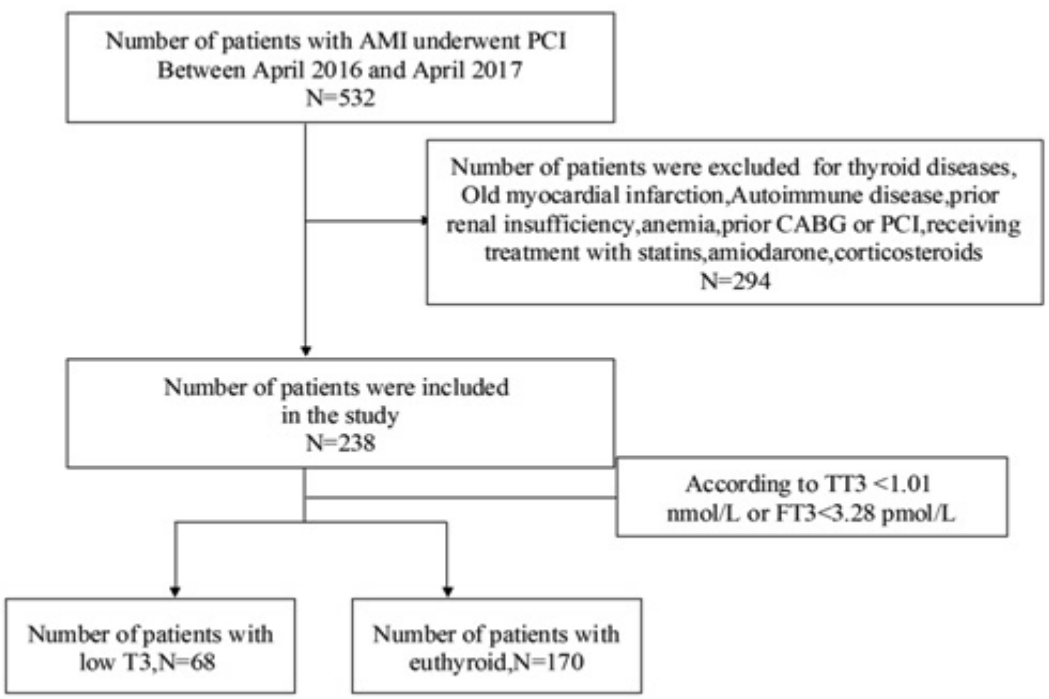

Fig. 1. *Study population and selection. AMI: acute myocardial infarction; PCI: percutaneous coronary intervention; CABG: coronary artery bypass grafting; TT3: Total triiodothyronine; FT3: free triiodothyronine.*

Table II. *Coronary angiography characteristics*

	Euthyroid (n =170)	LT3S (n = 68)	P values
*vs*1-vessel, n (%)	96(56.5)	19(27.9)	0.000
*vs*2-vessel, n (%)	56(32.9)	27(39.7)	0.402
*vs*3-vessel, n (%)	18(10.6)	21(30.8)	0.000
LM, n (%)	12(7)	12 (17.6)	0.027
TO, n (%)	8(4.7)	7(10.2)	0.191
P LAD ,n (%)	13(7.6)	6(8.8)	0.970
SVC, n (%)	10(5.8)	11(16.2)	0.023
CBL, n (%)	2(1.2)	5(7.3)	0.034
HTB, n (%)	10(5.8)	12(17.6)	0.010
CTO, n (%)	8(4.7)	7(10.2)	0.191
Failed PCI rate, n(%)	9(5.3)	14(20.6)	0.001
Gensini score	38(22-54)	51(32.5-80)	0.001
cTnI, ng/mL	3.53(0.67-11.62)	7.16(1.94-18.36)	0.009
NTproBNP, pg/mL	1450(906-2200)	3645(1250-10925)	0.009
LVEF < 50%, n (%)	13(7.6)	18(26.5)	0.000
Mace,n (%)	6(3.5)	6(8.8)	0.174
Length of stay, days	4(3-5.25)	6(4-8)	0.000
TT3(nmol/L)	1.27(1.14-1.38)	0.89(0.76-0.98)	0.000
FT3(pmol/L)	4.75(4.42-5.19)	4.14(3.86-4.43)	0.000
FT4(pmol/L)	11.07(9.85-12.25)	11.03(9.88-13.36)	0.811
TSH(mIU/ml)	1.76((1.055-2.695)	1.83(1.07-2.63)	0.753
WBC, G/L	8.15(6.68-10.18)	9.18(7.14-12.27)	0.229
NE, G/L	5.59(4.25-8.08)	6.96(5.01-9.79)	0.012
Hb, g/L	150((141.74-160)	141.5(132.2-153)	0.000
TC, mmol/L	4.68(3.99-5.34)	3.12(3.68-4.96)	0.008
TG, mmol/L	1.44(1.11-2.16)	1.30(0.87-2.21)	0.094
HDL-C, mmol/L	1.02(0.86-1.22)	0.99(0.84-1.14)	0.222
LDL-C, mmol/L	3.04(2.45-3.66)	2.55(2.22-3.24)	0.009
hsCRP, mg/L	4.56(1.67-11.27)	9.81(1.88-32.12)	0.006
UA umo1/L	335.3(278.65-412.45)	333.5(272.4-450.12)	0.715
HCY umol/L	13.6(9.7-18.3)	13.9(8.9-20.8)	0.421

Vs1:2:3-vessel: Vascular stenosis was greater than 75%; LM: left main disease; TO: two vascular occlusion; PLAD: proximal left anterior descending coronary artery lesions; SVC: severe vascular calcification; CBL: coronary bifurcation lesions; HTB: high thrombus burden; CTO: chronictotal occlusion; LT3S: low triiodothyronine syndrome; cTnI: cardiac troponin I; NTproBNP: N-terminal pro-brain natriuretic peptide; LT3S: low triiodothyronine syndrome; LVEF: left ventricular ejection fraction; Mace: major adverse cardiac events was defined as in-hospital cardiovascular death and adverse cardiac events which was defined as re-infarction: Fatal arrhythmia: stroke. TT3: total triiodothyronine; FT3: free
Triiodothyronine; WBC: white blood cell count; NE: Neutrophil count; Hb: Hemoglobin; TC: total cholesterol; TG:t otal triglyceride; HDL-C: high-density lipoprotein cholesterol; LDL-C: low-density lipoprotein cholesterol; hsCRP: high-sensitivity C-reactive protein; UA: Uric acid; HCY: Homocysteine; LT3S: low triiodothyronine syndrome.

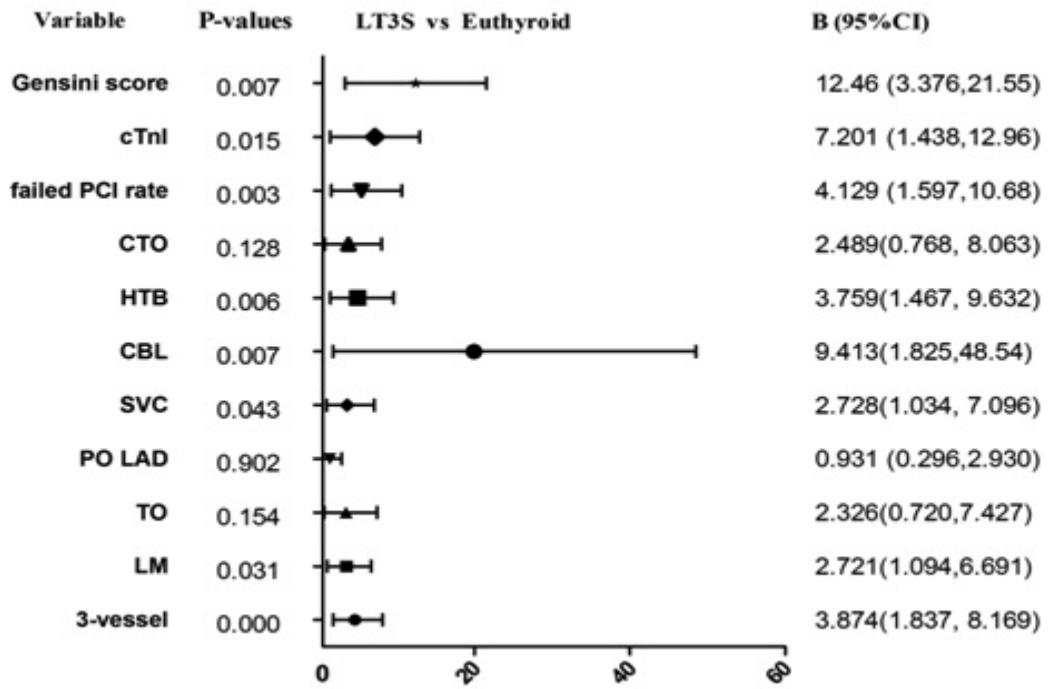

Fig. 2. *Linear or logistic regression analysis of LT3S and PCI risk factors; cTnI: cardiac troponin I; 3-vessel: Three vascular stenosis was greater than 75%; LM: Left main vessel lesion; TO: Two vascular occlusion; POLAD: Proximal occlusion of left anterior descending coronary artery; SVC: Severe vascular calcification; CBL: Coronary bifurcation lesions; HTB: High thrombus burden; CTD: chronic total occlusion; LT3S: low triiodothyronine syndrome. Adjusted for gender, age, smoking, hypertension, diabetes, dyslipidemia.*

DISCUSSION

The time delay in PCI typically increases the mortality rate (8). Some factors that determine the success rate and complexity of PCI include multiple vascular lesions, proximal LAD lesions, left main vessel lesion, high thrombus burden, bifurcation vessel lesions, chronic total occlusion and Gensini scoring (9-12). Our study showed that more tripe-vessel stenosis, left main stenosis, bifurcation lesions, severe vascular calcification, thrombus burden, and Gensini scores in the LT3S group were higher than the euthyroid group. This suggests that AMI patients with LT3S have a more complex presentation and are therefore more challenging candidates for PCI. Furthermore, this study showed that the failure rate of PCI was higher in the LT3S group. Although the MACE events after PCI were not statistically significant, there was an increased trend in the LT3S group. Our study also found that hsCRP and neutrophils in the LT3S groups were higher. This also suggests that serious inflammatory reaction occurs after AMI. We also found that the peak hypersensitive troponin I and peak NTproBNP in the LT3S group was higher, while the cardiac ejection fraction was lower and the length of stay was longer than the euthyroid group. This suggests that the LT3S group had more severe myocardial injury, resulting in increased procedure complexity in emergency PCI.

In conclusion, we report that AMI patients with LT3S had more complex coronary artery lesions, resulting in higher PCI surgery failure rate and more severe myocardial damage. Therefore, we believe that LT3S is associated with the complexity of emergency PCI.

REFERENCES

1. Abdulaziz Qari F. Thyroid hormone profile in patients with acute coronary syndrome. Iran Red Crescent Med J 2015; 17:e26919.
2. Vidart J, Wajner SM, Leite RS, Manica A, Schaan BD, Larsen PR, Maia AL. N-acetylcysteine administration prevents nonthyroidal illness syndrome in patients with acute myocardial infarction: a randomized clinical trial. J Clin Endocrinol Metab 2014; 99(12):4537-45.
3. Jankauskien E, Orda P, Rumbinait E. Left ventricular function by speckle-tracking echocardiography in patients with low-T3 syndrome and acute myocardial infarction. Medicina (Kaunas) 2015; 51(4):209-16.
4. Jefferies JL, Towbin JA. Dilated cardiomyopathy. Lancet 2010; 375(9716):752-62.
5. Pol CJ, Muller A, Zuidwijk MJ, et al. Left-ventricular remodeling after myocardial infarction is associated with a cardiomyocyte-specific hypothyroid condition. Endocrinology 2011; 152(2):669-79.
6. Thygesen K, Alpert JS, Jaffe AS, et al. Third universal definition of myocardial infarction. Eur Heart J 2012; 33:2551-67.
7. Erkan AF, Tanindi A, Kocaman SA. Epicardial adipose tissue thickness is an independent predictor of critical and complex coronary artery disease by Gensini and Syntax scores. Tex Heart Inst J 2016; 43(1):29-37.
8. McNamara RL, Wang Y, Herrin J, et al. Effect of door-to-balloon time on mortality in patients with ST-segment elevation myocardial infarction. J Am Coll Cardiol 2006; 47:2180-86.
9. Lee MS, Shlofmitz E, Kaplan B, Shlofmitz R. Percutaneous coronary intervention in severely calcified unprotected left main coronary artery disease: Initial experience with orbital atherectomy. J Invasive Cardiol 2016; 28(4):147-50.
10. Rawlins J, Sambu N, O'Kane P. Strategies for the management of massive intra-coronary thrombus in acute myocardial infarction. Heart 2013; 99(7):510.
11. Antoni ML, Yiu KH, Atary JZ, et al. Distribution of culprit lesions in patients with ST-segment elevation acute myocardial infarction treated with primary percutaneous coronary intervention. Coron Artery Dis 2011; 22(8):533-36.
12. Watanabe H, Morimoto T, Shiomi H, et al. Chronic total occlusion in non-infarct-related artery is associated with increased short-and long-term mortality in patients with ST-segment elevation acute myocardial infarction complicated by cardiogenic shock (from the CREDO-Kyoto AMI registry). Catheter Cardiovasc Interv 2018; 92(3):455-63.

LETTER TO THE EDITOR

CHITOOLIGOSACCHARIDES INHIBIT A549 LUNG CANCER CELL LINE PROLIFERATION BY REGULATING CELL AUTOPHAGY

HF. LI[1], LF. HUANG[1] and LH. CHEN[2]

[1]Medical College, Hangzhou Normal University, Hangzhou, China; [2]College of Animal Sciences and Technology, Zhongkai University of Agriculture and Engineering, Guangzhou, China

Received May 6, 2019 – Accepted June 18, 2019

To the Editor,

Chitooligosaccharides (COS) are water-soluble polysaccharides prepared from chitosan by two methods: chemically or enzymatically. COS possess a wide spectrum of indications in medicine, including antibacterial, antiviral, antifungal (1), and anti-tumoral activities (2, 3). Autophagy is a highly conserved normal physiological process in the cytoplasm of eukaryotic cells (4), mainly involved in the degradation of long-lived proteins and organelles. Autophagy disorders are associated with different human pathologies (5). The level of autophagy in cancer cell lines is lower than that in normal cells. Even in the absence of serum or amino acid starvation, the level of autophagy in cancer cells cannot be increased (6, 7). To date, 30 autophagy-related proteins that influence the distinct stages of autophagy have been reported by researchers (8). In the process of mammalian autophagic vacuole formation, Atg3, Atg5, Atg7, Atg10, Atg12 and microtubule-associated protein 1 light chain 3 (MAP1-LC3) participate in two ubiquitin-like protein processing modification processes: Atg12 binding process and LC3 modification process. Atg12 binding process is associated with the formation of pre-autophagic vesicles, and LC3 modification process is essential for the formation of autophagic vesicles (9). Therefore, LC3 can be used as a molecular marker for autophagy. A549 cells are adenocarcinomic human alveolar basal epithelial cells, widely used to test new drugs for lung cancer treatment. This study aimed to investigate the inhibitory effects of COS on apoptosis, proliferation, and autophagy of A549 lung cancer cell lines. LC3 was used as a marker for autophagy evaluation.

MATERIALS AND METHODS

Preparation of COS

COS was prepared by metal-coordinating oxidative degradation of chitosan. Firstly, 0.5 g chitosan was dissolved in acetic acid solution and then stirred with deionized water (60 mL). Copper acetate (80 mg) was dissolved in deionized water (10 mL), and then added to the solution of chitosan in acetic acid. After 6.5 h of stirring, the metal ions were removed from the solution by 732 cation-exchange resin and COS was obtained by freeze-drying. COS samples were stored at -20°C until analysis.

Cell culture

A549 cells were seeded onto 25 cm^2 flasks in 3 mL medium (RPMI 1640 medium, Shanghai Guangyu Biotechnology Co., Ltd., China). Cell density was adjusted to 5×10^5 cells/mL in culture medium and then inoculated into other culture flasks for culture. Cell adhesion and growth were observed.

Key words: chitooligosaccharide; autophagy; A549 lung cancer cell line; apoptosis; proliferation

Corresponding Author:
Dr Liehuan Chen,
College of Animal Sciences and Technology,
Zhongkai University of Agriculture and Engineering,
No. 501 Zhongkai Road,
Guangzhou 510225, China
e-mail: chenliehuan_zkuae@163.com

0393-974X (2019)

MMT assay for inhibition of cell proliferation

A549 cells were seeded onto 96-well culture plates (180 µg/well) and allowed to adhere. After cell adherence, fresh culture medium (180 µl) containing the following concentrations of COS: 1.0, 2.0, 3.0, 4.0, and 5.0 mg/mL, were introduced. Each group was divided into five parallel wells, and a negative control group was set up. After 12 and 24 h of culture, the supernatants were discarded and the cells were cultured with 20 µL MTT solution (5.0 mg/mL) for 4 h and then the supernatant was discarded, and 150 µL dimethylsulfoxide (DMSO) (Suzhou Lianxiong Chemical Technology Co., Ltd., China) was added. After 10 min of oscillation, the optical density (OD) value was measured at 490 nm, and the growth inhibition rate was calculated using the following formula:

Growth inhibition rate% = (1-OD value $_{\text{experimental group}}$/ OD value $_{\text{control group}}$) ×100%

Effects of COS on cell morphology

A549 cells in logarithmic phase were cultured with 5.0 mg/mL COS for 24 h. The morphology of A549 cells was observed under an inverted microscope (Shanghai Caikang Optical Instrument Factory, China).

Wright and Giemsa staining

A549 cell suspension was prepared by adjusting the cell density of $1x10^5$ cells/mL and laid in a 6-well plate (2 mL/hole) and cultured overnight with 5.0 mg/mL COS. The samples were worked in four replicates, and negative control was set up. After culture, the supernatant was discarded, the cells were washed with phosphate buffered saline (PBS) three times, fixed with 95% ethanol for 10 min, stained with dye for 20 min, washed with PBS three times, and the cell morphology was observed under an inverted microscope (Shanghai Caikang Optical Instrument Factory, China).

Acridine orange/ethidium bromide (AO/EB) staining

A549 cells were cultured with COS as previously described; they were washed three times with PBS, fixed with 95% ethanol for 10 min, and stained with 8 µL AO/EB staining solution for 10 min. Then the staining solution was discarded, the supernatant was washed with PBS three times, and sealed tablets were added. The cover slide was taken out and the cell morphology was observed under a fluorescence microscope (DFM-60D Inverted Fluorescence Microscope, Shanghai Shangguang Instrument Co., Ltd., China).

Detection of apoptosis

A549 cells were cultured at the logarithmic growth stage. The cell concentration was adjusted to $1x10^5$ cells/mL. The cell suspension was added to a 25 cm^2 flask with 3 mL 5%CO_2 in each bottle and incubated overnight at 37°C. After cell adherence, the old culture medium was discarded, and 3 mL cell culture medium containing 5.0 mg/mL COS was added and incubated for 24 h. A negative control group was also used. After incubation, trypsin was added for digestion. The cells were collected by centrifugation at 800 r/min, then were washed with PBS for three times to adjust the cell concentration to $1x10^6$/mL. According to the manufacturer's protocol, 10 µL Annexin V-FITC and 5 µL propidium iodide (PI) were added to the cell suspension and incubated for 30 min at 4°C. After incubation 300 µL combined buffer solution was added for flow cytometry. The Raman signals were generated by light from an argon ion laser (488 nm), fluorescein isothiocyanate (FITC) was stimulated with green fluorescence, and PI was red fluorescent. The experiments were carried out in triplicates. The percentage of apoptotic cells was calculated using the following formula:

Apoptotic rate (%)=(number of apoptotic cells/total number of cells)x100.

Immunohistochemistry (IHC) analysis

A549 cells cultured with COS as previously described were washed three times with PBS, dried with ice-acetone for 15 min, and then washed three times with PBS for 3 min. 0.5% Triton X-100 was added and incubated for 20 min to break the membrane and then the culture was washed twice with PBS. Afterward, 5% bovine serum albumin (BSA) was added and incubated for 30 min, followed by Anti-Bax, Bcl-2, and survivin (dilution, 1:400) and incubated overnight at 4°C. After incubation, the culture was washed with PBS, and the cells were incubated for 1 h in the dark with sheep anti-mouse IgG antibody (dilution, 1:400) followed by rabbit polyclonal anti-complement complement C3 antibody (dilution, 1:400). After incubation, the cultures were washed with PBS and dyed with DAB for 3 to 10 min, followed by washing twice with nonionic water for 1 min each

time. Finally, the cells were re-stained with 10.0 μg/mL hematoxylin for 5 min, washed with deionized water, and observed under an inverted microscope.

Monodansylcadaverine (MDC) staining

A549 cell cultured with COS as previously described were washed for three times with PBS, and 2 mL 4% paraformaldehyde (PFA) was added to each well and kept for 15 min. After PFA fixation, 200 μL MDC (50 μmmol/l) dye solution was added and culture for 60 min at 37°C for 60 min. Finally, the cells were washed three times with PBS and observed under a fluorescence microscope.

Immunofluorescent staining

The cells were cultured with COS as previously described and fixed with 4% PFA. After fixation, the cells were washed three times with PBS and incubated with 1 mL 0.2% Triton x-100 for 15 min at room temperature. The supernatant was discarded and the cells were washed three times with PBS before incubation with 1 mL LC3 antibodies (1:1000) at 4°C overnight in a wet box, then washed three times with PBS. Then, the cells were cultured with 1 mL secondary antibody (1:1000) for 3 h at room temperature in the dark. The cells were colored with DAPI and observed under a fluorescence microscope.

Protein detection

Two mL cell culture medium containing COS (5.0 mg/mL) was used to treat A549 cells (cell density, $1x10^5$ cells/mL) for different time periods (4, 8, 12 h). Cells were washed three times with PBS, then digested with trypsin and collected in sterilized tubes (Eppendorf, Germany) and centrifuged at 4°C and 800 r/min for 10 min. The extraction of protein was carried out after 100 μL cell protein lysate (RIPA lysate) was added with 12% sodium dodecyl sulfate polyacrylamide gel electrophoresis (SDS-PAGE) at constant voltage of 150 V. After electrophoresis, polyvinylidene difluoride (PVDF) membrane was transported to a semi-dry membrane and treated with methanol for 5 s at a constant voltage of 20 V, and then transferred for 30 min. At the end of conversion, the membrane was immersed in TBST containing 0.5% BSA and sealed for 1 h at 37°C. The membrane was rinsed three times for 5 min and then incubated with LC3 antibody (1:1000) or β-actin (1:1000) at 37°C for 1 h, washed three times with TBST and incubated with the second antibody sheep anti-mouse IgG antibody (1:1000) at 37°C for 1 h and washed three times with TBST. Finally, the film was colored according to the manufacturer's instructions and visualized.

Statistical analysis

SPSS 19.0 software was used for statistical analysis. The results were expressed by inhibition rates. The data in the two groups were tested by *t*-test, and the data in the multiple groups were analyzed by one-way analysis of variance (ANOVA). $P < 0.05$ was considered as statistical difference.

Table I. *Inhibitory effects of COS on the proliferation of A549 cells.*

Drug concentrations	12 h		24 h	
	OD±SD	Inhibition rates (%)	OD±SD	Inhibition rates (%)
Negative control group	0.998±0.012	0	1.004±0.006	0
1.0mg/mL	0.942±0.007**	6.63	0.821±0.005**	19.16
2.0mg/mL	0.873±0.011**	13.74	0.727±0.006**	25.46
3.0mg/mL	0.758±0.009**	24.16	0.638±0.007**	36.13
4.0mg/mL	0.703±0.010**	30.21	0.554±0.009**	44.83
5.0mg/mL	0.612±0.009**	38.54	0.438±0.008**	55.91

*Compared with negative control, * P<0.05; ** P<0.01*

RESULTS

Inhibitory effects of COS on the proliferation of A549 cells

Table I shows that different concentrations of COS can inhibit the proliferation of A549 cells, and with the increase of drug concentrations and the prolongation of action time, the inhibition rate also increases, demonstrating a time- and dose-dependent manner.

Effects of COS on the morphology of A549 cells

After 24 h of exposure to 5.0 mg/mL COS, the morphological changes of A549 cells were observed under an inverted microscope. In the control group, A549 cells were spindle-shaped with clear cell outline and fewer dead cells. After COS treatment, the majority of the cells showed cell shrinkage, smaller size, round cells, and larger cell gap. A great number of exfoliated and dead cells and cell fragments appeared in the culture flask, however, the number of cells significantly decreased (Fig. 1A).

Wright and Giemsa staining showed that the membrane of A549 cells in the control group was intact, and the nucleolus and chromatin were distributed in the nucleus. After COS treatment, the

Table II. *Number of positive cells and IHC scores.*

Group	A(%)	B	IHS
Bax-A549 control group	19	2	38
Bax-A549 5.0mg/mL COS	38	3	114
Bcl-2-A549 control group	64	3	192
Bcl-2-A549 5.0mg/mL COS	27	2	54
Survivin-A549 control group	50	3	150
Survivin-A549 5.0mg/mL COS	10	1	10

A: grade of positive cells; B: color intensity of positive cells. IHC=A×B

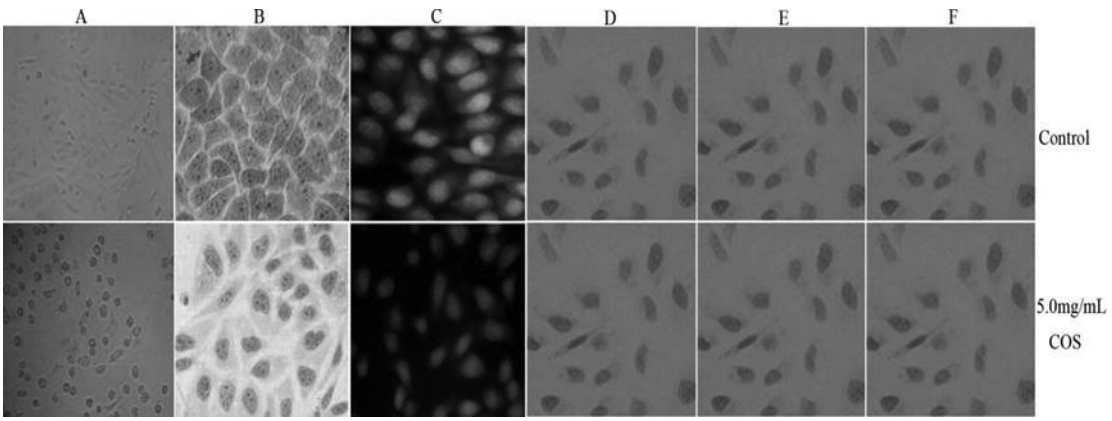

Fig. 1. *Morphological changes of A549 cells and the effects of COS treatment on the expression of Bax, Bcl-2, and survivin in A549 cells (×200).* ***A)*** *Morphology of A549 cells treated with COS, ×200;* ***B)*** *Wright and Giemsa staining, ×400;* ***C)*** *AO-EB staining, ×200;* ***D)****: expression of Bax in A549 cells, ×200;* ***E)*** *expression of Bcl-2 in A549 cells, ×200;* ***F)*** *expression of survivin in A549 cells, ×200).*

number of cells notably decreased compared to the control group. The treatment determined a decreased ability of cells adherence. Cell chromatin aggregates and marginalizes, and apoptotic bodies appeared around or outside the cell membrane (Fig. 1B).

AO-EB staining (Fig. 1C) showed that the normal living cells have normal structure and green fluorescence in the nucleus. The non-apoptotic dead cells have normal structure and a part of the nucleus was orange-red. The apoptotic cells were spherical or pyknotic and the nucleus was orange-red. Compared with the control group, there was a significant difference in apoptosis after COS treatment.

The apoptotic rate of A549 cells after 24 hours of treatment with COS was found to be 37.68%.

Expression levels of Bax, Bcl-2, and Survivin in A549 cells

Compared with the control group, the expression level of Bax in the COS group was strongly positive and up-regulated, while the expression levels of Bcl-2 and Survivin were down-regulated. Compared with Bcl-2, the expression level of survivin was lower (Fig. 1, D-F).

The expression of Bax increases, while the expression of Bcl-2 and survivin decrease in A549 cells treated with COS (Table II).

Observation of autophagy formation by MDC staining

The positive signals of MDC were mainly concentrated in the perinuclear area and the number of MDC positive cells in A549 cells treated with COS increased after COS treatment (Fig. 2A).

Observation of autophagy formation by immunofluorescence staining

Only a limited number of LC3 positive particles in the control group were located in individual cytoplasm, showing bright-spot fluorescence, and the number of positive autophagic cells was small. LC3 positive particles were mainly found in the cytoplasm of the COS treatment group, indicating that the number of autophagic cells increases. Immunofluorescence staining further showed that COS could induce autophagic cell death (Fig. 2B).

Changes of LC3II/LC3I ratios detected by Western blotting

The amount of LC3I in A549 cells treated with COS for 4 h was significantly higher than that of LC3II. With the prolongation of COS treatment time to 8 h, the amount of LC3I decreased, while the amount of LC3II increased. After treating with

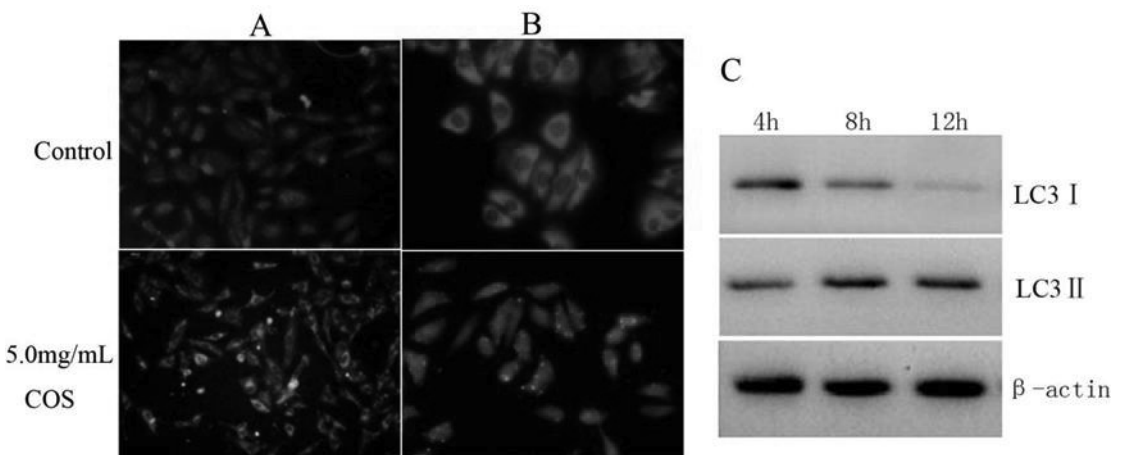

Fig. 2. ***A)*** *MDC staining, (x 200);* ***B)*** *Immunofluorescence staining, (x200);* ***C)*** *the effects of COS at different treatment time points on the expression level of LC3 protein in A549 cells*

COS for 12 h, LC3I mainly transformed into LC3II, indicating that the number of autophagic cells gradually increased (Fig. 2C).

DISCUSSION

It has been reported that COS has natural anti-tumor activity, can inhibit the proliferation of a variety of cancer cells, and has no toxic effects on normal organisms (10). Our results showed that COS could significantly inhibit the proliferation of A549 cells in a time- and dose-dependent manner. According to Muzzarelli's findings (11), the anti-tumor activity of COS is related to their potential of inducing apoptosis and necrosis in tumor cells. Pae et al. (12) showed that COS could inhibit the proliferation of HL-60 cells by inducing apoptosis. In our study, the COS treated cells were stained with Wright and Giemsa and appeared round, with contracted cytoplasm, and apoptotic bodies appeared. The apoptotic rate of A549 cells treated with COS (5.0 mg/ml) reached 37.68% after 24 h, confirming the above hypothesis.

Our results demonstrated that the anticancer effect of COS can be determined by three mechanisms: by promoting the apoptosis of cancer cells through inhibiting the expression level of Bcl-2, by up-regulating the expression level of Bax or by inhibiting the expression of survivin. In the current study, LC3 antibody was used to detect the number of autophagic vesicles in A549 cells treated with COS. Cytoplasmic LC3 (LC3I) can enzymatically hydrolyze a small segment of polypeptide and transform it into the autophagic membrane (LC3II), which is another key step in autophagy. This study demonstrates that, with the prolongation of COS treatment time, the proportion of LC3II/LC3I increases gradually, suggesting that COS can inhibit cell proliferation by inducing autophagy in tumor cells.

REFERENCES

1. Aam BB, Heggset EB, Norberg AL, Sørlie M, Vårum KM, Eijsink VG. Production of chitooligosaccharides and their potential applications in medicine. Mar Drugs 2010; 8(5):1482-517.
2. Kadry MO, Abdel-Megeed RM, El-Meliegy E, Abdel-Hamid A-HZ. Crosstalk between GSK-3, c-Fos, NFκB and TNF-α signaling pathways play an ambitious role in Chitosan Nanoparticles Cancer Therapy. Toxicol Rep 2018; 5:723-27.
3. Shen KT, Chen MH, Chan HY, Jeng JH, Wang YJ. Inhibitory effects of chitooligosaccharides on tumor growth and metastasis. Food Chem Toxicol 2009; 47(8):1864-71.
4. Jin S, White E. Role of autophagy in cancer: management of metabolic stress. Autophagy 2007; 3(1):28-31.
5. Kondo Y, Kanzawa T, Sawaya R, Kondo S. The role of autophagy in cancer development and response to therapy. Nat Rev Cancer 2005; 5(9):726-34.
6. Amaravadi RK, Lippincott-Schwartz J, Yin XM, et al. Principles and current strategies for targeting autophagy for cancer treatment. Clin Cancer Res 2011; 17(4):654-66.
7. Sani TA, Mohammadpour E, Mohammadi A, et al. Cytotoxic and apoptogenic properties of dracocephalum kotschyi aerial part different fractions on calu-6 and mehr-80 lung cancer cell lines. Farmacia 2017; 65(2):189-99.
8. Sui X, Chen R, Wang Z, et al. Autophagy and chemotherapy resistance: a promising therapeutic target for cancer treatment. Cell Death Dis 2013; 4:e838.
9. Pan JA, Ullman E, Dou Z, Zong WX. Inhibition of protein degradation induces apoptosis through a microtubule-associated protein 1 light chain 3-mediated activation of caspase-8 at intracellular membranes. Mol Cell Biol 2011; 31(15):3158-70.
10. Galluzzi L, Pietrocola F, Bravo-San Pedro JM, et al. Autophagy in malignant transformation and cancer progression. Embo J 2015; 34(7):856-80.
11. Muzzarelli RA. Biomedical exploitation of chitin and chitosan via mechano-chemical disassembly, electrospinning, dissolution in imidazolium ionic liquids, and supercritical drying. Mar Drugs 2011; 9(9):1510-33.
12. Pae HO, Seo WG, Kim NY, et al. Induction of granulocytic differentiation in acute promyelocytic leukemia cells (HL-60) by water-soluble chitosan oligomer. Leuk Res 2001; 25(4):339-46.

LETTER TO THE EDITOR

EXPRESSIONS OF SALL4, Bmi-1 AND p27 AND THEIR CORRELATION IN LARYNGEAL SQUAMOUS CELL CARCINOMA

LQ. WANG[1], Y. WANG[2], H. JIN[3], L. YAN[4], HF. LIU[5], J. LIANG[6] and LC. ZHANG[1]

[1]Department of Otolaryngology, Hongqi Hospital Affiliated to Mudanjiang Medical University, Mudanjiang, China; [2]Medical Functional Laboratory, Mudanjiang Medical University, Mudanjiang Medical University, Mudanjiang, China; [3]Department of Clinical Laboratory, Hongqi Hospital Affiliated to Mudanjiang Medical University, Mudanjiang, China; [4]Department of Histology and Embryology, Mudanjiang Medical University, Mudanjiang, China; [5]Heilongjiang Key Laboratory of Anti-fibrosis Biotherapy, Mudanjiang Medical University, Mudanjiang, China; [6]Stem Cell Institute, Mudanjiang Medical University, Mudanjiang, China

Received March 12, 2019 – Accepted May 24, 2019

To the Editor,

With more than 95% cases of squamous cell carcinoma, laryngeal cancer is one of the most common types of malignant tumors (1). At present, the prognosis of laryngeal cancer is still poor and its 5-year survival rate is less than 70% (2). Recently, molecular targeted therapy has become a research hotspot in the field of cancer therapy due to its high specificity and low invasiveness.

P27 can negatively regulate cell cycle, and the down-regulation or knockout of p27 expressions can lead to uncontrolled cell cycle progression, enhanced cell proliferation and blocked apoptosis, all of which may aid the malignant transformation of the cells (3). SALL4 is abnormally expressed in a variety of malignant tumors (4, 5). It has also been proved that SALL4 can inhibit the transcription of p27 gene (6), thus affecting the regulation of cell cycle (7). At the same time, it was revealed that SALL4 can bind to the promoter of Bmi-1 gene to initiate Bmi-1 transcription, thus affecting the expression level of the Bmi-1 gene (8). In addition, SALL4 and Bmi-1 both play an important role in maintaining the self-renewal and unlimited proliferation of stem cells (9, 10). However, there are few studies on SALL4, Bmi-1 and p27 in laryngeal squamous cell carcinoma. Therefore, in this study, expressions of SALL4, Bmi-1 and p27 in laryngeal squamous cell carcinomas were detected by an immunohistochemical method to clarify their roles and correlation in the development of laryngeal carcinoma, so as to provide a theoretical basis for developing molecular targeted therapies in the treatment of laryngeal cancer.

MATERIALS AND METHODS

Subjects

From May 2016 to December 2017, 60 patients (57 males and 3 females) with laryngeal squamous cell carcinoma from Hongqi Hospital Affiliated to Mudanjiang Medical University were enrolled in this study. Subsequently, 60 samples of laryngeal squamous cell carcinoma were collected as the experimental group, while 60 normal samples of laryngeal mucosa or inflammatory lesions were collected from sites adjacent to laryngeal squamous cell carcinoma as the control group. Informed

Key words: laryngeal squamous cells; SALL4; Bmi-1; P27 protein

Corresponding Author:
Dr Lichen Zhang,
Department of Otolaryngology,
Hongqi Hospital Affiliated to
Mudanjiang Medical University, No. 5 Tongxiang Road,
Mudanjiang, Heilongjiang Province, China
e-mail: zhanglichen5830@126.com

0393-974X (2019)

consent was signed by all patients and the experiment was approved by the ethics committee of Hongqi Hospital Affiliated to Mudanjiang Medical University.

The ages of the 60 patients ranged from 36 to 73 years median 52.5 years); 36 patients were over 52.5 years, and 24 patients were under 52.5 years; 33 patients smoked more than 1 cigarette/day, while 27 patients smoked less than 1 cigarette/day. The primary tumor size was larger than 3 cm in 23 patients and smaller than 3 cm in 37 patients. According to the primary location of the tumors, there were 25 cases of supraglottic type, 21 cases of glottic type, and 14 cases of subglottic type. Staging of laryngeal squamous cell carcinoma was determined using the TNM staging criteria. Thirty-five patients were of stage I and stage II, while 25 patients were at stages III and stage IV. According to the degree of tumor differentiation, 14 patients showed high differentiation (G1), 28 patients showed moderate differentiation (G2), and 18 patients showed poor differentiation (G3). In addition, 23 patients had lymph node metastasis, and 37 patients had none.

Immunohistochemical staining and judgment of results

The laryngeal cancer and paracancerous tissues were fixed in 10% formalin (Beijing Zhongshanjinqiao Biological Co., Ltd., China) and paraffin-embedded using a fully automatic embedding machine (LEICA, Germany). Four 4-μm thick pathological sections were cut from each wax block by a slicing machine (LEICA, Germany). Three of the slices were used for immunohistochemical staining and one slice was used as the negative control. The slices were baked in an oven at 65°C (Shanghai Sunshine Experimental Instrument Co., Ltd., China) for 12 h and incubated at room temperature before an immunohistochemical staining kit SP-9001 (Beijing Zhongshan Jinqiao Biological Co., Ltd., China) was used. The specific steps of staining were as follows: The slices were baked in at 65°C, and then dewaxed in xylene I and xylene II in turn. Thereafter, the slides were soaked in anhydrous ethanol I, anhydrous ethanol II, 95% ethanol, 80% ethanol, a phosphate buffered saline (PBS) buffer (Beijing Zhongshan Jinqiao Biological Co., Ltd., China) and an ethylene diamine tetraacetic acid (EDTA) buffer (Beijing Zhongshan Jinqiao Biological Co., Ltd., China) in turn. Finally, the slides were sealed and cooled to 20°C after being repaired in a high-pressure pot. After soaking and rinsing in PBS, the slides were subjected to light-proof repair in a wet box by adding 3% methanol and hydrogen peroxide onto the slides. After soaking and rinsing the slides in PBS, a goat serum working fluid was added onto the slides dropwise, and the slides were sealed and placed in a 37°C thermostat (Shanghai Sunshine Experimental Instrument Co., Ltd., China) before anti-1 (diluted at 1:200) antibodies were added onto the slides dropwise. The PBS buffer was used as the control. Then, the slides were incubated overnight in the wet box at 4°C. After 24 h, the slides were taken out from the wet box and soaked in the PBS buffer for 30 min before secondary antibodies were added onto the slides dropwise. The slides were then placed in the wet box and incubated at 37°C. After soaking and rinsing the slides in PBS, a diaminobenzidine (DAB) developer (Beijing Zhongshanjinqiao Biological Co., Ltd., China) was added to stain the slides. After successful staining, the slides were put into distilled water to stop DAB reaction, countered stained with hematoxylin, rinsed with water, differentiated in hydrochloric acid alcohol, developed using ammonia water, and rinsed with water. Finally, the slides were dehydrated using gradient alcohol of 80% ethanol, 95% ethanol, anhydrous ethanol I, and anhydrous ethanol II. After being dried and sealed in neutral gum, the slides were observed under an optical microscope (OLYMPUS, Japan).

The intensity of the positive expression of SALL4, Bmi-1 and p27 was judged by the staining intensity and percentage of positive cells on the slides. The multiplied score of SALL4, Bmi-1 and p27 was used as the immunohistochemical score of each slide (10). Score of staining intensity was: 0, no staining; 1, weak staining; 2, moderate staining; and 3, strong staining. The percentage of positive tumor cells: 0, the percentage of positive cells lower than 5%; 1, the percentage of positive cells 5%-25%; 2, the percentage of positive cells 26% - 50%; 3, the percentage of positive cells 51%-75%; and 4, the percentage of positive cells higher than 75%. Immunohistochemical score of SALL4: 0-1, negative (-); 2-4, weakly positive (+); 6-8, moderately positive (++); and 9-12, strongly positive (+++). The immunohistochemical score of Bmi-1 and p27: 0, negative (-); 1-2, weakly positive (+); 3-8, moderately positive (++); and 9-12, strongly positive (+++). Overall, +~+++ was deemed positive and – was deemed negative.

Statistical analysis

SPSS 21.0 statistical software was used for statistical analysis. The data were analyzed by χ^2 tests. The

difference was statistically significant when P was < 0.05. Spearman grade correlation analysis was used to analyze the correlation among SALL4, Bmi-1 and p27 expressions. The difference was statistically significant when P was < 0.05.

RESULTS

Expressions of SALL4, Bmi-1 and p27

The positive staining of SALL4, Bmi-1 and p27 in the experimental group was mainly located in the nucleus as gray or dark gray granules, as shown in Fig. 1. In the experimental and the control groups, the positive expression rates of SALL4 were 65% and 46.7%, respectively, and the difference was statistically significant (P < 0.05). The positive expression rates of Bmi-1 in the experimental and the control groups were 66.7% and 10%, respectively, and the expression of Bmi-1 in the experimental group was significantly higher (P < 0.05). The positive expression rates of p27 in the experimental and the control groups were 46.7% and 70%, respectively, and the expression level of p27 in the experimental group was significantly lower (P < 0.05). The detailed results are shown in Table I.

Relationship between the clinicopathological features of laryngeal squamous cell carcinoma and the expression of SALL4, Bmi-1 and p27

The positive expression rate of SALL4 in the stage I + II group (51.4%) was lower than that in the stage III + IV group (84.0%). In addition, a higher clinical stage of laryngeal cancer was associated with a higher level of positive expression of SALL4 (P < 0.05). Moreover, the positive expression rate of SALL4 gradually increased in highly (83.7%), moderately (67.9%) and lowly (33.3%) differentiated laryngeal cancer (P < 0.05). Finally, the positive expression rate of SALL4 in the group (87%) with lymph node metastasis was significantly higher than that in the group without lymph node metastasis (51.4%) (P < 0.05). The detailed results were shown in Table II below.

The later the clinical stage of laryngeal cancer, the higher the positive expression of Bmi-1. The positive expression rate of Bmi-1 in stage I+II patients (51.4%) was significantly lower than that in stage III+IV patients (88.0%) (P < 0.05). In highly (35.7%), moderately (71.4%) and lowly (83.3%) differentiated laryngeal cancer tissues, the positive rate of Bmi-1 expression increased over a decreasing

Table I. *Expressions of SALL4, Bmi-1 and p27 in experimental and control groups.*

Gene	Group	Number	Expression				Z	P
			-	+	+ +	+ + +		
SALL4 (%)	Control group	60	32 (53.3)	17 (28.3)	8 (13.3)	3 (5.0)	-2.142	0.034*
	Experimental group	60	21 (35.0)	8 (13.3)	18 (30.0)	13 (21.7)		
Bmi-1 (%)	Control group	60	54 (90.0)	3 (5.0)	2 (3.3)	1 (1.7)	-4.287	0.001*
	Experimental group	60	20 (33.3)	12 (20.0)	9 (15.0)	19 (31.7)		
p27 (%)	Control group	60	18 (30.0)	8 (13.3)	20 (33.3)	14 (23.3)	-2.661	0.007*
	Experimental group	60	32 (53.3)	15 (25.0)	9 (15.0)	4 (6.7)		

** P < 0.05.*

degree of laryngeal cancer differentiation ($P < 0.05$). In addition, the positive expression rate of Bmi-1 in the group (82.6%) with lymph node metastasis was higher than that in the group (56.8%) without lymph node metastasis ($P < 0.05$). The detailed results are shown in Table II.

The positive expression rate of p27 in highly (64.3%), moderately (46.4%) and lowly (33.3%) differentiated laryngeal cancer decreased over the decreasing degree of differentiation ($P < 0.05$). The positive expression rate of p27 in the group (21.8%) with lymph node metastasis was significantly lower than that in the group (61.2%) without lymph node metastasis ($P < 0.05$). In addition, although the positive expression rate of p27 in the stage I + II group (40.0%) was lower than that in the stage III + IV group (56.0%), the difference was not significant ($P > 0.05$). The detailed results are shown in Table II.

SALL4, Bmi-1 and p27 expressions in laryngeal squamous cell carcinoma

The correlation among SALL4, Bmi-1 and p27 expressions in laryngeal squamous cell carcinoma was analyzed by hierarchical correlation analysis. The results showed the presence of a positive correlation between Bmi-1 and SALL4 expressions ($r=0.379$, $P=0.007$), a negative correlation between Bmi-1 and p27 expressions ($r=-0.380$, $P=0.008$), and a negative correlation between p27 and SALL4 expressions ($r=-0.309$, $P=0.027$).

DISCUSSION

The results of this study showed that the expression rate of SALL4 in the experimental group was higher than that in the control group ($P < 0.05$), and the expression of SALL4 increased over the increasing clinical stage and the degree of malignance of laryngeal cancer ($P < 0.05$), indicating that SALL4 can be considered as a molecular marker for the diagnosis and prognosis evaluation of laryngeal cancer. The results of this study showed that the expression rate of Bmi-1 in the experimental group was higher than that in the control group ($P <$

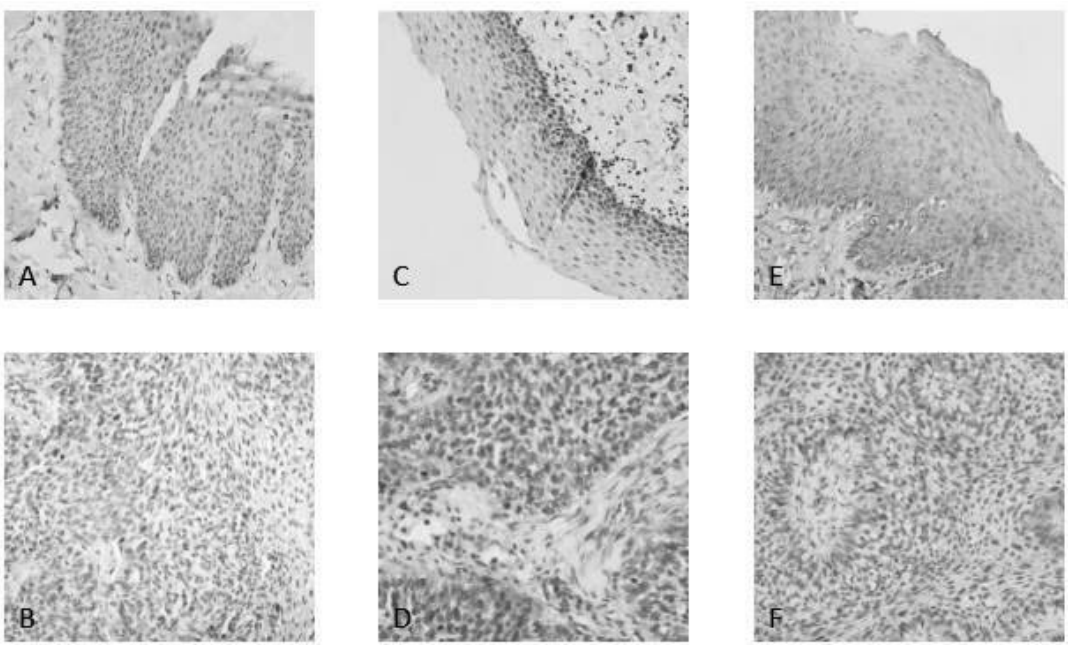

Fig. 1. *The expression of SALL4, Bmi-1 and p27 in the experimental and the control groups.* ***A)*** *Negative SALL4 expression in the control group;* ***B)*** *positive SALL4 expression in the experimental group;* ***C)*** *negative Bmi-1 expression in the control group;* ***D)*** *positive Bmi-1 expression in the experimental group;* ***E)*** *positive p27 expression in the control group;* ***F)*** *negative p27 expression in the experimental group, 200x.*

Table II. *The relationship between SALL4, Bmi-1 and p27 expression and clinicopathological features in the experimental group.*

Clinicopathological features		Number	SALL4				Bmi-1				p27			
			(+~+++)	(-)	χ^2	P	(+~+++)	(-)	χ^2	P	(+~+++)	(-)	χ^2	P
Gender	Male	57	36	21	-	0.645	37	20	-	0.664	25	32	-	0.531
	Female	3	3	0			3	0			3	0		
Age	≤51.5	24	14	10	0.535	0.461	13	11	2.556	0.112	9	15	1.775	0.186
	>52.5	36	25	11			27	9			19	17		
Smoking volume	≤365	27	18	9	0.437	0.509	18	9	0.160	0.695	12	15	0.011	0.923
	>365	33	21	12			22	11			16	17		
Differentiation of tumors	G1	14	12	2	7.065	0.028	5	9	7.961	0.018	9	5	8.236	0.017
	G2	28	19	9			20	8			13	15		
	G3	18	6	12			15	3			6	12		
Primary tumor size	≤3cm	37	24	13	0.304	0.576	22	15	0.164	0.683	18	19	0.052	0.815
	>3cm	23	15	8			18	5			10	13		
Lymph node metastasis	No	37	19	18	5.039	0.024	21	16	4.195	0.042	23	14	5.551	0.020
	Yes	23	20	3			19	4			5	18		
TNM staging	I+II	35	18	17	4.118	0.043	18	17	9.117	0.004	14	21	1.459	0.226
	III+IV	25	21	4			22	3			14	11		
Primary site of tumor	Supraglottic type	25	16	9	1.679	0.433	17	8	1.567	0.457	13	12	0.495	0.783
	Glottic	21	11	10			15	6			9	12		
	Subglottic type	14	12	2			8	6			6	8		

0.05), and the expression of Bmi-1 increased over the increasing clinical stage ($P < 0.05$) and decreasing degree of tumor differentiation ($P < 0.05$) of laryngeal cancer, suggesting that knockout or knockdown of the Bmi-1 expression may aid the treatment of laryngeal cancer and improve its prognosis. The results of this study showed that the expression of p27 in the experimental group was lower than that in control group ($P < 0.05$). The expression of p27 decreased over a decreasing degree of differentiation in laryngeal squamous cell carcinoma. In the group with lymph node metastasis, the expression of p27 also decreased ($P < 0.05$), suggesting that laryngeal cancer may be treated by restoring or up-regulating the expression of p27. The results of this study showed that in laryngeal cancer, the expression of both Bmi-1 and SALL4 was correlated with the expression of p27. Therefore, these three factors play a synergistic role in the occurrence and development of laryngeal cancer.

To sum up, the expression of SALL4, Bmi-1 and p27 in laryngeal squamous cell carcinoma was closely related to the occurrence, invasion and metastasis of laryngeal cancer. Therefore, the joint detection of the expression of SALL4, Bmi-1 and p27 in laryngeal cancer may help the diagnosis and prognosis prediction of laryngeal cancer.

ACKNOWLEDGEMENTS

This study was supported by the scientific research project of basic research fund in Heilongjiang Provincial Universities (2017-kyywfmy-0679); Mudanjiang Science and Technology Planning Project (Z2018s043).

REFERENCES

1. Marioni G, Marchese-Ragona R, Cartei G, Marchese F, Staffieri A. Current opinion in diagnosis and treatment of laryngeal carcinoma. Cancer Treat Rev 2006; 32(7):504-15.
2. Rudolph E, Dyckhoff G, Becher H, Dietz A, Ramroth H. Effects of tumour stage, comorbidity

and therapy on survival of laryngeal cancer patients: a systematic review and a meta-analysis. Eur Arch Otorhinolaryngol 2011; 268(2):165-79.
3. Oka K, Suzuki Y, Nakano T. Expression of p27 and p53 in cervical squamous cell carcinoma patients treated with radiotherapy alone: radiotherapeutic effect and prognosis. Cancer 2000; 88(12):2766-73.
4. Bai S, Wei S, Ziober A, Yao Y, Bing Z. SALL4 and SF-1 were sensitive and specific markers for distinguishing granulosa cell tumors from yolk sac tumors. Int J Surg Pathol 2013; 21(2):121-25.
5. Deisch J, Raisanen J, Rakheja D. Immunohistochemical expression of embryonic stem cell markers in malignant rhabdoid tumors. Pediatr Dev Pathol 2011; 14(5):353-59.
6. Gartel AL, Shchors K. Mechanisms of c-myc-mediated transcriptional repression of growth arrest genes. Exp Cell Res 2003; 283(1):17-21.
7. Yang J, Chai L, Liu F, et al. Bmi-1 was a target gene for SALL4 in hemato-poietic and leukemic cells. Proc Natl Acad Sci U S A 2007; 104(25):10494-99.
8. Guarino M. Epithelial-mesenchymal transition and tumour invasion. Int J Biochem Cell Biol 2007; 39(12):2153-60.
9. Kobayashi D, Kuribayshi K, Tanaka M, Watanabe N. SALL4 was essential for cancer cell proliferation and was overexpressed at early clinical stages in breast cancer. Int J Oncol 2011; 38(4):933-39.
10. Detre S, Saclani Jotti G, Dowsett M. A "quickscore" method for immunohistochemical semiquantitation: validation for oestrogen receptor in breast carcinomas. J Clin Pathol 1995; 48(9):876-78.

LETTER TO THE EDITOR

CLINICAL EFFICACY OF A SERIES OF CHINESE HERBAL MEDICINES IN THE TREATMENT OF STABLE CHRONIC OBSTRUCTIVE PULMONARY DISEASE BASED ON SYNDROME DIFFERENTIATION

X. YU[1], W. WANG[2] , H. ZHENG[1], XJ. QIAN[1] and P. JIANG[1]

[1]Department of respiration, Tianjin First Center Hospital, Tianjin, China; [2]Department of Endocrinology, Tianjin First Center Hospital, Tianjin, China

Received January 8, 2019 – Accepted July 9, 2019

To the Editor,

Chronic obstructive pulmonary disease (COPD) is the fourth leading cause of death in the United States (1), and is expected to become the third leading fatal disease globally by 2020 (2). COPD is a chronic airway inflammatory disease characterised by airflow limitation (3). The functions of multiple organs apart from the lungs are also affected (4). A significant reduction in quality of life, nutritional status and exercise ability are reported in patients presenting with obvious dyspnoea (5), and this inflammation may lead to chronic hypoxia in many organs as well as a reduction in the immune system (6). Traditional Chinese medicine (TCM) emphasises holism and syndrome differentiation, and multi-target and multi-site treatments are some of its advantages. Modern Chinese medicine believes that COPD mainly causes spleen *qi* deficiency, lung *yang* deficiency and kidney *yin* deficiency, three types of TCM syndrome. Western medicine can alleviate the clinical symptoms of COPD, but attacks often recur. Therefore, combined with Western medicine, different Chinese medicines are used to treat COPD patients based on the TCM syndromes. The aim of this study is to fundamentally treat COPD. Accumulating evidence has revealed that TCM alone or a combination of TCM and Western medicine has a good clinical effect in the treatment of stable COPD (7, 8).

This study investigated the efficacy of TCM for patients with stable COPD. Treatment was given based on syndrome differentiation on the basis of conventional Western medical treatments. The prescriptions were chosen based on the symptoms of weakness of the lungs, spleen and kidneys (9). In order to provide an objective basis for further clinical application, the clinical efficacy of the combination of TCM and Western medicine was evaluated in the treatment of stable COPD.

MATERIALS AND METHODS

A total of 120 patients with moderate-stage COPD in the stable period, who were admitted to hospital between January 2016 and January 2017, completed the study process. The diagnostic criteria were consistent with that for stable COPD in the Guidelines for the Diagnosis and Management of Chronic Obstructive Lung Disease (2013 revised edition), developed by the COPD group of the Respiratory Medicine Society of the Chinese Medical

Key words: stable chronic obstructive pulmonary disease; Strengthening body resistance; Chinese medicine syndrome differentiation; traditional Chinese medicine; Western medicine

Corresponding Author:
Dr Xi Yu,
Department of Respiration,
Tianjin First Center Hospital,
No. 24 Rehabilitation Road, Nankai District,
Tianjin 300192, China
Tel.: +86 13682198585 - Fax: +86 022 23626600
e-mail: xiyu_dr@163.com

0393-974X (2019)

Association (3). Patients who had COPD but who were experiencing an acute exacerbation of the disease, or had other pulmonary diseases, were excluded from the study.

The patients enrolled were 67 males and 53 females (ages 51-75 years; average 63.34±9.87 years). The course of the disease ranged between 10 and 20 years, with an average of 14.17±4.06 years. This study was a single-blind randomised controlled study after syndrome differentiation of TCM. The patients were randomly divided into a control group (n = 60) and an observation group (n = 60). All patients received improved health education and were instructed to quit smoking and prevent the inhalation of dust, smoke and harmful gases. Patients in the observation group were treated with symptom-guided Chinese herbal medicines in addition to the treatment received by the control group. The differences in age, gender, course of the disease and lung function before treatment were not statistically significant between the two groups. The study

Table I. *Functions and applicable symptoms of Chinese herbs.*

Chinese herb	Functions	Applicable symptoms
Heterophyllya false starwort root	Nourish *yin* and moisten the lungs.	Chronic cough; blood in phlegm.
Astragalus	Anti-inflammatory; immunostimulant; antioxidative; anti-cancer; anti-diabetic; cardioprotective; hepatoprotective; antiviral activities.	*Qi* deficiency syndrome; empyrosis; nephritis; diabetes mellitus; hypertension; cirrhosis; leukaemia; uterine cancer.
Lily	Nourishing *yin* and moistening the lungs.	Chronic cough; blood in phlegm.
Schisandra berry	Pulmonary astringency; kidney nourishment; tonifying body fluid; sweating; astringent essence.	Treatment of asthma and cough due to lung deficiency; thirst due to dry mouth; spontaneous sweating; night sweating; fatigue and thin wounds; sleeping droppings; prolonged diarrhoea and dysentery.
Gecko	Activating collaterals and dispersing knots.	Malignant tumours; tuberculosis; osteomyelitis and syrinx.
Codonopsis pilosula	Replenishing *qi*; relieving thirst; tonifying the spleen and lungs; nourishing the blood.	Spleen and lung *qi* deficiency; fatigue; cough asthma; insufficiency of *qi* and blood.
Poria cocos	Tonifying the spleen and stomach.	Diabetes mellitus; dysentery; chronic fatigue syndrome; diarrhoea; dizziness; oedema; insomnia; kidney problems.
Atractylodes macrocephala	Tonifying the spleen; replenishing *qi*.	Spleen deficiency.
Rhizoma zingiberis	Tonifying the spleen.	Spleen deficiency.
Fructus ziziphi jujubae	Replenishing *qi*; nourishing the blood.	Spleen deficiency.
Fructus corni	Nephroprotective activities.	Kidney deficiency.
Oriental waterplantain rhizome	Clearing away heat and nourishing *yin*; tonifying the kidneys; promoting the secretion of saliva.	Kidney deficiency.
Prepared rehmannia	Replenishing *qi*; nourishing the *yin.*	Blood deficiency.
Cinnamomum cassia	Invigorating the *yang.*	Kidney *yang* deficiency.
Monkshood	Replenishing the *yang*; expelling chill and dampness; stopping pain	Kidney *yang* deficiency.
Salvia miltiorrhiza	Invigorating the *yang*; clearing away heat.	Kidney deficiency.
Chuanxiong rhizome	Dispersing blood stasis; promoting blood and *qi* circulation; dispelling wind and relieving pain.	Cough; toothache; wind chill; too much spit and nasal discharge.
Herba epimedii	Warming the kidney *yang*.	Kidney *yang* deficiency syndrome.
Couchgrass root	Dispelling wind; dredging collaterals; harmonising stomach ventilation.	Wind chill; easing pain.
Polygala root	Expectorant and sedative.	Insomnia; amnesia; depression; palpitations with anxiety; memory improvement.

was approved by the Ethics Committee of Tianjin First Central Hospital and all participants provided written informed consent.

Patients in the control group only inhaled seretide (salmeterol/fluticasone propionate; GlaxoSmithKline PLC, UK; Drug Import Registration Certificate no. H20140164; specifications: 250 μg/50 μg × 60 inhalations) twice daily (morning, evening) for treatment, 1 inhalation/time. Other drugs were not taken during the treatment.

Based on the Diagnostic Efficacy of Standard TCM Syndrome (2012 edition) (8), the observation group patients were divided into three types according to TCM syndrome differentiation: lung *qi* deficiency (group A), spleen *yang* deficiency (group B) and kidney *yang* deficiency (group C). As well as the inhalation of 250/50 μg of seretide, patients with different types of symptom took different TCM oral prescriptions (every prescription was a granular preparation with independent packing) once in the morning and once in the evening. The course of treatment was three months. The TCM prescriptions used in this study were purchased from Jiangyin Traditional Chinese Medicine Group. The error of these medicines was about 0.1, which meets the quality control standard of new TCM.

Group A was comprised of 17 patients with lung *qi* deficiency. Coughing was the principal manifestation of the disease during attacks. The sound of the cough was clear, and most were single or intermittent, more frequent during the day than at night, and the amount of phlegm was small. After controlling the acute symptoms, patients sweated easily, easily caught a cold and had a fear of wind. The tongue was normal or had a slightly light colour, and the coating of the tongue was thin and white. The pulse was wiry and thready or slow and thready. Herbal prescription: 30 g of heterophylla false starwort root, 30 g of raw astragalus, 30 g of lily, 20 g of schisandra berry and a pair of geckos (approximately 10 g) (Table I).

Group B was comprised of 32 patients with spleen *yang* deficiency. Patients often had wet coughs during attacks, which usually manifested as repeated coughs, severe at night and mild during the day. The cough discharge was mucus or serous sputum, the volume of which was often > ++. After controlling the acute symptoms, patients lost their appetites, experienced abdominal distension after meals, their faces became swollen and their stools were soft and semi-fluid. Their tongues were light or swollen and often had teeth marks, and the coating of the tongue was white or white and greasy. The pulse was

Table II. *Comparison of total syndrome scores, CAT scores and FEV1/Pred% before and after treatment between the observation group and control group.*

Observation index	Number	Observation group	Control group	*P*-value
Syndrome score before treatment	60	16.47±4.14	16.98±3.85	0.007
Syndrome score after treatment	60	5.44±1.85	8.95±2.11	0.011
P-value			0.026	
CAT score before treatment	60	16.28±4.93	16.43±4.52	0.009
CAT score after treatment	60	7.97±2.19	11.23±2.18	0.016
P-value			0.019	
FEV1/Pred% before treatment (%)		66.51±12.97	65.43±14.11	0.087
FEV1/Pred% after treatment (%)		65.24±6.09	66.78±8.18	0.091
P-value			0.103	
GOLD 2		Moderate	Moderate	

moist and slow or slippery. The herbal prescription was 30 g of astragalus, 30 g of *Codonopsis pilosula*, 30 g of *Poria cocos* from Yunnan, China, 20 g of *Atractylodes macrocephala*, 15 g of *Rhizoma zingiberis*, and 20 g of *Fructus ziziphi jujubae* (Table I).

Group C was comprised of 11 patients with kidney *yang* deficiency. Patients often had dry coughs during attacks, which mostly manifested as paroxysmal and were more severe at night than during the day. The volume of sputum varied from + to +++. After controlling the acute symptoms, patients experienced mild lumbago and weakness of the limbs. During a coughing attack, patients suffered from enuresis or frequent nocturia, experienced dizziness and tinnitus, felt cold in the body and limbs and were short of breath. When moving, patients were characterised as having shortness of breath. Their tongues were light and swollen or had blood stasis. The coating of the tongue was white, smooth and moist. The pulse was often thready (deep and thready, wiry and thready, or thready and rapid). The herbal prescription was 30 g of *Fructus corni*, 30 g of *Poria cocos* from Yunnan, China, 15 g of Oriental waterplantain rhizome, 30 g of prepared rehmannia, 10 g of Cinnamomum cassia, 10 g of monkshood, 15 g of *Herba epimedii*, 30 g of couchgrass root, 15 g of polygala root, 15 g of *Salvia miltiorrhiza*, and 10 g of Chuanxiong rhizome (Table I).

Symptom and sign scores and curative effect scores before and after treatment

The evaluation criteria for curative effect were established according to the Diagnostic Efficacy of Standard TCM Syndrome (4).

Criteria for phlegm volume score (the volume of phlegm for one whole day): no phlegm, 0 points; 10–50 mL, 2 points; 51–100 mL, 4 points; >100 mL, 6 points.

Criteria for cough score: no obvious cough, 0 points; mild cough, 2 points; relatively obvious cough, 4 points; very obvious cough, 6 points.

Criteria for wheezing score: no wheezing, 0 points; occasional mild wheezing that does not affect rest or activities, 2 points; frequent wheezing that does not affect sleep, 4 points; obvious wheezing, the patient cannot lie in a supine position and affecting sleep or activity, 6 points.

Criteria for lung rale score: no rales, 0 points; scattered dry rales or few wet rales, 2 points; a large number of dry and wet rales, but not fully distributed in the whole lungs, 4 points; dry and wet rales that are fully distributed in the whole lungs, 6 points.

Clinical control: main symptoms disappeared or basically disappeared and objective indexes returned to normal levels. The more the symptom score was reduced, the more obvious the clinical effect was.

Pulmonary function

Pulmonary function was determined using a lung function tester (Jaeger, Germany) based on the criteria established by the American Thoracic Society (ATS) (2, 3). The instrument was calibrated every day after the machine was turned on, including environmental calibration (altitude, atmospheric pressure, temperature and humidity were measured and recorded), volume calibration and box calibration, to ensure that the lung function tester was in good working condition for each test. Pulmonary function data were measured in the standard output state. The forced expiratory volume in one second (FEV1)/measured forced vital capacity (FVC)

Table III. *Comparison of the frequency of acute exacerbation and the average duration of acute exacerbation between the observation group and control group.*

Group	Number	Frequency of acute exacerbation (times)	Average duration of acute exacerbation (days/year)
Observation group	60	1.75±1.25	16.56±9.09
Control group	60	2.35±1.32	21.61±7.96
P-value		0.032	0.041

and FEV1/predicted% (FEV1/Pred%) were measured and recorded (2, 3). These tests were performed before treatment on the first day, in the third month of treatment, and the sixth and twelfth month after treatment.

Quality of life

The quality of life score was evaluated using the commonly used COPD assessment test (CAT) (2, 3). CAT is mainly used as a simple and reliable evaluation of the health status of COPD patients. It is simple and fast and covers a wide range of health concerns, such as symptoms and the ability to exercise.

Frequency of acute attacks

The definition of acute exacerbation was based on the Guidelines for the Diagnosis and Management of Chronic Obstructive Lung Disease (2013 revised edition) (3). The diagnosis of acute exacerbation of COPD mainly depends on the description of a patient's own observations of their daily symptoms. Acute exacerbation is characterised by abnormal changes in the symptoms of a patient's conscious respiratory system beyond daily fluctuations and the patient needing to change their daily medication. The main manifestation is the aggravation of dyspnoea, which is often accompanied by wheezing, chest tightness, exacerbation of the cough, increased phlegm, changes in colour and/or viscosity of sputum, and fever.

Safety index

Safety indexes included routine blood indexes, routine urine indexes, glutamic pyruvic aminotransferase and urea nitrogen and creatinine tests, which were undertaken before and after the treatment.

The adverse reactions caused by the use of drugs in the course of treatment were observed.

Statistical analysis

Data were statistically analysed using statistical software SPSS 17.0. Normally distributed measurement data were expressed as mean ± standard deviation (x±SD). Measurement data were compared between the two groups using an independent sample *t*-test, and count data were compared between the two groups using a *Chi*-squared test. $P<0.05$ was considered statistically significant.

RESULTS

The balance in gender between the two groups was evaluated using a *t*-test, the *P*-value of which was >0.05, suggesting that the difference in gender between these two groups was not statistically significant. The balance in age, course of the disease, syndrome score and lung function (FEV1/Pred%) between these two groups was evaluated using a *t*-test, the *P*-value for which was >0.05 for all, suggesting that the differences in all parameters between the two groups were not statistically significant.

In the observation group, the total score of clinical syndrome was 16.47±4.14 before treatment and 5.44±1.85 after treatment, which was a significant decrease. In the control group, the total score of clinical syndrome was 16.98±3.85 before treatment and 8.95±2.11 after treatment, which was also a significant decrease. The total score after treatment between the two groups was statistically evaluated, with the *P*-value being 0.026 ($P<0.05$), suggesting that the difference between the two groups was statistically significant (Table II).

In the observation group, the CAT score was 16.28±4.93 before treatment and 7.97±2.19 after treatment, which was a significant decrease. In the control group, the CAT score was 16.43±4.52 before treatment and 11.23±2.18 after treatment, which was also a significant decrease. The CAT score after treatment between the two groups was statistically evaluated, with the *P*-value being 0.019 ($P<0.05$), suggesting that the difference between the two groups was statistically significant (Table II).

In the observation group, the FEV1/Pred% was 66.51±12.97% before treatment and 65.24±6.09% after treatment, which was not a significant decrease. In the control group, the FEV1/Pred% was 65.43±14.11% before treatment and 66.78±8.18% after treatment, which was not a significant change. The FEV1/Pred% after treatment between the two groups was statistically evaluated, with the *P*-value being 0.103 ($P>0.05$), suggesting that the difference between the two groups was not statistically significant (Table II).

Long-term anti-recurrent efficacy in one year was compared between the two groups. Differences in the frequency of acute exacerbation and the average

duration of acute exacerbation between the two groups were statistically significant (Table III).

None of the patients in the two groups had obvious adverse reactions during the treatment.

DISCUSSION

Although the present treatment of Western medicine can effectively relieve the symptoms and complications of COPD, few studies have researched the drugs and methods that can effectively prevent and reverse the progress of COPD (10). TCM treatment follows the principle of attaching the symptoms for acute diseases and clearing up the original cause of chronic diseases. Although the centuries-old medical system's foundations are still unknown, by following its principles we have successfully prevented the progress of COPD in some cases and even reversed its progress. This study of TCM has emphasised that in the stable period of COPD it is necessary to strengthen the body's resistance to reduce acute attacks and delay the progress of the disease (11). This study aimed to investigate the efficacy of TCM combined with Western medicine in the treatment of COPD. From the results obtained, it can be concluded that syndrome scores and CAT scores were significantly decreased in both groups, and better efficacy was observed when COPD patients were treated with both TCM and Western medicine. The study's hypothesis can be further demonstrated by the comparison of the frequency of acute exacerbation and the average duration of acute exacerbation between the observation group and control group. In the observation group, the frequency and duration of acute exacerbation was less than in the control group, which indicates that TCM combined with Western medicine could mitigate the recurrence of COPD attacks. Furthermore, it could be a promising therapeutic method for COPD patients.

REFERENCES

1. GBD 2015 Chronic Respiratory Disease Collaborators. Global, regional, and national deaths, prevalence, disability-adjusted life years, and years lived with disability for chronic obstructive pulmonary disease and asthma, 1990-2015: a systematic analysis for the Global Burden of Disease Study 2015. Lancet Respir Med 2017; 5:691-706.
2. Global Initiative for Chronic Obstructive Lung Disease (GOLD): Global Strategy for the Diagnosis, Management and prevention of Chronic Obstructive Pulmonary Disease. (2017 REPORT). http://www.goldcopd.org.
3. Chronic obstructive pulmonary disease group of the Chinese Medical Association for respiratory diseases. Guidelines for the diagnosis and treatment of chronic obstructive pulmonary disease (2013 Revised Edition). Chin J of Tuberc Resp Dis 2013; 36:255-64.
4. Ge JB, Xu YJ. Internal Medicine (Eighth Edition). Beijing: People's Medical Publishing House; 2013.
5. Dai PJ, Ji XJ, Wang HH, Liang H. Therapeutic effect of tiotropium bromide combined with Shah Mette Lo / propionate in the treatment of stable chronic obstructive pulmonary disease. J Chin PR Diag Ther 2013; 27:68-70.
6. Liu WB, Huang LS, Ding XJ. Effect of integrated traditional Chinese and Western Medicine on immune function of patients with chronic obstructive pulmonary disease. Zhejiang J Tradit Chin Med 2014; 49:290.
7. Yang JQ, Wang Z, Lou YF, Xu JP, Hong HH, Chen RL, Yu NN. Clinical observation of Yiqi Jianpi granules combined with Western medicine in the treatment of 60 cases of chronic obstructive pulmonary disease at stable stage of lung and spleen deficiency. J Tradit Chin Med 2013; 54:1933-36.
8. Li Hang, Huang HT, Zhan SF, Liu XH. Therapeutic effect of therapy of reinforcing earth to strengthen metal for stable phase of chronic obstructive pulmonary disease: a meta-analysis. J Guangzhou Univ Tradit Chin Med 2017; 34:132-39.
9. State Administration of Traditional Chinese Medicine. Standard of traditional Chinese medical syndrome diagnosis. Beijing: Chinese medicine publishing house; 2012.
10. He QY. The 2015 revised edition of the global prevention and treatment of chronic obstructive pulmonary disease. Chin J Resp Crit Care Med 2015; 14:125-27.
11. The Ministry of Health of the People's Republic of China. Clinical guidelines for new drugs in Chinese medicine. Beijing: Chinese Medicine Science and Technology Publishing House; 2002.

LETTER TO THE EDITOR

BACTERIOLOGICAL AND BIOCHEMICAL ANALYSIS OF RAW MILK SAMPLES FROM MASTITIC SAHIWAL COWS OF THE PUNJAB PROVINCE

H. SATTAR[1], S. FIRYAL[1], A.R. AWAN[1], H. REHMAN[2], M. WASIM[1], M. TAYYAB[1] and A.A. ANJUM[3]

[1]Institute of Biochemistry and Biotechnology, University of Veterinary and Animal Sciences, Lahore, Pakistan; [2]Department of Physiology, University of Veterinary and Animal Sciences, Lahore, Pakistan; [3]Department of Microbiology, University of Veterinary and Animal Sciences, Lahore, Pakistan

Received April 16, 2019 – Accepted July 12, 2019

To the Editor,

Mastitis results from an intramammary infection caused by pathogenic microorganisms, and is a significant disease in the dairy industry. Bacteriological etiology is very important for mastitis prevention and control (1). Mastitis negatively affects the quality and quantity of milk by reducing milk production, and inducing changes in milk composition (including increase in somatic cell count SCC), and milk discards (2). Mastitis not only affects animal health, but it can also have major implications on the financial situation of dairy farms. Despite recent technological advances in veterinary medical care, mastitis is still a frequent and costly disease in the dairy industry.

Pakistan is ranked at third position in the world for milk production (3). Bovine mastitis is one of the major diseases of dairy herds worldwide and the dairy industry in Pakistan is often negatively impacted by a high incidence and prevalence of mastitis (4). The etiopathology of bovine mastitis is multifaceted and usually includes: a combination of environmental conditions, exposure to pathogenic microorganisms and host defense mechanisms (5). The organisms responsible for mastitis can be classified by their nature as contagious and environmental. The most predominant infectious agents are streptococci, coliforms, coagulase-negative staphylococci, as well as *Staphylococcus aureus* (6). The aim of this study was to assess three main forms of bacterial contamination in mastitic milk from a dairy cow herd in comparison to normal raw cow milk. The results of this study will provide information on mastitis-causing bacteria for rapid detection, correct mastitis prevention and control.

MATERIALS AND METHODS

In the present study, biochemical and bacteriological analysis was carried out in the Microbiology Laboratory, Department of Microbiology, University of Veterinary and Animal Sciences, Lahore, Pakistan.

Animals

A total of 360 Sahiwal cows with clinical (n=120), and subclinical (n=120) mastitis infections, as well as healthy animals (n=120) were included in this study. The samples were collected from different Government farms of the Punjab province [Khanewal (Jahangirabad, Qadirabad); Okara (Bahadurnagar, Shergarh); Sheikhupura and

Key words: mastitis; cow milk; bacteriological analysis; biochemical analysis; Sahiwal cow

Corresponding Author:
Dr Sehrish Firyal,
Institute of Biochemistry and Biotechnology,
University of Veterinary and Animal Sciences,
Lahore, Pakistan
Tel.: +92 3336573392
e-mail: sehrishfiryal@uvas.edu.pk

0393-974X (2019)

Lahore]. Punjab has the largest cattle population with 48% of the total population and is the major milk producing province with an annual milk production of 9.35 million liters (Government of Pakistan, 2008). For the detection of subclinical mastitis, a Surf Field mastitis test was performed in the field (7). To this end, foremilk samples were mixed with equal volumes of 3% household detergent solution (Surf Excel, Lever Brothers Pakistan) in the four receptacles of the Surf Test paddles. The mixture was swirled for about 15 s and monitored for gel formation (i.e. thickening of the mixture).

Collection of milk sample

Milk samples (4-5 mL) from 360 Sahiwal cows were collected aseptically from each of the selected animals after sanitizing the teat ends with 70% ethyl alcohol. Before collection of the sample, the end of each teat was carefully and vigorously scrubbed with a cotton swab moistened with 70% ethyl alcohol for 12-15 sec. A separate swab was used for each teat being sampled (even of the same cow). Teats were dried thoroughly, and then two to three streams of milk were extracted to minimize the chance of contamination. Subsequently, milk samples

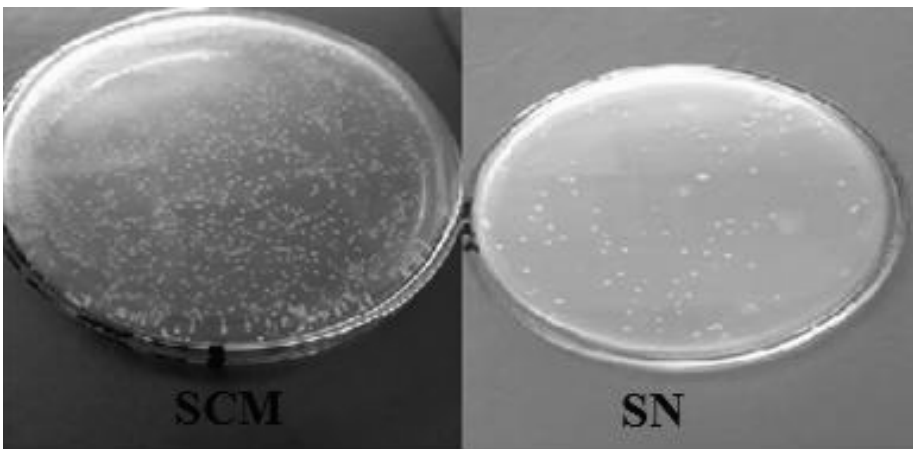

Fig. 1. *Isolated bacterial colonies on blood agar plates of clinical mastitis (SCM), and normal (SN) Sahiwal cow's milk sample.*

Table I. *Biochemical test results of clinical, subclinical and normal raw milk samples from Sahiwal cows*

Sample type	Gram stain	Coagulase	CT	Ind	NT	SH	OX	Identified bacteria
Clinical	-	-	+	+	+	-	-	*E.coli*
	+	+	+	-	+	-	-	*S. aureus*
	+	-	-	-	-	-	-	*S. agalactiae*
Subclinical	-	-	+	+	+	-	-	*E.coli*
	+	+	+	-	+	-	-	*S. aureus*
	+	-	-	-	-	-	-	*S. agalactiae*
Healthy	-	-	+	+	+	-	-	*E.coli*
	+	-	-	-	-	-	-	*S. agalactiae*
	+	+	+	-	+	-	-	*S. aureus*

were collected in sterilized collection vials. The samples were placed on ice immediately after collection and were taken to the microbiology laboratory and stored temporarily at -20°C.

Preparation of serial dilution

Before plating, each milk sample was diluted. Sterilized distilled water was used to make an initial10-fold dilution. From this, further serial 10 dilutions were prepared i.e., 10^{-2}, 10^{-3}, 10^{-4}, 10^{-5}. Known volumes of these serial dilutions were spread onto blood agar plates to obtain cell counts.

Isolation of different pathogens from milk sample

Three differential media, blood agar, mannitol salt agar, and eosin methlene-Blue (EMB) were used to differentiate the three main bacterial species commonly associated with mastitis i.e., *Staphylococcus aureus* (*S. aureus*), *Escherichia coli* (*E. coli*), and *Streptococcus agalactiae* (*S. agalactiae*).

Biochemical testing

Besides gram staining, numerous biochemical tests were performed for identification. Screening tests included, Catalase test (CT), Oxidase test (OX), coagulase test, Starch hydrolysis (SH), Nitrate test (NT), and Indole test (Ind). Bacteria were identified on the basis of the test result pattern.

RESULTS

A total of 360 milk samples of clinical mastitis,

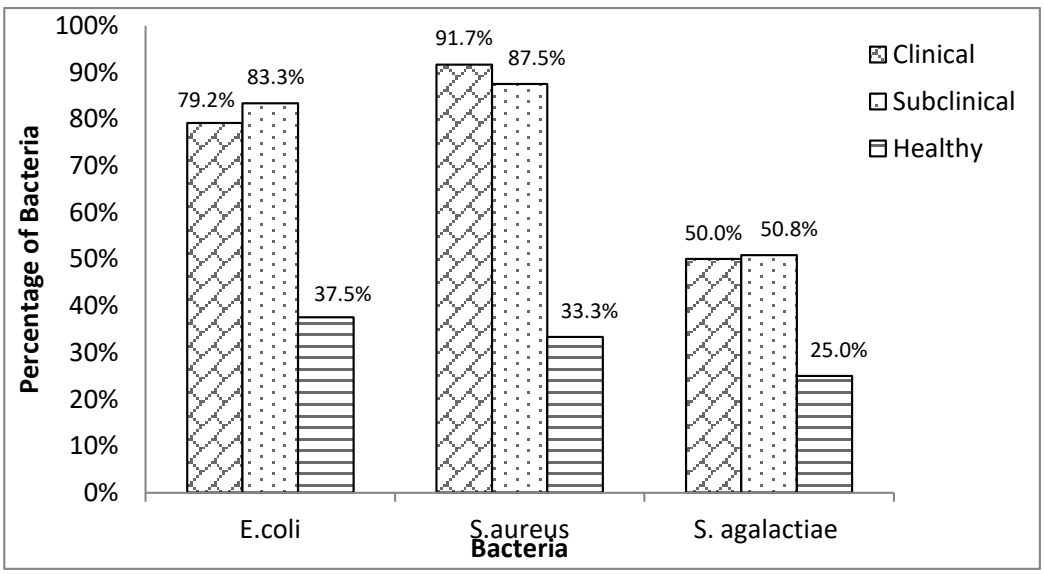

Fig. 2. *Bacterial percentage in Sahiwal cow clinical, subclinical and healthy milk samples.*

Table II. *Bacteria isolated from clinical, subclinical and healthy Sahiwal cow milk samples.*

Sample type	Total sample	Microorganism isolated		
		E. coli	***S. aureus***	***S. agalactiae***
Clinical	120	95	110	60
Subclinical	120	100	105	61
Healthy	120	45	40	30
Total	360	240	255	151

subclinical mastitis and normal Sahiwal cows were collected. The milk samples were initially inoculated onto surface of Blood agar under aseptic conditions and incubated at 37°C for 24-48 h. The growth on plates is shown in Fig. 1. The suspected colonies were purified on specialized media. Speciation of mastitis isolates was carried out by running a relatively small battery of biochemical screening tests: catalase test (CT), coagulase test, nitrate test (NT), oxidase test (OX), indole test (Ind), and starch hydrolysis (SH). The results of biochemical tests are shown in Table I.

The percentage of samples in each mastitis status group testing positive to each of the bacteria was calculated. *E. coli* was detected in 79.2% (n=95), 83.3% (n=110) and 37.5% (n=45) clinical, subclinical mastitis and normal milk samples, respectively. *S. aureus* was detected in 91.7% (n=110), 87.5% (n=105) and 33.3% (n=40) clinical, subclinical mastitis and normal milk sample respectively. *S. agalactiae* was detected in 50% (n=60), 50.8% (n=61) and 25% (n=30) clinical, subclinical mastitis and normal milk sample respectively. The result of positive samples and percentages are shown in Table II and Fig. 2.

DISCUSSION

In the present study, 360 milk samples from Sahiwal cows with clinical mastitis, subclinical mastitis or healthy were randomly collected from different dairy farms of the Punjab, Pakistan. These samples were subjected to bacteriological and biochemical analysis for the three types of bacteria, *S. aureus, E. coli*, and *S. agalactiae*, commonly associated with mastitis. Microorganisms that can easily grow in milk, and are often found to contaminate milk include *Coliform*, *Staphylococcus*, *Streptococcus*, *Lactobacillus*, *Salmonella*, and *Micrococcus* (8, 9).

The cows in the current study were placed into three groups: a clinical (n=120), a subclinical (n=120) and a control/healthy group (n=120). Our results show that *S. aureus* was the most common isolate (*E. coli*, *S. agalactiae*) among the three species most commonly associated with mastitis. The results revealed that *S. aureus*, *E. coli* and *S. agalactiae* were isolated as the top ranking pathogens for mastitis positive cases. These results are in agreement with Fook et al. (10) and Demme and Shimeles in 2015 and Saglam et al. in 2017 (11, 12). The results of the present study indicate that the percentage of *S. aureus* is high as compared to *E. coli* in both the clinical and subclinical groups. The presence of *S. agalactiae* is less frequent in both clinical and subclinical groups as compare to *S. aureus* and *E. coli.*

This study indicates that mastitis is most commonly caused by *S. aureus*, followed by *E. coli,* and is one of the major problems of the dairy industry. The distribution of pathogens in dairy herds has a substantial economic impact resulting from mastitis. In addition to the economic importance of mastitis, these infections constitute a significant public health risk. Therefore, mastitis requires appropriate diagnosis and treatment measures.

REFERENCES

1. Grifoen K, Hop GE, Holstege MM, Velthuis AG, Lam TJ. 1Health4Food – Dutch Mastitis Diagnostics Consortium. Dutch dairy farmers' need for microbiological mastitis diagnostics. J Dairy Sci 2016; 99:5551-61.
2. Harmon RJ. Physiology of mastitis and factors affecting somatic cell counts. J Dairy Sci 1994; 77:2103-12.
3. Carvajal A, Huircan P, Lepori A. Single nucleotide polymorphisms in immunity-related genes and their association with mastitis in Chilean dairy cattle. Genet Mol Res 2013; 12(3): 2702-11.
4. Dahlin A. Genetic studies on Sahiwal cattle in Pakistan. PhD Thesis, Swedish Univ Agri Sci Uppsala, Sweden, 1998.
5. Zadoks RN, Allore HG, Barkema HW, Sampimon OC, Wellenberg GJ, Grohn YT, Schukken YH. Cow- and quarter-level risk factors for *Streptococcus uberis* and *Staphylococcus aureus* mastitis. J Dairy Sci 2001; 84:2649-63.
6. Poppert S, Riecker M, Wellinghausen N. Accelerated identification of *Staphylococcus aureus* from blood cultures by a modified fluorescence in situ hybridization procedure. J Med Microbiol 2010;

59:65-68.

7. Muhammad G, Naureen A, Asi MN, Saqib M. Evaluation of a 3% Surf solution (surf field mastitis test) for the diagnosis of subclinical bovine and bubaline mastitis. Trop Anim Health Prod 2010; 42 (3):457-64.
8. Brito JRF, Dias JC. Sensitivity and specificity of the California mastitis test as a diagnostic tool for subclinical mastitis with regard to counting of somatic cells. Braz Vet Res 1997; 17:49-53.
9. Fonseca LFL, Santos MV. Milk quality and control of mastitis. Sao Paulo: Lemos Editorial Press 2000; 39-141.
10. Fook CY, Abdullah A, Ayob MK. Bacteriological quality and safety of raw milk in Malaysia, Food Microbiology 2004; 24:535-41.
11. Demma B, Abegaz S. Isolation and identification of major bacterial pathogen from clinical mastitis cow raw milk in Addis Ababa, Ethiopia. Acad J Anim Dis 2015; 4(1): 44-51.
12. Saglam AG, Sahin M, Celik E, Celebi O, Akca D, Otlu S. The role of staphylococci in subclinical mastitis of cows and lytic phage isolation against to Staphylococcus aureus. Veterinary World 2017; 10(12):1481-85.

LETTER TO THE EDITOR

CORRELATION BETWEEN KRAS GENE MUTATIONS AND CLINICOPATHOLOGICAL FEATURES OF PATIENTS WITH INTRAHEPATIC CHOLANGIOCARCINOMA

J. WANG[1], MX. XU[2], LQ. WANG[3], HY. LI[4], ZL. WANG[5] and LJ. LI[6]

[1]Department of Physical Diagnosis, Affiliated Hongqi Hospital, Mudanjiang Medical University, Mudanjiang, China; [2]Department of Clinical Laboratory, Affiliated Hongqi Hospital, Mudanjiang Medical University, Mudanjiang, China; [3]Department of Ear-Nose-Throat, Affiliated Hongqi Hospital, Mudanjiang Medical University, Mudanjiang, China; [4]Department of Quality Control Office, Affiliated Hongqi Hospital, Mudanjiang Medical University, Mudanjiang, China; [5]Section of Graduate student training, First Clinical College, Mudanjiang Medical University, Mudanjiang, China; [6]Department of Pathology, Affiliated Hongqi Hospital, Mudanjiang Medical University, Mudanjiang, China

Received March 7, 2019 – Accepted July 5, 2019

To the Editor,

Intrahepatic cholangiocarcinoma (ICC) ranks second among primary malignant tumors of the liver. It has been shown that bile duct stones, liver cirrhosis, and HBV infection are risk factors of ICC (1). In recent years, the incidence of ICC has been increasing. According to the data in the Surveillance Epidemiology and End Results (SEER) database, the annual incidence of ICC was only 0.9/100,000 per year between 1995 and 1999. However, this number jumped to 16/100,000 per year between 2000 and 2011, and the Asian population are at the highest risk (2). The RAS signaling pathway is one of the most extensively studied pathways in ICC. Among the numerous associated genes, the Kirsten rat sarcoma viral oncogene homologue (KRAS) gene is closely related to the RAS signaling pathway in ICC.

KRAS is a small intracellular GTPase and a node protein of the epidermal growth factor receptor (EGFR) and tyrosine kinase receptor signaling pathways (3). Activation of the EGFR and KRAS signaling pathways may lead to occurrence, progression, invasion, and metastasis of colorectal malignant tumors. In addition, mutations in the KRAS gene downregulate GTPase activity, thus activating the KRAS signaling pathway (4, 5). In this study, we analyzed the relationships between the mutations in codons 12 and 13 of the KRAS gene and the clinicopathological features of ICC, including patients' gender, age, tumor size, tumor type, pathological type, degree of differentiation, and Tumor node metastasis (TNM) stage to provide new insights for developing effective treatments of ICC.

MATERIALS AND METHODS

Subjects

Forty cases of paraffin-embedded tissue samples of ICC diagnosed by histopathological examination (all tissue specimens were from the biopsies of resected specimens) in The Affiliated Hongqi Hospital, Mudanjiang Medical University from June 2015 to June 2018 were selected for this study. The clinicopathological information of these samples, including the patients' gender, ages, tumor diameters, gross tumor morphology, pathological

Key words: KRAS gene; codon; ICC; gene mutation; YB-1 protein expressions

Corresponding Author:
Dr Lijuan Li,
Department of Pathology,
Affiliated Hongqi Hospital, Mudanjiang Medical University,
No.5 Tongxiang Road, Mudanjiang 157011,
Heilongjiang Province, China
e-mail: lilijuan_mdjmu@163.com

0393-974X (2019)

classifications, degrees of differentiation, TNM stages, presence of lymphatic and distant metastases, presence of hepatolithiasis (upper level of the left and right hepatolithiasis) and the levels of preoperative CA199 and CEA, was collected. None of the ICC patients had been treated with chemotherapy or radiotherapy before surgery. The ICC tumors were staged postoperatively according to the TNM staging system of the 7th edition of the American Joint Cancer Commission (AJCC) and the International Union against Cancer (UICC). Signed informed consent was obtained from all patients. This study was approved by the Ethics Committee of The Affiliated Hongqi Hospital, Mudanjiang Medical University.

Inclusion criteria of the experimental group: ICC diagnosed by histopathological examinations; complete medical data; no other primary tumors in addition to ICC; paraffin-embedded tissue samples collected within one year; no history of chemotherapy before surgery.

Sample collection, processing, and storage

Fresh tissue specimens of ICC were excised (20×20mm) and immersed into the stationary liquid formalin (Anhui Ante Biochemistry Corporation, China). The specimens were dehydrated with low to high gradients of ethanol and then immersed in the xylene solution (Anhui Ante Biochemistry Corporation, China) after complete dehydration. The specimens were then placed in dissolved paraffin and kept in an incubator (Jiangsu Taicang Instrument and Equipment Biotech Corporation, China) at 37°C. The specimens were completely immersed and embedded in paraffin. The tissue blocks were then sliced into sections of about 5 μm in thickness. Finally, the sections were flattened in 52°C water, attached to slides, and baked in a thermostat oven at 80°C.

Conventional dewaxing of paraffin-embedded tissue sections

The Hematoxylin-Eosin (HE) staining method was selected. The prepared paraffin sections were baked in an oven at 65°C for 1 h. Then, the sections were dewaxed with xylene and dehydrated with different concentrations of alcohol. Next, the sections were stained by hematoxylin (Shanghai Sangon Biotech, China) for 5 min and rinsed with tap water for 6 min. The sections were then immersed in a 0.5% eosin solution (Shanghai Sangon Biotech, China) for 3 min, and washed with tap water for 30 s. After being dehydrated till transparent, they were finally mounted with cover glasses, and allowed to dry. Paraffin-embedded tissue blocks with cancer tissues confirmed by HE staining were selected. Subsequently, 3 tissue sections of 10 μm in thickness were cut from each tissue block, after which 1 mL of xylene (Jiangsu Taicang Instrument and Equipment Biotech Corporation, China) was added to dissolve the sample before being centrifuged at 13000rpm (Sigma Biotech Corporation, China) for 2 min. The supernatant was discarded, and the absolute ethanol was dried. After standing for 10 min, the paracancerous tissues and ICC tissues were observed under an electron microscope.

Extraction of sample DNA

After conventional dewaxing treatment, protease K (Cwbio IT Group, China) and sodium dodecyl sulfate (SDS) (Cwbio IT Group, China) were added to reach the final concentrations of 1mg/mL and 2%, respectively. After being incubated for 24-36 h, the sample was centrifuged at 15 000r/min for 15 min at 4°C. The liquid under the paraffin layer was extracted. According to the manufacturer's instructions (Wujiang Corning Life Sciences, China), the DNA of paraffin sections was extracted.. The preparation tube was placed in a 2 mL centrifuge tube, and the obtained mixture was transferred into the preparation tube and centrifuged at 4°C and 6000 r/min for 1 min. The filtrate was discarded, and 500 μL of Buffer W1 was added to the preparation tube before being centrifuged at 4°C and 12000 r/min for 1 min. The filtrate was discarded, and 700 μL of Buffer W2 was added and centrifuged at 4°C and 12000 r/min for 1min. A second round of 700 μL Buffer W2 was added and centrifuged again in the same manner. The preparation tube was then placed into a 15 mL clean, enzyme-free centrifuge tube provided with the kit. DNA was subsequently extracted by using 30 mL of eluent. The concentration of the extracted DNA product was measured by an ultraviolet spectrophotometer (Shimadzu Corporation, Japan) adjusted to 100μg/mL and stored at -20°C.

PCR amplification of the KRAS gene

Primerpremier 5.0 software and the online primer design software on the website of Invitrogen were used to design primers for different loci of KRAS based on the gene sequence of KRAS (NM_004985.3) collected in the PubMed database. The primers were synthesized and

purified by Shanghai Biotechnology. The specific primer sequence and the polymerase chain reaction system were as follows:

The sequence of exon 2 of the wild type KRAS gene in the PubMed database was as follows: ATGA CTGAATATAAACTTGTGGTAGTTGGAGCTGGT-GGCGTAGGCAAGAGTGCC.

In the KRAS gene 01, the sequences corresponding to Forward and Reverse primers were 5′: AGGCCTGCTGAAAATGACTG-3′ and 5′: ATCAAAGAATGGTCCTGCAC-3′ respectively.

In the KRAS gene 02, the sequences corresponding to Forward and Reverse primer were 5′: GCCTGCTGAAAATGACTGAA-3′ and 5′: GAATGGTCCTGCACCAGTAA-3′ respectively.

The polymerase chain reaction system contained 25 μL, 4 μL, 2 μL, 2 μL and 17 μL of MiX (2*), a DNA template, a forward primer, a reverse primer, and deionized water respectively, with a total volume of 50 μL.

The PCR instrument (BIO-RAD, USA) was employed for polymerase chain reaction. The conditions were as follows: predenaturation at 96°C for 1 min, denaturation at 96°C for 10 s, annealing at 50°C for 5 s, and extension at 60°C for 4 min. A total of 25 cycles were performed. The temperature was maintained at 4°C. A total of 7 samples were randomly selected from the obtained PCR amplification products and subjected to 1% agarose gel electrophoresis to determine the correctness of the synthesized bands.

Tissue protein lysis and concentration determination

In the histopathological study of patients with ICC, fresh cholangiocarcinoma tissues of 7 patients (numbered Pat. 1-7) and their corresponding paracancerous tissues were randomly selected. The mortar was pre-cooled with liquid nitrogen, and 10 mg of the tissues were placed within and ground. Liquid nitrogen was added continuously during the grinding process. The obtained tissue powder was transferred to a 1.5 mL EP tube, added with 1 mL RIPA lysis buffer (Shanghai Beyotime Biotechnology, China), incubated for 30 min on ice, and centrifuged at 13,000 rpm for 10 min. The supernatant was collected and stored at -80°C. To determine the concentration, the protein standard was first diluted with gradient RIPA lysis buffer; 2 uL of RIPA lysis buffer (blank control), diluted protein standards, and samples were sequentially pipetted into a 96-well plate. Then, 20 mL of freshly prepared working solution and 200 uL of reagent B were then added into each well. The plate was mixed thoroughly by using a plate shaker at room temperature for 15 min. Finally, the plate was placed on a Tecan infinite M200 enzyme mark instrument with a wavelength of 450 nm visible light to measure the absorbance value of each well. A standard curve was plotted, and the protein concentration of the sample to be tested was determined through the standard curve.

Detection of tissue protein expressions by Western blot

After plotting the standard curve based on the measured concentrations of each protein sample, the volume required for each sample was calculated so that the total protein amount of each supernatant sample was equal. Loading buffer was added before the samples were boiled and placed in the SDS-polyacrylamide gel for electrophoresis (Bio-Rad, USA) for about 1 h. Then, the gel was removed and placed on a nitrocellulose membrane (Shanghai Beyotime Biotechnology, China). A BIO-RAD membrane transfer apparatus (manufactured in the United States) at a constant current of 220 mA was used to transfer the membrane for 2 h. The nitrocellulose membrane was then dyed with Ponceau S solution (Shanghai Beyotime Biotechnology, China) to observe the efficiency of membrane transfer. TBST solution was used for washing to remove the Ponceau S staining solution. The membrane was then immersed in the blocking solution and incubated on a horizontal shaker at room temperature for 1 h. Two cycles of TBST washing, each for 5 min, were applied. Next, the nitrocellulose membrane was immersed in the diluted primary antibody solution and incubated on a horizontal shaker at 4°C overnight. The membrane was then washed and immersed in the diluted secondary antibody solution before being incubated on a horizontal shaker for 1 h at room temperature. After incubation, the secondary antibody was discarded, and the membrane was washed three times, 10 min each time. The reagents A and B in the ECL chemiluminescence kit (Peqlab Corporation, Germany) were mixed in equal volume and added dropwise to the nitrocellulose membrane. After being incubated for 3-5 min, the excess color developing solution was discarded, and the membrane was placed in the Chemi-smart 5100 chemiluminescence imaging system (Peqlab Corporation, Germany) to harvest the exposure images.

Statistical analysis

SPSS19.0 statistical software was used for the statistical analysis of experimental data. Homogeneity test of normal variance was carried out for all experimental results, which were then expressed as mean ± standard deviation. The data between the two groups were compared by *t*-test (for both homogeneous variance and corrected variance). The test level was α=0.05, and P <0.05 was considered statistically significant. In addition, the correlations between variables were analyzed by Pearson correlation.

RESULTS

Detection of PCR amplification products by agarose gel electrophoresis

DNA was extracted from paraffin-embedded tissue samples of 40 ICC cases. The target fragments were amplified by PCR and detected by electrophoresis. The successfully extracted DNA was used as a template for PCR amplification, and the products of PCR amplification were detected by 1% agarose gel electrophoresis. The results showed a specific band near 176bp, which was consistent with the theoretical value (Fig. 1). After purification, the PCR products were sequenced and detected.

KRAS gene mutations in codons 12 and 13 of ICC

A total of 40 paraffin-embedded tissues of intrahepatic cholangiocarcinoma were acquired, among which, there were mutations in 13 cases (Table 1A). Of these 13 cases, 12 (12/13, 92.3%) had mutations in codon 12, including 8 GGT>GAT mutation (8/13, 61.5%), 3 GGT>GTT mutation (3/13, 23.1%), and 1 GGT>GCT mutation (1/13, 7.7%). When the groups with codon 12 mutations were compared, the differences were statistically significant (χ^2=39, P<0.05). GGC>GAC mutation of codon 13 was found in 1 patient (1/13, 7.7%), and significant differences (χ^2=13, P<0.05) were observed when the mutations of codons 12 and 13 were compared.

The correlation between the mutations of codons 12 and 13 of the KRAS gene and the clinicopathological characteristics of patients with ICC

As shown in Table I, there were no significant differences in gender, age, tumor size, and lymphatic metastasis.

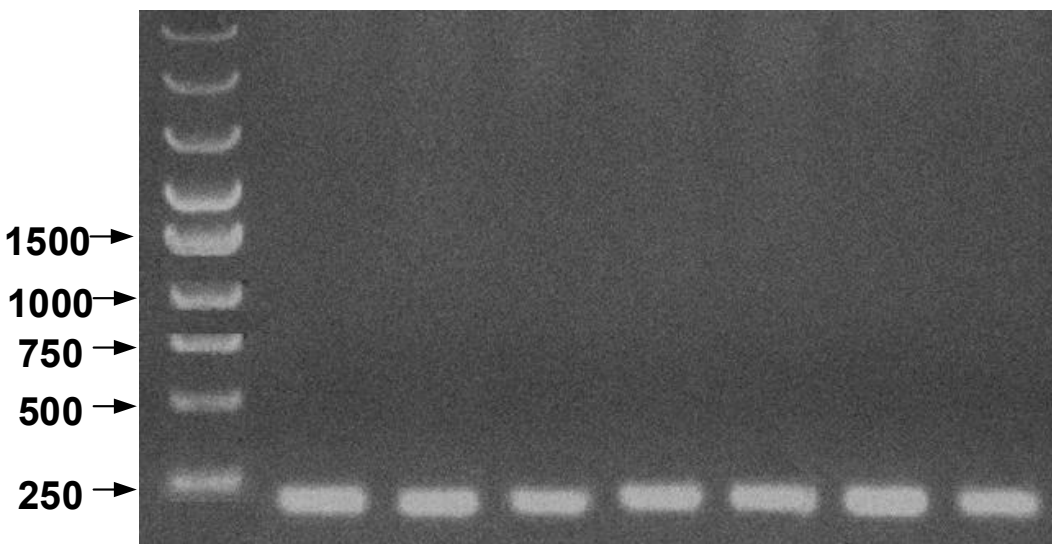

Fig. 1. *Agarose gel electrophoresis of KRAS gene PCR products.*

Table I. *Summary of KRAS gene in patients with ICC.*

	Types of KRAS gene mutations		Quantity (n=X)	Ratio (%)	χ^2	P Value
A	12 codon GGT>GAT mutation		8	61.5	39.00	0.01
	12 codon GGT>G TT mutation		3	23.1		
	12 codon GGT>GCT mutation		1	7.7		
	Mutations of codon 12		12	92.3	13.00	0.05
	13 codon GGC>GAC mutation		1	7.7		
	Mutations of codons12 and 13		13	100.0		
	Statistical items		Quantity	KRAS mutations (case)	Mutation rate (%)	P Value
B	Gender	Male	28	9	32.1	0.943
		Female	12	4	33.3	
	Age (years)	<65	23	7	30.4	0.753
		≥65	17	6	35.3	
	Tumor size	<5cm	19	6	31.6	0.909
		≥5cm	21	7	33.3	
	Tumor typing	Mass	22	8	61.5	0.748
		Peripheral infiltration	12	4	33.3	
		Intrahepatic	2	0	0.0	
		Combined	4	1	25.0	
	Lymphatic metastasis	Valid teaming modes:	9	6	66.7	0.032
		None	31	7	22.6	

A) *KRAS gene mutation analysis;* ***B)*** *Relationship between KRAS gene mutations and clinicopathological features of ICC*

Abnormal expressions of YB-1 protein in ICC

Correlation analysis was performed on the ICC tissues and paracancerous tissues, and the results are shown in Fig. 2. Western blot (WB) assays showed that the protein expressions of YB-1 in all ICC samples were significantly higher than those in paracancerous normal tissues (Fig. 2A). Immunohistochemical staining also showed similar results. For instance, the expression of YB-1 protein was almost undetectable in paracancerous tissues (Fig. 2C), with only a small amount of YB-1 protein seen in bile duct cells. In contrast, YB-1 proteins were clearly expressed in cholangiocarcinoma cells (Fig. 2B). In addition, high levels of YB-1 proteins were seen in the cytoplasm of 75.9% (22/29) ICC tissues, and 40.9% of all YB-1 positive tissues with YB-1 nuclear stainings (Fig. 2D, Fig. 2E). Furthermore, positive staining of YB-1 was also found in the lymph nodes of one patient (Fig. 2F).

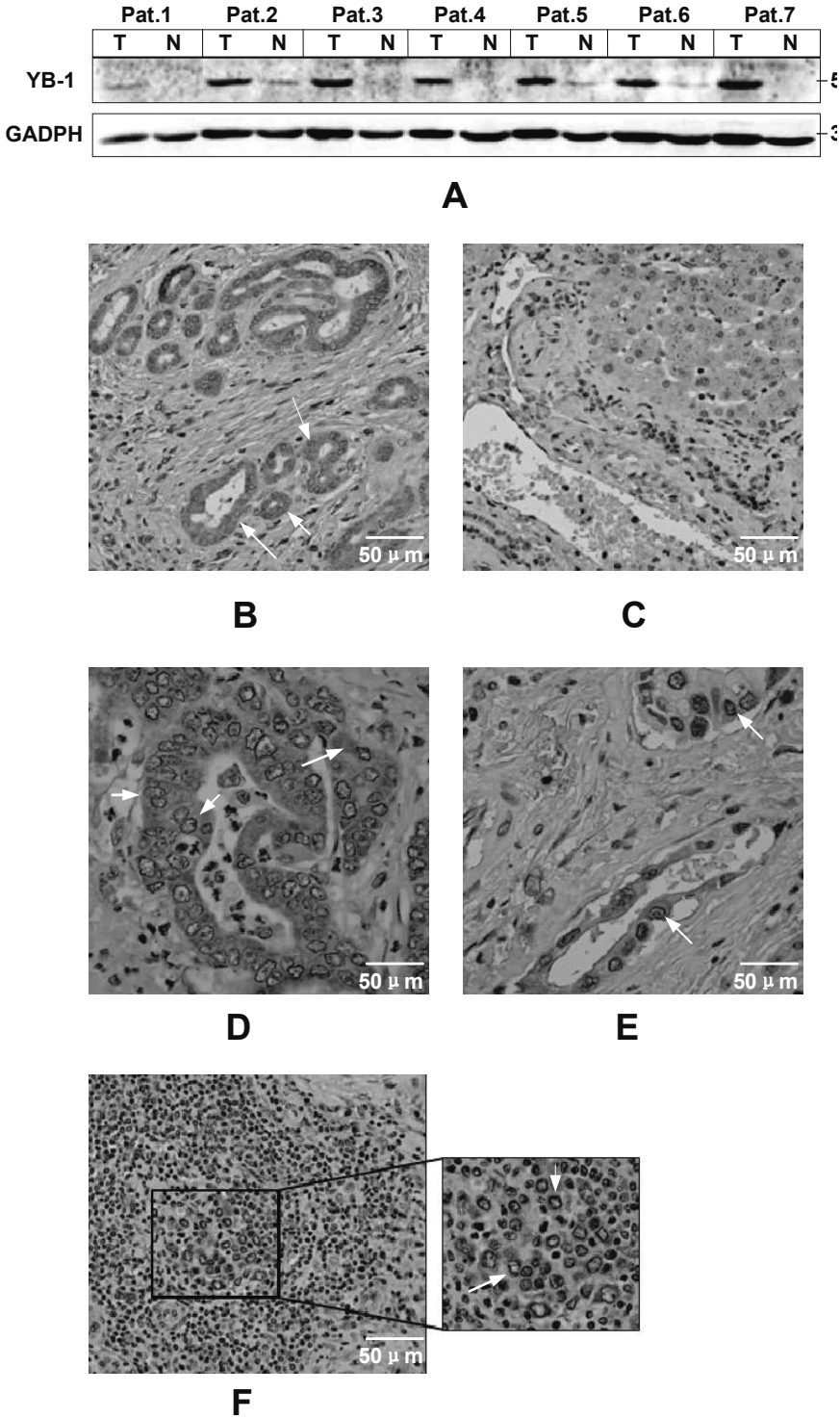

Fig. 2. *Detection of YB-1 expressions in ICC tissues and paracancerous tissues.* ***A****) Detection of YB-1 expressions in ICC by Western blot;* ***B****) Detection of YB-1 expressions in ICC tissues by immunohistochemical staining;* ***C****) Detection of YB-1 expressions in paracancerous tissues by immunohistochemical staining;* ***D****) Detection of YB-1 positive expressions in YB-1 cytoplasm of paracancerous tissues by immunohistochemical staining;* ***E****) Detection of YB-1 positive expressions in YB-1 nuclei of paracancerous tissues by immunohistochemical staining;* ***F****) Detection of YB-1 positive expressions in metastatic lymph node tissues by immunohistochemical staining) (200* electron microscopy). T: tumor tissues, N: paracancerous tissues, Pat.1-7: Number of patients.*

DISCUSSION

As a family of primitive and conservative genes, RAS genes belong to the category of proto-oncogenes. RAS was first found in the offspring genes of Kirsten murine sarcoma virus (Ki2M SV) and Harver murine sarcoma virus (Ha2MSV). The RAS family contains three functional genes, namely KRAS, HRAS, and NRAS. These genes are located on human chromosomes 12, 1 and 11 (6), respectively. The KRAS gene influences most heavily on human tumors and is highly expressed in colorectal cancer, pancreatic cancer, ICC and other malignant tumors of the digestive tract (7). The mutation sites of the KRAS gene are usually located at codons 12 and 13, although rare mutations are also seen at codon 61. Sartore-Bianchi et al. (7) found that the mutations sites of the KRAS gene often occur at codons 12 and 13, with the majority of mutation types being GGT>GAT and GGT>GTT (9).

As a multi-functional protein, YB-1 is also closely related to cell proliferation regulation (10). Early studies have shown that a high expression of YB-1 or its nuclear localization is associated with markers of cell proliferation, and may also affect cell proliferation through p21 protein (11, 12).

In summary, this study indicated the correlation between the mutations of codons 12 and 13 of the KRAS gene in intrahepatic cholangiocarcinoma and the clinicopathological features of patients. Markers of proliferation of cancer cells such as intrahepatic cholangiocarcinoma and lymph tissues were also found. Our results may provide an experimental basis for subsequent clinical treatment of ICC.

ACKNOWLEDGEMENT

This work was supported by The foundation of HongQi (2018HQ-03).

REFERENCES

1. Morine Y, Shimada M. The value of systematic lymph node dissection for intrahepatic cholangiocarcinoma from the viewpoint of liver lymphatics. J Gastroenterol 2015; 50(9):913-27.
2. Gu J, Jeong S, Xia Q. Intrahepatic cholangiocarcinoma arising from HBV infection may be a highly selected population for liver transplantation. Hepatology 2017; 66(5):1703-04.
3. Soh J, Toyooka S, Matsuo K, et al. Ethnicity affects EGFR and KRAS gene alterations of lung adenocarcinoma. Oncol Lett. 2015; 10(3):1775-82.
4. Fitzgerald TL, Lertpiriyapong K, Cocco L, et al. Roles of EGFR and KRAS and their downstream signaling pathways in pancreatic cancer and pancreatic cancer stem cells. Adv Biol Regul 2015; 59:65-81.
5. Baldelli E, Bellezza G, Haura EB, et al. Functional signaling pathway analysis of lung adenocarcinomas identifies novel therapeutic targets for KRAS mutant tumors. Oncotarget 2015; 6(32):32368-79.
6. Nishimura M, Watanabe T, Yagi S, Yamanaka T, Fujimuro M. Kaposi's sarcoma-associated herpesvirus ORF34 is essential for late gene expression and virus production. Sci Rep 2017; 7(1):329.
7. Sartore-Bianchi A, Trusolino L, Martino C, et al. Dual-targeted therapy with trastuzumab and lapatinib in treatment-refractory, KRAS codon 12/13 wild-type, HER2-positive metastatic colorectal cancer (HERACLES): a proof-of-concept, multicentre, open-label, phase 2 trial. Lancet Oncol 2016; 17(6):738-46.
8. Zhou L, Baba Y, Kitano Y, et al. KRAS, BRAF, and PIK3CA mutations, and patient prognosis in 126 pancreatic cancers: pyrosequencing technology and literature review. Med Oncol 2016; 33(4):32.
9. Raub CB, Lee CC, Shibata D, Taylor C, Kartalov E. HistoMosaic Detecting KRAS G12V mutation across colorectal cancer tissue slices through in situ PCR. Anal Chem 2016; 88(5):2792-98.
10. Kim H, Hwang H, Lee H, Hong HJ. L1 Cell adhesion molecule promotes migration and invasion via JNK activation in extrahepatic cholangiocarcinoma cells with activating KRAS mutation. Mol Cells 2017; 40(5):363-70.
11. Huang WC, Tsai CC, Chan CC. Mutation analysis and copy number changes of KRAS and BRAF genes in Taiwanese cases of biliary tract cholangiocarcinoma. J Formos Med Assoc 2017; 116(6):464-68.
12. Tamás J, Vereczkey I, Tóth E, Csernák E, Purcsi K, Pete I. Mixed ovarian tumor composed of Brenner tumor and adult-type granulosa cell tumor: a case report of a very rare mixed ovarian tumor and a review of the literature. Int J Surg Pathol 2018; 26(4):382-87.

JOURNAL OF BIOLOGICAL REGULATORS & HOMEOSTATIC AGENTS Vol. 33, no. 5, 1559-1563 (2019)

LETTER TO THE EDITOR

PARTICIPATION OF TLR4 AND NEUROINFLAMMATION IN THE HIPPOCAMPUS IN VASCULAR COGNITIVE IMPAIRMENT OF HYPERTENSIVE STROKE-PRONE RATS

Y. LIU and M. GU

Department of Neurology, Chongqing Three Gorges Central Hospital, Chongqing, China

Received June 12, 2019 – Accepted July 26, 2019

To the Editor,

Vascular cognitive impairment (VCI) is a cognitive disorder linked to vascular brain injury including mild cognitive impairment to dementia (1). Vascular dementia is the second most common cause of dementia worldwide after Alzheimer's disease (AD) (2). In general, vascular dementia is caused by cerebral hypoperfusion (3). The risk factors include advanced age, diabetes, hypertension, and cardiovascular disease (1, 2). Brain ischemia is a subtype of vascular cognitive impairment because of small-artery disease in hypertensive stroke, however, the molecular mechanisms leading to brain damage during the disease are not yet fully understood.

Toll-like receptors (TLRs) are the key players of the innate and adaptive immune pattern recognition receptors in the inflammatory process (4). Along with immune system-related cells, TLRs are involved in brain development and diseases. TLRs (1–9) are endogenous factors regulating neural plasticity during brain development (5). TLR2, TLR4, and TLR9 are described mainly as tumor promoting (5). Microglial activation of TLR2 and TLR4 is involved in Alzheimer's disease. Inflammatory systems are involved in the progression of ischemic brain injury (6). Particularly, TLR4 plays an important role among these TLRs ,whereas the TLRs are involved in the acute ischemia/reperfusion brain injury (7, 8). Notably, protection of ischemic post conditioning against transient focal ischemia-induced brain damage in the early phase of ischemia is associated with inhibition of TLR2 and TLR4 pathways (8). Nevertheless, the role of TLR4 in regulating hypertensive stroke-mediated cerebral immune signals needs to be studied.

Inflammation is a part of signal pathways in the process of VCI and proinflammatory cytokines (PICs) are essential modulators involved in the responses during VCI. Thus, we hypothesized that TLR4, IL-1β, IL-6 and TNF-α are upregulated in the hippocampus of spontaneously hypertensive stroke-prone rats (SHRSP). We further hypothesized that inhibition of TLR4 signal decreases activities of IL-1β, IL-6 and TNF-α, accompanied with attenuation of Caspase-3 and Caspase-9, indicating cellular apoptosis, thereby improving impaired learning performance in SHRSP rats.

MATERIALS AND METHODS

Animals

All animal protocols were in accordance with the guidelines of the International Association for the Study of Pain and approved by the Institutional Animal Care and Use Committee of Chongqing Three Gorges Central Hospital. Rats were housed in individual cages with free access to food and water and were kept in a temperature-controlled room (25°C) on a 12/12 h light/dark cycle.

Key words: vascular cognitive impairment; hypertension; stroke; neuroinflammation; signal pathway

Corresponding Author:
Dr. Meiying Gu,
Department of Neurology,
Chongqing Three Gorges Central Hospital,
Chongqing, China, 165 Xincheng Road,
Wanzhou District, Chongqing 404000, China
Tel.: +86 02358104352
e-mail: gumeiying3g@gmail.com

0393-974X (2019)

DISCLOSURE: ALL AUTHORS REPORT NO CONFLICTS OF INTEREST RELEVANT TO THIS ARTICLE.

Male SHRSP and Wistar Kyoto (WKY) rats aged at 16-18 weeks were used for experimentation. The rats were placed in individual chambers on a heated platform and arterial pressure was measured using tail-cuff plethysmography. Before measurements, the rats were trained for 5 consecutive days to adapt to the environment. Mean systolic blood pressure was obtained as the average of 10 measurements. Systolic blood pressure was 185±12 mmHg in SHRSP and 121±8 mmHg in WKY (P<0.05, SHRSP *vs* WKY) animals. In rats treated with TLR4 inhibitor, TAK-242 (Millipore Sigma Co.) was infused (5 mg/kg; i.p.) for 4 weeks by osmotic minipumps (model 2004, Alzet, Cupertino, CA, USA). The behavioral experiments were started on the fourth week after TAK-242.

ELISA measurements

The levels of IL-1β, IL-6 and TNF-α (Wuhan Fine Biotech) in the CA1 region of the hippocampus were determined using a two-site immunoenzymatic assay (ELISA) according to the provided description. Briefly, polystyrene 96-well microtitel immunoplates were coated with affinity-purified rabbit anti-IL-1β (Cat#ERB0062), anti-IL-6 (Cat#ERB0068) and anti-TNF-α antibodies (Cat#ERB0126). Parallel wells were coated with purified rabbit IgG for evaluation of nonspecific signal. After overnight incubation at room temperature and 2 h of incubation with the coating buffer containing 50 mM carbonate buffer in 2% BSA, the plates were washed with 50 mM Tris-HCl. After washing, the diluted samples and the standard solutions of IL-1β/IL-6/TNF-α were distributed in each plate and left at room temperature overnight. The plates were washed and incubated with anti-IL-1β/IL-6/TNF-α galactosidase, then washed and incubated with substrate solution. After incubation of 2 h at 37°C, the optical density was measured using an ELISA reader (575 nm wavelength).

Western blot analysis

The protein expression of TLR4, cleaved form of Caspase-3 and Caspase-9 in CA1 region of the hippocampus were determined by using a standard Western blot analysis. In brief, the tissues from individual rats were sampled. Total protein was extracted by homogenizing samples in ice-cold immunoprecipitation assay buffer with protease inhibitor cocktail kit. The lysates were centrifuged and the supernatants were collected for measurements of protein concentrations using a bicinchoninic acid assay reagent kit. After being denatured by heating at 95°C in an SDS sample buffer, the supernatant samples were loaded onto 4-20% Mini-Protean TGX Precast gels and then electrically transferred to a polyvinylidene fluoride membrane. Membranes were incubated with the rabbit anti-TLR4, anti-Caspase-3 and anti-Caspase-9 primary antibodies (1:500, obtained from Neuromics or Abcam Co). After being fully washed, the membrane was incubated with horseradish peroxidase-linked anti-rabbit secondary antibody (1:250) and visualized for immunoreactivity. The membrane was also processed to detect β-actin for equal loading. The bands recognized by the primary antibody were visualized by exposure of the membrane onto an X-ray film. The film was then scanned and the optical densities of protein bands were analyzed using the Scion image software.

Learning performance

Learning behavior was first tested using the hidden platform task in the Morris water maze (maze diameter: 110 cm, water depth: 50 cm, platform diameter: 7cm, four large black-and-white cues). For habituation purposes, all animals were allowed to explore the water maze without platform on the day before the experiments started. On day 1, the platform was inserted (1–2 cm below the water level), and each animal was randomly assigned to one of four different platform locations. From day 1 through day 7, each animal was given six consecutive trials to reach the platform, and the starting points were randomly chosen (six out of eight different positions). When the animal failed to reach the platform within 60 s, it was manually placed on the platform. In any case, the animal was allowed to stay for another 30 s on the platform, before it was placed back into its cage. After 60 s recovering time in the cage, the next trial was started. In the Morris water maze, the animal was tracked using the Ethovision Color software (Noldus Beijing, China) in order to analyze swimming speed and swimming path length.

In addition, spatial working memory performance was assessed one week after antibody infusion, by recording spontaneous alternation performance in a Y-maze. The maze was made of grey-painted vinyl-chloride. Each arm was 50 cm long, 30 cm high and 10 cm wide and converged at an equal angle. Each rat was placed at the center of the maze and allowed to move freely through

it during an 8-minute period. The numbers of arm entries were recorded for 8 minutes. An alternation was defined as entries into all arms. The percentage of alternation was calculated as (actual alternations/total entered-2) x100.

Statistical analysis

All data were analyzed using one-way repeated-measure analysis of variance. As appropriate, Tukey's *post hoc* tests were used. Values are presented as means±standard error. For all analyses, differences were considered significant at $P < 0.05$. All statistical analyses were performed by using SPSS for Windows version 15.0.

RESULTS

The protein expression of TLR4 was significantly increased in the hippocampus of SHRSP rats as compared with WKY rats ($P<0.05$, n=10 in each group) (Fig. 1A). Also, the protein expression of Caspase-3 and Caspase-9 was significantly elevated in the hippocampus of SHRSP rats (Fig. 1B). Fig. 1C shows that IL-1β, IL-6 and TNF-α were elevated in the hippocampus of SHRSP rats (n=20; $P < 0.05$ *vs* WKY rats) as compared with WKY rats (n=15). Infusion of TAK-242 attenuated the upregulation of

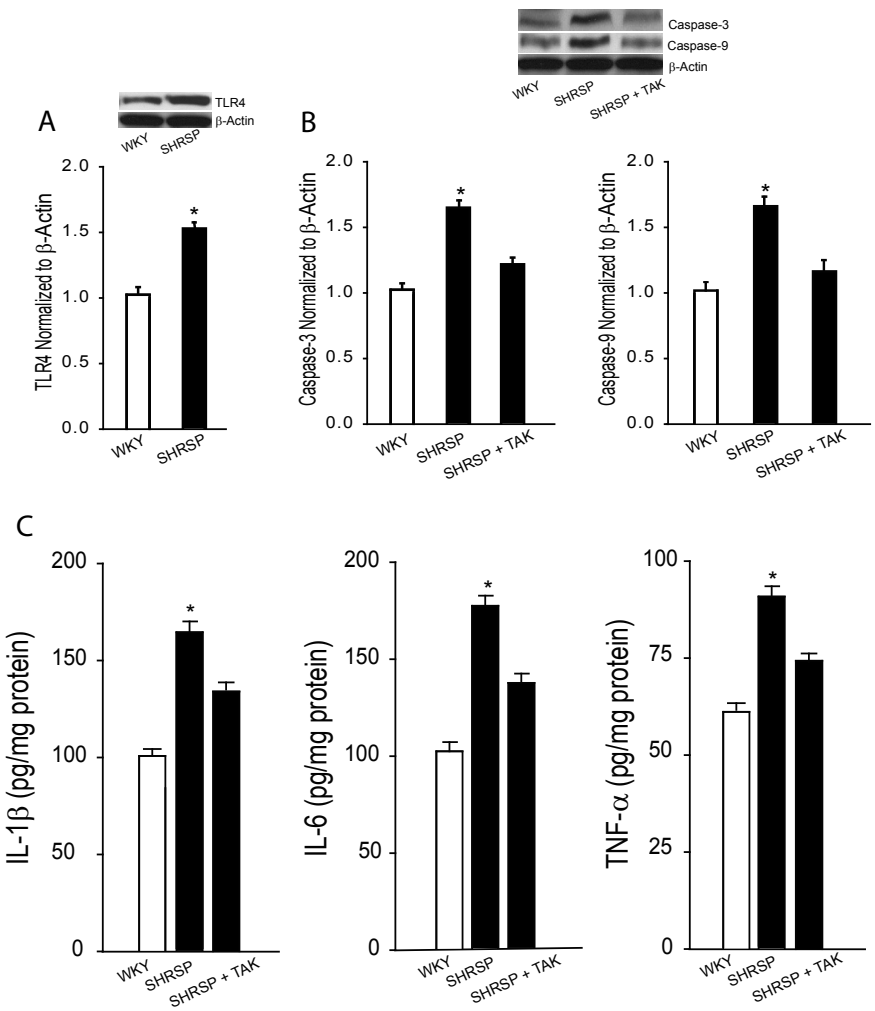

Fig. 1. *Expression of TLR4, PICs and Caspase-3/Caspase-9. Averaged data and typical bands show increases in TLR4 (**A**), Caspase-3 and Caspase-9 (**B**), and proinflammatory IL-1β, IL-6 and TNF-α (**C**) in the hippocampus CA1 region of WKY rats and SHRSP rats. As compared with WKY, TLR4, Caspase-3/Caspase-9 and IL-1β/IL-6/TNF-α were increased in SHRSP and a chronic infusion of TAK-242 (a TLR4 inhibitor) attenuated the increases of Caspase-3/Caspase-9 and IL-1β/IL-6/TNF-α. In A, *P < 0.05 vs WKY; n=10 in each group. In B, *P < 0.05 vs WKY and SHRSP with TAK-242; n=8-10 in each group. In C, *P < 0.05, SHRSP (n=20) vs WKY (n=15) and SHRSP with TAK-242 (n=15).*

Caspase-3 and Caspase-9 as well as elevation of IL-1β, IL-6 and TNF-α in SHRSP rats (n=15).

As can be seen in Fig. 2A, the swimming path length (cumulatively for six consecutive trials) was significantly higher in SHRSP rats compared to WKY animals ($P < 0.05$, SHRSR/n=20 *vs* WKY/n=15). It is noted that TAK-242 shortened the swimming path length observed in SHRSP rats ($P < 0.05$, SHRSP *vs* SHRSP with TAK-242/n=15). In addition, to assess the possible effects of motor activity in SHRSP rats, swimming speed was examined and the results showed that there were insignificant differences in the swimming speed in these different experimental groups ($P > 0.05$ among groups) (Fig. 2B).

Moreover, spontaneous alternation performance was examined. In this experiment, the number of arm entries was determined by counting the number of arms each animal entered in the maze during the test as a measure of activity level. No significant differences in the number of arm entries were observed between the WKY group and SHRSP group. The number of arm entries for each group was 16.5±2.2 in WKY rats (n=15) and 16.8±2.5 in SHRSP rats (n=20; $P > 0.05$ between two groups). The spatial working memory performance was then assessed by recording spontaneous alternation performance. The percentage of spontaneous alternation was impaired in SHRSP rats (n=20) as compared with WKY rats (n=15; $P < 0.05$, between WKY and SHRSP) (Fig. 2). A decrease of spontaneous alternation was alleviated in SHRSP rats after infusion of TAK-242 (n=15; $P < 0.05$, SHRSP *vs* SHRSP with TAK-242).

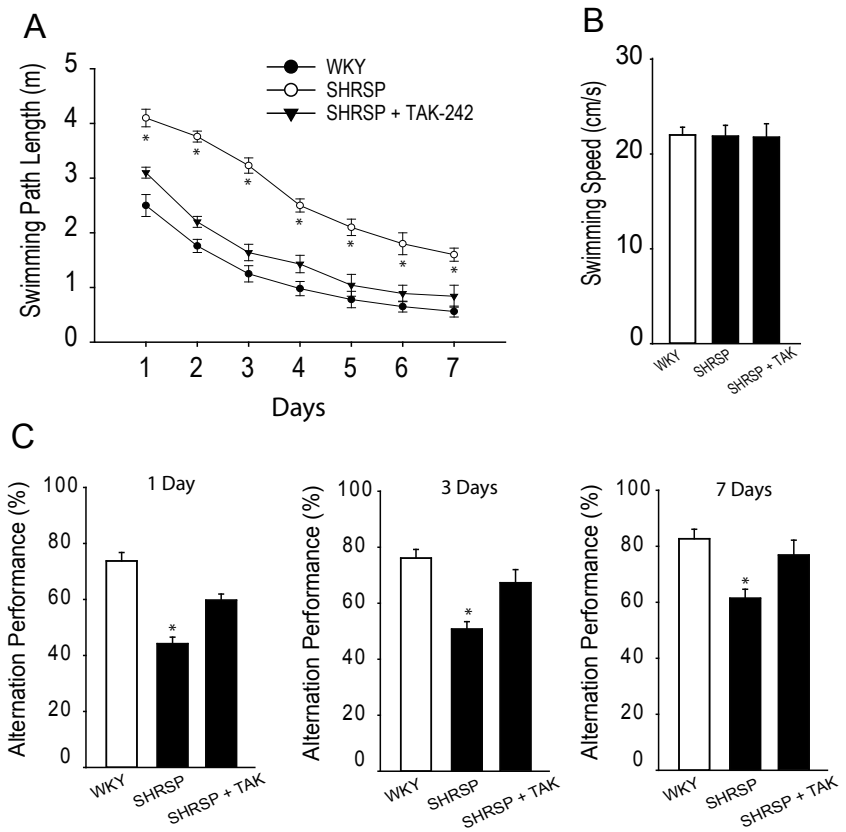

Fig. 2. *Learning performance in SHRSP rats and WKT rats.* ***A****) The cumulative swimming path length on 7 consecutive days in the Morris water maze for three experimental groups, showing increases of swimming path length in SHRSP rats (n=20) as compared to WKY rats (n=15). A chronic infusion of TAK-242 attenuated increases of swimming path length observed in SHRSP rats (n=15). *P < 0.05 vs WKY rats and SHRSP rats with TAK-242.* ***B****) Insignificant difference was observed in the swimming speed in three groups (P > 0.05).* ***C****) Spontaneous alternation performance in rats. The learning performance was examined at day 1, 3 and 7 during the fourth week of TAK-242 infusion. *P < 0.05, SHRSP rats/n=20 vs WKY rats/n=15 and SHRSP rats with TAK-242/n=15.*

DISCUSSION

SHRSP is a unique genetic model of severe hypertension and cerebral stroke. In this animal model, behavioral tests, including water maze task and spontaneous alternation performance, appear abnormal (9). Thus, this rat model was employed in the current study and we observed impairment of the learning performance in SHRSP rats. Our data further demonstrated that TLR4 was amplified in the hippocampus of SHRSP rats as compared with WKY rats. In SHRSP, increases of apoptotic Caspase-3/Caspase-9 and IL-1β, IL-6 and TNF-α were also found. Interestingly, blocking TLR4 attenuated IL-1β, IL-6 and TNF-α signaling pathway, which was accompanied with decreases of Caspase-3 and Caspase-9.

Elevated levels of PICs in the hippocampus are associated with increased disease vulnerability such as cell death, and PICs are involved in alterations of cellular damage related to development of memory deficits, and significant increases in IL-1β, IL-6 and TNF-α in the brain were observed following Aβ (1-42) injection to impair cognitive function in rats (10). Consistently, we further demonstrated that, in SHRSP with impaired memory, IL-1β, IL-6 and TNF-α were increased in the hippocampus tissues. Inhibition of TLR4 has a protective effect against transient focal ischemia-induced brain damage and neurological deficits (8). In particular, our data showed that chronic infusion of TAK-242 blocking TLR4 attenuated amplification of IL-1β, IL-6 and TNF-α. This also attenuated impairment of learning performance in SHRSP rats.

Caspases regulate the apoptotic cascade and neuro-degeneration as predominant target involved in PIC-mediated apoptosis in neuronal cells during memory impairment (11). We found that Caspase-3/Caspase-9 were increased in the hippocampus of SHRSP rats and inhibition of TLR4 attenuated their levels, suggesting the role of TLR4 in regulating neuronal apoptotic process in SHRSP.

In conclusion, TLR4 and PICs are amplified in the hippocampus of SHRSP rats. In this process, TLR4 has a regulatory effects on IL-1β, IL-6, TNF-α and Caspase-3/Caspase-9. The data may offer clues for the development of therapeutic strategies to target specific TLR4-PICs pathways for managing neurological symptoms observed in patients with hypertensive stroke.

REFERENCES

1. Rincon F, Wright CB. Vascular cognitive impairment. Curr Opin Neurol 2013; 26:29-36.
2. Vos T, Allen C, Arora M, Barber RM, Bhutta ZA, Brown A. Global, regional, and national incidence, prevalence, and years lived with disability for 310 diseases and injuries, 1990-2015: a systematic analysis for the Global Burden of Disease Study 2015. Lancet 2016; 388:1545-602.
3. Roman GC, Erkinjuntti T, Wallin A, Pantoni L, Chui HC. Subcortical ischaemic vascular dementia. Lancet Neurol 2002; 1:426-36.
4. Shi D, Das J, Das G. Inflammatory bowel disease requires the interplay between innate and adaptive immune signals. Cell Res 2006; 16:70-74.
5. Barak B, Feldman N, Okun E. Toll-like receptors as developmental tools that regulate neurogenesis during development: an update. Front Neurosci 2014; 8:272.
6. Fu Y, Liu Q, Anrather J, Shi FD. Immune interventions in stroke. Nat Rev Neurol 2015; 11:524-35.
7. Wang PF, Fang H, Chen J, et al. Polyinosinic-polycytidylic acid has therapeutic effects against cerebral ischemia/reperfusion injury through the downregulation of TLR4 signaling via TLR3. J Immunol 2014; 192:4783-94.
8. Wang Y, Ge P, Yang L, Wu C, Zha H, Luo T, Zhu Y. Protection of ischemic post conditioning against transient focal ischemia-induced brain damage is associated with inhibition of neuroinflammation via modulation of TLR2 and TLR4 pathways. J Neuroinflammation 2014; 11:15.
9. Gooch J, Wilcock DM. Animal models of vascular cognitive impairment and dementia (VCID). Cell Mol Neurobiol 2016; 36:233-39.
10. Su F, Bai F, Zhang Z. Inflammatory cytokines and Alzheimer's disease: a review from the perspective of genetic polymorphisms. Neurosci Bull 2016; 32:469-80.
11. Yun N, Lee YM, Kim C, et al. Anamorsin, a novel caspase-3 substrate in neurodegeneration. J Biol Chem 2014; 289:22183-95.

LETTER TO THE EDITOR

CORRELATION BETWEEN SERUM INDICATORS OF CHILD OBESITY METABOLIC SYNDROME AND THE INCIDENCE OF CARDIOVASCULAR DISEASES

ZZ. CHEN[1] and SK. LIU[2]

[1]Department of Pediatrics, The People's Hospital of Putuo Zhoushan, Zhoushan City, Zhejiang Province, China; [2]Department of Cardiology, The People's Hospital of Putuo Zhoushan, Zhoushan City, Zhejiang Province, China

Received April 8, 2019 – Accepted July 29, 2019

To the Editor,

The endothelial cell protein C receptor (EPCR) is a type-I transmembrane glycoprotein receptor mainly secreted by vascular endothelial cells (1). If vascular endothelial cells are damaged, the membrane-type EPCR (mEPCR) is released into the blood circulation (2), thereby increasing the serum level of soluble EPCR (sEPCR) (3). It has been indicated that sEPCR shows a certain correlation with clinical diseases and can be used as a molecular marker of vascular endothelial damage and the severity of vascular lesions (4). The soluble intercellular adhesion molecule-1 (sICAM-1) can trigger immunological and vascular inflammatory reactions and promote the adhesion of inflammatory cells to endothelial cells and the infiltration of inflammatory cells through blood vessel walls (5). Therefore, the increased content of sICAM-1 is an indicator of vascular endothelial injuries caused by inflammation. By comparing the levels of sEPCR and sICAM-1 in child patients of obesity and child patients with both obesity and metabolic syndromes (MS), this paper explored the correlation between the activity of the above indicators and the incidence of obesity, MS, and other associated cardiovascular diseases in children, thus providing the clinical basis for using functional changes of endothelial cells in child patients of obesity and MS as early indicators to achieve early diagnosis and comprehensive prognosis of these diseases.

MATERIALS AND METHODS

Cases

A total of 80 child obesity patients treated at the child endocrine outpatient department of the The People's Hospital of Putuo Zhoushan from March 2014 to December 2018 were enrolled in this study. The patients were divided into two groups in accordance with their conditions; 42 patients were allocated to the obesity group with metabolic syndrome (group A) and 38 patients were allocated to the simple obesity (non-metabolic syndrome obesity) group (group B). In accordance with the age and gender of patients, a total of 40 healthy child volunteers were randomly selected as the control group (group C). The study was approved by the Ethics Committee of The People's Hospital of Putuo Zhoushan and all subjects included in the study signed an informed consent to participate in the study or informed written consent was given by the family or guardian.

The Diagnostic Criteria for MS in Children and Adolescents, jointly recommended by the endocrine genetics and metabolism research group, the cardiovascular research group, and the child health research group of the

Key words: cardiovascular; soluble endothelial cell protein C receptor; soluble intercellular adhesion molecule-1; vascular endothelial cell

Corresponding Author:
Dr Shankuan Liu,
Department of Cardiology,
The People's Hospital of Putuo Zhoushan,
No. 19 Donggangwenkang Street,
Zhoushan City, 316100, Zhejiang Province, China
e-mail: liushankuan_sea1@163.com

0393-974X (2019)

Chinese Pediatric Society, Chinese Medical Association, was used for diagnostic criteria. For obesity patients with an age of ≥10 years and <16 years, their precondition of diagnosis was central obesity, i.e. a waist circumference (WC) of ≥ the 90th percentile (P90) of children with the same age and gender. MS was diagnosed by the presence of at least two of the following conditions: i) hyperglycemia: impaired fasting blood glucose (IFG): fasting plasma glucose (FPG) ≥5.6mmoL/L; or impaired glucose tolerance (IGT): oral glucose tolerance test (OGTT) 2 h ≥7.8mmoL/L and <11.1mmoL/L; ii) hypertension: systolic blood pressure (SBP) ≥ P95 of the blood pressure in children of the same age and gender, or diastolic blood pressure (DBP) ≥ P95 of the blood pressure in children of the same age and gender (6); iii) high-density lipoprotein-cholesterol (HDL-C) < 1.03mmoL/L or non-HDL-C ≥ 3.76mmoL/L; and iv) triglyceride (TG) ≥ 1.47mmoL/L.

The diagnostic criteria for non-MS obesity: Children aged 2 to 18 years with a body mass index (BMI) in the 85th~95th percentile of that in children of the same age and gender, who were diagnosed as overweight with an increased risk of obesity. If their BMI exceeded P95, the children were diagnosed as obese except that their conditions were caused by the following factors: endocrine diseases including thyroid-associated diseases and the hyperadrenocorticism syndrome, diseases of the central neurotrophin system including the deformation or damage to the hypothalamus, the long-term use of a hormone therapy, and genetic metabolic diseases including the Laurence-Moon-Bield syndrome and the Prader-Will syndrome.

Measurement of physical indicators

The subjects underwent physical examinations in the morning for the measurements of weight (W), height (H), body mass index (BMI), waist circumference (WC), and hip circumference (HC). Blood pressure measurements were carried out using a vertical mercury column sphygmomanometer with a standard cuff: after a 10-min rest, the subjects were seated to measure the SBP and DBP of their right brachial artery. For each subject, the measurement was repeated twice, and the average was recorded in mmHg.

Blood biochemistry assays

After a 12h-overnight fasting, blood samples of the subjects in all groups were collected to measure FPG, fasting insulin (FINS), serum total cholesterol (TC), TG, low-density lipoprotein (LDL), and high-density lipoprotein (HDL). Afterward, the obesity and MS patients (group A and group B) took an oral dose of 1.75 g glucose/kg (up to 75g) within 3~5 min of blood sampling to measure the plasma levels of glucose and insulin at 0.5h, 1h, 2h, and 3h later. The steady-state model was utilized to calculate HOMA-IR (homeostasis model assessment of insulin resistance) (HOMA-IR=FPG×FINS/22.5) and AI (atherosclerotic index) (AI= [TC-HDL]/HDL). In addition, LogFINS and LogHOMA-IR indicated logarithmic (base 10 Log) conversion of the obtained FINS and HOMA-IR values.

Serum sEPCR and sICAM assays

All blood samples were centrifuged for 30 min at 3000 rpm to separate the serum and erythrocytes. The upper serum layer was collected and stored at -80°C. Enzyme-linked immunosorbent assay (ELISA) was applied to determine the concentrations of serum sEPCR and sICAM using the following operation processes.

A 10× sample diluent was diluted 1:10 by distilled water. Before the assessment, the serum samples were diluted at least 20 times with the sample diluent. Preparation of the standard solution: a 200ng/mL solution was obtained using dilution with distilled water. A total of 8 centrifuge tubes (1.5 mL each) were taken: 900 uL of standard diluent was added to tube 1, and 500 uL of standard diluent was added to the other tubes. Next, 100 uL of 200 ng/mL standard solution was added to tube 1 and mixed evenly on the vortex mixer. Then, 500 uL of the mixed solution were pipetted out from tube 1 and added into tube 2. The procedures were repeated to dilute the liquid in the tubes. Then, 500 uL of the mixed solution were pipetted out from tube 7, and tube 8 was set as the blank control. Washing solution was diluted with double distilled water (double distilled water refers to water that had been distilled twice in a row). The reaction plate was equilibrated at room temperature for 20 min before 100 uL/well of the standard solutions or sample solutions were added. After mixing, the plate was incubated at 37°C for 40 min, washed 4~6 times with a washing solution and dried with filter paper. Then, 50 uL of distilled water and 50 uL of primary antibody were added into each well, respectively, (except for the blank control). After mixing, the plate was incubated at 37°C for 40min, washed 4~6 times with a

washing solution and dried with filter paper. Then, 100uL/well of the ELISA working fluid was added and the plate was incubated at 37°C for 40 min, washed 4~6 times with a washing solution and dried with filter paper. Afterward, 100uL/well of the TMB solution was added and the plate was incubated at 37°C for 15 min in the dark, followed by the addition of 10uL/well of the terminating solution and mixing. The concentrations of sEPCR and sICAM were determined within 30 min at 450 nm using a plate reader.

Statistical analysis

All collected data were analyzed by SPSS 22.0 statistics software. The data were subjected to the normality test. The data with a normal distribution were expressed as mean ± standard deviation ($\bar{x}\pm s$), while the data with a non-normal distribution were converted to data with a normal distribution using logarithmic transformations. Inter-group comparisons were analyzed by One-way ANOVA, while paired comparisons were analyzed by the Least-Significance Difference (LSD) method. Categorized variables were tested by the *Chi*-squared test, while ranked data were tested by the Spearman-associated analysis. The correlation between sEPCR/sICAM-1 concentrations and other indicators was analyzed by multiple stepwise regression. $P<0.05$ was considered statistically significant.

RESULTS

Measurement of each clinical indicator

Physical measurement: Compared with group C, group A showed significantly increased levels of H, W, BMI, WC, HC, waist-hip ratio (WHR), waist-height ratio (WHtR), SBP, and DBP ($P<0.05$), while group B showed significantly increased levels of W, BMI, WC, HC, WHR, WHtR, SBP, and DBP ($P<0.05$). Compared with group B, group A showed a significantly increased level of WHtR ($P<0.05$). Although the values of other physiological indicators showed no significant differences among the 3 groups ($P<0.05$), they all

Table I. *Comparison of each clinical indicator.*

Indicators		Group A	Group B	Group C	P1	P2	P3
Physical measurement	Age (years old)	11.92±2.34	11.52±2.97	11.61±2.72	0.272	0.341	0.263
	Height (cm)	157.92±10.31	154.22±11.22	150.13±13.43	0.026	0.518	0.172
	Weight (Kg)	76.51±16.46	68.57±21.31	45.33±13.11	0.000	0.000	0.088
	BMI (Kg/cm^2)	30.74±4.34	28.98±5.87	18.65±2.74	0.000	0.000	0.198
	WC (cm)	93.34±14.46	91.74±13.65	61.02±7.42	0.000	0.000	0.554
	HC (cm)	102.56±11.32	98.85±13.73	79.24±10.36	0.000	0.000	0.364
	WHR	0.98±0.05	0.89±0.07	0.76±0.06	0.000	0.000	0.514
	WHtR	0.61±0.06	0.48±0.08	0.40±0.03	0.000	0.000	0.041
	SBP (mmHg)	116.73±12.35	109.44±9.16	100.09±13.34	0.000	0.034	0.309
	DBP (mmHg)	75.22±9.87	71.25±7.79	65.68±7.65	0.000	0.012	0.118
Saccharometabolism	FPG (mmoL/L)	5.43±0.49	5.28±0.48	4.51±0.34	0.000	0.000	0.531
	LogFINS*	1.48±0.22	1.36±0.25	1.01±0.16	0.000	0.000	0.126
	LogHOMA-IR*	0.84±0.27	0.72±0.25	0.30±0.12	0.000	0.000	0.129
Lipometabolism	TC (mmoL/L)	4.69±0.85	4.37±0.55	4.03±0.67	0.001	0.058	0.192
	TG (mmoL/L)	1.73±0.81	1.19±0.47	0.88±0.38	0.001	0.000	0.001
	HDL (mmoL/L)	1.08±0.21	1.31±0.44	2.16±0.51	0.000	0.000	0.056
	LDL (mmoL/L)	2.93±0.75	2.61±0.54	1.56±0.27	0.000	0.000	0.048
	AI	3.58±0.91	2.60±0.73	0.96±0.26	0.000	0.000	0.000
sEPCR (ng/mL)		156.22±91.15	134.11±52.33	98.34±33.46	0.014	0.038	0.076
sICAM-1 (ng/mL)		314.74±31.35	285.41±20.72	245.83±19.38	0.012	0.014	0.508

*P1: group A vs group C; P2: group B vs group C; P3: group A vs group B. * indicates logarithm conversion before analysis.*

increased significantly (Table I).

Saccharometabolism: Compared with group C, the levels of FPG, LogFINS, and LogHOMA-IR of children in groups A and B increased significantly (P<0.01). Compared with group B, the levels of GLU2h and LogFINS1h in group A increased significantly (P<0.05); the levels of FPG, LogFINS, LogFINS0.5h, LogFINS2h, LogFINS3h, and LogHOMA-IR in group A showed increased trends (Tables I and II) but the difference was not significant (p>0.05).

Lipometabolism: Compared with group C, levels of TC, TG, LDL, and AI of children in group A increased significantly (P<0.01), while levels of HDL decreased significantly (P<0.01). Compared with group C, levels of TG, LDL, and AI of children in group B increased significantly (P<0.01), while levels of HDL decreased

Table II. *Comparison of OGTT and insulin releasing test results between group A and group B (obesity and MS).*

Plasma glucose (mmoL/L)	FPG	0.5h	1h	2h	3h
Group A	5.38±0.43	8.29±1.12	8.54±1.34	7.21±1.62	5.69±1.31
Group B	5.25±0.48	8.07±1.53	7.75±1.61	6.51±0.67	5.40±1.32
P Values	0.523	0.541	0.125	0.027	0.514
Insulin	LogFINS*	LogFINS0.5h*	LogFINS1h*	LogFINS2h*	LogFINS3h*
Group A	1.49±0.26	2.31±0.18	2.37±0.14	2.28±0.26	1.90±0.45
Group B	1.39±0.24	2.31±0.19	2.24±0.31	2.17±0.25	1.76±0.57
P Values	0.121	0.332	0.035	0.082	0.265

** Logarithm conversion before analysis*

Table III. *Correlation between sEPCR and other indicators.*

Indicator	sEPCR		sICAM-1	
	r	P	r	P
W	0.186	0.125	0.235	0.008
BMI	0.232	0.007	0.481	0.000
SBP	0.241	0.026	0.095	0.368
DBP	0.289	0.008	0.312	0.001
WC	0.301	0.005	0.463	0.000
HC	0.234	0.034	0.265	0.006
WHR	0.014	0.015	0.615	0.000
FPG	0.235	0.032	0.492	0.000
TC	0.177	0.107	0.282	0.005
TG	0.116	0.365	0.407	0.000
HDL	-0.212	0.064	-0.414	0.000
LDL	0.248	0.026	0.574	0.000
AI	0.202	0.068	0.586	0.000
LogHOMA-IR	0.246	0.025	0.546	0.000
WHtR	0.431	0.001	0.617	0.000
LogFINS	0.228	0.038	0.525	0.000

significantly (P<0.01). TC showed increased trends but the difference was not significant (P>0.05). Compared with group B, the differences in TG, LDL, and AI in group A were statistically significant (P<0.05), and the differences in TC and HDL were not significant (P>0.05). However, compared with group B, TC levels of children in group A showed increased trends while HDL levels showed decreased trends (Table I).

sEPCR and sICAM-1 levels: Compared with group C, the levels of sEPCR and sICAM-1 of children in groups A and B increased significantly (P<0.05). Compared with group B, levels of serum sEPCR and sICAM-1 in group A showed increased trends (Table I), but the differences were not significant (P>0.05).

Relationship of sEPCR and sICAM-1 to other indicators

The level of sEPCR was positively correlated with the levels of BMI, SBP, DBP, WC, HC, WHR, WHtR, LDL, FPG, LogFINS, and LogHOMA-IR (P<0.05 or P<0.01), while no correlation was found between the level of sEPCR and the levels of W, TC, TG, HDL, and AI (P>0.05). The level of sICAM-1 was positively correlated with the levels of W, BMI, DBP, WC, HC, WHR, WHtR, TC, TG, LDL, AI, FPG, LogFINS, and LogHOMA-IR (P<0.05 or P<0.01), and negatively correlated with the level of HDL (P<0.01). In addition, no correlation was found between the level of sICAM-1 and the level of SBP (P>0.05) (Table III).

Multiple stepwise regression of sEPCR and sICAM-1 expressions

Using sEPCR/sICAM-1 as independent variables and other indicators as dependent variables, a multiple stepwise regression was performed to find that WHtR was an independent risk factor affecting the concentration of sEPCR in the subjects (P=0.001). The regression equation was Y=2.271+37.38x, in which Y was sEPCR (ng/mL) and x was WHtR. The independent risk factors affecting the concentration of sICAM-1 in the subjects were BMI (P=0.002), WHR (P=0.022), and LDL (P=0.000). The regression equation was Y=22.38x1+85.48x2+86.5 3x3-120.769, in which Y was sICAM-1 (ng/mL), x1 was BMI, x2 was WHR, and x3 was LDL.

DISCUSSION

The variation in serum sEPCR concentrations could be used as a specific molecular marker of endothelial cell damage (7). The damage to vascular endothelial cells and an increased level of sEPCR would promote blood coagulation and reduce fibrinolysis, thereby aggravating the damage of vascular endothelial cells and accelerating the onset of atherosclerosis (AS) (8, 9). In addition, it was suggested that there were different vascular endothelial damage and dysfunctions in child obesity patients, especially those with damaged saccharometabolism and abnormal insulin concentrations. Meanwhile, as levels of serum sEPCR increased, the risk of thrombosis also increased, aggravating the damage to vascular endothelial cells.

An increased level of sICAM-1 indicated an increased risk of cardiovascular diseases (10, 11). Experimental data showed that sICAM-1 mediated the adhesion and migration of inflammatory cells via endothelial cells, thereby triggering the onset of AS. It was also found that levels of sICAM-1 were positively correlated with multiple risk factors of cardiovascular diseases, including BMI, WHR, WHtR, DBP, saccharometabolism disorder, and insulin tolerance. Moreover, levels of sICAM-1 were negatively correlated with HDL, while BMI, WHR, and LDL were independent risk factors for an increased level of sICAM-1. Therefore, it was further demonstrated that obesity, especially central obesity, was closely related to an abnormality in lipid metabolism and adhesion of vascular endothelial cells in obese children.

In summary, it was hypothesized that sEPCR and sICAM-1 might be involved in the pathophysiological process of endothelial damage in child obesity patients with MS. Moreover, sEPCR and sICAM-1 might also be used as sensitive indicators for functional damages to vascular endothelial cells and severity of inflammatory diseases.

REFERENCES

1. Mohan Rao LV, Esmon CT, Pendurthi UR. Endothelial cell protein C receptor: a multiliganded and

multifunctional receptor. Blood 2014; 124(10):1553-62.
2. Huang Y, Long Y, Deng D, et al. Alterations of anticoagulant proteins and soluble endothelial protein C receptor in thalassemia patients of Chinese origin. Thromb Res 2018; 172:61-66.
3. Esmon CT. The discovery of the endothelial cell protein C receptor. J Thromb Haemost 2010; 8(1):2-5.
4. Navarro S, Bonet E, Estellés A, et al. The endothelial cell protein C receptor: its role in thrombosis. Thromb Res 2011; 128(5):410-16.
5. Moughal NA, Adonogianaki E, Thornhill MH, Kinane DF. Endothelial cell leukocyte adhesion molecule-1 (ELAM-1) and intercellular adhesion molecule-1 (ICAM-1) expression in gingival tissue during health and experimentally-induced gingivitis. J Periodontal Res 1992; 27(6):623-30.
6. Xu J, Esmon NL, Esmon CT. Reconstitution of the human endothelial cell protein C receptor with thrombomodulin in phosphatidylcholine vesicles enhances protein C activation. J Biol Chem 1999; 274(10):6704-10.
7. Boomsma MM, Stearns-Kurosawa DJ, Stegeman CA, Raschi E, Meroni PL, Kurosawa S, Tervaert JW. Plasma levels of soluble endothelial cell protein C receptor in patients with Wegener's granulomatosis. Clin Exp Immunol 2002; 128(1):187-94.
8. Bilgic MA, Yilmaz H, Bozkurt A, et al. Relationship of late arteriovenous fistula stenosis with soluble E-selectin and soluble EPCR in chronic hemodialysis patients with arteriovenous fistula. Clin Exp Nephrol 2015; 19(1):133-39.
9. Karabıyık A, Yılmaz E, Eğin Y, Akar N. The effects of endothelial protein C receptor gene polymorphisms on the plasma sEPCR level in venous thrombosis patients. Turk J Haematol 2012; 29(1):55-62.
10. Witkowska AM, Borawska MH. Soluble intercellular adhesion molecule-1 (sICAM-1): an overview. Eur Cytokine Netw 2004; 15(2):91-98.
11. Glowinska B, Urban M, Peczynska J, Florys B. Soluble adhesion molecules (sICAM-1, sVCAM-1) and selectins (sE selectin, sP selectin, sL selectin) levels in children and adolescents with obesity, hypertension, and diabetes. Metabolism 2005; 54(8):1020-26.

LETTER TO THE EDITOR

IgA NEPHROPATHY AND RENAL CELL CARCINOMA: MOLECULAR GENETIC ANALYSIS

HN. LI[1,2,3], H. CHEN[4], XX. YANG[2], YY. XU[4], Y. CAO[4], JS. GENG[1,2], XM. JIN[1] and HX. MENG[1,2]

[1]Department of Pathology, Harbin Medical University, Harbin, China; [2]Department of Pathology, Harbin Medical University Cancer Hospital, Harbin, China; [3]Department of Pathology, The First Affiliated Hospital of Hei Longjiang University of Chinese Medicine, Harbin, China; [4]Department of Urinary Surgery, Harbin Medical University Cancer Hospital, Harbin, China

Received March 17, 2019 – Accepted July 30, 2019

To the Editor,

Immunoglobulin A nephropathy (IgAN), the most common form of primary glomerulonephritis worldwide, has been suggested to be associated with malignant tumors (1). Recent studies have suggested that IgAN is associated with solid tumors such as kidney cancer, bronchial cancer, lung cancer, gastric cancer, carcinoma of the esophagus, rectal cancer and mesothelioma (2-9). However, the molecular genetic changes and pathogenesis of tumor-associated IgAN is unknown. Here, we report a patient with IgA nephropathy and renal cell carcinoma, along with details of molecular genetic analysis.

MATERIALS AND METHODS

Case description

A 57-year-old female was hospitalized at the First Affiliated Hospital of Hei Longjiang University of Chinese Medicine complaining of back and right flank pain. A urinalysis was performed and found to be positive for hematuria and proteinuria (300 mg/24 h), no other abnormalities were identified on physical examination. A renal biopsy was performed immediately. A kidney tumor with a diameter of 3 cm had been identified on the same kidney, but on a different site, with a previous renal biopsy 3 years previously. No other abnormalities were identified during physical examination. The results of urinalysis were as follows: proteinuria, 1.0 g/l; positive for hematuria; urinary cast examination was negative. The patient gave informed and signed consent to publish her case details.

Histopathologic parameters of renal injury

IgAN were categorized according to the Oxford classification. The pathologic variables of the Oxford classification were scored as follows: mesangial score less than or equal to 0.5 (M0) or greater than 0.5 (M1), segmental glomerulosclerosis absent (S0) or present (S1), endocapillary hypercellularity absent (E0) or present (E1), and tubular atrophy/interstitial fibrosis less than or equal to 25% (T0), 26–50% (T1), or more than 50% (T2), crescent formation absent (C0) or present (C1).

After surgery resection, tumor and adjacent normal tissues were fixed with formalin, and subsequently embedded in paraffin (FFPE). Tumor cells, adjacent normal tissues, and their junction cells were scraped from each slide, respectively. Genomic

Key words: IgA nephropathy; renal cell carcinoma; genetic analysis; tumor manifestation

Correspondence Author:
Prof. Hongxue Meng, MD. PhD
Department of Pathology,
Harbin Medical University Cancer Hospital,
150 Haping Road, Harbin, China
Tel.: +86 451 85718261
e-mail: menghongxue15@163.com

0393-974X (2019)

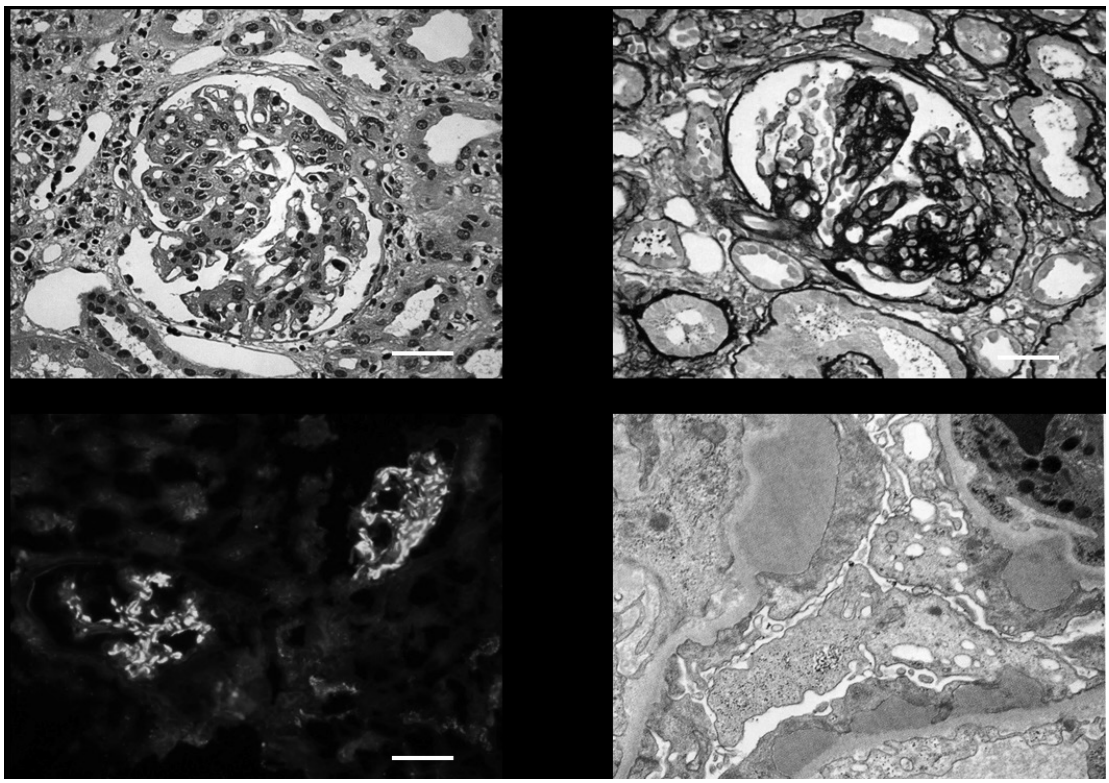

Fig. 1. *Light microscopic examination showed segmental sclerotic, glomerular mesangial cell hyperplasia, and tubular atrophy by hematoxylin-eosin staining (**A**) and periodic acid-Schiff stain (**B**). Immunofluorescence was positive for IgA (**C**). Electron microscopy showed marked mesangial and stromal hyperplasia with electron-dense deposits (**D**). Bars, 200 μm.*

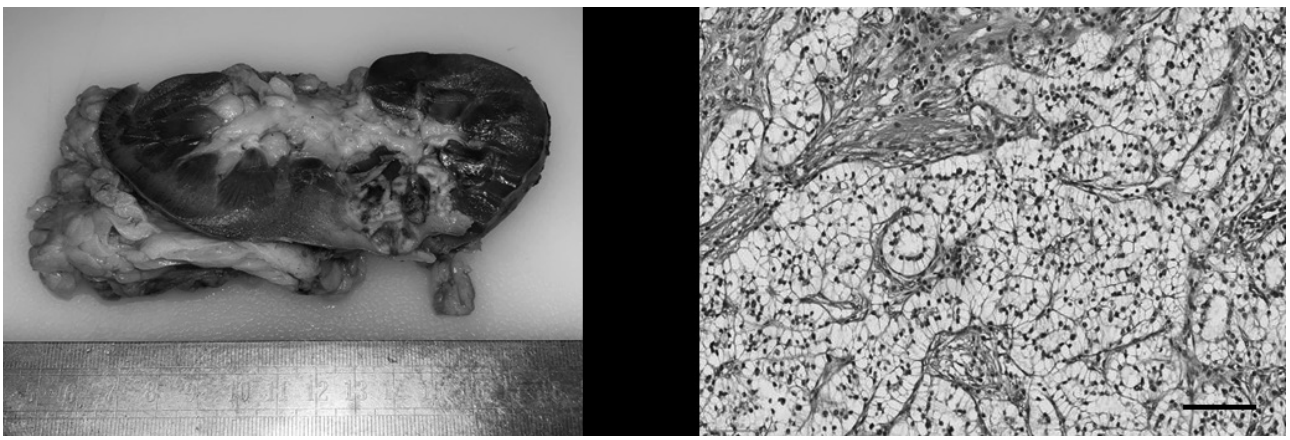

Fig. 2. *A kidney tumor was identified with a diameter of 3 cm (**A**), with the diagnosis of renal clear cell carcinoma at Grade 2 (WHO/ISUP classification) (**B**). Bars, 200 μm.*

DNA were extracted from each samples using the GeneRead DNA FFPE Kit (Qiagen). The analysis of the patient samples was approved by the Ethics Committee of the First Affiliated Hospital of Hei Longjiang University of Chinese Medicine.

Genomic DNA was sheared into fragments with the size of ~200 bp. The adapters were added to both ends, then were purified with Agencourt AMPure SPRI beads (Beckman Coulter, Inc., Brea, CA, USA). Ligation-mediated PCR was performed to amplify the extracted DNA. For enrichment the PCR product was hybridized to the SureSelect biotinylated RNA library (Agilent Technologies, Santa Clara, CA, USA) according to the manufacturer's instructions. Paired-end multiplex samples were sequenced with the IlluminaHiSeq 2000 System. Sequencing depth was ~20 × per sample.

VarScan1 was used for built-in filters in the present study to detect the single-nucleotide variations. The filtering criteria was applied, coverage of reads ≥ 10 in tumor DNA and variant frequency ≥ 10% ($P < 0.0001$) for calling a somatic site.

Alternatively, MuTect2 was used for built-in filters to detect the single-nucleotide variations. The filtering criteria was applied, total read count ≥ 15 in tumor DNA and variant frequency ≥ 10% in tumour DNA. Removal of variants in positions was listed in the dbSNP129 database (www.ncbi.nlm.nih.gov/SNP/).

Renal biopsy findings

Light microscopic examination of a renal biopsy specimen revealed nine glomeruli, one of which was segmental sclerotic (periodic acid-silver methenamine; Fig. 1A). The remaining glomeruli showed endocapillary hypercellularity, glomerular mesangial cells with mild-to-moderate stromal hyperplasia, and tubular atrophy (Fig. 1B). The renal biopsy result was E1M1S1T1 according to Oxford classification. Immunofluorescence was positive for IgA (2+) but negative for IgG, IgM, C3, and C1q (Fig. 1C). Electron microscopy showed marked mesangial and stromal hyperplasia with electron-dense deposits (Fig. 1D).

The patient was administered piperazine ferulate tablets (200 mg, oral, three times a day), irbesartan (150 mg, oral, once a day) and a Tripterygium wilfordii capsule, a traditional Chinese medicine drug made from herbs, (500 mg, oral, three times a day) for three months, and the 24-h proteinuria returned to the normal value (<150 mg/24 h). Over frequent monitoring (every 3 months for 2 years), no abnormalities were observed.

The patient received kidney surgery immediately at Harbin Medical University Cancer Hospital, which validated the diagnosis of renal clear cell carcinoma at Grade 2 (WHO/ISUP classification) (Fig. 2, A and B). The tumor was staged IA (T1aN0M0), according to the Tumor-Node-Metastasis staging system.

Molecular genetic analysis

To explore the genomic characteristics underlying IgA nephropathy-associated cancer, we performed an investigation using high-throughput sequencing of DNA obtained from renal carcinoma tissue and IgAN biopsy tissue. Genomic DNA sequencing revealed the same driver gene mutations (EGFR mutation; Early Growth Response 1, EGR1 mutation; MUC20 mutation; MUC3A mutation) in tumor cells and IgAN biopsy cells, but not in para-carcinoma tissue (distance form tumor > 5cm) which were diagnosed by a pathologist. EGFR, MUC20 and MUC3A are oncogene usually observed in RCC, and EGR1 is an anti-oncogene according to previous reports (5-7). These findings support the hypothesis that IgA nephropathy may be a tumor manifestation in kidney tumor.

DISCUSSION

Association between malignant tumors and IgAN has been reported, but the precise mechanism and genetic changes have not been elucidated. There have been several reports on patients with tumor-associated IgAN (Table I) (2-4). The most common reported malignancy with IgAN was renal cell carcinoma (4 cases).

Previous studies demonstrated that minor glomerular abnormalities may be associated with the immune response of malignant tumors (1). Tumor cells may release antigens which stimulate the production of antibodies. Subsequently, antigen-antibody immune complexes, such as self-

Table I. *Malignant tumors associated with IgAN as reported in the literature.*

Associated tumor type	Age (years)	Sex	Sequence of two diseases	Immunofluorescence	Year published
Breast cancer	57	F	Simultaneous	IgA+	1986 (Yin et al.)
Renal cancer	61	M	Simultaneous	IgA and C3+	1991 (Tanaka et al.)
Bronchial cancer	45	No data	IgAN then cancer	No data	1996 (Schutte et al.)
Small cell lung cancer / gastric cancer	66	M	Cancer then IgAN	No data	1998 (Tomoda et al.)
Esophageal cancer	70	M	IgAN then cancer	IgA, IgM and C3+	1998 (Lam et al.)
Lung cancer	55	M	IgAN then cancer	No data	2008 (Yacoub et al.)
Renal cancer	58	M	IgAN then cancer	IgA and IgM+	2009 (Mimura et al.)
Renal cancer	66	M	IgAN then cancer	IgA/IgM/C3+	2010 (Mimura et al.)
Renal cancer	59	M	Simultaneous	IgA/IgM/C3+	2011 (Mimura et al.)
Mesothelioma	65	M	Cancer then IgAN	IgA/C3+	2012 (Fawole et al.)
Rectal cancer	68	M	Cancer then IgAN	IgA/IgG/IgM/C3+	2013 (Yahata et al.)
Gastric cancer	58	M	Cancer then IgAN	IgA positive	2013 (Kocyigit et al.)
Breast cancer	31	F	IgAN then cancer	IgA positive	2018 (Jiang et al.)

polymeric IgA 1 in IgA nephropathy, or as a joint auto-antigen complement C3, may be formed (9). The IgA and/or IgG antibody complexes may be formed and deposited in the glomerular mesangium. Pathogenic IgA has been suggested to be crucial to the pathogenesis of IgAN (10).

In the present case study, the principal clinical manifestations were hematuria and proteinuria. The present study hypothesized that the patient may exhibit IgAN prior to renal cancer. A study estimated that ~25% patients >60 years old with membranous glomerulonephritis experienced an associated cancer, and the overall incidence of cancer in membranous glomerulonephritis was 7.9% (11). As the strongest association was observed between membranous glomerulonephritis and solid tumors, it has been recommended that any patient with nephrotic syndrome >40 years of age should be screened for cancer (12).

In addition, whether kidney disease is associated with specific types of cancer remains unknown and requires additional study. Genomics will serve an essential role in understanding the pathogenesis underlying IgAN-associated cancer.

ACKNOWLEDGEMENTS

This work was supported by the National Nature Science Foundation of China (81600539), Natural Science Foundation of Heilongjiang Province of China (LC2016038), Nn10 program of Harbin Medical University Cancer Hospital (Nn10 2017-03), Harbin Special fund project for Science and technology innovation (2016RAQXJ203), Youth elite training Foundation of Harbin Medical University Cancer Hospital (JY2016-06) and Outstanding Youth Foundation of Harbin Medical University Cancer Hospital (JCQN-2018-05).

REFERENCES

1. Pani A, Porta C, Cosmai L, et al. Glomerular diseases and cancer: Evaluation of underlying malignancy. J Nephrol 2016; 29:143-52.
2. Yin P, Chen W and Chen G. Clinical report of 4 cases of malignant tumor complicated with glomerular disease. New Med 1986; 7:354-55.
3. Mimura I, Tojo A, Kinugasa S, Uozaki H, Fujita T. Renal cell carcinoma in associated with IgA nephropathy in the elderly. Am J Med Sci 2009; 338:431-32.
4. Yahata M, Nakaya I, Sakuma T, Sato H, Aoki S, Soma J. Immunoglobulin a nephropathy with massive paramesangial deposits caused by anti-vascular endothelial growth factor therapy for metastatic rectal cancer: A case report and review of the literature. BMC Res Notes 2013; 6:450.
5. Zhong JT, Wang HJ, Yu J, Zhang JH, Wang SF, Yang X, Su W. Correlations of the expressions of c-Jun and Egr-1 proteins with clinicopathological features and prognosis of patients with nasopharyngeal carcinoma. Cancer Biomark 2017; 19:213-20.
6. Kong X, Ding LJ, Wang ZX. Mucin expression profile of benign and malignant cervical tissues and correlation with clinical-pathologic parameters. Eur J Gynaecol Oncol 2017; 38:350-55.
7. Oh F, Todhunter D, Taras E, Vallera DA, Borgatti A. Targeting EGFR and uPAR on human rhabdomyosarcoma, osteosarcoma, and ovarian adenocarcinoma with a bispecific ligand-directed toxin. Clin Pharmacol 2018; 10:113-21.
8. Liu F, Shangli Z, Hu Z. CAV2 promotes the growth of renal cell carcinoma through the EGFR/PI3K/Akt pathway. Onco Targets Ther 2018; 11:6209-6216.
9. Faria TV, Baptista MA, Burdmann EA , Cury P. Glomerular deposition of immune complexes as a first manifestation of malignant melanoma-a case report. Ren Fail 2010; 32: 1223-25.
10. Hongxue M, Huining L, Rintaro O, et al. TSLP in tonsillar follicular dendritic cells correlates with elevated serum IgA titer by promoting tonsillar IgA class switching in IgA nephropathy. Transl Res 2016; 176:1-17.
11. Zech P, Colon S, Pointet P, Deteix P, Labeeuw M, Leitienne P.. The nephrotic syndrome in adults aged over 60: Etiology, evaluation and treatment of 76 cases. Clin Nephrol 1982; 17:232-36.
12. Jiang D, Zhang X, Liu J, Deteix P, Labeeuw M, Leitienne P. Triple negative breast cancer and immunoglobulin A nephropathy: A case report and literature review. Oncol Lett 2018; 15:979-83.

LETTER TO THE EDITOR

ENDOSCOPIC SUBMUCOSAL DISSECTION FOR TREATING GASTRITIS CYSTICA PROFUNDA

J-A. LI, Y-L. TIAN, L. CONG, S. FAN and L-W. DUAN

Gastroenterology and center of Digestive Endoscopy, The Second Hospital of Jilin University, Changchun, Jilin, China

Received May 8, 2019 – Accepted August 5, 2019

To the Editor,

Gastritis cystica profunda (GCP), also known as cystic gastritis, was first described by Franzin in 1981 (1). GCP is a relatively rare disorder characterized by growth in deeper layers of gastric mucosa spreading into submucosa layer of stomach. The condition is accompanied by gastric cystic dilatation (2). Due to the lack of specificity of symptoms, physical signs and endoscopic findings associated with this disease, it can be easily misdiagnosed prior to surgery as stromal tumors, ectopic pancreas and other submucosal lesions. Here, we report the treatment of GCP in a 57-year-old female.

Medical history and treatment

A 57-year-old female patient was admitted to our hospital (The Second Hospital of Jilin University, China) with a gastric sinus mass that had developed one month earlier. The patient experienced the symptoms of acid reflux after food ingestion, hunger at night, and reported weight loss of approximately 10 kg in the course of one year prior to admission. The patient had previously undergone a uterine and bilateral accessory resection due to endometrial cancer and had a history of hypertension for the previous 20 years. Upon admission, the investigation showed that the patient had a fasting blood glucose level of 7.24 mmol/L, triglyceride (TG) at 3.62 mmol/L, total cholesterol of 6.6 mmol/L, and low density lipoprotein (LDL) cholesterol of 5.03 mmol/L. The test for hepatitis B (HBV) was positive. Endoscopic investigation of the stomach revealed a 2.0 cm × 1.5 cm bulging lesion in the giant curvature of the antrum. (Fig. 1A). Endoscopic ultrasound examination found that the third layer of the gastric wall of the bulge had a moderate echo position, the internal echo was uneven, the boundary was clear and there were no echogenic tubular structures inside. The largest section of the mass was found to be about 9.1 mm x 5.8 mm (Fig. 1B). The preoperative diagnosis for the patient was described as gastric antrum mass, type II diabetes, hypertension grade 2 and hyperlipidemia. After the diagnosis, the endoscopic mucosal dissection was performed. The post-operative pathological examination revealed chronic inflammation of gastric mucosa with acute activity. At the same time, mucosal lamina propria and mucosal muscle layer showed hyperplastic dilated glands (Fig. 2 A,B). After surgery, acid suppression, fluid replacement and infection prevention treatments were administered. The patient successfully recovered and was subsequently discharged. Half a year after the operation, no abnormalities were detected by endoscopic examination.

The patient signed an informed consent for publication of her data.

Key words: gastritis cystica profunda; endoscopic submucosal dissection; gastric cancer; submucosal lesions

Corresponding Author:
Li-Wei Duan,
Gastroenterology and center of Digestive Endoscopy,
The Second Hospital of Jilin University,
218 Ziqiang Street, Changchun,
Jilin 130041, P.R.China
e-mail: dliwei@aliyun.com

0393-974X (2019)

DISCUSSION

Gastritis cystica profunda (GCP) is defined by formation of multiple benign cystic gastric glands within the submucosa of the stomach. The pathogenesis of this condition probably involves the loss of the integrity of the muscularis mucosa and the consequent migration of epithelial cells to the submucosal layer (3). Due to the low incidence of GCP, there are no major clinical reports on the condition in the literature. The precise causes and pathogenesis of GCP are still largely unknown. Published reports indicate that the condition is more common among patients who had previously undergone gastric surgery. For this reason, surgical damage to the mucosa around the incision site and the consecutive epithelial implantation is considered as a causative factor (4, 5). However, in spite of improvements, ofendoscopic techniques and subsequent drastic reduction in the incidence of traumatic surgery, cases of GCP are still reported. Nowadays, most physicians believe that chronic inflammation and ischemia are the main causes of GCP (1). Gastric mucosal epithelial cells can invade the submucosal layer along the mucosal muscle layer at the injury site. This eventually leads to the

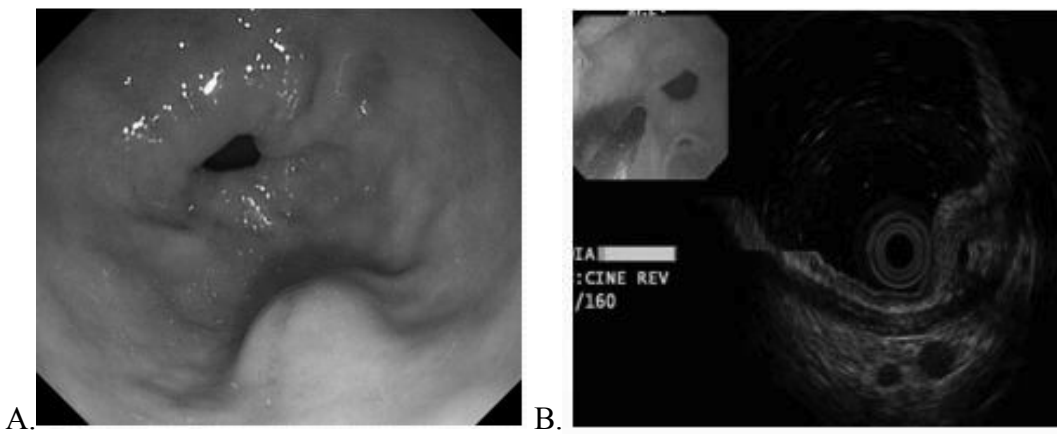

Fig. 1. ***A)*** *Endoscopic view showing the 2.0 cm ×1.5cm bulging lesions in giant curvature of the antrum.* ***B)*** *Endoscopic ultrasound of the lesions in the gastric curvature of the antrum.*

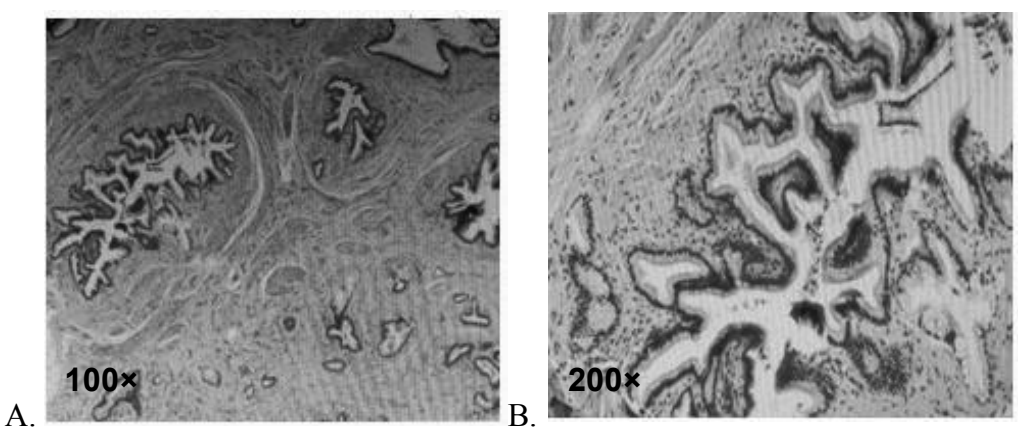

Fig. 2. *Pathological Hematoxylin and Eosin staining. Mucosal lamina propria and mucosal muscle layer showing hyperplastic dilated glands:* ***A)*** *100×;* ***B)*** *200×.*

formation of glands in the mucosal muscle layer and submucosal layer, thus forming cystic dilatation. The deletion in the Kcne2 gene and the infections with Epstein-Barr virus (EBV) and *Helicobacter pylori* were reported to be closely associated with the occurrence of GCP (6–8). The definite diagnosis of GCP requires pathological investigation of resected tissues by microscopic analysis. The pathological changes characteristic of GCP include glandular connective tissue hyperplasia, invasive gastric gland, pyloric gland or metaplastic gland invasion into the deep mucosa and infiltration into the submucosal layer and muscle layer. However, the morphology of the glandular tissue remains normal (1, 10). Pathological analysis clearly showed that the hyperplasia expands into cystic glands. GCP is considered to be a benign lesion, although it is also viewed as a precancerous lesion (10, 11) associated with early gastric cancer (12). With the development of endoscopic techniques, endoscopic mucosal resection (EMR) and endoscopic submucosal dissection (ESD) can be used to fully remove the lesions (13), which significantly improved the prognosis of patients.

The clinical manifestations of GCP are not specific but some of them can be revealed by chance during physical investigation. The most common clinical symptoms of GCP are upper abdominal pain and bloating, which may be accompanied by nausea, loss of appetite, weight loss, hemoptysis and anemia due to bleeding at the site of lesion. Occasionally, pyloric obstruction may occur due to formation of large lesions. In the case described in this article, the patient reported a sense of hunger and acid reflux in the upper abdomen. The patient had a history of gynecologic surgery at the lower abdomen 20 years previously. When examined with a white light endoscope, GCP appears as submucosal bulging lesions with a smooth surface and normal color. However, due to deep location of the lesions, it is difficult to use the conventional endoscopic procedure to obtain a biopsy. This complicates the distinguishing of GCP lesions from the lesions associated with stromal tumors, ectopic pancreas, hypertrophic gastritis and other diseases. In some cases, endoscopic ultrasonography reveals characteristic features of GCP, such as multiple anechoic cysts or submucosal cysts (9). In the present case, the third layer of the ultrasound structure of the patient's stomach wall showed an anechoic tubular structure, suggesting the existence of a cystic structure. Some GCPs can be seen under endoscopic ultrasonography as gastric wall thickening or submucosal hypoechoic areas, which need to be differentiated from gastric stromal tumors and gastric cysts. Gastric stromal tumors generally show hypoechoic changes in the mucosal layer or muscularis propria, while gastric cysts usually appear as single-shot hypoechoic dark areas. However, the findings of ultrasonography can be inconclusive, in which cases the pathological diagnostics is required.

Regarding the treatment strategies for GCP, it is generally considered that ESD resection should be performed for GCP with no malignant changes, and surgical resection is recommended for GCP with suspected malignant changes. Currently, the correct diagnostics of GCP prior to surgery remains difficult, and further research is needed to address this issue. With continuing improvement of endoscopic ultrasonographic techniques, the identification of anechoic or submucosal cysts becomes easier, which in turn provides a substantial help in the diagnostics. ESD and EMR are becoming the treatments of choice for benign GCP. In our patient, the diagnosis of GCP was established by endoscopic ultrasonography. The lesion was completely removed by ESD, and the surgical trauma was avoided. There was no recurrence at the follow-up examination by gastroscopy. The case demonstrates that ESD can be used instead of traditional surgical methods for the removal of GCP lesions that are not accompanied by malignant tumor formation.

REFERENCES

1. Franzin G, Novelli P. Gastritis cystica profunda. Histopathology 1981; 5:535-47.
2. McCurdy KR, Parmar K, de Melo SW. Gastritis cystica profunda: a deeper problem. ACG Case Rep J 2016; 3:e125.
3. Enis D, Fatih A. Multiple gastritis cystica profunda in a patient without gastric surgery history. Arch Iran

Med 2018; 21:608-61.
4. Kondo K, Kondo K, Kojima H, Akiyama S, Ito K, Takagi H. Pathogenesis of adenocarcinoma induced by gastrojejunostomy in Wistar rats: role of duodenogastric reflux. Carcinogenesis 1995; 16:1747-51.
5. Lee TH, Lee JS,Jin SY. Gastritis cystica profunda with a long stalk. Gastrointest Endosc 2013; 77:821-2; discussion 822.
6. Roepke TK, Purtell K, King EC, La Perle KM, Lerner DJ, Abbott GW. Targeted deletion of Kcne2 causes gastritis cystica profunda and gastric neoplasia. PLoS One 2010; 5:e11451.
7. Kim L, Kim JM, Hur YS, et al. Extended gastritis cystica profunda associated with Epstein-Barr virus-positive dysplasia and carcinoma with lymphoid stroma. Pathol Int 2012; 62:351-5.
8. Wiedemann T, Loell E, Mueller S, Stoeckelhuber M, Stolte M, Haas R, Rieder G. Helicobacter pylori cag-Pathogenicity island-dependent early immunological response triggers later precancerous gastric changes in Mongolian gerbils. PLoS One 2009; 4:e4754.
9. Tsuji T, Iwahashi M, Nakamori M, et al. Multiple early gastric cancer with gastritis cystica profunda showing various histological types. Hepatogastroenterology 2008; 55:1150-2.
10. Yamashita M, Hirokawa M, Nakasono M, et al. Gastric inverted hyperplastic polyp. Report of four cases and relation to gastritis cystica profunda. APMIS 2002; 110:717-23.
11. Moon SY, Kim KO, Park SH, et al. Gastritis cystica profunda accompanied by multiple early gastric cancers. Korean J Gastroenterol 2010; 55:325-30.
12. Ogasawara N, Noda H, Kondo Y, et al. A case of early gastric cancer arising from gastritis cystica profunda treated by endoscopic submucosal dissection. Case Rep Gastroenterol 2014; 8:270-5.
13. Machicado J, Shroff J, Quesada A, Jelinek K, Spinn MP, Scott LD, Thosani N. Gastritis cystica profunda: Endoscopic ultrasound findings and review of the literature. Endosc Ultrasound 2014; 3:131-4.

LETTER TO THE EDITOR

EXPRESSION OF CYCLIN-DEPENDENT KINASE SUBUNIT 2 IN UTERINE LEIOMYOSARCOMA CELLS

WW. CHEN[1], YW. HUANG[2], DY. HU[3] and ZG. ZHAO[1]

[1]Department of Pathology, The Second Affiliated Hospital and Yuying Children's Hospital of Wenzhou Medical University, Wenzhou, Zhejiang, China; [2]Department of Oncology, The Third Affiliated Hospital of Wenzhou Medical University Wenzhou Zhejiang, China; [3]Department of Radiology, The Second Affiliated Hospital of Wenzhou Medical University, Jiangnan Hospital, Wenzhou, Zhejiang, China

Received May 6, 2019 – Accepted July 25, 2019

To the Editor,

Uterine smooth muscle tumors (USMT) are the most common types of benign gynecological tumors (1). USMT mainly consisted of smooth muscle tissues and connective tissues. As a pathological type of uterine sarcoma, USMT can be divided into primary and secondary tumors (2). Compared with primary leiomyosarcoma, secondary leiomyosarcoma has better prognosis and a complete tumor capsule.

In order to treat ULMS, many researchers have studied the expression of related genes and proteins that may play a role in ULMS. Cyclin-dependent kinase subunit (CKS) is a family of widely distributed small molecule proteins (3). There are two kinds of CKS proteins in human cells, i.e., CKS1 (cyclin-dependent kinase subunit 1) and CKS2 (Cyclin-dependent kinase subunit 2), which are composed of 79 amino acids and share 81% homology (4). It has been shown that the CKS family can promote the proliferation and apoptosis of tumors (5). CKS1 and CKS2 proteins are also involved in cell apoptosis. Knockout of CKS1 can increase the apoptosis rate of breast cancer cells, while CKS2 can protect prostate cancer cells against programmed cell death by regulating cell apoptosis, although the mechanism underlying the role of CKS1 in cell apoptosis remains unclear (6). The P27 expression is low in malignant tumors of the digestive system, breast, and the urinary system (7).

In conclusion, uterine leiomyosarcoma is often misdiagnosed before surgery, and the therapeutic effect of molecular targeted drugs remains unclear. The expression of CKS2 and its roles in leiomyosarcoma of the uterus were explored. The clinical significance and mechanism were discussed, to provide a new hypothesis for the treatment of ULMS.

MATERIALS AND METHODS

Cell culture and passage

In this study, human uterine leiomyosarcoma cell lines SK-UT-1 and SK-UT-2 were selected as experimental groups, while the corresponding uterine leiomyoma cell lines were selected as control groups. The uterine leiomyosarcoma tissues used in this study were from patients with a median age of 44 years (range 28-77 years). None of the patients had received chemotherapy or radiotherapy prior to surgery. Informed consent was signed by all patients or their families and this experiment was approved by the Ethics Committee of The Second

Key words: uterine leiomyosarcoma; CKS2M; SK-UT-1; SK-UT-2; cell cycle

Corresponding Author:
Dr Zhiguang Zhao,
Department of Pathology,
The Second Affiliated Hospital
and Yuying Children's Hospital of Wenzhou Medical University,
109 Xueyuan Road, Wenzhou, Zhejiang, 325027, China
e-mail: feycww1220@163.com

0393-974X (2019)

Affiliated Hospital and Yuying Children's Hospital of Wenzhou Medical University.

SK-UT-1 and SK-UT-2 cells were cultured in accordance with the culture conditions recommended by American type culture collection (ATCC). Cells were cultured in a 37°C cell culture incubator (Shanghai Jingan Biotechnology Co., Ltd., China) under 5%CO_2. The tube containing SK-UT-2 cells which had been conserved at –80°C were directly placed in a 37°C water bath to thaw rapidly. The melted liquid in the tube was then transferred into a 1.5 mL Eppendorf tube for centrifugation at 1000r/min for 5 min. After centrifugation, the supernatant was discarded and the pellet was suspended in 4 mL of fresh medium for subsequent culture. When the cells reached 80-90% confluence, they were detached by 1 mL of 0.25% trypsin-EDTA (ethylenediamine tetraacetic acid, Shanghai Yaxin Biotechnology Co., Ltd., China) and subcultured.

Cell transfection

The cells were trypsinized one day before transfection using 0.25% trypsin-EDTA. After counting the cells, they were seeded into 6-well plates at 5×10^5 cells per well in 2 mL of non-resistant medium. After 12-15 h of cell culture, the cells were transfected using Lipofectamine 2000 following the manufacturer's protocol.

Detection of cell cycle by flow cytometry

After 48 h of transfection, 800 g of cells were collected by digestion with trypsin containing EDTA. After centrifugation for 5 min, the supernatant was discarded. After 2 washes with cold PBS (phosphate buffer saline) (Beijing Institute of Biological Products, China) via centrifugation, the cells were suspended in 250 ul of cold PBS (Beijing Solebo Technology Co., Ltd., China), then 750 uL of anhydrous ethanol were slowly added and mixed. The cells were incubated overnight at 4°C, centrifuged for 5 min at 2000 g, and washed and suspended in cold PBS. Subsequently, 20 uL of RnaseA solution (Shanghai Huashun Biotechnology Co., Ltd., China) were added to each sample prior to 30 min of incubation in a 37°C water bath. Then, the cell suspension was filtered with 400 mesh screens and a propidium Iodide (PI) dye (Shanghai Huashun Biotechnology Co., Ltd., China) was added. After gentle mixing and incubation at 4°C for 30 min, the samples were analyzed by flow cytometry (Beckman Coulter, Inc., USA).

Real-time quantitative PCR (RT-PCR)

The length of Foxp3 gene was 109bp and the primer sequences were as follows:

F terminal: TTCGACGAACACTACGAGTACC; F terminal: GGACACCAAGT CTCCTCCAC;

The length of GAPDH gene was 225bp and the primer sequences were as follows:

F terminal: GTCAAGGCTGAGAACGGGAA; F terminal: AAATGAGCCCCAGCCTTCTCC;

After the liquid in the culture plate was aspirated, the cells were washed twice with PBS and lysed with Trizo1 (Nanjing Institute of Bioengineering, China) to extract cell RNA following the manufacturer's protocol. The concentration and quality of extracted RNA were evaluated by measuring the optical density (OD) on an ultraviolet spectrophotometer. Then, cDNA template of each RNA sample was obtained by reverse transcription using the reaction system shown in Table I. The procedure of reverse transcription was 30 min at 42°C and 10 min at 4°C on a thermal cycler (BIO-RAD, USA) followed by cooling on ice. The obtained cDNA was directly used for subsequent real-time PCR.

Table I. *Reaction system of reverse transcription.*

Component	Volume
cDNA	1 μL
SYBR Green	5 μL
Upstream primers	0.3 μL
Downstream primers	0.3 μL
RNase Free ddH_2O	3.4 μL

Determination of protein concentrations by BCA (bicinchoninic acid) assay

After cell culture medium was discarded, cells were washed three times by PBS, gently scraped off and transferred into Eppendorf (EP) tubes placed on ice. The collected cells were centrifuged at 3000 r/min for 5 min and the cell pellet was lysed for 30 min under shaking in a lysis buffer containing 100:1 of RIPA (Radio Immunoprecipitation Assay):PMSF (Phenylmethanesulfonyl fluoride). Then, the EP tubes

were centrifuged at 12000 r/min for 15 min at 4°C and the supernatant was transferred into new EP tubes for storage. Afterwards a 0.5mg/mL protein standard was prepared with PBS. According to the number of samples extracted, BCA reagents A and B were mixed in a proportion of 50:1 to form BCA working liquid. The products of 0, 1, 2, 4, 8, 12, 16, 20 μL were added to standard wells of a 96-well plate, respectively, and PBS was added until 20μL/well; 2 μL samples were added to a 96-well plate, and PBS was added until 20μL/well; 200 μL BCA working fluid was added to each well and incubated at 37°C for 20-30 min. The absorbance of each well was measured by enzyme labeling instrument, and the standard curve (y = ax + b) was drawn. The protein concentration of the samples was calculated according to the standard curve.

Detection of the target protein expression by Western blotting

The volume of each sample was adjusted so that the total protein content in each sample was equal. After the samples were mixed with a sample buffer, they were boiled, loaded onto an SDS polyacrylamide gel (Bio-Rad company, USA), electrophoresed for about 1 h, and then transferred onto a nitrocellulose membrane by wet transfer or 1.5 h at a constant voltage of 100V. Then, the membrane was rinsed with TBST (the mixture of Tris-Hcl, NaCl, and tween20) buffer, blocked [20 mL TBST, 0.75 g BSA (Bovine serum albumin), 3 spoons of skimmed milk powder] for 60 min at room temperature, incubated overnight at 4°C with primary antibodies (Biyun Tian Biological Co., Ltd., China), washed three times with TBST, incubated with the corresponding secondary antibody (1:5000 dilution) at room temperature for 1 h under shaking, washed again with PBS for 4 times, and analyzed by image pro plus software (BIO-RAD, USA). The gray values of target protein bands were compared with those of beta-actin protein band to obtain the relative protein expression.

Statistical analysis

SPSS22.0 was used for data analysis. *Chi*-squared test was used for categorical variables while *t*-test was used for continuous variables. $P < 0.05$ suggested the presence of significant difference.

RESULTS

Analysis of CKS2 mRNA and protein expressions in uterine leiomyosarcoma cells transfected with si-CKS2

The expression of CKS2 in ULMS SK-UT-1 and SK-UT-2 cells decreased significantly after the transfection with si-CKS2 ($P<0.01$) (Fig. 1). After SK-UT-2 cells were transfected with si-CKS2, the protein expression of CKS2 decreased significantly ($P < 0.01$) (Fig. 1B).

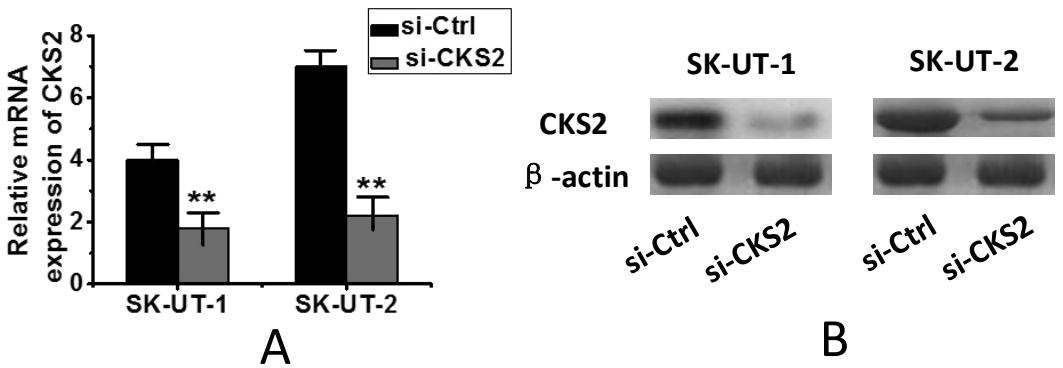

Fig. 1. *The expression of CKS2 in ULMS cells transfected with si-CKS2.* ***A)*** *The expression of CKS2 in ULMS cells transfected with si-CKS2;* ***B)*** *The CKS2 protein expression in ULMS cells transfected with si-CKS2; (Compared with the control group, * $P < 0.05$ indicated statistical significance, and ** $P < 0.01$ indicated statistical significance.*

Effect of si-CKS2 transfection on uterine leiomyosarcoma cells

The proliferation of SK-UT-2 cells decreased significantly at 24 hours after the transfection with si-CKS2 ($P < 0.01$) (Fig. 2). The proportion of SK-UT-1 cells in the G1 phase increased significantly after transfection ($P < 0.05$) (Fig. 2C), along with a decreased proportion of S cells ($P < 0.05$). In addition, there was no significant difference between different groups in terms of the proportion of cells in the G2 phase. As seen in Fig. 2D, SK-UT-2 cells in the transfection group showed an increased proportion of G1 cells ($P < 0.01$) and a decreased proportion of S cells ($P < 0.05$) compared with the control group, while no significant difference was seen between the two groups in terms of the proportion of cells in the G2 phase.

Effect of si-CKS2 transfection on viability of uterine leiomyosarcoma cells

From Fig. 3A, it can be seen that the number of SK-UT-1 and SK-UT-2 cells passing through an ordinary Transwell compartment was significantly lower in the si-CKS2 transfection group than that in the control group ($P < 0.01$). The experimental results seen in Fig. 3B showed that in the si-CKS2 transfection group of SK-UT-1 and SK-UT-2 cells, the number of cells passing through an ordinary Transwell compartment

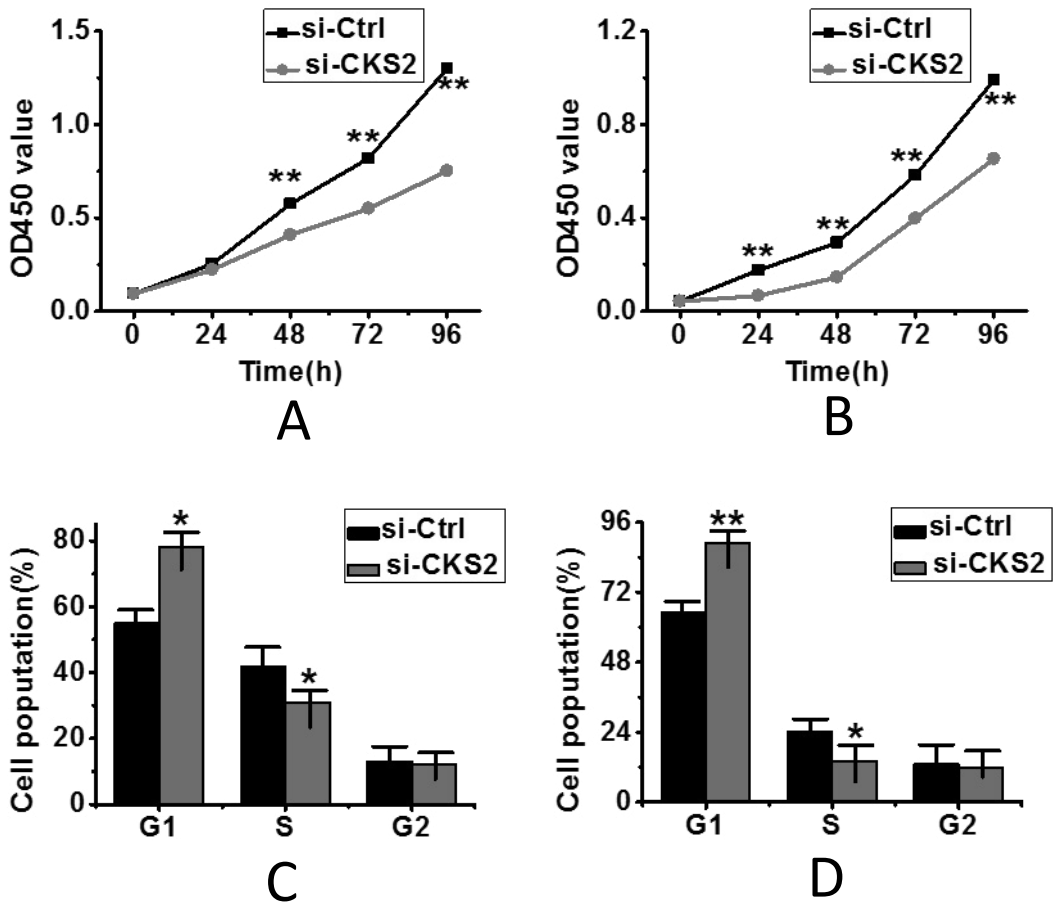

Fig. 2. *Influencing factors of ULMS cells transfected with si-CKS2. **A**) Cell proliferation of SK-UT-1 cells transfected with si-CKS2; **B**) Cell proliferation of SK-UT-2 cells transfected with si-CKS2; **C**) Changes of cell cycle after transfection of SK-UT-1 cells with si-CKS2; **D**) Changes of cell cycle after transfection of SK-UT-2 cells with si-CKS2; (Compared with the control group, * $P < 0.05$ indicated statistical significance, and ** $P < 0.01$ indicated statistical significance.*

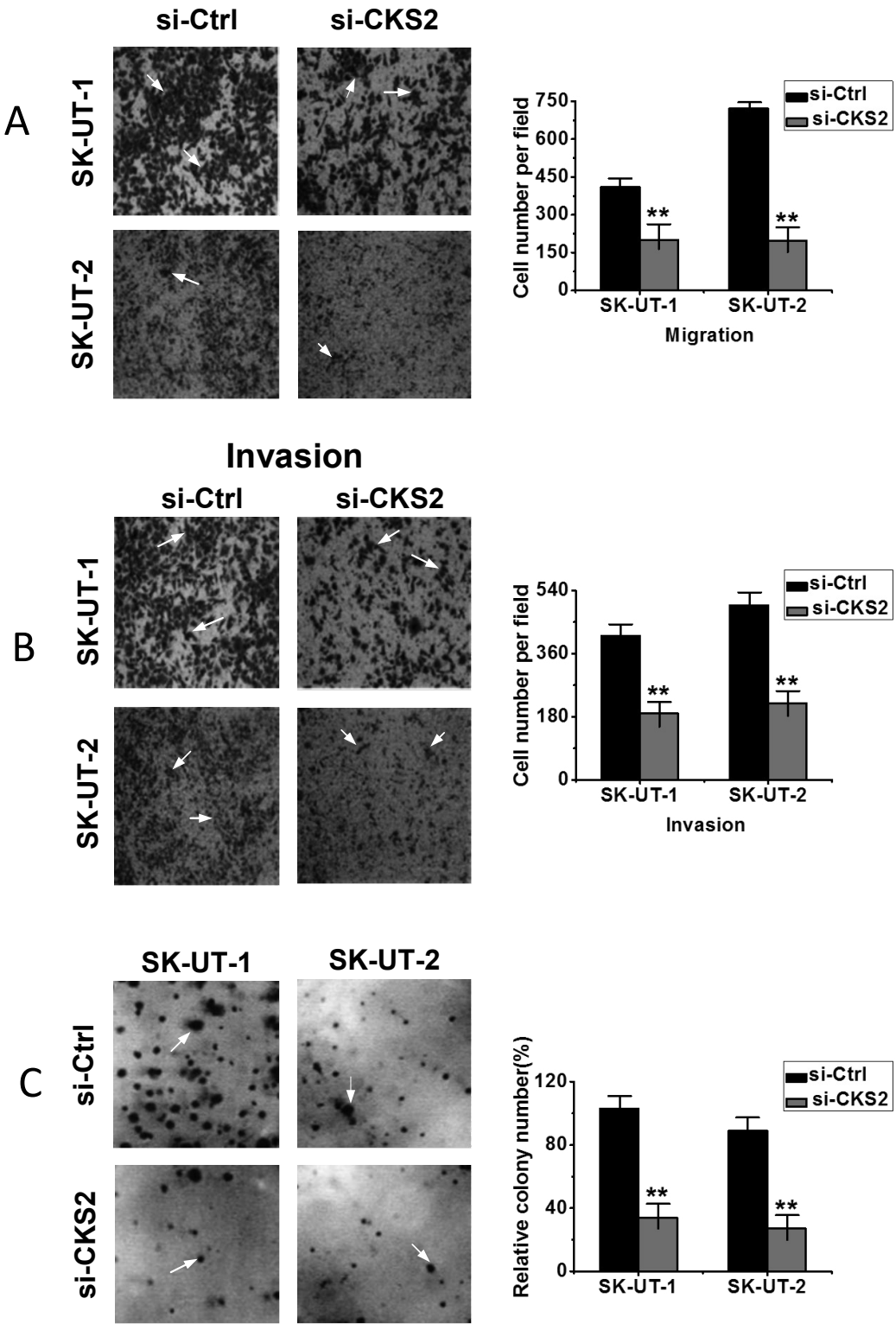

Fig. 3. *Effects of si-CKS2 transfection on the migration, infiltration and plate cloning of ULMS cells.* ***A****) The results of migration ability of ULMS cells transfected with si-CKS2;* ***B****) The results of infiltration capacity of ULMS cells transfected with si-CKS2;* ***C****) Plate cloning ability of ULMS cells after si-CKS2 transfection; (Compared with the control group, * P < 0.05 indicated statistical significance, and ** P < 0.01 indicated statistical significance.*

was significantly reduced ($P < 0.01$). Compared with the si-Ctrl group, the number of SK-UT-1 and SK-UT-2 clones in the si-CKS2 group decreased significantly ($P < 0.01$) (Fig. 3C).

DISCUSSION

Characterized by early metastasis, high recurrence, and poor prognosis, uterine leiomyosarcoma is a type of tumor commonly seen in women aged 40-60 years (8). At present, uterine leiomyosarcoma is mainly treated by surgery (9, 10). It has been shown that silencing the CKS2 gene can inhibit the proliferation of early embryonic cells and arrest embryonic development. In the present study, it was found that the mRNA and protein expression of CKS2 in UMS SK-UT-1 and SK-UT-2 cells was significantly decreased after the transfection with si-CKS2 ($P<0.01$).

Cell cycle checkpoint plays an important safeguard role in cells by ensuring the accuracy and integrity of DNA during DNA replication and mitosis. Cell cycle checkpoint can also effectively prevent cell cycle progression of cells carrying DNA errors (11, 12). In this study, the proliferative capacity of SK-UT-2 cells decreased significantly at 24 h after the transfection with si-CKS2 ($P<0.01$). In transfected SK-UT-1 and SK-UT-2 cells, the proportion of G1 phase cells increased ($P<0.05$) and the proportion of S phase cells decreased ($P<0.05$). In addition, the number of clones was significantly decreased ($P<0.01$). In summary, the silencing of CKS2 in uterine leiomyosarcoma cells could promote their apoptosis, offering a new hypothesis for the treatment of ULMS.

REFERENCES

1. Johnson AJ, Wu MJ. The new role for an old kinase: protein kinase CK2 regulates metal ion transport. Pharmaceuticals (Basel) 2016; 9(4):80.
2. Robboy SJ, Bentley RC, Butnor K, Anderson MC. Pathology and pathophysiology of uterine smooth-muscle tumors. Environ Health Perspect 2000; 108 Suppl 5:779-84.
3. Takatani-Nakase T. Zinc Transporters and the progression of breast cancers. Biol Pharm Bull 2018; 41(10):1517-22.
4. You H, Lin H, Zhang Z. CKS2 in human cancers: Clinical roles and current perspectives (Review). Mol Clin Oncol 2015; 3(3):459-63.
5. Lan Y, Zhang Y, Wang J, Lin C, Ittmann MM, Wang F. Aberrant expression of Cks1 and Cks2 contributes to prostate tumorigenesis by promoting proliferation and inhibiting programmed cell death. Int J Cancer 2008; 123(3):543-51.
6. Wang XC, Tian J, Tian LL, et al. Role of Cks1 amplification and overexpression in breast cancer. Biochem Biophys Res Commun 2009; 379(4):1107-13.
7. Lan Y, Zhang Y, Wang J, Lin C, Ittmann MM, Wang F. Aberrant expression of Cks1 and Cks2 contributes to prostate tumorigenesis by promoting proliferation and inhibiting programmed cell death. Int J Cancer 2008; 123(3):543-51.
8. Ricci S, Stone RL, Fader AN. Uterine leiomyosarcoma: Epidemiology, contemporary treatment strategies and the impact of uterine morcellation. Gynecol Oncol 2017; 145(1):208-216.
9. Smith EA, Gole B, Willis NA, et al. DEK is required for homologous recombination repair of DNA breaks. Sci Rep 2017; 7:44662.
10. Godfrey AL, Chen E, Massie CE, et al. STAT1 activation in association with JAK2 exon 12 mutations. Haematologica 2016; 101(1):e15-9.
11. Oswald F, Rodriguez P, Giaimo BD, et al. A phospho-dependent mechanism involving NCoR and KMT2D controls a permissive chromatin state at Notch target genes. Nucleic Acids Res 2016; 44(10):4703-20.
12. Kambe T, Matsunaga M, Takeda T. Understanding the contribution of zinc transporters in the function of the early secretory pathway. Int J Mol Sci 2017; 18(10):2179.

LETTER TO THE EDITOR

A DOUBLE INFUSION OF TRANEXAMIC ACID REDUCES TRANSFUSION REQUIREMENTS FOLLOWING TOTAL HIP ARTHROPLASTY COMPARED TO SINGLE-DOSE ADMINISTRATION

C. LEGNANI[1], G. ORIANI[2], F. PARENTE[3] and A. VENTURA[1]

[1]IRCCS Istituto Ortopedico Galeazzi, Sport Traumatology and Minimally Invasive Surgery Center, Milan, Italy; [2]IRCCS Istituto Ortopedico Galeazzi, Department of Anesthesiology, Milan, Italy; [3]IRCCS Istituto Ortopedico Galeazzi, Hip and Knee Arthroplasty Surgery Center I, Milan, Italy

Received January 28, 2019 – Accepted May 27, 2019

To the Editor,

Total hip arthroplasty (THA) is a major orthopedic procedure, responsible for potential significant blood loss and complications of anaemia requiring tranfusions (1). Several treatment options exist in order to reduce perioperative anaemia, including perioperative red cell salvage, hemodilution, controlled hypotension, use of recombinant human erythropoietin (2).

Hyperfibrinolysis following surgical trauma is a major factor causing bleeding in patients undergoing THA. Therefore pharmacological agents able to inhibit hyperfibrinolysis are currently adopted in the management of perioperative blood loss (3). Tranexamic acid (TXA) has demonstrated as an excellent safety profile without increasing the risk of adverse events, including thromboembolism (4, 5), and many papers have shown that its use can significantly reduce transfusion requirements following joint replacement surgery (6-11). However, there are huge variations in the way in which TXA is administered in joint replacement surgery, with dosing regimens ranging from 10 to 135 mg/kg, and regimen duration ranging from a single shot to multiple injections, to continuous infusion for up to 3 days (6-11). As a result, no consensus about the starting time, methods, or volume of usage of TXA exists and the optimal dose for TXA in joint replacement surgery has yet to be determined.

A retrospective study was conducted comparing the efficacy of combined pre- and post-operative infusion of TXA 15 mg/kg to single pre-operative infusion in patients undergoing THA.

MATERIALS AND METHODS

Eight hundred and one patients who underwent primary THA at our Institution between January 2016 and December 2016 were retrospectively reviewed. 356 patients received a single pre-operative dose of 15 mg/ kg TXA (Single Dose, SD group), while 445 received a single pre-operative dose of 15 mg/ kg TXA followed by a second post-operative dose of 15 mg/kg TXA 6 hours postoperatively (Double Dose, DD group). Blood loss was calculated from haematological values and perioperative transfusions. Major complications, such as thrombotic events were recorded up to one year from surgery. A haemoglobin threshold of 8 g/ dl in patients without comorbidities, and a threshold of 10 g/dl in patients with pre-existing cardiac pathology was set to administer blood transfusion

Key words: hip osteoarthritis; total hip arthroplasty; tranexamic acid; blood transfusion

Corresponding Author:
Dr Claudio Legnani,
IRCCS Istituto Ortopedico Galeazzi,
Via Monreale 18,
20148 Milan, Italy
Tel.: +39 02 487851 - Fax: +39 02 48785233
e-mail: claudio.legnani@grupposandonato.it

0393-974X (2019)

DISCLOSURE: ALL AUTHORS REPORT NO CONFLICTS OF INTEREST RELEVANT TO THIS ARTICLE.

in accordance with international guidelines (12). Written informed consents were provided by all the subjects who were included in the study. Statistical analysis was performed using *Chi*-squared test to evaluate differences between the groups. IBM SPSS Statistics for Windows® software, Version 21.0 (IBM Corp., Armonk, NY, USA) was used. Statistical significance was set at $p<0.05$.

RESULTS

None of the patients who completed TXA therapy reported adverse events. A detailed overview of the results is reported in Table I. No statistically significant differences in the amount of blood loss examined through drainage after the 24th hour were reported between the two groups (p = n.s.). Similarly, no statistically significant differences in the value of postoperative haemoglobin concentrations were reported between patients in the SD and DD group (p = n.s.). A significant difference between the two groups in terms of blood transfusion administration was reported (<0.05): 52 patients (14%) underwent blood transfusion in the SD group, while the rate inthe DD group was significantly lower (6.1%, 27 patients).

DISCUSSION

The most important finding of the present study is that combined pre- and post-operative intravenous administration of TXA 15 mg/kg is more effective compared to single pre-operative infusion reducing the need for postoperative transfusions following THA.

Several papers reported that TXA can be safely and effectively used to reduce blood loss and transfusion requirements following joint replacement surgery (6-11). None of the patients in our case series reported venous or arterial thromboembolic events, thus confirming safety of the procedure as previously reported (4, 5). Regarding TXA administration, currently there is no consensus about starting time, methods, or optimal dose of TXA to be used during THA, and dosing regimens as well as regimen duration consistently vary among authors (6-10).

Several studies demonstrated the efficacy of a single bolus of TXA of 1g to reduce blood loss (6, 7). George et al. analyzed reported a significant reduction in blood loss after administering a single perioperative intravenous bolus on patients undergoing primary hip and knee arthroplasty (6). Similarly, Figar et al. reported an average transfusion rate of 0.6 units/patient after a single TXA administration compared to 1.53 units/patient in the control group (7).

More recent studies have suggested multiple dose regimens to be more effective compared to a single dose regimen (8, 9) and recently administration of up to 5 doses of TXA have been tested (10). In the present study, a single dose of TXA was compared to a doubled regimen.

A low transfusion rate was reported in the

Table I. *Comparison of perioperative blood loss between groups.*

	Single Dose Group	Double Dose Group	p value
Hb change (g/dL)			
- Pre-operative	14.7 (SD: 4.2)	14.3 (SD: 5.7)	p = n.s.
- Post-operative	10.9 (SD: 1.4)	11.0 (SD: 0.9)	p = n.s.
Blood loss (ml)	199 (SD: 152.1)	192 (SD: 174.1)	p = n.s.
Transfusion rate (%)	52/356 (14.0%)	27/445 (6.1%)	p < 0.05

SD: standard deviation

DD group compared to the SD group, although no statistically significant difference in terms of decrease of haemoglobin was reported between the two cohorts.

Limitations of the present study include its retrospective nature and its non-randomized design. Further prospective randomized studies are needed to substantiate these findings.

Combined pre- and post-operative infusion of TXA 15 mg/kg was associated with diminished transfusion requirements compared to single pre-operative infusion. No serious treatment-related adverse effects were reported following intravenous administration of TXA for hip replacement surgery.

ACKNOWLEDGEMENTS

This research was supported by the Italian Ministry of Health.

REFERENCES

1. Trevisan C, Klumpp R, Auriemma L, Compagnoni R. An algorithm for predicting blood loss and transfusion risk after total hip arthroplasty. Transfus Apher Sci 2018; 57(2):272-76.
2. Gwam CU, Mistry JB, Etcheson JI, et al. Decline in allogeneic blood transfusion usage in total hip arthroplasty patients: National Inpatient Sample 2009 to 2013. Hip Int 2018; 28(4):382-90.
3. Mannucci PM. Hemostatic drugs. N Engl J Med 1998; 339(4):245-53.
4. Fillingham YA, Ramkumar DB, Jevsevar DS, et al. the safety of tranexamic acid in total joint arthroplasty: a direct meta-analysis. J Arthroplasty 2018; 33(10):3070-82.
5. Marmotti A, Mattia S, Mangiavini L, et al. Tranexamic acid effects on cartilage and synovial tissue: an in vitro study for a possible safe intra-articular use. J Biol Regul Homeost Agents 2016; 30(4 Suppl 1):33-40.
6. George DA, Sarraf KM, Nwaboku H. Single perioperative dose of tranexamic acid in primary hip and knee arthroplasty. Eur J Orthop Surg Traumatol 2015; 25(1):129-33.
7. Fígar A, Mc Loughlin S, Slullitel PA, Scordo W, Buttaro MA. Influence of single-dose intravenous tranexamic acid on total hip replacement: A study on transfusions, collateral complications, and readmissions. Orthopade 2017; 46(4):359-65.
8. Xie J, Hu Q, Ma J, Huang Q, Pei F. Multiple boluses of intravenous tranexamic acid to reduce hidden blood loss and the inflammatory response following enhanced-recovery primary total hip arthroplasty: a randomised clinical trial. Bone Joint J 2017; 99-B(11):1442-49.
9. Xie J, Ma J, Yao H, Yue C, Pei F. Multiple boluses of intravenous tranexamic acid to reduce hidden blood loss after primary total knee arthroplasty without tourniquet: a randomized clinical trial. J Arthroplasty 2016; 31(11):2458-64.
10. Lei Y, Huang Q, Huang Z, Xie J, Chen G, Pei F. Multiple-dose intravenous tranexamic acid further reduces hidden blood loss after total hip arthroplasty: a randomized controlled trial. J Arthroplasty 2018; 33(9):2940-45.
11. Legnani C, Oriani G, Parente F, Ventura A. Reducing transfusion requirements following total knee arthroplasty: effectiveness of a double infusion of tranexamic acid. Eur Rev Med Pharmacol Sci 2019; 23(5):2253-56.
12. American Society of Anesthesiologists Task Force on Perioperative Blood Management. Practice guidelines for perioperative blood management: an updated report by the American Society of Anesthesiologists Task Force on Perioperative Blood Management. Anesthesiology 2015; 122(2):241-75.

LETTER TO THE EDITOR

CLINICAL APPLICATIONS OF SHOCK WAVES IN DENTISTRY

F. GOKER[1], V. SANSONE[2,3], R.C. APPLEFIELD[3], S. TASCHIERI[1,3] and M. DEL FABBRO[1,3]

[1]Department of Biomedical, Surgical and Dental Sciences, University of Milan, Milan, Italy; [2]Department of Biomedical Sciences for Health, University of Milan, Milan, Italy; [3]IRCCS Istituto Ortopedico Galeazzi, Milan, Italy

Received February 7, 2019 – Accepted June 6, 2019

To the Editor,

Shock waves (SWs) are acoustic pulses of pressure disturbances that propagate rapidly in 3 dimensional space. Extracorporeal Shock Wave Therapy (ESWT) is a well-established, non-invasive and multidisciplinary clinical treatment used in orthopedics, physical therapy, urology and cardiology. ESWT improves bone regeneration using high-energy acoustic waves that deliver a mechanical force to body tissues (1). ESWT may induce neovascularization, increase expression of several growth factors (such as bone morphogenetic proteins) and stimulate osteoblastic lineage cells (2, 3). The range of medical applications for ESWT is impressive and it continues to broaden as our knowledge of the mechanisms behind their potential grows. Current use of ESWT for musculoskeletal disorders is aimed to induce interstitial and extracellular responses leading to tissue regeneration (4). For example, orthopedic applications for SWs, such as the treatment of long bone fracture nonunions, were found to have a success rate ranging from 50 to 85% (5). Other studies yielded promising results in the treatment of osteonecrosis of the femoral head and heterotropic ossifications with high-energy flux Density EFD (1, 2), and on soft tissues (superficial lesions like cutaneous ulcers) with planar waves (6).

Given such premises, it seems reasonable that ESWT could be applied also for the treatment of certain challenging oral and maxillofacial conditions (eg. granuloma, cysts, bone defects associated with periodontal, peri-implant and periapical disease, graft healing, osteonecrosis of the jaws) where the treatment target of bone regeneration often resembles the therapeutic targets of orthopaedic conditions such as osteonecrosis and pseudoarthrosis.

The primary aims of this systematic review were to evaluate whether ESWT may be advantageous in oral procedures for: a) improving healing of bone and soft tissue; b) reducing the incidence of any complications and side effects; c) improving patients' quality of life (by reducing pain, swelling and other common symptoms) in the post-operation period; and d) increasing treatment acceptance by patients.

MATERIALS AND METHODS

An electronic search was performed on the following databases using search terms and Boolean operators: MEDLINE, Scopus, Web of Science, Cochrane Central Register of Controlled Trials (CENTRAL). Grey literature databases were searched. A hand search of the main dental journals from 2000 up to the last issue available, was undertaken. The last search was performed on 11 April

Key words: Extracorporeal shockwave therapy; oral surgery; bone regeneration; tissue healing

Corresponding Author:
Dr Massimo Del Fabbro,
Department of Biomedical, Surgical and Dental Sciences,
Università degli Studi di Milano
IRCCS Istituto Ortopedico Galeazzi,
Via Riccardo Galeazzi 4, 20161, Milan, Italy
Tel.: +39 02 50319950 - Fax: +39 02 50319960
e-mail: massimo.delfabbro@unimi.it

0393-974X (2019)

DISCLOSURE: ALL AUTHORS REPORT NO CONFLICTS OF INTEREST RELEVANT TO THIS ARTICLE.

2019. The reference list of the retrieved literature reviews and of the included studies was also manually checked for possible additional eligible studies. Clinical studies reporting results of ESWT in oral surgical procedures for regeneration purposes were included. Studies where regeneration was not the aim, such as extracorporeal shock wave lithotripsy (ESWL) in clinical use for the treatment of salivary gland stones, were not considered suitable and were excluded. No restrictions were placed regarding the language and the year of publication. Both prospective and retrospective studies were considered. No limitation on sample size was placed. The studies had to provide details on the timing, duration, type, energy flux density, pulse rate, focal area of the shock wave therapy at the time of the oral procedure. They also had to provide clear definitions of the success criteria, and details on the operative protocol.

The title and abstract of articles retrieved through the electronic and manual searches were independently screened by two reviewers. The full text of all eligible studies was independently assessed by the same two reviewers to check whether studies met all inclusion criteria. Cases of disagreement were discussed together until agreement was reached. For articles excluded at this stage, the reason for exclusion was recorded. The identified suitable articles were subject to data extraction and analysis, and were also assessed for their methodological quality, and for their suitability to

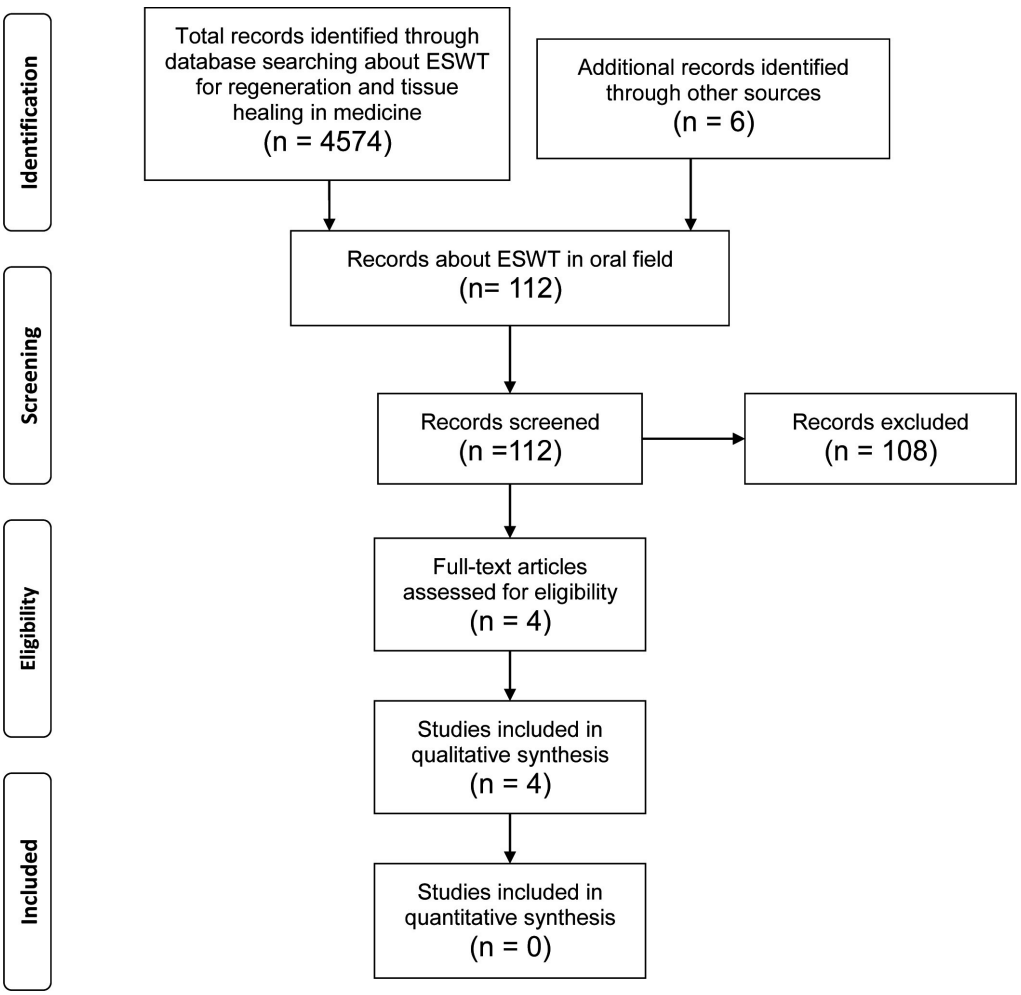

Fig. 1. *Flowchart of the study selection process.*

include in a meta-analysis. Two reviewers extracted the data independently (MDF and FG), using an *ad hoc* data collection form. Cases of disagreement were subject to joint evaluation until an agreement was reached.

The following methodological parameters were used for risk-of-bias assessment: for randomized studies (if any), the random sequence generation method and allocation concealment; for all studies: clear definition of inclusion and exclusion criteria, clear definition of outcomes assessment and success criteria; number of operators involved; completeness of the outcome data reported, recall rate (it was assumed adequate if dropout <20%), explanation for dropouts/withdrawal (when applicable), sample size (it was assumed adequate if >20 patients treated), and length of follow-up period (it was assumed adequate if the mean duration was ≥2 years). All the criteria were assessed as adequate, unclear, or inadequate. Studies were considered at low risk of bias if more than 2/3 of the parameters were judged as adequate. Studies were considered at high risk if more than one parameter was judged as inadequate.

As meta-analysis was not feasible due to absence of studies with similar features, only qualitative analysis was carried out and the outcomes were presented in a narrative way.

RESULTS

Fig. 1 shows a flowchart summarizing the screening process. The first raw search on SWs and regeneration/tissue healing provided 4574 articles. Six additional articles were found by hand-searching. After focusing to oral applications, 112 articles were found. After a screening of the titles and abstracts only 4 articles reporting results of comparative clinical studies were included (7-10). The general features of these studies, all performed in a University setting, are summarized in Table I. Of the four articles included, three were related to the same randomized clinical trial, consisting of 60 adult patients undergoing orthodontic treatment (7-9). Patients were included if they had mesially directed orthodontic movement of the mandibular second molar into the extraction site of the mandibular first molar. In this trial, performed at the Medical University of Vienna, Austria, the effect of focused ESWT on tooth mobility, pulpal blood flow and stability of the temporary anchorage devices, was assessed up to 6 months of follow-up (7-9). The authors reported promising results of ESWT for most of the parameters investigated.

Another randomized trial, with a split-mouth design, was performed at the University of Frankfurt and at the University of Cologne, Germany, on 24 patients undergoing mandibular third molar extraction (10). This study investigated the effect of focused ESWT on socket healing, evaluating the quantity and quality of BMP-2 and growth factors in patients' blood samples by biochemical analysis. The authors concluded that there were no benefits of ESWT in increasing the amount of the investigated growth factors (10).

Table I. *Main characteristics of the included studies and outcomes.*

Study ID	Type of study	Country	N. of samples (C/T)	Instrument	SW Parameters	Type of treatment	Follow-up	Risk of bias	Outcome Variable	Result
Falkensammer 2014 (7)	RCT	Austria	25(13/12)	Orthogold 100, MTS/TNT	Focused Single 1000 impulse 0.19–0.23 mJ/mm^2 5 pulses/sec	Orthodontic	4 mo	Low	Stability of TADs	No Positive effect
Falkensammer 2015 (8)			60(30/30)				6 mo		Pulpal blood flow (laser Doppler)	Positive effect but not significant
Falkensammer 2016 (9)			60(30/30)				6 mo		Tooth Mobility (Periotest)	Positive effect but not significant
Pfaff 2016 (10)	RCT(SM)	Germany	48(24/24)	Duolith SD1 T	Focused Single 1000 impulse 0.25 mJ/mm^2	Tooth Extraction	2 mo	Medium	Growth Factors in Blood & Bone Marrow	No Positive effect

RCT: randomized control trial; SM: split mouth; C: control; T: test; mo: month; TAD: temporary anchorage devices; SW: shock waves

DISCUSSION

This review highlighted the paucity of evidence-based comparative studies investigating the effects of ESWT in the oral field. The results of the randomized study by Falkensammer et al. were published in three different papers (7-9). That study was well designed and well performed. It focused on healthy adult orthodontic patients, and reported in general a trend for positive effects of ESWT, though they were transient and not statistically significant. The authors also reported absence of any adverse effects and encouraged the use of ESWT in an expanded range of applications, especially in pathological conditions. In this study, the parameters of ESWT (energy, frequency, number of applications) were applied empirically. Though the authors report that they were based on previous shock-wave studies focusing on bone regeneration, the latter refer to animal (rat) models (11, 12). Therefore, direct translation of the findings of such studies to humans should be done with caution. The same authors acknowledged a limited generalizability of their results. In fact, the treatment was confined to the mandible, in a selected population of patients, it was performed in a single center and the sample size was relatively low.

The other study that was included, aimed to identify the amount of a few growth factors implied in bone regeneration following bilateral mandibular wisdom tooth extraction, after applying ESWT to one side of the jaw (10). Though higher levels of Insulin Growth Factor-1 and Vascular Endothelial Growth Factor were found, the other investigated growth factors did not show any significant increase as compared to control. However, only biochemical evaluation was performed: no follow-up assessment was reported, so it was not possible to evaluate clinically or radiographically the effect of ESWT on alveolar bone regeneration.

Other experimental studies in the literature reveal that the use of shock waves in dentistry may have potential benefits in several oral applications, such as the removal of tooth biofilm, the regeneration of alveolar bone, the eradication of periodontal pathogens, and the reduction of tooth mobility after active orthodontic movement. We hope that such considerations might stimulate researchers to perform additional randomized studies with large sample size in order to confirm the beneficial effects of ESWT in oral procedures.

REFERENCES

1. Mayer-Wagner S, Ernst J, Maier M, et al. The effect of high-energy extracorporeal shock waves on hyaline cartilage of adult rats in vivo. J Orthop Res 2010; 28:1050-56.
2. Tam KF, Cheung WH, Lee KM, Qin L, Leung KS. Shockwave exerts osteogenic effect on osteoporotic bone in an ovariectomized goat model. Ultrasound Med Biol 2009; 35:1109-18.
3. Catalano MG, Marano F, Rinella L, et al. Extracorporeal shockwaves (ESWs) enhance the osteogenic medium-induced differentiation of adipose-derived stem cells into osteoblast-like cells. J Tissue Eng Regen Med 2017; 11:390-99.
4. Ogden JA, Tóth-Kischkat A, Schultheiss R. Principles of shock wave therapy. Clin Orthop Relat Res 2001; 387:8-17.
5. Elster EA, Stojadinovic A, Forsberg J, Shawen S, Andersen RC, Schaden W. Extracorporeal shock wave therapy for nonunion of the tibia. J Orthop Trauma 2010; 24:133-41.
6. Mittermayr R, Antonic V, Hartinger J, et al. Extracorporeal shock wave therapy (ESWT) for wound healing: technology, mechanisms, and clinical efficacy. Wound Repair Regen 2012; 20:456-65.
7. Falkensammer F, Rausch-Fan X, Arnhart C, Krall C, Schaden W, Freudenthaler J. Impact of extracorporeal shock-wave therapy on the stability of temporary anchorage devices in adults: a single-center, randomized, placebo-controlled clinical trial. Am J Orthod Dentofac Orthop 2014; 146:413-22.
8. Falkensammer F, Rausch-Fan X, Schaden W, Kivaranovic D, Freudenthaler J. Impact of extracorporeal shockwave therapy on tooth mobility in adult orthodontic patients: a randomized single-center placebo-controlled clinical trial. J Clin Periodontol 2015; 42:294-301.
9. Falkensammer F, Schaden W, Krall C, Freudenthaler J, Bantleon HP. Effect of extracorporeal shockwave therapy (ESWT) on pulpal blood flow after

orthodontic treatment: a randomized clinical trial. Clin Oral Invest 2016; 20:373-79.

10. Pffaf JA; Boelck B, Bloch W, Nentwig GH. Growth Factors in bone marrow blood of the mandible with application of extracorporeal shock wave therapy. Implant Dent 2016; 25:606-12.
11. Hazan-Molina H, Reznick AZ, Kaufman H, Aizenbud D. Assessment of IL-1beta and VEGF concentration in a rat model during orthodontic tooth movement and extracorporeal shock wave therapy. Arch Oral Biol 2012; 58:142-50.
12. Sathishkumar S, Meka A, Dawson D, et al. Extracorporeal shock wave therapy induces alveolar bone regeneration. J Dent Res 2008; 87:687-91.

LETTER TO THE EDITOR

IMPLANT-PROSTHODONTIC REHABILITATION OF A PATIENT WITH A LARGE CYST-LIKE PERIAPICAL LESION: 2-YEAR CLINICAL AND RADIOLOGIC FOLLOW-UP

A. LANZA, F. DI FRANCESCO*, V. GRASSIA*, M. VITALE, L. NUCCI, R. FEMIANO, L. FEMIANO, G. DE MARCO* and F. FEMIANO

Multidisciplinary Department of Medical, Surgical and Dental Sciences, Campania University Luigi Vanvitelli, Naples, Italy

Received April 3, 2019 – Accepted June 14, 2019

*These Authors contributed equally to this work

To the Editor,

Mandibular lesions may arise from both odontogenic and non-odontogenic origins (1-2). Among them, the cyst-like periapical lesion represents the most common disease concerning lesions of jaws (1). The radicular cyst is an inflammatory odontogenic cyst of endodontic origin and usually has benign nature, slow evolution, centrifugal growth with expansion and displacement, erosion or even perforation of adjacent anatomical structures such as buccal or lingual cortical bone. Nowadays, there is no consensus concerning timing and type of treatment for large osteolytic lesions of endodontic origin. Several treatment options are available for cyst-like periapical lesion such as non-surgical and surgical treatments. The choice of treatment depends on the size and localization of the lesion, on the bone integrity of the cystic wall, and on its proximity to vital structures (3).

Several studies showed interesting outcomes concerning the nonsurgical endodontic treatment for large periapical lesions associated with non-vital teeth (4, 5). However, periapical lesions not healing after adequate endodontic treatment or having an unusual radiographic image should be submitted to surgical excision (5). If affected teeth are considered hopeless, the surgical treatment should be programmed in relation to the following prosthetic rehabilitation. Implant-prosthetic rehabilitation may represent the best choice in terms of cost-benefit ratio. Nevertheless, a large osteolytic lesion may be a severe risk of failure for the following implant-prosthetic rehabilitation. Different treatment approaches have been employed for implant replacement of infected hopeless teeth with osseous defects (5), one of which is the extraction of compromised teeth, debridement, guided bone regeneration (GBR), and delayed implant placement (6).

The aim of this clinical report is to describe the successful surgical and prosthetic management of a complex case of cyst-like periapical lesion of endodontic origin, employing bone regeneration techniques and delayed implant placement protocol.

MATERIALS AND METHODS

A 40-year-old male patient, non-smoker in good general health, presented spontaneous localized pain and gingivitis in the right second mandibular premolar (4.5) and the right first mandibular molar (4.6), both

Key words: dental implant; implant rehabilitation; implant restauration; osteolytic lesion; socket preservation

Corresponding Author:
Prof. Alessandro Lanza,
Prosthodontics Division,
Multidisciplinary Department
of Medical, Surgical and Dental Sciences,
Campania University Luigi Vanvitelli
Via Luigi De Crecchio 7, 80138 Naples Italy
e-mail: alessandro.lanza@unicampania.it

0393-974X (2019)

DISCLOSURE: ALL AUTHORS REPORT NO CONFLICTS OF INTEREST RELEVANT TO THIS ARTICLE.

significantly and structurally compromised (Fig. 1A). Clinical examination showed the presence of gingivitis and coronal destruction of 4.5 and 4.6, the latter of which had been endodontically treated four years before our observation. 2D and 3D radiographic examinations showed a large osteolytic lesion in relation to the root apex of 4.5 and 4.6 (Fig. 1, B and C). The mandibular right first molar was a non-vital tooth with second degree mobility, therefore, cyst-like periapical lesion of endodontic origin was suspected. Cone beam computed tomography (CBCT) showed that this lesion was approximately 2 cm in diameter, reaching buccal bone and producing a fenestration (Fig. 1C). Both teeth (4.5, 4.6) were considered hopeless, due to their compromised residual structure and the presence of large periapical lesion. The patient's general health did not present a risk for surgery; accordingly, an implant-prosthetic rehabilitation was planned. Restoration of periodontal health was carried out, through scaling and root planning sessions. Good periodontal health had been achieved at follow-up after 30 days.

The first stage, i.e. periodontal treatment, resulted in the resolution of gingivitis. The hopeless teeth were revealed as the maxillary right third molar, the mandibular right second premolar and the mandibular right first molar, therefore, surgical treatment was started. First, 4.5 and 4.6 were extracted through a minimally invasive approach (Fig. 2A), then the enucleation of the large lesion was carried out with careful alveolar revision in order to remove all residual fragments (Fig. 2B). During the enucleation of the lesion, the preservation of the residual buccal bone, intra- and inter-alveolar bone marrow and mesial and distal interproximal height of bone were performed (Fig. 2C). Socket preservation and buccal fenestration repair were carried out in order to compensate alveolar bone dimensional changes of post-extractions sockets (Fig. 2, D and E). The socket was filled with deproteinized bovine bone graft in small particles (Bio-Oss; Geistlich, Switzerland). The graft was then carefully covered with absorbable collagen membrane 25x25 mm (Bio-Gide; Geistlich, Switzerland), stabilized with

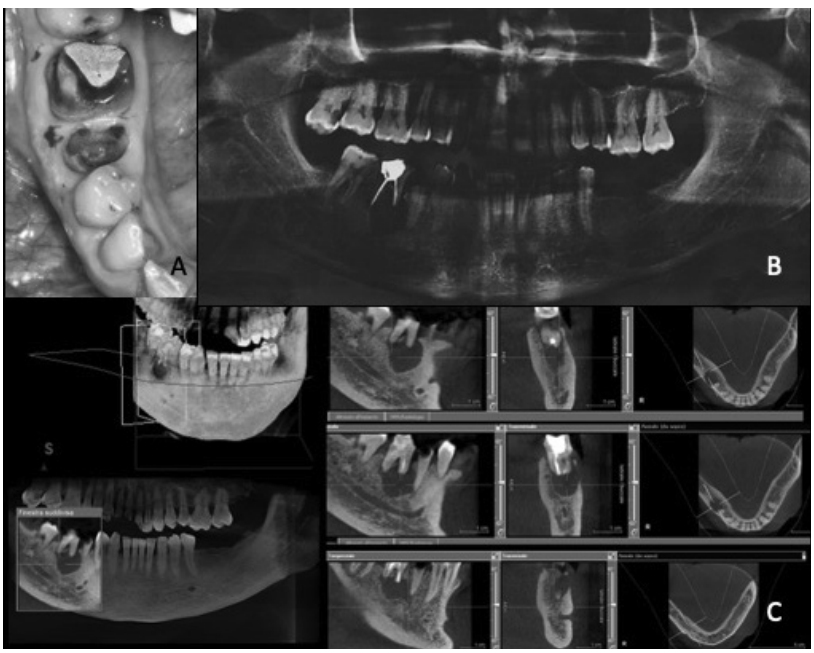

Fig. 1. ***A)*** *Initial clinical situation showed the presence of gingivitis and coronal destruction of 4.5 and 4.6.* ***B)*** *Orthopantomography examination showed a large osteolytic lesion in relation to the root apex of 4.5 and 4.6.* ***C)*** *Axial, Coronal and sagittal views of Cone beam computed tomography showed that this lesion was about 2 cm in diameter reaching buccal bone and producing a fenestration.*

dedicated pin (Fig. 2F). Horizontal mattress suturing technique employing a non-absorbable e-PTFE suture (Expanded Polytetrafluorethylene, Gore-Tex) was used, thus the membrane was covered with the mucoperiosteal flap. After surgery, antibiotic therapy with amoxicillin and clavulanic acid twice a day for 5 days and 0.20% chlorhexidine rinses three times a day for 4 weeks were prescribed. The second stage, i.e. the surgical treatment, resulted in the extraction of compromised teeth, the enucleation of the periapical lesion and the simultaneous socket preservation. The suture points were removed after seven days and follow-ups were carried out at 14, 21, 28 days. Once complete epithelial closure was obtained (Fig. 2G), follow-ups were performed twice a month for two months and once a month for six months. Nine months after enucleation of the lesion and contextual guided bone regeneration occurred, the third stage, i.e. implant placements, were initiated. The contextual socket preservation allowed the restitution *ad integrum* of the compromised buccal bone and the preservation of transverse diameter of the bone ridge, inter-radicular bone of the mandibular right first molar and buccal bone coronal to fenestration. Two cylindrical implants were inserted with the help of a surgical guide. The employed dimensions of implants were 4 mm in diameter and 11 mm in length in correspondence of the second lower right premolar, 5.0 mm in diameter and 9 mm in length in correspondence of first lower right molar (OsseoSpeed TX S Dentsply Implants) (Fig. 3, A and B). Cover screws were inserted and gaps between the implant shoulder and the buccal bone were filled with deproteinized bovine bone graft in small particles (Bio-Oss; Geistlich, Switzerland) (Fig. 3C). Simple interrupted suturing technique was adopted using a non-absorbable e-PTFE (Expanded Polytetrafluorethylene, Gore-Tex) suture was used

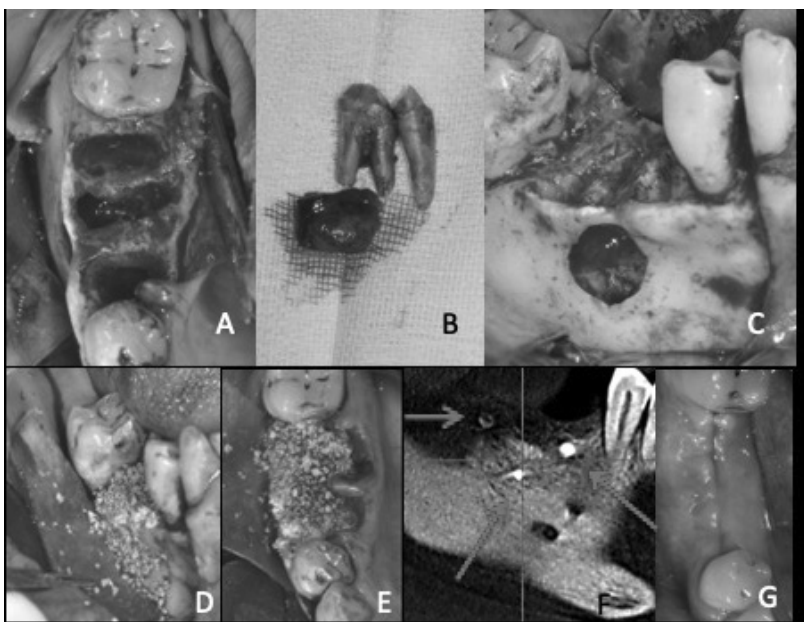

Fig. 2. ***A)*** *Extraction of mandibular right second premolar and the mandibular right first molar;* ***B)*** *Enucleation of the large lesion with careful alveolar revision;* ***C)*** *Preservation of the residual buccal bone, intra and inter-alveolar bone marrow, and mesial and distal interproximal height of bone.* ***D)*** *Lateral clinical view of the employed deproteinized bovine bone graft in small particles and absorbable collagen membrane.* ***E)****. Occlusal clinical view of the employed deproteinized bovine bone graft in small particles and absorbable collagen membrane.* ***F)*** *Radiographic view of the employed graft dedicated pin stabilizing a membrane.* ***G)*** *Seven days after surgery.*

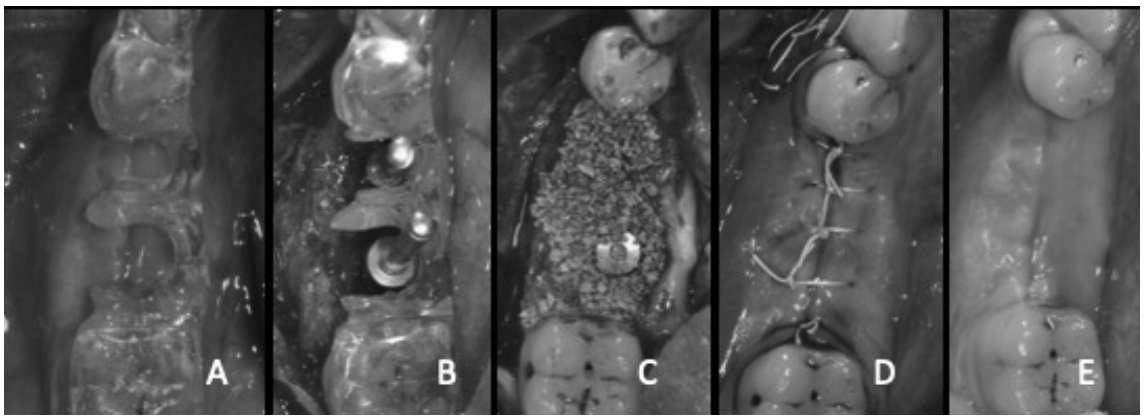

Fig. 3. ***A)*** *Implant placement through surgical guide.* ***B)*** *Checking parallelism between implants.* ***C)*** *Contextual guided bone regeneration.* ***D)*** *Simple interrupted suturing technique using a non-absorbable e-PTFE suture.* ***E)*** *Seven days after surgery.*

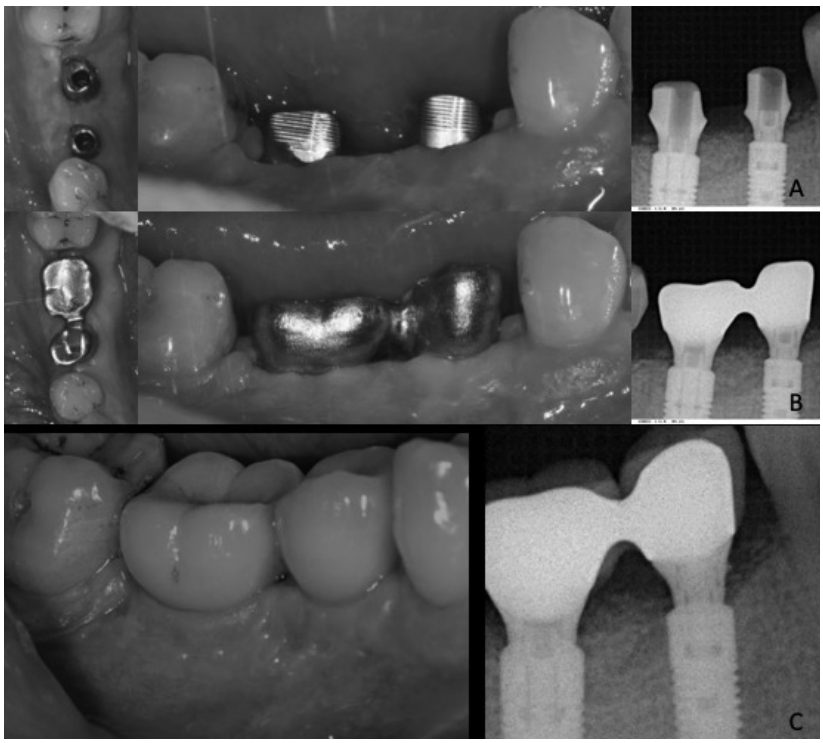

Fig. 4. ***A)*** *Clinical and radiographic checking of abutments.* ***B)*** *Clinical and radiographic checking of metal structures.* ***C)*** *Clinical and radiographic outcomes, two years follow-up.*

(Fig. 3D).

The suture points were removed after seven days, and follow-ups were performed at 14, 21, and 28 days. Once obtained a complete epithelial closure (Fig. 3E), follow-ups were carried out twice a month for two months, then once a month.

After 16 weeks, the prosthodontic phase was started. The implant exposures were performed, following a minimally invasive technique (Flapless guided implant uncovering) (4). This technique

allowed to reduce the total time of prosthetic phase and to anticipate the impression phase which was carried out employing one-stage impression technique (Impregum™ Penta™ Polyether Impression Material, 3M ESPE). Through Atlantis™ WebOrder, two custom titanium abutments and two machined metal structures in Cr-Co were realized. Therefore, clinical and radiographic checks of abutments and metal structures were carried out, in particular the precision-fit of implant-abutment interface and of abutment-structure interface (Fig. 4 A and B). Two splinted crowns were realized, thus aesthetic and functional controls of crowns were performed The crowns were then cemented using provisional cement (Temp-Bond™ Kerr). Follow-ups were planned at 1 month, 3 months, 6 months, and at 1 and 2 years.

To date, two years of follow-up have been carried out with excellent clinical and radiographic outcomes, suggesting stability of soft and hard peri-implant tissues levels (Fig. 4C).

The patient was informed and signed consent to participate in this study.

DISCUSSION

Interesting outcomes after nonsurgical endodontic treatments of large periapical lesions associated with non-vital teeth have been reported (1,2). However, periapical lesions not healing after adequate endodontic treatment or having an unusual radiographic image should be submitted to surgical excision (3). On the other hand, implant-prosthetic rehabilitation after enucleation of jaw cysts and bone grafting, is an acceptable and well-documented procedure in clinical practice (4, 5). Therefore, the gold standard for the treatment of most cyst-like periapical lesion is enucleation, especially in large lesions. The main goal of the surgical treatment is to ensure complete enucleation of the lesion, however, a conservative treatment respecting both adjacent bone tissue and teeth is desirable. After the enucleation of a large lesion, the socket may be treated with or without bone grafting. The employment of bone grafting materials after the enucleation of a lesion is a topic still to be discussed, especially in large bone defects (6). Several studies highlighted that the residual cystic cavities should be filled with bone graft in order to guide hard and soft tissue healing, increasing the ability to place delayed implants in the correct three-dimensional positioning supporting buccal bone (7-9). Conversely, the cavity remaining after enucleation may heal spontaneously without using filling materials, as shown by several studies (7-9). The spontaneous healing in large bone defect may lead to bone regeneration, allowing the implant-prosthetic rehabilitation (2, 3, 7), however, large osseous defects may occur after the removal of large lesions (5). Socket preservation and buccal fenestration repair have been described as successful surgical techniques in order to compensate alveolar bone dimensional changes of post-extractions sockets and to guide the healing of hard and soft tissues (5-8). Conversely, a non-guided healing could compromise the correct and three-dimensional delayed placement of implants in an ideal restorative position (5-8). Autogenous bone grafting is still considered the gold standard among reconstructive techniques in oral implantology (9, 10), although it is often related to disadvantages such as limited availability and donor site morbidity (9, 10). In order to overcome these limitations, different biomaterials have been employed to fill mandibular cyst cavities after enucleation of lesions (11, 12), thus avoiding donor site morbidity and no limited quantities (11, 12). The outcomes obtained in this clinical report support guided bone regeneration through deproteinized bovine bone graft covered with an absorbable collagen membrane, in agreement with other studies (7-12). When large bone defects required a socket preservation, submerged implant placement should be recommended in order to ensure a sufficient primary stability and better bone healing, as well as to avoid risk of inflammation during the osseointegration of the implant. Submerged implant placement needs second surgery, starting the prosthodontic phase. The aim of the second stage should not be limited to uncovering the screw, but to also preserving the continuity of the keratinized tissue band. After the osseointegration of the implant, minimally invasive techniques are desirable in order to preserve soft and hard peri-implant tissues,

especially when augmentation procedures of hard tissue have been carried out. This minimally invasive approach optimizes soft tissue profile around the implant components and reduces peri-implant bone resorption over time.

Within the limits of a case report, the present work showed how the employment of accredited surgical and prosthetic techniques can successfully manage cases of large osteolytic lesions, which may be a severe risk of failure for the following implant-prosthetic rehabilitation. In cases where the large lesion has to be excised, the surgical treatment should be programmed in relation to the following planned implant-prosthetic rehabilitation. Furthermore, a multidisciplinary approach is always to be preferred in such cases.

REFERENCES

1. Lin LM, Ricucci D, Lin J, Rosenberg PA. Nonsurgical root canal therapy of large cyst-like inflammatory periapical lesions and inflammatory apical cysts. J Endod 2009; 35:607-15.
2. Kahler B. Healing of a cyst-like lesion involving an implant with nonsurgical management. J Endod 2015; 41:749-52.
3. Santos Soares SM, Brito-Júnior M, de Souza FK, et al. Management of cyst-like periapical lesions by orthograde decompression and long-term calcium hydroxide/chlorhexidine intracanal dressing: a case series. J Endod 2016; 42:1135-41.
4. Lanza A, Scognamiglio F, De Marco G, Lanza M, Femiano F, Minervini G. Flapless guided implant uncovering (FGIU): Minimally invasive healing abutment connection surgery. Dent Oral Craniofac Res 2016; 2:1000188.
5. Pradel W, Eckelt U, Lauer G. Bone regeneration after enucleation of mandibular cysts: comparing autogenous grafts from tissue-engineered bone and iliac bone. Oral Surg Oral Med Oral Pathol Oral Radiol Endod 2006; 101:285-90.
6. Chiapasco M, Rossi A, Motta JJ, Crescentini M. Spontaneous bone regeneration after enucleation of large mandibular cysts: a radiographic computed analysis of 27 consecutive cases J Oral Maxillofac Surg 2000; 58:942-48.
7. Sculean A, Nikolidakis D, Schwarz F. Regeneration of periodontal tissues: combinations of barrier membranes and grafting materials - biological foundation and preclinical evidence: a systematic review. J Clin Periodontol 2008; 35:106-16.
8. Darby I, Chen ST, Buser D. Ridge preservation techniques for implant therapy. Int J Oral Maxillofac Implants 2009; 24:260-71.
9. Sakkas A, Wilde F, Heufelder M, Winter K, Schramm A. Autogenous bone grafts in oral implantology is it still a "gold standard"? A consecutive review of 279 patients with 456 clinical procedures. Int J Implant Dent 2017; 3:23.
10. Traianedes K, Russell JL, Edwards JR, Stubbs HA, Shanahan IR, Knaack D. Donor age and gender effects an osteoinductivity of demineralized bone matrix. J Biomed Mater Red Part B Appl Biomater 2004;70B:21-29.
11. Velich N, Nemeth Z, Hrabak K, Suba Z, Szabo G. Repair of bony defect with combination biomaterials. J Craniofac Surg 2004; 15:11-15.
12. Sanz M, Ferrantino L, Vignoletti F, de Sanctis M, Berglundh T. Guided bone regeneration of non-contained mandibular buccal bone defects using deproteinized bovine bone mineral and a collagen membrane: an experimental in vivo investigation. Clin Oral Implants Res 2017; 28(11):1466-76.

LETTER TO THE EDITOR

EFFECTS OF ISCHEMIC PRECONDITIONING WITH RESVERATROL ON EPIGASTRIC RAT FLAP: NEW PERSPECTIVES FOR HEAD AND NECK RECONSTRUCTION

P. PETRONE[1], E.M.C. TRECCA[2], M. CASSANO[2], N.A.A. QUARANTA[3], M.L. FIORELLA[3], V. DE SANTIS[4], M. RESSA[4], E. DALENA[1], P. DALENA[5], F. FORTUNATO[6], A. PORTINCASA[7], L. CECCHINO[7] and A. ARMENIO[4]

[1]Department of Otorhinolaryngology, San Giacomo Hospital, Monopoli, Bari, Italy; [2]Department of Otorhinolaryngology,University Hospital of Foggia, Foggia, Italy; [3]Department of Otorhinolaryngology, University of Bari "Aldo Moro" , Bari, Italy; [4]Department of Plastic and Reconstructive Surgery, IRCCS Istituto Tumori, "Giovanni Paolo II", Bari, Italy; [5]Department of Otorhinolaryngology, Catholic University of the Sacred Heart, Rome, Italy; [6]Department of Medical and Surgical Sciences, University Hospital of Foggia, Foggia, Italy; [7]Department of Plastic and Reconstructive Surgery, University Hospital of Foggia, Foggia, Italy

Received March 25, 2019 – Accepted June 4, 2019

To the Editor,

Currently, skin and soft tissue reconstruction after trauma or neoplasm excision, or for the correction of malformation, represents one of the most significant challenges in head and neck surgery. Although alloplastic and bioengineering materials have recently given new impetus to reconstructive surgery, autologous tissues are still the top choice in clinical practice (1). It is not always possible to rely upon local flaps in cases of large defects or complicated injuries. Microvascular free flaps are an increasingly popular option for extended soft tissue defects. However, this surgery is still associated with complications, the most common involving ischemia, hypoxia, and transient ischemia with post-ischemic reperfusion injury. Furthermore, in cases involving intraoperative complications with continuation and/or reiteration of the ischemic phase, such damage may cause partial or complete necrosis and flap failure (2, 3).

The goal of this study was to examine the outcomes of ischemic preconditioning (IPC) plus administration of resveratrol on the vitality of epigastric rat flaps. Histological and immunohistochemical assessments were used to evaluate the tissue changes after IPC and the administration of resveratrol into the flap circulation.

MATERIALS AND METHODS

Animals

The study was conducted on fifteen Sprague-Dawley rats weighing 450–500 g, received from the Experimental Animal Center, University of Bari, from September 2012 through December 2012. The rats were housed in pairs at ambient temperature on a 12:12 h light-dark cycle and supplied with adequate water and laboratory chow throughout the study. All animals were treated according to "The Directive for the Protection of Vertebrate Animals

Key words: microsurgery; ischemic preconditioning; resveratrol; flap; reconstruction

Corresponding Author:
Eleonora Maria Consiglia Trecca, M.D.
Department of Otorhinolaryngology
University Hospital of Foggia
Viale L. Pinto 1, 71122, Foggia, Italy
Tel.: +39 339 7006689 - Fax: +39 0881 736031
e-mail: eleonoramc.trecca@gmail.com

0393-974X (2019)

used for Experimental and other Scientific Purposes (86/609/CEE)", the European guidelines on animal experimentation. The research was approved by the University of Bari Experimental Animals Ethics Committee.

Surgical procedure

Operations were carried out under general anesthesia. The Sprague-Dawley rats received intra-peritoneal injection of 30–40 mg/kg sodium pentobarbital. Supplementary injections of 15 mg/kg were administered when necessary. When the animals were sedated, fur was shaved from their bellies with an electric razor. Sterile surgeries were performed. The rats were maintained at a comfortable temperature with heaters until they woke up after the operation. In all rats, an epigastric flap was raised. The right flap was assigned as the control flap (C flap), and the left as the resveratrol treated flap (R flap). The skin paddle (4 cm x 3.5 cm) was shaped on the upper abdomen between both anterior axillary lines. The flap originated exclusively from the inferior epigastric vascular pedicle. The procedures were performed under an operating microscope. After flap elevation, the C and R flaps were sutured back in their normal position. The skin close to the pedicle was exposed to reach the vessels for clamping. The area was covered with hydrated gauze. All flaps (C flaps and R flaps) were subjected to IPC, consisting of 1 hour of normothermic ischemia (25°C), and then reperfusion. No other ischemic insults were applied to the flaps. During the week after the operation, resveratrol at a dose of 0.2 cc was administered in the inferior epigastric artery of the R flap (4, 5). After fourteen days, viable areas of C flaps and R flaps were calculated, and collected for histological assessment with hematoxylin-eosin staining and CD34 immunostaining (Ventana-Roche, monoclonal JC70 mouse). On completion of the experiment, the rats were sacrificed using an intraperitoneal overdose of sodium pentobarbital.

Macroscopic evaluation

Examiners who were blinded to the surgical procedure conducted post-operative assessment (1). Macroscopic modifications that occurred during follow-up were observed and noted. Skin viability was determined by studying the color, texture and appearance of the flaps. After fourteen days, the viable flap zones were analyzed using clinical photographs and ImageJ (6), an image-elaborating software. The areas of flap survival in C and R flaps were calculated in cm^2 and as fractions of vital site estimated as: extension of vital area × 100% total area (necrosis: total area minus viable area). A score of 1 to 3 was assigned to define the extension of necrosis, respectively, as mild (≤15%,), moderate (16-75%), or marked (≥ 76% of the total area).

Histological evaluation

On day 14 post-surgery, specimens for histological evaluation were collected from C and R flaps. Tissue specimens were fixed in formalin. The specimens were treated in the standard manner, embedded in paraffin, partitioned to 4 μm slices and prepared for hematoxylin-eosin and $CD34^+$ hematopoietic progenitor cell evaluation. Each section was assessed microscopically in order to evaluate and quantify the presence of edema, the degree of inflammatory cell infiltration, and angiogenesis. A blinded histopathological analysis of all samples was performed. Two pathologists assigned the scores separately and the mean value was calculated in order to ensure reliability and increase the objectivity and accuracy of the results (1). The differences between C flaps and R flaps were evaluated on a scoring system modified as follows. A score of 1 to 3 was assigned to define the presence of edema as: 1= mild, 2= moderate or 3= marked. The degree of inflammatory cell infiltration was scored from 1 to 3 according to the amount of inflammatory cells identified per high power field (HPF) (x400). Each sample was assigned a score of 1, 2 or 3, respectively, when less than 3, 3 to 40, or greater than 41 inflammatory cells were observed. For the degree of angiogenesis, $CD34^+$ hematopoietic progenitor cell analysis was performed and a score of 1 to 3 was assigned as follows: 1=less than 5, 2= 6 to 19, 3= greater than 20 blood vessels and capillary buds estimated in 6 HPF per section (7).

Statistical analysis

All results are presented with the mean ± standard

deviations (SD). The investigation of significant differences among the mean values of continuous variables was performed using *t*-tests for independent samples. The threshold for statistical significance was set at a *p* value =0.05. Calculations were made using software STATA-MP 10.1 for Mac OS X.

RESULTS

Out of the study group, 6 rats (40%) died; rats number 1 and 2 due to anesthesia overdose (13.3%), rats number 4 and 10 due to hypothermic shock (13.3%), and rats number 14 and 15 as the result of post-operative bleeding (13.3%). Scoring data revealed a statistically significant improvement ($p<0.05$) in R flaps compared to C flaps in respect to all of the investigated parameters (edema, lymphoplasmacytic infiltrate, necrosis, angiogenesis). The mean scores of each variable in C and R flaps with their standard deviation (SD) and p values are shown in Table I.

Pathological evaluation

Control (C) group. Muscle fibers in the C group were characterized by a reduction of hematoxylin-eosin within the cytoplasm, fiber bulge, partial rupture, and leak of routinely striated aspect compared to those in R group. Multiple skin ulcers with bacterial infections and some chronic granulocytic abscesses were observed. Rats number 5, 6 and 13 displayed extensive areas of necrosis, with giant cells of chronic inflammation and large numbers of granulocytes and plasma cells. Even areas without inflammation displayed ischemic and necrotic spots (Fig. 1). The foreign body granulomas around the residue stitches in C group specimens were much larger than in R group specimens. The $CD34^+$ hematopoietic progenitor cell analysis in C group specimens showed poor angiogenesis.

Resveratrol (R) group. In all R group specimens, the areas of acute inflammation were less extensive than those in the C group. R group tissues exhibited increased microvessel density (a "starry-sky" appearance) with a large sprouting angiogenesis and less ischemic necrosis than C specimens (Fig. 2). Resveratrol administration failed in rats number 6, 9 and 11. However, a relatively diffused "starry-sky" pattern was observed in all R specimens, including rat numbers 6, 9 and 11. The CD34+ analysis in R specimens demonstrated the growth of blood vessel walls and an increase in neoangiogenic vessels (Fig. 2). In all R flaps, plasma

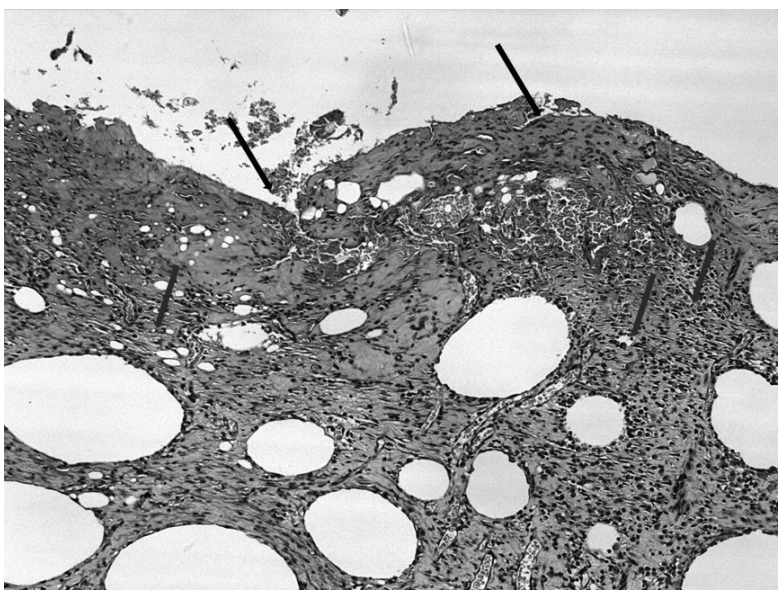

Fig. 1. *Control flap (C flap): rat number 7 (hematoxylin-eosin, X10). Note the skin and the phlogosis.*

Table I. *Mean value with standard deviation (SD) and p value of each variable in C and R flaps.*

Variable	CONTROL FLAPS	RESVERATROL FLAPS	p value
	Mean (SD)	Mean (SD)	
Edema	3 (0)	1.4 (0.7)	0.0000
Lymphoplasmacytic infiltrate	1 (0)	2.6 (0.7)	0.0000
Necrosis	3 (0)	1.4 (0.7)	0.0000
Angiogenesis	1 (0)	2.6 (0.7)	0.0000

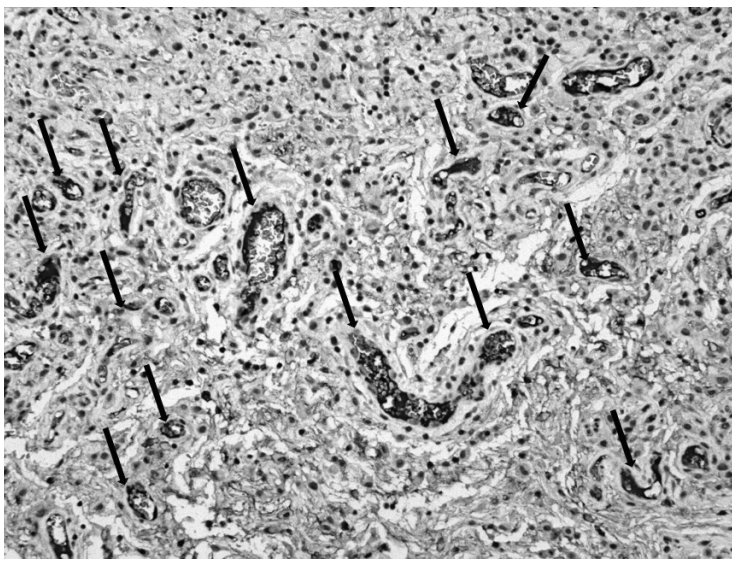

Fig. 2. *Resveratrol treated flap (R flap): rat number 7 (CD34+ hematopoietic progenitor cell analysis, high-magnification image). Note angiogenesis with growth of blood vessel walls and the increase of vessels.*

cells, non-degranulating mast cells, and a reduction in acute inflammation areas were noted; furthermore, neither giant chronic inflammatory cells nor chronic granulocytic abscesses or foreign body granulomas like those seen in C flaps were observed. The large lymphoplasmacytic infiltrate, observed in all R flaps, is characteristic of chronic regenerative processes, and a reliable marker of the end of the acute inflammatory response. These histological results indicated that resveratrol could reduce tissue damage after ischemia and reperfusion of a flap.

DISCUSSION

Free flap surgery is considered the gold standard in oncologic surgery and head and neck reconstruction. This technique can result in severe complications, such as total flap necrosis (8, 9). Current research aims at reducing tissue necrosis (4, 5).

IPC is a surgical method that improves tissue survival during repeated ischemia/reperfusion (I/R) cycles. The current research suggests that the use of external stressors in addition to IPC induces a better tolerance compared to IPC alone. However, there are no standard protocols for use of IPC alone or IPC plus external stressors (10). We decided to associate IPC with the administration of resveratrol to increase ischemic tolerance in myocutaneous flap. Resveratrol has antioxidant and anti-inflammatory properties (11). In this study, the

results of the combined use of IPC and resveratrol were investigated with histological examinations. At least two challenges exist for doing so. First, the IPC time protocols vary among different studies. Second, a protocol for resveratrol administration in IPC does not exist. Hsieh et al. (4) demonstrated in their animal study that resveratrol protracts allograft survival. In their protocol, they treated 4 groups of rats with diverse quantities of resveratrol (0.1 or 0.5 mg/kg) for one week. Ciloglu et al. (5) studied the outcomes of resveratrol on flap viability in diabetic rats. One week after flap surgery, the resveratrol group received intraperitoneally 10 mg/kg of resveratrol in 1 ml and the controls physiological saline solution. In our protocol the C flaps were treated only with IPC, while the R flaps received IPC followed by 0.2 cc. of resveratrol. Our data demonstrated that IPC plus resveratrol induced enhanced flap viability over IPC alone. However, this experimental study will likely be difficult to replicate in humans because the factors associated with IPC will differ from those in rats, and the use of resveratrol, as an angiogenic growth factor (12), requires further investigation.

ACKNOWLEDGEMENTS

We would like to express our gratitude to Professor Michele Pascone, whose dedicated career in plastic surgery helped establish the prestige of the Puglia region in this field within Italy and internationally. We are also immensely grateful to Dr. Davide Russo for the histopathological assessment in this study.

This work was presented as a scientific oral presentation at the American Academy of Otolaryngology—Head and Neck Surgery (AAO-HNSF) Annual Meeting & OTO EXPO, Vancouver (Canada), in the section Facial Plastic and Reconstructive Surgery, on September 30, 2013.

REFERENCES

1. Portincasa A, Trecca EMC, Ciancio F, et al. The role of lipofilling in reconstructions with dermal regeneration template: clinical and histological assessment. J Biol Regul Homeost Agents 2018; 32(1):171-76.
2. Portincasa A, Cecchino L, Trecca EMC, et al. A rare case of Brooke-Spiegler syndrome: integrated surgical treatment of multiple giant eccrine spiradenomas of the head and neck in a young girl. Int J Surg Case Rep 2018; 51:277-81.
3. Nicoli F, Chilgar RM, Sapountzis S, et al. Reconstruction after orbital exenteration using gracilis muscle free flap. Microsurgery 2015; 35(3):169-76.
4. Hsieh YH, Huang SS, Wei FC, Hung LM. Resveratrol attenuates ischemia - reperfusion-induced leukocyte - endothelial cell adhesive interactions and prolongs allograft survival across the MHC barrier. Circ J 2007; 71(3):423-28.
5. Ciloglu NS, Zeytin K, Aker F. The effects of resveratrol on flap survival in diabetic rats. J Plast Surg Hand Surg 2014; 48(4):234-37.
6. Schindelin J, Rueden CT, Hiner MC, Eliceiri KW. The ImageJ ecosystem: An open platform for biomedical image analysis. Mol Reprod Dev 2015; 82(7-8):518-29.
7. Karayannopoulou M, Papazoglou LG, Loukopoulos P, et al. Locally injected autologous platelet-rich plasma enhanced tissue perfusion and improved survival of long subdermal plexus skin flaps in dogs. Vet Comp Orthop Traumatol 2014; 27(5):379-86.
8. Copelli C, Tewfik K, Cassano L, Pederneschi N, Catanzaro S, Manfuso A, Cocchi R. Management of free flap failure in head and neck surgery. Acta Otorhinolaryngol Ital 2017; 37(5):387-92.
9. Ciudad P, Orfaniotis G, Socas J, et al. Technical considerations to avoid microvascular complications during groin lymph node free flap transfer. Arch Plast Surg 2015; 42(5):650-52.
10. Marian CF, Jiga LP, Ionac M. Ischemic preconditioning of free muscle flaps: An experimental study. Microsurgery 2005; 25:524-31.
11. Olas B, Wachowicz B. Resveratrol, a phenolic antioxidant with effects on blood platelet functions. Platelets 2005; 16 (5): 251-60.
12. Athar M, Back JH, Tang X, Kim KH, Kopelovich L, Bickers DR, Kim AL. Resveratrol: a review of preclinical studies for human cancer prevention. Toxicology and Applied Pharmacology 2007; 224 (3): 274-83.

JOURNAL OF BIOLOGICAL REGULATORS & HOMEOSTATIC AGENTS Vol. 33, no. 5, 1609-1613 (2019)

LETTER TO THE EDITOR

INNOVATIONS IN ORAL AND MAXILLOFACIAL SURGERY: BIOMIMETICS MEETS PHYSIOLOGY

A. CICCONETTI[1], A. PASSARETTI[1], C. RASTELLI[2], E. RASTELLI[2] and G. FALISI[2]

[1]Department of Oral and Maxillofacial Sciences, Sapienza University of Rome, Italy; [2]Department of Life, Health and Environmental Sciences, School of Dentistry, University of L'Aquila, L'Aquila, Italy

Received May 2, 2019 – Accepted May 27, 2019

To the Editor,

Reconstructive surgery is the best method for reconstruction of bone defects of various origins: this branch is very important for the improvement of the quality of life of patients who suffer significant trauma on parts of the face or mouth, which may be the result of accidents or interventions for cancer reasons. Reconstruction plays the fundamental role of allowing a correct and rapid functional re-organization and a social reintegration of the treated patients.

The biomimetic approach

The term "biomimetic" derives from the Greek words "*bios*" (life) and "*mimesi*" (to be imitated). Biomimetics deals with the study of natural phenomena to understand their mechanisms and apply them to science, engineering and medicine. The biggest challenge is to determine how nanostructures and microstructures work in relationship to the organism and the environment. There are various hybrid compositions inspired by nature, manufactured and used as a model able to regulate biological processes. Several in-depth studies have been conducted to biomimic biological systems and develop biomedical materials and devices using natural and synthetic polymers. The development of innovative biomaterials allows molecular modulation and cell binding. A modified surface, that is biomimetic, can represent a sort of artificial extracellular matrix able to provide biological stimuli suitable for guiding the formation of new tissue. The signals can generally favor adhesion but can also be selective for some cell types and therefore induce a specific response (1).

Extracellular matrix is the new scaffold

The newly formed bone is the result of a series of actions that begins with the recruitment of osteo-progenitor cells. In the early phases of adhesion to the substrate, the osteogenic cells secrete specific proteins in the surrounding environment, which aggregate into a sort of natural scaffold or the extracellular matrix (ECM). By adhering to this support, the cells proliferate, differentiate and organize themselves for the formation of the neo-tissue. Within the ECM, highly ordered organic fibers are dispersed, consisting of 90% of collagen and the remaining part of numerous proteins such as: osteocalcin, osteonectin, osteopontin, fibronectin, proteoglycans, albumins and immunoglobulins. In the inorganic portion of the intracellular substance, minerals consisting predominantly of calcium and phosphate salts are deposited.

The presence of mineral gives the material strong mechanical properties such as hardness and resistance to the load, while the composition

Key words: biomimetics; oral surgery; mechanobiology

Corresponding Author:
Prof. Andrea Cicconetti,
Department of Oral and Maxillofacial Sciences,
Sapienza University of Rome,
Piazzale Aldo Moro 5, 00185 Roma, Italy
Tel./Fax: +39 06 49911
e-mail: cicconetti.sapienza@libero.it

0393-974X (2019)

DISCLOSURE: ALL AUTHORS REPORT NO CONFLICTS OF INTEREST RELEVANT TO THIS ARTICLE.

and distribution of the protein components gives elasticity and resistance to fractures. Two main types of bone can be detected: cortical bone tissue and trabecular bone tissue. The mechanical properties of the bone are very variable depending on the species, age (Table I) and anatomical site.

The mechanical properties of trabecular bone are due to the characteristics of the individual trabeculae and its highly porous structure. The content of minerals in a bone shows little changes as we age, and this tendency is reflected in its rigidity.

Bone properties in biomimetic strategies

Bone is known for its ability to self-heal, but defects with critical dimensions hinder the natural healing process of bone and do not allow complete healing of the fracture. The study of tissue engineering allowed the development of 3D scaffolds that imitate the ECM, providing a mechanical support able to help the formation of new bone tissue.

Scaffolds designed to promote bone growth should promote cell adhesion, survival, migration and proliferation, accelerate bone remodelling, provide osteoinductive structural guidance, and in some cases release substances such as antibiotics or gene therapy.

To meet these requirements, the scaffolds must be biocompatible, biodegradable and non-toxic; they should have mechanical properties similar to human bone which has a compressive strength between 2 and 12 MPa and an elastic modulus between 0.1 and 5 GPa; finally, they should have a degree of essential porosity for correct cell growth and migration, a correct flow of nutrients and vascularization.

The scaffolds can be made of natural or synthetic materials (Table II), within which elements such as calcium and phosphate, physiological mineral components of the bone, can be present. Synthetic materials are designed to summarize many of the characteristics necessary for the performance of bone substitutes. Aliphatic polyesters are the most used polymers, while the metallic materials are particularly suitable for the construction of structures capable of bearing loads without the risk of large elastic deformations, therefore they are suitable for the replacement of hard tissues such as bones and teeth (2).

The main condition that must be respected by the materials used for the construction of dental implants is biocompatibility. Biocompatibility is defined as the tolerance of vital tissues in relation to the material in use. The biocompatible materials are subdivided into resorbable materials and non-resorbable materials.

Titanium is the non-resorbable material that is currently most used in implant prosthetic applications. Titanium is particularly popular in dental implantology because it has an elastic modulus similar to that of bone, a low specific weight and very low thermal conductivity. These characteristics allow the absorption of chewing loads through the implant structure without the development of tensions. Recently, the analysis of mechanical properties confirms that the three-dimensional titanium meshes have sufficient rigidity to prevent deformation due to external stresses, stabilizing the bone grafts present within the area of the peri-implant bone defect (3).

To avoid a second operation aimed at the removal of non-resorbable membranes, a whole series of resorbable membranes have been developed. These membranes are characterized by the fact that during the regeneration phases they undergo a reabsorption process by hydrolysis. This process takes place at a pace that allows adequate bone regeneration. The resorbable membranes are subdivided into collagen membranes and synthetic membranes resulting from the combinations of polyglycolide and/or polylactide.

Polymers and resorbable solutions

Polylactic acid (PLA) and polyglycolic acid (PLG) are aliphatic synthetic polymers that have demonstrated good clinical applications. PLA and PLG are disrupted by the body through a hydrolysis process, respectively to lactic and glycolic acid. These two substances are subsequently metabolized to CO_2 and H_2O through the Krebs cycle. The PLA membrane can be molded in hot water. When the desired shape is obtained, the membrane is cooled and becomes rigid.

Collagen membranes have a composition similar to the periodontal connective tissue and are degraded through enzymatic reactions. The resorbable membranes in collagen are mainly produced with collagen of bovine and porcine origin. Compared to

Table I. *Maximum resistance of cortical bone of human femur.*

	Mechanical Properties							
Age		10-20	20-30	30-40	40-50	50-60	60-70	70-80
		Maximum resistance (MPa)						
	Stress	114	123	120	112	93	86	86
	Compression	-	167	167	161	155	145	-
	Curvature	151	173	173	162	154	139	139
	Torsion	-	57	57	52	52	49	49

Table II. *Materials used to manufacture scaffolds for bone tissue engineering and their main advantages and limitations.*

Materials	Examples	Advantages (+) / Limitations (-)
Metals	NiTi, titanium alloy , magnesium alloy	+ Young's module; + High resistance to compression; - Not degradable; - Releasing of Ions;
Ceramic materials	TiO_2, HAp, ?-TCP, Bioglasses	+ Biocompatible; + Biodegradable; - Fragility; -Risk of fracture;
Natural Polimers	Collagen, chitosan, hyaluronic acid	+ Biocompatible; + Biodegradable; + Osteogenic; - Low resistance to stress;
Synthetic Polimers	PLGA, PCL	- Acid degradation; - Rapid degradation *in vivo*

synthetically derived products, collagen membranes have hemostatic abilities, promote a rapid stabilization of the clot, have chemiotactic properties against fibroblasts and are semi-permeable, so they do not hinder the passage of nutrients. These membranes have demonstrated rapid angiogenesis, thus promoting regeneration. Furthermore, they have also been shown to prevent epithelial growth in the defect space during the initial post-surgical healing phase (2,3).

CONCLUSIONS

In maxillofacial surgery, as well as in many branches that deal with oncology or traumatology and/or regenerative, the greatest limit is that of predictability of the result with a *restitutium ad integrum* tissue (4-7). The technological evolution, today, with a synergy between various interfaces, allows us to have at our disposal the means with which to realize substitutes of materials, hard and soft, with a fidelity equal to the native material. We have treatments biologically advanced for well-known pathologies affecting bone tissues, such as osteoporosis, by using innovative support to regenerative procedures, such as tissue engineered scaffolds (8). The scientific research has addressed several pathogeneses, thus leading to a significant loss of biological tissues: the pathogenesis, in fact, may depend on different co-factors, such as syndromic conditions (9), inflammation (10), infections and other systemic conditions. Currently, the most promising therapies have been developed with strategic merging of scaffolds and mesenchymal stem cells from different sites (11). Along with therapies, the future challenge is also to improve the diagnosis (12) and the ability of surgeons to treat each kind of pathology with the most advanced technologies with the aim of reducing hospitalization time.

The morphology of bone defects is the key to the correct technique of reconstructive surgical approach to restore the anatomy and physiology of the minus point. A bias that still afflicts the correct analysis of the surgical case is the variability of the classification profiles of bone defects. There are classifications based on the walls of the defect, based on the morphology of the defect, based on the region where it is located, and so on. Therefore, a critical analysis of these classifications, also defining other types of defects that include the analysis of contact surfaces, could be the viaticum to create a new and overall classification of minus in terms of reconstruction of the defect with custom-made prostheses.

In oro-maxillo-facial surgery, during the intervention programming phase, imaging techniques and computer programs are used that allow to predict the result of the intervention, with a three-dimensional image, permitting the possibility to accurately transfer the simulated intervention onto the computer in the operating room. In addition to imaging there is the possibility of making prostheses that fill the defect or plates in Poly-DL-lactic acid or titanium that allow to guide the surgery in the direction of planning already obtained virtually. The expected result will be a *restitutio ad integrum* with a high predictability of result.

REFERENCES

1. Reddy R, Reddy N. Biomimetic approaches for tissue engineering. J Biomater Sci Polym Ed 2018; 29(14):1667-85.
2. De Witte TM, Fratila-Apachitei LE, Zadpoor AA, Peppas NA. Bone tissue engineering via growth factor delivery: from scaffolds to complex matrices. Regen Biomater 2018; 5(4):197-211.
3. Lee SH, Moon JH, Jeong CM, Bae EB, Park CE, Jeon GR, Lee JJ, Jeon YC, Huh JB. The mechanical properties and biometrical effect of 3D preformed titanium membrane for guided bone regeneration on alveolar bone defect. Biomed Res Int 2017; 2017:7102123.
4. Di Bari R, Coronelli R, Cicconetti A. An anatomical radiographic evaluation of the posterior portion of the mandible in relation to autologous bone harvest procedures. J Craniofac Surg 2014; 25(5):e475-83.
5. Di Bari R, Coronelli R, Cicconetti A. Intraosseous vascularization of anterior mandible: a radiographic analysis. J Craniofac Surg 2014; 25(3):872-79.
6. Di Bari R, Coronelli R, Cicconetti A. Radiographic evaluation of the symphysis menti as a donor site for an autologous bone graft in pre-implant surgery. Imaging

Sci Dent 2013; 43(3):135-43.
7. Cicconetti A, Guttadauro A, Riminucci M. Ulcerated pedunculated mass of the maxillary gingiva. Oral Surg Oral Med Oral Pathol Oral Radiol Endod. 2009; 108(3):313-17.
8. Aulino P, Costa A, Chiaravalloti E, et al. Muscle extracellular matrix scaffold is a multipotent environment. Int J Med Sci 2015; 12(4):336-40.
9. Inchingolo F, Tatullo M, Abenavoli FM, et al. Non-syndromic multiple supernumerary teeth in a family unit with a normal karyotype: case report. Int J Med Sci 2010; 7(6):378-84.
10. Tatullo M, Gentile S, Paduano F, Santacroce L, Marrelli M. Crosstalk between oral and general health status in e-smokers. Medicine (Baltimore) 2016; 95(49):e5589.
11. Paduano F, Marrelli M, Amantea M, et al. Adipose tissue as a strategic source of mesenchymal stem cells in bone regeneration: a topical review on the most promising craniomaxillofacial applications. Int J Mol Sci 2017; 18(10).
12. Tatullo M, Marrelli M, Amantea M, Paduano F, Santacroce L, Gentile S, Scacco S. bioimpedance detection of oral lichen planus used as preneoplastic model. J Cancer 2015; 6(10):976-83.

LETTER TO THE EDITOR

SUBLINGUAL SUFENTANIL NANOTAB PATIENT-CONTROLLED ANALGESIA SYSTEM/15 MCG IN A MULTIMODAL ANALGESIC REGIMEN AFTER VERTEBRAL SURGERY: A CASE-SERIES ANALYSIS

A. VERGARI[1], M. DI MURO[1], A. DE ANGELIS[1], R. NESTORINI[1], M.C. MELUZIO[2], L. FRASSANITO[1], F.C. TAMBURRELLI[2] and M. ROSSI[1]

[1] Department of Anesthesiology, Intensive Care Medicine and Toxicology, A. Gemelli University Hospital Foundation, Catholic University of the Sacred Heart, Rome, Italy;
[2]Department of Spine Surgery, A. Gemelli University Hospital Foundation, Catholic University of the Sacred Heart, Rome, Italy

Received February 25, 2019 – Accepted June 20, 2019

To the Editor,

Acute post-operative pain (POP) is an important public health issue worldwide. Undertreatment of POP can result in increased morbidity, limitation of active rehabilitation, delayed discharge, worsening of outcome, and it is highly predictive of chronic post-surgical pain.

Intravenous (IV) Patient-Controlled Analgesia (PCA) with morphine has been considered the gold standard for acute severe pain management, but fell into disuse in our clinical practice, given the invasive route and the workload on medical and nursing staff. Moreover, IV morphine can delay early mobilization and negatively interfere with gut function, affecting recovery. A multimodal, opioid-sparing approach has thus gained increasing popularity, according to Enhanced Recovery After Surgery (ERAS) protocols.

Recently, a Sufentanil Sublingual Tablet System (SSTS) has been marketed in Europe by Grünenthal GbmH (Aachen, Germany) (1). The SSTS is a PCA system approved for the management of acute moderate-to-severe pain in adult patients in hospital setting (2, 3). This pre-programmed drug/device combination product delivers a fixed dose of 15 mcg of sufentanil tablets as needed, in a non-invasive sublingual dosage form. Sufentanil is a μ-opioid agonist which lacks active metabolites, has a high therapeutic index and a rapid plasma/CNS equilibration half-life, ensuring a rapid and consistent onset of action (4, 5). The sublingual route of administration overcomes the high peak levels and short duration of action associated with IV administration due to sufentanil's highly lipophilic nature, also avoiding the first-pass metabolism associated with the "per os" route of administration (5-9).

The primary objective of this study was to determine the efficacy of the SSTS as part of multimodal analgesia by assessing POP intensity at 24 h. Secondary endpoints included patients' reports of pain intensity at 48 and 72 h, patients' satisfaction at discharge, side effects, length of hospital stay after surgery and nursing team satisfaction.

MATERIALS AND METHODS

A retrospective analysis of 19 consecutive patients

Key words: pain; postoperative; sublingual sufentanil; spinal fusion; spondylolisthesis

Corresponding Author:
Dr Alessandro Vergari,
Department of Anesthesiology,
Intensive Care Medicine and Toxicology,
A. Gemelli University Hospital Foundation,
Catholic University of the Sacred Heart, Rome, Italy
Tel.: +39 0630154507 - Fax: +39 063013450,
e-mail: alessandro.vergari@policlinicogemelli.it.

0393-974X (2019)

scheduled for elective lumbar fusion surgery who received SSTS 15 mcg with a 20-minute lockout interval in the postsurgical period was performed. The study protocol and statement of informed consent to data treatment were approved by the local ethics committee (31120/18). Participants gave written informed consent to data analysis and publication. The study was registered at ClinicalTrials.gov on February 20, 2018 [CTN03459404].

Exclusion Criteria to post-operative sublingual sufentanil administration were:

- Age <18 yrs or >75 yrs
- Opioid tolerance
- Documented sleep apnoea or home oxygen therapy
- History of alcohol or drug abuse
- Allergy or hypersensitivity to opioids.

The patients enrolled were suffering from intractable lumbar pain, with or without lower limb radiation, walking limitation (neurogenic claudication) and different degrees of daily life activity limitation. The most frequent pathogenesis of the lumbar pain was degenerative or isthmic spondylolisthesis, lumbar stenosis, and spinal deformities. The surgical treatment consisted in decompression of neurologic structures (when required) and different procedures of vertebral fusion. On the day before surgery, patients were instructed on the use of the device.

Intraoperative management was standard (general anaesthesia inducted with propofol, fentanil or sufentanil, rocuronium and desflurane). In the post-anaesthesia care unit (PACU), patients were given SSTS when awake and cooperative (score 1 in Modified Wilson Sedation Scale) (10). They consequently self-administered SSTS as needed for pain relief for a maximum duration of 72 h. All patients were given acetaminophen, ketoprofen and metoclopramide "per os" in an 'around-the-clock' (ATC) dosing regimen. Ondansetron was prescribed as rescue drug in case of persistent nausea or vomiting. Tramadol "per os" was prescribed as rescue drug for pain control. Pain intensity was estimated during the 72 h after surgery using an 11-point NRS, ranging from 0 (no pain) to 10 (the worst pain imaginable). NRS was quantified before the surgical procedure and post-operatively at baseline (in PACU before the first administration of sublingual sufentanil), at 30 min, 1, 2, 6, 12, 24, 48 and 72 h. Side effects (nausea, vomiting, sleepiness, itching, dizziness, others) and length of stay after surgery were also reported.

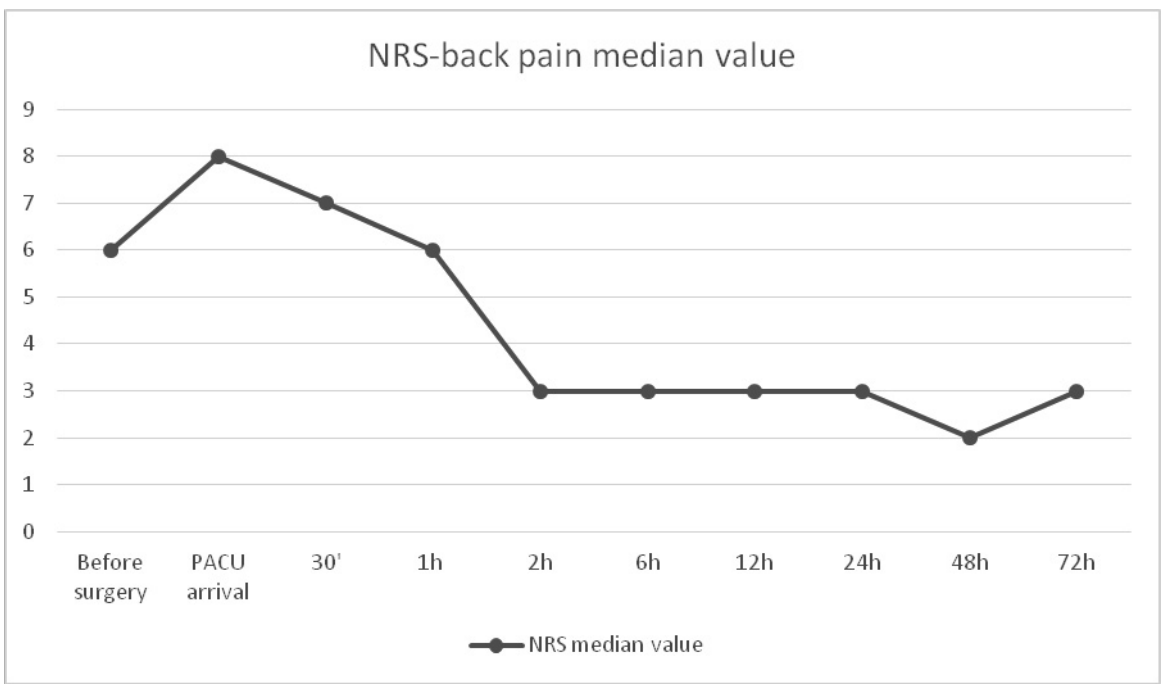

Fig. 1. *NRS median value.*

Patient and nurse satisfaction were assessed using a specific Ease-of-Care (EOC) Questionnaire, each adapted from validated patient (11) and nurse (12) EOC Questionnaire. The patient EOC Questionnaire included 20 questions, 18 of which were collected into 6 categories (confidence with the device, understanding, comfort with the device, movement, dosing confidence, pain control) and scored on a scale of 0 to 3 (0 not at all, 1 somewhat, 2 a great deal, 3 a very great deal). The remaining 2 questions (satisfaction with level of pain control and satisfaction with method of administration of pain medication) were scored on a scale of 0 to 3 (from extremely dissatisfied to extremely satisfied). The nurse EOC Questionnaire had 9 questions, 7 of which focused on the time-consuming and bothersome features of the device and were scored on a scale of 0 to 2 (0 not at all, 1 somewhat, 2 a great deal). The remaining 2 questions (satisfaction with level of pain control and satisfaction with the device) were scored on a scale of 0 to 2 (0 unsatisfied, 1 satisfied, 2 extremely satisfied). Statistical analysis was performed using SPSS 15.0. Data are expressed as mean and standard deviation.

RESULTS

Nineteen consecutive patients eventually met inclusion criteria for SSTS use. In 2 patients the treatment was interrupted (1 for intractable post-operative vomiting and 1 for technical malfunction of the device). The 17 remaining patients were analysed: 11 women and 6 men, mean age 59±10 years, mean Body Mass Index (BMI) 22.5±3.53. Average surgery time was 250 min (mean 258±73.9 min). In the PACU, mean time to first SSTS use after recovery from anaesthesia was 22.5±5.6 min.

During the pre-anaesthetic interview, patients estimated the intensity of their low-back pain as moderate. At the arrival in PACU, NRS score median value was 8, reduced to 6 at 1 h and 3 at 2, 6 and 12 h

Table I. *NRS and tablets consumption, mean and median values. Tablet consumption refers to each span of time from the previous entry.*

	NRS ***Mean value ±DS***	**NRS** ***Median value***	**Tablets consumed** ***Mean value ±DS***	**Tablets consumed** ***Median value***
Before surgery	6.05±2.5	6	-	-
PACU arrival	7±2	8	-	-
30'	6.6±2.1	7	0.9±0.2	1
1h	5.7±2.1	6	0.7±0.6	1
2 hrs	3.5±2	3	0.9±1	1
6 hrs	2.8±2.2	3	1.1±0.9	1
12 hrs	3.5±1.9	3	1.3±1.1	1
24 hrs	2.8±2	3	3.8±2.5	3
48 hrs	1.9±1.5	2	6.4±4.4	6
72 hrs	2.3±1.5	3	4.4±5.6	3.5

Table II. *Patient and Nurse EOC Questionnaire.*

Patient EOC Questionnaire		
		Mean±DS
	CONFIDENCE WITH THE DEVICE	**2.6±0.4**
1	I liked being in control of my pain medication.	2.47±0.6
2	I have never been worried that the device would run out of medication.	2.7±0.7
3	I have never been afraid of having to ask for help to use the device.	2.8±0.3
	UNDERSTANDING	**2.7±0.1**
4	The instructions provided by the nurse/doctor were useful.	2.8±0.3
5	I understood how often I could press the button to get my pain medication.	2.7±0.4
6	I have never needed help from nurses to use and/or adjust the device.	2.7±0.4
	COMFORT WITH THE DEVICE	**2.8±0.2**
7	I never had problems pressing the button because I was drowsy and/or feeling weak.	2.7±0.5
8	The device was easy to use.	2.9±0.2
9	Releasing the drug was easy, regardless the position in which I was lying in the bed.	2.8±0.3
	MOVEMENT	**2.6±0.5**
10	I have never been afraid of walking away from the device (in order to reach the chair, the bathroom, the unit hallway..).	2.7±0.8
11	It is easy to carry.	2.5±0.8
	DOSING CONFIDENCE	**2.7±0.4**
12	I have never been worried that nurses or doctors were not monitoring how much pain medication I was taking.	2.9±0.2
13	I have never been afraid of becoming addicted to the pain medication.	2.6±0.7
14	I have never been worried that I might be taking more medication than I was supposed to.	2.8±0.5
15	I have never been worried that I might not assume enough medication to control pain.	2.6±0.7
	PAIN CONTROL	**2.1±0.5**
16	Problems with device use have never prevented me from controlling pain.	2.8±0.3
17	Pain never woke me up from sleep.	1.8±0.8
18	Pain never went up and down (i.e. sometimes the pain was bad and other times it was under control).	1.7±0.8
	SATISFACTION	**Mean±DS**
19	How satisfied were you with the level of the pain control?	**2.4±0.5**
20	How satisfied were you with the way in which your pain medication was administered?	**2.5±0.5**

Nurse EOC Questionnaire		
	I considered time-consuming/bothersome..	**Mean±DS**
1	Learn how to use the device.	0.7±0.4
2	Maintaining device function.	0.2±0.4
3	Changing or adjusting the device due to malfunction.	0.3±0.6
4	Educating/ re-instructing patient on how to use the device.	0.5±0.5
5	Positioning, moving or transferring the patient with the device.	0.1 ± 0.3
6	Managing breakthrough pain.	0.1 ±0.3
7	Treating patient problems related to the device (identification thumb tag damage, problems with drug release..).	0.2 ± 0.5
	SATISFACTION	
8	How satisfied were you with the pain control provided by the device?	**1.7±0.4**
9	Please rate your overall satisfaction with the device	**1.7±0.4**

The patient EOC Questionnaire included 20 questions, 18 of which were collected into 6 categories (confidence with the device, understanding, comfort with the device, movement, dosing confidence, pain control). The questions were scored on a scale of 0 to 3 (0 not at all, 1 somewhat, 2 a great deal, 3 a very great deal). The higher the score, the better the corresponding value. The remaining 2 questions (satisfaction with level of pain control and satisfaction with method of administration of pain medication) were scored on a scale of 0 to 3 (from extremely dissatisfied to extremely satisfied). The nurse EOC Questionnaire had 7 questions scored on a scale of 0 to 2 (0 not at all, 1 somewhat, 2 a great deal): a lower score meant a better experience in the use of the device. The remaining 2 questions (satisfaction with level of pain control and satisfaction with the device) were scored on a scale of 0 to 2 (0 unsatisfied, 1 satisfied, 2 extremely satisfied): higher value corresponded to a greater satisfaction. Data are expressed as mean and standard deviation.

from the arrival. At 24 h after surgery, median NRS value was 3 (primary endpoint, mean value 2.8±2). Median NRS values were 2 and 3 at 48 and 72 h, respectively (secondary endpoints). Table I and Fig. I show all mean and median NRS values recorded. The patients self-administered a total of 20 sufentanil tablets (median value, see Table I). Only 1 patient required a rescue dose of tramadol. Only 1 patient reported itching. 7 out of 17 patients experienced mild nausea (only 2 of them requested antiemetic rescue therapy). Many patients reported sleepiness (9 out of 17) and 4 patients felt dizziness. No other side effects were reported. After surgery, many patients spent 3 days in hospital (14 out of 17), but 1 patient was discharged prior to 48 h and 2 patients from 48 to 72 h. The patient satisfaction with level of pain control and SSTS method of administration corresponded to a median value of 2 (from 0 to 3) and 3 (from 0 to 3), respectively (see Table II). The nursing team also reported to be extremely satisfied with the method of drug administration (median value of 2 in a scale from 0 to 2, Table II).

DISCUSSION

Although a certain limit of this report is the lack of a control group and its snall sample, this preliminary investigation has the advantage of portraying our clinical practice.

A moderate-to-severe POP follows surgical treatment, mostly because of injury of paravertebral musculature and acute restoration of spinal sagittal balance and segmental lordosis. The peak of pain is generally experienced on the first days after surgery, causing a mobility restriction. Conversely, our patients portrayed a median NRS back pain value of 3 at 24 h post-op, with the greatest reduction in pain intensity experienced during the first 2 hours. Patients also began mobilization on post-op day 1, with a single physical therapy session a day. In our view, mobilization sessions were more beneficial compared to standard: the patients not only got to sit up on post-op day 1 (as common in our daily practice), but most of them managed to stand up and ambulate, promptly resuming activities of daily living. The improved pain control also shortened the length of hospital stay, permitting early discharge after surgery (less than 48 hours, against the usual discharge occurring in our experience at least 72–96 hours after surgery).

SSTS in a multimodal analgesic regimen proved to be safe: no major events or post-operative respiratory depression episodes occurred. At the end of the treatment, patients felt comfortable with self-providing pain medication, declaring a high level of satisfaction with the achieved pain control. The nursing team likewise expressed great satisfaction, evaluating the system both effective and inexpensive in terms of time and effort.

In conclusion, the SSTS, in multimodal analgesia, can be considered very effective in the management of moderate-to-severe POP in lumbar fusion surgery. The improvement in pain management and its 'easy-to-use' features could implement early mobilization protocols following major surgery, according to the new paradigms of ERAS.

DISCLOSURE

Alessandro Vergari has served as Advisory Board Member for Grünenthal Italia.

Grünenthal Italia srl sustained publication fees.

REFERENCES

1. Sacerdote P, Coluzzi F, Fanelli A. Sublingual sufentanil, a new opportunity for the improvement of postoperative pain management in Italy. Eur Rev Med Pharmacol Sci 2016; 20:1411-22.
2. Melson TI, Boyer DL, Minkowitz H, et al. Sufentanil sublingual tablet system vs. intravenous patient-controlled analgesia with morphine for postoperative pain control: a randomized, active-comparator trial. Pain Pract 2014; 14:679-88.
3. Meijer F, Cornelissen P, Sie C, et al. Sublingual sufentanil for postoperative pain relief: First clinical experiences. J Pain Res 2018; 11:987-92.
4. van de Donk T, Ward S, Langford R, Dahan A. Pharmacokinetics and pharmacodynamics of sublingual sufentanil for postoperative pain management. Anaesthesia 2018; 73:231-37.
5. Minkowitz H, Singla NK, Evashenk MA, Hwang SS, Chiang YK, Hamel LG, Palmer PP. Pharmacokinetics of sublingual sufentanil tablets and efficacy and safety in the management of postoperative pain. Reg Anesth Pain Med 2013; 38:131-39.
6. Ringold FG, Minkowitz H, Gan TJ, Aqua KA, Chiang YK, Evashenk MA, Palmer PP. Sufentanil sublingual tablet system for the management of postoperative pain following open abdominal surgery: A randomized, placebo-controlled study. Reg Anesth Pain Med 2015; 40:22-30.
7. Jove M, Griffin DW, Minkowitz H, Ben-David B, Evashenk MA, Palmer PP. Sufentanil sublingual tablet system for the management of postoperative pain after knee or hip arthroplasty: A randomized, placebo-controlled study. Anesthesiology 2015; 123:434-43.
8. Fisher DM, Chang P, Wada DR, Dahan A, Palmer PP. Pharmacokinetic properties of a sufentanil sublingual tablet intended to treat acute pain. Anesthesiology 2018; 128:943-52.
9. Willsie SK, Evashenk MA, Hamel LG, Hwang SS, Chiang YK, Palmer PP. Pharmacokinetic properties of single- and repeated-dose sufentanil sublingual tablets in healthy volunteers. Clin Ther 2015; 37:145-55.
10. Némethy M, Paroli L, Williams-Russo PG, Blanck T

J. Assessing sedation with regional anesthesia: Inter-rater agreement on a modified Wilson sedation scale. Anesth Analg 2002; 94:723-28.

11. Harding G, Schein JR, Nelson WW, Vallow S, Olson WH, Hewitt DJ, Polomano RC. Development and validation of a new instrument to evaluate the ease of use of patient-controlled analgesic modalities for postoperative patients. J Med Econ 2010; 13:42-54.
12. Harding G, Vallow S, Leidy NK, et al. Ease of care with patient controlled analgesia systems: Questionnaire development and validation. J Adv Nurs 2007; 59:530-41.

LETTER TO THE EDITOR

TREATMENT OF DENTAL DILACERATIONS

C. MASPERO, A. FAMA, D. CAVAGNETTO, A. ABATE and M. FARRONATO

Fondazione IRCCS Ca' Granda, Ospedale Maggiore Policlinico, Department of Orthodontics University of Milan, Italy

Received January 15, 2019 – Accepted June 25, 2019

To the Editor,

Dilaceration is defined as a dental element with a noticeable alteration in the axial inclination between the crown and the root, or in the root axial inclination only (1). In the first case, the dilaceration occurs in the coronary-root junction level with a deformation of the CEJ. In the second case, it may be present anywhere along the root surface and includes any axial modification during the root formation process (2). According to a study by Farronato et al., the most commonly involved teeth are the permanent maxillary incisors, followed by the mandibular anterior teeth (1). Dilacerations are more frequent in the upper rather than in the mandibular arch. Occasionally, primary teeth are also involved. Additionally, root dilaceration is more common than coronary dilaceration (3). There is no universal consensus in the literature regarding the frequency of dental dilaceration. Data may differ according to the different ethnic groups as ethnicity may influence the result. Referring to a study by Ezoddini et al., approximately 40% of the population present dental abnormalities, the most common being dilacerations, which represent about 15% of the total number (3). According to another study dilacerations are present in about 3% of dental elements. They are more common in men than in women and a family history of dental abnormalities was found in one-third of the cases examined. Different methods have been proposed in the relevant literature in order to provide good aesthetics and functionality in cases of particularly important dilacerations.

MATERIALS AND METHODS

Search strategy

The review of the literature was conducted through the following electronic databases: Medline, Pubmed, Embase and Cochrane Library. Key words selected were: "dilacerated tooth", "dilacerated root", "dilacerated crown", "dilaceration". Only articles with reliability or accuracy of the diagnostic method were considered. Articles with information about etiology, diagnosis and therapy and specific articles regarding the role of surgical and rehabilitative treatment were considered.

Inclusion and exclusion criteria

Only articles between 1970 and 2017 were selected. Using the "limits" option, only articles referring to "Humans" were considered. The following types of studies were included in this review: case-reports and series, reviews and clinical trials. Commentaries, letters to the editor, short communication, articles referring to non-dentistry topic and those published before 1970 were not considered. Criteria for this study are summarized in Table I.

Key words: dilacerated dental elements; dilacerations; orthodontic treatment; impacted teeth

Corresponding Author:
Maspero Cinzia. MD DDS
Department of Orthodontics, University of Milan,
Fondazione IRCCS Ca' Granda,
Ospedale Maggiore Policlinico,
via Francesco Sforza 35, 20122. Milano, Italy
Tel.: +39 0255032520 - Fax: +390255032842
e-mail: cinzia.maspero@unimi.it

0393-974X (2019)

DISCLOSURE: ALL AUTHORS REPORT NO CONFLICTS OF INTEREST RELEVANT TO THIS ARTICLE.

RESULTS

Initially 1,023 articles were found. Three additional studies from non-peer-reviewed journals (gray literature) were also considered. After elimination of duplicates, the primary search resulted in 390 articles. Two hundred seven articles were screened from database. Successively 156 articles as non-relevant on the basis of abstract, title and study design were excluded. Full texts of 51 articles were read to exclude additional irrelevant studies. Only 31 articles met the inclusion criteria. The research refers to the Preferred Reporting Items for Systematic Reviews and Meta-Analyses (PRISMA). The PRISMA flow chart (Fig.1) shows the search methodology and results.

A meta-analysis was not possible due to the heterogeneity of the variability in study designs. No reportable limitations exist as the PRISMA guidelines were followed.

The Quality Assessment of Diagnostic Accuracy Studies tool-2 (QUADAS-2) was used to evaluate risk of bias. The reviewers assessed the risk of bias of each study independently and discrepancies were resolved by a third reviewer.

Data extraction

Two reviewers among the authors were responsible for article selection without blinding to the authors. Disagreements were resolved by discussion or the involvement of another review author. Data extracted were collected on the following items: journal and year of publication, study design, therapeutic outcomes, ethnicity and author's conclusion.

DISCUSSION

The dilaceration of a permanent element usually is the consequence of a trauma in the primary tooth, intrusive or avulsion (4). This association was found in 90% of cases and is particularly significant in the upper incisors, the most exposed to trauma. When the angle between the root and the crown is very sharp, it is unlikely that the element can reach the physiological position. This association is due to the close relationship between the root of deciduous elements and the crown of the germs of permanent teeth. It is important to follow-up the post-traumatic patients in order to make an early diagnosis of a possible dilaceration. The severity of the lesion depends on several factors: the tooth formation stage, the intensity, and the direction of the traumatic force. When trauma occurs before the permanent teeth have erupted, the outcome is a dilacerated tooth, which usually requires assistance to erupt correctly. Other trauma-related clinical problems such as ankylosis and invasive cervical root resorption can cause unerupted teeth. The etiopathogenesis of dilaceration has been related to disorders of crown formation, mechanical interference during eruption, flogistic processes of deciduous teeth and some developmental syndromes such as Axenfeld-Rieger syndrome, Smith-Magenis syndrome, hypermobility type Ehlers-Danlos syndrome and cleidocranial

Table I. *Inclusion and exclusion criteria*

INCLUSION CRITERIA	EXCLUSION CRITERIA
Articles published between 1970-2017	Articles published before 1970
Humans	Non-human topics
Case-reports	Commentaries
Case series	Letters to editor
Reviews	Short communication
Clinical trials	
No language limit	

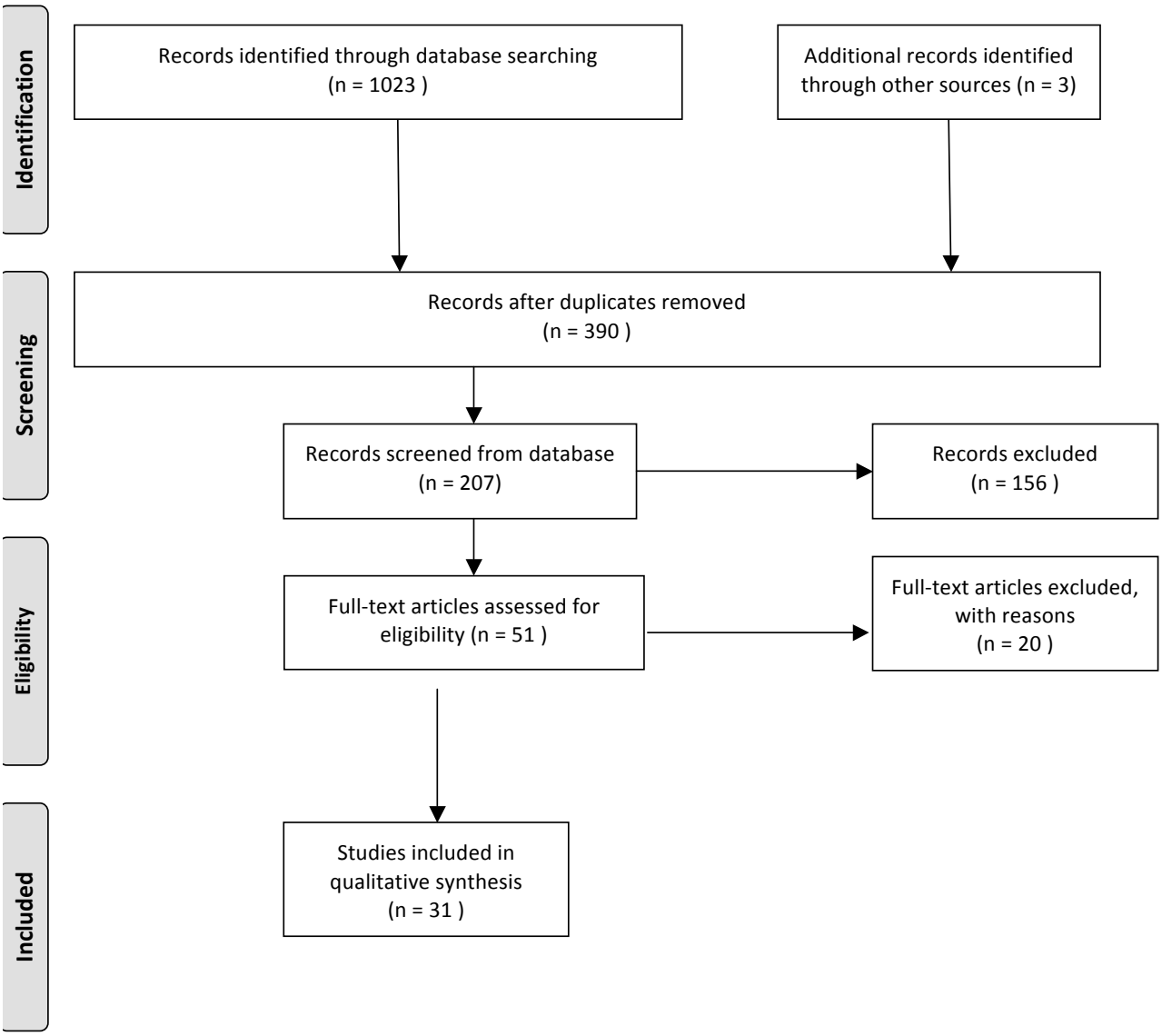

Fig. 1. *Prisma flow chart*

dysplasia (5). Root dilaceration of deciduous elements could be due to medical procedures, such as neonatal laryngoscopy and endotracheal intubation.

The main diagnostic problem is the difficulty in establishing the prognosis and the treatment plan by radiological evaluation (6-8). The first examinations for the diagnosis are represented by periapical radiographs according to Clark technique, orthopantomography and teleradiography. In cases of dilacerated elements in vestibular position, it is possible to use an occlusal radiography. In some cases transversal slice imaging technique can be used which allows the evaluation of the space of the periodontal ligament, root resorption and radicular morphology. The study by Sawamura et al., conducted on maxillary dental elements, confirmed the TC has a significantly greater specificity and sensitivity than conventional radiographs (7) (Fig. 2).

Advanced imaging techniques are an essential requirement for a correct diagnosis and for planning surgical access and bond placement, as

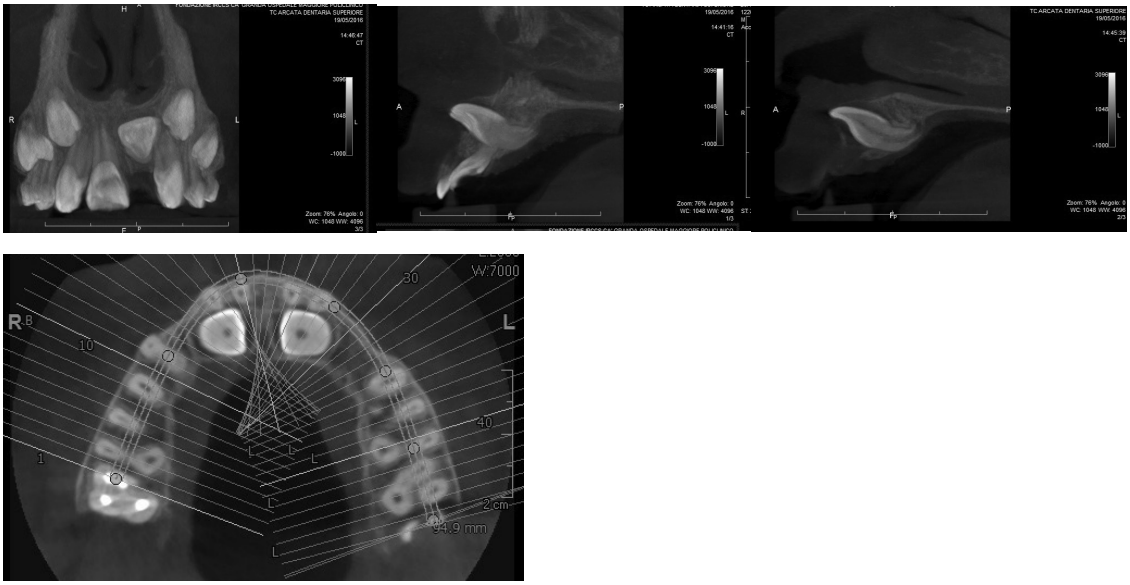

Fig. 2. *Contemporary CBCT exam*

well as in defining the optimal and most efficient path for extrusion into the oral cavity, that avoids or minimizes collateral damage (9-12).

In conclusion, early diagnosis facilitates orthodontic, surgical and endodontic treatment. The therapeutic options proposed in the literature are particularly optimistic for young patients with non-severe dilaceration. Adequate periodontal support and tooth vitality can be maintained with the use of light (30-40 gr.) and continuous orthodontic forces. Surgical solutions are preferred in case of particularly compromised dental elements. In case of autotransplantation, there is no evidence of long-term stability. Prosthetic solutions can be performed in order to avoid the extraction of the dilacerated element. The distance from the mucogengival line, the quantity and quality of the adherent gingiva and the position of the dilacerated tooth influence the surgical disinclusive approach.

Combined orthodontic-surgical options should be studied in long-term longitudinal studies. There is no evidence in which way ethnicity may influence therapeutic options.

REFERENCES

1. Farronato G, Giannini L, Galbiati G, Maspero C. A 5-year longitudinal study of survival rate and periodontal parameter changes at sites of dilacerated maxillary central incisors. Prog Orthod 2014 Jan 6; 15:3.
2. Andrade MG, Weissman R, Oliveira MG, Heitz C. Tooth displacement and root dilaceration after trauma to primary predecessor: an evaluation by computed tomography. Dent Traumatol 2007; 23(6):364-67.
3. Ezoddini AF, Sheikhha MH, Ahmadi H. Prevalence of dental developmental anomalies: a radiographic study. Community Dent Health 2007; 24(3):140-44.
4. Farronato G, Maspero C, Farronato D. Orthodontic movement of a dilacerated maxillary incisors in mixed dentition treatment. Dent Traumat 2009; 25 (4):451-56.
5. de Araujo MR, de Oliveira Ribas M, Koubik AC, Mattioli T, de Lima AA, França BH. Fanconi's anemia: clinical and radiographic oral manifestations. Oral Dis 2007; 13(3):291-95.
6. Broer N, Fuhrmann A, Bremert S, Schulze D, Kahl-

Nieke B. Evaluation of transversal slice imaging in the diagnosis of tooth displacement with special consideration of the upper canines. J Orofac Orthop 2005; 66(2):94-109.

7. Sawamura T, Minowa K, Nakamura M. Impacted teeth in the maxilla: usefulness of 3D Dental-CT for pre-operative evaluation. Eur J Radiol 2003;47(3):221-26.
8. Kapila S, Conley RS, Harrell WE Jr. The current status of cone beam computed tomography imaging in orthodontics. Dentomaxillofac Radiol 2011; 40:24-34.
9. Lucchese, A., Carinci, F., Brunelli, G., & Monguzzi, R. Everstick® and Ribbond® fiber reinforced composites: Scanning Electron Microscope (SEM) comparative analysis. Euro J Inflam 2011; 9(3 S):73-79.
10. Farronato G, Cannalire P, Martinelli G, Tubertini I, Giannini L, Galbiati G, Maspero C. Cleft lip and/or palate. Minerva Stomatol 2014; 63(4):111-26.
11. Manuelli M, Huanca Ghislanzoni L, Farronato M, Martintoni A, Marcolina M, Lucchese A. Comparison of linear transverse measures between plaster and resin printed digital models. J Biol Regul Homeost Agents 2018; 32(2 Suppl. 2):81-85.
12. Lo Giudice A, Portelli M, Militi A et al. Is static friction affected by aging and amount of elastomeric ligatures in orthodontic sliding mechanics? An in-vitro investigation. J Biol Regul Homeost Agents 2018; 32(2 Suppl. 2):67-73.

LETTER TO THE EDITOR

BROMELAIN AFTER ORAL OR DENTAL PROCEDURES: AN UPDATE

A. MOFFA[1], F. FRACCAROLI[2], S. CARBONE[2], V. RINALDI[2], A. COSTANTINO[2], M.A. LOPEZ[2], M. CASSANO[1] and M. CASALE[1]

[1]Unit of Otolaryngology, University of Foggia, Foggia, Italy; [2]Unit of Otolaryngology, UOS ORL TI, Campus Bio-Medico University, Rome, Italy

Received May 15, 2019 – Accepted June 25, 2019

To the Editor,

Oral diseases are very common chronic diseases and represent an important public health problem due to their social and economic impact. In most cases, oral and dental surgical procedures are performed in a surgery clinical setting, under local anesthesia, with minimal recovery time (1). These procedures frequently produce pain, trismus and facial swelling in the postoperative period, and in clinical practice, nonsteroidal anti-inflammatory drugs (NSAIDs) are widely used in order to control these symptoms (2). However, NSAIDs present several side effects, such as gastrointestinal, renal, and haematological problems, especially in elderly people. Efficient, safe, and natural molecules with anti-inflammatory properties and no major side effects should be considered for controlling pain, oedema, and trismus. Among these molecules, bromelain has been recently used. It is a general name of a family of a natural sulfhydryl proteolytic enzymes obtained from *Ananas comosus*. Bromelain concentration is high in the pineapple stem. Bromelain containing several proteinases, shows a range of biological properties from platelet aggregation inhibition to anti-inflammatory effects. In particular, this molecule reduces existing oedema and prevents oedema formation, increasing tissue permeability by fibrinolysis and promoting reabsorption of fluid into blood circulation. To date, bromelain has been widely used in a variety of conditions related to surgical practice. There is already a recent meta-analysis (3) including five studies on bromelain efficacy on health outcomes after third molar surgery, specific notoriously painful surgical dentistry procedure. The authors concluded that bromelain is effective controlling post-operative pain for 48-72 h after surgery, but did not achieve a significant effect in comparison to the control group with regard to oedema or trismus. The aim of our study is to systematically review the published literature regarding all the therapeutic effects of bromelain after oral and dental surgery underlining the proposed bromelain schedule and evaluating the most effective parameters.

METHODS

Search strategy and selection criteria

A search was made of the PubMed, Google Scholar and Ovid databases according to the PRISMA guidelines using the following key words or in the case of PubMed, medical subject headings: “bromelain” and “dentistry”, “periodontitis”, “gingivitis”, “mucositis”, “implant”, “teeth”, “gingiva”, “stomatitis”, “oral ulcers”, “oral scars”, “oral tumour”, “oral lesions”, “oroantral communication”, “oroantral fistula”, “oral cavity”, “mucositis”, “tonsillectomy”, “adenoidectomy”, “wound

Key words: bromelain; dentistry; oral surgery; third molar extraction; pain; oedema; trismus

Corresponding Author:
Antonio Moffa, MD
Department of Otolaringology,
University of Foggia,
71122 Foggia, Italy
Tel.: +39 388 3639207
e-mail: moffa.antonio1@gmail.com

0393-974X (2019)

DISCLOSURE: ALL AUTHORS REPORT NO CONFLICTS OF INTEREST RELEVANT TO THIS ARTICLE.

healing", "oral surgery", "third molar extraction", "teeth extraction", and "odontostomathology" with no limit selected for the year of publication. We included only articles in English language and all randomized controlled clinical trials on humans aged >18 years, covering the effect of the bromelain in patients undergoing dental surgical procedures. Articles published in languages other than English, reviews, cohort studies, case-control studies, laboratory studies and studies for which the full article was not available, were excluded. Two authors independently assessed the full-text version of each publication, making their selection based on content and excluding papers that did not include the specifically required content. The reference lists of articles that met the first criteria were fully reviewed to identify useful articles that were not included in the initial electronic search. During the research phase, in each of the journals, articles strictly coherent with the topic were first identified, while *in vitro* studies or studies on animal models were excluded after the primary selection.

At the end of our study selection process, nine studies with a total of 527 patients were included: eight studies evaluated the effects of bromelain administration after third molar extraction while one study after bimaxillary orthognathic surgery (Fig. 1).

RESULTS

Features of each single study are reported in Table I.

Third molar extraction: bromelain vs control group

Ordesi et al. (4) conducted another similar study including 80 patients: 40 treated with one bromelain tablets every 12 hours for 7 days with paracetamol as an analgesic if required, and 40 received only paracetamol if required. The authors evaluated pain, oedema, erythema and consumption of analgesics. Patients treated with bromelain showed a significant improvement in pain, oedema and erythema and a reduced consumption of analgesic compared to the control group. Tan and Li (5) investigated the effects of bromelain in patients with hematologic tumour after third molar extraction during chemotherapy. They included 72 patients: 36 used oral bromelain

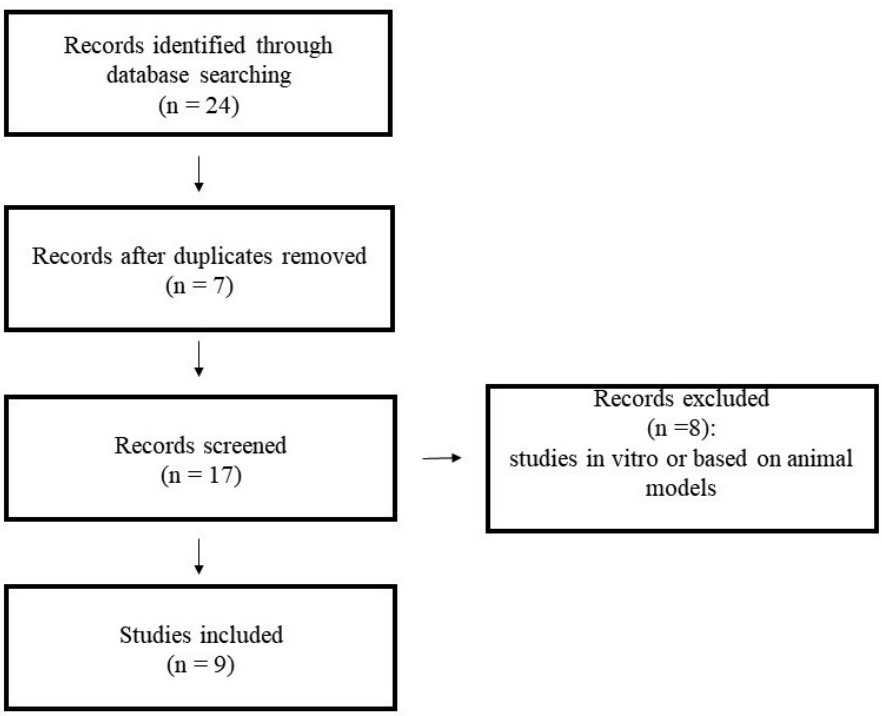

Fig. 1. *Article search strategy.*

capsule (three times/day, for three days) and 36 patients were treated with cold-hot compresses. The authors evaluated pain, swelling and limitation of mouth opening and values of the following molecular markers (IL-25, TNF-alfa, EGFR, beta-FGF) and QOL. Patients treated with bromelain showed that pain, swelling and mouth opening in the bromelain group significantly improved compared to the control group. Additionally, the levels of IL-25 and TNF-α in the bromelain group were significantly lower than the control group, suggesting less inflammatory response. On the other hand, EGFR and β-FGF were significantly higher in patients treated with bromelain supporting the activation of tissue repair pathways. QOL scores were significantly better in the bromelain group. De la Barrera-Núñez et al. (6) evaluated the role of bromelain after impacted lower molar extractions. In this study, 34 patients were included: 16 patients received bromelain 150 mg tablet per day for 3 days and 100 mg tablet on days 4 to 7 while 18 patients received placebo in the same dosage. The authors evaluated pain, swelling and trismus before and after surgery. Although there were no statistically significant differences between the two groups, better values were recorded for swelling and improved oral aperture in the group treated with bromelain than the placebo group. No significant differences were observed in the assessment of pain between the two groups. Omer Waleed Majid et al. (7) investigated the effect of bromelain on the postoperative sequelae and quality of life after surgical removal of lower third molars in 45 patients divided into three groups: 15 patients with bromelain, 15 with diclofenac and 15 with placebo. The patients took one capsule every 6 hours, starting the morning before the day of surgery and continued for 4 days. The authors evaluated pain, swelling, trismus, and quality of life (QOL) after surgery. Both bromelain and diclofenac groups showed a significant reduction in pain compared with the placebo. Diclofenac also resulted in a significant reduction of swelling at 3 and 7 days, and bromelain resulted in an insignificant reduction. A nonsignificant reduction in trismus occurred in both treatment groups compared with the placebo group. Both treatment groups also showed a comparable significant difference in the effect on QOL in most subscales and total scores without difference.

Third molar extraction: bromelain vs NSAIDs and corticosteroids

The study conducted by Inghingolo et al. (8) included 46 patients suitable for exodontia of 3.8 and 4.8 teeth. After 3.8 teeth exodontia, the patients used cephazolin sodium (1 g/12 h/i.m. along 6 days) together with bromelain (40 mg/6 h/os, for 6 days). After 60 days, the patients were also subjected to 4.8 teeth exodontia and used cephazolin sodium together with ketoprofen (100 mg/12 h/os, for 6 days). The authors evaluated postoperative pain and oedema, at 30 days distance, in both surgery phases (3.8 compared with 4.8) in the same patients, detecting the profile of the left hemiface (60 days after treatment) in respect to the right hemiface in the treated area. Data analysis showed similar reduction of postoperative pain and oedema, because of bromelain or ketoprofen administration, therefore the bromelain group was not statistically different from the ketoprofen group, evaluated 60 days after the two above-mentioned surgical sessions. Ghensi et al. (2) evaluated the effect of bromelain on discomfort after surgical extraction of impacted third molar. They included 80 patients, divided into four groups: group A (21 patients) without drug, group B (19 patients) with 40 mg bromelain taken orally every 6 hours for 6 days, group C (20 patients) with 4 mg dexamethasone sodium phosphate as a submucosal injection, and group D (20 patients) with pre-operative 4 mg dexamethasone sodium phosphate as a submucosal injection plus postoperative 40 mg bromelain taken orally every 6 hours for 6 days. The authors evaluated facial oedema and swelling, pain, trismus and number of analgesics before and after surgery, on postoperative days 2 and 7. The results showed on postoperative day 2 that there was a statistically significant reduction in facial oedema only in C and D groups compared with the A group. On post operative day 7, Group D showed a statistically significant reduction in postoperative swelling and in the number of analgesics than A group.

Drugs containing bromelain together with other substances

Isola et al. (9) investigated the effect of a

Table I. *Effects of included studies.*

Authors	Patients distribution	Mean age	Surgical procedure	Therapy	Efficacy parameters	Results
Ordesi P, et al.	80 patients: Control group (40); Experimental group (40)	Control group (30); Experimental group (28.7)	Third molar extraction	Experimental group: one bromelain tablet every 12 hours for 7 days with paracetamol as an analgesic if required. Control group: only paracetamol as an analgesic if required.	Pain, oedema, and erythema.	Significantly improvement in pain, oedema and erythema and a reduced consumption of analgesic than control group.
Yi Tan and Ping Li	72 patients: Control group (36); Experimental group (36)	Control group (23.7); Experimental group (24.3)	Third molar extraction	Control group: cold-hot compress for two days. Experimental group: bromelain enteric-coated capsules on the day of the surgery. Dosage: 30,000 units every time, three times/day, for three days.	Pain, swelling, limitation of mouth IL-25 in gingival crevicular fluid and levels of TNF-α, EGFR, and β-FGF in serum.	Pain, swelling and mouth opening in the bromelain group significantly improved than control group. the levels of IL-25 and TNF-α in the bromelain group were significantly lower than control group. EGFR and β-FGF were significantly higher in patients treated with bromelain. QOL scores were significantly better in the bromelain group.
De la Barrera-Núñez M et al.	34 patients: Control group (17); Experimental group (17)	Control group (23); Experimental group (24)	Third molar extraction	Experimental group: bromelain 150mg per day for three days and 100mg on days 4 to 7. Control group: placebo in the same dosage.	Postoperative pain, swelling and the degree of trismus.	Better values have been recorded for a swelling and improved oral aperture in the bromelain group than placebo group.
Omer Waleed Majid, et al.	45 patients: Bromelain group (15); Diclofenac group (15); Placebo group (15)	Bromelain group (23.7); Diclofenac group (22.8); Placebo group (23.8)	Third molar extraction	Both groups: 1 capsule every 6 hours, starting the morning before the day of surgery and continued for 4 days.	Pain, facial swelling, trimus and QOL.	Both bromelain and diclofenac groups showed a significant reduction in pain compared with the placebo. Diclofenac also resulted in a significant reduction of swelling at 3 and 7 days, and bromelain resulted in an insignificant reduction. Both treatment groups also showed a comparable significant difference in the effect on QOL in most subscales and total scores without difference.
Inchingolo F, et al	46 patients: Bromelain group; Ketoprofen group		Third molar extraction	After 3.8 teeth exodontia, the patients used cephazolin sodium (1 g/12 h/i.m. along 6 days) together with bromelain (40 mg/6 h/os, along 6 days). After 60 days, the patients were also subjected to 4.8 teeth exodontia, then they used cephazolin sodium together with ketoprofen (100 mg/12 h/os, along 6 days).	Pain and oedema.	Similar reduction of postoperative pain and oedema, because of bromelain or ketoprofen administration, therefore bromelain group was not statistically different from ketoprofen group, evaluated after the two up mentioned surgical sessions at 60 days distance.
Ghensi P, et al.	80 patients: Group A (21); Group B (19); Group C (20); Group D (20)	Group A (27.3); Group B (26.9); Group C (27.1); Group D (27.1)	Third molar extraction	Group A: no drug; group B: 40mg bromelain every 6hours for 6 days; group C: 4mg dexamethasone sodium phosphate as a submucosal injection; group D:d before the surgical operation 4 mg dexamethasone sodium phosphate as a submucosal injection plus postoperative 40mg bromelain every 6hours for 6 days.	Facial oedema and swelling, pain, trismus and number of analgesic before and after surgery, on postoperative day 2 and 7.	On postoperative day 2, there was a statistically significant reduction in facial oedema only in C and D groups compared with the A group. On post operative day 7, Group D showed a statistically significant reduction in postoperative swelling and in the number of analgesic than A group. .
Isola G, et al.	82 patients: Placebo group (27); Ibuprofen group (27); Experimental group (28)	Mean age: 26.8	Third molar extraction	Placebo group: sugar pill, Sucratol Capsules twice a day for 5 days; Ibuprofen group: 600 mg of this drug, twice a day for 5 days; experimental group: phytotherapeutic drug (baicalin, bromelain and escin) twice a day for 5 days.	Pain, swelling, trismus.	Phytotherapeutic drug significantly improved only postoperative pain score at 12 h and 48 h after surgery compared to placebo and ibuprofen groups while the mean reduction of swelling and trismus was similar between groups.
Bormann K, et al.	68 patients: Bromelain 1000 FIP (21); Bromelain 3000 FIP (23); Bromelain 4500 FIP (24)	Bromelain 1000 FIP (19.5); Bromelain 3000 FIP (20.6); Bromelain 4500 FIP (20.3)	Third molar extraction	Postoperative Bromelain 1000, 3000, or 4500 FIP units/day for 9 days oral route	Swelling and pain.	They have shown that there is no superiority about swelling of treatment with 3000 FIP and 4500 FIP versus 1000 FIP.
Shetty V, et al.	30 patients: Control group (15); Experimental group (15)	Control group (24); Experimental group (24)	Bimaxillary orthognathic surgery	Experimental group: twice-daily dose of systemic enzyme therapy. Control group: placebo.	Thickness of the soft tissue.	Patients treated with systemic enzyme, showed a significant improvement in soft tissue thickness than placebo.

phytotherapeutic drug with herbal extracts on postsurgical discomfort after third molar surgery in 82 patients divided into three groups: 27 treated with placebo, 27 with ibuprofen and 28 with a phytotherapeutic drug composed of baicalin (190 mg), bromelain (50 mg) and escin (30 mg). They measured postoperative pain, swelling and trismus. The authors showed that the phytotherapeutic drug significantly improved only postoperative pain score at 12 h and 48 h after surgery compared to the placebo and ibuprofen groups while the mean reduction of swelling and trismus was similar between groups. Shetty et al. (10) evaluated the effect of systemic enzyme therapy for the control of oedema in 30 patients undergoing bimaxillary orthognathic surgery: 15 patients received a twice-daily dose of systemic enzyme tablet, which contained a combination of trypsin, (96 mg), bromelain (180 mg) and rutoside trihydrate (200 mg), for five days and 15 patients received placebo. The authors measured the thickness of the soft tissue before and after surgery. At the end of the treatment, patients treated with systemic enzyme, showed a significant improvement in soft tissue thickness than placebo.

Third molar extraction and bromelain: comparison between different dosages

Bormann et al. (11) investigated the effect of bromelain in patients after wisdom teeth extraction, comparing the registered dosage 1000 FIP (Federation International Pharmaceutique) against higher dosages of 3000 FIP and 4500 FIP. In particular, the authors included 68 patients divided into three treatment groups for nine days; 21 patients received Bromelain 1000 FIP, 23 patients 3000 FIP and 24 patients 4500 FIP. The patients underwent two surgery sessions: one study period being conducted under treatment with bromelain and the other with placebo. The authors evaluated postoperative swelling and pain in comparison with baseline. They showed that there is no superiority regarding swelling of treatment with 3000 FIP and 4500 FIP *vs* 1000 FIP.

DISCUSSION

Based on our research, different clinical outcomes were analyzed: edema and pain (nine studies), trismus (five studies), analgesic consumption (two studies) and QOL score (two studies). From the analysis of four clinical trials comparing bromelain and placebo, Ordesi et al. (4), Tan and Li (5), Omer Waleed Majid et al. (7), observed a significant improvement of pain in the bromelain group compared to the control group, while only De la Barrera-Núñez et al. (6) did not register any significant difference. De la Barrera-Núñez et al. (6), Ordesi et al. (4) and Tan and Li (5) also recorded a significant amelioration in oedema in the bromelain group compared to the control group. From the analysis of the two studies evaluating the consumption of analgesics, only Ordesi et al. (4) recorded a significant reduction during bromelain treatment compared to the control group, while Ghensi et al. (2) did not registered any difference. There are two studies in which bromelain was used in combination with other substances: Shetty et al. (10) experienced bromelain, trypsin and rutoside composition, while Isola et al. (9) used the association of bromelain, escin and baicalin. One study conducted (5) cytokine detection and analysis, showing that bromelain reduced the levels of IL-25 and TNF-alfa, inflammatory cytokines, and improved EGFR and beta-FGF levels, supporting the activation of tissue repair pathways. There was no consensus regarding the dose, frequency and duration of treatment. Thus, we suggest research on the optimal dosage of the bromelain medication and the performance of more randomized clinical trials with methodological rigor and standardization. It might be interesting to evaluate the effects of bromelain in other oral surgical procedures, such as in implant dental surgery, after tonsillectomy, or in other common oral diseases like stomatitis, gingivitis, leucoplakia, and ulcers. It may be useful to evaluate the potential effects of topical bromelain administration directly on the surgical site area (12). Bromelain may be used to reduce NSAIDs dosage or for long-term treatments, eliminating patient exposure to the adverse effects associated with these medications. No serious adverse events have been reported with the consumption of bromelain. Data deriving from the present review of nine clinical studies suggest that, due to its positive action

on pain and oedema, bromelain administration plays a pivotal role in the postoperative period of patients undergoing third molar extraction. Further laboratory-based research and large-scale randomized controlled clinical trials on a larger scale are advisable to confirm these promising results.

REFERENCES

1. Casale M, Moffa A, Vella P et al. Hyaluronic acid: Perspectives in dentistry. A systematic review. Int J Immunopathol Pharmacol 2016; 29(4):572-82.
2. Ghensi P, Cucchi A, Creminelli L Tomasi C, Zavan B, Maiorana C.. Effect of oral adminis-tration of bromelain on postoperative discom-fort after third molar surgery. J Craniofac Surg 2016; 2017(28):e191-97.
3. De A C Almeida R, de Sousa Lima FCM, do E Vasconcelos BC. Is bromelain an effective drug for the control of pain and inflammation associated with impacted third molar surgery? Systematic review and meta-analysis. Int J Oral Maxillofac Surg 2018; 48(5):651-58.
4. Ordesi P, Pisoni L, Pierluigi N Macchi M, Borloni R, Siervo S. Therapeutic efficacy of bromelain in impacted third molar surgery: A randomized controlled clinical study. Quintessence Int 2016; 2014(45):679-84.
5. Tan Y, Ping Li P. Bromelain has significant clinical benefits after extraction of the third molar during chemotherapy in patients with hematologic tumour. Oncol Lett 2018; 15(3):2962-66.
6. De la Barrera-Núñez M, Yáñez-Vico M, Batista-Cruzado A, et al. Prospective double-blind clinical trial evaluating the effectiveness of Bromelain in the third molar extraction postoperative period. Med Oral Patol Oral Cir Bucal 2014; 19(2):e157-62.
7. Omer Waleed Majid Al-Mashhadani BA. Perioperative bromelain reduces pain and swelling and improves quality of life measures after mandibular third molar surgery: a randomized, double-blind, placebo-controlled clinical trial. J Oral Maxillofac Surg 2016; 2014 (72):1043.
8. Inchingolo F, Tatullo M, Marrelli M et al. Clinical trial with bromelain in third molar exodontia. Euro Rev Med Pharmacol Sci 2010; 14:771-74.
9. Isola G, Matarese M, Ramaglia L. Iorio-Siciliano V, Cordasco G, Matarese G. Efficacy of a drug composed of herbal extracts on postoperative discomfort after surgical removal of impacted mandibular third molar: a randomized, triple-blind, controlled clinical trial. Clinical Oral Investigations 2018; 23(5):2443-53.
10. Shetty V, Mohan A. A prospective, randomized, double-blind, placebo-controlled clinical trial comparing the efficacy of systemic enzyme therapy for edema control in orthognathic surgery using ultrasound scan to measure facial swelling. American Association of Oral and Maxillofacial Surgeons J Oral Maxillofac Surg 2013; 71(7):1261-67.
11. Bormann K, Kristina Weber K, Kloppenburg H Staude P, Koch A, Meiser P, Gellrich NC. perioperative bromelain therapy after wisdom teeth extraction – a randomized, placebo- controlled, double-blinded, three-armed, cross-over dose-finding study. Phytother Res 2016; 30(12):2012-19.
12. Casale M, Moffa A, Cassano M et al. Saline nasal irrigations for chronic rhinosinusitis: From everyday practice to evidence-based medicine. An update. Int J Immunopathol Pharmacol 2018; 32:2058738418802676.

JOURNAL OF BIOLOGICAL REGULATORS & HOMEOSTATIC AGENTS Vol. 33, no. 5, 1635-1639 (2019)

LETTER TO THE EDITOR

ANALYSING THE ROLE OF STAT3 IN HIV-1 INFECTION

S.V. IBBA[1*], C. FENIZIA[2*], P. SERNA ORTEGA[1], V. MERCURIO[1], I. SAULLE[1], E.M. LORI[1], D. TRABATTONI[1], M. CLERICI[2,3] and M. BIASIN[1]

[1]Department of Biomedical and Clinical Sciences "L. Sacco", University of Milan, Milan; [2]Department of Pathophysiology and Transplantation, University of Milan, Milan; [3]Don Carlo Gnocchi Foundation, IRCCS, Milan, Italy

Received April 2, 2019 – Accepted June 28, 2019

[*]These Authors contributed equally to the manuscript

To the Editor,

Signal transducer and activators of transcription-3 (STAT3) is differentially regulated in viral infections, including HIV-1 infection (1). Indeed, STAT3 stimulation by viral proteins results in the transcription of several inflammatory proteins and micro RNAs (miRNAs) that are possibly involved in the recruitment and activation of lymphocytes and can be endowed with either pro- or anti-viral properties (1, 2). STAT3, like the other members of the STAT family, is activated by cytokine and growth factor receptors on the cellular membrane, and in turn regulates gene transcription (2, 3). In particular, STAT3 main activators are interleukin (IL)-6, IL-10, IL-23, IL-21, IL-12, interferon (IFN)γ, tumor necrosis factor (TNF)α, granulocytic colony stimulating factor (G-CSF), monocyte chemoattractant protein (MCP1), CCL3 and CCL5/RANTES (2–5). STAT3 activation plays a role in a number of processes including cell cycle, differentiation, pluripotency and apoptosis (3). STAT3 is activated by phosphorylation (mainly via JAK) and translocates into the nucleus, where it binds to its specific DNA consensus sequences, including IFN-stimulated response elements (ISRE), to regulate targets transcription (2, 4). STAT3 is endowed with multiple functions, some of which appear to be contradictory (6). Thus, STAT3 might act as a negative regulator of type I IFNs, depending on the cellular context (2, 4). Moreover, even un-phosphorylated STAT3 was shown to regulate the transcription of multiple genes *via* NFκB, triggering a pro-inflammatory response and the induction of IL12 production (6, 7).

HIV-1 infection activates STAT3, mostly as a consequence of its interaction with Nef (1, 4); the net result of such activation is not fully clarified and is the topic of this study.

MATERIALS AND METHODS

PBMCs isolated from 20 healthy controls were infected *in vitro* with HIV-1_{BaL}, as elsewhere described (8), in presence/absence of a specific STAT3 inhibitor (Stat3 inhibitor V, Stattic®). Cells were pre-treated with Stattic for 3 h before infection and analyzed on day 7 post-infection. Stattic selectively inhibits activation, dimerization, and nuclear translocation of STAT3. Healthy volunteers signed an informed consensus, following Helsinki regulation. Since STAT3 inhibitor reduces cell viability, a curve dose-response was assessed

Key words: STAT3; HIV-1; STAT3 inhibitor; miRNA29

Corresponding Author:
Dr Claudio Fenizia,
Dept. of Pathophysiology and Transplantation,
University of Milan,
Via F. Sforza 35, 20122, Milan
Tel.: +39 02 50319678
e-mail: claudio.fenizia@unimi.it

0393-974X (2019)

DISCLOSURE: ALL AUTHORS REPORT NO CONFLICTS OF INTEREST RELEVANT TO THIS ARTICLE.

and a non-toxic concentration was thoroughly identified at 2.5 μM. Cell viability was assessed by counting the total number of cells and the fraction of vital cells by ADAM MC Automated Mammalian Cell Counter (NanoEnTek Inc). p24 viral antigen was measured in cell supernatant by ELISA (ExpressBio). Expression level of 84 genes involved in the STAT3 pathway was analyzed 7-days post infection by real time PCR array (Qiagen). Donors were pooled for such arrays. Changes in expression level > 1.5-fold between the untreated control and those STAT3 inhibitor-treated were confirmed by real time PCR (9, 10). CCL3 (MDSystem), IL-1β (Thermofisher), IL-12b/p40 (Novusbio), IL-6 (Thermofisher) and pan-IFNα (StemCell) production was measured by ELISA. MiRNAs were isolated and quantified by real time PCR 7-day post infection, as elsewhere described (5). Results were corrected for outlier calculation and the samples excluded from analyses. Unpaired *t*-tests were performed by GraphPad Prism.

RESULTS

STAT-3 inhibitor reduces in vitro HIV-1 infection in PBMCs

In vitro HIV-1 infection of PBMCs was consistently reduced by the STAT3 inhibitor, according to p24 concentration in supernatants (Fig. 1a). The overall inhibition of HIV-1 replication *in vitro* was 54.3% for STAT3 inhibitor treated cells as compared to untreated condition (p value < 0.02).

STAT-3 inhibitor induces antiviral cytokines/ chemokines in HIV-1 infected cells

Gene expression analysis was performed using a real-time PCR array that screens simultaneously 84 genes involved in viral infections (Table I); the results are shown in Fig. 1b and were confirmed by real time PCR (Fig. 1c). Gene expression analysis showed that the expression of a number of immune proteins with a known anti-HIV effect including CCL3 (p value < 0.006), IL-1β (p value < 0.02) and IFNα (p value < 0.02) (Fig. 1c) was significantly increased by STAT3 inhibition. Notably, we also observed a 23-fold increase in the mRNA expression of IL-12b (p value < 0.01) but not in that of IL-12a (data not shown). IL-6 was significantly reduced by the STAT3 inhibitor (p value < 0.02) and, although changes did not reach statistical significance, an upregulation of cytotoxic activity genes, including granzyme and IFNγ mRNA was seen (data not shown). These results were confirmed by analysis of cytokine production. Thus, CCL3 (p value < 0.03), IL-1β (p value < 0.001) and IL-12b (subunit p40) (p value < 0.004) were increased by the STAT-3 inhibitor (Fig. 2a). Finally, IL-6 was decreased and IFNα was increased by STAT-3 inhibition, even if statistical significance was not reached.

STAT-3 inhibitor downregulates miRNA29 family

miRNA29 family, isoforms a, b and c, were shown to exert a protective function against HIV-1 infection. The STAT3 inhibitor reduced miRNA29 a, b, c expression 7 days post-infection (Fig. 2b), although these differences did not reach statistical significance. These data are consistent with the previously described ability of miRNA29 to down regulate IL-12b mRNA expression (11).

DISCUSSION

STAT3 is a well-known transcription factor involved in the anti-HIV-1 immune response. Indeed, STAT3 is activated by viral proteins and this leads to the release of several inflammatory proteins, such as interferon-stimulated genes and the pro-inflammatory cytokine IL-6 (6). In order to better understand the role of STAT3 during HIV-1 infection, we selectively inhibited STAT3 activation. Unexpectedly, STAT3 inhibition led to an increased *in-vitro* protection against HIV-1 infection. STAT3 relies on multiple mechanisms of action and comprises different activation pathways (3). In fact, STAT3 inhibition still resulted in a significant upregulation of multiple genes with immune anti-HIV properties, including CCL3, IL-1β, IFNα and IL-12b. Although IL-12 classically includes both IL-12a and b subunits, IL-12b itself can homo-dimerize and bind its receptor, preserving cytokine effects (11). Moreover, this is consistent with the observed decrease of miRNA29. In fact, as previously reported, miRNA29 can bind IL-12b in order to downregulate it (7). STAT3 is one of the transcription factors responsible for miRNA29

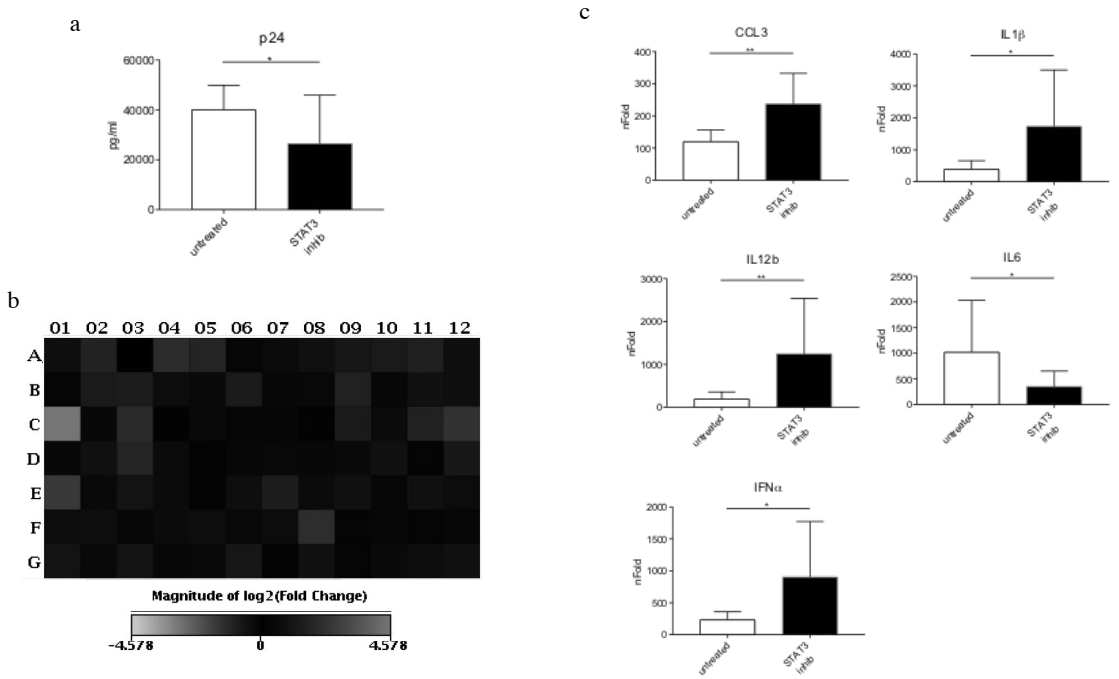

Fig. 1. ***a****) p24 viral antigen in untreated (white) or 2.5 µM STAT3 inhibitor treated (black) PBMCs' supernatant at day 7 post-infection (p value < 0.02).* ***b****) Heat map of differential gene expression by real-time PCR array on pooled untreated or 2.5 µM STAT3 inhibitor treated PBMCs' mRNA at day 7 post-infection.* ***c****) Real time PCR in untreated (white) or 2.5 µM STAT3 inhibitor treated (black) PBMCs at day 7 post-infection. Statistic was assessed by unpaired t-test (n =20). Bars represent standard error.*

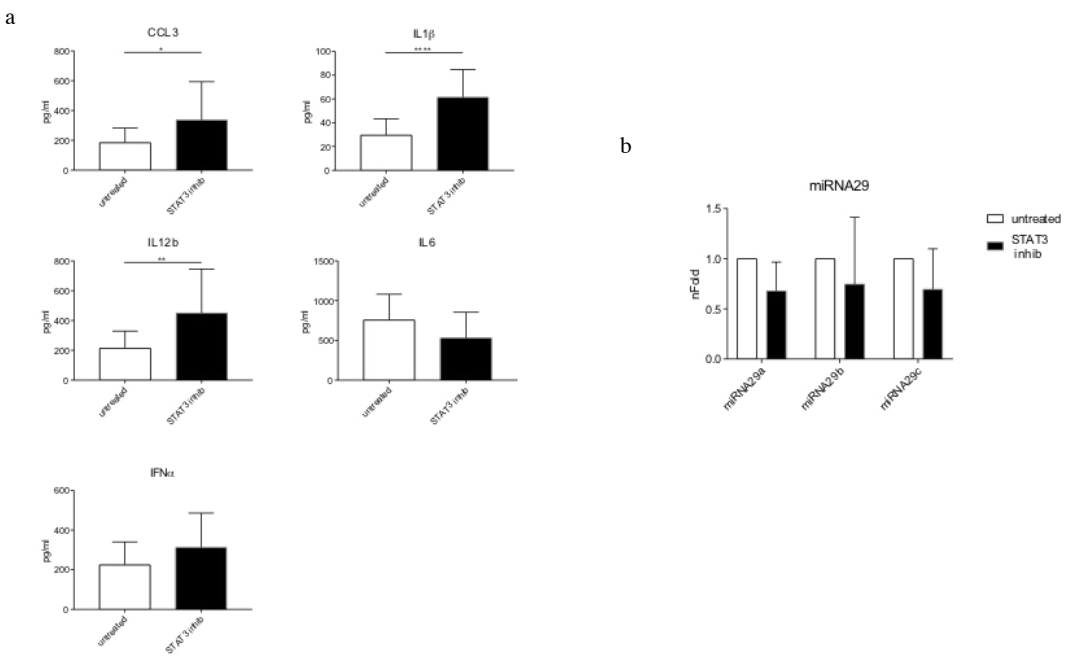

Fig. 2. ***a****) ELISA on supernatant of untreated (white) or 2.5 µM STAT3 inhibitor treated (black) PBMCs at day 7 post-infection. Statistic was assessed by unpaired t test (n =20). Bars represent standard error.* ***b****) quantification by real time PCR of miRNA29a, -b or –c in untreated (white) or 2.5 µM STAT3 inhibitor treated (black) PBMCs at day 7 post-infection. Statistic was assessed by unpaired t-test (n =20). Bars represent standard error.*

Table I. *Genes analyzed by PCR array, referred to the heat map depicted in Fig. 1b.*

Layout	01	02	03	04	05	06	07	08	09	10	11	12
A	AKT1 -1.32	APCS 3.16 B	BIRC3 1.00	BPI 4.15 B	CAMP -2.09 B	CARD6 -1.07	CARD9 1.45 A	CASP1 -1.37	CASP8 -1.59	CCL3 2.46	CCL5 -1.93	CD14 1.75 B
B	CHUK -1.06	CRP 2.43 B	CTSG 2.60 B	CXCL1 -1.24 B	CXCL2 1.42	DMBT1 2.50 B	FADD -1.12	HSP90AA1 1.35	IFNA1 2.99 B	IFNB1 1.29 B	IKBKB -1.40	IL12A 1.73
C	IL12B 23.89	IL18 1.29	IL1B 3.94	IL6 -1.83	CXCL8 1.37	IRAK1 1.18	IRAK3 1.21	IRF5 -1.03	IRF7 -1.72	JUN -1.23	LBP 3.06 B	LCN2 4.77 B
D	LTF 1.30 B	LY96 -1.38	LYZ 3.37	MAP2K1 -1.24	MAP2K3 1.08	MAP2K4 -1.09	MAP3K7 -1.17	MAPK1 -1.14	MAPK14 -1.19	MAPK3 -1.43	MAPK8 -1.05	MEFV 2.31 B
E	MPO 5.92 B	MYD88 -1.15	NAIP -1.49	NFKB1 -1.24	NFKBIA 1.07	NLRC4 -1.31	NLRP1 -1.83	NLRP3 -1.22	NOD1 -1.41	NOD2 -1.07	PIK3CA -1.42	PRTN3 1.54 B
F	PSTPIP1 -1.25	PYCARD -1.33	RAC1 -1.10	RELA -1.21	RIPK1 -1.30	RIPK2 1.35	SLC11A1 1.52	SLPI 4.21 B	SUGT1 -1.06	TICAM1 -1.11	TICAM2 1.12	TIRAP -1.09
G	TLR1 -1.49	TLR2 1.41	TLR4 2.07 A	TLR5 1.27 B	TLR6 -1.17	TLR9 -1.60	TNF 1.07	TNFRSF1A -1.43	TOLLIP 1.14	TRAF6 -1.20	XIAP -1.28	ZBP1 -1.43

expression (5, 11). Thus, it is not surprising to find miRNA29 downregulated upon STAT3 inhibition. IL-6 was previously reported to have a protective function against HIV infection (11, 12). By inhibiting STAT3 we observed a decrease in IL-6 expression, which unexpectedly was coupled with a reduction of HIV-1 replication. We believe that this is not contradictory with the protective role of IL6 in HIV-1 infection as, upon STAT3 inhibition, the antiviral immune response relies on other pivotal mechanisms, possibly driven by NFκB. Notably, STAT3 inhibition is associated with the elicitation of both innate and adaptive immune antiviral mechanisms, suggesting that the inhibition of STAT3 activity should be investigated for the design of novel therapeutic agents against HIV infection.

REFERENCES

1. Gong G, Waris G, Tanveer R, Siddiqui A. Human hepatitis C virus NS5A protein alters intracellular calcium levels, induces oxidative stress, and activates STAT-3 and NF-κB. Proc Natl Acad Sci U S A 2001; 98:9599-604. doi:10.1073/pnas.171311298.
2. Costa-Pereira AP, Tininini S, Strobl B, et al. Mutational switch of an IL-6 response to an interferon-γ-like response. Proc Natl Acad Sci U S A 2002; 99:8043-47. doi:10.1073/pnas.122236099.
3. Yu H, Pardoll D, Jove R. STATs in cancer inflammation and immunity: a leading role for STAT3. Nat Rev Cancer 2009; 9:798-809. doi:10.1038/nrc2734.
4. Wang W-B, Levy DE, Lee C-K. STAT3 Negatively Regulates Type I IFN-Mediated Antiviral Response. J Immunol 2011; 187:2578-85. doi:10.4049/jimmunol.1004128.
5. Ortega PA s, Saulle I, Mercurio V, et al. Interleukin 21 (il-21)/microrna-29 (mir-29) axis is associated with natural resistance to Hiv-1 infection. Aids 2018; 32:2453-61. doi:10.1097/QAD.0000000000001938.
6. Suarez AAR, Renne NV, Baumert TF, Lupberger J. Viral manipulation of STAT3: Evade, exploit, and injure. PLOS Pathog 2018; 14:e1006839. doi:10.1371/journal.ppat.1006839.
7. Brain O, Owens BMJ, Pichulik T, et al. The Intracellular Sensor NOD2 Induces MicroRNA-29 Expression in Human Dendritic Cells to Limit IL-23

Release. Immunity 2013; 39:521-36. doi:10.1016/j.immuni.2013.08.035.

8. Sironi M, Biasin M, Cagliani R, et al. A Common Polymorphism in TLR3 Confers Natural Resistance to HIV-1 Infection. J Immunol 2012; 188:818-23. doi:10.4049/jimmunol.1102179.
9. Fenizia C, Fiocchi M, Jones K, et al. Human T-Cell Leukemia/Lymphoma Virus Type 1 p30, but Not p12/p8, Counteracts Toll-Like Receptor 3 (TLR3) and TLR4 Signaling in Human Monocytes and Dendritic Cells. J Virol 2014; 88:393-402. doi:10.1128/JVI.01788-13.
10. Vaccari M, Fenizia C, Ma Z-M, et al. Transient increase of interferon-stimulated genes and no clinical benefit by chloroquine treatment during acute simian immunodeficiency virus infection of macaques. AIDS Res Hum Retroviruses 2014; 30:355-62. doi:10.1089/aid.2013.0218.
11. Adoro S, Cubillos-Ruiz JR, Chen X, et al. IL-21 induces antiviral microRNA-29 in CD4 T cells to limit HIV-1 infection. Nat Commun 2015; 6:7562. doi:10.1038/ncomms8562.
12. Vanpouille C, Introini A, Morris S, et al. Distinct cytokine/chemokine network in semen and blood characterize different stages of HIV infection. Aids 2016; 30:193-201. doi:10.1097/QAD.0000000000000964.

JOURNAL OF BIOLOGICAL REGULATORS & HOMEOSTATIC AGENTS Vol. 33, no. 5, 1641-1646 (2019)

LETTER TO THE EDITOR

A NEW HISTOLOGICAL METHOD TO STUDY ORAL SOFT TISSUE PENETRABILITY TO IODINE AND OPTIMIZE ORAL USE OF IODINE SOLUTIONS

D. ZAFFE[1], S. SPINATO[2] and C. BERTOLDI[3]

[1]Department of Biomedical, Metabolic and Neural Sciences, University of Modena and Reggio Emilia, Modena, Italy; [2]Private Practice, Sassuolo MO, Italy; [3]Department of Surgery, Medicine, Dentistry and Morphological Sciences with Transplant Surgery, Oncology and Regenerative Medicine Relevance, University of Modena and Reggio Emilia, Modena, Italy

Received June 6, 2019 – Accepted July 18, 2019

To the Editor,

Iodine tincture, formulated in 1908, was initially used as skin disinfectant but caused burns due to high iodine-content (7%). The formulation of 'tamed' iodine solutions including carriers, for example polyvinylpyrrolidone (PVP), complexed with 1% iodine content or lower, have almost completely eliminated problems created by iodine tincture. In addition to skin disinfectant, tamed iodines replaced iodine tincture and, after demonstrating effectiveness against several pathogens, have been widely used in both dentistry and periodontology (1). In addition to its disinfectant capacity, iodine reacts histochemically with glycogen and has been used for over half a century to discriminate cancer areas of the cervix and esophagus (2), more clearly identify the mucogingival junction, and more recently, to detect oral lesions (2).

Excluding Xiao's et al. investigations (3), no other evidence of iodine penetration has been produced histologically after treatment with either iodine or povidone-iodine solutions, due to the extreme solubility of iodine compounds in water solutions. Xiao et al. achieved good results from the brown iodine staining of tissues (3), but required the freezing of the tissue in dry ice-acetone (-78°C), cryostatic sectioning, xylene treatment and immediate photographing of samples, due to the rapid disappearance of the brown iodine-staining of tissue. Furthermore, no simultaneous revelation of cell or tissue structures results, as water immediately removes the brown color of the iodine-stained tissue.

The aim of this work is to establish a histological method to fix iodine inside slides of treated oral mucosa more permanently in order to allow section counterstaining and facilitate improved clinical and experimental studies on iodine penetration.

MATERIALS AND METHODS

The present study was performed on samples of oral mucosa taken from 15 patients, aged between 18 and 47 years, requiring extraction of a partially erupted third molar. All patients considered in this perspective study signed an informed consent detailing all procedures of the treatment, as requested by the Helsinki protocols.

After administration of 4% articaine solution with adrenaline 1:100.000 (Artin, Omnia, Fidenza, Italy), the oral mucosa was cleansed for 2 min with a 10% povidone-iodine solution (Betadine, Mundipharma,

Key words: histology; oral mucosa; microbiota; povidone iodine; staining; wisdom tooth.

Corresponding Author:
Prof. Carlo Bertoldi,
Dipartimento Chirurgico, Medico,
Odontoiatrico e di Scienze Morfologiche
Università di Modena e Reggio Emilia,
Via del Pozzo 71, 41124, Modena, Italy
Tel.: ++39 0594224101 - Fax: ++39 0594373428
e-mail: carlo.bertoldi@unimore.it

0393-974X (2019)

DISCLOSURE: ALL AUTHORS REPORT NO CONFLICTS OF INTEREST RELEVANT TO THIS ARTICLE.

Basel, Switzerland) to disinfect the third-molar area before extraction. A vestibular incision along the bone ridge was performed. A full-thickness flap was elevated in order to expose the third-molar crown. The extraction was then carried out using levers and traditional high speed steel drills (Zekrya, Dentsply Maillefer, Ballaigues, Switzerland) with cool irrigation. High speed drills were sometimes used to create space for lever insertion and subsequent luxation or to perform a coronoidectomy. In the latter case, levers were also used to separate tooth fragments, in agreement with standard surgical protocols. After complete root removal, sockets were curetted of all soft tissue debris. Sutures (Vicryl, Ethicon) were carried out to close the flap. At this time, a 3×4 mm sample was taken when an excess of oral mucosa occurred (which should be eliminated) of this partially erupted third-molar area. When excess oral mucosa was largely abundant, an additional small sample had to be taken and it was used as control mucosa (4). Amoxicillin (Ratiopharm GmbH, Ulm, D89079 Germany), 1 g, twice-a-day for 6-7 days and, if required, Synflex forte 550mg (Recordati SpA, 20148 Milano, Italy) as analgesic were recommended after surgery. The patients were instructed to use a chlorhexidine mouthwash (0.12%) twice a day and to avoid brushing the surgical site for one week. Sutures were removed 7 days after surgery.

Taking care to keep the epithelium facing upwards, 3×4 mm excised mucosa fragments were immediately treated for 2 min with one of the following solutions: A) 1% Silver nitrate in 0.1 M potassium nitrate in water; B) 1% Silver nitrate in 0.1 M potassium nitrate in 25% ethanol; C) 1% Silver nitrate in 75% ethanol. After silver nitrate treatment, mucosa (silver mucosa) samples were rinsed for 5 seconds in fresh 0.15 M potassium nitrate. The 5-second potassium nitrate rinse was then repeated for each mucosa sample. Samples were then sutured individually onto pieces of cardboard using silk stitches, always taking care to keep the epithelium facing upwards. Samples were then fixed in 4% paraformaldehyde in water for 2-4 h at room temperature. Samples were then treated first with 70% ethanol, then dehydrated and were then methyl methacrylate (MMA)-infiltrated as reported elsewhere (4). The MMA infiltrated mucosa samples were then removed from the cardboard and placed between two 1-cm thick (plane-parallel) poly methyl methacrylate (PMMA) blocks and inserted into a container filled with polymerizing solution. Polymerization was performed using a water bath at 4°C. Control mucosa samples were only paraformaldehyde-fixed and methyl methacrylate-embedded.

The transparent PMMA silver mucosa samples were sectioned by a plane orthogonal to the epithelium layer. Five-µm sections were individually laid down onto 127-µm-thick copper (999‰) plates, covered with a small polyethylene sheet and placed at 65°C for 24 h. Each copper plate was then fastened to a Philips aluminum stub using biadhesive tape. A few drops of acetone were then poured onto the surface of each PMMA section, adhering it to the copper plate and, after acetone evaporation, the acetone process was repeated up to 4-5 times until total PMMA dissolution.

Silver mucosa specimens were then analyzed under scanning electron microscope (SEM Quanta 200 (FEI) equipped with X-ray energy dispersive microscopy chemical microanalysis (EDS INCA-350, Oxford instruments, Abingdon, United Kingdom) in order to analyze the different effects of treatment with the 3 silver nitrate solutions. Analysis was performed in a low vacuum water-saturated conductive atmosphere (0.53 Torr) at 20 KV, with no metal sputtering, using a solid state backscattered electron detector. The chemical composition of analyzed surfaces was checked using EDS microanalysis.

The PMMA blocks containing the embedded silver mucosa treated with the most efficacious of the 3 silver nitrate solutions, as well as the PMMA blocks containing the control mucosa, were later sectioned to obtain 5-µm sections that were lain on glass slides and were then covered by a polyethylene sheet and kept at 65°C for 24 h. After PMMA removal by methyl acetate/xylene, silver mucosa sections were hydrated through graded ethanols to water, washed in distilled water for 5 min and then treated with high-contrast photographic developer, for 5 min. After a short wash in distilled water, slides were fixed in 5% sodium thiosulphate for 5 min. Silver mucosa sections were then washed in 3 subsequent distilled water baths (1 min each) and then counterstained with either 0.05% Fast Green in 0.05% Acetic acid or with 0.05% Azure II in water (1 min each). After tap water washing, stained sections were dehydrated, cleared in xylene, and D.P.X. (Sigma-Aldrich, St. Louis MO) mounted. Control mucosa sections were hydrated, stained with 0.05% Azure II and mounted. After PMMA removal and subsequent rehydration, some silver

mucosa slides were used to stain the glycogen component by periodic acid-Schiff reaction (3). After water washing, sections were counterstained with Fast Green, washed, dehydrated, cleared and D.P.X.-mounted.

RESULTS

Morphological analyses performed under scanning electron microscope (SEM) highlighted the presence of elements with the greatest atomic numbers in white or light gray when observed by backscattered detector (Fig. 1) in all examined sections of mucosa treated with povidone-iodine and silver nitrate (silver mucosa). Silver mucosa samples showed the presence of light colored material in the external layer of the epithelium with different outcomes produced by the

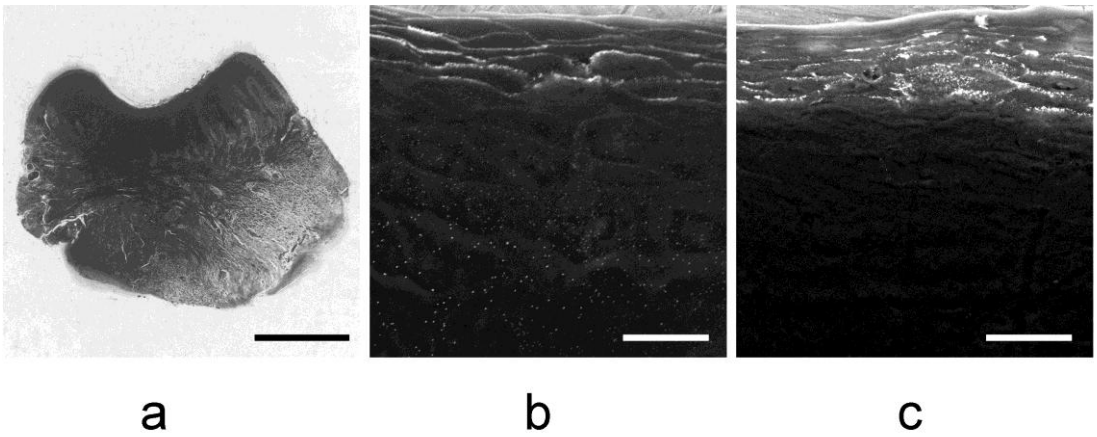

Fig. 1. *Backscattered SEM images (SEM Quanta 200 FEI, 20 kV, 0.53 Torr, no sputtering) showing a 5-µm section of povidone-iodine treated mucosa at low magnification (**a**), and, at high magnification, the external side of the epithelium of mucosa treated with the silver nitrate solution B (**b**) and C (**c**). Notice the lesser amount of white/light gray granular material surrounding some peripheral cells of the epithelium (b) and the greater amount of white/light gray granular material, also spreading into the keratinocyte cytoplasm (c). Bars: a = 1 mm; b = c = 25 µm.*

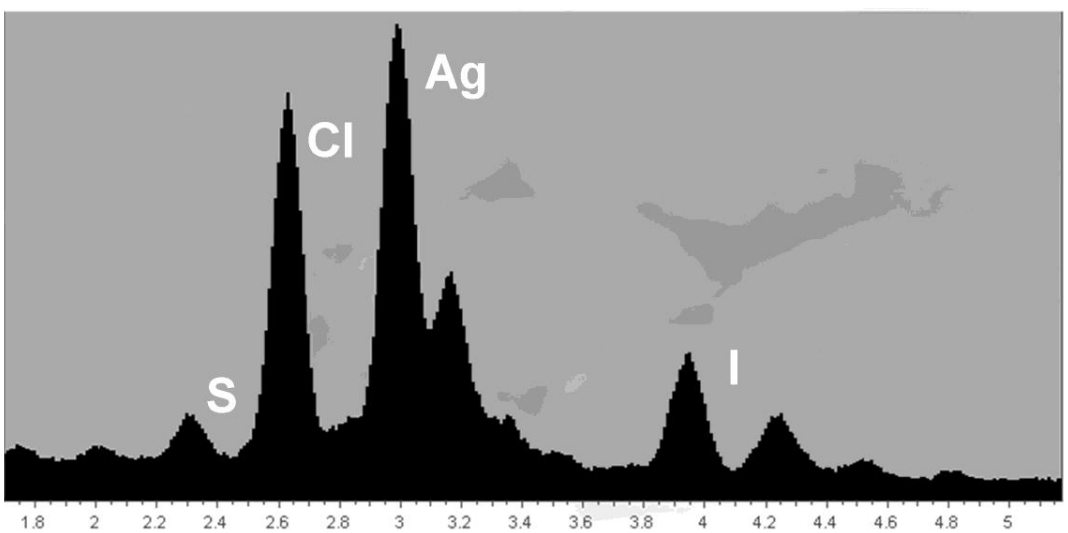

Fig. 2. *X-ray microanalysis of the granular material of mucosa treated with (alcoholic) silver nitrate solution 3 (see Fig. 1c). The X-ray microanalysis shows that, in addition to sulphur (S) and chlorine (Cl), due to the underlying membrane/cytoplasm components of keratinocytes (sulphur protein and intracellular electrolyte, respectively), the granular material resulted to be composed of silver (Ag), with two distinctive peaks, at 2.98 KeV-Lα and 3.15 KeV-Lβ and iodine (I) with two distinctive peaks, at 3.94 KeV-Lα and 4.22 KeV-Lβ.*

3 different silver nitrate solutions. Treatment with the aqueous solutions (solutions A and B) produced a faint outline of only a few cells of the external layer of the epithelium (Fig. 1b). On the contrary, treatment with the alcoholic solution (solution C) produced a larger amount of granular material which also spread into the keratinocyte cytoplasm (Fig. 1c). X-ray microanalysis showed that this granular material, highlighted by backscattered SEM analysis (Fig. 1b), was composed of silver, chlorine and, in a lesser amount, sulfur in samples treated with solutions A and B. On the contrary, X-ray microanalysis showed that granules, highlighted by backscattered SEM analysis (Fig. 1c), in samples treated with the alcoholic solution C were composed of silver, and also iodine, chlorine and, in a lesser amount, sulfur (Fig. 2).

Silver mucosa sections processed with solution C and treated with photographic developer highlighted that silver precipitation, i.e. povidone-iodine propagation, formed a layer almost parallel to the external surface of the epithelium, irrespective of epithelium thickness (Fig. 3). Povidone-iodine propagation proceeded as far as surrounding keratinocytes, even if some spreading into the cytoplasm of some cells could be seen, particularly in the innermost cell ranks (Fig. 3). Povidone-

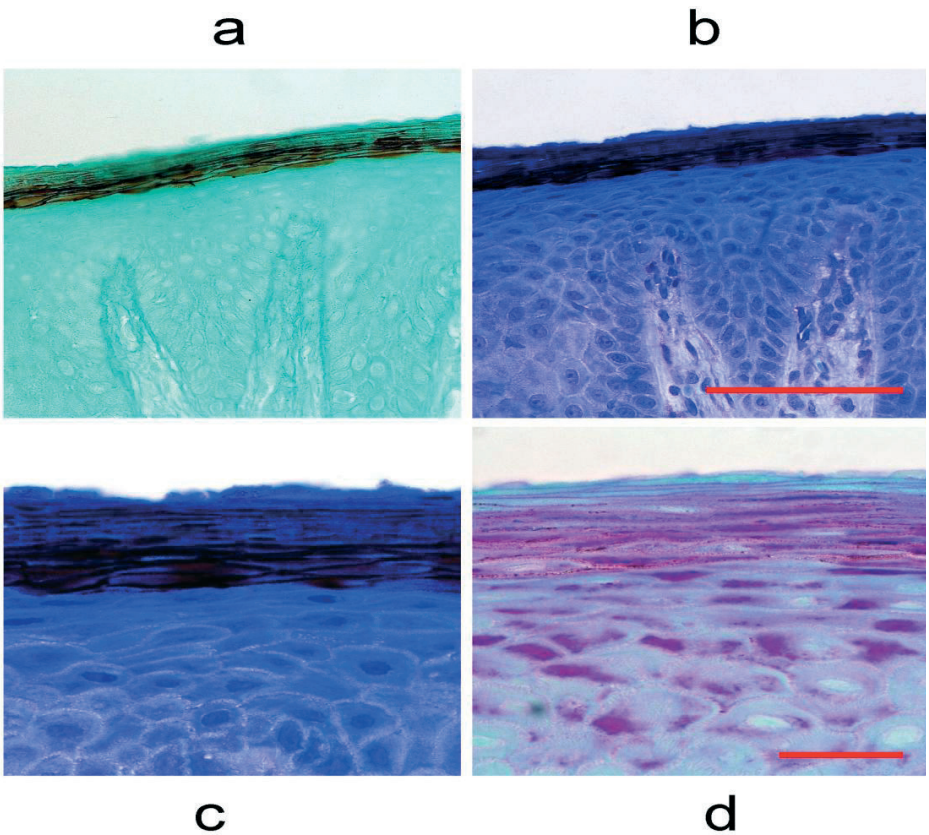

Fig. 3. *Histological sections of povidone-iodine-treated mucosa undergoing silver reduction and counterstained (**a**) with Fast Green and (**b**) Azure II (low magnification); (**c**) undergoing silver reduction and Azure II counterstaining, and (**d**) not undergoing silver reduction but stained with PAS reaction to highlight the glycogen content (high magnification). Notice in a and b how the reduced silver layer (corresponding to iodine propagation) forms almost parallel to the external surface of the epithelium, irrespective of local epithelium thickness, and in c how the silver layer, progressing uniformly from the external to the basal surface of the epithelium, reached the middle of the of the prickle cell layer. Notice in d how silver salts reacted with Schiff's reagent, forming red/pink lines contouring cells, thus creating an artifact. Bars: a = b = 100 µm; c = d = 25 µm.*

iodine layer thickness ranged from 25 to 30 μm and povidone-iodine propagation concerned the more peripheral to the middle cells of the prickle cell layer (Fig. 3). The PAS reaction treatment of silver mucosa sections, treated with silver nitrate but not treated with photographic developer, highlighted that silver halides had reacted with the Schiff's reagent used after periodic acid oxidation (Fig. 3d). In the layer corresponding to presence of silver (i.e. povidone iodine propagation) cells were surrounded by a red/pink granular material which did not spread into their cytoplasm.

PMMA blocks and sections of silver mucosa exposed to daylight for 6-12 months before photographic developing resulted much less effective than sections of silver-treated mucosa photographically developed immediately after PMMA polymerization. The latter slides remained unchanged after 12 months of exposure to daylight.

DISCUSSION

Tissue healing and regeneration depends on several variables: healthy systemic conditions (5), materials and techniques used on soft and hard tissues (6, 7), and devices used to apply these materials (8). However, the control of infection and inflammation is fundamental (9, 10). Iodine solutions are effective against several pathogens but only at an effective strength (11). Currently, no methods are available to define the degree of penetration of iodine solutions into tissues, therefore it is impossible to study their clinical and diagnostic effectiveness.

Povidone iodine is a stable complex of polyvinylpyrrolidone (povidone, PVP) and I_3^- (12). In aqueous media, $I_3^- \leftrightarrow I_2 + I^-$ and $I_2 + H_2O \leftrightarrow HOI + I^- + H^+$ release iodine ions (12). These two reactions may explain why Xiao et al. (3) worked with frozen sections and xylene, as iodine compounds quickly decay in water solutions. The povidone-iodine and silver nitrate reaction profit from both equilibrium reactions to form insoluble silver iodide.

In accordance with the study of Xiao et al. (3), alcoholic solution (75% ethanol) produces the best results as it is similar to the solvent composition of the iodine tincture, allowing silver nitrate dissolution and preventing iodine diffusion, thus allowing silver iodine formation. Reagents to process povidone-iodine treated mucosa must be chosen carefully without halides or other anions reacting with silver, and paraformaldehyde should be dissolved in water not buffered solutions. Methacrylate embedding was chosen for two reasons. The first, and most important, is the transparency of PMMA allowing mucosa biopsy identification and correct sectioning. The second is that PMMA is the usual embedding media in the Authors' bone laboratory. However, other suitable embedding media, such as paraffin, celloidin, Spurr's resin, after careful checking for undesirable silver reactions, can be used.

Contrary to Xiao et al.'s air-unsteady, no counterstained and low-contrast iodine method (3), the histological method we propose produces good results. Developed iodide has a high contrast, allowing easy discrimination with most counterstain processes. Some staining techniques require different procedures: halides must be removed with one or more 5% sodium thiosulphate baths, before, for instance, PAS which reacts with silver salts. The best results are obtained immediately after PMMA polymerization. Although povidone-iodine stained compounds remained unchanged after 1 year of exposure to daylight, keeping PMMA blocks in the dark is beneficial for stained slide preservation and silver reactivity.

In conclusion, transforming iodine into a stable histological formation inside tissues is particularly useful for histological analysis of clinical and experimental iodine treatments. In the field of oncology, this method can be applied to povidone-iodine-treated (human or animal) mucosa or skin, to organs treated with iodine tincture or Lugol's solution, to oral lesion detection and to mucogingival junction identification.

REFERENCES

1. Van der Sluijs M, Van der Sluijs E, Van der Weijden F, Slot DE. The effect on clinical parameters of periodontal inflammation following non-surgical periodontal therapy with ultrasonics and chemotherapeutic cooling solutions: a systematic

review. J Clin Periodontol 2016; 43:1074-85.
2. Kurita H, Kurashina K. Vital staining with iodine solution in delineating the border of oral dysplastic lesions. Oral Surg Oral Med Oral Pathol Oral Radiol Endod 1996; 81:275-80.
3. Xiao T, Kurita H, Li X, Qi F, Shimane T, Aizawa H, Uehara S. Iodine penetration and glycogen distribution in vital staining of oral mucosa with iodine solution. Oral Surg Oral Med Oral Pathol Oral Radiol Endod 2014:117:754-59.
4. Bertoldi C, Zaffe D, Generali L, Lucchi A, Cortellini P, Monari E. Gingival tissue reaction to direct adhesive restoration: A preliminary study. Oral Dis 2018; 24:1326-35.
5. Bertoldi C, Balli F, Tanza D, Bertolani P, Chiarini L Experimentation and clinical analysis of the interrelationships between dental damage and celiac disease. Minerva Stomatol 1995; 44:395-405.
6. Consolo U, Bertoldi C, Zaffe D. Intermittent loading improves results in mandibular alveolar distraction osteogenesis. Clin Oral Implants Res 2006; 17:179-87.
7. Bertoldi C, Bencivenni D, Lucchi A, Consolo U. Augmentation of keratinized gingiva through bilaminar connective tissue grafts: a comparison between two techniques. Minerva Stomatol 2007; 56:3-20
8. Bertoldi C, Pradelli JM, Consolo U, Zaffe D Release of elements from retrieved maxillofacial plates and screws. J Mater Sci Mater Med 2005; 16: 857-61.
9. Bertoldi C, Pellacani C, Lalla M, Consolo U, Pinti M, Cortellini P, Cossarizza A Herpes Simplex I virus impairs regenerative outcomes of periodontal regenerative therapy in intrabony defects: a pilot study. J Clin Periodontol 2012; 39:385-92.
10. Bertoldi C, Bellei E, Pellacani C, et al. Non-bacterial protein expression in periodontal pockets by proteome analysis. J Clin Periodontol 2013; 40:573-82.
11. Managutti A, Managutti SA, Patel J, Puthanakar NY. Evaluation of post-surgical bacteremia with use of povidone-iodine and chlorhexidine during mandibular third molar surgery. J Maxillofac Oral Surg 2017; 16:485-90.
12. Gottardi W. Iodine and disinfection: theoretical study on mode of action, efficiency, stability, and analytical aspects in the aqueous system. Arch Pharm (Weinheim) 1999; 332:151-7.

LETTER TO THE EDITOR

TRANSIENT DISCOLORATION AND APICAL BREAKDOWN AFTER TRAUMA IN PERMANENT DENTITION

L. CASULA[1], E. COTTI[2], P. CAPPARÈ[1] and D. MUSU[3]

[1]Oral Surgery Specialization School, Vita-Salute University San Raffaele, Milano, Italy; [2]Department of Conservative Dentistry and Endodontics, University of Cagliari, Italy; [3]Department of Endodontology, Academic Centre for Dentistry Amsterdam (ACTA), Amsterdam, Netherlands

Received March 3, 2019 – Accepted July 18, 2019

To the Editor,

Post-traumatic color change is a well-known phenomenon. However, color alterations can range from a lack of translucency to pink, bluish or grey discoloration and have different clinical implications (1). A pink-to-red coronal discoloration can be associated with pulpal haemorrhage and it represents a direct evidence of disruption of the pulpal neurovascular bundle (2). This event presents at first as a pinkish hue that turns bluish as the haemocomponents disintegrate and changes into greyish-blue when seen through the grey enamel (3). The scientific literature supports a conservative approach for the management of post-traumatic discoloration in the primary dentition (4, 5) and in immature or open apex permanent teeth due to their healing potential (6). Thus, the trend is to delay the endodontic treatment until clear signs of pulpal and periapical pathosis have developed (7). In permanent dentition, the presence of coronal discoloration along with a negative response to sensibility tests and evidence of periapical radiographic involvement are related to pulp necrosis (6). In addition, post-traumatic pink discoloration can be permanent (8) and root canal therapy has been suggested (9). Although some authors support the post-traumatic presentation as a transient pathology, there is a lack of a consensus in the scientific literature, as far as coronal discoloration is concerned, hindering the forward recognition of signs of reversibility (6, 10). The current case study reports an eight-year follow-up case of a post-traumatic transient coronal discoloration on a permanent tooth with mature apex managed with a conservative approach. This paper supports the role of the radiographic sign of apical breakdown as an early indicator of post-traumatic pathology reversibility.

Case presentation

A 35-year-old female Caucasian patient with non-contributory general medical history was referred for endodontic examination three days after she experienced acute facial trauma. The clinical examination revealed injuries to the extra-oral soft tissues, exhibiting a laceration of her upper lip that had been sutured in the emergency room, and a bruised chin. The maxillary central incisors showed an enamel-dentin coronal fracture involving the incisal ridge and the mesial marginal ridge (Ellis class 2) (Fig. 1). The clinical tests revealed tenderness to percussion and no response to sensibility test (cold test) for both teeth. In addition, the upper right central incisor showed a first-degree mobility. A direct composite restoration (Ceram.X Universal, Dentsply De Trey, Konstanz,

Key words: crown fracture; dental traumatology; endodontics; subluxation; transient coronal discoloration; transient apical breakdown

Corresponding Author:
Dr. Davide Musu,
Strada 18 n°10, Poggio dei Pini,
Capoterra, Cagliari, Italy
Tel.: +39 3492735089
e-mail: davidemusu.dds@gmail.com

0393-974X (2019)

DISCLOSURE: ALL AUTHORS REPORT NO CONFLICTS OF INTEREST RELEVANT TO THIS ARTICLE.

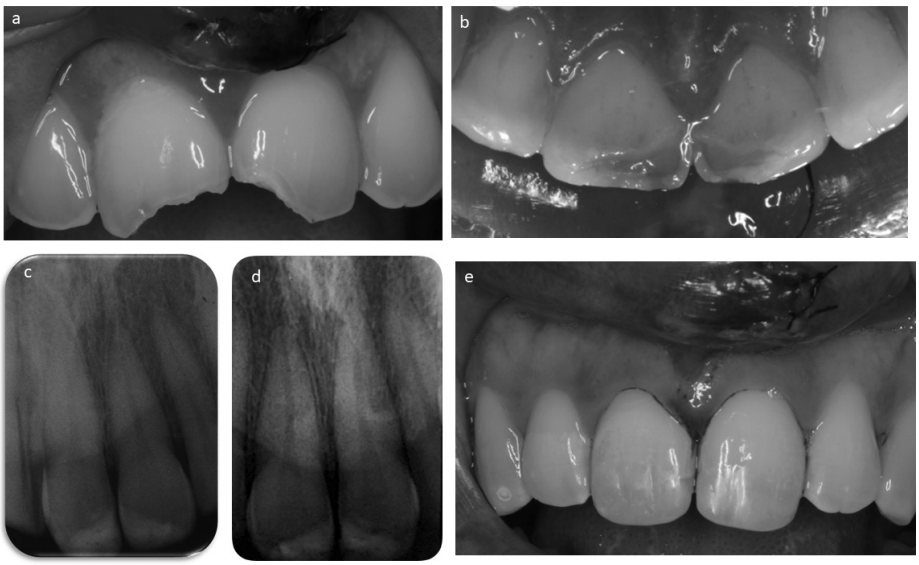

Fig. 1. *Clinical and radiological presentation of the patient showing an enamel-dentin coronal fracture of the involved teeth and laceration of the upper lip.* ***a)*** *Vestibular view.* ***b)*** *Palatal view.* ***c)*** *Parallax periapical radiograph.* ***d)*** *Parallel periapical radiograph.* ***e)*** *Teeth after restoration.*

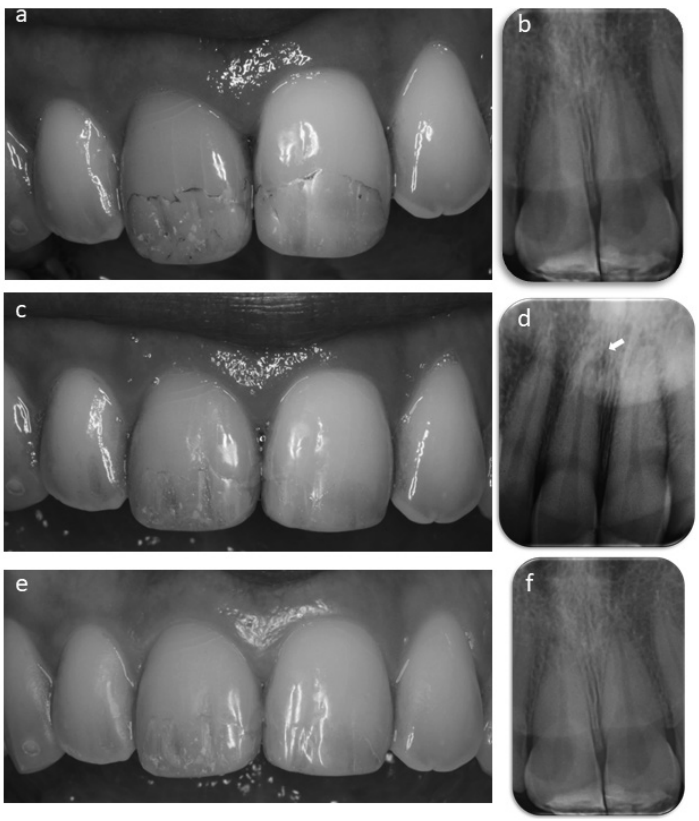

Fig. 2. ***a)*** *Post-traumatic pink discoloration of the right central incisor two weeks after the trauma.* ***b)*** *Periapical radiograph depicting no sign of periapical pathology two weeks after the trauma.* ***c)*** *Attenuation of the discoloration one month after the trauma.* ***d)*** *Periapical radiograph showing a transient apical breakdown (arrow) one month after the trauma.* ***e)*** *Complete regression of the discoloration two months after the trauma.* ***f)*** *Periapical radiograph depicting a reduction of the periapical ligament widening two months after the trauma.*

Germany) over a thin layer of resin-modified glass-ionomer cement (RMGIC, Vitrebond, 3M ESPE) was placed on both teeth under rubber dam isolation and parallel and parallax periapical radiographs were taken (Fig. 1). According to the Internal Association of Dental Traumatology guidelines (IADT) (9) an additional diagnosis of concussion of the left central incisor and subluxation of the right central incisor was made. Despite the age and evidence of complete apical closure, endodontic treatment was postponed in view of a possible pulpal recovery. However, a strict follow-up schedule was arranged with the patient. The patient was reviewed again after two weeks for the finishing and polishing of the restorations, and the maxillary right central incisor appeared discolored (Fig. 2). The tooth presented a pinkish hue and the clinical tests were repeated. The cold test was still negative for both teeth, whereas tenderness to percussion was attenuated. No periapical change was detectable on the radiograph, therefore root canal treatment was not performed (Fig. 2, a and b). At the follow-up one month after trauma, the cold test turned positive for both teeth, tenderness to percussion was diminished and the discoloration of the right central incisor was still present but attenuated (Fig. 2c). A periapical radiograph revealed some periapical changes such as a periapical ligament widening and an internal surface resorption due to the transient apical breakdown, suggesting spontaneous repair processes (Fig. 2d). Two months after trauma, the cold test was still positive for both teeth and the tenderness to percussion was within normal parameters. The right incisor showed a complete color reversal and its appearance was normal in comparison with the other teeth (Fig. 2e). At the periodical recall visits the patient was asymptomatic, the color of the upper central incisor was normal, sensibility test (cold test) was positive and tenderness to percussion was absent (Fig. 3a). The periodic periapical radiographs revealed no signs of periapical pathosis (Fig. 3b). At the last review eight years later, the patient was still asymptomatic with both teeth responding to the cold test. The restorations appeared in good condition with no signs of pigmentation, and the periapical radiograph was negative for periapical pathologic changes (Fig. 3, c and d).

DISCUSSION

According to the IADT guidelines, at least two signs and symptoms are necessary to make

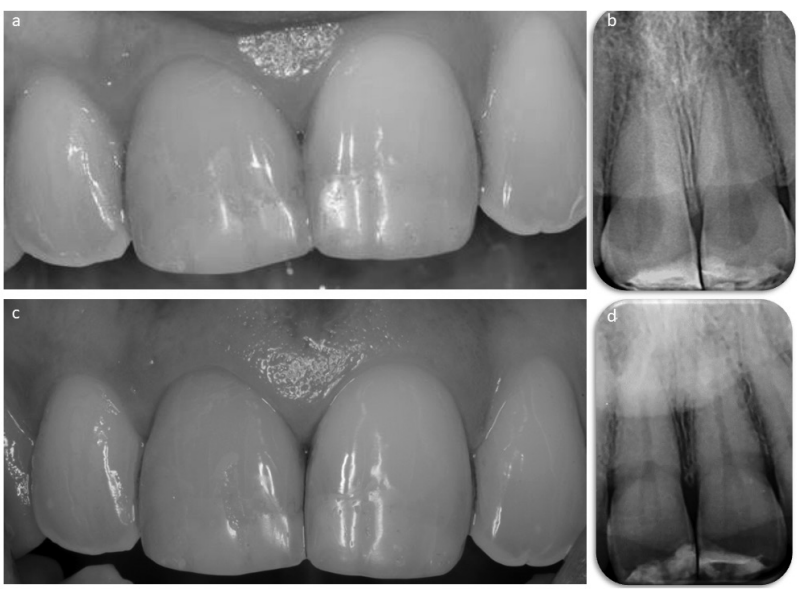

Fig. 3. *Periodical follow-up visits.* ***a)*** *Clinical presentation at the 3-year periodical review.* ***b)*** *Radiological presentation at the 3-year periodical review.* ***c)*** *Clinical presentation at the 8-year periodical review.* ***d)*** *Radiological presentation at the 8-year periodical review.*

a diagnosis of pulp necrosis, such as crown discoloration, negative sensibility testing and periapical radiolucency (9). Nevertheless, the scientific literature recommends the importance of considering a temporary negative answer to sensibility tests after a traumatic injury (1). Furthermore, as reported by Bastos et al., neural regeneration in traumatized teeth is slower (or even absent) than vascular regeneration so that the tooth may save vitality even though it does not respond to sensibility tests (10). Interestingly, in the present case, discoloration attenuated contemporarily with the restoration of the thermal sensibility and the radiographic evidence of the apical breakdown. Transient apical breakdown is a mechanism that allows a temporary enlargement of the apical foramen in mature traumatized teeth permitting the ingrowth of new vessels, and it is usually visualized on periapical radiograph as a widening of the periodontal ligament space and internal surface resorption at the apex of the involved tooth (6, 11). After the revascularization is completed, the blood metabolites in the pulp chamber and dentinal tubules can be cleared up so that the discoloration can disappear (12).

The present case depicted the conservative management of a rarely reported clinical situation, a post-traumatic transient discoloration in the permanent dentition of an adult patient, where signs of color reversibility were detected as early as one month, in association with a full recovery of the pulp sensibility. In addition, this report highlights the role of the radiographic event of the transient apical breakdown which can be used as an indicator of repair. Thus, in absence of clear signs of both pulp healing and periapical pathosis, the observation of the apical breakdown can serve as a diagnostic aid to support the delay of root canal treatment.

REFERENCES

1. Andreasen FM, Andreasen JO. Luxation Injuries of permanent teeth: general findings. In: Andreasen JO, Andreasen FM, Andersson L, editors. Textbook and color atlas of traumatic injuries of teeth. Oxford: Blackwell Munksgaard; 2007.
2. Heithersay GS, Hirsch RS. Tooth discoloration and resolution following a luxation injury: significance of blood pigment in dentin to laser Doppler flowmetry readings. Quintessence Int 1993; 24:669-76.
3. Lauridsen E, Hermann NV, Gerds TA, Ahrensburg SS, Kreiborg S, Andreasen JO. Combination injuries 2. The risk of pulp necrosis in permanent teeth with subluxation injuries and concomitant crown fractures. Dent Traumatol 2012; 28:371-78.
4. Hyun HK, Shin TJ, Kim YJ. The post-traumatic colour change of primary incisors: a colourimetric and longitudinal study. Int J Paediatr Dent 2016; 26:291-300.
5. Aguiló L, Gandía JL. Transient red discoloration: report of case. ASDC J Dent Child 1998; 65:346-48.
6. Cohenca N, Karni S, Rotstein I. Transient apical breakdown following tooth luxation. Dent Traumatol 2003; 19:289291.
7. Cardoso M, Carvallo Rocha MJ. Association of crown discoloration and pulp status in traumatized primary teeth. Dent Traumatol 2010; 26:413-16.
8. Wong M, Schmidt JC. Vital bleach of hemorrhagic discoloration. J Endod 1991; 17:242-43.
9. Diangelis AJ, Andreasen JO, Ebelesender KA et al. Guidelines for the Management of Traumatic Dental Injuries: 1. Fractures and Luxations of Permanent Teeth. Pediatric Dent 2017; 39:401-11.
10. Bastos JV, Goulart EM, de Souza Côrtes MI. Pulpal response to sensibility tests after traumatic dental injuries in permanent teeth. Dent Traumatol 2014; 30:188-92.
11. Andreasen FM. Pulpal healing after luxation injuries and root fracture in the permanent dentition. Endod Dent Traumatol 1989; 5:111-31.
12. Liao Q, Ye W, Yue J et al. Self-repaired process of a traumatized maxillary central incisor with pulp infarct after horizontal root fracture monitored by laser doppler flowmetry combined with tissue oxygen monitor. J Endod 2017; 43:1218-22.

JOURNAL OF BIOLOGICAL REGULATORS & HOMEOSTATIC AGENTS Vol. 33, no. 5, 1651-1656 (2019)

LETTER TO THE EDITOR

SATISFACTION GRADE ASSESSMENT OF PATIENTS TREATED WITH ZYGOMATIC IMPLANTS WITH SELF-TAPPING APEX AND MACHINED BODY

A. SCARANO[1], R. CONTE[2], G. MURMURA[1] and F. LORUSSO[3]

[1]Department of Medical, Oral and Biotechnological Sciences and CeSi-MeT, University of Chieti-Pescara, Chieti, Italy; [2]Private Practice, Padova, Italy; [3]Department of Medical, Oral and Biotechnological Sciences, University of Chieti-Pescara, Chieti, Italy

Received June 7, 2019 – Accepted August 2, 2019

To the Editor,

The treatment of maxillary severe atrophies related to the traumatic loss of the dental elements, incorrect prosthetic loads or oncologic resection needs reconstructive surgery procedures, preparatory to implant-prosthetic support (1). Many different regeneration techniques to increase hard and soft tissue reconstruction with autologous bone have been proposed, such as the use of bone intraoral and/or extraoral grafts, sometimes associated with Type I Le Fort osteotomies (2).

In this context, the use of auxiliary surgical techniques, such as the use of zygomatic implants, may represent a treatment option in cases of severe partial or complete atrophy of the maxillary. Brånemark et al. has described a positioning technique that involved the insertion of implants through the sinus intra route and guided insertion through the execution of a lateral trapdoor bone, without lifting the Schneider membrane, experiencing a high predictability of the procedure (3). The original technique has been modified to provide for the preservation and lifting of the sinus membrane, contextual to the procedure.

Stella and Warner have proposed a variant of the zygomatic implant placement technique (sinus slot technique), which does not require detachment of the Schneider membrane (4). In this regard, a further technical variant with extrasinus approach has been proposed, the implant route of which is completely external to the cavity of the maxillary sinus. In the literature, different geometries and implant designs have been proposed in order to facilitate an optimal positioning of the fixture and a long-term maintenance of osseointegration of the placed implants (5-7).

The aim of this work was to clinically evaluate the survival rate and patient satisfaction before and after prosthetic rehabilitation of zygomatic implants with machined body and self-tapping apex.

MATERIALS AND METHODS

A total of twelve patients affected by extreme atrophy of the maxilla, who needed prosthetic implant-borne maxillary rehabilitation, were treated from May 2016 to January 2019 in the Department of Medical Sciences, Oral and Biotechnology, University of Chieti-Pescara. Healthy patients with non-contributory past medical history, 7 women and 5 men, all non-smokers, mean age 51 years, (range 49–61 years) were included in this study.

The inclusion criteria were extreme atrophy jaw with unstable implants accompanied by wounds, sores and associated functional and aesthetic discomfort. In the

Key words: zygomatic implants; maxillary atrophy; fixed prosthesis

Corresponding Author:
Prof. Antonio Scarano,
Department of Medical, Oral
and Biotechnological Sciences and CeSI-Me,
University "G. D'Annunzio" of Chieti-Pescara,
Via dei Vestini, 31, 66100 Chieti (CH), Italy
Tel.: +39 0871 3554084
e-mail: ascarano@unich.it

0393-974X (2019)

DISCLOSURE: ALL AUTHORS REPORT NO CONFLICTS OF INTEREST RELEVANT TO THIS ARTICLE.

period of study (including a 1-year follow-up), twenty-four zygomatic implants (Isomed, Padova, Italy) and 24 standard implants (Isomed, Padova, Italy) were inserted in the premaxilla area. The implants used in this study are characterized by a self-tapping apex of 13 mm with surface treatment, while the remaining part by a machined surface (Fig. 1A). The implant has an internal hexagonal connection that allows screwing a Multi-Unit Abutment (MUA) to allow prosthetic anchoring.

The subjects underwent screening according to the following inclusion criteria: absence of lesions in the oral cavity and insufficient residual bone volume to receive standard implants. In addition, patients who agreed to participate in a postoperative program were included.

The exclusion criteria were: i) smoking more than 20 cigarettes a day, or excessive consumption of alcohol (about 1 litre a day of wine); ii) local radiation therapy of the oral cavity, anti-cancer chemotherapy; iii) blood disorders, liver or kidney disease, immunodepressed patients; iv) patients receiving corticosteroids; v) pregnancy; vi) autoimmune and inflammatory diseases of the oral cavity.

After examination by three-dimensional X-ray (CBCT) and oral impressions, investigations proceeded with a 3D printing of the atrophic jaws (Fig. 1B) in order to simulate the surgery and confirm the previously planned implant length using 3D planning software (Isomed, Padova, Italy). All patients received two zigomatic implants and two standard implants. The zygomatic implants used in this study had a diameter of 4.1 mm and a length of 40 mm.

Data collection

Before the surgical treatment, radiographic examinations were performed such as radiographs, orthopantomographies (OPT) and tomographic scans (CBCT). In the period of follow-up, OPT and radiographical data were collected and processed by a dedicated software (ITK-SNAP, Penn Image Computing and Science Laboratory, University of Pennsylvania, USA). The rate of successful implantation was evaluated according to the following criteria:

(i) absence of persistent pain or dysesthesia;

(ii) absence of peri-implant infection with suppuration;

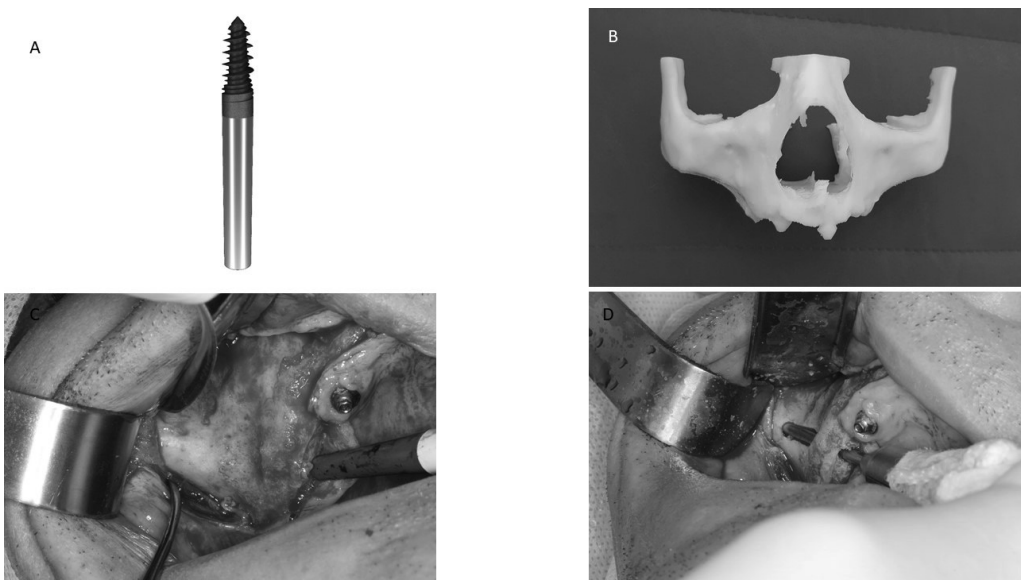

Fig. 1. ***A)*** *Zygomatic implants with machined body and self-tapping apex used in the present study.* ***B)*** *3D printing of the atrophic jaws in order to simulate the surgery and confirm the previously planned implant length using 3D planning software.* ***C)*** *After crestal incision a modified mucoperiosteal triangular flap was performed. The zygomatic region was exposed and remained clearly visible with through retractor for the whole duration of the intervention.* ***D)*** *The second bur perforates the cortical bone of the maxillary sinus and enters in the zygomatic bone for about 14 mm, impacting forwards at about 1 cm from the orbital cavity.*

(iii) absence of mobility;

(iv) absence of persistent peri-implant bone resorption visible in orthopantomography.

In this study zygomatic implants were used which had a spiral self-tapping apex and a machined body.

Surgical technique and prosthetics

All patients were treated following the same surgical protocol, with an antimicrobial prophylaxis of 500 mg amoxicillin twice daily for 5 days starting from one hour before the intervention. The shape and volumes of the maxillary were studied using Cone Beam Computed Tomography (CBCT). Impressions were vertical dimension (VDO), centric relation (CR) and skeletal relationship of the jaw. A stereolithography model was realized by the DICOM files and a 3D printer, which is a particularly indicated for this type of surgery as it faithfully reproduces the bony anatomy of each case, allowing to assess the exact size and position of the implants. Local anesthesia was induced by infiltration of articaine/epinephrine Articaine Pierrel (Pierrel, Milano, Italy) and the postsurgical analgesic treatment was carried out with 600 mg of ibuprofen twice a day for 3 days.

After crestal incision, a modified triangular mucoperiosteal flap, recently described and used in the large sinus lift, was raised (Fig. 1C), proceeding with the exposure of the zygomatic region, leaving it clearly visible (through retractor) for the whole duration of the intervention (Fig. 1D) (7).

An initial osteotomy was performed with a 5 mm round bur in the highest part of the bone ridge. A furrow in the crestal direction was performed with a second diamond bur with machining tip. The third bur perforated the cortical bone of the maxillary sinus and entered the zygomatic bone for about 14 mm, impacting forwards at about 1 cm from the orbital cavity. The distance between the point of crestal bone and the apical point was measured with a probe, based on the tomography measurement. The suitable length of the implant was confirmed and it was screwed into the implant bed. The relationship between the alveolar crest and zygomatic area influences the implant position, and the final preparation was performed with a calibrated bur to the predetermined length (Fig. 2A). The implant was inserted with an axis extending from the second premolar or canine

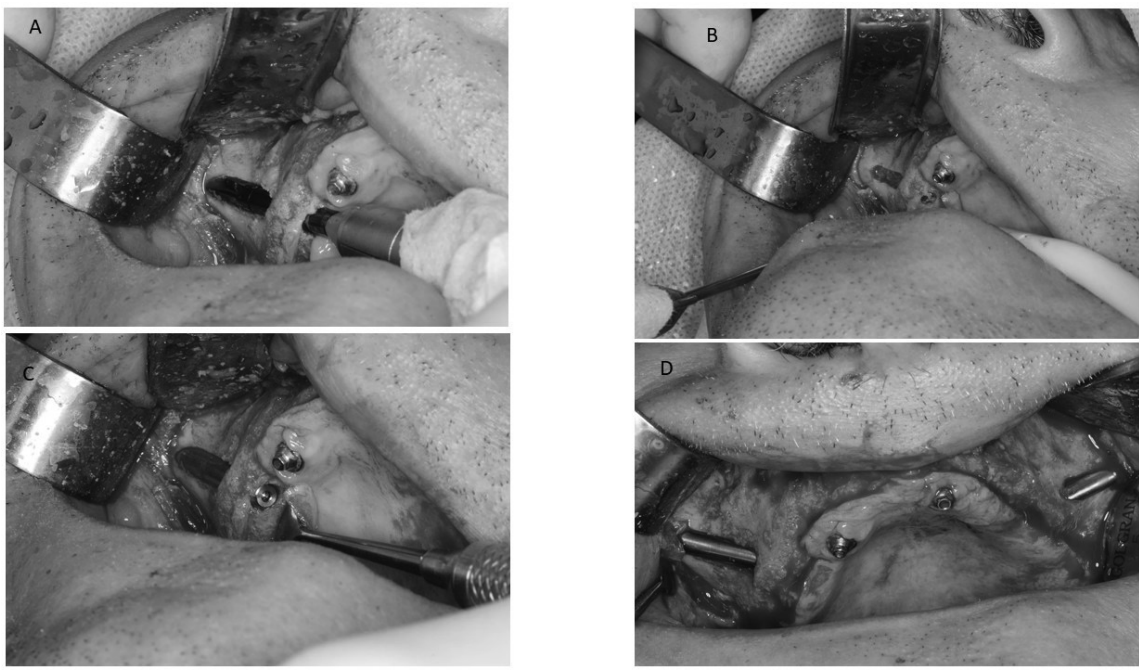

Fig. 2. ***A)*** *The final preparation was carried out with a calibrated bur of a predetermined length.* ***B)*** *The maxillary sinus after a small detachment of the Schneider's membrane.* ***C)*** *Zygomatic implant placement.* ***D)*** *Placement of two conventional and two zygomatic implants.*

from the highest point of the cheekbone, exactly in the corner formed by the frontal and temporal process. The point of entry was palatally in the premolar area. During the placement, the implant leans against the wall of the maxillary sinus after a small detachment of the Schneider's membrane (Fig. 2B). The implants used present a geometric shape characterized by self-tapping threads that allow an easy positioning and, above all, a high primary stability (Fig. 2C) This shape allows the implant to slide along the osteotomy and to be engaged in the zygomatic hole in a simple and predictable way (fig. 2D). The flaps were sutured with non-absorbable thread 4.0 (Assut Europe, Magliano dei Marsi, Italy) leaving the distal outlet free to facilitate inflammatory exudate drainage in the first hours after surgery (7).

At the end of the procedure, an intravenous infiltration of dexamethasone (4 mg) was performed. Orthopantomography was carried out after surgery to evaluate the correct position of the fixtures (Fig. 2 A, B). A warm and soft diet was recommended for two weeks, supported by a thorough oral hygiene protocol. In order to preserve the intestinal microbiome, the intake of lactic acid bacteria (Biocult Strong, Italfarmacia, Rome-Italy) was also prescribed. Seven days after the procedure the surgical suture was removed. Before the next implant uncovering, patients were allowed to use removable dentures with the aid of adhesive pastes. The second surgical phase was carried out after 3 months, in which the healing abutments of the implants were positioned. A temporary restoration was carried out in acrylic resin, finished, polished and cemented approximately 4 weeks after the second phase implant surgery. The final prosthetic restoration was screwed in and completed after 8 weeks of loading with the acrylic prosthesis. All the subjects were included in a rigid oral hygiene recall program. Patients were asked to complete a questionnaire to measure the degree of satisfaction before and after prosthetic rehabilitation with a score ranging from 1 to 10, where 10 represented the maximum level of comfort of masticatory function comparable to the natural teeth, and 1 corresponded to poor results comparable to a mobile and unstable dental prosthesis. The questionnaire was completed 1 month after surgery and 6 months after loading with the final prosthesis.

RESULTS

After the surgical procedure all patients reported the sensitivity of the area but no cases of neurological damage were observed. No pain or purulent secretion on palpation were reported to be associated with any of the inserted implants either conventional or zygomatic. The postoperative radiographs showed the implants engaged in zygomatic bone following a sinus path as per the planning of the surgical treatment. One patient reported extensive bruising of the face which resolved almost completely after 5 days. All implants appeared stable and the patients showed a high degree of satisfaction 6±0.4, while before treatment patients attributed a score 1±0.3, and after 6 months, the degree of satisfaction was 8±0.4. No cases of implant loosening or fracture were observed during the period of follow-up.

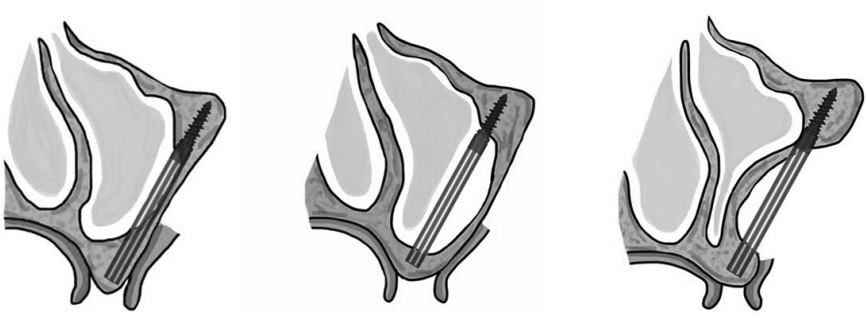

Fig. 3. *An intrasinusal technique and extra-sinus procedure approach depends upon the concavity or convexity that describes the outer wall of the maxillary sinus.*

DISCUSSION

The zygomatic implant proved to be an effective option in the management of atrophic edentulous maxilla, as well as defects in the maxillectomia (8).

The use of multiple zygomatic implants (two or three on each side) combined with two or four anterior maxillary axial implants to support a prosthesis has been suggested by Bothur and coll. (9). The technique for atrophic patients, not subjected to maxillectomia, involves the opening of the maxillary sinus without lifting the sinus membrane to drive the cutter towards the zygomatic bone (5). There are essentially two surgical techniques for the insertion of the zygomatic implants: an intrasinusal technique and an extra-sinus procedure, and the approach depends upon the concavity or convexity that describes the outer wall of the maxillary sinus The sinus morphology affects the passage or otherwise of the alveolar crest to anchor to the zygomatic bone (Fig. 3).

Several retrospective studies document a percentage of implant survival rate of 90-100% (9-10). Contraindications to the zygomatic treatment include chronic infectious sinusitis, maxilla or zygomatic disease, the use of bisphosphonates, and smoking more than 20 cigarettes a day (7). Computed tomography is crucial for the evaluation of the zygomatic implant site and the sinus condition, as well as for the implant path.

The use of this new technique provides for the possibility of an extra-sinus implant path, with promising results (11). In this research we used one zygomatic implant per side and 2 implants in the anterior maxilla. The post procedure management is very important, in fact a soft diet was prescribed for 12 weeks, the time consistent with the proper periimplant healing intended as bone remodelling induced by the load.

After 18 weeks, the subjects introduced foods with greater consistency to the exclusion of hard foods, and those which require the application of strong masticatory forces. After 24 weeks the patients were given freedom of choice of food. Even the occlusion is important, patients were given a bilateral occlusion with a front group, the cusps were also little accentuated in order to limit the lateral components of the occlusal forces. The results observed in the present study show the ease of implant placement with self-tapping apex which makes it possible to easily center the hole in the zygomatic bone. The zygomatic implants represent a good alternative to regenerative surgery, taking advantage of the available bone anchored in the zygomatic region to native and non-regenerated bone with obvious biomechanical advantages (3).

ACKNOWLEDGEMENTS

The authors acknowledge the helpful technical assistance of Dr. Mauro di Berardino (radiology technician) for elaboration of CBCT.

REFERENCES

1. Wagner F, Dvorak G, Nemec S, Pietschmann P, Figl M, Seemann R. A principal components analysis: how pneumatization and edentulism contribute to maxillary atrophy. Oral Dis 2017; 23(1):55-61.
2. Schlund M, Nicot R, Lauwers L, Raoul G, Ferri J. Le Fort 1 osteotomy and calvarial bone grafting for severely resorbed maxillae. J Craniomaxillofac Surg 2016; 44(7):859-67.
3. Brånemark P-I, Gröndahl K, Ohrnell L-O, et al. Zygoma fixture in the management of advanced atrophy of the maxilla: technique and long-term results. Scand J Plast Reconstr Surg Hand Surg 2004; 38(2):70-85.
4. Stella JP, Warner MR. Sinus slot technique for simplification and improved orientation of zygomaticus dental implants: a technical note. Int J Oral Maxillofac Implants 2000; 15(6):889-93.
5. Lima de Andrade C, Carvalho MA, Bordin D, da Silva WJ, Del Bel Cury AA, Sotto-Maior BS. Biomechanical behavior of the dental implant macrodesign. Int J Oral Maxillofac Implants 2017; 32(2):264-70.
6. Scarano A, Degidi M, Perrotti V, Degidi D, Piattelli A, Iezzi G. Experimental evaluation in rabbits of the effects of thread concavities in bone formation with different titanium implant surfaces. Clin Implant Dent Relat Res 2014; 16(4):572-81.
7. Scarano A, Lorusso F, Arcangelo M, D'Arcangelo C, Celletti R. Lateral sinus floor elevation performed with trapezoidal and modified triangular flap designs:

a randomized pilot study of post-operative pain using thermal infrared imaging. Int J Environ Res Public Health 2018; 15(6): pii: E1277.

8. Araújo PP, Sousa SA, Diniz VB, Gomes PP, da Silva JSP, Germano AR. Evaluation of patients undergoing placement of zygomatic implants using sinus slot technique. Int J Implant Dent 2016; 2(1):1-10.
9. The treatment of maxillary severe atrophies related to the traumatic loss of the dental elements, incorrect prosthetic loads or oncologic resection needs reconstructive surgery procedures, preparatory to implant-prosthetic support (1).
10. Scarano A, Crocetta E, Quaranta A, Lorusso F. Influence of the thermal treatment to address a better osseointegration of Ti6Al4V dental implants: histological and histomorphometrical study in a rabbit model. Biomed Res Int 2018; Doi: 10.1155/2018/2349698.
11. Scarano A, Carinci F, Mangano C, Quaranta A, Piattelli A. Removal torque values of titanium implants inserted into bone defects filled with hydroxyapatite: a histologic and histomorphometric analysis in rabbit. Int J Immunopathol Pharmacol 2007; 20(1 S1):49-53.
12. Bothur S, Jonsson G, Sandahl L. Modified technique using multiple zygomatic implants in reconstruction of the atrophic maxilla: a technical note. Int J Oral Maxillofac Implants 2003; 18(6):902-4.

LETTER TO THE EDITOR

P53 AND VEGF EXPRESSION IN HUMAN TEMPOROMANDIBULAR JOINT DISCS WITH INTERNAL DERANGEMENT CORRELATE WITH DEGENERATION

S. CASTORINA[1*], C. LOMBARDO[1*], P. CASTROGIOVANNI[2], G. MUSUMECI[2], E. BARBATO[3], L.E. ALMEIDA[4] and R. LEONARDI[5]

[1]Department of Medical, Surgical and Advanced Technological Sciences "G.F. Ingrassia", University of Catania, Catania, Italy; [2]Department of Biomedical and Biotechnological Sciences, Section of Anatomy and Histology, University of Catania, Italy; [3]Department of Odontostomatologic and Maxillofacial Sciences, "Sapienza" University, Rome, Italy; [4]Department of Surgical Sciences, Oral surgery, Marquette University School of Dentistry, Milwuakee, Wisconsin, USA; [5]Department of General Surgery and Medical-Surgical Specialties, University of Catania, Italy

Received February 13, 2019 – Accepted June 18, 2019

*These authors contributed equally to the research

To the Editor,

Temporomandibular joint (TMJ) disorders are one of the most relevant causes of chronic facial pain and disability, internal derangement (ID) is the most common TMJ arthropathy and is often related to disc damage (1). ID could be considered as an earlier stage of histopathologic changes of the TMJ disc tissue including breakup of dense collagen fiber bundles, new vessel generation and innervation of the central zone, cell proliferation and an increased number of cell types.

Anterior disc displacement with (ADDwR) and without reduction (ADDwoR) are the most common types of ID. In ADDwR, the disc slides into and out of its normal functional position when the jaw opens and closes; in ADDwoR the disc slides anteriorly to a lower rest position, remaining stuck in the anterior joint recess and failing to revert to its normal position with condylar movement. When the disc slips out of place or is displaced, it can determine improper condyle movement, causing dysfunction.

Human tumor protein p53, is known as a "guardian of the genome", and its target genes are involved in cell-cycle control and induction of apoptosis. As tumor suppressor protein, p53 can act as transcription factor for genes of pro-apoptotic effector proteins and it is also implied in transcription-independent cellular signaling that leads to cell death via pathways localized in the mitochondria or the cytosol. Furthermore, p53 determines transcription of DNA repair enzymes that promote cell survival. This highlights the functional double role of p53, namely apoptosis or promoting cell survival. In physiological conditions, cellular p53 level expression is low and the protein has a short half-life of 20 min. Upon DNA damage, p53 levels increase primarily through stabilization of the protein (2-3).

Vascular endothelial growth factor (VEGF) has a pivotal role in increasing capillary vessel permeability and acts in angiogenesis of inflamed TMJ synovial tissue (4).

The aim of the present research was to analyzed p53 and VEGF immunoexpression patterns in disc patients with ID, with ADDwR and ADDwoR and to

Key words: temporomandibular joint; internal derangement; p53; VEGF; immunohistochemistry

Corresponding Author:
Prof. Claudia Lombardo,
Department of Biomedical
and Biotechnological Sciences,
Human Anatomy and Histology Section,
School of Medicine, University of Catania,
Via S. Sofia 87, 95125 Catania, Italy
e-mail: claudialombardodoc@gmail.com

0393-974X (2019)

correlate the results with the degeneration grade. The purpose is to gain insight into the pathophysiological mechanisms underlying the morphological changes of the different areas of the articular disc.

MATERIALS AND METHODS

Tissue samples

TMJ disc specimens, surgically obtained from patients with TMJ ID, were provided by the Pontifical Catholic University of Paranà, Brazil (5). After project approval by the Ethics Committee of the same University, each patient signed an informed consent form before tissue collection. The discs had been obtained from 11 females and 7 males aged 24 to 41 years with TMJ ID, 8 with ADDwR and 10 with ADDwoR diagnosed on the basis the following parameters: history, clinical examination, and magnetic resonance imaging data. Mean patient age was 34.2±5.4 years; mean disease duration from ID symptom onset to surgery was 8.7±1.2 months.

Unassisted maximum mouth opening (MMO) and a visual analog scale (VAS) for pain were used to evaluate the disease severity. MMO was calculated with a millimeter ruler as interincisor distance; pain intensity in the preceding week was rated on a 100 mm VAS from 0 (no pain) to 100 (the worst pain imaginable). The diagnosis that led to the surgical procedure was painful ID with functional impairment. The inclusion criteria for disc excision were: i) unsuccessful conservative management; ii) tenderness to TMJ palpation; and iii) TMJ pain or interference with jaw movement. Exclusion criteria were: i) other TMDs; ii) dentofacial deformity; iii) major jaw trauma; iv) previous TMJ surgery; and v) prior TMJ treatment with steroid injections. The discs appeared macroscopically deformed and none had preserved a normal biconcave shape. The anterior, intermediate and posterior band were preserved in all specimens.

Four TMJ discs from the collection of the Anatomy Institute of Catania University were also included in the study as controls. They were autopsy specimens from one male and three female donors (mean age 49.7±4.4 years) that were selected, as previously reported (5), for their virtually normal shape and condition, since none had macroscopic signs of joint degeneration and/or inflammatory outlook on dissection and were not displaced; in addition the donors' clinical histories were negative for general joint disease or TMJ arthropathy.

Immunohistochemistry

Sections were processed as described previously (5). Briefly, they were incubated for 30 min in 0.3% H^2O^2/methanol and rinsed with phosphate-buffered saline (PBS; BioOptica, Milano, Italy). The antigen retrieval was performed using a microwave oven, as already described (5). Then slides were incubated with the following primary antibodies: a rabbit polyclonal anti-p53 antibody (FLN-393:sc-6243; Santa Cruz Biotechnology, Inc., Dallas, USA) and an anti-VEGF antibody (A-20:sc-152; Santa Cruz Biotechnology, Inc., Dallas, USA.) diluted 1:100 in PBS, 0.1 % bovine serum albumin, and incubated overnight at 4°C. The secondary antibody, biotinylated anti-mouse/anti-rabbit IgG, was applied for 30 min at room temperature followed by the avidin-biotin-peroxidase complex (Vector Laboratories, Burlingame, CA, USA). The immunoreaction was demonstrated by 4 min incubation in 0.1 % 3,3'-diaminobenzidine and 0.02% hydrogen peroxide solution (DAB substrate kit, Vector). Finally, sections were counterstained with Mayer's hematoxylin (Histolab Products AB, Goteborg, Sweden), mounted on GVA mount (Zymed Laboratories, San Francisco, CA, USA) and observed with an Axioplan Zeiss light microscope (Carl Zeiss, Oberkochen, Germany) and photographed with a digital camera (AxioCam MRc5, Carl Zeiss, Oberkochen, Germany).

Positive and negative controls

In order to test the specificity of the primary antibodies, we used esophagus and lung tissue as positive control and some of the disc sections that were tested with normal rabbit serum, without primary antibody.

Computerized image analysis

The antibodies-staining (p53 and VEGF) status was identified as either negative or positive. Immunohistochemical positive staining was demonstrated by the presence of brown chromogen detection on the edge of the hematoxylin-stained cell nucleus, distributed within the cytoplasm or in the membrane via evaluation by light microscopy. Fifteen fields, the area of which was about 600,000 μm^2, randomly selected from each section, were

analyzed and the percentage areas stained with antibodies (p53 and VEGF) were calculated using a software for image acquisition and histomorphometric analysis (AxioVision Release 4.8.2 - SP2 Software, Carl Zeiss Microscopy GmbH, Jena, Germany), which quantifies the area of positive immunolabelling in each field, expressed as % positive, dark brown pixels of the analyzed fields, as described previously (6). Digital micrographs were taken using the Zeiss Axioplan light microscope (Carl Zeiss, Oberkochen, Germany) fitted with a digital camera (AxioCam MRc5, Carl Zeiss, Oberkochen, Germany). Evaluations of immunohistochemical localizations were made by three blinded investigators, whose evaluations were assumed to be correct if values were not significantly different. In case of dispute concerning interpretation, the case was reconsidered to reach a unanimous agreement.

Histopathological degeneration score

Some paraffin sections were stained with H&E in order to identify histopathological degeneration and evaluate them by a histopathological degeneration score (HDS). The score considers the changes and the degree of modification observed in pathological samples, i.e. collagen bundles, non-specific degenerative changes, and the presence of blood vessels, and ranged in a score from 0 (normal tissue) to 8 (severe tissue degeneration). The HDS was estimated by three observers, two anatomists and a histologist (7) who used the mean value of scores as the value of each sample.

Statistical analysis

P53 and VEGF expression of all discs was compared among them and with the HDS. All experiments were made in triplicate. Data were tested for normality with the Kolmogorov-Smirnov test. All variables were normally distributed. The anterior, intermediate, and posterior bands in sections from patients with ADDwR and ADDwoR were considered for comparisons. Comparison between immunoexpression (p53- and VEGF-) and HDS was performed through Spearman's test. Immunohistochemical comparisons between means from the different bands were tested with One-way ANOVA post-test: Tukey-Kramer Multiple Comparisons Test; a p level < 0.05 was considered significant, p level < 0.01 was considered very significant. All data were analyzed with SPSS software (SPSS release 16.0, Chicago, IL, USA). Data are presented as the mean±SD.

RESULTS

Immunohistochemistry

To investigate the expression of p53 and VEGF, we analyzed discs of patients with ID ADDwR and

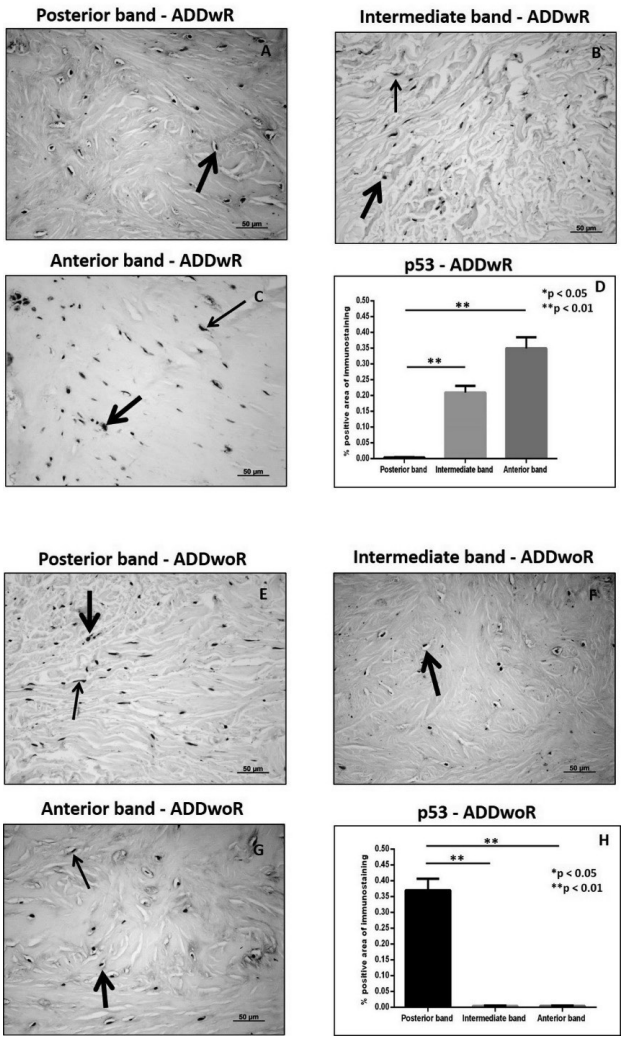

Fig. 1. *P53 immunoexpression in sections from patients with ADDwR and ADDwoR.* ***A)*** *posterior band - ADDwR.* ***B)*** *intermediate band - ADDwR.* ***C)*** *anterior band - ADDwR.* ***D)*** *Graph. A bar chart representing a comparison of the % p53 immunostained area in the posterior, intermediate and anterior bands of ADDwR samples.* ***E)*** *posterior band - ADDwoR.* ***F)*** *intermediate band - ADDwoR.* ***G)*** *anterior band - ADDwoR.* ***H)*** *Graph. A bar chart representing a comparison of the % p53 immunostained area in the posterior, intermediate and anterior bands of ADDwoR samples. Thick arrows: chondrocyte-like cells; thin arrows: fibroblast-like cells. Data are presented as mean±SD. *p<0.05, **p<0.01. Scale bar: 50 µm.*

ADDwoR. In particular, p53 immunoexpression was detected in fibroblast- and chondrocyte-like cells. In ADDwR, the histomorphometric analysis demonstrated an expression of p53 principally in the anterior and the intermediate disc areas when compared to the posterior band, in fact the percentage of immunostained area was significantly higher in the anterior and the intermediate bands compared with the posterior one ($p<0.0$) as shown in Fig. 1, A-D. On the contrary, in ADDwoR, a very low (not detectable) expression of p53 was noticed in the anterior and the intermediate bands and a high expression intensity in the posterior band; the percentage of immunostained areas was much higher in the posterior band when compared to the anterior and the middle ones ($p<0.01$) (Fig. 1, E-H). The expression of VEGF was detected in endothelium of newly formed vessels, in fibro- and chondrocyte-like cells. ADDwR histomorphometric analysis demonstrated a higher percentage of immunostained area in the anterior and intermediate bands compared to the posterior band ($p<0.05$) (Fig. 2, A-D). Instead, in ADDwoR, a lower percentage of immunostained area was detected in the anterior and the intermediate areas when compared to the posterior band ($p<0.01$) (Fig. 2, E-H). Moreover, increased immunoexpression of p53 and VEGF was correlated with the increase of the HDS ($p<0.05$).

TMJ discs from cadavers (control) showed a not detectable expression of both p53 and VEGF.
In the negative control sections immunoexpression was not detected.

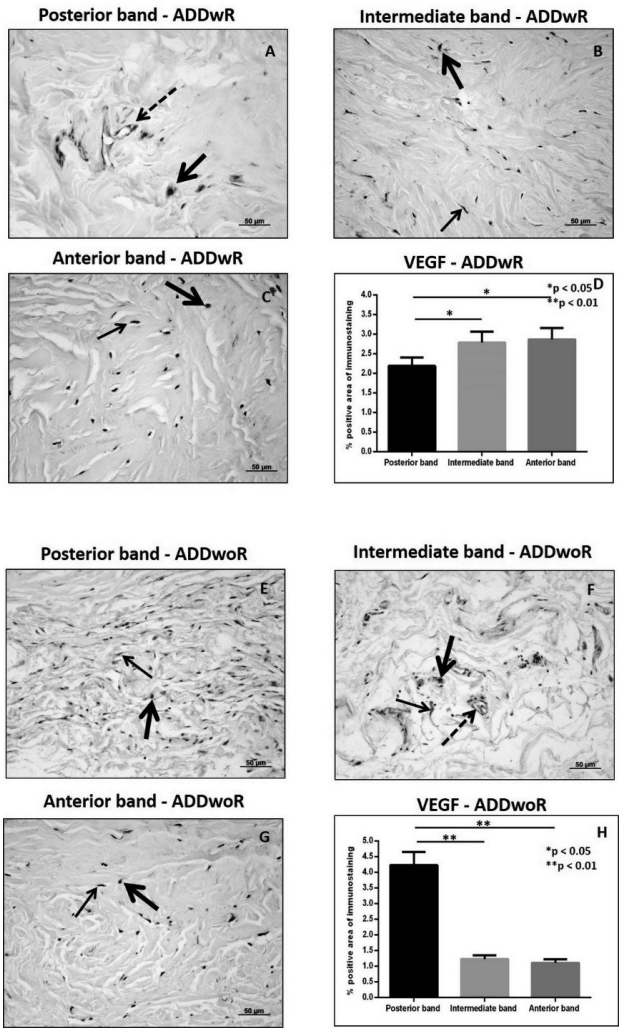

Fig. 2. *VEGF immunoexpression in sections from patients with ADDwR and ADDwoR.* ***A)*** *posterior band - ADDwoR.* ***B)*** *intermediate band - ADDwoR.* ***C)*** *anterior band - ADDwoR.* ***D)*** *Graph. A bar chart representing a comparison of the % VEGF immunostained area in the posterior, intermediate and anterior bands of ADDwoR samples.* ***E)*** *posterior band - ADDwoR.* ***F)*** *intermediate band - ADDwoR.* ***G)*** *anterior band - ADDwoR.* ***H)*** *Graph. A bar chart representing a comparison of the % VEGF immunostained area in the posterior, intermediate and anterior bands of ADDwoR samples. Thick arrows: chondrocyte-like cells; thin arrows: fibroblast-like cells; dashed arrows: vessels. Data are presented as mean±SD. *p<0.05, **p<0.01. Scale bar: 50 µm.*

Histopathological degeneration score

In H&E-stained pathological discs, a reduced number of cells was shown, a decreased number of fibroblast-like cells and a number of chondrocyte-like cells increased in relation to the severity of the morphological damage with abnormal collagen fiber arrangement, collagen bundle fragmentation and tearing. The histopathological score was 3.93±0.6. Differently, control discs showed no signs of cellular or tissue alterations and histopathological score ranged from 0 to 1 points (7-8).

DISCUSSION

The present study gave insights of this synergy of p53 and VEGF expression showing the different patterns of immunodetection in the three areas of TMJ discs in patients with ID ADDwR and correlated these results with the histopathological grading score.

In vivo studies on rodents have underlined the pivotal role of apoptosis in articular cells of displaced rabbit discs and rat TMJ tissues after acute inflammation (9). Also Fas ligand (FasL), an apoptotis-inducing factor activated by distinct signal pathways, was shown to be highly immunostained in ADDwR (10). In this context p53 plays an important role as it is activated by cellular stress and may act promoting DNA repair when the DNA damage is limited or induces apoptosis, in relation to high DNA damage, to re-establish the tissue integrity (11). Leonardi et al. (7) proved an overexpression of death receptor-5 (DR5) and ligand tumor necrosis factor-related apoptosis-inducing ligand (TRAIL), which triggers cell death in ID TMJ discs of patients with both ADDwR and ADDwoR. Our previous investigations have already demonstrated an increased expression of VEGF in human dysfunctional TMJ discs. In particular, VEGF immunolocalization was found related with angiogenesis, morphogenesis and differentiation of chondrocytes. The present study showed VEGF immunolocalization is related not only with the histopathological grading score, but also with the different insults exercised in the three bands in patients with ADDwR and ADDwoR (12). Liu et al. (11) demonstrated, on rat degenerated intervertebral disc tissues, that both p53 and VEGF are involved in the process of neovascularization and capillary infiltration, in particular p53 and VEGF immunoexpressions were significantly higher in tissue areas of increased load, indicating that p53 is likely involved in neovascularization and degenerated disc areas (12). According to our results, it can be assumed that when more histopathological changes in the disc are relieved, major levels of p53 and VEGF are produced. In conclusion, the present study may be useful for further investigations, despite the limitation determined by the relatively small number of samples, in the pathogenesis of TMJ disc degeneration and to stimulate the design of new therapeutic pharmacological strategies.

ACKNOWLEDGEMENTS

The study was funded by the Department of Bio-Medical Sciences, University of Catania.

We thank members of our laboratory.

REFERENCES

1. Mintz SS. Craniomandibular dysfunction in children and adolescents: a review. Cranio 1993; 11:224-31.
2. Reinhardt HC, Schumacher B. The p53 network: cellular and systemic DNA damage responses in aging and cancer. Trends Genet 2010; 28:128-36.
3. Christmann M, Kaina B. Transcriptional regulation of human DNA repair genes following genotoxic stress: trigger mechanisms, inducible responses and genotoxic adaptation. Nucleic Acids Res 2013; 41:8403-20.
4. Zhang S, Cao W, Wei K, et al. Expression of VEGF-receptors in TMJ synovium of rabbits with experimentally induced internal derangement. Br J Oral Maxillofac Surg 2013; 51:69-73.
5. Loreto C, Chiarenza GP, Musumeci G et al. ADAM10 localization in temporomandibular joint disk with internal derangement: an ex vivo immunohistochemical study. Acta Histochem 2016; 118:293-98.
6. Musumeci G, Trovato FM, Pichler K, Weinberg AM, Loreto C, Castrogiovanni P. Extra-virgin olive oil diet and mild physical activity prevent cartilage degeneration in an osteoarthritis model: an in vivo and in vitro study on lubricin expression. J Nutr Biochem 2013; 24:2064–75.
7. Leonardi R, Almeida LE, Trevilatto PC, Loreto C. Occurrence and regional distribution of TRAIL and DR5 on temporomandibular joint discs:comparison of disc derangement with and without reduction. Oral Med Oral Patho Oral Radiol Endod 2010; 109:244-51.
8. Leonardi R, Loreto C, Barbato E, Polimeni A, Caltabiano R, Lo Muzio L. A histochemical survey of the human temporomandibular joint disc of patients with internal derangement without reduction. J Craniofac Surg 2007; 18:1429-33.
9. Spears R, Oakes R, Bellinger LL, Hutchins B. Tumour necrosis factor-alpha and apoptosis in the rat temporomandibular joint. Arch Oral Biol 2003; 48:825-34.
10. Camejo Fde A, Almeida LE, Doetzer AD, et al. FasL expression in articular discs of human temporomandibular joint and association with osteoarthrosis. J Oral Pathol Med 2014; 43:69-75.
11. Liu XW, Kang J, Fan XD, Sun LF. Expression and

significance of VEGF and p53 in rat degenerated intervertebral disc tissues. Asian Pac J Trop Med 2013; 6:404-6.

12. Leonardi R, Lo Muzio L, Bernasconi G, Caltabiano C, Piacentini C, Caltabiano M. Expression of vascular endothelial growth factor in human dysfunctional temporomandibular joint discs. Arch Oral Biol 2003; 48:185-92.